Known and potential types of gold mineralization in the Muruntau gold district

Alexander Antonov[1], Vladimir Tsoy[2]
[1]*Canada Eurasia Chamber of Commerce, Uzbekistan Chapter, Tashkent, Uzbekistan*
[2]*Institute of Mineral Resources, Tashkent, Uzbekistan*

Abstract. The conducted assessment of structural features of Muruntau district's gold deposits together with clarification of their mineral composition has revealed that besides the well-known and mined mineralization in sandstone/shale strata, mineralization of Carlin type, represented by "invisible" micron and nano-sized gold particles in carbonate sedimentary rocks, may be revealed in the mineralized zones. It is shown that gold-bearing zones of silicification concordant to hosting rocks at the super-large Muruntau deposit are metasomatically altered carbonate sedimentary rocks. One of the criteria for the original carbonate nature of the concordant silicification zones is the predominance of carbon dioxide in the gas-liquid inclusions of the ore matrix. The highest probability for discovering Carlin-type mineralization is f the Kokpatas-Okzhetpes trend in the northern part of the Muruntau district. Further studies of ore zones and the presence of invisible nano-sized gold can stimulate the improvement of ore processing flowsheets and increase the gold recovery at the processing mills of the district.

1 Introduction

Muruntau (Central Kyzylkum) district is one of the largest gold districts in the world (Shayakubov 1998). The discovered reserves and resources are of similar amounts to the gold systems in northeastern Nevada (Carlin trend, etc.).

Large sediment-hosted gold deposits (Daugyztau, Amantaytau, Kokpatas, etc.), including the super large Muruntau deposit (initial reserves about 180 Moz), were formed in the area at the end of the Hercynian epoch (Permian-Triassic) after the Turkestan Paleo-ocean closure.

In contrast to the north-eastern Nevada deposits, where terrigenous and carbonate layers are interbedded, the Muruntau district's deposits are hosted by terrigenous sandstone-shale units. The opinion that gold-bearing fluids do not penetrate limestones and are blocked by the Devonian carbonate rocks dominated the local literature in the past. The nature of primary carbonate within the silicified layers in the predominantly terrigenous Besapan ore-bearing suite was not recognized.

The authors disagree that the ore-bearing strata of interbedded sandstones, siltstones, shales and flints has no interlayers of carbonate rocks. Tsoy (2001) proposed the theory of "apo-carbonate" origin of interlayers and lenses of quartzite and flint. They are considered as the original carbonate rocks - limestone and dolomite, altered during the metasomatism until complete replacement by silica.

This extended abstract considers the results of the analyses of silicified, interbedded rocks at the Kokpatas deposits in the Muruntau district. At the north-eastern flank of Muruntau, 2200-meter-deep boreholes intersect flat ore bodies of apo-carbonate origin, concordant to the bedding of the sedimentary rock.

The Kokpatas deposit is considered by the authors as the most realistic target, within the Muruntau district, for detecting Carlin type mineralization including invisible gold. This extended abstract draws attention to the insufficient study of micron- and nano-sized gold inclusions in sulfide minerals. It is indicated by Sanakulov et al. (2019) that the concentration of invisible gold can reach 2-5 g/t for the entire gold-bearing ore mass. The study of "invisible" gold and exploration of Carlin type mineralization in the Muruntau district can have great economical impact.

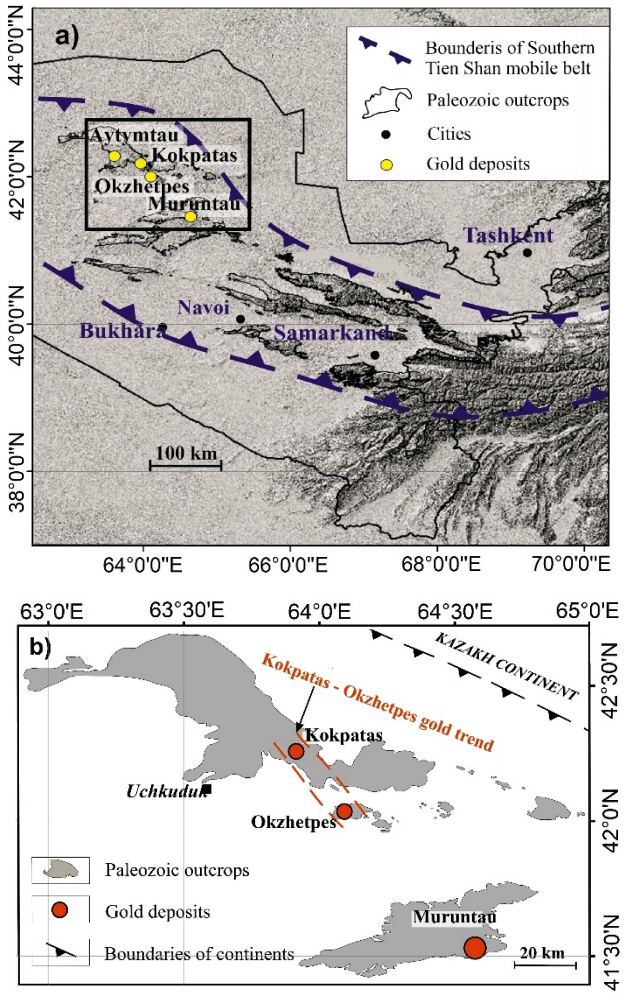

Figure 1. a Location of the Muruntau gold district in the Southern Tien-Shan mobile belt (box; see part b); **b** Schematic map of gold deposits in the Muruntau district from which samples were taken.

2 Methodology

The mineralized zones exposed by boreholes and trenches were studied during the research. Various samples were taken for further mineralogical-petrographic and geochemical studies.
The chemical composition of ores and ore-bearing rocks was studied by total silicate analysis. Contents of main and associated components were determined by spectral semi-quantitative, ICP mass-spectrometric, atomic absorption methods.
Mineral composition of ores, their structural-textural features, and hydrothermal alteration characteristics are determined by research of thin sections, polished thin sections (Nikon Eclipse LV100 Pol), and mineralogical analysis of heavy fractions. The composition of the main and associated components was identified by X-ray spectral local analysis on a microprobe (JEOL "Superprobe" JXA -8800R).
Fluid inclusion study of different quartz taken from the deep drill holes shows that one of the main components of vacuole fluids is carbon dioxide. The presence of carbonic acid in the gas-liquid inclusions indicates the original carbonate composition of layered or metamorphogenic quartz veins.

3 Apocarbonate mineralization: metasomatic processes cause limestone and dolomite layers to be altered into silicified, concordant gold-bearing zones.

The presence of carbonate rocks at the Muruntau and Daugyztau deposits, where the main gold value is associated with concordant silicification zones, is confirmed by silicate analysis (Table 1). The gold content of the carbonate rocks depends on the degree of silicification. Intensely silicified dolomites and limestones usually contain higher gold mineralization. Less silicified carbonate rocks, when their original composition is distinguishable, contain gold up to tenths of g/t. In addition to gold, scheelite, pyrite, arsenopyrite, stibnite?, and other minerals are found in these rocks.
Silicified carbonate interlayers, lenses altered into quartzites and jasperoids with gold and antimonite mineralization were identified at the Daugyztau deposit. XRD phase analysis revealed quartz, dolomite and sericite in apocarbonate formations.
Table 1 lists the results of silicate analyses of two metallurgical samples suggesting that ore-bearing rocks contain carbonates (dolomite and ankerite) in the amount of CaO – 1,06-3,23 wt% and MgO – 1,25-1,08 wt%. The converted mineral composition is presented by quartz, feldspars, carbonates (dolomite and ankerite), hydromicas, kaolinite, carbonaceous matter, jarosite, goethite, hydrogetite, pyrite, arsenopyrite, skorodite, galenite, sphalerite, valentinite, chalcopyrite, cerargyrite, embolite, Ag sulphosalts, native gold and silver, confirming the former findings of Zairi (1992).
These results show that the ore-bearing rocks contain carbonate interlayers, which were silicified, with the formation of quartzites, flints, and jasperoids. In the latter, antimonite mineralization was identified.
According to Graupner et al. (1999) layered and intersecting Muruntau quartzes have differences in gas-liquid inclusions. Thus, in layered quartz phase separation does not occur, whereas in intersecting quartz there is evidence for phase separation. Layered quartz is less gold-bearing, opposite to the intersecting ones. The composition of the gas phase is dominated by carbon dioxide. These facts confirm the validity of our point of view with regards to the apocarbonate nature of layered quartz.

Table 1. Results of silicate analyses of metallurgical samples at Daugyztau deposit (Irgiredmet data).

Component	Content, %		Component	Content, %	
	sample № 48	sample № 65		sample № 48	sample № 65
SiO2	61,46	64,32	S total	2,34	1,76
Al2O3	14,72	12,08	S sulf.	0,44	1,75
Fe2O3	6,53	3,73	As	0,04	0,09
TiO2	0,36	0,35	Sb	0,04	0,028
CaO	1,06	3,23	C total	1,07	
MgO	1,25	1,08	C organic	0,11	
K2O	2,92	2,18	Au g/t	1,8	1
Na2O	1,24	1,24	Ag g/t	4	53,2

4 Prospects for discovery of Carlin type gold deposits in the structures of the Kokpatas - Okzhetpes trend

The northwest striking Kokpatas - Okzhetpes trend is one of 10 trends in the Kyzylkum ore district, at the marginal sutural zone of the closed Turkestan Ocean (Antonov and Nurtayev 2022).
The Kokpatas and Okzhetpes deposits are most similar to the Carlin-type mineralization. In contrast to other Kyzylkum trends, ore bodies are mostly localized in limestone layers (Bulutkan, Barkhanniy, zones 2, 9, Sardor of Okzhetpes ore cluster). We define silicified carbonate interlayers and lenses in terrigenous formations at the Kokpatas-Okzhetpes trend. They are similar to those identified in the Muruntau deposit, which were previously mapped as metamorphosed quartz veins. The findings of our research confirm the data of Graupner et al. (1999) on the compositional differences of gas-fluid inclusions in: 1) layered, and 2) intersecting quartz-vein systems. The layered quartz veins lack evidence for phase separation, whereas the intersecting quartz veins record phase separation. Importantly, layered quartz is less gold-bearing than intersecting quartz. Carbon dioxide predominates in the gas phase. These facts indicate the apo-

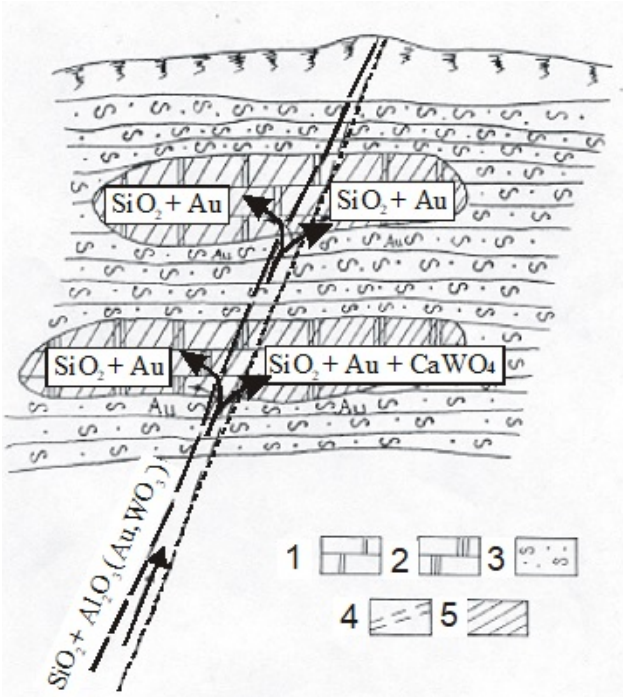

Figure 2. Scheme of the formation of apocarbonate gold mineralization at the Muruntau district. 1-dolomites, 2-quartzites, 3-terrigeenous rocks, 4- ore-bearing fault, 5- ore bodies.

carbonate nature of layered quartz. The following pattern of gold mineralization formation is assumed for the reviewed deposits, including the Kokpatas-Okzhetpes trend.

Carbonate and terrigenous rocks with lenses, interlayers of carbonate rocks (at the Kosmanachi strata, Taskazgan, Besapan, Kokpatas and other suites) are affected by hydrothermal siliceous fluids with gold and WO3 anions, resulting in the formation of quartzites, jasperoids, gold-hosting flints, scheelite, locally stibnite and others. Gold is deposited in the process of the neutralization of acidic hydrothermal fluids in interaction with carbonate rocks. The association of gold mineralization with carbonate relics in quartz is commonly observed under the microscope and on the raster images of microprobe studies (Figure 3 a and b).

The Kokpatas-Okzhetpes trend's deposits have one more feature similar to the Carlin-type mineralization - the presence of micron- and nano-sized gold inclusions. Sanakulov (2019), Koneev et al. (2019), and Tsoy et al. (2011) provide evidence that colloidal and ionic forms of disseminated gold prevail in the "black-shale" ore deposits of gold-sulfide type, whereas the native form is predominantly represented by fine-dispersed nano-sized particles.

Its practical significance is that the main losses in the commercial gold extraction are associated with micron- and nano-sized gold fines. According to the above analytical studies, the amount of nano-sized gold contained in sulfide, arsenide and other ore minerals reaches 2-5 g/t for the whole mass of the gold-bearing ore.

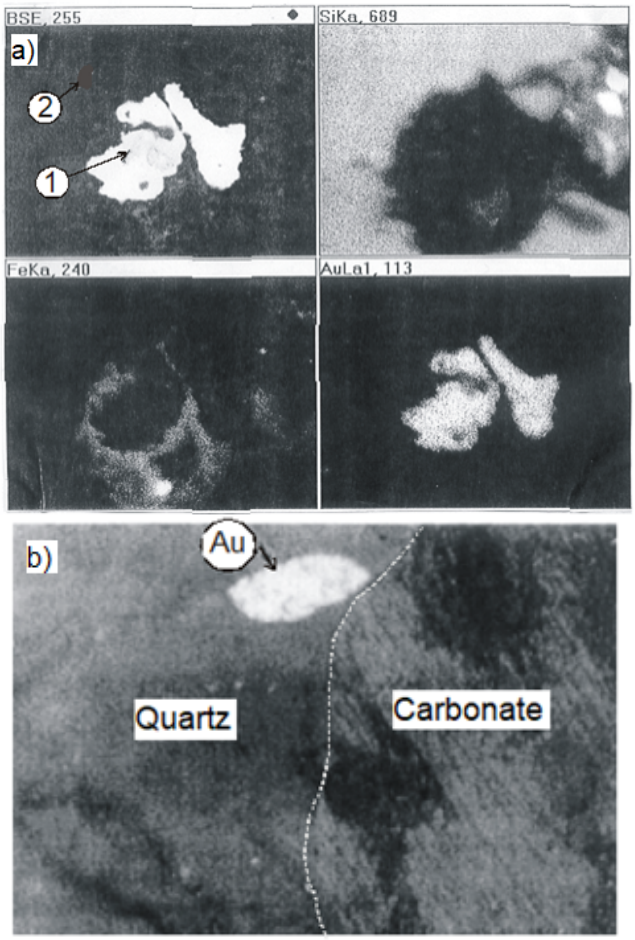

Figure 3. **a** Native gold (1) in quartz (2). Raster pictures show the presence of Si, Fe, Au. Photo from the Barkhanniy deposit, magnification 2000x zoom. **b** Native gold (1) in quartz (2). Raster pictures show the distribution of Si, Fe, Au. Photo from the Barkhanniy deposit, 2000x zoom

5 Conclusions

The study of mineralogical features in deposits from the Muruntau district shows that, in addition to long-term developed and mined gold deposits in sandstones-shales sequences, gold mineralization in limestones and dolomites of Carlin style can be revealed. We have concluded that the nature of layered silicified gold-bearing zones in the Muruntau ore field is primary carbonate, which is supported by the predominance of carbon dioxide in the gas phase of vacuoles. "Invisible" micron- and nano-sized gold dissemination, which can reach 20-30% of the total amount, is widespread in the deposits of the Kokpatas-Okzhetpes gold trend. Additional study of "invisible" gold will help increasing gold recovery in processing plants of the Muruntau gold district (Sanakulov et al. 2021).

References

Antonov AE, Nurtayev BS (2022) Typical features of Carlin type gold deposits (CTGD)how consistent are they? KTGD (Kyzylkum type gold deposits), Uzbekistan, Southern Tien-Shan, vs CTGD. Proceedings of the 16th SGA Biennial Meeting, 28-31 March 2022, 2:5-8

Graupner T, Kempe U, Spooner ETC, Bray CJ, Kremenetsky AA (1999) Characterization of fluids from the giant Muruntau Au-ore field, Uzbekistan, utilizing fluid inclusion microthermometry, volatile and dissolved anion/cation data. Mineral Deposits: Processing, Stanley et al. (eds), Balkema, Rotterdam.

Koneev RI, Khalmatov RA, Krivosheeva AN (2019) Forms of occurrence and micro-nano ensambles of gold as indicators of formation conditions, spatial distribution, and type of orogenic deposits in Uzbekistan (South Tien Shan), Zapiski RMO (Proceedings of the Russian Mineralogical Society). Vol. 148, N. 4, pp 30-46

Sanakulov K, Adizov LA, Tkachenko ES (2021) Improvement of technological processes for processing gold-containing ore at Hydrometallurgical plant № 2. Gorniy Vestnik of Uzbekistan #4 (87), pp 51-55 (in Russian)

Sanakulov KS, Khvan AB (2019) Nanogold and the possibility of its extraction (review). Gorniy Vestnik of Uzbekistan#1 (76), pp 96-102

Shayakubov TSh (ed.) (1998) Gold deposit Muruntau. FAN, Tashkent, 539 pp (in Russian)

Tsoy VD (2001) Quartz-carbonate-gold (apocarbonate) formation and its role in the expansion of the mineral resource base of Uzbekistan. Proc. of Conf. Actual Problems of Development of Mineral Deposits. Tashkent, pp 136-137 (in Russian)

Tsoy VD, Koroleva IV, Munduzova MA et al. (2011) Unconventional apocarbonate type of gold mineralization in Uzbekistan. Tashkent: GP NIIMR. 174 pp (in Russian)

Zairi NM (1992) Isotopic-geochemical models of formation of deposits of gold-carbon formation: Abstract. Dissertation. 46 pp (in Russian)

Distribution of Elements in Gold Grains: Implications for Mineralization

David Banks[1,2], Robert Chapman[1], Olga Borovinskaya[3]
[1] School of Earth and Environment, University of Leeds, Leeds, LS2 9JT, U.K.
[2] Department of Geological Engineering, Istanbul University-Cerrahphasa, Istanbul, Turkiye.
[3] TOFWERK, Thun, Switzerland.

Abstract. Multi-element analyses by LA-ICPMS is a well-established technique for many minerals. The superior detection limits compared with EPMA offers the possibility that many elements can be used to understand the mineralizing process and act as discriminants between deposits. In studies of placer gold grains, different elements have been used to infer the style of mineralization and the possible source. However, the mode of occurrence of elements within the gold grains is largely unknown and therefore has implications when data is interpreted. LA-ICPMS(ToF) element mapping of gold grains, at a resolution of 5µm, revealed different modes of occurrence. Ag is always an alloy element and where their concentration is high enough as are Cu, Hg, Sb and Pd. A variety of mineral inclusions are also present with pyrite containing a large number of elements that are not present in the gold. Other elements, such as the PGE's, are present but predominantly as nanoparticles. Interpretation of analyses must consider how elements are present and associated with each other.

1 Introduction

Natural gold grains are an alloy of different elements, the most common and in the highest concentration being silver. Other frequent alloy elements are copper, mercury, antimony and palladium which can have concentrations at the percent level but are usually much lower. Many additional elements can be present at ppm or ppb concentrations (Banks et. al. 2018). Analysis by EPMA depends on the concentration and frequently for the latter elements is below the detection limits. Grains are often not homogeneous and may contain inclusions of different minerals which can observed and identified by SEM-BSE (Chapman et. al. 2021a). However, inclusions come in a range of sizes and the smallest are often not identified or may be below the surface. Thus, when analysed by Laser Ablation the data may erroneously be attributed to the composition of the gold especially when prior SEM investigation of the polished grains is not carried out (Chapman et. al. 2021b). This is evident in some previous research.

LA-ICPMS is an established technique for determining the spatial distribution of elements in various minerals. In ore deposit studies pyrite is commonly analysed and the element concentrations and distributions has led to a greater understanding of mineralizing processes. Mass spectrometry analysis utilises a sequential measurement of the individual elements. Recent advances in instrumentation have greatly reduced the time for a sweep through the masses chosen, improving the ability to determine elemental associations. However, the elements to be determined must be chosen prior to analysis. This study uses Laser Ablation with Time of Flight Mass Spectrometry (LA-ToFMS) of the different elements. This essentially determines the presence of all elemental isotopes, that are above the detection limit, instantaneously. This avoids missing elements that are present, but were not chosen to be analysed, and a better understanding of element associations.

2 Analytical Method

Placer gold grains were mounted in resin blocks with the flattest surface at 90^{o} to the horizontal plane. These were then polished to expose the maximum area of the centre and the minimum of the external surface. The selected grains were ablated, and the material analysed by ToF-MS at TOFWERK, Thun, Switzerland using an ArF excimer laser at 20 Hz frequency, continuously scanning over lines at 100 µm/s, providing no interpixel overlap. An area of 550 µm x 500 µm could be mapped at 5-µm resolution in 12 min, with all isotopes measured simultaneously for each 5-µm pixel. The element maps in Figures 1-3 are based on the signal intensity and not concentration.

3 Element Distributions

As gold is a metal, the nature of the bonding with elements that form an alloy is different to other minerals. Alloys are defined by their metallic bonding and can be classified as substitutional where a gold atom is replaced by another element, most commonly silver. Where substitution does not occur as the replacement element is too small to fit in the structure the alloy is deemed to be interstitial in nature. Where different elements are present, the alloy may be both substitutional and interstitial. Alloys can be manufactured using different elements to produce desirable characteristics. In nature silver is the most common alloy element and may also include copper and mercury in many instances with antimony and palladium in a lesser number of cases. Whether individual gold grains are a homogeneous alloy is a matter of chance. In Figure 1, the first grain shows a homogeneous alloy of gold silver and, to a degree, mercury. There is increased gold and decreased silver around the edges which is normal for grains from a placer environment.

In Figure 2 an area of with a high number if inclusions (part of Figure 1) is shown in greater

Figure 1. Element maps of two gold grains at a resolution of 5µm. The top 3 images show a homogeneous distribution of Au and Ag and to a slightly lesser degree Hg. Au concentrations are highest at the edge and Ag lowest. Hg shows a diffusion from the center to the edge where the concentration is highest. The second grain (middle and bottom 6 images) shows variability in the Au and Ag concentrations and is not homogeneous. Hg has areas of very high concentrations and again a diffusion to grain boundaries. This grain has several different mineral inclusions of variable size and different element content.

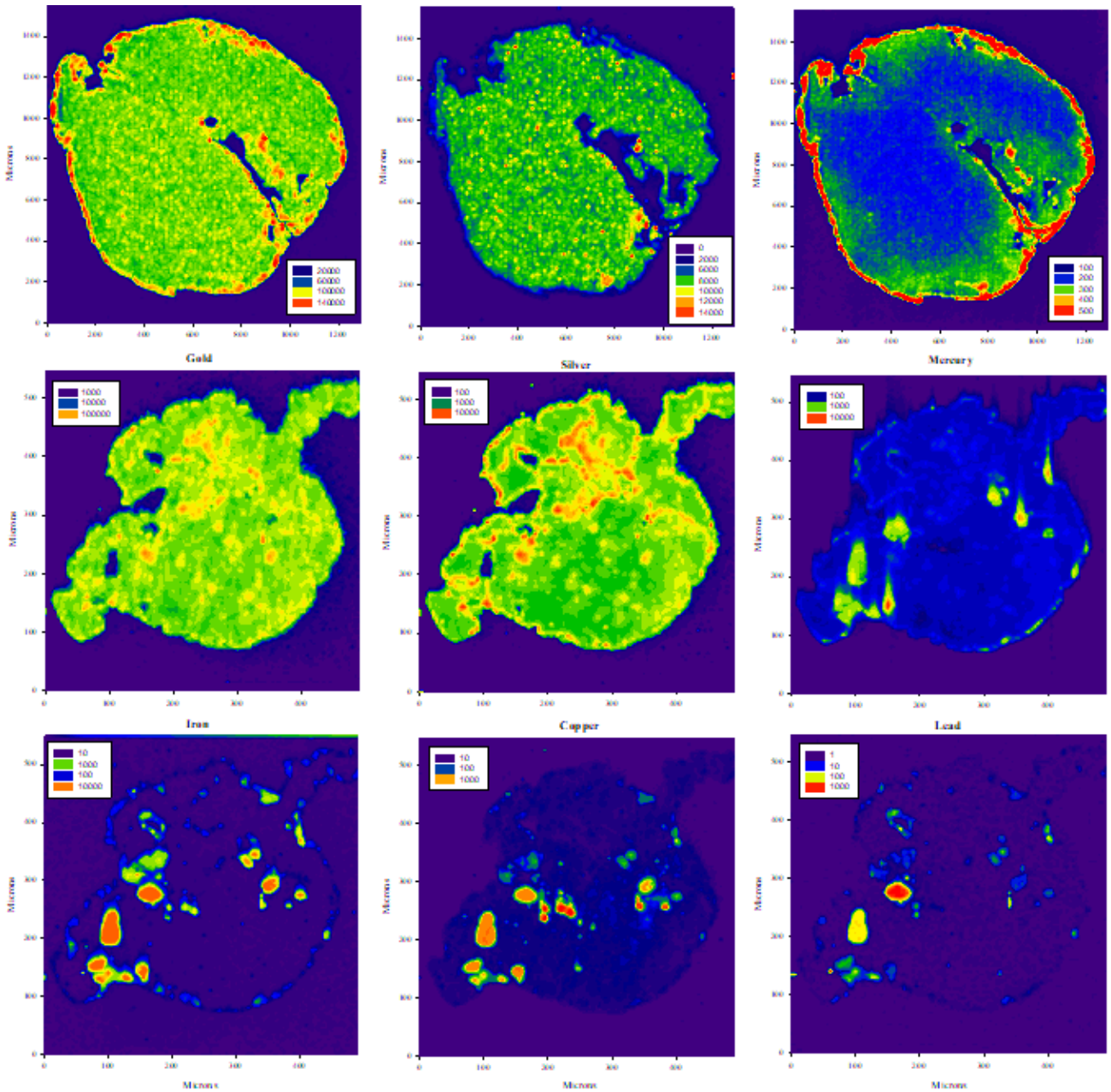

detail. Iron (pyrite) is greater than copper in some inclusions but there are also copper only inclusions with very low concentrations of iron. Other elements shown are also contained in the pyrite. The 4 copper inclusions have no other associated elements. Bismuth and lead are associated with pyrite and together with uranium, tellurium and antimony also occur as much smaller inclusions. All REE were determined, but these are not distributed evenly within the pyrite or relative to each other, cerium being an example. Clearly there is information from the analyses of the different inclusions that can be combined with the alloy data to improve interpretation of the mineralization process.

Figure 2. Element maps of some of the larger mineral inclusions. Pyrite is the host for the majority of elements, including those not shown here. Mn, Hg, Ce, for example, are not homogeneously distributed in the pyrite and may be different minerals or exsolution features.

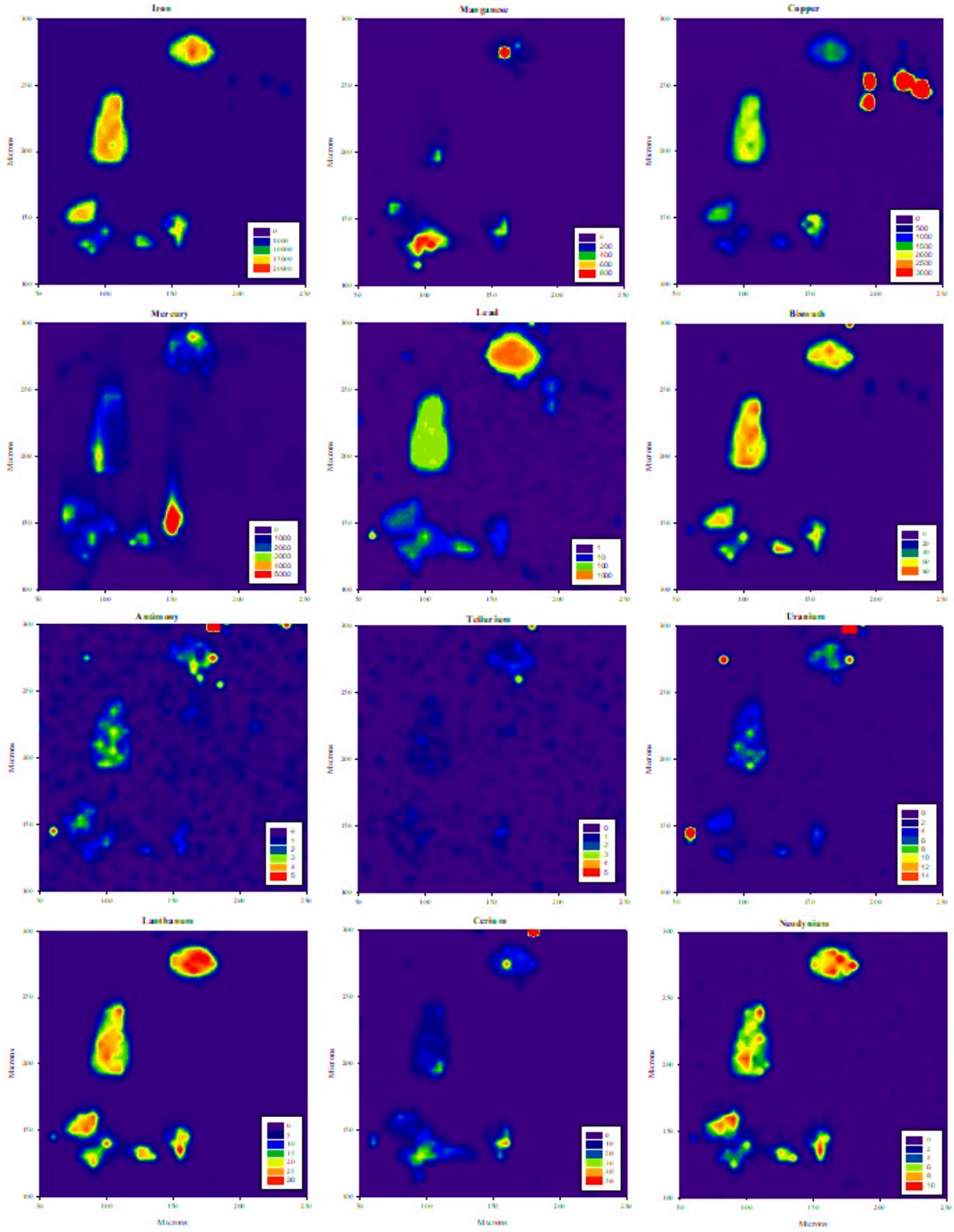

In Figure 3 there are examples of elements that are present as inclusions at ppb or lower concentrations contained in one 5µm ablation spot They are best described as nanoparticles, possibly transported by the mineralizing fluid and trapped as the gold was precipitated or co-precipitated with the gold particles. Other PGE and transition metals can occur in the same manner. Rhenium-osmium and platinum-iridium always show a strong association.

Analysis of gold grains by LA-ICPMS(ToF) clearly shows that any elemental analyses needs to be carefully considered with respect to how it may be present in the sample. The location for ablation must exclude any visible inclusions, but these may be present beneath the surface and hence unavoidable when ablated. SEM observation should be made to identify any visible inclusions which can then be used to interpret their element analyses after laser ablation.

4 Conclusions

Figure 3. PGE element maps with nanoparticles in individual ablation spots. These are likely to have been transported in this form and trapped as the gold precipitated.

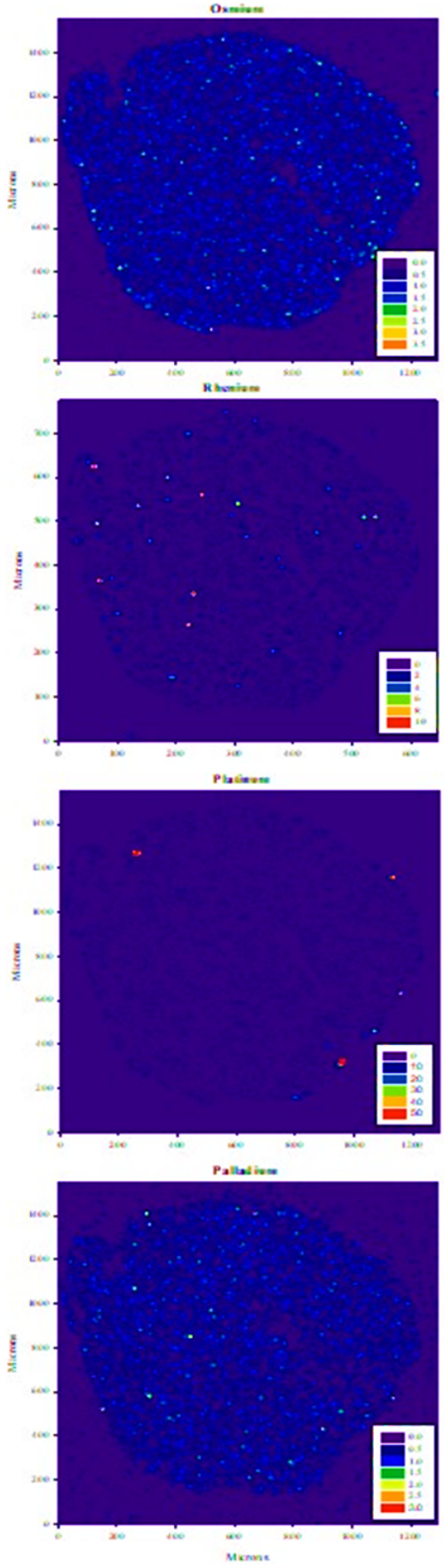

Analyses from a single ablation per grain can lead to a false analytical impression of the homogeneity of the alloy composition. Therefore, many grains per location and for some grains many ablations are required to ensure a representative analysis is obtained. There is a wealth of data possible from ToFMS and the analyses represents the best overall composition of the gold grains.

The analyses of elements trapped in mineral inclusions can be used to interpret the style of mineralization and be used as a means of discriminating different sources. We have observed that most elements are present in pyrite, and other minerals contain far fewer elements and at much lower concentrations. Discrete nanoparticles of different elements/minerals also appear to be a ubiquitous feature. It is likely that mineral inclusions, the elements they contain, and the presence of nanoparticles may be more diagnostic of the source deposit type. Apart from diffusion of mercury within the gold grains it appears that there is no diffusion of elements from inclusions into the gold or vice versa. The presence of some elements as nanoparticles poses a problem for analysis by quadrupole mass spectrometry. They are so small that they do not persist long enough to ensure they would be detected and if they are they are likely to represent a single small signal. Such signals are considered as spikes and have been ignored in the past when they are real analyses. The presence of PGE's may be indicative of mafic-ultramafic involvement. Other nanoparticles we have observed, such as Ga, Cd, Se, Sn, U, Th, may be specific to a particular style or source of gold mineralization.

References

Banks, DA., Chapman, RJ., Spence-Jones, C. 2018. Detrital gold as a deposit-specific indicator mineral by LA-ICP-MS analysis. Geoscience BC Report 2018-21.

Chapman, RJ., Banks, DA., Styles, MT., Walshaw, RD., Piazolo, S., Morgan, DJ., Grimshaw, MR., Spence-Jones, C., Matthews, TJ., Borovinskaya, o. 2021a. Chemical and physical heterogeneity within native gold: Implications for the design of gold particle studies. Mineralium Deposita, 56, 1563-1588.

Chapman, RJ., Craw, D., Moles, NR., Banks, DA., Grimshaw, MR. 2021b. Evaluation of the contributions of gold derived from hypogene, supergene and surficial processes in the formation of placer gold deposits. Geological Society of London, Special Publication 516.

Mapping Auriferous Fluid Flow along the Cadillac Larder Lake Fault Zone (Abitibi Belt, Canada)

Georges Beaudoin[1,2], Benoit Quesnel[1,2], Christophe Scheffer[1,2], Guillaume Raymond[1,2]
[1]*Département de géologie et de génie géologique, Université Laval, Québec QC Canada*
[2] *Centre de recherche sur la géologie et l'ingénierie des ressources minérales (E4m)*

Abstract. The O-H isotope composition of orogenic gold-bearing veins along the Cadillac Larder Lake Fault Zone (CLLFZ) between Val-d'Or and Kirkland Lake is documented in detail to unravel the fluid sources of orogenic gold deposits. Coexisting vein minerals show common oxygen isotope equilibrium, which yields temperatures between ~250 and ~550°C. Temperature covariation with fluid O and H isotope compositions demonstrates mixing between a higher temperature (> 500°C), deep-seated metamorphic fluids with high $\delta^{18}O_{H2O}$ (>9‰), low δD_{H2O} (<-40‰), with lower temperature (<250°C) upper crustal fluids with lower $\delta^{18}O_{H2O}$ (<4 ‰), and higher δD_{H2O} that ranges from 0 to 30‰. Along the Augmitto-Bouzan segment (Rouyn-Noranda), decreasing temperatures from 420ºC at 700 m depth, to 230ºC at 100 m depth, show the vertical ascent of the deep-seated metamorphic fluids along the CLLFZ. In the eastern part of the CLLFZ (Val-d'Or to Malartic) the metamorphic fluid has an end-member O isotope composition of 9-10‰, whereas to the west from Malartic to Kirkland Lake, it has a $\delta^{18}O_{H2O}$ between 11-13‰. The switch in metamorphic fluid reservoirs occurs where the CLLFZ has an inflection in strike. The upper crustal fluids, that cannot be distinguished despite differences in the composition of the country rocks hosting the orogenic gold deposits.

1 Introduction

The typical mineralizing fluid in orogenic gold deposits is aqueous-carbonic with a moderate temperature (250-500ºC), low salinity (3-12 wt.% NaCl eq.) near neutral pH, CO_2-rich composition (<10 mol%), but the source of the fluids and the processes leading to metal deposition remains debated (Goldfarb et al., 2005). The fluids have high $\delta^{18}O_{H2O}$ (~2 to10‰) and variable δD_{H2O} (-60 to 30‰) values (Quesnel et al. in press). The two most proposed sources of fluids are magmatic and metamorphic, despite evidence for a magmatic source being questioned (Goldfarb and Pitcairn 2023, Quesnel et al. in press). Beaudoin and Chiaradia (2016) showed that the auriferous fluids in the Val-d'Or vein field were the product of mixing between a deep-seated, high-temperature (>550ºC), high $\delta^{18}O_{H2O}$ (>9‰) and low δD_{H2O} (<-60‰), and upper crustal fluids with a lower temperature (<250ºC), lower $\delta^{18}O_{H2O}$ (<2‰) and higher δD_{H2O} (>0‰). A similar mixing trend is characteristic of the orogenic deposit class (Quesnel et al. in press).

Documenting the mixing of deep-seated and upper crustal fluids in orogenic gold deposits requires detailed district-scale studies such as that of the Val-d'Or vein field by Beaudoin and Pitre (2005). Here we extend this study along the 250 km length of the Cadillac Larder Laker Fault Zone (CLLFZ), between Val-d'Or and Kirkland Lake, to document the sources of auriferous fluids in this classical orogenic gold vein field.

2 Geological Setting

The Cadillac-Larder Lake Fault Zone (CLLFZ) is one of the most endowed orogenic gold-rich shear zone worldwide (Robert, 1994). The CLLFZ is a 250 km long east-west structure that separates the southern volcanic zone of the Abitibi Subprovince, to the

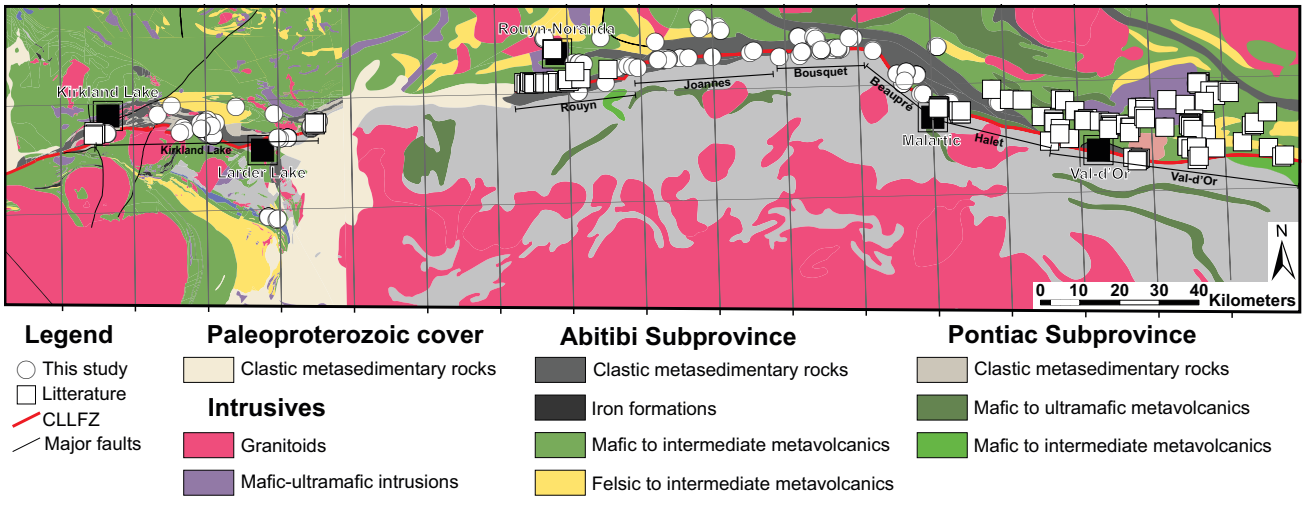

Figure 1. Geology along the Cadillac Larder Lake Fault Zone, with location of samples.

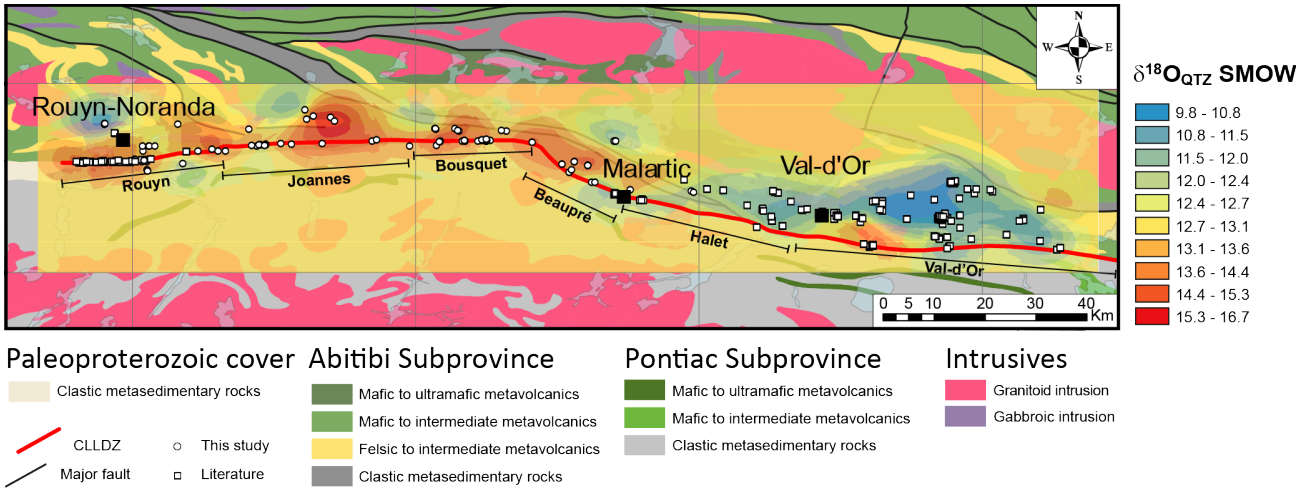

Figure 2. Distribution of quartz d18O values along the CLLFZ, between Val-d'Or and Rouyn-Noranda.

north, from the Pontiac metasedimentary Subprovince, to the south (Fig. 1). The CLLFZ has been divided into six segments, between Val-d'Or and Rouyn-Noranda, to better understand the distribution of gold mineralization along the CLLFZ (Bedeaux et al. 2017). Here we add one additional segment for the Kirkland-Larder Lake area (Fig. 1).

3 Sampling and Methods

The samples (n=168) have been collected in orogenic gold deposits and veins, mostly composed of quartz-tourmaline-carbonate (QTC), hosted in higher order shear zones, along the CLLFZ between Kirkland Lake and Val-d'Or. These samples yield 214 $\delta^{18}O$ values from quartz (n=168) and tourmaline (n=46), and 44 δD values from tourmaline.

Samples of quartz and tourmaline were reacted with BrF_5 at the Stable Isotope Laboratory of Université Laval. The evolved CO_2 was analyzed by a Micromass Isoprime 100 isotope ratio mass spectrometer coupled to a Micromass MicroGas system in continuous flow mode at GEOTOP. Samples of tourmaline were crushed and loaded into a zero-blank auto sampler. The hydrogen isotopic composition was measured using a Thermo-Finnigan thermo-combustion elemental analyzer coupled to a Thermo-Finnigan MAT253 Continuous-Flow Isotope-Ratio Mass Spectrometer) at Queen's Facility for Isotope Research. Isotope ratios are reported in the δ-notation relative to Vienna Standard Mean Ocean Water (VSMOW) with a precision better than 0.2‰ for O and 3‰ for H.

4 Results

The QTC vein quartz $\delta^{18}O$ values along the CLLFZ from this study and literature range from 9.2 to 18.5‰. The spatial distribution of quartz $\delta^{18}O$ values along the CLLFZ are contoured in Figure 2 between the Val-d'Or and Rouyn segments, where sufficient data exist for spatial analysis. Figure 2 shows that higher quartz $\delta^{18}O$ values, above 13‰, are mostly found west of Malartic, in contrast to the eastern segments of the CLLFZ where $\delta^{18}O$ values are as low as 9.8‰. There is a zone of overlap in the Beaupré segment, where there is an inflection in the strike of the CLLFZ near Malartic (Fig. 2). There is, however, no systematic change in quartz $\delta^{18}O$ values along the strike of the CLLFZ west or east of Malartic. Quartz $\delta^{18}O$ values tend to decrease north of the trace of the CLLFZ, as shown in the Val-d'Or vein field by Beaudoin and Pitre (2005). Figure 2

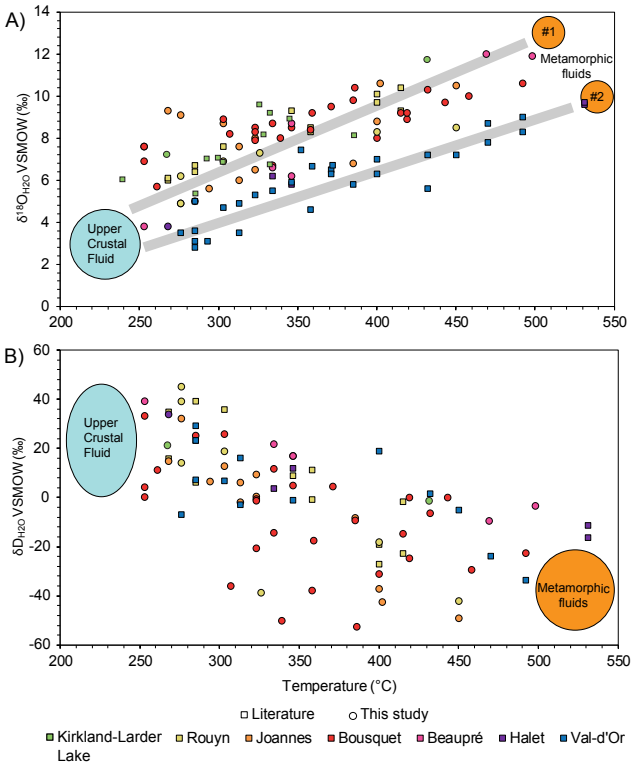

Figure 3. A) Covariation of $\delta^{18}O_{H2O}$ with the quartz-tourmaline temperature of equilibrium along the CLLFZ. Composition of the 2 metamorphic fluids (#1 and #2) and of the Upper Crustal fluid end-members are shown. B) Covariation of δD_{H2O} with quartz-tourmaline temperature of equilibrium along the CLLFZ. End-member Upper Crustal and Metamorphic fluids compositions are shown.

shows that the E-W distribution of $\delta^{18}O$ values is not correlated with the types of country rocks.

Tourmaline $\delta^{18}O$ values from this study and literature range from 6.1 and 13.6‰, with a spatial distribution similar to that of quartz. Tourmaline δD values range from -132 to -17‰, but no systematic east-west variation in composition is documented.

Tourmaline and quartz display oxygen isotope equilibrium at temperatures between 240 and 530ºC. There is no systematic variation of temperature along the CLLFZ. The water in equilibrium with quartz and tourmaline, using the quartz-H_2O oxygen fractionation of Sharp et al. (2016) and the tourmaline-H_2O hydrogen fractionation of Kotzer et al. (1993), yields a correlation between temperature and O-H isotope compositions (Fig. 3). Water compositions of the CLLFZ segments west of Malartic have higher $\delta^{18}O_{H2O}$ values than those from segments east of Malartic, defining two sub-parallel arrays (Fig. 3). Both arrays converge towards a common lower temperature (<250ºC), low $\delta^{18}O_{H2O}$ (<4‰), and high δD_{H2O} (>0‰) end-member fluid composition. The two sub-parallel arrays define two slightly different high temperature (>550ºC), high $\delta^{18}O_{H2O}$ (11-13‰, west of Malartic; 9-10‰ east of Malartic), and low δD_{H2O} (<-60‰) end-members.

The spatial variation of $\delta^{18}O_{H2O}$ values along the CLLFZ is similar to that of quartz $\delta^{18}O$ values (Fig. 3) but the number of locations where a quartz-tourmaline pair enables calculation of the temperature of equilibrium and fluid composition does not allow for spatial analysis as in Figure 3. The distribution of δD_{H2O} values along the CLLFZ does not show a systematic trend, consistent with the single array of temperature-δD_{H2O} in Figure 3B.

5 Discussion

As shown by Beaudoin and Pitre (2005) for the Val-d'Or vein field and by Quesnel et al. (in press) mixing between deep-seated metamorphic and upper crustal fluids is common for the class of orogenic gold deposits. We show here that mixing of these fluid reservoirs occurs along the 250 km length of the CLLFZ. In the Rouyn segment, Raymond (2022) has documented a vertical temperature gradient of 30ºC/km, from 420ºC at 700 m depth to 230ºC at 100 m depth, showing the vertical ascent of the deep-seated metamorphic, and mixing with the upper crustal, fluids along a sub-vertical panel of the CLLFZ at the Augmitto-Bouzan deposit.

Along the CLLFZ, the temperature-water O-H isotope composition indicates a common low temperature (<250ºC), low $\delta^{18}O_{H2O}$ (<4‰) and high δD_{H2O} (>0‰) Upper Crustal fluid reservoir (Fig. 3). These characteristics are most compatible with surface water that has resided for some time in the porosity of the regional country rocks, where it has become heated, and its isotope composition has been modified by water-rock reactions. In the Archean setting of the orogenic gold deposits along the CLLFZ, the ultimate fluid source was likely seawater.

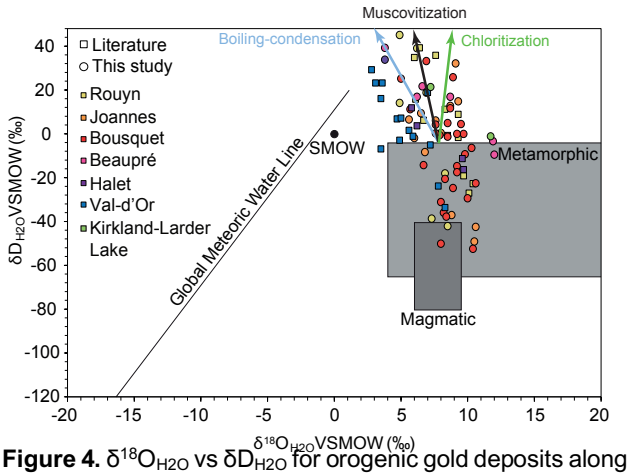

Figure 4. $\delta^{18}O_{H2O}$ vs δD_{H2O} for orogenic gold deposits along the CLLFZ. O-H isotope trends during boiling-condensation, and of muscovite and chlorite alteration of host rocks are from Quesnel et al. (in press). Fields for metamorphic, magmatic and meteoric waters, and seawater (SMOW) are from Sheppard (1986).

There is a spread of δD_{H2O} values (0 to 40‰, Fig. 4) that is common to orogenic gold deposits worldwide (Quesnel et al. in press). Two processes most likely explain the high δD_{H2O} values: 1) boiling-condensation cycles and 2) formation of hydrothermal mica in vein and wallrock alteration. Boiling-condensation cycles are likely due to the dynamic pressure fluctuation environment of orogenic gold deposits (Robert et al. 1995). Quesnel et al. (in press) showed that the high δD_{H2O} values can result from successive events of flash boiling during pressure drop, enabling migration of light hydrogen vapor along the vein network, leaving heavier hydrogen water in the veins. Furthermore, muscovite and chlorite are common in veins and wall rock alteration of orogenic gold deposits. Precipitation of mica in veins and alteration halos will also yield heavier hydrogen residual water because of the negative H fractionation between water and mica. Thus, it is likely that the wide spread of δD_{H2O} values at any given temperature in Figure 3 is the results of these two processes during vein formation. The deep-seated metamorphic fluids (Fig. 4) most likely are the product of prograde metamorphism of the regional country rocks at depth, consistent with the high temperature (>550ºC), high $\delta^{18}O_{H2O}$ (>9‰) and low δD_{H2O} (<-60‰). Although some water compositions in Figure 4 could be compatible with magmatic water, the probability of such an occurrence is unlikely due to the lack of a systematic spatial and temporal association with magmatic rocks, as discussed for orogenic gold deposits by Goldfarb and Pitcairn (2023).

The two arrays in the temperature-$\delta^{18}O_{H2O}$ diagram (Fig. 3) show that slightly different metamorphic fluid reservoirs were tapped on each side of the strike inflection along the CLLFZ, near Malartic. The two reservoirs have similar fluid temperatures and δD_{H2O} values but are different in the oxygen isotope composition. Metamorphic fluid

#1, west of Malartic, has a higher $\delta^{18}O_{H2O}$ values (11-13‰) than that of Metamorphic fluid #2 (9-10‰), east of Malartic. The difference in composition suggests that Metamorphic fluid #1 is sourced from country rocks with a higher proportion of sedimentary, or low temperature altered, country rocks that would yield prograde metamorphic fluids with a heavier oxygen isotope composition.

The fact that both metamorphic fluid end-members display no variation along the CLLFZ strike indicates a homogenized metamorphic fluid source at depth on each side of the inflexion in strike near Malartic. In contrast, there is no evidence of compositional differences of the Upper Crustal fluid end-member on both sides of the inflexion point along the CLLFZ, indicating a largely similar fluid composition in the country rocks resident pore fluids. In addition, this suggests that fluid-rock isotope exchange at the site of mineralization did not significantly modify the composition of the auriferous fluids.

It is intriguing that there is an overlap of both fluid reservoirs at the regional inflexion in strike of the CLLFZ. According to Bedeaux et al. (2018), a NE-SW segment could have linked, on each side, two E-W segments of the CLLFZ during the main N-S deformation event in the southern part of the Abitibi Subprovince. The main N-S shortening was followed by late dextral strike-slip deformation. This would be consistent with our fluid reservoir mapping that shows that metamorphic reservoirs #1 and #2 are yielding slightly different fluid compositions on each side of the linking NE-SW segment.

6 Conclusion

We show that the orogenic gold deposits along the CLLFZ formed by mixing two slightly different, deep-seated metamorphic fluids, with common upper crustal fluids. The two metamorphic reservoirs provided fluids along E-W segments of the CLLFZ that are separated by an inflexion of the trace of the fault zone, which likely segmented fluid sources from the two reservoirs.

Acknowledgements

We thank Canada First Research Excellence Fund Metal Earth program for funding this study.

References

Beaudoin G, Pitre D (2005) Stable isotope geochemistry of the Archean Val-d'Or (Canada) orogenic gold vein field. Mineralium Deposita 40:59-75.

Beaudoin G, Chiaradia M (2016) Fluid mixing in orogenic gold deposits: Evidence from the H-O-Sr isotope composition of the Val-d'Or vein field (Abitibi, Canada). Chemical Geology 437:7-18.

Bedeaux P, Pilote P, Daigneault R, Rafini S (2017) Synthesis of the structural evolution and associated gold mineralization of the Cadillac Fault, Abitibi, Canada. Ore Geology Reviews 82:49-69.

Bedeaux P, Rafini S, Pilote P, Daigneault R (2018) Modelling Seismically Induced Mesothermal Goldfields along the Deep-Rooted Cadillac-Larder Lake Fault, Abitibi, Canada. Geofluids 2018:21.

De Souza S, Dubé B, McNicoll V, Dupuis C, Mercier-Langevin P, Creaser R, Kjarsgaard IM (2017) Geology and Hydrothermal Alteration of the World-Class Canadian Malartic Gold Deposit: Genesis of an Archean Stockwork-Disseminated Gold Deposit in the Abitibi Greenstone Belt In: Monecke T, Mercier-Langevin P, Dubé B (eds) Archean Base and Precious Metal Deposits, Southern Abitibi Greenstone Belt, Canada. Society of Economic Geologists, pp 263-291.

Goldfarb RJ, Baker T, Dubé B, Groves DI, Hart CJR, Gosselin P (2005) Distribution, character, and genesis of gold deposits in metamorphic terranes In: Hedenquist JW, Thompson JFH, Goldfarb RJ, Richards JP (eds) Economic Geology 100th Anniversary Volume. Society of Economic Geologists, pp 407-450.

Goldfarb RJ, Pitcairn I (2023) Orogenic gold: is a genetic association with magmatism realistic? Mineralium Deposita 58:5-35.

Quesnel B, Scheffer C, Beaudoin G, in press. The light stable isotope (hydrogen, boron, carbon, nitrogen, oxygen, silicon, sulfur) composition of orogenic gold deposits. In Huston D and Gutzmer J (eds) Isotopes in Economic Geology. SpringerNature. ISBN 978-3-031-27896-9.

Raymond G, 2022. Variation spatiale des conditions de circulation des fluides à l'origine de la minéralisation en or orogénique dans le segment Augmitto-Bouzan (Sous-Province de l'Abitibi, Québec, Canada). MSc thesis, Université Laval 107p.

Robert F (1994) Vein fields in gold districts: The example of Val-d'Or, southeastern Abitibi province. Current Research Part C. Geological Survey of Canada, pp 295-302.

Robert F, Boullier A-M, Firdaous K (1995) Gold-quartz veins in metamorphic terranes and their bearing on the role of fluids in faulting. Journal of Geophysical Research 100:12861-12879.

Sheppard SMF (1986) Characterization and isotopic variations in natural waters. Reviews in Mineralogy and Geochemistry 16:165-183.

In situ geochronology of hydrothermal events in the Upper Beaver Au-Cu deposit, Abitibi greenstone belt, Canada

Bin Lin [1, 2], Crystal Laflamme [1], Georges Beaudoin [1], Chris McFarlane [3]
[1] *Department of Geology and Geological Engineering, Université Laval, QC G1V 0A6, Canada*
[2] *Institute of Mineral Resources, Chinese Academy of Geological Sciences, BJ 100037, China*
[3] *Department of Earth Sciences, University of New Brunswick, NB, E3B 5A3, Canada*

Abstract. Three hydrothermal events were identified in the Archean Upper Beaver Au-Cu deposit, Abitibi greenstone belt (Canada). Extensive epidote, K-felspar, carbonate, sericite, chlorite, minor andradite, and hematite, magnetite alteration, as concordant stratabound replacement, with chalcopyrite, pyrite, pyrrhotite, Au, and Bi and Te-bearing minerals represent the early Dog's Breakfast event. The main hydrothermal event consists of discordant veins of quartz-carbonate ± chlorite ± anhydrite, minor tourmaline, with chalcopyrite, magnetite, pyrite, molybdenite, scheelite, cobaltite, pyrrhotite, Au, Bi and Te-bearing minerals. The late hydrothermal event is characterized by quartz-carbonate-chlorite ± epidote ± tourmaline ± anhydrite veins with minor chalcopyrite, pyrite, specularite, scheelite and Au. In situ U-Pb dating of hydrothermal zircon and xenotime constrain the timing of the main and late hydrothermal events at about ca. 2679 Ma and 2575 Ma, respectively, indicating multi-hydrothermal events in the formation of Upper Beaver, and refining the time-framework for Au metallogeny in the southern Abitibi greenstone belt.

1 Introduction

The Abitibi greenstone belt, one of the word-class Archean gold mineralization regions, is in the southern Superior Province (Fig.1A). Despite a relative structural framework, efforts to constrain the timing of formation of numerous gold deposits in Abitibi greenstone belt yield a timespan of > 100 million years (Dubé and Mercier-Langevin 2020). Geochronological data from molybdenite, rutile, and titanite indicate that several orogenic gold deposits in the southern Abitibi greenstone belt (Val-d'Or region) formed between 2660 and 2640 Ma. New structural-geochronological evidence from the Val-d'Or district indicates that orogenic gold formed during three discrete hydrothermal events at 2686 ± 15 Ma, 2643 ± 3 Ma and 2607 ± 5 Ma, respectively (Herzog et al. 2023). Whereas the relationships and relative timing between the gold deposits and regional volcanism, magmatism, and lithospheric-scale faults are well documented, the absolute age for hydrothermal event remains unclear in other Archean gold districts in the southern Abitibi greenstone belt (e.g., Kirkland Lake, Larder Lake). More geological and geochronological data show that not all Au events are solely orogenic, some of them can be closely related to magmatism with Cu mineralization (e.g., Upper Beaver).

The Upper Beaver Au-Cu deposit is associated with an intrusive complex in the southern Abitibi greenstone belt. In situ LA-ICP-MS (laser ablation-inductively coupled plasma-mass spectrometry) U-Pb geochronology from accessory minerals (zircon, xenotime) is used to refine the multi-phased hydrothermal events based on detailed core logging and petrography. It provides an improved timeframe for the Upper Beaver deposit and regional Au metallogeny of the Abitibi greenstone belt.

2 Regional geology and deposit geology

The Abitibi greenstone belt consists of volcano - sedimentary rocks of low to moderate-grade metamorphism between ca. 2750 and 2695 Ma (Fig.1A). The volcanic units are unconformably overlain by sedimentary basins of the Porcupine and Timiskaming groups (Fig.1B). Several intrusions are distinguished according to the emplacement ages and petrology, including syn-volcanic, pre-Timiskaming (post-volcanic), early- to syn-Timiskaming, and post-Timiskaming categories (Dubé and Mercier-Langevin 2020). Two major first-order structures are related to major precious and base metal deposits in the southern Abitibi greenstone belt: the Destor-Porcupine fault zone (DPfz) and the Larder Lake-Cadillac fault zone (LLCfz) (Fig.1B).

The Upper Beaver deposit lies roughly 8 km north of the LLCfz and 30 km east of Kirkland Lake (Fig.1B). It is hosted in a succession of volcanic and volcaniclastic rocks of the Blake River and Tisdale assemblages. Simplified surface map, and a composite cross section show the geology and distribution of mineralization in Figure 2. The Upper Beaver deposit is an atypical Au-Cu deposit that contrasts with orogenic gold deposits as it preserves widespread and pervasive magnetite, K-feldspar, epidote, carbonate, and sericite alteration, surrounding the polyphase of Upper Beaver Intrusive Complex (UBIC). The UBIC consists of several magmatic pulses as diorite or monzodiorite with different compositions and textures, but were named mafic syenite porphyry, mafic syenite altered breccias, mafic syenite, crowded porphyry, and spotted porphyry in the mine, respectively. All these intrusions are cut by a Proterozoic diabase dike (Fig.2).

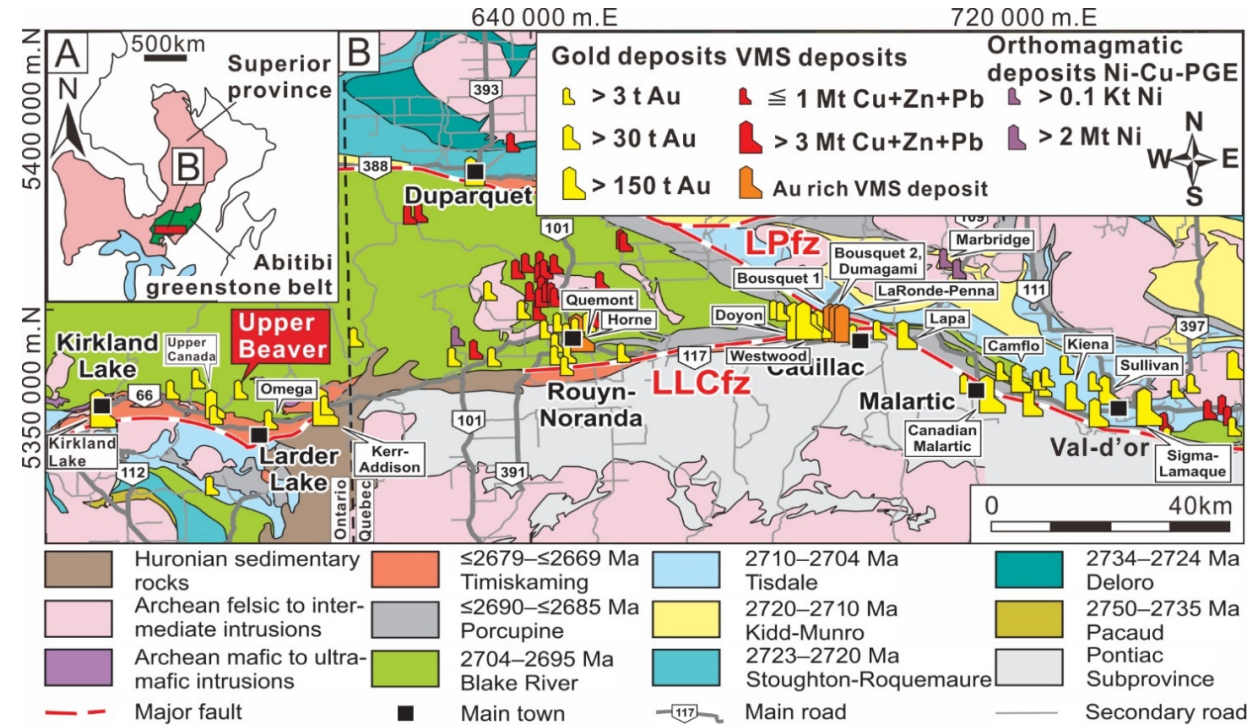

Figure 1. Location (A) and geological map (B) of the southern Abitibi greenstone belt (modified from Monecke et al. 2017)

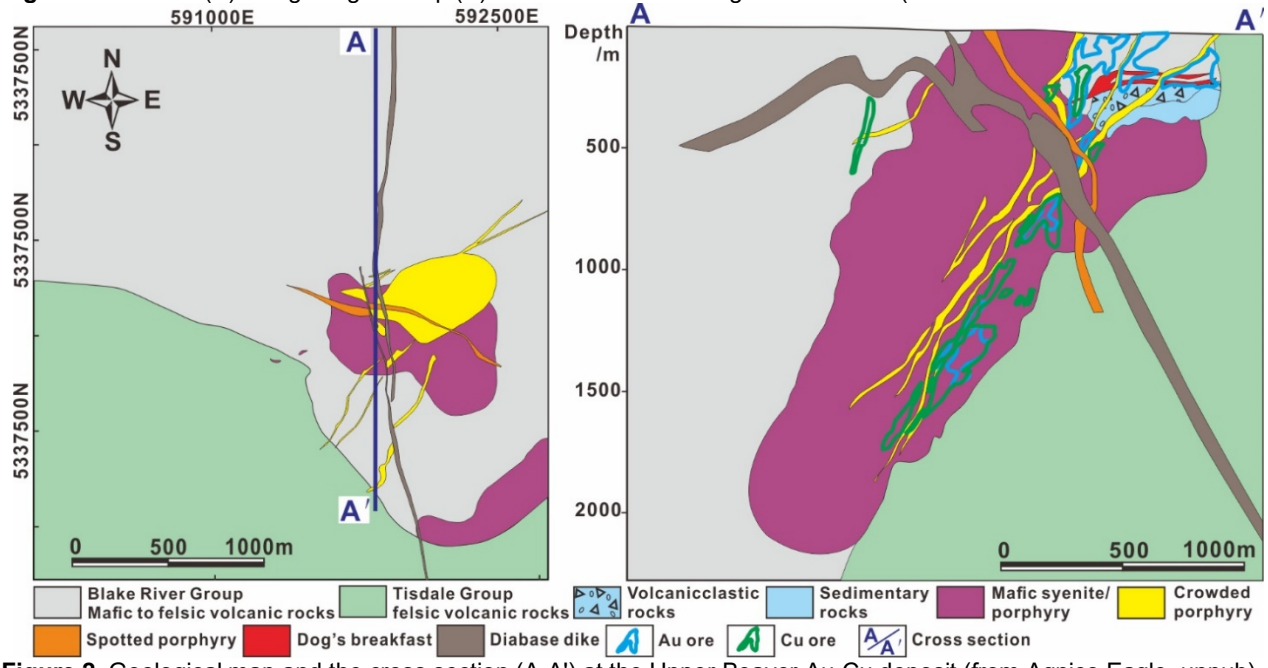

Figure 2. Geological map and the cross section (A-A') at the Upper Beaver Au-Cu deposit (from Agnico Eagle, unpub)

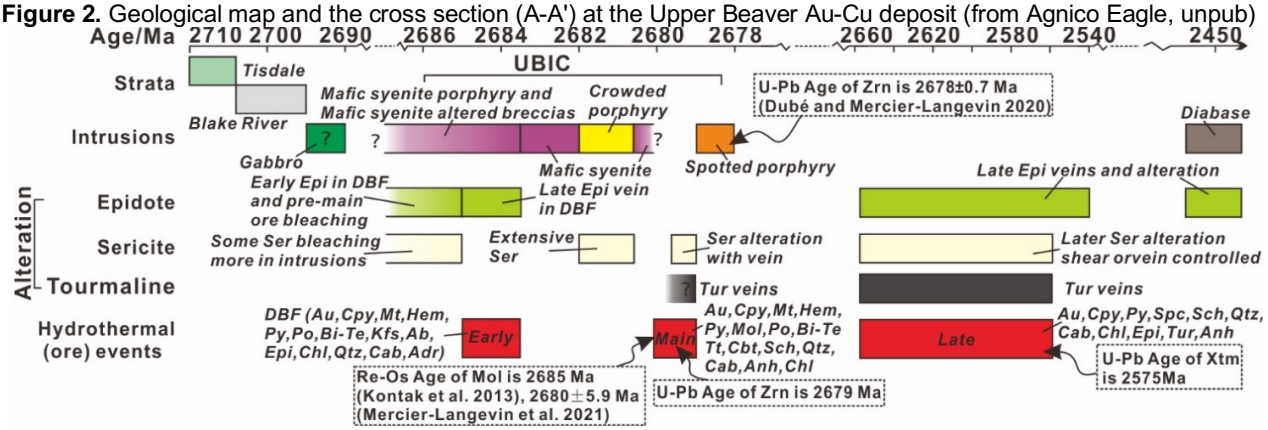

Figure 3. Timeline of geology and hydrothermal events in the Upper Beaver Au-Cu deposit (modified from Agnico Eagle, unpub). Abbreviation: Adr-andradite, Anh-anhydrite, Cab-carbonate, Chl-chlorite, Cpy-chalcopyrite, Cbt- cobaltite, DBF-Dog's Breakfast, Epi-epidote, Kfs-K feldspar, Mol-molybdenite, Mt-magnetite, Po-pyrrhotite, Py-pyrite, Sch-scheelite, Ser-sericite, Spc- specularite hematite, Tur-tourmaline, Zrn-zircon.

3 Methods

To constrain the timing of hydrothermal events in the Upper Beaver deposit, in situ U-Pb geochronological data was acquired on hydrothermal zircon and xenotime in veins associated with the main and late hydrothermal events. Petrography, micro-X-ray fluorescence (μXRF) mapping, energy dispersive spectrum (EDS) and electron microprobe (EPMA) analysis were conducted to reveal the presence, location, and major and trace element composition of these accessory minerals in thin sections. Zircon, and xenotime in different hydrothermal events were analyzed for in situ U-Pb geochronology using LA-ICP-MS at the University of New Brunswick, Canada.

4 Results

From the main hydrothermal event, zircons from the quartz - carbonate ± chlorite ± anhydrite± tourmaline veins are colorless and forms 8 ~ 50 um prismatic grains The zircon grains occur primarily in equilibrium with vein-hosted sulfide minerals (molybdenite, pyrite). Petrography and the REE composition of zircon indicate that they are hydrothermal in origin (Hoskin 2005). A total of 19 zircon grains yields a concordia age of ca. 2674 Ma (n=23 analyses spots) and a weighted mean $^{207}Pb/^{206}Pb$ age of ca. 2679 Ma (n=23) (Fig.3).

The quartz ± carbonate ± chlorite ± epidote ± tourmaline ± anhydrite veins represent the late hydrothermal event. Xenotime grains from these veins are up to 20 μm in diameter and occur either in equilibrium with sulfide minerals (chalcopyrite, pyrite) and Au, or in equilibrium with gangue minerals (quartz, carbonate). The xenotime grains are moderately to strongly enriched in MREE and HREE, with a subtle or no negative Eu anomaly, and a wide range in Lu contents, which suggests a hydrothermal origin (Herzog et al. 2023). Xenotime analyses yield a concordia age of 2582 Ma (n=41 analyses in 40 grains) and a weighted mean $^{207}Pb/^{206}Pb$ age of ca. 2575 Ma (n = 34).

5 Discussion

The main Cu-Au mineralization crosscuts the 'crowded porphyry' and is cut by the 'spotted porphyry'. A zircon ID-TIMS U-Pb age from the spotted porphyry is ca. 2678 ± 0.7 Ma (Fig.3) (Dubé and Mercier-Langevin 2020) constraining the timing of the main gold mineralization to earlier than ca. 2678 Ma. Two N-TIMS molybdenite Re-Os date from this hydrothermal event constrains it at ca. 2685 (Kontak et al. 2013) or. 2680 ± 5.9 Ma (Mercier-Langevin et al. 2021). The new in-situ U-Pb age of hydrothermal zircon at ca. 2679 Ma represents the absolute age for the hydrothermal event and confirms the timing of main Au-Cu event at Upper Beaver. It coincides with Re-Os age (2675 ± 6 Ma) from quartz-molybdenite-Au vein in Kirkland Lake (Ispolatov et al., 2008) and in situ U-Pb age of xenotime (2686 ± 15 Ma) from quartz-carbonate veins at the S-50 Kiena deposit (Herzog et al., 2023).

The late quartz ± carbonate ± chlorite ± epidote ± tourmaline ± anhydrite veins which cut the spotted porphyry (ca. 2678 Ma) indicate that a later hydrothermal event affected the Upper Beaver deposit. In situ U-Pb age of hydrothermal xenotime is ca. 2575 Ma (Fig.3), younger than the time of main Au-Cu event and much younger than the spotted porphyry. Only minor sulfides (chalcopyrite, pyrite) and Au occur in late hydrothermal event veins.

6 Conclusions

Upper Beaver is an Archean Au-Cu deposit with close spatial and temporal relationships with the UBIC in southern Abitibi greenstone belt. In-situ U-Pb dating of hydrothermal zircon and xenotime confirms that the timing of main hydrothermal event is at about 2679 Ma, consistent with zircon U-Pb age of younger spotted porphyry. The age of xenotime from later veins suggests a late hydrothermal evet at about 2575 Ma. The geochronology of hydrothermal events in Upper Beaver help to reveal its genesis and refine the Au metallogeny in southern Abitibi greenstone belt.

Acknowledgement

The authors greatly appreciate the financial support for this study by NSERC and Agnico-Eagle Mines Limited.

References

Dubé B, Mercier-Langevin P (2020) Gold deposits of the Archean Abitibi Greenstone Belt, Canada. Econ Geol Spec Pub 23:669–708. https://doi. org/10.5382/SP.23

Herzog M, LaFlamme C, Beaudoin G, Marsh J, and Guilmette C (2023) U–Pb vein xenotime geochronology constraints on timing and longevity of orogenic gold mineralization in the Malartic-Val-d'Or Camp, Abitibi Subprovince, Canada: Miner Deposita 58:105–133. https://doi.org/10.1007/ s00126 - 022-01131-1.

Hoskin P W O (2005) Trace - element composition of hydrothermal zircon and the alteration of Hadean zircon from the Jack Hills, Australia. Geochim Cosmochim Acta 69, 637–648.

Ispolatov V, Lafrance B, Dubé B, Creaser R, and Hamilton M (2008) Geologic and structural setting of gold mineralization in the Kirkland Lake-Larder Lake gold belt, Ontario: Econ Geol 103:1309–1340. https://doi.org/ 10.2113/gsecongeo.103.6.1309.

Kontak D J, Dubé B, McNicoll V, Creaser R, and Kyser T K (2013). The Upper Beaver Au-Cu deposit, Kirkland Lake, Ontario, Canada: An Archean IOCG analogue or just an intrusion-related iron oxide copper gold deposit(?) Geological Association of Canada-Mineralogical Asso- ciation of Canada (GAC-MAC) Annual Joint Meeting,122.

Mercier-Langevin P, Creaser R A, Dubé B, Dubé J, Kontak D J, Sutton J, and Côté-Mantha O (2021) Molybdenite Re-Os ages of a gold-rich vein, Porphyry zone, Upper Beaver deposit, Abitibi greenstone belt, Ontario; Geological Survey of Canada, Open File 8789, 13. https://doi.org/ 10.4095/328239

Monecke T, Mercier-Langevin P, Dubé B, Friedman M (2017) Geology of the Abitibi Greenstone Belt: Rev. Econ Geol 19:7–50. https:// doi.org/10.5382/ Rev.19. 01.

Using Chlorite and White Mica Mineral Chemistry as Footprints at Alta Floresta Mineral Province – Brazil.

Márcia Elisa Boscato Gomes[2]; Maria José Mesquita[1]; Igor de Camargo Moreira[1]; Renata Augusta Sampaio Paes[1]; Hevelyn Eduarda da Silva Martins[1]; José Henrique Matos[1]; Alberto Ruggiero[1]; Guilherme Primo[1]; Diego Fernando Ducart[1]; João Gabriel da Silva[1]; Luciano Poggi[1]; André Massanobu Ueno Kunifoshita[1], Leonardo Zanchetta de Laurentis[1].
[1]Universidade Estadual de Campinas -Unicamp
[2]Universidade Federal do Rio Grande do Sul – UFRGS

Abstract. The mineral chemistry of chlorite and white mica from Type 1, Type 2 and Type 3 ore deposits from Alta Floresta Mineral Province, Brasil were investigated to develop footprints of their alteration processes. Mg-rich chlorite and Mg- and Si-rich phengite are footprints for the older orogenic-gold event with high crystallisation temperature (420-300ºC) and variable pressure (3-7 kbar). Fe-rich and Al-Fe-rich chlorite and white mica are the footprints for younger magmatic-hydrothermal event with porphyry and epithermal undeformed alterations respectively. The temperatures (380-120ºC) and low pressures (4.6-0.6 kbar) are coherent to the cooling of a shallow hydrothermal-magmatic system. These data contribute to the understanding of the two ore events overprint.

1 Introduction

White mica and chlorite mineral chemistry is a sensitive indicator of hydrothermal and metamorphic processes (Sillitoe 2010; Gaillard *et al.* 2018). These minerals frequently show a wide compositional range in different ore deposits in response to the activities of water, Si and Al, pH and redox, P and T (Guidotti and Sassi 1998; Halley *et al.* 2015) and can provide valuable footprints of hydrothermal fluid pathways in and around the deposits. In this abstract we evaluate chemical patterns of chlorite and white micas from the Paleoroterozoic Alta Floresta Mineral Province (AFMP). The results from Paraiba, Peteca, and Serrinha do Guarantã deposits, and Luiz Bastos target of the Type-1, União do Norte District of Type-2, and Juruena District of Type-3 (Mesquita et al, 2022) are discussed to develop footprints of Type-1, -2, and -3 deposits and their alteration processes.

2 Geology

The AFMP is one of the promising Brazilian provinces for gold and copper. It comprises an inlier nucleus of 2.05 to 1.97 Ga arc-related rocks surrounded and cut by younger 1.82 to 1.52 Ga magmatic-arc rocks.

The current mineralization models defined three deposit types: Type-1 Au ± Cu shear zone-hosted veins, entirely hosted in the older granitic, granitic-gneiss and metamafic rocks of the inlier, and Type-2 Au-Cu porphyry deposits and Type-3 Au ± Ag ± base metals epithermal deposits, in the younger rocks. (Detailed geology and location of the studied deposits are in Mesquita et al. 2022.)

3 Results

We constructed a database of 680 quantitative electron microprobe analyses (EPMA), including revised previous data and new chlorite and white mica chemical compositions.

In the Type-1 deposit, chlorite and white mica substitute for biotite in the chlorite–carbonate alteration (Fig. 1a). In Type-2 and -3 deposits, the analysed chlorite and muscovite are from the phyllic/sericitic, chlorite–sericitic and chloritic alteration zones (Fig.1b, c).

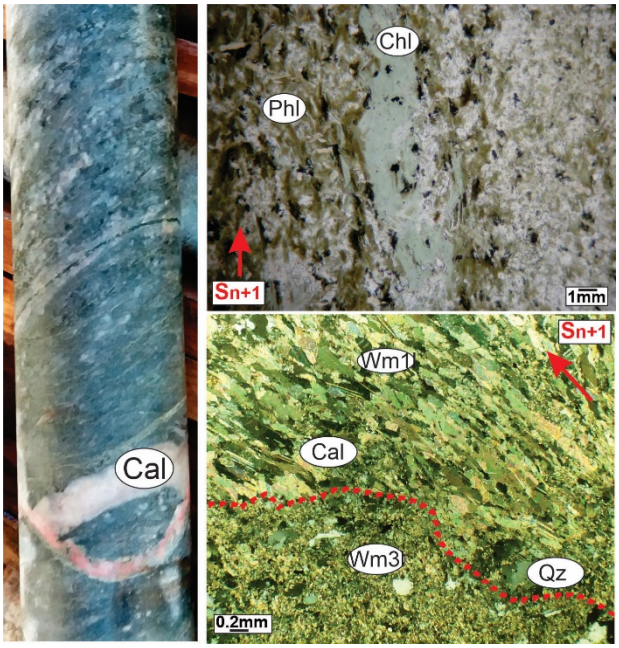

Figure 1. a) chlorite phyllonite cut by calcite (Cal) vein; (b) Phlogopite (Phl) and sulfide (black) alteration replaced by chlorite (Chl) and sulfide; (c) White mica (Wm-3), quartz (Qz) and pyrite overprinting the Sn+1 foliation defined by white mica (Wm-1) and calcite in a muscovite phyllonite.

3.1 Chlorite

Most chlorite classifies as brunsvigite; however, the Fe# allows a general characterization of Type-1deposits chlorite as more magnesian (Fe#, 0.43), and Types-2 and -3 as the Fe-richest (Fe#. 0.5).

In Type-1 deposits, the chlorite composition is strongly controlled by Mg^{2+} for Fe^{2+} substitution. chlorite from distal propylitic (Mg 3.5–4.1 apfu) and proximal sericitic (Mg 3–3.3 apfu) alterations of the Portera–Buriti deposit and the biotite–phlogopite

(Mg 3.1–3.3 apfu) and chlorite–carbonate (Mg 3.1–3.5 apfu) alterations and ore quartz vein (Mg 2.5–2.7 apfu) of the Paraíba deposit are individualized in small clusters with less extensive replacements. Peteca and Luiz Bastos chlorite of chloritic–carbonate alteration clusters in two populations in the high-Fe extreme.

In the Type-2 and -3 deposits, Serrinha de Matupá's chlorite has a broad range of Mg↔Fe exchange reactions, with those from incipient alterations showing an intermediate to high Mg (1.6–3.0 apfu), those of sericitic alteration high Mg (2.4–4.0 apfu), and the Fe-richest ones (0.8–1.4 apfu) in the Mn chloritic ore. In the high-Mg (Serrinha do Matupá and Buriti-Porteira sericitic alterations) and particularly in the high-Fe extremes (Luiz Bastos and Serrinha de Matupá Mn chlorite alteration), other variables than Fe–Mg substitution modify the chlorite's composition.

The Tschermak substitution (Si^{IV} + (Mg +Fe^{2+}) ^{VI} = (^{IV} Al + ^{VI} Al) best describes the chlorite's chemical behaviour in most deposits. In Type-1 deposits, the highest chlorite (Si + Fe +Mg) values are found in Serrinha de Guarantã deposit and chlorite–carbonate alteration (Ch-2) of the Paraíba deposit. The opposite occurs in Ch-1 of Type-1 Luiz Bastos deposit, which plots in the higher Al extreme. Although the Tschermak is also the essential substitution in chlorite formation from Type-2 and -3 deposits, especially those of the Paraíba and Peteca deposits and Serrinha de Matupá,the data are much more spread out than in Type-1 deposits.

The classification diagram Si v. R^{2+} by Wiewióra and Weiss (1990) combines composition and temperature estimations. Most Type 1 deposits' chlorite plots over the zero vacancies line, clustering around intermediate R^{2+} and R^{3+}, indicating the octahedral site's total occupation and high crystallization temperature (Fig. 2a). The Type-2 and -3 deposits' chlorite shows (Fig. 2b) increasing Si, R^{2+} and vacancies and lower crystallization temperatures. The Type-3 Luiz Bastos chlorite composition remarkably extends to decreasing R^{2+} and increasing Si (Fig. 2c). These data suggest that the di-trioctahedral substitution also plays an important role, increasing vacancies in the mineral structure and decreasing temperature (up to 100°C). Applying the quantitative geothermometer of Inoue et al. (2009), the temperatures obtained for chlorite of Type-1 deposits were between 250 and 498°C. The Type-2 chlorite exhibits scattered temperatures between 152 and 402°C. The Type-3 chlorite shows the lowest and variable temperatures (68–378°C).

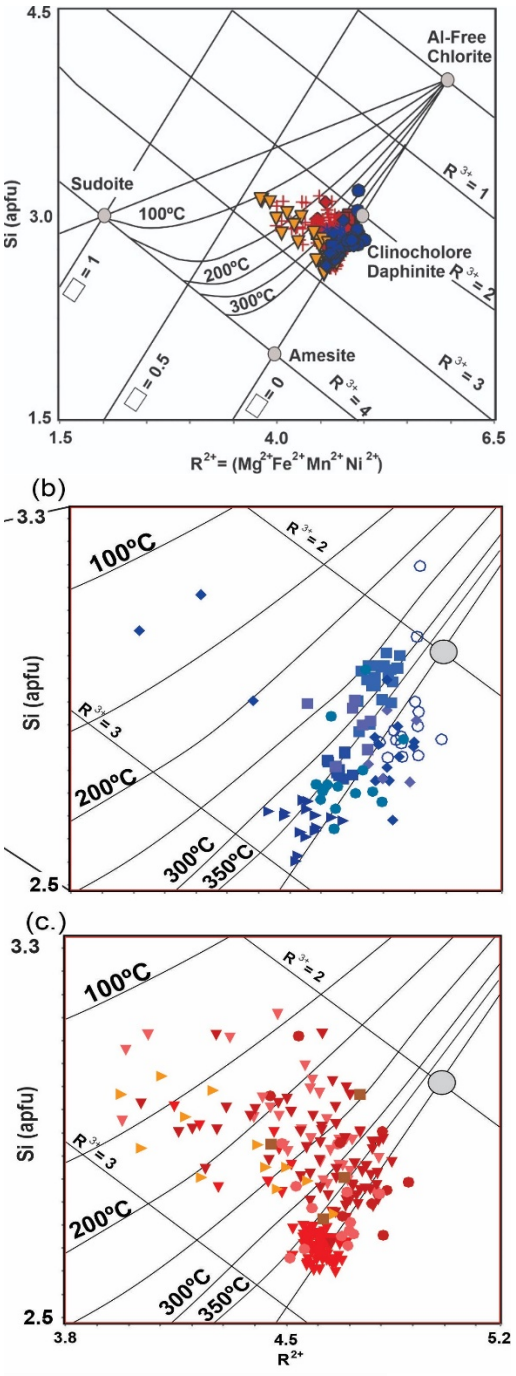

Figure 2. R^{2+} v. Si (apfu) proposed by Wiewióra and Weiss (1990), in which R2 = Fe^{Tot} + Mg + Mn+ Ni, allows identification of the chlorite composition and the correlation to the presence of vacancies, R3 (Al^{Tot} +Cr + Ti) and temperature (Bourdelle and Cathelineau 2015).

3.2 White Mica

The major white mica has an interlayer population 0.8 apfu and a Si excess over 3 apfu, characteristically phengitic in composition.

The general broad compositional field depicted in Figure 3 indicates that the control of chemical variations in white micas is the ferriphengite–ferrimuscovite–phengite(FPh–FMu–Ph) compositional substitutions (Guidotti 1987). The main substitution from the ideal muscovite follows the tie-line muscovite–ferriphengite (Mu–FPh) end members. This chemical approach highlights the muscovite–Fe–phengitic compositions of the white micas from the Type-1 deposits. The Type-2 and -3 white micas show a compositional field's enlargement towards the ferrimuscovite trend. The Type-3 Luiz Bastos and Trairão deposits white micas fall essentially on the Mu–FPh join. Even with no Fe^{2+}–Fe^{3+} distinction by EPMA analysis, the Mu deviation to ferrimuscovite suggests that $Fe^{3+} \leftrightarrow Al^{3+}$ substitution could also have occurred (Guidotti 1987). The Type-2 and -3 samples show significant variations from Mu to FMu, suggesting the Fe^{3+} replacing Al^{VI}.

Considering all samples, the Tschermak exchange reaction is the most significant controller of compositional variations since most points cluster around the negative linear correlation of (Fe + Mg + Si) v. total Al. The Type-1 white mica plots in the field of higher phengitic substitution (Ph), those of muscovite–phyllonite being more aluminous and those of chlorite–carbonate phyllonite showing a broader substitution interval. Tschermak substitution within the white mica of the Type-2 Serrinha de Matupá and Peteca deposits is the most extensive, from muscovite to phengite end members, and their compositional trends overlap. The substitutions along this general negative trend are associated with samples from different hydrothermal alteration zones of Type-2 and -3.

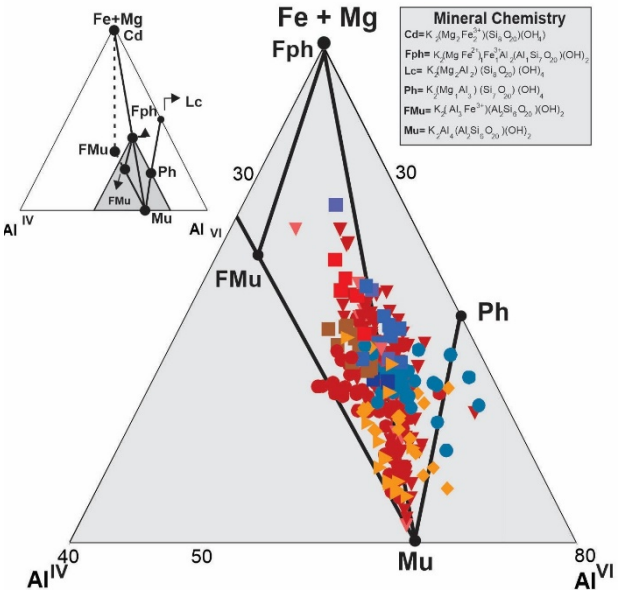

Type-1 deposit

- Paraíba (Wm-1) - Barren Mu alteration
- Paraíba (Wm-2) - Ore Chl-Cb alteration
- Paraíba - Ore Qtz vein
- Peteca (Wm-1) - Ore Chl-Cb alteration

Type-2 deposit

- Paraíba (Wm-3) - Barren Sericitic
- Paraíba (Wm-4) - Ore Sericitic
- Peteca (Wm-2 e Wm-3)- Propylitic/Chloritic
- Serrinha de Matupá (Wm-1) - Incipient alteration
- Serrinha de Matupá (Wm-2 e Wm-3) - Ore Mn-Chloritic/Sericitic

Type-3 deposit

- Luiz Bastos (Wm-1) - Sericitic
- Trairão

Figure 3. Mineral chemistry of white mica. $^{IV}Al - {}^{VI}Al - (Mg + Fe^{Tot})$ diagram classification of white mica with all AFMP data (Guidotti 1987). White mica end members: Mu, muscovite; Ph, phengite; FMu, ferrimuscovite; FMu*, ferrimuscovite; Fph, ferriphengite; Lc, leucophyllite; Cd, celadonite.

The pressures obtained using the phengite barometer in the Paraíba deposit distal muscovite alteration zone (Wm-1) is between 2.7 and 3.7 kbar. However, the Paraíba proximal Chl–Cb phyllonite ore veins and Peteca white mica are predominantly over 4.0 kbar. The pressures calculated using the phengite barometer define a broad field from 1 to 5 kbar. However, the pressures of the ore zones in all deposits are more limited and higher, from 3 to 4.5 kbar.

4 Conclusions

Chlorite and white micas in phyllonite and mineralization of the orogenic gold deposits (Paraíba, Peteca, and Serrinha de Guarantã deposits) have characteristic Mg- and Si-rich footprints. The chlorite broadly shows a high-Mg brunsvigitic to clinochlore composition, mainly controlled by the Fe↔Mg and Tschermak exchanges. The consistent high temperatures (above 350°C) and the $Si < 3 < 4 < R^{2+} < 5$, and $2 < R^{3+} < 3$ ranges (apfu) correspond to metamorphic chlorite and support the correlation to the metamorphic and metamorphic–hydrothermal environments with pressures over 4 kbar, as indicated by the Peteca and Paraíba phyllonites. These temperatures and the Mg-high tendency are consistent with the typical mesozonal orogenic gold deposits elsewhere.

The white mica shows Mg- and Si-rich composition (Mg = 0.63, Si = 3.4) with restricted compositions controlled by the end members phengite, $K(Mg\ Fe^{2+})_{0.5}\ Al_{1.5}\ Si_{3.5}\ Al_{0.5}\ O^{10}\ (OH)^2$ and ferriphengite, $K(Mg\ Fe^{2+})_{0.5}\ Fe^{3+}{}_{0.5}\ Al\ Si_{3.5}\ Al_{0.5}\ O_{10}(OH)^2$. High fluid pressures favour the production of phengitic mica (Ernst 1963), compatible with a

3.0–6.5 kbar field defined for the orogenic gold deposits assemblages. According to this author, the higher P and T favour the more significant extension of the solid solution between phengite and ferriphengite, which is also a characteristic feature of the phyllonites Wm-1 and Wm-2. The P–T, depth and fluid conditions are comparable with those proposed for orogenic gold mineralizations globally (5–15 km, e.g., Goldfarb and Groves 2015).

The magmatic–hydrothermal event formed the porphyry–epithermal deposits (Type-2 and -3 deposits). In the Paraíba deposit, the phengite of pervasive porphyry phyllic alteration (Wm-3) overprinted the Wm-1, obliterating the Sn+1 of the older muscovite phyllonite related to the orogenic gold phase. The Peteca deposit porphyry propylitic/chloritic alteration formed over a wide range of P–T (1–4 kbar and 290–380°C), yet at lower pressures than the earlier Peteca chlorite–carbonate phyllonite related to the orogenic gold phase. Both porphyry–epithermal deposits have the Fe-rich chlorite and ferrimuscovite trend as the common characteristic footprint, but the porphyry (Type-2) and epithermal (Type-3) deposits display in detail distinct characteristics. Porphyry chlorite (Serrinha de Matupá, and parts of the Paraíba, Peteca deposits) is mainly high-Fe brunsvigite to ripidolite. The temperatures range from intermediate to high (270–370°C) and have 1–5 kbar pressures.

White mica compositions are controlled mainly by the end members' muscovite, $KAl_2\ Si_3\ Al\ O^{10}(OH)^2$ and ferrimuscovite, $KFe^{3+}{}_{0.5}\ Al_{1.5}\ Si_3\ Al\ O^{10}(OH)^2$. The mean Si ranges from 3.45 to 3.12 apfu, the total Al ranges from 2.34 to 2.25 afpu, and the Fe + Mg + Mn ranges from 0.32 to 0.65 apfu, indicating that muscovite is not an end member but contains important ferriphengite compositions. The observed chemical variations are controlled mainly by theTschermak substitution. Porphyry white mica, especially Wm-3 and Wm-4 from Paraíba and Wm-2 and Wm-3 from the Peteca deposit, scatter the Tschermak substitution line towards lower Al values, which suggest variable amounts of Fe^{2+} and Fe^{3+} in the structure.

The epithermal-type chlorite and white micas (Luiz Bastos and Trairão deposits), on the other hand, have Al- and Fe-rich main footprints. Chlorite varies from diabanite to ripidolite, with high-Fe and Al (Al^{VI} 1.97, Fe^{tot} 0.61), controlled by Tschermak substitution. The vacancy variations (0–0.5) are governed by di-trioctahedral substitution. Temperatures range between 120°C and 260°C, and pressure ranges from 0.6 to 3 kbar. The white mica is dominantly in the muscovite–ferrimuscovite trend, richer in the muscovite end member and displaying the same scattering from the Tschermak substitution line, suggesting Fe^{3+} substitution. These high-Al and lower-Fe^{tot} characteristics of epithermal white mica are, however, also seen in part of Serrinha de Matupá and Peteca porphyry white mica. This fact and the extensive chlorite deviation from the amesite–clinochlore line towards higher vacancies and the Si of these hydrothermal populations could represent an evolution of the porphyry alterations with decreasing temperature. Interestingly, the Serrinha de Matupá incipient and phyllic alteration P–T field superimposes the Luiz Bastos chlorite–sericite alteration field, suggesting that the Serrinha de Matupá porphyry may have evolved towards an epithermal system.

Finally, the phyllonites' chlorite and white mica chemical composition have characteristic Mg-rich chlorite and Mg- and Si-rich muscovite–phengite footprints. The consistent high crystallization temperature (above 350°C) and almost zero vacancies suggest metamorphic chlorite. In contrast, Fe-rich and Al–Fe-rich alterations are the main footprints for the porphyry and epithermal deposits, respectively.

Acknowledgements

The authors are grateful to the Institute of Geosciences of the University of Campinas, and the Microprobe Laboratory of Institute of Geosciences – UFRGS for supporting the analytical data.

References

Bourdelle, F. and Cathelineau, M. 2015. Low-temperature chlorite geothermometry: a graphical representation based on a T–R2+–Si diagram. *European Journal of Mineralogy*, **27(5)**, 617-626. https://doi.org/10.1127/ejm/2015/0027-2467

Ernst, W. G. 1963. Significance of phengitic micas from low-grade schists. *American Mineralogist: Journal of Earth and Planetary Materials*, ***48*(11-12)**, 1357-1373.

Gaillard, N., Williams-Jones, A.E. et al. 2018. Mica composition as a vector to gold mineralization: deciphering hydrothermal and metamorphic effects in the Malartic district, Quebec. Ore Geology Reviews, 95, 789–820, https://doi.org/10.1016/j.oregeorev.2018.02.009

Goldfarb, R.J. and Groves, D.I. 2015. Orogenic gold: Common or evolving fluid and metal sources through time. Lithos, 233, 2–26, https://doi.org/10.1016/j.lithos.2015.07.011

Guidotti, C.V. and Sassi, F.P. 1998. Petrogenetic significance of Na–K white mica mineralogy: recent advances for metamorphic rocks. European Journal of Mineralogy, 10, 815–854, https://doi.org/10.1127/ejm/10/5/0815

Halley, S., Dilles, J.H. and Tosdal, R.M. 2015. Footprints: hydrothermal alteration and geochemical dispersion around porphyry copper deposits SEG Newsletter, 100, 1–17, https://doi.org/10.5382/SEGnews.2015-100.fea

Mesquita et al. 2022. Paleoproterozoic gold deposits at AFMP, Brazil: two overprinted mineralizing events? From: Torvela, T., Lambert-Smith, J. S. and Chapman, R. J. (eds). Recent Advances in Understanding Gold Deposits: from Orogeny to Alluvium. Geological Society, London, Special Publications, 516. https://doi.org/10.1144/SP516-2021-64

Sillitoe, R.H. 2010. Porphyry copper systems. Economic Geology, 105, 3–41, https://doi.org/10.2113/gsecongeo.105.1.3

Wiewióra, A. and Weiss, Z. 1990. Crystallochemical classifications of phyllosilicates based on the unified system of projection of chemical composition: II. The chlorite group. Clays and Clay Minerals, 25, 83–92, https://doi.org/10.1180/claymin.1990.025.1.09

Gold in the Sardis Placer Deposit: Composition and Source of King Croesus's Gold

Gülcan Bozkaya[1], David A. Banks[2,3], Ömer Bozkaya[1]
[1] *Department of Geological Engineering, Pamukkale University, Denizli, Türkiye*
[2] *School of Earth and Environment, University of Leeds, Leeds, LS2 9JT UK*
[3] *Department of Geological Engineering, Istanbul University-Cerrahpaşa, Türkiye*

Abstract. In history, Sardis was important for its wealth derived from placer gold in the Pactolus River which erodes an alluvial fan containing the gold, thought to be derived from erosion of the Menderes Massif. We have shown that the exterior of gold grains was modified in the placer by biological and chemical processes. LA-ICPMS analyses indicate the presence of significant numbers of PGE particles and mineral inclusions that cast doubt on the source of the material in the alluvial fan. We propose that the gold in this alluvial fan was derived from laterization of the ophiolites that now form the Çaldağ laterite deposit prior to tectonic movement of the ophiolite unit to the NW. This is a Ni deposit and contains gold in some of the laterite units. The mineralogy in the alluvial fan at Sardis is also similar to some laterite units at Çaldağ.

1 Introduction

The legend of King Midas, and all that he touched turning to gold, is an etiological myth used to explain the rich alluvial gold deposits of the Pactolus River. In the legend, King Midas asked for the power to turn everything he touched into gold because he believed it would bring him great wealth and prosperity. According to the myth, King Midas was granted his wish by the god Dionysus, but he soon realized that his newfound power was more of a curse than a blessing as all he touched, including his daughter, turned to gold. Midas prayed to Dionysus to remove his power, who replied that this could only be done by washing in the river Pactolus. Thus, the power was transferred to the river and all the alluvium was turned to gold. The Legend of King Midas probably relates to King Croesus who ruled the Lydian empire from 560 to 546 BC. So rich was the gold resources in the river that the Lydians based their economy on its resources. An estimate of the richness can be made by the offering Croesus made to the Oracle at Delphi prior to his battle with Cyrus. The offering included 117 ingots of pure gold each weighing 150 lbs, a pure gold lion weighing 600lbs and a golden vat weighing some 522lbs. In total approximately 10,000 troy ounces with a current value of approximately $15 million. Lydia acquired great wealth and influence from the gold extracted from the Pactolus River and by the development of a process that separated gold and silver from electrum. This process ensured that for the first-time coins of a reliable and consistent value were used for commerce.

2 Location

The Pactolus River, now called Sart Çayı, from where the gold was extracted, originates from Mount Tmolus and runs north through ancient Sardis into the Gediz river which in ancient times was called the river Hormus. This cuts the same alluvial fans that are currently exploited commercially for several mineral resources including gold. However, despite there being a succession of alluvial fans in the Sardis area and along the margins of the Menderes Massif and the Gediz basin it is only in the oldest Neogene alluvial fan at Sardis is there any appreciable gold in specific conglomerate layers (Topkaya 1975). Today it does not have a steep gradient and its flow is quite inconsequential and would not have been able to account for the amount of placer gold recovered. Possibly tectonic movement has reduced the flow rate and the ability for gold to be eroded.

The study area is part of the larger extensional domain of the Alpine-Himalayan belt. The basement rocks of the study area are the Precambrian-early Mesozoic metamorphic rocks (Menderes Massif) and Upper Cretaceous-Paleocene ophiolitic rocks (Çaldağ unit) (Figure 1). Metamorphic rocks of the Menderes Massif were derived from a micro-continental block (the Anatolide–Tauride Block) and collision with the Sakarya continent,belonging to Eurasia during? the Mesozoic (Şengör and Yılmaz 1981). This metamorphic core-complex forms the western nuclei of the Anatolides and comprises a pre-Alpine "gneissic core" and an Alpine "schist and marble envelope". The core of the Menderes Massif consists, in ascending order of migmatites, para- and orthogneisses (leptites), amphibolites, granulites and eclogites (Candan et al. 2001).

3 External Features

The gold grains are flat, sub-rounded and essentially two dimensional, approximately 2-3 mm in size with the surface having a porous texture.

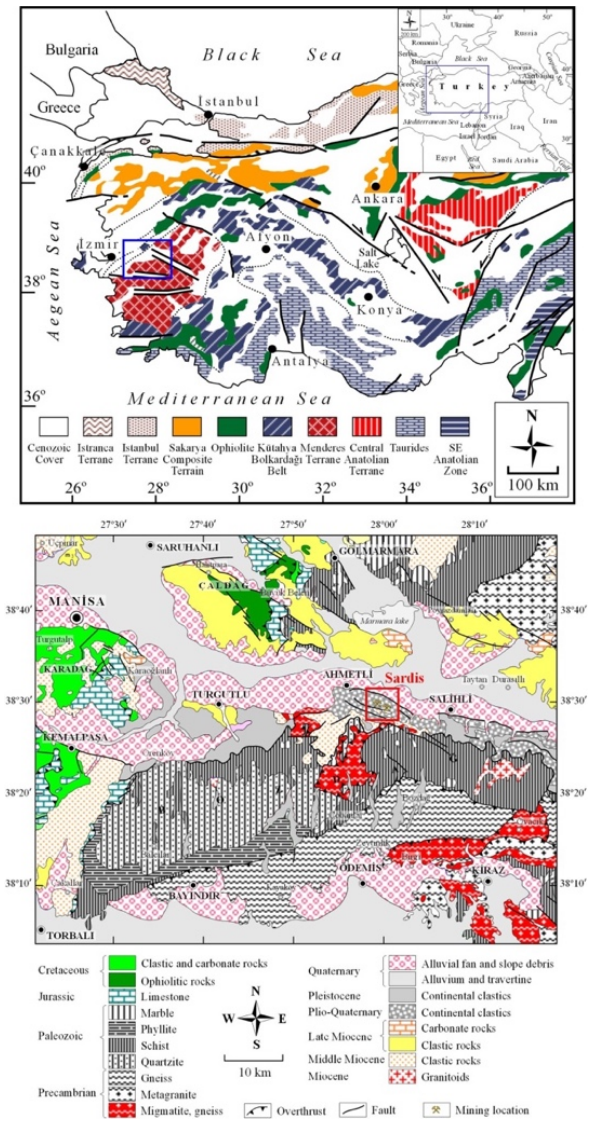

Figure 1. The distribution of the main Alpine terranes in Turkey and regional geology of Sardis and surrounding area (top). Modified from MTA (2002) and Göncüoğlu et al. (1997). Location of Sardis is at the western end of the Gediz basin close to Izmir in Western Turkey. The alluvial fan located on the fault adjacent to the Menderes Metamorphic Complex to the south. The Çaldağ deposit and ophiolite are now located to the NW (bottom).

SEM images (Figure 2) shows this to be the result of the growth of new gold on top of the original gold grains. Layers of new gold are commonly seen to form a columnar structure (Figure 2a, c) with layers of gold stacked on top of each other. It is within these spaces that calcite, baryte and clays have been precipitated on top of the gold. These are the latest phase of mineral precipitation and always on top of the gold.

The outermost areas of the gold grains (Figure 3) have features that are consistent with a biological origin. All the features are of gold and are generally elongate with a smooth appearance. They are likely of bacterial origin, possibly as a result of conditions at the bacteria-water interface that was conducive to gold deposition. Similar features are found in gold grains from placer deposits in New Zealand (Reith et al. 2006). Certain bacteria can generate sub-micron gold particles or at the bacterial-water interface.? the conditions may induce the precipitation of gold nanoparticles. On all the smooth bacterial surfaces there are aggregates of gold particles (Figure 3. d,e g, h, i). that can be seen to be made from clusters of much smaller gold particles and may eventually reach the size of the ball-like accumulation in Figure 3e. The size of the individual particles is approximately 20nm or less. These particle aggregates are also found on the plate-like growths of the new gold described in the previous section (Figure 2c).

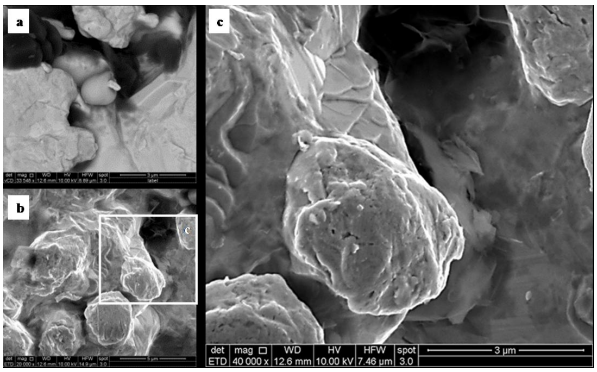

Figure 2. Exterior surface showing the presence of new euhedral gold crystals and columnar structures made from plates of new gold. These structures create the impression of porosity on the grain surfaces.

SEM-BSE images of polished grains (Figure 4) shows these have a dark core. Au and Ag element maps indicate Ag is depleted around the edges leaving an almost pure gold surface (Figure 4. a,b,c) Numerous mineral inclusions are also present in the centre of the grains involving elements such as Ni, Sb, Fe, Sn, Cu, As and Pt (Figure 4d. e,f). The example in Figure 4 shows a euhedral crystal and several smaller crystals of a Sb-Ni phase.

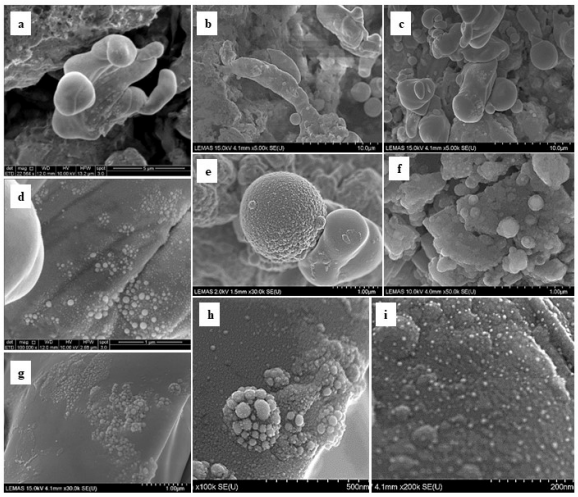

Figure 3. Bacterial-like features coated in Au on the surface of the grains. At high magnification these can be seen to be coated with nano-particles (20nm) of Au that aggregate to form larger spherical structures that can reach c. 1µm.

4 LA-ICPMS Analyses

The LA-ICPMS system uses an Agilent 7500c quadrupole mass spectrometer, with a Geolas ablation system to determine the composition of individual grains. The Geolas ablation system uses a Compex 103 ArF excimer laser at a wavelength of 193nm, delivering an energy density of 6 Jcm^{-2} on the sample surface at a pulse frequency of 5Hz with spot sizes of 50 and 100µm. Calibration of the different elements was made using the standards AuRM2, MASS-1, NIST481 and 610.

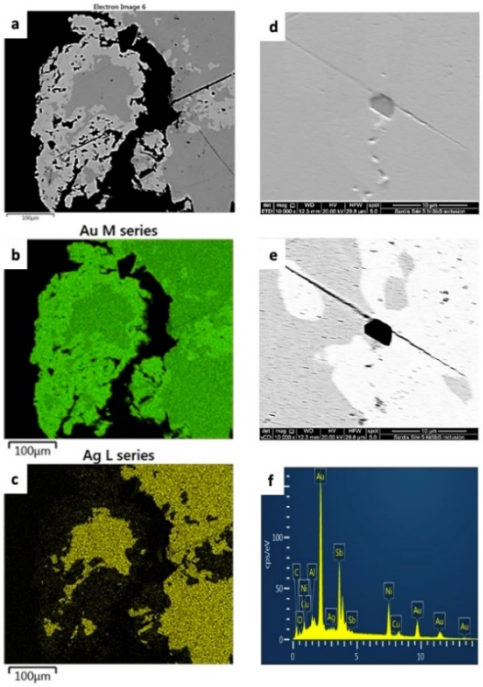

Figure 4. SEM-BSE images of the polished gold grains showing an Au-rich-edge and an Au-Ag alloy in the centre. Inclusion of a mineral trapped as the gold was precipitated. It is located at the margin of the Au-Ag alloy and the au-rich rim.

The analyses of the new formed gold on the outside of the original grains shows it is almost pure with Au content that averages 99.4% with low Ag averaging 0.4%. Many transition elements are present in the grains at low ppm or ppb levels except for Fe which is between a few 100's to 1000's ppm and Hg which is between a few 10's to a few 100's. The presence of a large number of elements likely arises from contamination whilst in the placer. The original placer grains have modified edges from the removal of Ag, in the placer environment, and show the same range and concentrations of transition elements as the newly formed gold. The main difference between new gold and the rims of the original placer grains are that Ag can be between 1 and 9% and Hg is between 100 and 3000 ppm which is much greater than in the newly formed gold.

The analyses from the central parts of the gold grains represent the original composition, essentially an alloy of Au, Ag, Hg and perhaps Cu and Sb which are homogeneously distributed at low concentrations. The concentrations of Au are between 90 and 80%, the Ag concentration is between 9 and 20% and Hg which has a reasonably consistent concentration between 3000 and 5000 ppm. All samples have effectively the same Cu concentration of 1 to 4ppm and unlike the other analyses low levels of Sb. Fe is present in less than half the analyses, occurring as small mineral inclusions, and averages 140 ppm. A few analyses contain Pb and Bi but these are due to mineral inclusions being ablated. Other elements present are from small inclusions within the grains. Examples of the elements that are part of the alloy and those that are present as particles are shown in Figure 5. The analysis of PGE's required a larger laser spot, longer dwell times on the elements and only Au and PGE being analysed. Rh, Pd, Re, Ir and Pt are recorded as individual spikes (Figure 6) averaging concentrations of a few 10's ppb. These nanoparticles are however relatively numerous. For 24 individual ablations the number of spikes recorded were Ru 17, Rh 41, Pd 29, Re 21, Os 13, Ir 52 and Pt 18.

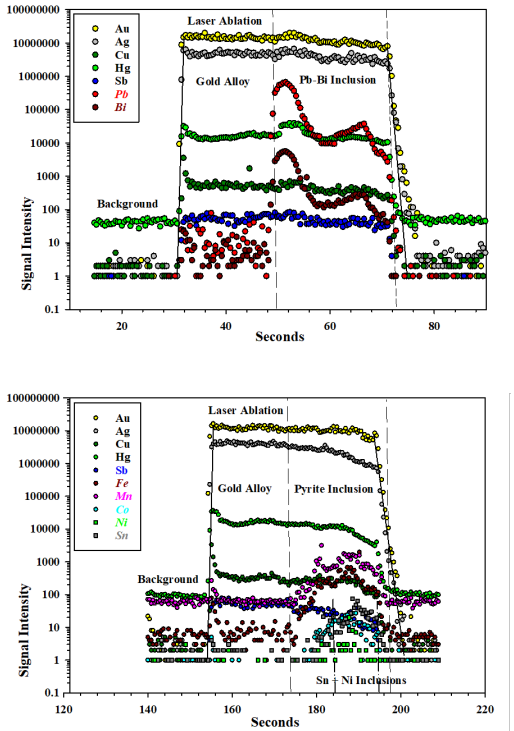

Figure 5. LA-ICPMS ablation profile of two gold grains. The alloy composition is Au, Ag, Cu Hg and Sb as indicated by their parallel profile. Beneath the surface there has been ablation of a Pb-Bi inclusion (top) and pyrite which contains some additional elements. There has also been ablation of Sn and Ni inclusions (bottom).

5 Discussion

Previous SEM analysis of the grains indicated they were almost pure gold (Rammage and Craddock 2000). This questioned the need for the process of separating gold and silver from electrum. If the grains were pure gold, then perhaps, they were actually separating the gold and silver from older

coins made from the electrum. It was also suggested that the porous surface of the grains was the result of grains being directly processed rather than beating gold grains to make thin sheets which were then processed to extract the silver. Our analyses show the grains are electrum but have a surface of pure gold consistent with previous SEM analyses that was used to assume the entire grains were pure gold.

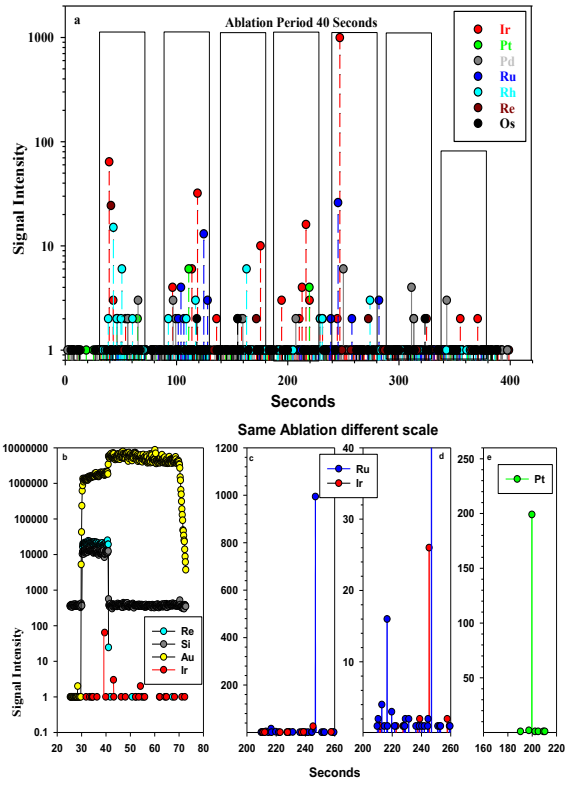

Figure 6. Several ablation profiles specifically for PGE's that are present as single large spikes indicating their presence as very small (nanoparticles?) inclusions in the grains.

A supposed distinctive feature of the artifacts recovered from Sardis is the presence of 50-150µm silver-coloured inclusions which when analysed are predominantly platinum, iridium alloys with some variable concentrations of osmium. These are observed in Achaemenian jewellery and Lydian coins (Young 1972) and are inferred to have been included in the gold. Similar gold artefacts were recovered from a royal tomb in Ur, Mesopotamia with the same size and composition of platinum, iridium osmium gold alloy. Such inclusions are uncommon in gold and only occur in specific geological environments such as ophiolites and related chromite deposits. Inclusions of PGE elements which were supposedly absent in Sardis grains led to interpretations that gold containing PGE's or only PGE's were brought to Sardis from different locations with various trade routes being proposed. However, we have shown that the gold does include numerous PGE inclusions that are consistent with the elements present in the artifacts.

The physical source of the placer gold is from the oldest alluvial fan on the northern margin of the Menderes Massif and it is thought that erosion of rocks of the massif was the source. However, the analyses of the gold with the presence of PGE elements and mineral inclusions with Pt, Ni, Sb, Sn, etc is more consistent with a ultramafic or ophiolitic source. The low concentrations of Cu and the appreciable concentrations of Hg together with the general absence of inclusions of pyrite, and galena are not consistent with an orogenic or magmatic style of mineralization. There is no indication that comparable units were present in the Menderes Massif. The Pactolus River is not very long or large and for the amount of recovered gold it must have been flowing through a very rich source in which the gold had been pre-concentrated.

We propose that the source of the gold was-the Çaldag Ni-laterite deposit, now to the NW, but was previously located at Sardis prior to relocation by lateral movement on the main faults. The deposit lies on the Çaldağ horst of the Gediz Graben and covers approximately 10 km^2. This developed from the ultramafic rocks of the Late Cretaceous - Early Paleocene ophiolitic mélange of the flysch zone, located on the northern edge of the Menderes Massif, within the Gediz Graben (Figure 1). The laterite also contains electrum that has an Au and Ag composition consistent with the grains we have analysed.

Acknowledgements

POMZA Export Company is thanked for supplying gold grains from their current mining operation.

References

Candan, O, Dora, OÖ, Oberhansli, R, Çetinkaplan, M, Partzsch, JH, Warkus, FC, Dürr, S (2001) Pan-African high-pressure metamorphism in the Precambrian basement of the Menderes Massif, western Anatolia, Turkey. Int. J. Earth Sci 89: 793-811.

Göncüoğlu, MC, Kozlu, H, Dirik, K (1997) Pre-Alpine and Alpine terranes in Turkey: explanatory notes to the terrane map of Turkey. Ann. Geol. Pays Helleniques, 37: 515-536.

Helvacı, C, Gundogan, I, Oyman, T, Sözbilir, H, Parlak, O (2013) Geology, Mineralogy and Geochemical Properties of the Caldag Ni-Co Laterite Deposits. Bulletin of the Earth Sciences Applications and Research Centre of Hacettepe University, 34: 101-132.

MTA (2002) 1: 500,000 scaled geological map series of Turkey. Izmir section. Miner. Res. Explor. Ankara.

Ramage, A, Craddock, P (2000) King Croesus' Gold: Excavations at Sardis and the History of Gold Refining. Harvard University Art Museums and the British Museum Press. 272p.

Reith, F, Rogers, SL, McPhail, DC., Webb, D. (2006) Biomineralization of Gold: Biofilms on Bacterioform Gold. Science, 313: 233-236.

Şengör, AMC, Yılmaz, Y (1981) Tethyan evolution of Turkey: a plate tectonic approach. Tectonophysics 75: 181-241

Topkaya, YA (1975) Recent Evaluation of the Sart Placer Gold Deposit. MTA Report.

Young, WJ (1972) The Fabulous Gold of the Pactolus Valley. Boston Museum Bulletin 70: 4-13.

Multiple sulphur isotope signatures of the Fenelon gold deposit, Abitibi Greenstone Belt, Canada: Constraints on fluid origin and ore-forming processes

Evan Slater[1], Sébastien Castonguay[2], Anthony Williams-Jones[1], James Clark[1], Richard Stern[3]
[1]McGill University, Montreal, Canada
[2]Geological Survey of Canada, Québec, Canada
[3]Canadian Centre for Isotopic Analysis, University of Alberta, Edmonton, Canada

Abstract. This study presents in situ multiple S isotope data (^{32}S, ^{33}S, ^{34}S) for sulphide phases from the Fenelon gold deposit (>4 Moz), in the Neoarchean Abitibi Greenstone Belt, to evaluate the nature of ore fluids and processes responsible for the formation of the deposit. Gold mineralization at Fenelon consists of two main stages: 1) auriferous quartz veins with molybdenite, and 2) gold- and sulphide-rich mineralization comprising early arsenopyrite, zoned and colloform pyrite, and lastly pyrrhotite-chalcopyrite-sphalerite-arsenopyrite-Bi-tellurides. All stages are interpreted to have formed during orogenic shortening. Multiple S isotope data for arsenopyrite and pyrite show near zero $\Delta^{33}S$ and positive $\delta^{34}S$ values. For zoned pyrite, $\delta^{34}S$ increases from grain cores (1.7‰ avg.) to rims (3.6‰ avg.), which is compatible with progressive reduction of the ore fluid. Chalcopyrite and pyrrhotite are characterized by near zero $\Delta^{33}S$ and similarly positive $\delta^{34}S$ values; however, there is a mixing trend with another S source with near zero $\delta^{34}S$ and positive $\Delta^{33}S$ (~0.5‰). The data are compatible with Fenelon having formed from magmatic fluids which incorporated S either from local country rock or by mixing with metamorphic-derived fluids near the site of deposition.

1 Introduction

The study of gold deposits in greenstone belts is challenging since regional metamorphism and deformation often overprint mineralization, masking geochemical signatures, ore textures and alteration parageneses. Therefore, an important question remains highly debated: whether Archean orogenic gold mineralization—i.e., synchronous with the main phase of shortening—form from dominantly metamorphic or magmatic fluids. The Fenelon gold deposit, a recent >4 Moz discovery in the Neoarchean Abitibi Greenstone Belt ('Abitibi'), Quebec, Canada, appears to have formed during shortening in a ductile-brittle environment, yet the mineralization has characteristics which differ from typical orogenic deposits. We have evaluated the mineralization at Fenelon by analysing multiple S isotopes to gain insight into the fluid origin and ore-forming processes.

The Abitibi is a prolific gold mining region with >200 Moz of past production and diverse mineralization styles (Dubé and Mercier-Langevin 2020 and references therein). Some deposits have been shown to pre-date the main phases of shortening such as the syngenetic Horne deposit and intrusion-related Coté gold deposit. However, most of the gold endowment of the Abitibi occurs within deposits that formed during the main phase of shortening when both metamorphism and magmatism were potentially active; e.g., the Young Davidson and Dome deposits. Such deposits are nevertheless considered to be orogenic, and there is ongoing debate on the origin of their ore fluids (e.g., Goldfarb and Pitcairn 2022).

1.1 S Isotopes in Ore Deposit Research

In most circumstances, the stable isotopes of S (^{32}S, ^{33}S, ^{34}S, and ^{36}S) fractionate during physicochemical processes proportional to their respective masses. Fractionation occurs dominantly because of the speciation of S, and the heavier isotope preferentially fractionates into the oxidized species (e.g., Hutchison et al. 2020). This mass dependent fractionation of sulphur (MDF-S), typically traced using $\delta^{34}S$, can be challenging to interpret as it is a function of both changes in the S reservoir and/or physicochemical processes including variations in pH, redox and temperature.

In Archean rocks, variations in $\delta^{34}S$ inherited form reservoir can be distinguished from physicochemical processes by tracking the mass independent fractionation of sulphur (MIF-S), traced by $\delta^{33}S$ ($\Delta^{33}S = [(\delta^{33}S/1000 +1) – (\delta^{34}S/1000 + 1)^{0.515}] \cdot 1000‰$; Farquhar et al. 2010); once set, $\delta^{33}S$ remains unaffected by physicochemical processes. In the Archean oxygen-poor atmosphere, through which ultraviolet rays could pass freely, volcanic SO_2 dissociated to oxidized and reduced species imparting MIF-S signatures (Farquhar and Wing 2003). The oxidized species have been shown to have both positive and negative $\delta^{33}S$ values, but reduced species have just positive values (Paris et al. 2014). These MIF-S signatures are preserved in rocks which interacted with the Archean atmosphere, mainly sediments, but also in magmatic rocks that incorporated sedimentary rocks or components of recycled oceanic lithosphere (LaFlamme et al. 2018a). Therefore, analysing $\delta^{34}S$ in combination with $\delta^{33}S$ can be a useful tool to evaluate fluid origin and evolution in Archean ore deposits (e.g., LaFlamme et al. 2018b).

2 Geology

2.1 Regional Geology

The Abitibi straddles the border between Ontario and Quebec in eastern Canada, and consists of east-west trending successions of folded

Neoarchean volcanic and sedimentary rocks settled between or faulted against intrusive domes and stocks (e.g., Monecke et al. 2017). Most gold deposits occur proximal to major E-W trending transcrustal fault zones such as the Destor-Porcupine and Larder Lake-Cadillac faults in the southern Abitibi (Dubé and Mercier-Langevin 2020, and references therein).

The Fenelon deposit is located within the Harricana-Turgeon Belt (Lacroix 1990), the most north-western belt in the Abitibi, which is bisected by the Sunday Lake Deformation Zone (SLDZ); the latter is a major E-W fault zone analogous to those in the southern Abitibi (Figure 2). Despite hosting the Detour Lake gold mine, the single largest such deposit in Canada (~40 Moz past production + reserves + resources; Leite et al. 2020), the belt and its ore deposits have seen limited research, most of which has focused on Detour Lake (Castonguay et al. 2020, and references therein). This belt shares many characteristics with the southern Abitibi including similar large-scale E-W trending deformation zones, syn-volcanic and syn-tectonic magmatism, sedimentary basins, and mineralization and alteration styles.

2.2 Local Geology

There are few outcrops in the deposit area, and thus the geology is interpreted mostly from diamond drill hole and aeromagnetic data (Fig. 1). Based on the latter, the stratigraphic units appear to be arranged in NW-SE trending packages. The immediate deposit area is dominated by ~2707 Ma argillite, which grades into <2705 Ma conglomeratic quartz-wacke (Carter 2022) to the southwest. Proximal to the SLDZ is a wedge of polymictic conglomerate which resembles 'Timiskaming-type' conglomerates associated with major deformation zones in the southern Abitibi (e.g., Bleeker 2015).

The sedimentary rocks are intruded by and interlayered with several calc-alkaline intrusions. To the northwest of the deposit lies the Jeremie Pluton, a polyphase granodiorite to diorite (Faure 2015). The ~2697 Ma Jeremie Diorite, possibly linked genetically to the Jeremie Pluton, is an important host rock for Au mineralization (Carter 2022). Mafic dykes of pyroxenite, gabbro and leucogabbro cut the sedimentary rocks and Jeremie diorite and are locally spatially associated with gold mineralization.

A penetrative foliation occurs throughout the deposit area affecting all rock types. To the northeast of the deposit and within it, a NW-SE-trending subvertical foliation is dominant whereas to the southwest the steep foliation is NE-SW trending.

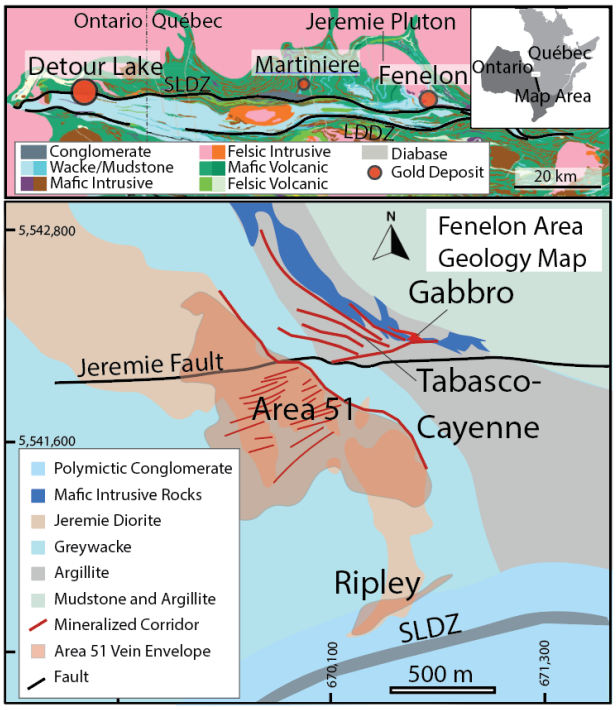

Figure 2. (Top) Geological map of the Harricana-Turgeon belt showing the locations of gold deposits (modified from Faure 2015). (Bottom) Fenelon deposit area geological map. The units are simplified, based on the geological model for the deposit interpreted from drill hole data. SLDZ – Sunday Lake Deformation zone, LDDZ – Lower Detour Deformation Zone. (Coordinates: UTM NAD83; zone 17).

2.3 Gold Mineralization

Gold mineralization at Fenelon is divided into several zones differentiated mainly by their host rocks and orientations (Figure 2). The Gabbro Zone consists of high-grade mineralization which follows steep SE-striking internal contacts and enclaves within a polyphase mafic sill. The Tabasco and Cayenne zones consist of steep SE-striking mineralized panels hosted in strained argillite that coalesce into the Contact Zone, which follows the near vertical contact of the Jeremie Diorite. There is an apparent spatial association between gold mineralization, graphitic argillite, and gabbroic intrusions in the Tabasco and Cayenne zones. Area 51 consists of multiple, parallel, ENE-striking, steeply dipping zones that are well mineralized in the Jeremie Diorite but also extend into the surrounding sedimentary rocks. To the south near the SLDZ is the Ripley zone which similarly consists of ENE-striking zones hosted mostly in a quartz diorite.

There are two main stages of mineralization at Fenelon. Stage 1 (M1) consists of sulphide-poor auriferous quartz veins with rare molybdenite. Stage 2 (M2) consists of sulphide-rich veins and lenses with three substages (Fig. 2): M2A is characterized by coarse-grained arsenopyrite; M2B comprises zoned and colloform pyrite; and M2C consists of intergrown pyrrhotite, chalcopyrite, sphalerite, arsenopyrite, Bi-tellurides, and native gold.

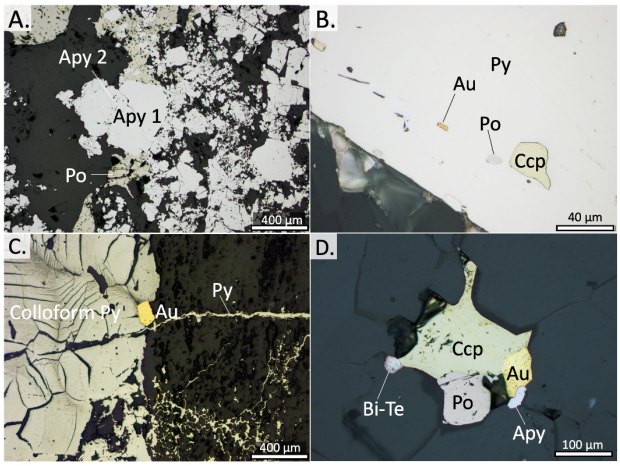

Figure 3. Reflected light images of sulphide mineralization from Fenelon. A) Coarse-grained M2A arsenopyrite (Apy 1) with fine-grained M2C arsenopyrite overgrowths (Apy 2) from Area 51. B) Zoned M2B pyrite with inclusions of gold (Au), pyrite (Py), pyrrhotite (Po), and chalcopyrite (Ccp) from Area 51. C) Colloform M2B pyrite associated with gold, and cut by pyrite veinlets in the Gabbro Zone. D) M2C gold intergrown with chalcopyrite, pyrrhotite, arsenopyrite and Bi-telluride (Bi-Te) from the Contact Zone.

3 Multiple S Isotopes

3.1 Methodology

Following a wholistic study of the mineralization at several scales, 17 representative polished sections that include the major ore zones were selected for isotopic analyses. From these, 19 regions of interest (2-4 mm diameter) were cored and arranged along with Canadian Centre for Isotopic Microanalysis (CCIM) reference materials into 25 mm diameter epoxy mounts. Backscattered electron (BSE) characterization of the samples was conducted by scanning electron microscopy (SEM) utilizing a Zeiss EVO M15 instrument.

Sulphur isotope ratios ($^{34}S/^{33}S/^{32}S$) were determined using the IMS-1280 multi-collector ion microprobe at the CCIM at the University of Alberta, Canada. Primary beam conditions utilized 20 keV $^{133}Cs^+$ ions focused to form a probe with a diameter of ~10 µm and beam current of ~ 1.2 nA. All secondary ions (^{32}S-, ^{33}S-, and ^{34}S-) were analysed simultaneously in Faraday cups (L2 using 1010Ω amplifier, L1 with 1012 Ω, and H1 with 1011 Ω, respectively) at a mass resolution of ~4000, sufficient to resolve potential isobaric interferences. The analytical protocol involved interspersing analyses of unknowns with CCIM primary reference material for pyrite (CCIM S0302A, $\delta^{34}S_{VCDT}$ = 0.0 ±0.2‰), pyrrhotite (S0322, $\delta^{34}S_{VCDT}$ = +1.2 ±0.1‰), chalcopyrite (CCIM S0321, $\delta^{34}S_{VCDT}$ = +0.2 ±0.2‰), and arsenopyrite (S0551, $\delta^{34}S_{VCDT}$ = +1.8 ±0.2‰). All primary reference materials have no known significant mass independent isotopic anomalies, i.e., $\Delta^{33}S$ = 0.

The standard deviations of $^{33}S/^{32}S$-, $^{34}S/^{32}S$-, and $\Delta^{33}S$ for the pyrite, pyrrhotite, chalcopyrite, and arsenopyrite reference materials ranged from 0.05‰ to 0.1‰. Propagated uncertainties in $\delta^{33}S_{VCDT}$ and $\delta^{34}S_{VCDT}$ are reported at 95% confidence level (2σ) and have typical values of ±0.15 – 0.3‰, and for $\Delta^{33}S$ are assigned a conservative ± 0.15‰.

3.2 Results

Multiple S isotope data are presented in Figure 4 and Figure **5**. Data for arsenopyrite (n = 26) show a narrow range of $\delta^{34}S$ (-1.0 to +3.6‰, avg. = +2.4‰) with all $\Delta^{33}S$ values near zero (-0.12 to +0.15‰, -0.02‰ avg.). In sample GRAB-5080-001 (Figure 3A) from Area 51, two stages of arsenopyrite were analysed (M2A and M2C). The $\delta^{34}S$ values for M2C Apy (+2.6-+3.6‰, +3.6‰ avg., n=6) are higher than those for M2A Apy (+1.5-+2.9‰, +2.4‰ avg., n=4).

Data for M2B pyrite show a consistent trend wherein $\delta^{34}S$ increases from core (+0.8 to +2.9‰, +1.7‰ avg.) to rim (+2.7 to +5.0‰, +3.6‰ avg.). Data for sample D00116475D indicate that the growth zone with Au, pyrrhotite and chalcopyrite inclusions has elevated $\delta^{34}S$ (+2.4-+3.3‰, +3.0‰ avg.) relative to earlier growth stages. Despite the variations in $\delta^{34}S$, $\Delta^{33}S$ is consistently near zero showing no evidence of MIF-S (-0.15 to +0.12‰, 0.00 avg.).

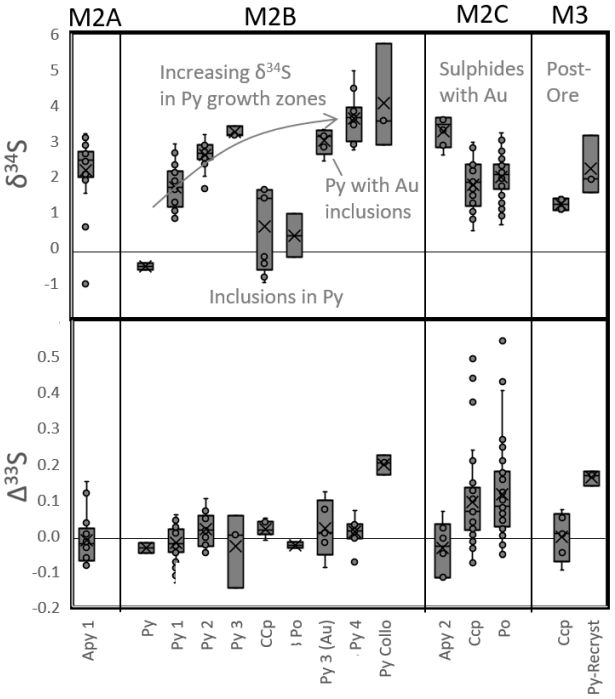

Figure 4. Whisker plots of multiple S isotope data grouped by paragenetic stage (M2A, M2B, M2C, M3) and sulphide phase. For M2B pyrite, $\delta^{34}S$ increases from core (py 1) to rim (py 2), yet $\Delta^{33}S$ stays near zero. The $\Delta^{33}S$ values for M2C chalcopyrite and pyrrhotite are elevated. Py – pyrite, Apy – arsenopyrite, Ccp – chalcopyrite, Po – pyrrhotite, Py – collo – Colloform pyrite.

Colloform pyrite from the Gabbro Zone yields positive $\delta^{34}S$ values (+2.9 to +5.7‰, +4.0‰ avg.)

and includes the highest $\delta^{34}S$ measured in this study. Data for post-ore pyrite that recrystallized from colloform pyrite indicates positive but slightly lower $\delta^{34}S$ values (+1.5-+3.2‰, +2.2‰ avg.). Both the colloform and recrystallized pyrite have $\Delta^{33}S$ values which are slightly positive (+0.14-+0.22‰, +0.18‰ avg.).

Chalcopyrite and pyrrhotite data cluster around $\delta^{34}S$ of ~+2.5‰ and $\Delta^{33}S$ of ~ 0‰, but some of the date appear to define a linear trend with a negative slope (Figure 5). Data for samples from the Tabasco and Contact zones have the most positive $\Delta^{33}S$ values (+0.37 to +0.54‰, +0.44 avg., and +0.13 to +0.28‰, +0.23‰ avg., respectively), indicating significant MIF-S. Inclusions of pyrrhotite and chalcopyrite in the zoned M2B pyrite from Area 51 have lower $\delta^{34}S$ values (-1.0 to +1.6‰, +1.1‰ average) than the rest of the data, and near zero $\Delta^{33}S$ (-0.10 to +0.07‰, 0.00‰ avg.). The inclusion analyses, therefore, diverge from the negative $\delta^{34}S$ vs. $\Delta^{33}S$ trend and do not show evidence of MIF-S.

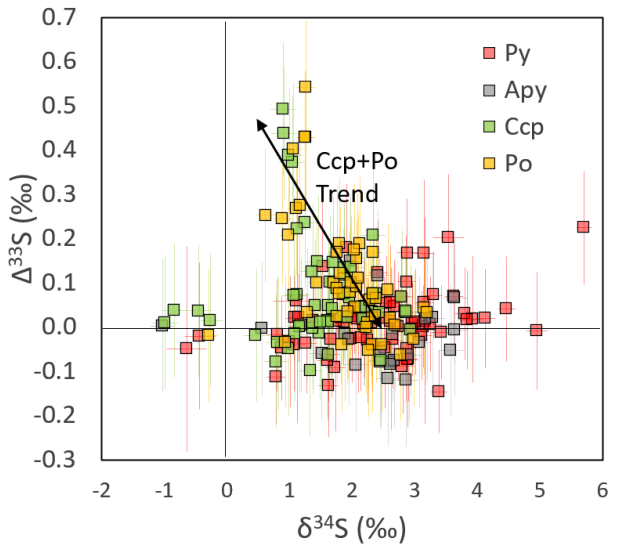

Figure 5. $\delta^{34}S$ vs. $\Delta^{33}S$ for all analyses coloured by mineral. Py – pyrite, Apy – arsenopyrite, Ccp – chalcopyrite, Po – pyrrhotite.

4 Conclusions

Multiple S isotope data indicate that gold mineralisation at Fenelon formed from a fluid dominated by mantle sulphur. This reservoir mixed with a small component of sedimentary S in the later stages of mineralisation, in association with elevated base metal concentrations. This is compatible with the main ore fluid being magmatic or metamorphic but derived from magmatic rocks (e.g., basalts). This fluid mixed with sedimentary S from either the country rock or metamorphic fluids with a sedimentary S component. A genetic model with predominantly magmatic fluids is favoured over metamorphic fluids to explain the elevated base metals in the deposit. Therefore, Fenelon is interpreted as a syn-orogenic intrusion-related deposit. It may be an example of a less common magmatic fluid-dominated endmember on a spectrum of orogenic deposits that form from predominantly metamorphic fluids, but with variable proportions of magmatic fluids.

Acknowledgements

This study was funded by Wallbridge Mining Company, the Targeted Geoscience Initiative (Geological Survey of Canada), and a NSERC Alliance Grant. We thank Wallbridge's exploration geology team for providing their expertise and support during the research.

References

Bleeker W (2015) Synorogenic gold mineralization in granite-greenstone terranes: the deep connection between extension, major faults, synorogenic clastic basins, magmatism, thrust inversion, and long-term preservation. Geological Survey of Canada, Open File 7852, pp 24–47

Carter J (2022) The geology of the Fenelon Deposit, Québec, Canada. M.Sc. Thesis, University of Toronto

Castonguay S, Dubé B, Wodicka N, Mercier-Langevin P (2020) Geological setting and gold mineralization associated with the Sunday Lake and Lower Detour deformation zones, northwestern Abitibi greenstone belt, Ontario and Quebec. Geological Survey of Canada, Open File 8712, pp 127–142

Dubé B, Mercier-Langevin P (2020) Gold Deposits of the Archean Abitibi Greenstone Belt, Canada. SEG Special Publications 23, pp 669–708.

Farquhar J, Wing BA (2003) Multiple sulfur isotopes and the evolution of the atmosphere. Earth Planet Sci Lett 213:1–13. https://doi.org/10.1016/S0012-821X(03)00296-6

Farquhar J, Wu N, Canfield DE, Oduro H (2010) Connections between sulfur cycle evolution, sulfur isotopes, sediments, and base metal sulfide deposits. Economic Geology 105:509–533.

Faure S (2015) Prolongement de la faille Sunday Lake (Mine Detour Gold, Ont) au Québec et son potentiel pour les minéralisations aurifères et en métaux de base. CONSOREM, rapport 2013-02

Goldfarb RJ, Pitcairn I (2022) Orogenic gold: is a genetic association with magmatism realistic? Miner Depos. https://doi.org/10.1007/s00126-022-01146-8

Hutchison W, Finch AA, Boyce AJ (2020) The sulfur isotope evolution of magmatic-hydrothermal fluids: insights into ore-forming processes. Geochim Cosmochim Acta 288:176–198. https://doi.org/10.1016/j.gca.2020.07.042

Lacroix S (1990) Géologie de la région des rivières Turgeon et Théo. Ministère des ressources naturelles du Québec, MB 90-28

LaFlamme C, Fiorentini ML, Lindsay MD, Bui TH (2018a) Atmospheric sulfur is recycled to the crystalline continental crust during supercontinent formation. Nat Commun 9. https://doi.org/10.1038/s41467-018-06691-3

LaFlamme C, Sugiono D, Thébaud N, et al (2018) Multiple sulfur isotopes monitor fluid evolution of an Archean orogenic gold deposit. Geochim Cosmochim Acta 222:436–446. https://doi.org/10.1016/j.gca.2017.11.003

Leite A, Dupont J-F, Raizman V, Fournier PA (2020) Detour lake operation Ontario, Canada NI 43-101 technical report

Monecke T, Mercier-Langevin P, Dubé B, Frieman BM (2017) Geology of the Abitibi Greenstone Belt. Reviews in Economic Geology 19:7–49

Paris G, Adkins JF, Sessions AL, et al (2014) Neoarchean carbonate-associated sulfate records positive δ33S anomalies. Science (1979) 346:739–741. https://doi.org/10.1126/science.1258211

Gold mineralizing fluids at the Imonga mineralization in the eastern part of the Democratic Republic of Congo

Inge Cools[1], Philippe Muchez[1], Stijn Dewaele[2]
[1]KU Leuven, Department of Earth & Environmental Sciences, Belgium
[2]Ghent University, Department of Geology, Belgium

Abstract. In order to understand the origin of the gold mineralizing fluid in Central Africa, the formation history of the quartz veins hosted gold mineralization at Imonga (eastern Democratic Republic of Congo) has been studied. Imonga is part of a metallogenic province known to host various types of mineralization, including Sn-W-Nb-Ta-Li-Au. The characterization of the mineralizing fluid comprises a detailed study of the paragenesis of the mineralization, microthermometry, Raman spectroscopy and modelling. The analysis of fluid inclusions in the mineralized quartz veins indicates an H_2O-NaCl-KCl-CO_2 fluid composition and a CO_2-N_2-CH_4(-H_2S) gaseous system, which is compatible with a metamorphic origin of the fluid. The presence of H_2S is characteristic for fluids carrying Au as reduced sulfur complexes. Calculated fluid salinity values range between 3.1 and 5.2 eq. wt% NaCl. The P-T formation window is proposed to range from 350°C to 400°C, with at 350°C an upper lithostatic pressure limit of 240 MPa, a burial depth of 9.2 km, and a lower hydrostatic pressure limit of 90 MPa. The corresponding density ranges between 0.78 g/cc and 0.91 g/cc. All observations allow the classification of the gold mineralization at Imonga as an orogenic gold deposit.

1 Introduction and geological setting

The Maniema province in the Democratic Republic of Congo (DRC) is part of the Central Africa Great Lakes area, well known for the occurrence of various types of mineralization, of which many are rich in elements critical for a high-tech and green industry. This metallogenic province also features substantial gold mineralization, of which the geological history is largely unknown. Previous studies of Walemba et al. (2004) and Fernandez-Alonso et al. (2012) linked the formation of the gold mineralization to the assembly of Gondwana, however, more recent studies propose an early Neoproterozoic timing linked to the assembly of Rodinia (Wouters et al. 2020).

In order to understand orogenic gold deposits in metamorphic belts, a thorough knowledge concerning the deformation, metamorphism and mineralization phases, age of the mineralization, characteristics and source of the mineralizing fluid, the architecture of the hydrothermal system and deposition mechanisms are required (Groves et al. 2003).

To enhance the knowledge on orogenic gold mineralizing fluids in Central Africa, more specifically in the Western Domain (WD) of the Karagwe-Ankole Belt (KAB), deposits and prospects within this area are being studied, among which the Imonga prospect. Besides a preliminary study of exploration drill cores and previous knowledge regarding gold mineralization at Imonga formulated by Van Eykeren (1950) and Kazmitcheff (1954, 1961), no in-depth studies concerning the gold mineralization at Imonga were carried out. The aim of this study is to characterize the mineralizing fluids and to deduce the precipitation conditions of the gold.

1.1 Geological setting

From a geological point of view, the southern part of Maniema is a complex area where the Mesoproterozoic Karagwe-Ankole Belt (KAB), Kibara Belt (KIB) and the Paleoproterozoic Rusizi-Ubende Shear Belt (RUB) meet (Figure 1) (Fernandez-Alonso et al. 2012). Within the KAB, two distinct structural domains are identified: (1) the Western Domain (WD), occurring in Rwanda, Burundi, Uganda and the DRC provinces of Kivu and Maniema, and (2) the Eastern Domain (ED) in Burundi and NW Tanzania (Tack et al. 2010).

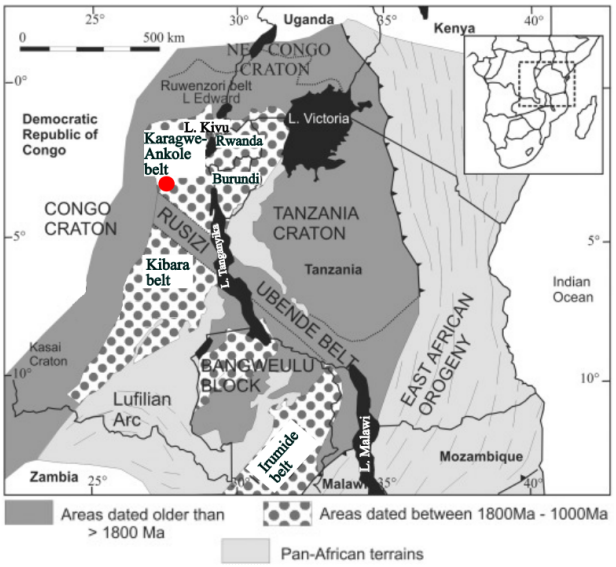

Figure 1. Tectonic setting of the KIB and the KAB in Central Africa (modified after Dewaele et al. 2015). The red dot indicates the study area.

1.2 The Imonga mine and prospect

The Imonga mine and prospect are located in the Maniema province, close to the border with South Kivu. This region hosts numerous gold mineralization of which some have been actively mined. The formation conditions of gold deposit, e.g., precipitation mechanism and P-T conditions, and the source of gold mineralization have, however, not been previously studied.

The Imonga prospect is part of the Imonga mine site (3°35'40.9"S 27°03'16.2"E) where alluvial and eluvial gold deposits were actively mined from 1931 until 1958 (Kazmitcheff 1961). Drilling was conducted near the mine site in order to perform a preliminary exploration (Kazmitcheff 1961). Representative rock samples from two cores have been preserved at the Royal Museum of Central Africa (RMCA) in Belgium.

2 Petrography and paragenesis

The current study started with a detailed petrographic and paragenetic study, of which results are discussed in Cools et al. (2022).

The host rocks of Imonga have been strongly altered, deformed and underwent foliation to the greenschist metamorphic grade. Post-foliation porphyroblasts of different minerals have been observed, with the characteristic occurrence of andalusite porphyroblasts. Four different generations of veins have been identified. The second vein generation (V2) consists of post-foliation quartz-ferroan dolomite-chlorite veins, that are strongly associated with sulfide (pyrite, chalcopyrite and arsenopyrite) and gold mineralization. This generation displays quartz deformation structures such as crystalplastic deformation (undulose extinction, bulging and subgrain recrystallization), as well as variation in vein growth morphology and inclusion bands which indicate crack-seal mechanisms. The third vein generation (V3) are post-foliation quartz-ferroan calcite-chlorite veins, strongly associated with sulfide (pyrite and chalcopyrite) mineralization.

Andalusite porphyroblasts in greenschist facies are thought to have formed post-foliation, both prior and after the second vein generation, thus closely related with the gold mineralization and can therefore be used to constrain the P-T window.

3 Methodology

The nature of the mineralizing fluid related to the gold mineralization has been studied by analyzing fluid inclusions (FI) in quartz crystals in three samples of V2 (IM78, IM79 and IM80) and one sample of V3 (IM77).

The analysis of the mineralizing fluid involved (1) a petrographic study of primary FI's, followed by (2) a microthermometric study using a Linkam THMSG 600 heating-freezing stage, mounted on an Olympus BX51 microscope, and (3) the analysis of the composition of the gaseous phases by Raman spectroscopy using a Horiba Labram HR Evolution, linked to an Olympus BX41 microscope. All the obtained data were used to (4) model the fluid characteristics and to (5) determine the P-T formation conditions using isochores.

4 Results and discussion

4.1 Fluid inclusion petrography

Two main types of primary FI's were distinguished in the veins studied: (1) FI's that consist of two phases, a liquid and a gaseous phase; (2) FI's that consist of three phases at room temperature, namely two liquid phases and a vapor phase. Both fluid inclusion types occur in the second vein generation, while in the third vein generation almost exclusively two-phase inclusions have been observed.

4.2 Microthermometry

Results of the microthermometric analysis have been incorporated in Table 1. The observed temperatures of phase transitions provide information regarding the composition of the fluid: (1) for both V2 and V3, Tm_{CO2} ranges from - 59.9 to - 56.6°C. Observations of Tm_{CO2} at lower temperatures than for a pure carbonic phase (- 56.6°C) indicate the presence of other gaseous components besides CO_2 (Shepherd et al. 1985). These additional gases have been identified by Raman spectroscopy of the gaseous phase (section 4.3); (2) Tfm ranges for both vein generations from - 24.5 to - 20.1°C. The comparison of the observed Tfm with eutectic temperatures of known systems (Goldstein and Reynolds 1994), indicates the presence of an H_2O-NaCl-KCl fluid. Eutectic temperatures lower than - 23.5°C indicate the presence of divalent salt cations; (3) final ice melting differs for both vein generations. Tm_{ice} of V2 ranges from - 8.7°C to - 5.4°C, while data for V3 vary between - 7.6°C and - 2.1°C; (4) Tm_{clath} ranges from + 6.4°C to + 10°C; (5) Th_{CO2} has only been observed for three-phase FI's of V2, ranging from + 27.5°C to + 31.2°C; (6) for V3, the low number of observations of Tm_{CO2} and Tm_{clath}, as well as the lack of Th_{CO2} observations, could indicate a limited occurrence of gaseous CO_2; (7) for both vein generations, the minimum formation temperature is initially estimated to lie between + 210°C and + 250°C, based on the Th_{tot}.

4.3 Raman spectroscopy

Molar fractions of CO_2, N_2 and CH_4 have been calculated based on peak area calculations of Raman spectroscopic analysis (Burke 2001; Frezzotti et al. 2012). Raman spectroscopic analyses show a range in the gaseous composition of V2 inclusions between 69 and 99 mol% CO_2, 0 and 31 mol% N_2 and between 0 and 5 mol% CH_4 with minor H_2S/HS^-. This composition is compatible with a metamorphic origin of the fluid (Dewaele et al. 2004; Kenis et al. 2005). Increasing N_2-content, linked to a decreasing CO_2-content, is interpreted to result from reactions during metamorphism and fluid-rock interaction during circulation of the fluids (Kenis et al. 2005).

The composition of the V3 inclusions ranges between 60 and 100 mol% N_2, 0 and 35 mol% CO_2 and between 0 and 10 mol% CH_4. None of the spectra indicates the presence of H_2S/HS^-. The high

N_2 content could indicate an increased influence of water-rock interaction (Kenis et al. 2005).

Table 1. Overview of the microthermometric data[1].

	V2	V3
Tm_{CO2}	- 59.3 to - 56.6°C $\bar{X}$ = - 56.9°C n = 73	- 57.7 to - 56.7°C $\bar{X}$ = - 57.0°C n = 3
Tfm	- 24.5 to - 20.1°C $\bar{X}$ = - 22.7°C n = 227	- 24.4 to - 20.1°C $\bar{X}$ = - 22.9°C n = 78
Tm_{ice}	- 8.7 to - 5.4°C $\bar{X}$ = - 6.8°C n = 189	- 7.6 to - 2.1°C $\bar{X}$ = - 5.5°C n = 84
Tm_{clath}	+ 6.4 to + 8.9°C $\bar{X}$ = + 7.4°C n = 73	+ 6.9 to + 10 °C $\bar{X}$ = + 8.9°C n = 4
Th_{CO2}	+ 27.5 to + 31.2°C $\bar{X}$ = + 29.9°C n = 17	No observations
Th_{tot}	+ 207 to + 250°C n = 43	+ 210 to + 250°C n = 9
Salinity (eq. wt% NaCl)	3.1 to 5.2 $\bar{X}$ = 4.4 n = 65	3.5 to 4.4 $\bar{X}$ = 4.0 n = 4
Density (g/cc)	0.74 to 0.95 g/cc $\bar{X}$ = 0.83 g/cc n = 70	0.85 to 0.90 g/cc $\bar{X}$ = 0.87 g/cc n = 4

[1] n = number of FI's; Tm_{CO2} = final melting of the carbonic phase; Tfm = first melting of the solid aqueous phase; Tm_{ice} = final ice melting; Tm_{clath} = melting of the clathrate; Th_{CO2} = homogenization of carbonic phases into the liquid phase; Th_{tot} = total homogenization.

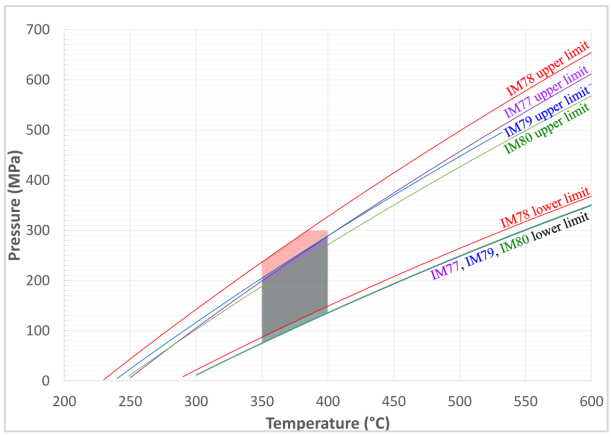

Figure 2. The upper and lower limit isochores, obtained by the 'Isoc' program (Bakker 1997, 2003) for each sample. The areas indicate the P-T formation conditions.

4.4 Fluid characterization and formation conditions

All obtained results have been used to characterize and model the fluid properties. The combination of the microthermometric and Raman spectroscopic results are indicative of the presence of a fluid with an H_2O-NaCl-KCl-CO_2-N_2-CH_4-H_2S composition.

Calculated salinity and density values, by the program 'Ice' (Bakker 1997, 2003), for both vein generations fall within the same range (Table 1). Salinity values range from 3.1 to 5.2 eq. wt% NaCl. The density values range from 0.74 to 0.95 g/cc.

Based on the isochores, constructed by the program 'Isoc' (Bakker 1997, 2003), the P-T conditions for the formation conditions of the two vein generations studied, have been determined. Constraints on the P-T window include: (1) the minimum formation temperature based on Th_{tot} which ranges between +200°C and +250°C; (2) the metamorphic grade of greenschist metamorphism characterized by andalusite porphyroblasts indicating a P-T range between 350°C and 450°C and 50 MPa and 300 MPa, respectively (Bushmin and Glebovitsky 2008); (3) quartz deformation structures that have been observed which are typically formed at temperatures from 300°C to 400°C (Passchier and Trouw 2005). The combination of all these constraints results in an applied temperature window ranging from 350°C to 400°C.

The P-T formation conditions deduced for both V2 and V3 fall within the same range (Figure 2) . For example, the isochores obtained for sample IM78 of V2 are discussed (Figure 2). At the proposed temperature of 350°C, an upper, lithostatic pressure limit of 240 MPa is deduced from the top isochore, corresponding to a depth of 9.2 km. The lower, hydrostatic, pressure limit corresponding to this depth is 90 MPa. The density of the fluids within this P-T formation window ranges from 0.78 up to 0.91 g/cc, with salinity between 3.1 to 5.2 eq. wt% NaCl. Combination of all the samples yields a highest upper limit of 240 MPa (9.2 km) and a lowest lower limit of 72 MPa (Figure 2).

5 Discussion and conclusion

Gold mineralization at Imonga has been observed in post-foliation V2 quartz-ferroan dolomite-chlorite veins, that formed closely related to andalusite porphyroblasts. It is associated with sulfide mineralization, including pyrite and chalcopyrite. The mineralizing fluid has an H_2O-NaCl-KCl-CO_2-N_2-CH_4-H_2S composition and a temperature between 350 and 400°C, compatible with a metamorphic origin (Kenis et al. 2005). The salinity of this fluid ranges from 3.1 to 5.2 eq. wt% NaCl, with a density between 0.87 and 0.94 g/cc. The presence of H_2S is characteristic for fluids carrying Au as an $Au(HS)^-_2$ or $Au(HS)_0$ complex (Robb 2005). The variation in the fluid pressure between 90 and 240 MPa can be explained as (cyclic) fluctuations between the lithostatic and hydrostatic pressure during vein development, as described by the fault-valve model for mesothermal and orogenic gold systems (Sibson et al. 1988).

An orogenic origin is proposed for the gold mineralization at Imonga, based on the correspondence with the fluid characteristics of orogenic gold in metamorphic belts, such as salinity and P-T formation conditions (Groves et al. 2003).

Gold at Imonga was most likely transported by gold-sulfur complexes. The close association between the gold and Fe-sulfides indicates that these complexes could have been destabilized through interaction of the mineralizing fluid with the iron-bearing host rock. Such interaction not only explains the precipitation of gold, but also of the Fe-sulfides. However, the variation in fluid pressure observed and which likely resulted from fault-valve activity, could also have contributed to the precipitation of gold (Mikucki 1998).

Acknowledgements

We would like to thank Herman Nijs (KU Leuven) for carefully preparing the thin, polished, and double polished sections. We are grateful to Florias Mees and the RMCA for providing access to the Imonga samples. The Raman equipment was acquired via the medium-scale research infrastructure FWO grant Raman-SIM2 (number I000718N).

References

Bakker, R.J. (1997) Clathrates: Computer programs to calculate fluid inclusion V- X properties using clathrate melting temperatures. Computers & Geosciences 23(1): 1–18. https://doi.org/10.1016/S0098-3004(96)00073-8

Bakker, R.J. (2003) Package FLUIDS 1. Computer programs for analysis of fluid inclusion data and for modelling bulk fluid properties. Chemical Geology 194(1):3–23. https://doi.org/10.1016/S0009-2541(02)00268-1

Burke, E.A.J. (2001) Raman microspectrometry of fluid inclusions. Lithos 55(1):139–158. https://doi.org/10.1016/S0024-4937(00)00043-8

Bushmin, S., Glebovitsky, V. (2008) Scheme of Mineral Facies of Metamorphic Rocks. Geology of Ore Deposits 50:659-669. https://doi.org/10.1134/S1075701508080011

Cools, I., Muchez, Ph., Dewaele, S. (2022) Mineralogical and geochemical study of the Au mineralization at Imonga, Maniema (DRC). Geologica Belgica vol. 25, nr. 3-4:185-190. https://popups.uliege.be/1374-8505/index.php?id=7030.

Dewaele, S., Muchez, P., Banks, D. A. (2004) Fluid evolution along multistage composite fault systems at the southern margin of the lower Palaeozoic Anglo-Brabant fold belt, Belgium. Geofluids 4(4):341–356. https://doi.org/10.1111/j.1468-8123.2004.00096.x

Dewaele, S., Hulsbosch, N., Cryns, Y., Boyce, A., Burgess, R., Muchez, P. (2015) Geological setting and timing of the world-class Sn, Nb-Ta and Li mineralization of Manono-Kitotolo (Katanga, Democratic Republic of Congo). Ore Geology Reviews 72:373-390. https://doi.org/10.1016/j.oregeorev.2015.07.004

Fernandez-Alonso, M., Cutten, H., De Waele, B., Tack, L., Tahon, A., Baudet, D., Barrit, S.D. (2012) The Mesoproterozoic Karagwe-Ankole Belt (formerly the NE Kibara Belt): the result of prolonged extensional intracratonic basin development punctuated by two short-lived far-field compressional events. Precambrian Research 216:63-86. https://doi.org/10.1016/j.precamres.2012.06.007

Frezzotti, M.L., Tecce, F., Casagli, A. (2012) Raman spectroscopy for fluid inclusion analysis. Journal of Geochemical Exploration 112:1–20. https://doi.org/10.1016/j.gexplo.2011.09.009

Goldstein, R.H., Reynolds, T.J. (1994) Systematics of fluid inclusions in diagenetic minerals. Society for Sedimentary Geology, SEPM Short Course Notes 31. https://doi.org/10.2110/scn.94.31

Groves, D.I., Goldfarb, R.J., Robert, F., Hart, C.J.R. (2003) Gold deposits in metamorphic belts; overview of current understanding, outstanding problems, future research, and exploration significance. Economic Geology and the Bulletin of the Society of Economic Geologists 98(1):1-29. http://dx.doi.org/10.2113/gsecongeo.98.1.1

Kazmitcheff, A. (1954) Etude des sondages d'Imonga & Résultats d'analyse et problème de l'or d'Imonga. Service des prospections Kampene, à COBELMIN. N° S.P. 20/54.

Kazmitcheff, A. (1961) Les roches albitiques et carbonatés des sondages d'Imonga (Maniema). Mémoires de l'Institut Géologique de l'université de Louvain. Tome XXII:69-96.

Kenis, I., Muchez, P., Verhaert, G., Boyce, A., & Sintubin, M. (2005) Fluid evolution during burial and Variscan deformation in the Lower Devonian rocks of the High Ardenne slate belt (Belgium); sources and causes of high-salinity and C-O-H-N fluids. Contributions to Mineralogy and Petrology 150(1): 102-118. https://doi.org/10.1007/s00410-005-0008-9

Mikucki, E.J. (1998) Hydrothermal transport and depositional processes in Archaean lode-gold systems: A review. Ore Geology Reviews 13:307–321. https://doi.org/10.1016/S0169-1368(97)00025-5

Passchier, C., Trouw, R. (2005) Microtectonics (2nd, Revised and Enlarged ed.). Springer, Berlin / Heidelberg. https://doi.org/10.1007/3-540-29359-0

Robb, L. (2005) Introduction to ore-forming processes. Blackwell, London.

Shepherd, T.J., Rankin, A.H. and Alderton, D.H. (1985) A Practical Guide to Fluid Inclusion Studies. Blackie and Sons, Glasgow.

Sibson, R., Robert, F., Poulsen, K. (1988) High-angle reverse faults, fluid-pressure cycling, and mesothermal gold-quartz deposits. Geology (Boulder) 16(6):551-555. https://doi.org/10.1130/0091-7613(1988)016<0551:HARFFP>2.3.CO;2

Tack, L., Wingate, M.T.D., De Waele, B., Meert, J., Belousova, E., Griffin, B., Tahon, A., Fernandez-Alonso, M. (2010) The 1375 Ma "Kibaran event" in Central Africa: Prominent emplacement of bimodal magmatism under extensional regime. Precambrian Research 180:63–84. https://doi.org/10.1016/j.precamres.2010.02.022

Van Eykeren, H. (1950) Les Gisements Aurifères de Mukukutshi, Itabatshi, Imonga et Katulu. Cobelmin – A.G.A., Rapport 6/50, RMCA Archives.

Walemba, K.M.A., Viljoen, M.J., Viljoen, R.P. (2004) Geological setting, genesis and evolution of the Twangiza gold deposit, Kivu, eastern D.R.Congo. in: Geoscience Africa 2004 Conference, Abstracts Volume 2,University of the Witwatersrand, Johannesburg, 12–16 July 2004, 682–683.

Wouters, S., Hulsbosch, N., Kaskes, P., Claeys, Ph., Dewaele, S., Melcher, F., Onuk, P., Muchez, Ph. (2020) Late orogenic gold mineralization in the western domain of the Karagwe-Ankole Belt (Central Africa): Auriferous quartz veins from the Byumba deposit (Rwanda). Ore Geology Reviews 125:103666. https://doi.org/10.1016/j.oregeorev.2020.103666

Timing of the Orogenic Jouhineva Au-Cu-Co and Huhta Au mineralization: Constraints from titanite U-Pb dating

Andressa A. Silva[1], Clifford G.C Patten[1], Jochen Kolb[1], Simon Hector[1], Benjamin Walter[1], Aratz Beranoaguirre[1], Elisabeth Eiche[1,2]
[1]Chair of Geochemistry and Economic Geology (EGG), Institute of Applied Geosciences (AGW), Karlsruhe Institute of Technology (KIT), Karlsruhe, Germany
[2]Laboratory for Environmental and Raw Materials Analysis (LERA), EGG-AGW, KIT Karlsruhe, Germany

Abstract. The Pojahnmaa Belt (PoB) hosts orogenic gold deposits with unusual metal contents. These deposits are hosted by metavolcanic and metasedimentary rocks and by similar structures as orogenic Au-only deposits. The reason for the different metal associations in the deposits is not well understood. This study investigates the Jouhineva Au-Cu-Co deposit and the Huhta Au occurrence from the PoB by combining in-situ titanite dating with detailed petrography. Six titanite types associated with the As-Au-Co and Cu-Au mineralization events were described and U-Pb dating from these titanite types was carried out. Jouhineva contains titanite associated with arsenopyrite veins ($Ttn_{1.1J}$), in the alteration halo ($Ttn_{1.2J}$), and with sericite-chlorite alteration (Ttn_{2J}). Huhta contains titanite in quartz-actinolite-pyrite-arsenopyrite veins ($Ttn_{1.1H}$) associated with arsenopyrite in the alteration halos ($Ttn_{1.2H}$). A titanite generation is associated with chalcopyrite, and sericite alteration (Ttn_{2H}). The dated titanite associated with the As-Au-(Co) mineralization was formed at 1854 ± 15 Ma ($Ttn_{1.1H}$) and 1816 ± 12 ($Ttn_{1.1J,}$ and $Ttn_{1.2J}$). The titanite associated with chalcopyrite and sericite-chlorite alteration was formed at 1760 ± 14 and 1744 ± 30 Ma (Ttn_{2H} and Ttn_{2J}, respectively). These ages indicate that the mineralization in the PoB was multi-stage and formed over, at least, three different periods.

1 Introduction

Orogenic Au deposits are generally considered Au-only deposits, where Au is the only commodity that can be mined economically (Goldfarb et al. 2005). Recently, several orogenic Au deposits have been discovered, particularly in Finland, which contain Cu, Co, Ni, Sb, U, and REE that are mined or of potential economic interest (Eilu 2015). Two hypotheses can account for this atypical endowment (1) an overprinted porphyry Cu mineralization by an orogenic Au one; or (2) a multi-stage orogenic Au mineralization (Eilu 2015, Patten et al. 2022, Hector et al. 2023).

The Paleoproterozoic Pohjanmaa Belt (PoB) is located in southwestern Finland and hosts the Jouhineva Au-Cu-Co deposit and the Huhta Au-only occurrence (Figure 1A-B; Hector et al. 2023). Jouhineva and Huhta are at a large scale controlled by the same structure, share the same host rocks, and are located close to felsic plutonic rocks (Figure 1C). We chose Jouhineva and Huhta because they form in the same conditions but have a different metal endowment. By comparing them we can characterize the key mechanisms. For this purpose, we combine careful petrography with in situ mineral dating.

2. Regional Geology

2.1 Pohjanmaa Belt

Finland sits within the Fennoscandia Shield which comprises the Archean Karelian provinces in the north, and Svecofennian domain in the south (Lahtinen et al. 2005). The PoB is located in the western Svecofennian domain (Lahtinen et al. 2005, 2014). This domain was formed during the Lapland-Savo, Fennian, Svecobaltic, and Nordic orogenies (Lahtinen et al. 2005). The Lapland-Savo orogeny (1930-1890 Ma) occurred due to the collision between Archean and Paleoproterozoic cratons, and the accretion of island arcs (Lahtinen et al. 2005). The Fennian orogeny (1900-1850 Ma) is related to the collision between the Keitele microcontinent and Karelian craton, and the accretion of volcano-sedimentary belts, such as the the PoB (Lahtinen et al. 2005, 2014). Between 1870 and 1850 Ma, associated with the Fennian Orogeny (Lahtinen et al. 2014), NNW-SSE shortening caused buckling of the orogen into the Bothnian orocline (Figure 1B; Lahtinen et al. 2005, 2014, 2018). The Svecobaltic orogen (1840-1780 Ma) was formed during the collision of the Sarmantia microcontinent with the southeastern margin of the Fennoscandian crustal segment. The Nordic orogen (1820-1770 Ma) was related to the collision of the Amazonia continent with the northwestern margin of Fennoscandia (Lahtinen et al. 2005). Orogenic collapse and voluminous intrusions between 1790 and 1770 Ma are followed by cooling until 1750 Ma (Lahtinen et al. 2018).

The Pohjanmaa Belt is characterized by volcano-sedimentary units that are stratigraphically divided into the Ylivieska and Eviärji fields (Kähkönen 2005). The Ylivieska field comprises volcanic, volcanoclastic, and related sedimentary rocks. The Evjärji field consists of graywackes, mudstone, shales, and volcanic rocks with mid-ocean-ridge basalt to within-plate basalt affinities (Kähkönen 2005). The metamorphic peak in the Ylieviaska field reached medium amphibolite facies conditions and in the Evijävi field lower-granulite facies conditions (Mäkitie 1999, 2000). Syn-orogenic granodiorite, granite, and tonalite of the Central Finland Granitoid Complex (CFGC) intruded the PoB at 1890-1870 Ga (Figure 1B-C; Nironen 2005). The Rautio batholith belongs to the Central Finland Granitoid Complex (Huhma 1986) and it has been suggested that

Rautio is related to a porphyry copper mineralization in the PoB (Geological Survey of Finland 2022a).

The Jouhineva deposit and Huhta occurrence are hosted in the Ylivieska field, located ~ 2.8 km from each other (Figure 1B, Geological Survey of Finland 2022a, 2022b). They are along with the same NW-SE trending structure and are located less than 1 km northeast of the Rautio Batholith. Both of them are hosted in metavolcanic rocks, plagioclase porphyrite, amphibolite, and biotite schist metamorphosed at lower amphibolite conditions (545 ± 30 °C) (Figure 1C; Hölttä et al. 2019; Hölttä and Heilimo 2017).

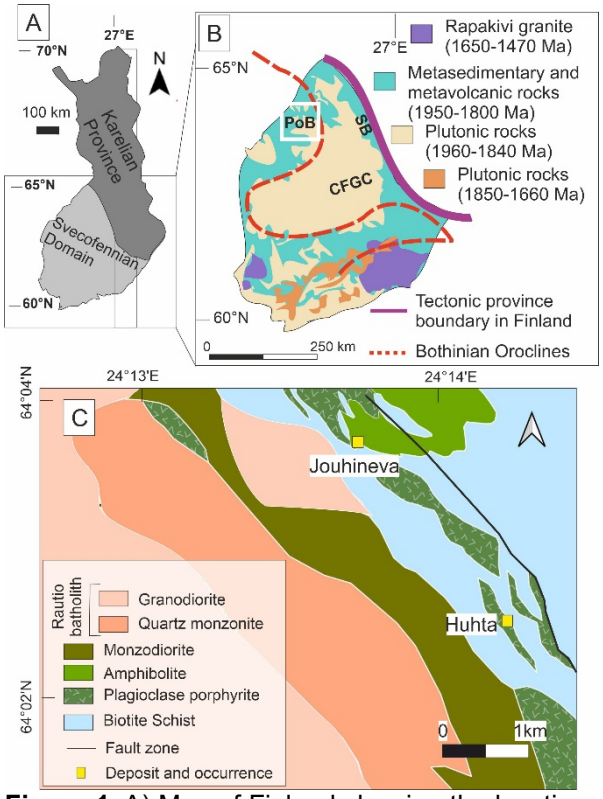

Figure 1. A) Map of Finland showing the location of the Archean Karelian province and Proterozoic Svecofennian Domain (Lahtinen et al. 2005). B) Geological map of the Svecofennian domain showing the Savo Belt (SB) localization. Central Finland Granitoid Complex (CFGC) and Pohjanmaa Belt (PoB) (Modified from Lahtinen et al. 2022). C) Geological map of the Jouhineva deposit, Huhta occurrence, and Rautio batholith. Map modified from Bedrock of Finland – DigiKP.

2.2 Jouhineva Au-Cu-Co deposit

The Jouhineva deposit contains total resources of 8.2 Mt Co, 3.6 Mt Cu, 3.5 t Ag and 0.39 t Au (Geological Survey of Finland, 2022a). Two ore mineral assemblages are described for Jouhineva: 1. Co- and Ni-bearing arsenopyrite with gold inclusions hosted in quartz veins; and 2. Chalcopyrite in actinolite-chlorite veins and free gold. This second vein type is associated with hydrothermal chlorite-sericite alteration in centimeter- to meter-scale wide halos around the auriferous veins (Hector et al. 2023).

2.3 Huhta Au occurrence

Huhta is characterized by mineralized quartz and actinolite veins (Geological Survey of Finland 2022b, Hector et al. 2023). It contains auriferous löllingite included in arsenopyrite hosted in quartz veins, and chalcopyrite-pyrite-pyrrhotite-sphalerite in actinolite-chlorite veinlets (Hector et al. 2023).

3. Sampling and Methodology

Four representative samples containing titanite associated with the different ore mineral assemblages were selected. Detailed transmitted and reflected optical microscopy was carried out to characterize the mineral assemblages and the titanite generations.

In-situ U-Pb dating of titanite by laser ablation-inductively coupled mass spectrometry (LA-ICP-MS) was done at the Laboratory for Environmental and Raw Materials (LERA) at the Karlsruhe Institute of Technology (KIT) using a Teledyne 193 nm Excimer Laser coupled with a ThermoFischer Scientific Element XR sector field mass spectrometer.

3 Results

3.1 Petrography and geochronology

3.1.1 Jouhineva Au-Cu-Co deposit

Two samples were studied from Jouhineva. The first sample has Co-bearing arsenopyrite, biotite, quartz, plagioclase, minor titanite-ilmenite, and sericite. Titanite ($Ttn_{1.1J}$) is subhedral to anhedral, 200-300 µm in diameter, and is on ilmenite rims. Titanite is often included in arsenopyrite. The alteration halo contains plagioclase, sericite, chalcopyrite, biotite, traces of arsenopyrite, titanite ($Ttn_{1.2J}$), ilmenite, actinolite, and pyrite. $Ttn_{1.2J}$ is intergrown with chalcopyrite. The second sample from Jouhineva is characterized by arsenopyrite and actinolite veins. The alteration halo contains plagioclase, quartz, actinolite, biotite, arsenopyrite, and traces of ilmenite. Biotite is strongly chloritized, plagioclase is strongly sericitized and ilmenite is replaced by titanite (Ttn_{2J}). The titanite associated with this alteration is anhedral, 300-500 µm in diameter, and is intergrown with pyrite.

$Ttn_{1.1J}$ and $Ttn_{1.2J}$ were analyzed (35 spots) and the concordia age for these spots is 1816 ± 12 (MSWD = 1.43, Figure 2A). The concordia age for Ttn_{2J} (9 spots) is 1744 ± 30 Ma (MSWD = 0.83, Figure 2B).

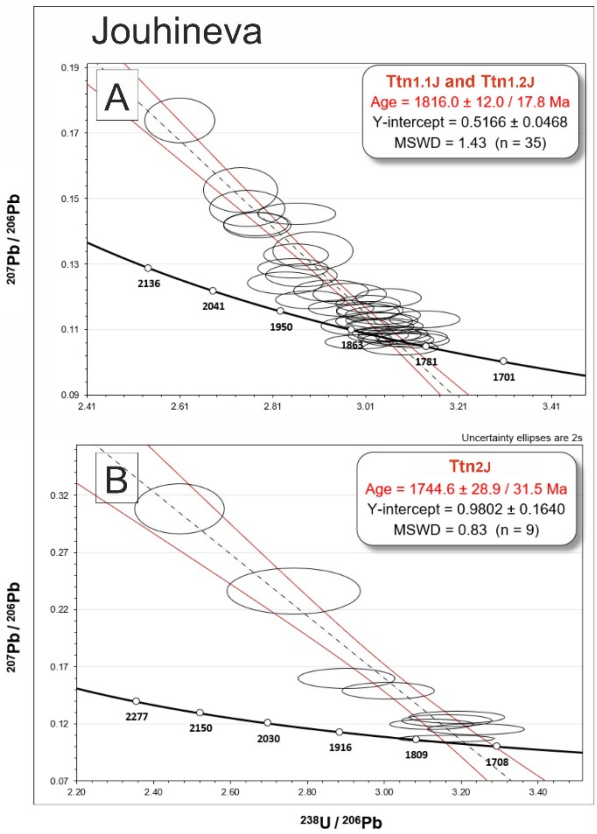

Figure 2. Titanite U-Pb concordia diagrams of A) $Ttn_{1.1J}$ and $Ttn_{1.2J}$ and B) Ttn_{2J}.

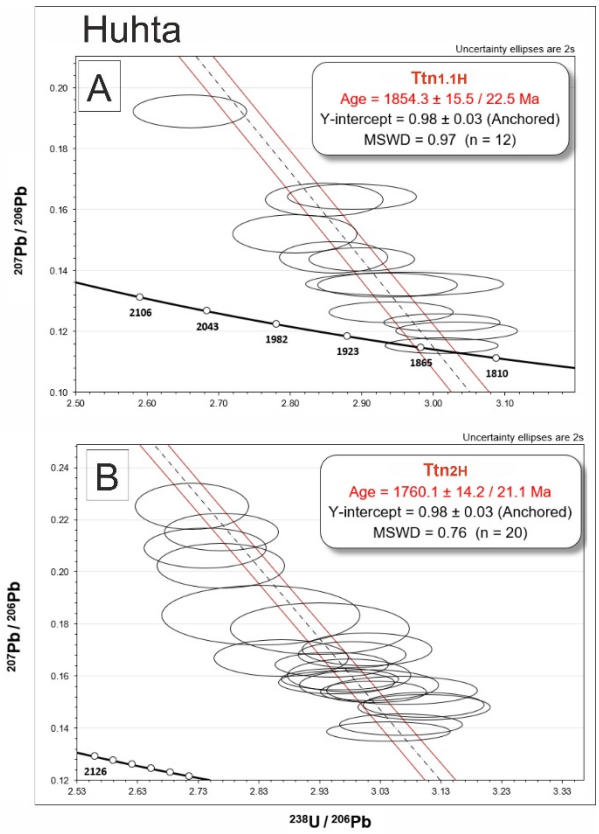

Figure 3. Titanite U-Pb concordia diagrams of A) $Ttn_{1.1H}$ and B) Ttn_{2H}.

3.1.2 Huhta Au occurrence

Two samples were studied from Huhta. The first sample contains vein-hosted arsenopyrite, quartz, pyrite, and prismatic actinolite$_1$ with traces of biotite and ilmenite replaced by titanite. Titanite ($Ttn_{1.1H}$) is subhedral, 100-300 µm in diameter, and is intergrown with pyrite and arsenopyrite.

The alteration halo of this vein consists of quartz, plagioclase, biotite, sericite, ilmenite rimmed by titanite, arsenopyrite, and traces of pyrite and chalcopyrite$_1$. Biotite forms clusters with titanite and arsenopyrite. Titanite ($Ttn_{1.2H}$) is 100-300 µm in diameter and anhedral.

The second sample from Huhta contains veins with actinolite$_2$, pyrrhotite, minor quartz, chalcopyrite$_2$, and ilmenite replaced by titanite. Actinolite$_2$ forms acicular grains obliquely oriented to prismatic actinolite$_1$. Titanite (Ttn_{2H}) is euhedral to subhedral, 100-300 µm in diameter, and is intergrown with chalcopyrite$_2$ and pyrrhotite. The alteration halo of this vein is characterized by sericite, chalcopyrite, pyrrhotite, and chlorite. Sericite replaces plagioclase and is associated with chalcopyrite$_2$.

The concordia age for the spots in $Ttn_{1.1H}$ is 1854 ± 15 Ma (MSWD = 0.97, Figure 3A). The concordia age from Ttn_{2H} (20 spots) is 1760 ±14 Ma (MSWD = 0.76, Figure 3B).

4. Discussion and conclusions

Our data indicate that the mineralization in Jouhineva and Huhta took place at least in three different periods: 1854 ± 15 Ma, 1816 ± 12 Ma, and a combined age between 1760 ±14 and 1744 ± 30 Ma.

Mineralization of quartz, arsenopyrite, pyrite, actinolite$_1$, and titanite ($Ttn_{1.1H}$) is dated at 1854 ± 15 Ma. The arsenopyrite mineralization is part of the As-Au mineralization event in Huhta (Hector et al. 2023). Based on isotopic Pb studies in galena from the PoB and Skellefte district, Sundblad et al. (1993) suggested that the gold mineralization in the PoB took place at approximately 1880-1850 Ma. It indicates that the gold mineralization in the studied area occurred during the Fennian orogeny when the PoB was accreted to the Keitele microcontinent (Lahtinen et al. 2005, 2014). Furthermore, the mineralisation age of the first event in Huhta (1854 Ma) is coeval with the buckling of the Fennian orogen, between 1870 and 1850 Ma (Lahtinen et al. 2014).

The mineralization of arsenopyrite, biotite, quartz, plagioclase, titanite ($Ttn_{1.1J}$ and $Ttn_{1.2J}$), and sericite in Jouhineva at 1816 ± 12 Ma postdates the first mineralization event in Huhta. Hector et al (2023) observed that gold is included in Co-bearing arsenopyrite in Jouhineva and concluded that arsenopyrite was formed during the As-Au-Co-Ni mineralization event. The different age for the Au-only mineralization in Huhta and As-Au-Co-Ni in Jouhineva indicates that mineralizing fluid metal

content might have evolved over time or was locally different. The younger age coincides with the Svecobaltic (1840 to 1780 Ma) and Nordic (1820 to 1770 Ma) orogenies. These orogenies are characterized by continent-continent collisions (Lahtinen et al. 2005).

The second generations of titanite in Jouhineva and Huhta (Ttn_{2J} and Ttn_{2H}) associated with chalcopyrite and chlorite-sericite alteration were dated at 1760 ±14 and 1744 ± 30 Ma, respectively. This period is coeval to orogenic collapse (Lahtinen et al. 2005, Kohrja et al. 2006) and close to the final cooling of the Fennoscandia orogen (Lahtinen et al. 2018).

Jouhineva was considered a porphyry copper overprinted by an orogenic gold deposit formed during the intrusion of the Rautio batholith (Eilu 2015, Geological Survey of Finland 2022a). However, Rautio was formed at 1890-1880 Ma (Höltä et al. 2019) and, thus, approximately 65 Ma before the first mineralization period in Jouhineva (1816 Ma). Moreover, the overprinted porphyry copper model for Johineva is unlikely due to the lack of porphyry copper alteration zones (Hector et al. 2023).

In conclusion, the results confirm that the mineralization of Au, Co, and Cu is multi-stage hydrothermal formed during the complex orogenic evolution of the PoB between 1850 and 1740 Ma.

Acknowledgments

The authors gratefully acknowledge the Ferenc Molnár and Geological Survey of Finland (GTK) for providing access to the national drill core archive in Loppi. This work is funding by the Deutsche Forschungsgemeinschaft (DFG, N° INST 121384/213-1 FUGG).

References

Eilu, P. (2015). Overview on Gold Deposits in Finland. In: Mineral Deposits of Finland. Elsevier 377–410.

Geological Survey of Finland (2022a) Jouhineva. Mineral Deposit Report n◦ 309.

Geological Survey of Finland (2022b) Huhta. Mineral Deposit Report n◦ 309.

Goldfarb RJ, Baker T, Dubé B, Groves DI, Hart CJR, Gosselin P (2005) Distribution, Character, and Genesis of Gold Deposits in Metamorphic Terranes. In: Hedenquist JW (ed) Economic geology: One hundredth anniversary volume : 1905-2005. Society of Economic Geologists, Inc, Littleton, CO, pp 407–450

Hector S, Clifford P, Kolb J, Silva AA, Walter B, Molnar F (2023) Orogenic Au deposits with atypical metal association (Cu, Co, Ni): insights from the Pohjanmaa Belt, western Finland. Ore Geology Reviews. https://doi.org/10.1016/j.oregeorev.2023.105326

Hölttä P, Heilimo E (2017) Metamorphic map of Finland. In: Nironen M (ed) Bedrock of Finland at the scale 1:1 000 000: Major stratigraphic units, metamorphism and tectonic evolution. Geological Survey of Finland, Espoo, pp 77–128

Hölttä P, Huhma H, Lahaye Y, Mänttäri I, Lukkari S, O'Brien H (2019) Paleoproterozoic metamorphism in the northern Fennoscandian Shield: age constraints revealed by monazite. International Geology Review 30:1–28. https://doi.org/10.1080/00206814.2019.1611488

Huhma, H. (1986). Sm-Nd, U-Pb and Pb-Pb isotopic evidence for the origin of the Early Proterozoic Svecokarelian crust in Finland. Bulletin.

Kähkönen Y (2005) Svecofennian supracrustal rocks. In: Lehtinen M, Nurmi PA, Rämö OT (eds) Precambrian geology of Finland: Key to the evolution of the Fennoscandian shield, 1. ed. Elsevier, Amsterdam, pp 343–406

Lahtinen R, Korja A, Nironen, M (2005) Palaeoproterozoic tectonic evolution of the Fennoscandian Shield. In: Lehtinen, M., Nurmi, P., R¨am¨o, T. (Eds.), The Precambrian Bedrock of Finland - Key to the evolution of the Fennoscandian Shield. Elsevier Science B.V, pp. 418–532.

Lahtinen R, Johnston ST, Nironen M (2014) The Bothnian coupled oroclines of the Svecofennian Orogen: a Palaeoproterozoic terrane wreck. Terra Nova 26:330–335. https://doi.org/10.1111/ter.12107

Lahtinen R, Huhma H, Sayab M, Lauri LS, Hölttä, P (2018) Age and structural constraints on the tectonic evolution of the Paleoproterozoic Central Lapland Granitoid Complex in the Fennoscandian Shield. Tectonophysics 745: 305–325.

Lahtinen R, Salminen PE, Sayab M, Huhma H, Kurhila M, Johnston ST (2022) Age and structural constraints on the tectonic evolution of Paleoproterozoic Saimaa orocline in Fennoscandia. Precambrian Research 369: 106477.

Mäkelä M (1984) Raahen Laivakankaan kvartsi-arseenikiisu-kultaesiintymä. (in Finnish): The quartz-arsenopyrite-gold mineralization of Laivakangas, Raahe, Finland. Unpublished M.Sc thesis, University of TurkuMäkitie H (1999) Structural analysis and metamorphism of Palaeoproterozoic metapelites in the Seinajoki-Ilmajoki area, western Finland. BULLETIN-GEOLOGICAL SOCIETY OF FINLAND 71:305–328

Mäkitie, H. (1999). Structural analysis and metamorphism of Palaeoproterozoic metapelites in the Seinajoki-Ilmajoki area, western Finland. BULLETIN-GEOLOGICAL SOCIETY OF FINLAND 71, 305–328.

Mäkitie, H. (2000). Granitoids (1.89-1.87 Ga), diatexites (1.89-1.88 Ga) and granitic pegmatites (1.80-1.79 Ga), and structural-metamorphic evolution in the Sein¨ajoki region, western Finland. Ph. D. Thesis.

Nironen, M. (2005). Proterozoic orogenic granitoid rocks. In: Lehtinen, M., Nurmi, P.A., R¨am¨o, O.T. (Eds.), Precambrian Geology of Finland: Key to the Evolution of the Fennoscandian Shield, 1. ed. Elsevier, Amsterdam, pp. 443–480.

Patten, C.G.C., Molnár, F., Pitcairn, I.K., Kolb, J., Mertanen, S., Hector, S. (2022). Multi-source and multi-stage metal mobilisation during the tectonic evolution of the Central Lapland Greenstone Belt, Finland: implications for the formation of orogenic Au deposits. Mineral Deposita.

Sundblad, K., Weihed, P., Billström, K., Markkula, H., Makelä, M. (1993). Source of metals and age constraints for epigenetic gold deposits in the Skellefte and Pohjanmaa districts, central part of the Fennoscandian Shield. Mineralium Deposita 28, 181–190.

Role of carbonaceous material in gold precipitation for orogenic gold deposits: a case study of the Bangbu gold deposit, China

Zhengpeng Ding[1], Xiaoming Sun[1]
[1]School of Earth Sciences and Engineering, Sun Yat-sen University, China

Abstract. Carbonaceous material (CM) is widely distributed at the Bangbu deposit. Despite being closely ore-related, the CM nature and genesis, as well as its possible role in gold metallogeny, remain unclear. Hence, we investigated the role of five ore-related CM types using Raman spectroscopy and thermodynamic modeling. CM1 only occurs in disseminated ores. Raman spectroscopy analysis shows that CM1 has undergone high-temperature metamorphism. Geochemical modeling shows that Au precipitation can be attributed to the fluid-rock interactions of CM1 and the ore fluids. CM2 occurs in quartz veins. Raman spectroscopy of CM2 experienced a temperature of ~455 °C. Methane is commonly found in fluid inclusions closely associated with CM2. Geochemical modeling shows that methane can be a more efficient Au-bisulfide reductant than CM2. CM3 intergrows in black veins, and its formation temperature is calculated at ~290 °C. During the sulfidation process, H_2S and CO_2 from the ore fluids may have reacted with Fe-bearing minerals, precipitating CM3 and Py3. CM4 occurs in the wall rocks and have similar structural features to semi-graphite but has no association with ores. Our study proposes the most likely roles of CM in gold precipitation, which bear important implications for a better understanding of the formation of ores.

1 Introduction

Carbonaceous material (CM) is carbon-rich material containing C-O and C-H bonds, including organic matter, graphite, bitumen, and hydrocarbons (Gaboury 2021), and is considered a crucial component of sedimentary rocks (Hu et al. 2017). Previous studies on gold deposits have indicated a significant correlation between various types of CM and different types of gold deposits (Large et al. 2011). Firstly, CM can serve as an effective carrier of gold and other trace elements in carbonaceous sedimentary rocks. Alternatively, metals may have been mobilized from the deeper parts of carbonaceous rocks into the carbonic fluids and migrated to the shallow crust (Gaboury 2013). Moreover, graphite and methane can act as efficient metal reductants that are responsible for gold precipitation (Fuchs et al. 2021), while hydrocarbons and petroleum may also play a role in gold migration in hydrothermal fluids (Crede et al. 2019).

The Bangbu gold deposit is situated in the southwestern part of Jiacha city, China. The disseminated ores are confined inside a fragmented zone of carbonaceous phyllite and have straight contact with stringer quartz veins. The vein-type ores are confined into large ore-controlling structures, which are mainly quartz veins. At Bangbu, different types of CM are widely reported in the ore bodies and wall rocks, yet its relations with the gold ores remain ambiguous (Ding et al. 2023). This study aims to integrate petrography, Raman spectroscopy, and thermodynamic modeling to reveal the origin of CM and its gold metallogenic role.

2 Analytical methods

The mineral assemblages and different types of CM in the ores were identified using a ZEISS AXIO microscope and SEM. Raman spectra of CM were measured using a Renishaw inVia Reflex Raman spectrometer. The analysis conditions included 9 mW output laser power, and a 100 to 3500 cm^{-1} spectroscopic range, which covers all CM peaks. Temperature is a key parameter for the origin and evolution of CM. Temperature is a crucial factor in the origin and evolution of CM. Based on prior research, CM areas can be identified and used to determine the temperature experienced by the CM (Rahl et al. 2005).

A quantitative evaluation of the role of different CM types in gold precipitation at Bangbu was carried out using the Geochemist's Workbench software. For a more intuitive representation of reaction-path modeling, carbonaceous sericite phyllite was defined as graphite and mixed as unmineralized rock. The LA-ICP-MS trace element data of individual fluid inclusion from Bangbu were used to define the initial ore fluid compositions (Zhao et al. 2020).

3 Results

3.1 Petrographic characteristics

Detailed petrographic observations reveal the spatial association of the five CM types (CM1-4 and methane), native gold, and three auriferous pyrite generations from the disseminated and vein-type ores. CM1 is exclusively present in the disseminated ores. CM1 occurs as an elongate or filamentous morphology in clusters in the disseminated ores and forms black conglomerate (Fig. 1a). Methane, commonly found as fluid inclusions in coarse vein-type ores, is spatially associated with CM2 (Fig. 1b).

CM3 occurs as black irregular particles or elongate bodies with an average diameter of 0.002 mm and are combined into randomly oriented black veinlets in coarse vein-type ores (Fig. 1c). In addition to Py2, CM3-Py3 veinlets coexist with quartz veins in the vein-type ores. CM4 appears as slivery white irregular semi-graphite in wall rocks and has a

stronger reflectance under the microscope than other types of CM (Fig. 1d). No petrographic relationships between CM4 and sulfides or native gold was observed.

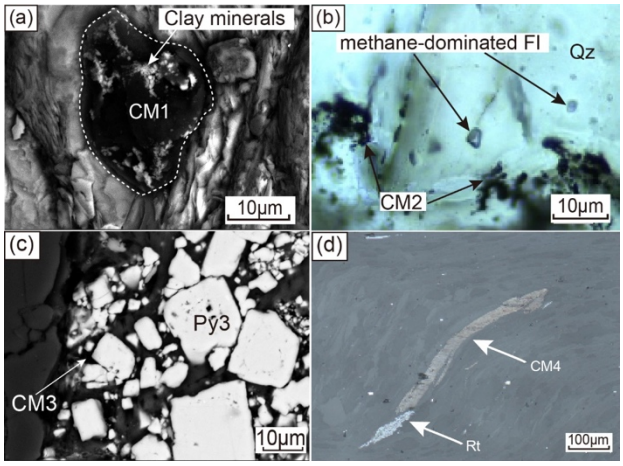

Figure 1. Photographs of CM1, CM2, methane, CM3, and CM4. Abbreviations: Py = pyrite; Qz = quartz; Rt = rutile.

3.2 Raman thermometer of solid CM

All four types of CM show well-developed D (1350 cm^{-1}) and G (1580 cm^{-1}) bands, as well as D2 (1600 cm^{-1}) and S1 (2690 cm^{-1}) bands, commonly accompanied by S2 (2940 cm^{-1}) and S3 (3200 cm^{-1}) bands (Fig. 2). CM1 has a strong G band, relatively weak D and D2 bands, an additional high S1 band, and a low S2 band, resembling typical flaky graphite with high crystallinity (Fig. 2a). Although CM2 has mostly similar spectra as CM1, the peak intensity was weaker (Fig. 2b). On the contrary, CM3 has a higher D band than the G band, and a lower D2 band than that of CM1 and CM2, indicating a disordered structure (Fig. 2c). CM4 is characterized by similar D and G bands, and clear D2, S1, S2, and S3 bands, suggesting that the experienced temperature of CM4 is lower than CM1 and CM2, but higher than CM3 (Fig. 2d). For the CM temperature calculation, it depends on the D, G, and D2 band area values. Using the thermometer of Rahl et al. (2005), the R1 and R2 of CM1-4 were calculated to be the averages of 510 °C, 455 °C, 290 °C, and 388 °C, respectively.

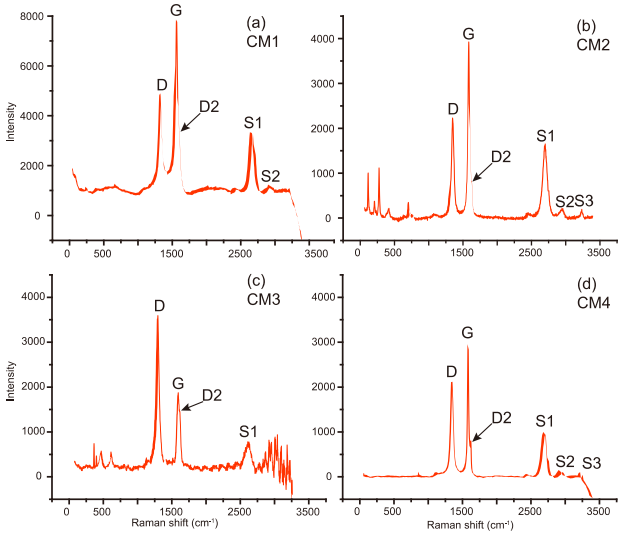

Figure 2. Raman spectra of the four CM types from Bangbu.

3.3 Thermodynamic modeling

We established several gold precipitation thermodynamic models for the different types of CM, based on petrographic observations, geochemical analyses, and mineral assemblages. In this study, the pH and temperature data of the ore fluids were provided by the ore-stage methane-dominated fluid inclusions (Zhao et al. 2020). Combined with the LA–ICP–MS data from individual fluid inclusions, the ore fluids were determined to be low temperature (avg. 250 °C), high sulfur activities (0.01mol as SO_4^{2-}), low-medium salinity (avg. 1mol/L NaCl), and weakly acidic to neutral (pH =5.2). The oxygen fugacity of the ore fluids to be -34 to -37 log units and are generally fixed below the QFM redox buffers.

4 Discussion

4.1 Role of CMs in gold precipitation

We defined the unmineralized wall rocks as a series of individual minerals, each containing 100g, including annite (representing biotite), graphite (representing CM), quartz, albite, K-feldspar, and chlorite, which reacted with the fluid under rock-buffer conditions, to establish the role of CM1 in gold precipitation with React module. Our reaction modeling indicates that 1g of CM1 would precipitate 43% of Au from the fluid (Fig. 3a). Meanwhile, further CM increases would not lead to major changes in the fluid in our model. We therefore suggest that this reaction can cause physico-chemical variations in the ore fluids and thereby promote redox and acid-base equilibria. Stability of Au complexes were thus destroyed and caused Au precipitation in Py1. Model results are consistent with patterns of observed mineral paragenesis in disseminated ores, further supporting this view.

In the phase separation process, the fugacity of methane was increased and accompanied by the decrease of Au concentrations in the ore fluids under acidic conditions. We consider that when the fluids

enter brittle-ductile shear zones in wall rocks, the pressure may have decreased and gradual transformation of liquid to vapor phase of methane may take place, causing the boiling of $methane_{(aq)}$ to $methane_{(g)}$ in the residual ore fluids and accompanied by a decrease of temperature. The significantly increased contact surface area between methane and the ore fluids, further exacerbating gold precipitation and may cause further driving the precipitation of Au.

We test the hypothesis of phase separation of methane in the ore fluids by the model 2, with adding methane to the initial fluids. As shown in Figures 3b, the reaction of only 1 g methane with 1 kg fluid would reduce the gold solubility from 100 to 22 ppb, resulting in the precipitation of Au^+ (78%). This model suggests that the methane phase separation is more effective for gold precipitation than fluid-rock reactions.

Sulfidation is commonly associated with orogenic-type gold ores (Groves et al. 2020). Au was incorporated into pyrite during the sulfidation process and usually caused the deposition of minerals. We propose that the deeper carbonic ore fluids ascended into the ore-hosting structures and that CO_2 and H_2S may have degassed from the fluids. During this reaction, the deposition of these sulfide phases might have depleted H_2S from the ore fluids, which destabilized Au-bisulfide complexes and drove Au deposition. To test our model in a simple way, we defined the sulfidation as a continuous addition of FeO, H_2S, and CO_2 to the initial fluid (model 3). The results are presented in Figures 3c, which show a drop in fluid Au^+ content (~20%) due to the deposition of Py3 and CM3. It is noteworthy that gold precipitation efficiency during the sulfidation is poor in this model and is unlikely to be the primary gold precipitation mechanism at Bangbu.

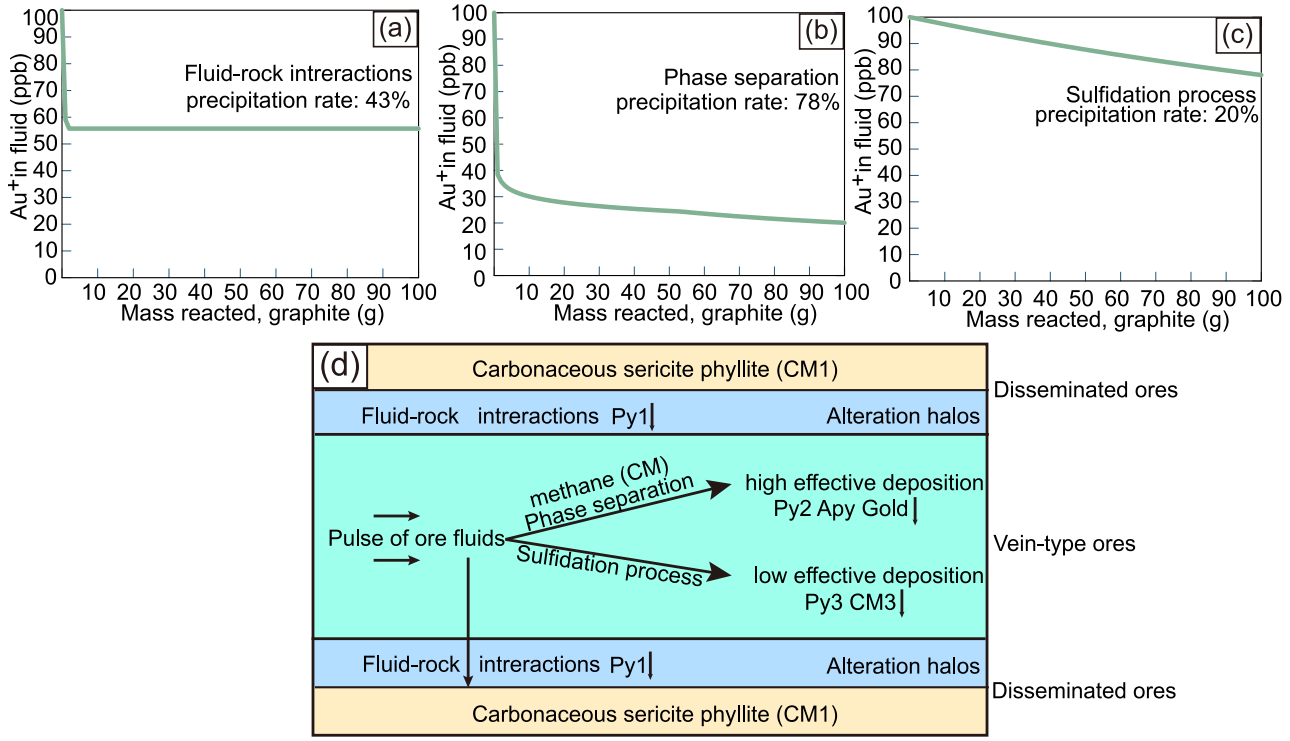

Figure 3. Thermodynamic modeling simulations of CMs added into the ore fluids: **a** Concentrations of Au^+ from model 1; **b** Concentrations of Au^+ from model 2; **c** Concentrations of Au^+ from model 3. The green line denotes the reacting concentration of Au^+ in the model; **d** The role of CM in the gold precipitation process illustrated in a pattern diagram.

Although our study indicates that many CMs could play an important role in gold precipitation, it may not be the case for all types of CM. Here, our data have shown that CM2 and CM4 have no role in gold precipitation, even though there is a spatial association between CM2, Py2, native gold, and methane-dominated fluid inclusions in the ores. Firstly, the experienced temperature of CM2 is much higher than the ore fluid temperature, which could indicate that CM2 could not have originated from the ore fluids, unlike CM3. CM2 was most likely sourced from indigenous CM and produced by the deep-lying carbonaceous rocks through pyrolysis or directly from CM1 particles via structural super-imposition and reformation. We suggested that CM2 would play a similar role in gold precipitation to that of CM1, but methane can precipitate more Au than CM2 in the ore fluids. Our study does not support that CM2 was a major reductant for gold precipitation but may have played a minor role. Secondly, CM4 is a completely different type with a unique flake structure compared to other types of CM and is similar to structural-bound semi-graphite. In addition, CM4 also occurs with hydrothermal sericite in wall rocks, but no auriferous minerals were identified. Meanwhile, Raman geothermometric results indicate that CM4

was formed during the post mineralization stage and had no relation to gold mineralization at Bangbu.

5 Implications

Different types of CM may have played a distinct role in the gold precipitation at Bangbu (Fig. 3d). Indigenous CM1 and hydrothermal CM3, representing fluid-rock interaction and sulfidation, respectively, could explain the formation of gold-poor pyrite. In contrast, methane may have played a key role in the formation of native gold grains. Considering CM has been widely distributed in other orogenic gold deposits, we propose that the different types of CM could be important associated mineral in sediment-hosted orogenic gold deposits worldwide. In practice, however, our study also suggests that there is no unique association between some hydrothermal CM (e.g., CM4) and gold mineralization in gold deposits. Each hydrothermal event may trigger the production of hydrothermal CM.

Acknowledgements

This research was financially supported by the National Natural Science Foundation of China (91855213, 41972070, 41672071, and U1302233).

References

Crede L, Liu W, Evans KA, Rempel KU, Testemale D, Brugger J (2019) Crude oils as ore fluids: An experimental in-situ XAS study of gold partitioning between brine and organic fluid from 25 to 250 °C. Geochimica Et Cosmochimica Acta 244: 352-365.

Ding ZP, Sun XM, Hu SY, Chen HJ, Li DF, Fu Y, Xu L, Wu ZY, Huang F (2023) Role of carbonaceous material in gold precipitation for orogenic gold deposits: A case study of the Bangbu gold deposit in southern Tibet, China. Ore Geology Reviews 152: 105231.

Fuchs S, Schumann D, Martin RF, Couillard M (2021) The extensive hydrocarbon-mediated fixation of hydrothermal gold in the Witwatersrand Basin, South Africa. Ore Geology Reviews 138: 104313.

Gaboury D (2013) Does gold in orogenic deposits come from pyrite in deeply buried carbon-rich sediments?: Insight from volatiles in fluid inclusions. Geology 41: 1207-1210.

Gaboury D (2021) The neglected involvement of organic matter in forming large and rich hydrothermal orogenic gold deposits. Geosciences 11: 344.

Groves DI, Santosh M, Deng J, Wang Q, Yang L, Zhang L (2020) A holistic model for the origin of orogenic gold deposits and its implications for exploration. Mineralium Deposita 55: 275-292.

Hu S, Evans K, Craw D, Rempel K, Grice K (2017) Resolving the role of carbonaceous material in gold precipitation in metasediment-hosted orogenic gold deposits. Geology 45: 167-170.

Large RR, Bull SW, Maslennikov VV (2011) A carbonaceous sedimentary source-rock model for Carlin-type and orogenic gold deposits. Economic Geology 106: 331-358.

Rahl JM, Anderson KM, Brandon MT, Fassoulas C (2005) Raman spectroscopic carbonaceous material thermometry of low-grade metamorphic rocks: Calibration and application to tectonic exhumation in Crete, Greece. Earth and Planetary Science Letters 240: 339-354.

Zhao X, Yang Z, Zhang X, Pei Y, Liu Y, Han D (2020) Geochemical compositions of ore-related pyrite, quartz and fluid inclusions of Bangbu gold deposit in the Indus–Yurlung Zangbo suture zone, Tibet. Ore Geology Reviews 120: 103441.

The role of crystal defects for the remobilisation of gold in pyrite

Denis Fougerouse[1,2], Dennis Sugiono[3], Sumail[3], Nicolas Thebaud[3], Steven M. Reddy[1,2]
[1]School of Earth and Planetary Sciences, Curtin University, Perth, Australia
[2]Geoscience Atom Probe Facility, John de Laeter Centre, Curtin University, Australia
[3]Centre for Exploration Targeting, The University of Western Australia, Crawley, Australia

Abstract. Gold hosted in sulfides represents a large proportion of the Au resource globally. Sulfide-hosted Au is refractory, meaning that its recovery necessitates a full oxidation of the minerals. Despite this characteristic, numerous evidence has been documented that Au can be remobilised naturally, through geological processes, improving the economic value of an ore deposit. However, the mechanistic process operating at the nanoscale for the remobilisation of Au in pyrite still remains poorly understood. In this study, we apply a correlative suite of techniques from the grain-scale to the nanoscale in order to determine the mechanism for Au mobility in pyrite. We selected samples from three orogenic Au deposits, including the Cambrian Huangjindong deposit (Jiangnan Orogen, China), the Archean Kanowna Belle and Jundee deposits (Yilgarn craton, Western Australia). Our data suggests a strong role of crystal defects, and in particular dislocations, for the remobilisation of Au from pyrite.

1 Introduction

Refractory Au ores are defined by trace amounts of Au hosted in sulfide minerals, mainly pyrite and arsenopyrite (Cook and Chryssoulis, 1990). Refractory Au ores represent a large proportion of global Au resources and it has been defined that Au can be hosted in the sulfide crystal lattice (Cabri et al., 1989), occur as discrete metallic nano- and microparticles (Palenik et al., 2004), and can be hosted in crystal defects such as dislocations (Fougerouse et al., 2021).

Secondary geological processes have been shown to affect the distribution of Au in sulfide and cause the liberation of gold from refractory ores, increasing the economic value of gold deposits. Remobilisation can improve the recovery of Au by simple cyanidation, but also be responsible for the formation of high-grade ore shoots (Fougerouse et al., 2016). The mineralogical processes responsible for Au remobilisation operate at the nanoscale, however the documentation of the distribution of trace elements at the nanoscale is notoriously difficult. In this study, we used a combination of advanced analytical instrumentation including electron backscattered diffraction (EBSD), nanoscale and time-of-flight secondary ion mass spectrometry (NanoSIMS and ToF-SIMS), transmission electron microscopy (TEM) and atom probe tomography (APT), in order to determine the mechanisms responsible for gold mobility in pyrite.

2 Samples and geological settings

Three samples from orogenic gold deposits were selected, including one mineralised sample from the Cambrian Huangjindong deposit (Jiangnan Orogen, China), and one from the Archean Jundee and Kanowna Belle deposit (Yilgarn craton, Western Australia).

The Huangjindong deposit is located in the Jiangnan Orogen (Southern China). Mineralisation at Huangjindong is dominated by gold-bearing pyrite and arsenopyrite (Zhang et al., 2018).

The Jundee deposit is hosted in the Yandal greenstone belt in the Eastern Goldfields province of the Archean Yilgarn craton. Mineralisation at Jundee is hosted in brecciated dolomite veins and is dominated by visible gold with a minor component of gold associated with arsenian pryrite (Yeats et al., 2001).

The Kanowna Belle deposit is located on the eastern edge of the Kalgoorlie terrane of the Yilgarn craton within the volcano-sedimentary units of the Black Flag Group (Sugiono et al., 2021). Gold at Kanowna Belle is hosted dominantly in laminated quartz-pyrite-gold veins.

3 Methods

The NanoSIMS and TEM measurements were performed at the Centre for Microscopy, Characterisation and Analysis, The University of Western Australia (CMCA, UWA), whereas the EBSD, ToF-SIMS and APT investigation were conducted at the John de Laeter Centre (JdLC), Curtin University.

We used a Tescan Clara field emission gun scanning electron microscope (FEG-SEM) equipped with an Oxford Symmetry EBSD detector at Curtin University, for quantifying crystal misorientation and define regions of interest for further work. A Cameca NanoSIMS 50L with a Cs^+ primary source (CMCA, UWA) and an IONTOF M6 ToF-SIMS instrument with a Bi^+ primary source (JdLC) were used to map the distribution of ^{75}As and ^{197}Au. The experiment conditions for both instruments resulted in a pixel size of approximately 100 nm.

TEM and APT specimens were prepared using a FEI Helios NanoLab G3 and a Tescan Lyra3 Ga^+ focused ion beam (FIB) instruments, respectively. TEM analyses were conducted on a FEI Titan G2 TEM (CMCA), whereas APT analyses were performed using a Cameca LEAP4000X HR (JdLC).

4 Results

4.1 Microscale results

EBSD results from all three samples investigated indicate that the internal pyrite misorientation is relatively weak. At Huangjindong, a maximum distortion of ~10° is accommodated by a low density of low-angle boundaries cutting across the grain. At Jundee, the pyrite studied is composed of an aggregate of grains. Each individual grain is weakly deformed but low-angle boundaries can be observed where grains impinge each other. At Kanowna Belle, evidence for crystal-plastic deformation can be observed in areas of the grain aggregate, but low-angle boundaries are associated with the growth zoning, mimicking the shape of the As-Au-rich domains (Fig. 1).

In all three samples investigated, the primary As and Au distribution is in the form of oscillatory bands following the pyrite crystal growth faces. Commonly, the cores of the pyrites are As and Au poor, whereas the rims of the grains are enriched in As and Au.

In the case of Jundee and Kanowna Belle, the primary oscillatory zoning is overprinted by pyrite with a dark backscattered (BSE) signal (Fig.1 E&I). The BSE-dark regions have sharp, curviplanar boundaries with the oscillatory zoned primary pyrite. NanoSIMS and ToF-SIMS analyses reveal that the BSE dark domains are As and Au poor compared to the oscillatory zoning (Fig 1. G, H, K&L). At Jundee, the BSE-dark zones are penetrating inward the pyrite from the grain edges and from low-angle boundaries. At Kanowna Belle, Within the As-Au-rich rim, convoluted As-depleted domains occur either parallel to the As-Au oscillatory zoning or as channels of As-depleted zones cutting across the oscillatory zone textures. Importantly, the location of the As-depleted zones at Kanowna Belle is associated with the presence of low-angle boundaries .

4.2 Nanoscale results

The APT analysis of a low-angle boundary at Huangjindong reveals that the boundary is composed by a succession of dislocations aligned within the boundary plane (Fig. 2). Dislocations are enriched in trace elements such as As, Ni, Cu, Sb, Pb and Au. Chemical profiles normal to the dislocations reveal a local depleted zone in proximity of the dislocation.

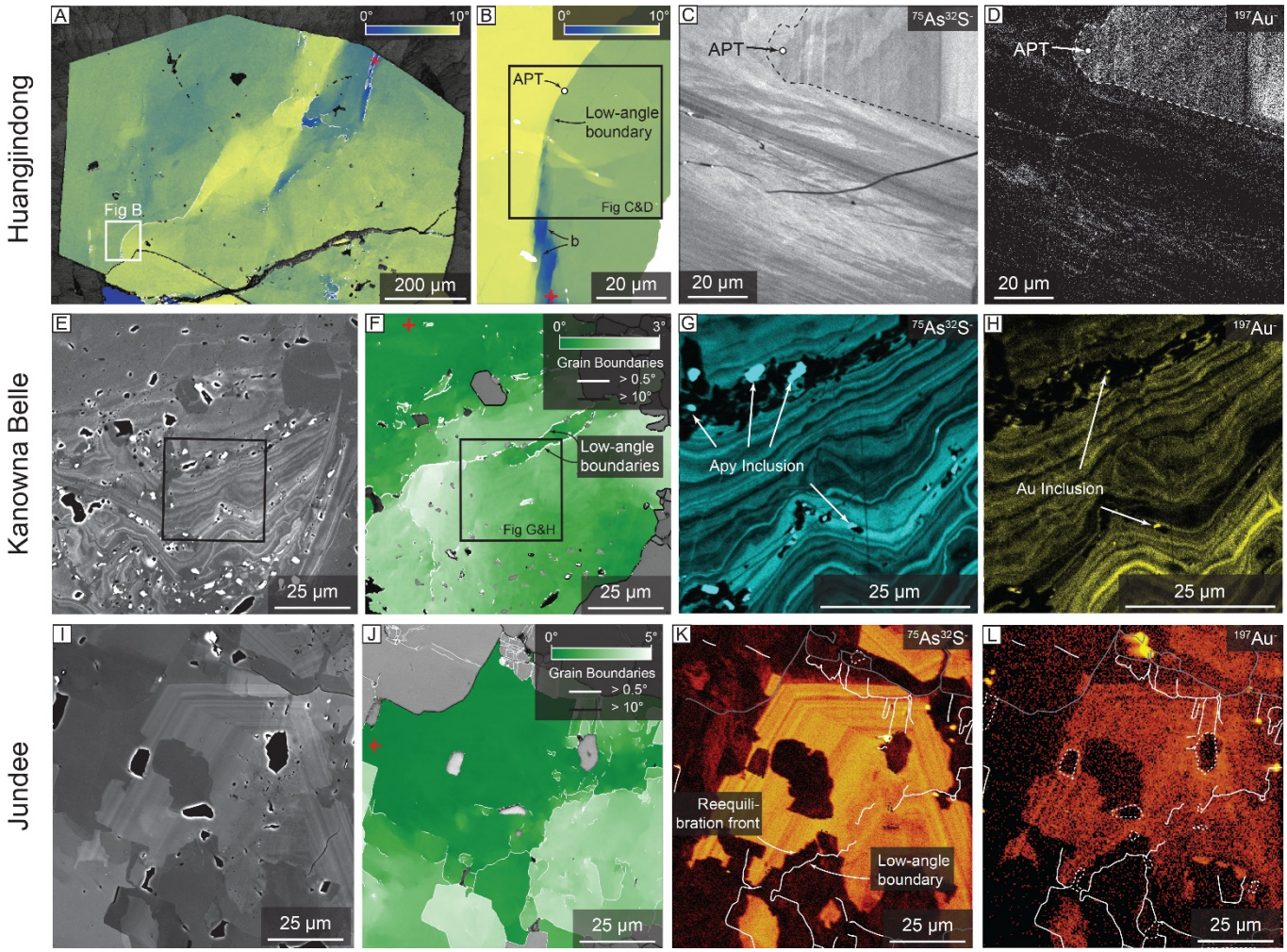

Figure 1. Microscale results for pyrites of the Huangjindong, Kanowna Belle and Jundee deposits. A, B, F and G) EBSD texture component maps showing crystal Distortion. Low-angle boundaries (>0.5°) are plotted in white and high-angle boundaries (>10°) in black; C, D, G and H) NanoSIMS maps for As and Au; E and I) BSE images; K and L: ToF-SIMS maps showing the distribution of As And Au.

TEM investigation of the Kanowna Belle textures reveal that the boundary of the domain depleted in Au and As is sharp at the nanoscale. The TEM analyses also revealed that in the As-Au-depleted zones, small arsenopyrite crystals and sub-micrometre gold particles are present. At Jundee, the APT investigation of the sharp boundary between the As-Au-rich and As-Au-poor domains reveal complex heterogeneities in the As distribution and the identification of crystal defects is ongoing.

5 Discussion

5.1 The role of crystal defect for gold mobility

The As-Au oscillatory zoning observed in all samples can be explained by the diffusion-limited self-organisation of ions at the crystal-fluid interface and is a reflection of growth kinetics rather than variations in fluid chemistry (Wu et al., 2019).
Secondary textures can be observed in all samples. At Huangjindong, a clear link between crystal-plastic deformation and the mobility of Au was established. Local concentration profiles suggest that Au was sourced from the pyrite, locally and migrated at the same time of the dislocation through the dislocation-impurity pair model (Fougerouse et al., 2021).
At Kanowna Belle, low-angle boundaries mimic the shape of the As-Au rim, indicating that they are not related to crystal-plastic deformation. The incorporation of large As atoms in pyrite leads to the staining and distortion of the crystal lattice (Simon et al., 1999). The close association of the low-angle boundaries and the high-As rim suggests that the low-angle boundary formed in response to lattice distortion caused by As incorporation.
In turn, within the As-Au-rich oscillatory zoned rim at Kanowna Belle, there is a relationship between the location of the low-angle boundaries and convoluted As-Au-poor domains. Similar observations are made at Jundee, with As-Au-poor domains cross-cutting As-Au-rich oscillatory zones. In both case studies, the As-Au-poor domains have sharp, curviplanar boundaries and penetrate inward the pyrite along grain boundaries and low-angle boundaries. These features are interpreted to form through a re-equilibration process. The driving force of the re-equilibration is the minimisation of free energy from a distorted pyrite lattice due to the incorporation of As and Au to a pyrite closer to stoichiometric composition. The fluid-mediated interface-coupled dissolution-reprecipitation model for re-equilibration is likely to be responsible for these textures (Fougerouse et al., 2016; Morey et al., 2008; Putnis, 2009).
In all three examples, we have documented a clear link between low-angle boundaries, crystal defects and the mobility of Au. Dislocations along low-angle boundaries can lead to several mechanisms for Au mobility. At Huangjindong, the dislocation-impurity pair model suggests that no fluids are necessary for the local redistribution of Au in pyrite. On the other hand, at Kanowna Belle and Jundee, re-equilibration textures forming through a fluid mediated process are well developed around low-angle boundaries. This relationship indicates that fluids, or H, preferentially utilise the microstructure network and dislocations to infiltrate pyrite and cause Au remobilisation.

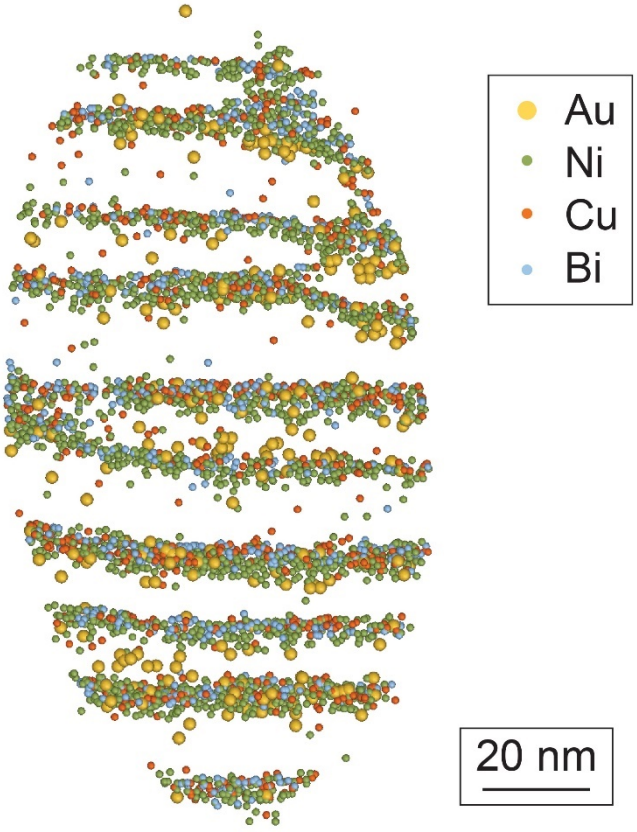

Figure 2. Nanoscale APT imaging of the low angle boundary indicated in Figure 1A-D. Each sphere represents an atom. The low angle boundary plane is composed of sub-horizontal Au, Ni, Cu and Bi enriched dislocations.

5.2 Implications

Refractory Au ores require oxidation to liberate Au locked in sulfides. The oxidation of sulfides requires significant amount of energy contributing to greenhouse gas emissions, produces acids and wastes rich in heavy metals.
Our study indicates that natural gold remobilisation processes exist and are efficient at the micrometre scale. Gold was observed in crystal defects along low-angle boundaries formed during deformation and fluids have been showed to use the low-angle boundary networks to initiate re-equilibration of pyrite. Such mechanism should be investigated for alternative method of selective or in situ leaching (Heath et al., 2008). Indeed, it has been demonstrated that crystal defects are more prone to dissolution than bulk crystal, thus reducing energy consumption necessary for extraction.

Acknowledgements
The study is supported by the Science and Industry Endowment Fund (SIEF RI13-01). DF acknowledges Australian Research Council

(DE190101307 and LP200200897) and Mineral Research Institute of Western Australia funding. We thank Northern Star Resources for providing samples and site access. The authors acknowledge the facilities, and the scientific and technical assistance of Microscopy Australia at the Centre for Microscopy, Characterisation & Analysis, The University of Western Australia, a facility funded by the University, State and Commonwealth Governments. Paul Guagliardo, William Rickard and David Saxey and thanked for their help with NanoSIMS, ToF-SIMS and APT, respectively.

References

Cabri L. J., Chryssoulis S. L., de Villiers J. P., Laflamme J. G. and Buseck P. R. (1989) The nature of" invisible" gold in arsenopyrite. *The Canadian Mineralogist* **27**, 353-362.

Cook N. J. and Chryssoulis S. L. (1990) Concentrations of invisible gold in the common sulfides. *The Canadian Mineralogist* **28**, 1-16.

Fougerouse D., Reddy S. M., Aylmore M., Yang L., Guagliardo P., Saxey D. W., Rickard W. D. and Timms N. (2021) A new kind of invisible gold in pyrite hosted in deformation-related dislocations. *Geology* **49**, 1225-1229.

Fougerouse D., Micklethwaite S., Tomkins A. G., Mei Y., Kilburn M., Guagliardo P., Fisher L. A., Halfpenny A., Gee M. and Paterson D. (2016) Gold remobilisation and formation of high grade ore shoots driven by dissolution-reprecipitation replacement and Ni substitution into auriferous arsenopyrite. *Geochimica et Cosmochimica Acta* **178**, 143-159.

Heath J., Jeffrey M., Zhang H. and Rumball J. (2008) Anaerobic thiosulfate leaching: Development of in situ gold leaching systems. *Minerals Engineering* **21**, 424-433.

Morey A. A., Tomkins A. G., Bierlein F. P., Weinberg R. F. and Davidson G. J. (2008) Bimodal distribution of gold in pyrite and arsenopyrite: examples from the Archean Boorara and Bardoc shear systems, Yilgarn Craton, Western Australia. *Economic Geology* **103**, 599-614.

Palenik C. S., Utsunomiya S., Reich M., Kesler S. E., Wang L. and Ewing R. C. (2004) “Invisible „gold revealed: Direct imaging of gold nanoparticles in a Carlin-type deposit. *American Mineralogist* **89**, 1359-1366.

Putnis A. (2009) Mineral Replacement Reactions. *Reviews in Mineralogy and Geochemistry* **70**, 87-124.

Simon G., Huang H., Penner-Hahn J. E., Kesler S. E. and Kao L.-S. (1999) Oxidation state of gold and arsenic in gold-bearing arsenian pyrite. *American Mineralogist* **84**, 1071-1079.

Sugiono D., Thébaud N., LaFlamme C., Fiorentini M., Martin L., Rogers J., Lorusso G. and McFarlane C. (2021) Integration of multiple sulfur isotopes with structural analysis unveils the evolution of ore fluids and source of sulfur at the Kanowna Belle Archean orogenic gold deposit, Yilgarn Craton, Western Australia. *Mineral. Deposita* **56**, 1471-1490.

Wu Y.-F., Fougerouse D., Evans K., Reddy S. M., Saxey D. W., Guagliardo P. and Li J.-W. (2019) Gold, arsenic, and copper zoning in pyrite: A record of fluid chemistry and growth kinetics. *Geology* **47**, 641-644.

Yeats C. J., Kohler E. A., McNaughton N. J. and Tkatchyk L. J. (2001) Geological setting and SHRIMP U–Pb geochronological evidence for ca. 2680–2660 Ma lode-gold mineralization at Jundee–Nimary in the Yilgarn Craton, Western Australia. *Mineral. Deposita* **36**, 125-136.

Zhang L., Yang L.-Q., Groves D. I., Liu Y., Sun S.-C., Qi P., Wu S.-G. and Peng J.-S. (2018) Geological and isotopic constraints on ore genesis, Huangjindong gold deposit, Jiangnan Orogen, southern China. *Ore Geology Reviews* **99**, 264-281.

Precise constraints on the lifespan of gold mineralization in the giant Yixingzhai gold deposit, North China Craton

Wen-Sheng Gao[1, 2, 3], Xiao-Dong Deng[1], Jian-Wei Li[1, 2], Dawid Szymanowski[3], Cyril Chelle-Michou[3]
[1]State Key Laboratory of Geological Processes and Mineral Resources, China University of Geosciences, China.
[2]School of Earth Resources, China University of Geosciences, China.
[3]Department of Earth Sciences, Eidgenössische Technische Hochschule (ETH) Zurich, Switzerland.

Abstract. The North China Craton hosts ~7000 t Au that was deposited in the Early Cretaceous. These deposits have been proposed to be of magmatic-hydrothermal origin with a low gold abundance of the source rock, indicating that the longevity of magmatic-hydrothermal processes might be key to achieving the giant size of some of the deposits. Here, we present results of zircon petrochronology with chemical abrasion isotope dilution thermal ionization mass spectrometry (CA-ID-TIMS) U-Pb dating to precisely constrain the timing and duration of gold mineralization in the Yixingzhai deposit (~100 t Au). The youngest zircons in two pre-ore and post-ore intrusions overlap within a short time interval of 0.04 ± 0.22 Ma in the Yixingzhai deposit. The results confirm a genetic link between gold mineralization and underlying magmatism. In addition, the findings suggest that it is possible to form a giant gold mineralization within a short time interval.

1 Introduction

The North China Craton (NCC) hosts several dozen gold deposits, which combined have proven reserves of ~7000 t Au (Wang et al. 2020a). These gold deposits are dated mainly at 140–120 Ma, coinciding with the peak of NCC decratonization during the late Mesozoic. Most of the gold deposits show a close temporal-spatial relationship to mafic/intermediate dykes/stocks (Yang et al. 2003). Recent studies on stable isotopes of ore and gangue minerals, noble gas geochemistry of fluid inclusions in Au-bearing pyrite, LA-ICP-MS melt inclusion analysis of the ore-related mafic/intermediate dikes, and gold and platinum group element contents of mantle xenoliths and basalts suggest that mafic/intermediate magmas from metasomatized lithosphere mantle have played a key role in the formation of the giant gold deposits in the NCC (Tan et al. 2012; Wang et al. 2020a; Wang et al. 2020b; Chang et al. 2021). Wang et al. (2020b) advocate that the extensive mantle metasomatism and hydration cannot form a gold-enriched mantle source because the basalts that are contemporary with lode gold have only negligibly high gold contents. Thus, gold pre-enrichment of the magma might not have played an essential role in the giant gold mineralization in the NCC. Instead, the volume and lifespan of the underlying magma and its physical and hydrothermal evolution processes at shallower levels may have been a key control.

Syn-mineralization porphyry intrusions provide snapshots of the evolution of the underlying magma reservoir. Trace elements in zircon, one of the most refractory minerals in porphyries, retain a key record of petrological evolution of the magma even in strongly hydrothermally altered samples. With the improvement of the high-precision zircon U-Pb dating procedures, the analytical precisions could be better than 0.03 % for a single zircon grain (Condon et al. 2015). Therefore, zircon petrochronology combined with high-precision zircon U-Pb dating provides a robust tool for establishing a temporal sequence of magmatic processes that contribute to forming magmatic-hydrothermal deposits (Chelle-Michou et al. 2014).

The Yixingzhai deposit (~100 t Au) in the Central Taihangshan District (CTD) of NCC is characterized by a suite of late Mesozoic intrusions and several different gold mineralization episodes during a short period (Zhang et al. 2020), making it an excellent place to constrain the duration of gold mineralization. In the present study, CA-ID-TIMS U-Pb zircon dates and in-situ zircon trace elements were obtained from the pre-, syn-, and post-ore intrusions at Yixingzhai to determine the timescale of gold mineralization in the deposit.

2 Geological background

The NCC is an ancient craton that consists of two blocks, the Western and Eastern block, which are separated by the Trans North China Orogen (Zhao et al. 2005; Figure 1A). The NCC experienced a long period of stability from the late Paleoproterozoic to the end of the Palaeozoic. However, the eastern part of the NNC was reactivated during the Mesozoic, as largely manifested by voluminous magmatism (granitoid intrusion, intermediate to mafic dikes, bimodal volcanic rocks) and widespread extensional tectonics (Figure 1A; Zhu et al. 2015). Within this period, many lode and disseminated gold deposits were formed in the eastern part of NCC (Figure 1 A; Chang et al. 2021).

The Yixingzhai gold deposit hosts several episodes of gold mineralization, such as breccia-hosted Fe-Au mineralization, lode gold mineralization, and porphyry-hosted disseminated gold mineralization (Figure 1B). Besides, various intermediate to felsic dikes/porphyries are identified at the pre-/syn-/post-ore stage of each gold mineralization (Figure 2; Gao et al. 2022). porphyry-hosted disseminated gold mineralization (~60 t Au) is the most economically important gold mineralization episode at Yixingzhai and is characterized by strong sericite alteration and

native gold-bearing sulfides (Zhang et al. 2018). It overprinted early felsite and early granite porphyry and was cut by a late granite porphyry (Figure 2). Zircon U-Pb dates of intrusions (ca. 140–135 Ma; Zhang et al. 2017), garnet U-Pb dates of breccia-hosted gold mineralization (ca. 140 Ma; Zhang et al. 2020), and sericite $^{40}Ar/^{39}Ar$ dates of porphyry-hosted disseminated gold and lode gold mineralization (ca. 139 Ma, Gao et al. 2022) all indicate a close temporal and possibly genetic relationship between the magmatism and mineralization at Yixingzhai (Figures 1 and 2).

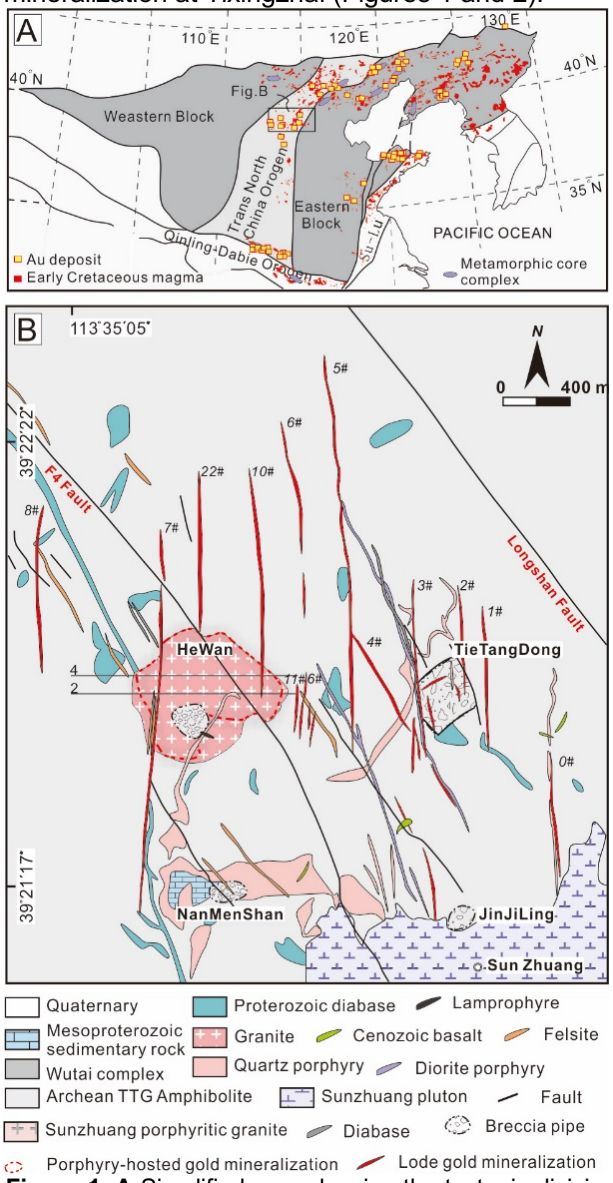

Figure 1. A Simplified map showing the tectonic division of the NCC and the location of the Yixingzhai deposit. The distribution of Early Cretaceous magmatism, gold deposits, and metamorphic core complexes are shown (Zhao et al. 2005). **B** Geological map of the various intrusions and mineralization in the Yixingzhai deposit (Zhang et al. 2017).

3 Samples and Methodology

Zircons were extracted from samples of the pre-ore early felsite (HW-1), pre/syn-ore early granite porphyry (HW-2), and post-ore late granite porphyry (HW-4), using conventional mineral separation techniques including jawbreaker, sieving, panning and heavy liquid mineral separation. Hand-picked zircons were annealed for 48 h at 900°C. Zircons were mounted in epoxy resin, polished, and imaged with cathodoluminescence (CL) on a JEOL JSM-6390LA Scanning Electron Microscope at the Department of Earth Sciences, ETH Zurich.

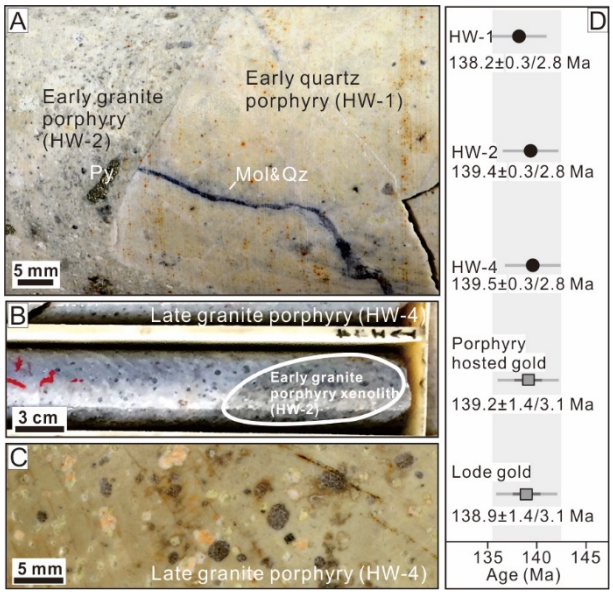

Figure 2. Photomicrographs showing the petrographic and textural features of the intrusions. **A** Early felsite clast enclosed by the early granite porphyry, both overprinted by the strong sericite alteration. **BC** Late granite porphyry with minor sericite alteration and a mineralized early granite porphyry xenolith. **D** Summary of the zircon U-Pb (black circle, this study) and sericite 40Ar/39Ar (grey box, Gao et al. 2022) data. Note the dark grey error bar is measurement uncertainty (2σ), while the grey error bar is full external uncertainty (2σ) plus decay constant. Py - Pyrite, Mol - Molybdenite, Qz - Quartz.

LA-ICP-MS geochemistry and geochronology analyses of cores and rims of individual crystals were conducted at ETH Zurich. NIST 610 glass was used as reference material for trace element analyses, with stochiometric concentrations of Si (zircon) as internal standards. The accuracy of the measurements was monitored by repeated analyses of secondary zircon standards (GJ-1, 91500, Plešovice, and synthetic zircon). Most trace elements have uncertainties better than ± 5% (2 RSD) based on secondary standard and glass standard reproducibility.

Fifteen zircons from the three samples showing no evidence of inheritance or contamination by inclusions were selected for CA-ID-TIMS analyses. The selected crystals were removed from the epoxy mount and chemically abraded for 12 h at 190°C using techniques modified from Mattinson (2005). Zircons were spiked with the EARTHTIME ^{202}Pb-^{205}Pb-^{233}U-^{235}U tracer solution (ET2535; Condon et al. 2015; McLean et al. 2015) and dissolved in high-pressure Parr bombs at 210°C for 60 h. Dissolved samples were dried and redissolved in 6N HCl at 190°C for 12 h. U and Pb were separated using a single-column HCl-based ion exchange

chromatography and loaded on outgassed Re filaments with a silica gel emitter. All measurements were performed at ETH Zurich employing a Thermo Scientific Triton Plus thermal ionization mass spectrometer. Pb and U were both measured in static mode.

4 High-precision zircon U-Pb dates and trace element compositions

Zircon LA-ICP-MS U-Pb dating results are graphically illustrated in Figure 2C. The weighted mean $^{206}Pb/^{238}U$ ages of the Hewan early felsite (HW-1), early granite porphyry (HW-2), and late granite porphyry (HW-4) are 138.2 ± 0.3/2.8 Ma, 139.4 ± 0.3/2.8 Ma, and 139.5 ± 0.3/2.8 Ma (2σ, analytical uncertainty/full external uncertainty including decay and calibration factors), respectively. They overlap with each other. These dates also overlap with the $^{40}Ar/^{39}Ar$ dating of the hydrothermal sericite, confirming a close temporal and genetic link between magmatism and mineralization.

Zircon ID-TIMS U-Pb dating results are graphically illustrated in Figure 3. Three of fifteen zircons were not considered due to high analytical uncertainties. The emplacement age interpretation for each sample is based on the youngest zircon. Thus, the ID-TIMS U-Pb data of the Hewan early felsite, early granite porphyry, and late granite porphyry are 138.25 ± 0.18 Ma, 137.93 ± 0.46 Ma, and 138.21 ± 0.12 Ma, respectively. All three ages overlap with each other within 2σ uncertainty. Zircon dates from the early felsite and late granite porphyries bracketing hydrothermal ore formation at Yixingzhai point to a maximum duration of mineralization of 0.04 ± 0.22 Ma, indicating a short period of ore-formation of porphyry-hosted disseminated gold at Yixingzhai. In addition, zircons from the pre-ore early felsite (HW-1) and the syn/post-ore granite porphyry (HW-2/HW-4) are accompanied by a pronounced difference in zircon geochemistry which may reflect the variety of magma origin and evolution (Figure 4). In contrast, zircons from the syn/post-ore granite porphyry (HW-2 and HW-4) exhibit overlapping trace element geochemistry, likely reflecting similar chemistry of the two porphyries (Figure 4).

5 Conclusion

Based on clear field relations and the state-of-art zircon petrochronology, the characteristic timescale of the porphyry-hosted disseminated gold mineralization at Yixingzhai is established to be no more than 0.04 ± 0.22 Ma, showing a short duration of ore-forming processes. In addition, the difference in zircon trace element compositions between the pre-ore felsite and post-ore granite might indicate they are derived from two different magma reservoirs. The results confirm a genetic link between gold mineralization and underlying magmatism. Furthermore, they suggest that it is possible to form a giant gold mineralization within a short time interval.

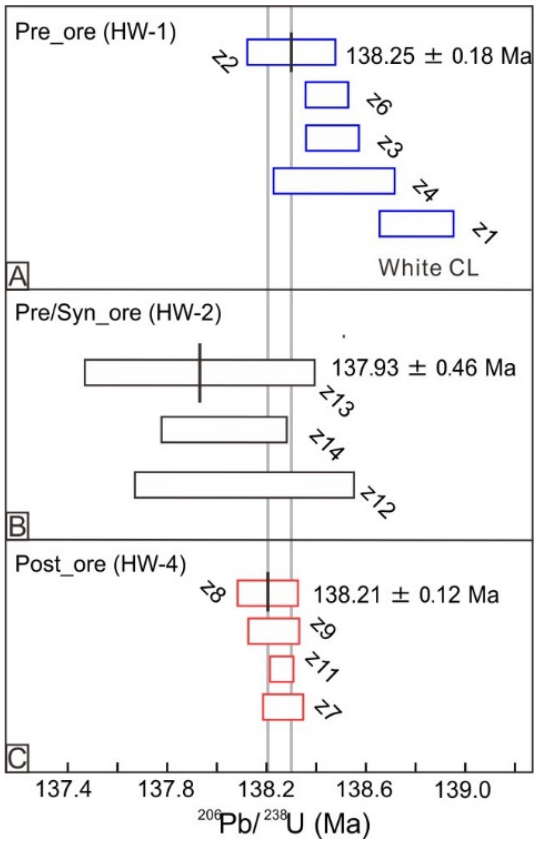

Figure 3. Summary of the zircon U-Pb ID-TIMS data (Th corrected, $Th/U_{(magma)}$ = 3.5) from the magmatic rocks in the Yixingzhai deposit.

Acknowledgments

This work is supported by the Ministry of Science and Technology of China (2016YFC0600104) and the MOST Special Fund from the GPMR, China University of Geosciences (Wuhan). Wensheng Gao acknowledges funding through the China Scholarship Council. We thank Yu-Xiang Li, Hong-Qiang Wang, Zhe Chi, Adrianna Luiza Virmond, Sava Markovic, Lorenzo Tavazzani, and Julien Allaz for their assistance with the fieldwork, sample preparation, SEM-CL, and LA-ICPMS analysis. We thank Chetan Nathwani for comments on an early version of the manuscript.

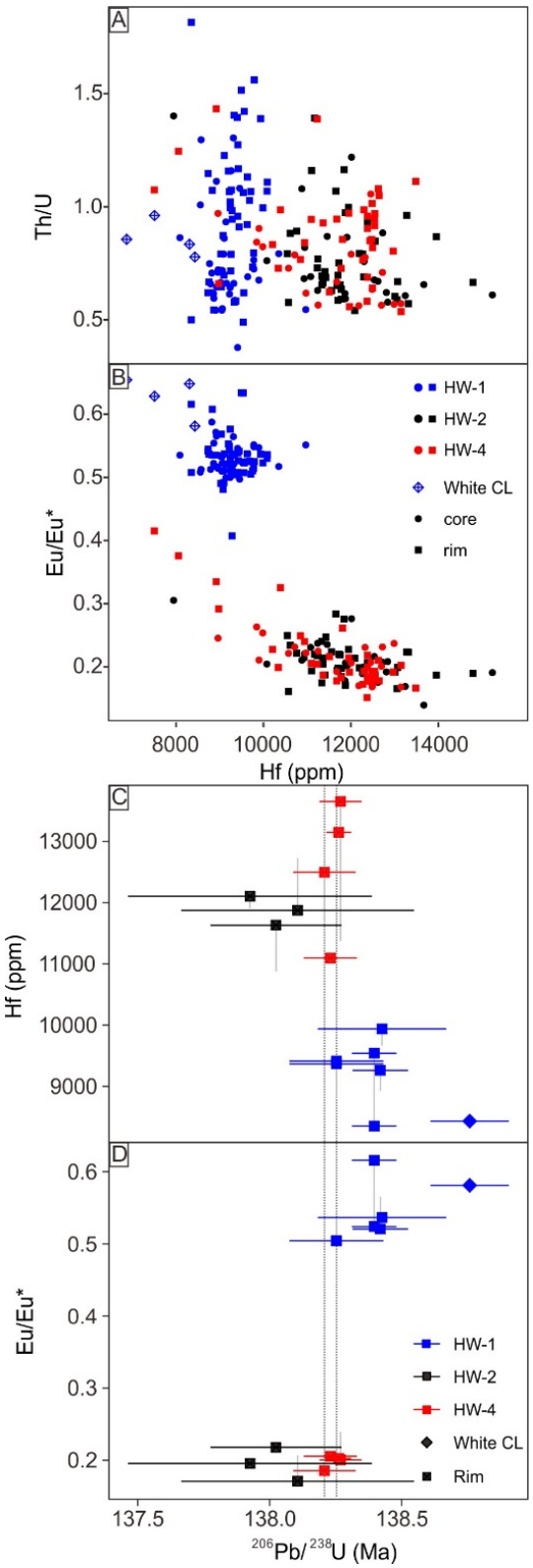

Figure 4. AB Trace element correlation diagrams for zircons from the Yixingzhai deposit. **CD** Trace element composition of ID-TIMS-dated zircons plotted against individual zircon crystallization ages. Note that the rim analyses are plotted as color-coded boxes with grey vertical lines extending to the compositions of the respective cores. Vertically dotted grey lines indicate the emplacement ages of the pre- and post-ore porphyry intrusions based on the youngest respective zircon.

References

Chang, J., Audétat, A., and Li, J.W. (2021): Tectono-magmatic controls on decratonic gold deposits, Contributions to mineralogy and petrology, v. 176, p. 1-18.

Chelle-Michou, C., Chiaradia, M., Ovtcharova, M., Ulianov, A., and Wotzlaw, J.F. (2014): Zircon petrochronology reveals the temporal link between porphyry systems and the magmatic evolution of their hidden plutonic roots (the Eocene Coroccohuayco deposit, Peru), Lithos, v. 198, p. 129–140.

Condon, D. J., Schoene, B., McLean, N.M., Bowring, S.A., and Parrish, R.R. (2015): Metrology and traceability of U-Pb isotope dilution geochronology (EARTHTIME Tracer Calibration Part I), Geochimica et Cosmochimica Acta, v. 164, p. 464–480.

Gao, W.S., Deng, X.D., Chelle-Michou, C., Zhang, L.Z., Li, J.W. (2022): 40Ar/39Ar ages constraints on lode gold and porphyry-hosted gold mineralization of the Yixingzhai gold deposit in Taihangshan District, North China Craton. SMRS 2022. Sustainable Mineral Resources Supply: Challenges for Future Generations. Geneva. p. 21.

Mattinson, J.M. (2005): Zircon U-Pb chemical abrasion ("CA-TIMS") method: combined annealing and multi-step partial dissolution analysis for improved precision and accuracy of zircon ages, Chemical Geology, v. 220, p. 47-66.

McLean, N. M., Condon, D.J., Schoene, B., and Bowring, S.A. (2015): Evaluating uncertainties in the calibration of isotopic reference materials and multi-element isotopic tracers (EARTHTIME Tracer Calibration Part II), Geochimica et Cosmochimica Acta, v. 164, p. 481–501.

Tan, J., Wei, J., Audétat, A., and Pettke, T. (2012): Source of metals in the Guocheng gold deposit, Jiaodong Peninsula, North China Craton: link to early Cretaceous mafic magmatism originating from Paleoproterozoic metasomatized lithospheric mantle, Ore Geology Reviews, v. 48, p. 70–87.

Wang, H.Q., Gao, W.S., Deng, X.D., and Li, J.W. (2020a): Zircon U-Pb dating reveals Late Jurassic gold mineralization in the Jidong district of the northern North China Craton, Ore Geology Reviews, 103798.

Wang, Z., Cheng, H., Zong, K., Geng, X., Liu, Y., Yang, J., and Wang, C.Y. (2020b): Metasomatized lithospheric mantle for Mesozoic giant gold deposits in the North China craton, Geology, v. 48, p. 169–173.

Yang, J.H., Wu, F.Y., and Wilde, S.A. (2003): A review of the geodynamic setting of large-scale Late Mesozoic gold mineralization in the North China Craton: an association with lithospheric thinning, Ore Geology Reviews, v. 23, p. 125–152.

Zhang, J.Q., Li, S.R., Santosh, M., Niu, S.D., Li, Q., and Lu, J. (2017): The magmatic-hydrothermal mineralization systems of the Yixingzhai and Xinzhuang gold deposits in the central North China Craton, Ore Geology Reviews, v. 88, p. 416–435.

Zhang, L.Z. (2018): Element geochemistry and age of the altered-porphyry gold mineralization in Yixingzhai gold deposit, Fanshi city, Shanxi Province, Geology and Mineral Resources of South China, v. 34, p. 134–141. (In Chinese with English abstract)

Zhang, L.Z., Chen, L., Wang, G.P., Deng, X.D., and Li, J.W. (2020): Garnet U–Pb dating constraints on the timing of breccia pipes formation and genesis of gold mineralization in Yixingzhai gold deposit, Shanxi Province, Earth Science, v. 45, p. 108–117. (In Chinese with English abstract)

Zhao, G.C., Sun, M., Wilde, S.A., and Li, S.Z. (2005): Late Archean to Paleoproterozoic evolution of the North China Craton: Key issues revisited, Precambrian Research, v. 136, p. 177–202.

Zhu, R., Fan, H., Li, J., Meng, Q., Li, S., and Zeng, Q. (2015): Decratonic gold deposits, Science China Earth Sciences, v. 58(9), p. 1523–1537.

The conglomerate-hosted Jacobina gold deposits, a modified paleoplacer of the Witwatersrand-type in Brazil

Enzio Garayp[1], Hartwig E. Frimmel [1,2]
[1]Bavarian Georesources Centre, Department of Geodynamics and Geomaterials Research, Institute of Geography and Geology, University of Würzburg, Am Hubland, D-97074 Würzburg, Germany
[2]Department of Geological Sciences, University of Cape Town, Rondebosch 7701, South Africa

Abstract. The genesis of the Neoarchean conglomerate-hosted Jacobina gold deposits in Brazil has been highly controversial, with both syngenetic and epigenetic models having been proposed. Here we show that they represent, analogous to Witwatersrand-type deposits (WTD), paleoplacers that became partly remobilized during later metamorphic overprint. Evidence of this includes strong lithological and sedimentological control on the Au grade, presence of detrital gold particles and other detrital clasts with gold inclusions. Detrital, syn-sedimentary and post-depositional pyrite generations can be distinguished. Syn-sedimentary pyrite has the highest Au content, from which elevated Au concentrations in Archean meteoric waters are inferred. The nature and extent of post-depositional alteration, mainly during the Paleoproterozoic Transamazonian Orogeny, distinguishes the Jacobina deposits from other WTD. Zr-in-rutile thermometry indicates peak metamorphic temperatures of >650°C, and chlorite thermometry retrograde local fluid infiltration at ca. 280°C-340°C. Local remobilized gold associated with Fe-oxides near intrusive rocks is attributed to late-Transamazonian mafic/ultramafic magmatism Remobilization during regional metamorphism was insufficient to form substantial secondary orebodies but led to purification of the gold particles that contain relatively little Ag and Cu and lack Hg.

1 Introduction

The Neoarchean metaconglomerate-hosted Jacobina gold deposits in the São Francisco Craton in eastern Brazil (Fig. 1) have been mined episodically on a small scale for more than 200 years. Presently operated by Yamana Gold Inc., they produce >6 t of Au per year. Current resource estimates indicate proven and probable resources of 100 t of Au at an average Au grade of 2.18 g/t with potential resources open at depth. The genesis of these deposits has been a matter of debate: some workers argued for a paleoplacer origin (Minter 1975; Hendrickson 1984; Molinari 1988) whereas others favored an entirely epigenetic formation (Teixeira et al. 2001; Milesi et al. 2002). This study aims at resolving this conflict on the basis of assessing the geological control on Au grade, textural observations, and mineral chemical analyses.

The gold-hosting Jacobina sequence is composed predominantly of quartzite with interlayered metaconglomerate beds and represents the fill of the Jacobina Basin, which is enclosed by the oldest terranes in South America, including a >3.4 Ga tonalite-trondhjemite-granodiorite (TTG) suite and 3.3 Ga granite-greenstone belts. Detrital zircon ages constrain the source of the Jacobina sediments to between 3251 ± 52 and 3614 ± 67 Ma (Teles et al. 2015). The Jacobina basin fill became squeezed into a major suture zone, the Contendas-Jacobina Lineament, in the course of collision of three Archean blocks during the ca. 2.0 Ga Transamazonian Orogeny (Fig. 1). This resulted in in westward thrusts and sinistral transcurrent faults due to east-west transpressive shortening. Cross-cutting abundant mafic/ultramafic sills and dikes, though not precisely dated, are probably related to the Transamazonian Orogeny.

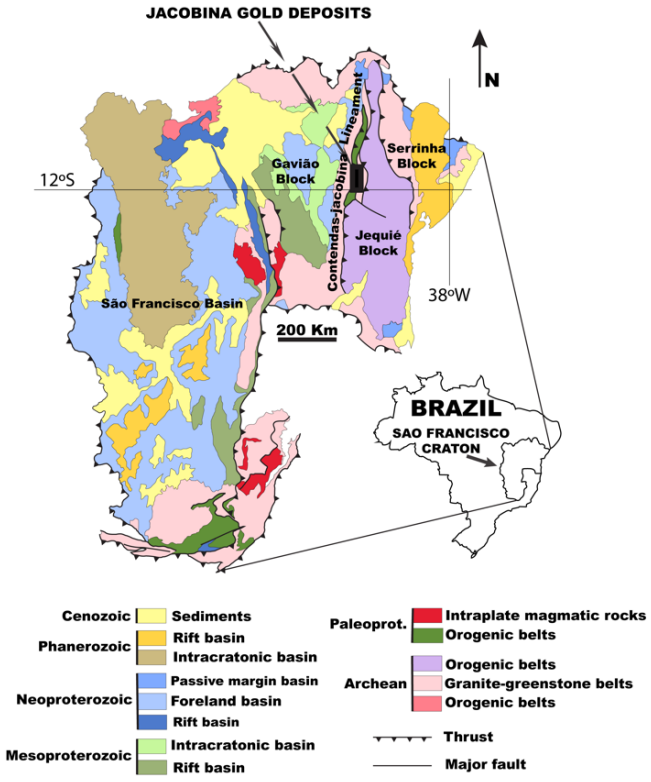

Figure 6 Location of the Jacobina gold deposits in the São Francisco Province, Brazil (modified from Delgado et al. 2003).

2 Results

Gold grade is strongly controlled by lithology: The bulk of the gold is hosted by metaconglomerates and subordinately pebbly quartzite. The orebodies (reefs) extend for several kilometers along strike and on dip at different stratigraphic levels (at least 13 reefs; Pearson et al. 2005). The Au grade is strongly related to sedimentary structures, such as specific small-pebble beds, the most densely packed conglomerates, or the bottom of large-pebble

conglomerate beds deposited at the base of channels or on unconformities.

A total of 74 polished thin sections from 12 different (reefs) were analyzed petrographically. Whereas well-rounded quartz pebbles and sand particles are undoubtedly detrital, pyrite occurs in a wide variety of textures: Round compact pyrite, which is the predominant type in most Archean conglomerates worldwide (e.g. England et al. 2002), is common also in Jacobina (Fig. 2 A). By analogy with round compact pyrite elsewhere, this type is regarded as detrital, a notion that has been consolidated throughout the years by petrography, trace element data, and isotope geochemistry (Frimmel 2014 and references therein; Guy et al. 2014). Variably rounded, inclusion-rich ("porous") pyrite is considered syn-sedimentary (Fig. 2B). Post-depositional pyrite occurs predominantly as overgrowth (Fig. 2C) and subordinately remobilized into veins with quartz (Fig. 3A).

Although a considerable proportion (ca. 25 %) of the gold occurs in texturally late positions, such as microfractures, and is thus clearly epigenetic, the majority occurs as interstitial grains within the conglomerate matrix, many of which display circular to elliptical outlines with smooth rounded boundaries in thin section (Fig. 3B). The latter are considered detrital. Of particular significance is the observation of gold inclusions within both detrital pyrite (Fig. 2A) and detrital quartz. Most of the post-depositional gold is associated with secondary pyrite but locally, near magmatic intrusive bodies, secondary gold is associated with hematite and goethite (Fig. 3C). In the latter case, hematite crystals overprint the metamorphic fabric, and oxidation affected both primary and secondary pyrite. The oxidized samples come from >600 m below surface, which precludes recent weathering.

The gold composition, as determined by electron microprobe, is, on average, 98.3 wt% Au, 1.54 wt% Ag, and 0.07 wt% Cu. Mercury was not detected. Systematic differences were noted between detrital and post-depositional gold: As an example, very pure gold veinlets contrast side by side with Ag-bearing gold inclusions in a quartz pebble, indicating that the late gold generation was depleted in Ag. This is also evident in Ag-depleted rims in detrital gold grains.

Trace element analyses of the various pyrite generations by LA-ICPMS (Table 1) revealed that the synsedimentary pyrite has the highest Au content (mean 1.86 ppm), followed by the detrital pyrite (mean 0.22 ppm) and the almost Au-free post-depositional pyrite (0.04 ppm). Relatively lower Au/Ag ratio in the post-depositional pyrite compared with the previous generations (Table 1) suggests that Au was decoupled from Ag during pyrite remobilization.

Abundant secondary pyrite and other metamorphic/hydrothermal minerals like chlorite, fuchsite, rutile, tourmaline and Fe-oxides are the most evident indicators of post-depositional alteration in the Jacobina ore assemblage. Zr-in-rutile thermometry (Meinhold 2010; Zack and Kooijman 2017) indicates peak metamorphic temperatures in excess of 650°C (ZrO_2 between 170 and 610 ppm, lower limit of detection = 160 ppm). Retrograde conditions were estimated by chlorite thermometry (Cathelineau 1988; De Caritat et al. 1993) as 280°C – 340°C. Based on its texture, most of the tourmaline is regarded as metamorphic, and its composition corresponds largely to that of tourmaline known from siliciclastic metasedimentary rocks (Fig. 4).

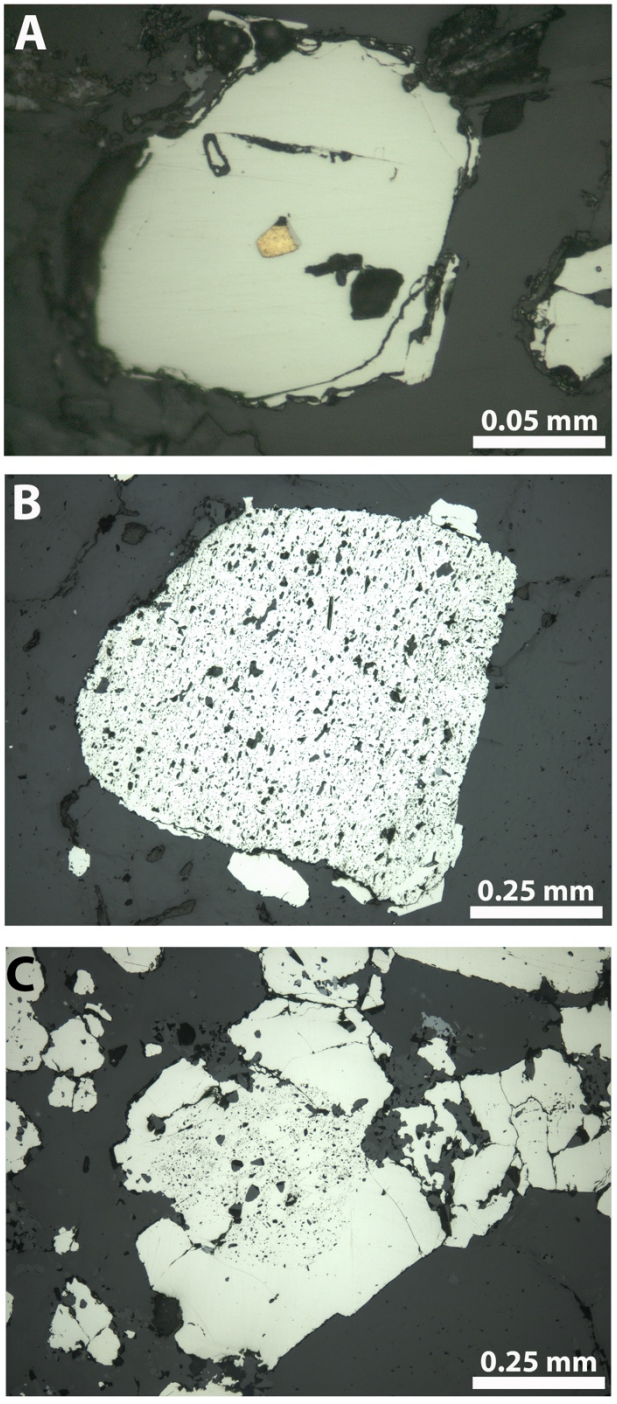

Figure 7. (A) Microphotograph of a compact detrital pyrite grain with gold-pyrrhotite inclusion in the center, (B) Microphotograph of a synsedimentary porous pyrite grain, (C) Microphotograph of euhedral pyrite overgrowth around synsedimentary pyrite (inclusion-rich core).

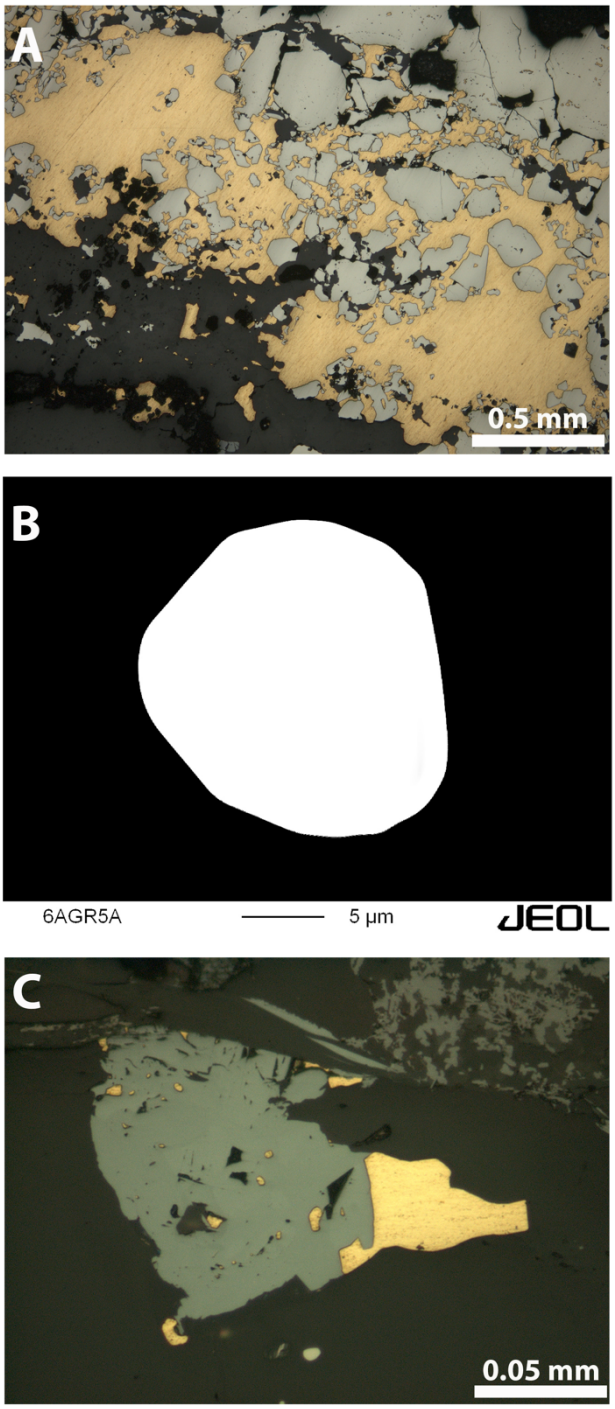

Figure 3. (A) Gold filling quartz-pyrite vein, (B) Back scattered image of a detrital gold grain (C) Remobilized gold with hematite.

Table 1 Trace element concentrations in different types of pyrite

Element	Round compact pyrite		Round porous pyrite		Secondary compact	
	Mean	Range (ppm)	Mean	Range (ppm)	Mean	Range (ppm)
As	202	30.7 – 703	833	32.5 – 9,180	320	0.61 – 1,121
Co	363	25.1 – 1,38	446	74.7 – 1,654	519	1.84 – 1,240
Ni	404	46.9 – 1,35	277	40.7 – 787	298	8.53 – 1,352
Pb	7.17	1.80 – 15.50	41.0	1.86 – 158	2.30	<0.01 – 53.3
Cu	1.70	<0.20 – 4.73	3.21	<0.20 – 11.4	0.68	<0.15 – 9.00
Au	0.22	0.11 – 0.39	1.34	0.07 – 10.9	0.04	<0.01 – 0.08
Ag	0.11	<0.02 – 0.22	0.33	0.03 – 1.82	0.04	<0.01 – 0.26
Tl	1.09	<0.01 – 3.86	0.09	<0.01 – 0.68	0.11	<0.01 – 2.90
Cd	0.21	<0.07 – 0.37	0.14	<0.07 – 0.23	0.20	<0.01 – 0.50
Au/Ag	2		4		1	

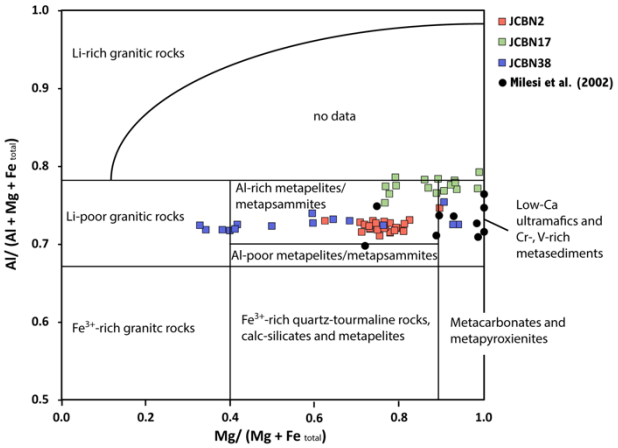

Figure 4. Tourmaline composition in the Al-Mg-Fe Diagram (Henry and Dutrow, 2018), classifying different genetic types.

3 Conclusions

There is substantial evidence of primarily placer gold concentration at Jacobina, that is, strong lithological and sedimentological control on Au grade at different scales, presence of detrital minerals with gold inclusions within heavy mineral layers, and the presence of detrital gold particles.

Three genetic types of pyrite were recognized: detrital, synsedimentary and post-depositional pyrites, analogous to Witwatersrand-type deposits elsewhere in the world. Each pyrite type had a particular role in the gold mineralization: whereas the detrital and the synsedimentary types accompanied gold accumulation, the post-depositional pyrite can be associated with Au dispersion by fluid-induced Au-depletion in detrital and synsedimentary pyrite.

The presence of synsedimentary pyrite with significantly higher Au concentrations in relation to the other pyrite types supports elevated Au contents, probably dissolved as Au-sulfide complex, in meteoric waters at the time as suggested for the Witwatersrand deposits (Frimmel 2014).

What distinguishes the Jacobina deposits from other Witwatersrand-type deposits are the nature and extent of the post-depositional alteration, mainly in the course of the Transamazonian Orogeny. Metamorphism and to a limited extent magmatism caused the partial dissolution and reprecipitation of various minerals including pyrite and gold. This remobilization changed their trace-element contents thus resulting in gold of greater fineness. It was, however, insufficient to form any substantial orebodies.

There is indication of local magmatic influence on the gold mineralization history. Mafic/ultramafic intrusives caused a thermal overprint, whereas late to post-tectonic granite emplacement triggered hydrothermal fluid circulation and further partial remobilization of ore components. The latter took place under very different redox conditions, evident from the presence of Fe-oxides/hydroxides associated with remobilized gold. This suggests

some gold remobilization after the Great Oxidation Event, probably by circulation of meteoric waters during uplift in the final stages of the Transamazonian Orogeny, which agrees with the age of the late to post-tectonic magmatism (1970 to 1800 Ma). In summary, based on the evidence of placer gold concentration and the intense post-depositional alteration, the modified paleoplacer model best fits the Jacobina gold deposits.

Acknowledgements

S. Höhn, U Schüßler and N. Koglin assisted with microprobe analyses, and H. Brätz is thanked for the LA-ICPMS analyses. We also thank Yamana Gold Inc. for providing access and logistic support to their operations in Jacobina. The analytical costs were covered by the Department of Geodynamics and Geomaterials Research at the University of Wuerzburg.

References

Cathelineau M (1988) Cation site occupancy in chlorites and Illites as a function of temperature. Clays and Clay minerals

De Caritat P, Hutcheon I, Walshe J L (1993) Chlorite geothermometry: A Review. Clays Clay Minerals 41: 219-239

Delgado IM et al. (2003) Geotectônica dos escudos das Guianas e Brasil-Central In: Bizzi LA, Schobbenhaus C, Vidotti RM, Gonçalves JH (eds) Geologia, Tectônica e Recursos Minerais do Brasil. Serviço Geológico do Brasil CPRM, Brasília, Brasil

England GL, Rasmussen B, Krapez B, Groves D (2002) Paleoenvironmental significance of rounded pyrite in siliciclastic of the Late Archean Witwatersrand Basin: oxygen-deficient atmosphere or hydrothermal alteration? Sedimentology 49:1133–1156

Frimmel HE (2014) A giant Mesoarchean crustal gold-enrichment episode: Possible causes and consequences for exploration. Society of Economic Geologists Inc. Special Publication 18:209–234

Guy BM, Ono S, Gutzmer J, Beukes NJ (2014) Sulfur sources of sedimentary “buckshot” pyrite in the auriferous conglomerates of the Mesoarchean Witwatersrand and Ventersdorp supergroups, Kaapvaal Craton, South Africa. Miner. Deposita 49:751–775

Henry DJ, Dutrow BL (2018) Tourmaline studies through time: contributions to scientific advancements. Journal of Geosciences 63:77-98

Hendrickson BR (1984) Stratigraphic position, mineralogy, depositional environment, and gold distribution of the Main Reef at Morro do Cuscuz and Morro do Vento near Jacobina, Bahia, Brazil. Unpublished MSc. Thesis, South Dakota School of Mines and Technology, Rapid City, USA

Meinhold G (2010) Rutile and its applications in earth sciences. Earth Sciences Reviews 102:1-28

Milesi JP et al. (2002) The Jacobina Paleoproterozoic gold-bearing conglomerates, Bahia, Brazil: a "hydrothermal shear-reservoir" model. Ore Geology Reviews 19:95–136

Minter WEL (1975) Sedimentological Aspects of the Serra do Córrego Formation with particular reference to the Main Reef Unit at Cuzcuz and Morro do Vento near Jacobina, Bahia, Brazil. Internal Report Unigeo Unpublished Report

Molinari L, Scarpelli L (1988) Depositos de Ouro de Jacobina in Principais Depositos Minerais do Brasil DNPM Brazil 3:463–478

Pearson W et al. (2005) Geology and gold mineralization of the Jacobina Mine and Bahia Gold Belt, Bahia, Brazil, and a comparison to Tarkwa and Witwatersrand. Window to the World: 2005 Symposium Proceedings Geological Society of Nevada Reno/Sparks 757–785

Teixeira JBG et al. (2001) Gold Mineralization in the Serra de Jacobina region, Bahia Brazil: tectonic framework and metallogenesis. Mineralium Deposita 36:332–344

Teles G, Chemale Jr. F, Oliveira CG (2015) Paleoarchean record of the detrital pyrite-bearing, Jacobina Au-U deposits, Bahia, Brazil Precambrian Research 256:289–313

Zack T Kooijman E (2017) Petrology and geochronology of rutile. Reviews in Mineralogy and Geochemistry 83(1):463-467

Revelio Aurum! uncovering invisible gold in N. America, China, and Europe

Philip Gopon[1,2], James O. Douglas[2,3], Benjamin Jenkins[2,4], Viktor Bertrandsson Erlandsson[1], Sandra Niederl[1], Patrick Sack[5], Zhuojun Xie[6], Peter Felfer[7]

[1] Dept. of Applied Geosciences and Geophysics, University of Leoben, 8770, Leoben, Austria
[2] Dept. of Materials, University of Oxford, OX1 3PH, Oxford, UK
[3] Dept. of Materials, Imperial College London, SW7 2AZ, London, UK
[4]Groupe de Physique de Matériaux, University of Rouen, 76800, Saint Etienne du Rouvray, FR
[5] Dept. of Energy, Mines, and Resources, Yukon Geological Survey, Y1A 2BF, Whitehorse, CA
[6] State Key Laboratory of Ore Deposit Geochemistry, Institute of Geochemistry, Chinese Academy of Sciences, 550081, Guiyang, P.R. China
[7] Dept. of Materials Science and Engineering, Friedrich-Alexander Universität Erlangen-Nürnberg, 91058, Erlangen, Germany

Abstract. Despite extensive study, Carlin-type gold (CTG) mineralization is still poorly understood. These deposits predominantly along major regional faults and are characterized by invisible gold thought to be hosted in sulfide minerals (Cline et al., 2005). CTG was until recently only thought to occur in central-Nevada, but discoveries in the Yukon Territory, China, and Kyrgyzstan have made us re-evaluate this. Additionally, a significant invisible gold component in other deposit types (epithermal, orogenic, porphyry, etc.) is drastically increasing the importance of these deposits. We investigated four invisible gold occurrences (Yukon, Nevada, Guizhou, and Austria) and reveal that gold is hosted in these deposits (in part) as lattice bound gold.

Our study combines high-resolution electron probe microanalysis and nano-secondary ion mass spectrometry with atom probe tomography to better understand the commonalities / differences in how gold is hosted in these geographically distant deposits and why sulfide minerals make such great hosts for gold and other critical metals. Furthermore, our atomic scale characterization suggests that the presence of arsenic is integral to the mechanisms by which gold is accommodated into the pyrite lattice, and is a commonality shared by all deposits we investigated.

1 Introduction

The Carlin-type gold (CTG) mineralization has been known in north-central Nevada since the early 1960s, but until the early 2000s was assumed to be a Nevadan phenomenon. In Nevada CTG deposits occur along 5 so called 'trends' which align with major regional faults, are hosted in silty-carbonate rocks, and are characterized by their large volume and generally low ore grade (Cline et al., 2005). Gold (the mineral) or electrum are rarely if ever reported, with the gold (element) being almost exclusively hosted in sulfide minerals.

The discovery of similar deposits in China, Kyrgyzstan, and Canada has forced us to re-think that Nevada is alone in hosting these massive and massively important gold deposits (Xie et al., 2018; Pinet et al., 2022). Furthermore, the presence of gold associated high-tech metals (ex. Te) in some of these deposits makes this deposit type potentially even more important for the Green Energy Transition and mineral resource security.

There are enough similarities between the host lithologies, tectonic setting, and gold occurrence (i.e. within sulfide minerals) but also enough dissimilarities in the same, where coming to a complete understanding of the ore-forming processes is still elusive. Notably, the most basic information, exactly how the gold is hosted in these sulfide minerals, is still something that is an open question for all of these deposits, and has large implications for the mineralization model as well as ore processing.

Our study has focused on the similarities and differences between the CTG deposits in N. America, China, and deposits with CTG like properties in Europe. The CTG deposits we investigate are all hosted in silty-carbonate host rocks, and al deposits investigated are associated or aligned with large regional fault structures. Some differences exist in the tectonic setting, but a common theme is a low energy and partially reducing depositional setting for the host rocks, be it a continental edge or an interior basin (Cline et al., 2005; Liang et al., 2021; Pinet et al., 2022). Gold is always hosted in arsenic containing pyrite which grows on top of a sedimentary or diagenetic pyrite core. The pyrite core, as well as the overgrowths, have variable trace elemental signatures as well as different textural forms. Despite this, all gold occurs as bound within the crystal lattice of arsenian-pyrite (Gopon et al., 2019), with an intimate link between arsenic and gold noted at the regional, meter, micrometer (Figure 1), nanometer (Figure 2), and atomic scale (Figure 2).

Our study combines high-resolution electron probe microanalysis (EPMA) and nano-secondary ion mass spectrometry (nanoSIMS) with atom probe tomography (APT). Using a select number of examples from North America, Europe, and China we present data that help to constrain how gold is hosted in these deposits, why sulfide minerals make such great hosts for gold and other critical metals, and share insights from atomic scale trace element and isotopic analysis into the formation mechanisms of these deposits.

2 Methods

2.1 High resolution mapping

High resolution maps where conducted using low voltage EPMA as well as a nanoSIMS to determine the micrometer scale distribution of trace elements in arsenic and gold containing pyrite. nanoSIMS analyses were conducted using a CAMECA 50L at Tianjin University and EPMA maps were acquired on a field emission gun sourced CAMECA SX5 at the University of Oxford.

2.2 Atomic probe tomography

Focused ion-beam scanning electron microscope (FIB-SEM) liftouts where taken from gold containing sub-domains identified in the high resolution maps. The liftouts on the three Carlin deposits (Yukon, Guizhou, and Nevada) were done using a Zeiss Crossbeam at the University of Oxford, and the liftouts from the Austria deposit (Flatschach district, Styria) where conducted on a FEI Helios at the University of Erlangen. APT experiments on the three Carlin deposits where conducted on a CAMECA LEAP 5000HR at the University of Oxford, and the Austrian gold containing pyrite was analyzed with a CAMECA LEAP 4000HR at the University of Erlangen.

3 Results

3.1 Mapping results

High resolution mapping of the gold containing pyrite from the three Carlin type deposits show similar features in terms of a barren sedimentary or detrital core overgrown by a gold and arsenic rich hydrothermal pyrite (Figure 1). The gold and arsenic tends to occur in complicated oscillatory zoned, micrometer scaled, overgrowths in the pyrite from Nevada and Guizhou. The Yukon gold containing overgrowths do not appear zoned at the micrometer scale and in general tend to be much smaller in size compared to those from Nevada and Guizhou (1-2 micrometers vs 5-20 micrometers). The Austrian gold containing pyrite showed a much more complicated zoning pattern within the pyrite compared to the CTG deposits, with no clear barren core- gold rich rim pattern discernible. The zoning appeared 'washed out' in places, in especially along fractures.

In all samples analyzed a correlation between high gold and high arsenic containing regions was noted, but not in all cases where high arsenic regions noted to be elevated in gold.

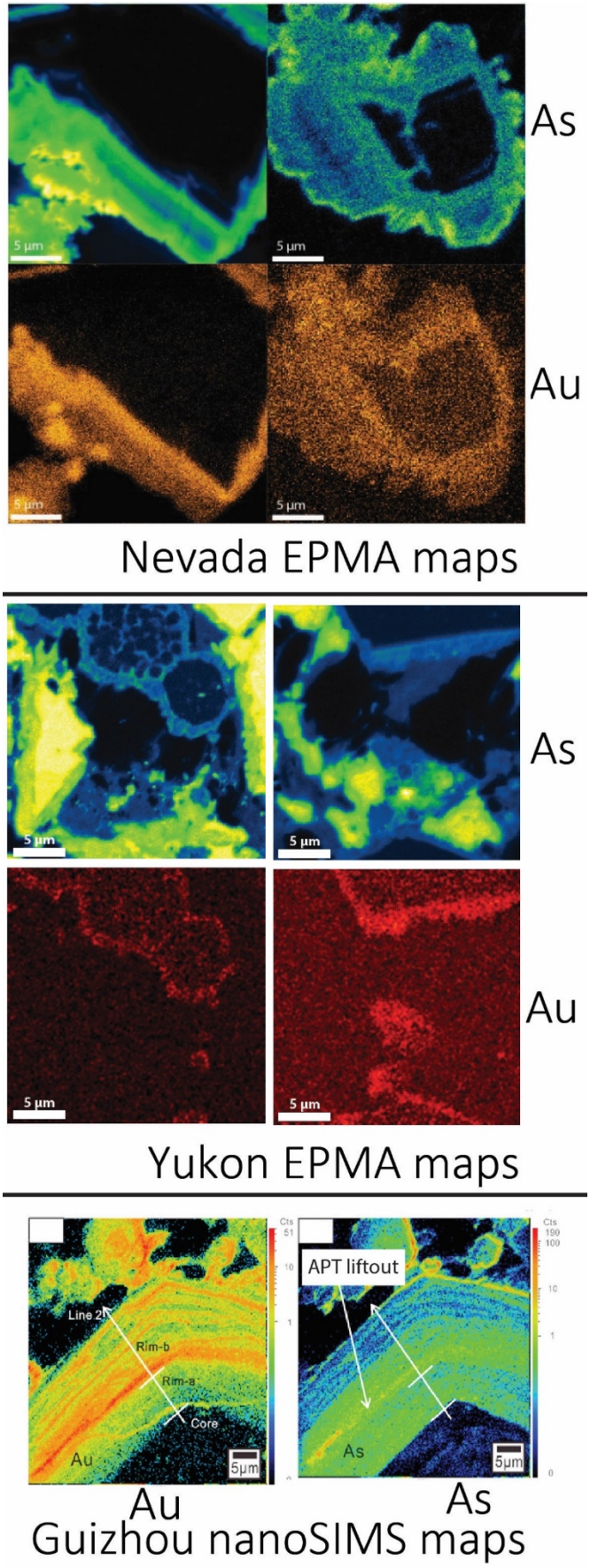

Figure 8. EPMA and nanoSIMS maps showing the distribution of arsenic and gold in pyrites from Nevada (top), Yukon (middle), and Guizhou (bottom).

3.2 APT results

Pyrite from the Yukon and Guizhou deposits showed nanoscale zoning, which were not noted in
APT datasets from the Nevadan pyrites. Within these zones, atomic scale characterization of the gold containing pyrite reveals homogenously distributed gold and arsenic (Figure 2). A correlation between high gold and arsenic was similarly noted within these nanoscale zones, as noted at the µm scale.
Atomic scale spatial analysis using the 3-depict software package revealed that there is higher arsenic concentration, compared to the matrix, surrounding individual gold atoms.

4 Discussion

High resolution mapping revealed similar textures (barren core, gold and arsenic containing rim) at the micrometer scale in all studied Carlin type deposits. The similarities of the host rock (interbedded shales and carbonates) of these deposits suggest that this lithology is important in the mineralization model for this deposit type (Muntean et al., 2011). Similarly, the oscillatory zoning that was present in all the Carlin deposits suggest similar processes where at work. This oscillatory zoning could have been caused by either growth from multiple fluid pulses, a constantly evolving single fluid pulse, or diffusion driven self-reorganization (Gopon, et al., 2019; Fougerouse et al., 2016).

The host rock (amphibolite) in the Austrian deposit is much different than the Carlin deposits. The deposit was originally mined as a Cu-Au resource in the Middle Ages-Renaissance, and visible gold and copper-sulfides where the primary minerals won. However, we note that the pyrite in the old mine waste piles, is similarly gold and arsenic rich as the pyrite from the Carlin deposits. It is notable that there is no barren (sedimentary or detrital) core to the pyrites, but simply a complicated oscillatory zoning that is often locally distributed, especially surrounding fractures in the pyrite. This suggests that the arsenic, and gold, were remobilized during later metamorphic overprinting.

5 Conclusion

Gold containing pyrite from three Carlin type deposits, show very similar textural features at the micrometer, nanometer, and atomic scale. Gold is contained within arsenic rich overgrowths, on a barren core. The non-Carlin deposit investigated showed very different core-rim patterns, but where found to be similarly oscillatory zoned as the overgrowth in the Carlin pyrites. Within the gold/arsenic rich zones, gold and arsenic is noted to be homogenously distributed (i.e. lattice bound). Moreover, our atomic scale spatial analysis shows that there is an enrichment of arsenic surrounding individual gold atoms, suggesting that arsenic is key to the incorporation mechanism of gold into the pyrite lattice (Gopon et al., 2019).

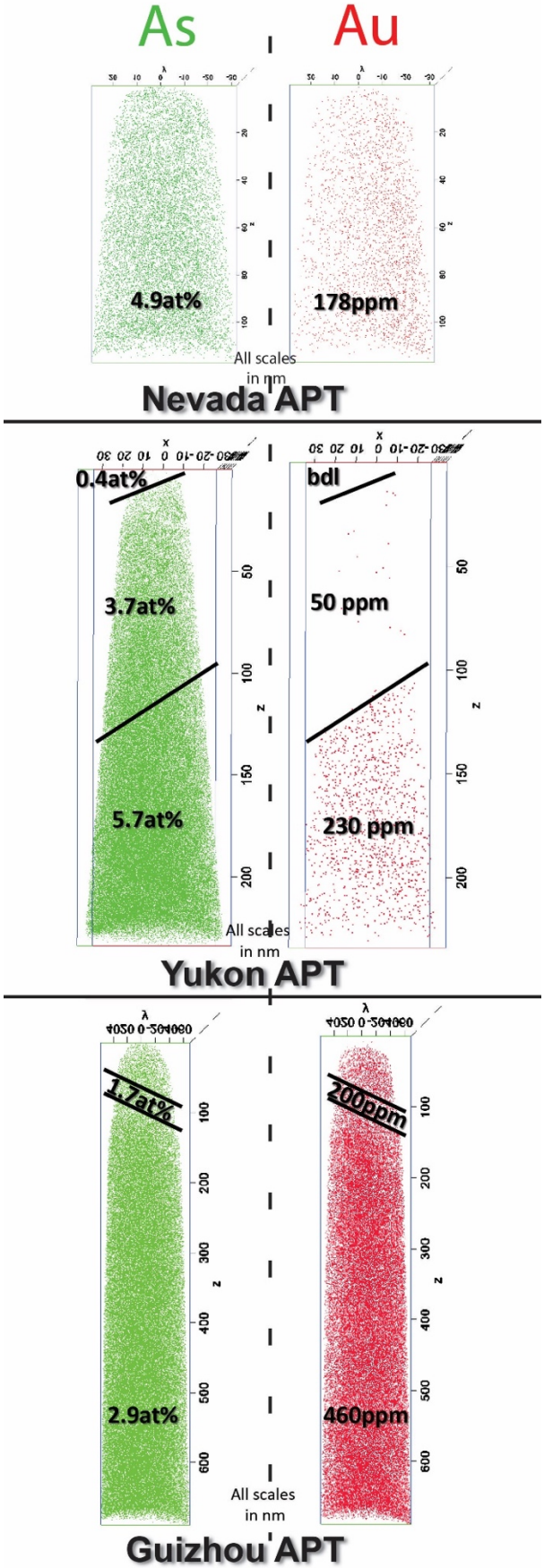

Figure 9. 3-D atom probe reconstructions showing the distribution of arsenic (left) and gold (right), in pyrite from Nevada (top), Yukon (middle), and Guizhou (bottom).

References

Cline, J.S., Hofstra, A.H., Muntean, J.L., Tosdal, R.M., and Hickey, K. a., 2005, Carlin-Type Gold Deposits in Nevada: Critical Geologic Characteristics and Viable Models: Economic Geology, v. 100th Anni, p. 451–484

Fougerouse, D., Reddy, S.M., Saxey, D.W., Rickard, W.D.A., Van Riessen, A., and Micklethwaite, S., 2016, Nanoscale gold clusters in arsenopyrite controlled by growth rate not concentration: Evidence from atom probe microscopy: American Mineralogist, v. 101, p. 1916–1919

Gopon, P., Douglas, J.O., Auger, M.A., Hansen, L., Wade, J., Cline, J.S., Robb, L.J., and Moody, M.P., 2019, A Nanoscale Investigation of Carlin-Type Gold Deposits: An Atom-Scale Elemental and Isotopic Perspective: Economic Geology, v. 114, p. 1123–1133

Liang, Q.L., Xie, Z., Song, X.Y., Wirth, R., Xia, Y., and Cline, J., 2021, Evolution of invisible au in arsenian pyrite in carlin-type Au deposits: Economic Geology, v. 116, p. 515–526

Muntean, J.L., Cline, J.S., Simon, A.C., and Longo, A. a., 2011, Magmatic–hydrothermal origin of Nevada's Carlin-type gold deposits: Nature Geoscience, v. 4, p. 122–127

Pinet, N. et al., 2022, Yukon's Carlin-Type Gold Deposits (Rackla Belt, Canada): Main Characteristics and New Insights on Alteration Styles and Geochemistry: Economic Geology, v. 117, p. 875–904

Xie, Z., Xia, Y., Cline, J.S., Koenig, A., Wei, D., Tan, Q., and Wang, Z., 2018, Are There Carlin-Type Gold Deposits in China ? A Comparison of the Guizhou , China , Deposits with Nevada , USA , Deposits: Reviews in Economic Geology, v. 20, p. 187–233

Reconnaissance mineral and cathodoluminescence studies of gold occurrences in the Pogo-Black Mountain area, eastern interior Alaska, USA

Garth E. Graham[1], Erin E. Marsh[1], Heather A. Lowers[1], Ryan D. Taylor[1]
[1]U.S. Geological Survey, Geology, Geophysics and Geochemistry Science Center, Denver, CO

Abstract. The Pogo Au deposit is the largest of a number of gold occurrences in eastern interior Alaska, that occur along a broad trend from west of Pogo to Black Mountain. Some of these occurrences are hosted in amphibolite facies gneisses and others in middle Cretaceous igneous rocks that intruded the older metamorphic rocks. All occurrences contain arsenopyrite and pyrite. Whole rock geochemical trends distinguish most metamorphic rock-hosted vein prospects (strong Bi-Te-Au correlations) and intrusion-hosted occurrences (weak As-Au correlations). Brecciated quartz veins in metamorphic rocks have paragentically late Bi-Te (±S) + Au that post-dates Fe-As sulphide deposition. High grade vein samples from the Tibbs Creek intrusion-hosted deposits contain pyrite and arsenopyrite, generally lack Bi-Te minerals, but can contain paragentically younger euhedral quartz, stibnite and carbonate. Cathodoluminescence (CL) studies of gold-rich samples indicate that quartz dissolution occurred during the syn- to post-tectonic Bi-Te-Au deposition, and the later stibnite event. In the case of metamorphic rock-hosted deposits (e.g., Pogo, Gray Lead), Bi-Te and gold deposition commonly occurs in microfractures within quartz veins; the limited quartz in these fractures have distinctive CL response. We propose that gold deposition is related to changes in pressure-temperature (P-T) conditions rather than fluid-rock chemical reactions. Similar quartz dissolution textures affect the void-filling euhedral quartz before or during stibnite and carbonate mineralization in high-grade Au samples from Blue Lead.

1 Introduction

Pogo is a significant quartz-vein-hosted Au mine (e.g., Rombach et al., 2002) operating in the Big Delta quadrangle, eastern interior Alaska. Historic and ongoing regional exploration programs have identified many additional gold prospects over the past several decades (Fig. 1). These include occurrences 40 km east in the vicinity of Black Mountain (Fig. 1; U.S. Geological Survey (USGS), 2018). Some prospects are hosted within gneiss and schist of the Lake George sequence and others are hosted in middle Cretaceous igneous rocks that intrude the metamorphic sequence (Foster et al., 1994; Teck Resources Inc., 1998; Dusel-Bacon et al., 2017). The two prevailing models for the genesis of Pogo and other deposits based on the presence of proximal Cretaceous intrusions: 1) magmatic-hydrothermal (e.g., Thompson and Newberry, 2000; Thompson, 2020), and 2) metamorphic fluid (orogenic) deposit (Goldfarb et al., 2007).

We present a reconnaissance-scale summary of geochemical signatures of mineralized rock from these deposits and quartz- and ore-mineral textural data on select high grade Au samples from certain occurrences. The observations provide relative timing of mineralization stages among the mineral occurrences. Kreiner et al. (this volume) provides complimentary details on the geochronology of igneous units and ore and gangue minerals.

2 Deposit and prospect characterisations

General descriptions of mineral occurrences discussed in the study area (Fig. 1) are provided in U.S. Geological Survey (2018) and Rimfire Minerals (2008). Examples of metamorphic rock-hosted occurrences examined in this study are from Pogo, Hill 4021 (Pogo property deposit), Gray Lead, and Boundary. Intrusion-hosted deposits include West Pogo, and Blue Lead/Michigan and other prospects north of Gray Lead on Black Mountain. Most of the sampling conducted in our study was in surface dumps and trenches, and samples from the Pogo mine were collected from faces and drill core was examined Black Mountain area deposits (Fig. 1).

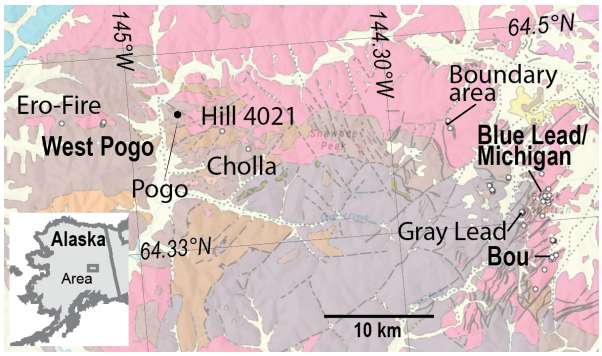

Figure 1. Location map of selected Au occurrences. Intrusion-hosted sites are bolded. Blue Lead, Gray Lead, and Bou occur along Black Mt. Pink=igneous rocks, yellows=cover, grays and browns=metamorphic rocks (Wilson et al., 2015).

Metamorphic rock-hosted quartz veins cut across foliation of amphibolite facies Lake George orthogneiss and paragneiss. At Pogo, where veins are up to 20 meters thick, alteration assemblages include early biotite and later sericite-dolomite. A surface exposure of an auriferous quartz vein at Gray Lead is approximately ~ 0.7-m true thickness with minor bleaching of wall rock. Veins in intrusive rocks can be meter-scale but are often narrower, typically sheeted to cross-cutting cm-scale-thickness vein sets in typically bleached/ sericitized granitoids (e.g., Blue Lead/Michigan.)

2.1 Whole Rock Geochemistry

Geochemical datasets (Graham et al., 2021; Rimfire Minerals, 2008) permit broad comparison of elemental ratios among different mineral occurrences. The Au:Bi ratios are highly correlative in Pogo, Gray Lead, and Boundary sites, where Bi and Au can exceed 1000 ppm and 100 ppm, respectively (Fig. 2a). Other metamorphic rock-hosted quartz vein occurrences proximal to Boundary contain high Bi (100s to ~3500 ppm), but relatively low <~1ppm Au. In contrast, Au:Bi does not correlate in most intrusion-hosted vein samples north of Gray Lead (Graham et al., 2021; tiny dots, Fig. 2a). These occurrences are generally Bi-poor despite gold concentrations locally exceeding ~20 ppm. Notable exceptions are the Blue Lead intrusion-hosted prospect and a four sample subset from West Pogo (Fig. 2a,b). The Te:Bi ratios have r^2 values of >0.86 for the Pogo, Grey Lead, and Boundary sites. Occurrences proximal to Boundary lack detectable Te (Fig. 2b). The intrusion hosted Blue Lead occurrence has a comparable Te:Bi correlation but with lower average Te and Bi concentrations then the suite of metamorphic hosted occurrences. A four sample subset collected at West Pogo also shows a distinct Te:Bi correlation.

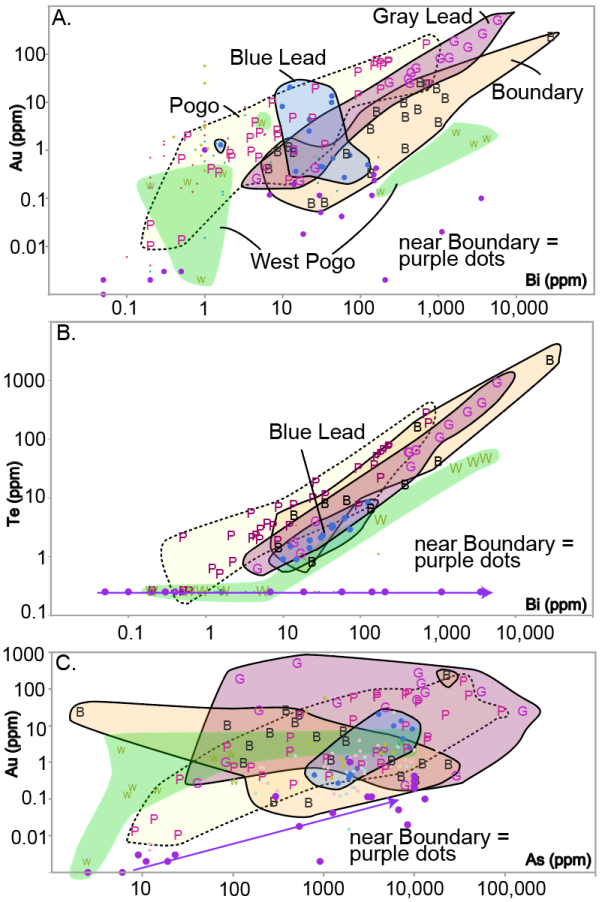

Figure 2. Grab sample whole rock geochemistry. (A) Bi vs Au, (B) Bi vs Te, and (C) As vs Au. Occurrences discussed in text are labelled. Data include Graham et al., 2021 and Rimfire Resources (2008).

Despite ubiquitous arsenopyrite(±loellingite) in all occurrences (see section 3.2), the Au:As correlation is relatively poor among occurrences. There is a qualitatively weak trend in our Pogo data as well as the near Boundary samples (Fig. 2c). Neither Gray Lead nor Boundary display a significant correlation. The Blue Lead intrusion-hosted system displays a somewhat tighter correlation, but with relatively more limited Au and As grades. There are some weak potential trends between Au:Sb, particularly for West Pogo, Blue Lead, and prospects near Boundary (Graham et al., 2021; not shown).

3 Vein textures

Mineralized vein samples from several different occurrences were examined initially using optical microscopy. Reconnaissance studies were then focused to samples that contain visible gold in thin sections. Samples from Pogo and Hill 4021 (Pogo project area), Gray Lead and Blue Lead/Michigan, and Boundary occurrences were included (Fig. 1).

Mineralized quartz veins from these occurrences typically demonstrate multi-stage development. There are one or more quartz generations and common evidence of brecciation, recrystallization, and dissolution. Sulphide and ore minerals are dominantly interpreted to be paragenetically late relative to one or more stages of quartz deposition.

3.1 Quartz and gangue mineral textures

Most of the quartz appears to be the earliest paragenetic stage. It is relatively coarse grained, with numerous secondary fluid inclusion trails/microfractures (Fig. 3a), and areas recrystallized to finer-grained mosaic quartz (not shown). Irregular boundaries are invariably present between quartz grains. White mica, chlorite, and Ti-oxides are present within the veins and are likely remnants of now-altered wall rock inclusions. Carbonate occurs as mm-scale through-going veins or spotty patches along some fractures in the Pogo samples. Samples from the Blue Lead and Michigan areas (Fig. 1) contain distinct late inward-terminating coarse quartz crystals overgrowing brecciated and recrystallized quartz. This texture suggests reopening of pre-existing veins. Carbonates can fill the remaining open space.

3.2 Sulphide/Bi±Te-Au mineralogy and textures

Petrographic and qualitative scanning electron microscopy (SEM) observations of the selected samples indicate similar, if incomplete parageneses among the different occurrences. Most deposits contain trace amounts of jamesonite, boulangerite, and/or other sulfosalts. Sulphide/ore mineral paragenesis in our sample suite broadly includes one or multiple stages of pyrite and arsenopyrite ± minor Au à Bi-Te-Au in most metamorphic-rock hosted occurrences. In a few of the intrusion hosted samples, minor As-Bi-Te-Au mineralization is

associated with brecciated quartz, whereas stibnite fills voids associated with the paragentically younger euhedral quartz.

Pyrite and arsenopyrite can occur as 10's of microns-scale euhedral crystals and aggregates as well as have highly milled textures, sometimes as mm's-scale masses and bands with broken edges and extensive fracturing, particularly in Pogo property (Pogo proper and Hill 4021) and Gray Lead samples. Gold has been observed within pyrite (but not our reconnaissance samples), and minor visible-Au is seen within arsenopyrite; Both sulphides can also locally be overgrown by Au or contain Au in cross-cutting fractures.

The vast majority of visible Au (electrum) in metamorphic rock-hosted occurrences is associated with influx of Bi/Bi-Te (±S) minerals. These minerals occur as complex 1-50+ µm intergrowths in late microfractures. When present with pyrite and arsenopyrite the Bi-Te-Au assemblages typically drape the sulphides. The late fractures can contain carbonate minerals.

In our selected high Au-grade samples from intrusion-hosted occurrences, arsenopyrite-pyrite bearing quartz vein generations are paragenetically early and associated with the older quartz described above. Bi-Te minerals are very rare. Late-stage massive stibnite and carbonate that fill the remaining space in these veins have irregular boundaries that cross-cut growth zones observed in CL in euhedral quartz, suggesting quartz dissolution in the vuggy space prior to or during stibnite deposition (not shown). Only one micron-scale gold grain was observed in massive stibnite. Euhedral quartz or massive stibnite were not observed in our metamorphic rock-hosted samples.

3.3 Vein Cathodoluminescence (CL) and Preliminary Raman Fluid Inclusion Analysis

CL imaging using a JEOL 8530F Plus at the USGS microbeam laboratory in Denver, Colorado, is a powerful tool for imaging quartz textures associated with sulphide and visible gold that were not obvious using standard optical microscopy (Fig. 3).

The CL spectral results demonstrate key aspects of the paragenesis among vein samples. First, at the ~2.8 eV position (broadly equivalent to the position of Ti in quartz), ghosts of original quartz, sometimes with preserved distinct growth/sector zoning are visible in what is now a series of mosaic quartz grains (Fig. 3a,c,d). Second, a later, spectrally distinct, lower intensity at the 2.8 eV position signature defines "microveinlets" – these correspond to zones of obvious and cryptic fractures in optical microscope images.

The imaging reveals important empirical relationships in the paragenesis of the occurrences. The images highlight: 1) the deformation and recrystallization of the original quartz; 2) sulphides (e.g., arsenopyrite in Fig. 3) cut across apparent growth zoning the now deformed quartz; 3) Bi-Te and Au minerals and lesser pyrite-arsenopyrite are almost ubiquitously in direct contact with the lower intensity quartz microveinlets. In the examples from the intrusion-hosted occurrences, the youngest euhedral quartz is partially dissolved, and space replaced by massive stibnite (not shown).

Preliminary Raman examination of the vapor phases in 2-phase liquid-gas fluid inclusion assemblages associated with low spectral-response quartz zones and sulphides (Fig. 3c,d) contain unquantified but distinct methane and CO_2 peaks.

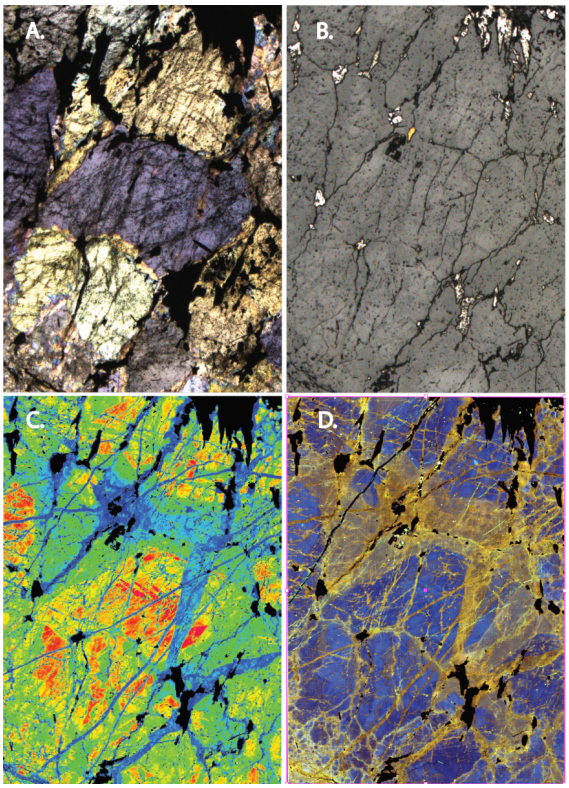

Figure 3. Arsenopyrite (upper right in images) and Bi-Te minerals and gold in quartz vein from Gray Lead. A. cross polarized image, B. reflected light, C. ~2.8 eV peak intensity, and D. false color RGB overlay. Image width = 2 mm.

4 Discussion

Gold mineralization involved at least two overlapping geochemical signatures. Low-grade gold was introduced, both as minor Au inclusions and possibly as enrichments within arsenopyrite, pyrite, and sulfosalts. The Bi-Te-Au assemblages, which produce significant free gold affected nearly wholly metamorphic rock-hosted quartz veins. This in part enhances the apparent grades of these occurrences. Interestingly, despite high Bi values in vein samples from prospects near Boundary (purple dots; Fig. 2) they lack high Au or Te grades, highlighting the relationship between Au and Te.

The cause of the chemical differences between prospects, and localized overprint of stibnite in some intrusion hosted occurrences is uncertain. Host rock composition (meta-sediment vs Cretaceous

intrusion), differential depths of emplacement/zoning and/or different fluid events (e.g. stibnite-rich zones observed in igneous-hosted Black Mountain occurrence) are some viable options.

The CL imaging provides important insights as to quartz-sulphide relationships that are not fully apparent using optical microscopy. Fe-As sulphide deposition (observed across prospects) appears to be syn- to post-deformation of original quartz veins. The CL imaging (Fig. 3) further shows that sulphide grains cross-cut growth zones in quartz and that Bi-Te-Au±sulphide minerals occur in "microveinlets" that do not always appear as distinct visible manifestations in the quartz they cut when examined by optical microscopy. These textures demonstrate that quartz was either soluble (case 1) or at least not being deposited in volume (case 2) during these mineralizing events. The "microveinlets" may represent alteration of quartz chemistry along the edges of micro-scale fractures.

The absence of quartz deposition during the main mineralizing events (and localized carbonate precipitation) may be related to CO_2-rich nature of the ore-forming fluids observed in preliminary Raman analyses. These fluids are likely equivalent to similarly described low salinity methane-CO_2-rich fluids, inferred to be syn-Au ore (Baker et al., 2006; Rombach et al. 2002). Modelling by Li et al. (2020) demonstrates that CO_2-rich fluids can cause retrograde quartz solubility we observe under reasonable conditions due to isobaric cooling or isothermal decompression; these types of fluids have been observed in fault-valve related orogenic gold deposits. The predominance of sulphides, and particularly Au-bearing assemblages in quartz veins, some in apparent isolation from wall-rock slivers (and suggestions of decreased Ti contents in fractures/ late quartz implied in CL) supports changes in pressure-temperature (P-T) conditions as a controlling factor. Similar chemistry across a broad area (Pogo property prospects to Gray Lead) suggests a reduced (metamorphic(?)) ore fluid, at least for the Au and Au-Bi-Te stages of mineralization in the metamorphic rock-hosted systems. Further study could help to enhance our understanding of the relationships between the metamorphic hosted occurrences and the intrusion-hosted deposits overprinted by the Sb-dominant event.

5 Conclusions

The Pogo-Black Mountain study area contains both metamorphic rock- and intrusion-hosted gold-rich deposits/occurrences. There may have been a relatively widespread Fe-As (Sb-Pb) mineralizing event. Bi-Te-Au deposition impacted predominantly metamorphic-rock-hosted prospects, whereas a late Sb± minor gold event affected the intrusion-hosted deposits on Black Mountain. The high-grade Bi-Te-Au event(s) (and Sb at Blue Lead/Michigan) identified in our limited sample set appear decoupled from quartz deposition. Relationships through space and time between metamorphic rock and igneous-hosted deposits could be refined with further research.

Acknowledgements

This work was funded as part of the U.S. Geological Survey Mineral Resource Program initiatives. Doug Kreiner and George Case provided thoughtful reviews. Any use of trade, firm, or product names is for descriptive purposes only and does not imply endorsement by the U.S. government.

References

Baker T, Ebert S, Rombach C, Ryan CG (2006) Chemical compositions of fluid inclusions in intrusion-related gold systems, Alaska and Yukon, using PIXE microanalysis. *Econ Geol 101*(2), 311-327.

Dusel-Bacon C, Holm-Denoma C, Jones III J, Aleinikoff J, Mortensen J. (2017) Detrital zircon geochronology and provenances of quartzose metasedimentary rock sfrom paraytochthonous north America, East-Central Alaska. Lithosphere, v.9 p.927-952.

Foster HL, Keith TE, and Menzie WD (1994) Geology of the Yukon-Tanana terrane of east-central Alaska. in The Geology of Alaska. edited Plafker G and Berg HC. Geol. Soc. Amer. Boulder CO, The Geology of North America, G-1:205-240

Goldfarb RJ, Marsh EE., Hart, CJR., Mair JL, Miller ML, and Johnson C. (2007) Geology and origin of epigenetic lode gold deposits, Tintina Gold Province, Alaska and Yukon: Chapter A in Recent U.S. Geological Survey studies in the Tintina Gold Province, Alaska, United States, and Yukon, Canada—results of a 5 year project. U.S Geological Survey Scientific Investigations Report 2007-5289, pA1-A18.

Graham GE, Peterson ML, Marsh EE, and Taylor RD (2021) Whole rock geochemical data from the eastern part of the Yukon-Tanana Upland region, Alaska, USA: U.S. Geological Survey data release, https://doi.org/10.5066/P95OKTU7.

Li XH, Klyukin YI, Steele-MacInnis, M, Fan, HR, Yang KF, Zoheir B, (2020) Phase equilibria, thermodynamic properties, and solubility of quartz in saline-aqueous-carbonic fluids: Application to orogenic and intrusion-related gold deposits: Geochim et Comochim. Acta, v. 283, p. 201-221.

Rimfire Minerals (2008) 2008 Technical Report on the Goodpaster district properties, Rimfire internal report. Last accessed on sedar: Feb 26, 2022.

Rombach, C.S., Newberry, R.J., Goldfarb, R.J., and Smith, M, (2002) Geochronology and mineralization of the Liese zones, Pogo deposit, Alaska [abs.]: Geol Soc of America Abstracts with Programs, v. 34, no. 6, p. 114.

Teck Resources Inc. (1998) Pogo project advanced exploration program, Stage II application and plan of operations: Teck Resources Inc. report, 75 p.

Thompson W (2020) Geochemical, spatial, and temporal relationships of the intrusives and meta-intrusives of the Pogo deposit, eastern interior Alaska. MS Thesis, University of Alaska, Fairbanks. 146p.

Thompson JFH, Newberry RJ (2000) Gold deposits related to reduced granitic intrusions. In: Hagemann SG, Brown PE (eds) Gold in 2000: Rev Econ Geol 13:377–400.

U.S. Geological Survey (2018) Alaska Resource Data File (ARDF): U.S. Geological Survey, http://ardf.wr.usgs.gov.

Wilson, FH, Hults CP, Mull CG, and Karl SM (2015) Geologic map of Alaska: U.S. Geological Survey Scientific Investigations Map 3340. compilers 2 sheets, scale. 10.3133/sim3340, 1:1,584,000, 196 p. pamphlet

Precipitation of gold by wallrock sulfidation in the Val-d'Or Vein Field, Abitibi Subprovince (Québec, Canada)

Michael Herzog[1], Crystal LaFlamme[1,2], Georges Beaudoin[1], Guillaume Barré[1], Laure Martin[2], Dany Savard[3]
[1]Département de géologie et de génie géologique, Université Laval, Québec, Canada
[2]Centre for Microscopy, Characterisation & Analysis, University of Western Australia, Western Australia, Australia
[3]Laboratoire des Matériaux Terrestres, Université du Québec à Chicoutimi, Québec, Canada

Abstract. Orogenic gold deposits hosted in meta-sedimentary basins are known to precipitate gold through coupled Au-As redox reactions, resulting in As-rich pyrite (As>>1 wt%) containing native Au inclusions and lattice-bound Au. Gold precipitation mechanisms in gold districts not hosted in meta-sedimentary wallrocks remain poorly understood. Five quartz-tourmaline-carbonate vein orebodies (Goldex, Triangle, Plug #4, Pascalis Gold Trend, Beaufor) of the Val-d'Or Vein Field, hosted in a greenstone belt sequence, contain gold in vein- and wallrock-hosted pyrite-rich (>95 vol%) sulfide aggregates, displaying a porous core (Py1; 0<Au<<30 ppm) and homogeneous rim (Py2; Au<1250 ppm). Py2 hosts bulk of the native Au or polymetallic (Au-Ag-Te-Bi) inclusions, primarily calaverite. An ubiquitous isotopic shift in $\delta^{34}S$ values (+3.0‰) from Py1 to Py2 in the orebodies suggests that fluid desulfidation-wallrock sulfidation controls gold precipitation. This mechanism leads to a decrease in fluid fS_2 by removal of $Au(HS)^-$ under reducing fO_2 conditions, supported by a corresponding decrease and consistently low contents in Co and Ni from Py1 (4500 ppm and 635 ppm) to Py2 (<550 ppm and <2200 ppm). Here, we show that a coupled decrease in fluid fS_2, fO_2, and fTe_2, induced by wallrock sulfidation, can lead to efficient gold deposition as inclusions in As-poor (<0.1 wt%) pyrite.

1 Introduction

Changes in fluid chemistry that result in the formation of orogenic gold deposits (OGD) depend on several physico-chemical parameters including temperature, pressure, as well as the fluid sulfur ($fS2$) and oxygen ($fO2$) fugacities. Both can have significant destabilizing impacts on reduced HS^- complexes, the most important Au-transporting ligands in OGD. Particularly, a decrease in fluid $fS2$ (i.e., removal of H_2S) and/or increase in fluid $fO2$ (i.e., removal of H_2), represent leading causes for gold precipitation (Palin and Xu 2000; Sugiono et al. 2022). Auriferous fluid chemistry may be traced using the $\delta^{34}S$ signature, as well as Au, Ag, As, Te, Co and Ni composition of precipitating sulfides, as these parameters are sensitive to $fS2$ and $fO2$. For instance, in As-rich sedimentary wallrocks, the As-content in pyrite can limit the incorporation of lattice-bound Au or coupled Au-As redox reactions can effectively form lattice-bound gold in OGD (Reich et al. 2005; Pokrovski et al. 2021). Moreover, Bi-rich fluids may scavenge gold through Bi-Te adsorption mechanisms on sulfide growth surfaces (Tooth et al. 2011).

However, in many As-poor, greenstone belt-hosted orogenic gold districts these fluid processes remain poorly understood at the sulfide mineral grain scale. Recent advances in in-situ microanalytical techniques, combined with detailed textural observations and a sulfide paragenesis, have the potential to elucidate these physico-chemical processes and, thereby, identify a gold precipitation mechanism. Here, we explore whether common physical fluid mechanisms (i.e., fluid immiscibility, fluid mixing, fluid-rock reactions) can control gold solubility in several orebodies (Goldex, Triangle, Plug #4, Pascalis Gold Trend, Beaufor) of an important gold district located in the Neoarchean, southern Abitibi subprovince, the Val-d'Or Vein Field (VVF).

2 Geological setting

The Neoarchean Abitibi and Pontiac subprovinces form the southeastern margin of the Superior Craton (Figure 1A) are juxtaposed by the sub-vertical, E-W trending Larder-Lake-Cadillac fault zone (LLCfz). Both subprovinces were affected by a major N-S shortening period (D2) during the Abitibi-Wawa orogenic cycle, between ca. 2669-2643 Ma, forming the transcrustal LLCfz and a penetrative E-W trending S2 foliation (Bedeaux et al. 2017).

The VVF, located in the southern Abitibi subprovince, contains ca. 54.7 Moz of orogenic gold mineralization (Figure 1B). It formed between ca. 2710-2685 Ma, comprising ultramafic, mafic and felsic submarine volcano-sedimentary rocks. These were intruded by contemporaneous tonalitic, granodioritic, dioritic and monzonitic sills that contain Fe-oxides, typically ilmenite, titanomagnetite and magnetite (Pilote et al. 2000) and all rocks were metamorphosed to sub- and upper greenschist-facies (Powell et al. 1995).

2.1 Orogenic gold mineralization

Metamorphosed intrusive and volcanic rocks contain the bulk of the VVF orogenic gold mineralization in brittle-ductile, fault-fill, shear and associated extensional veins, formed during D2 shortening at ca. 2643 Ma, sub-parallel to S2 with a dominant dip to the south (Robert and Brown 1986; Herzog et al. 2022). These veins consist of quartz-tourmaline-carbonate (QTC) and can display m-wide, strongly chloritized quartz-tourmaline-albite-muscovite-pyrite alteration halos. Pyrite-rich, vein- and wallrock- hosted sulfide assemblages contain gold either as native Au or polymetallic (Au-Ag-Te-Bi) inclusions in pyrite, together with minor base metal inclusions (Robert and Brown 1986).

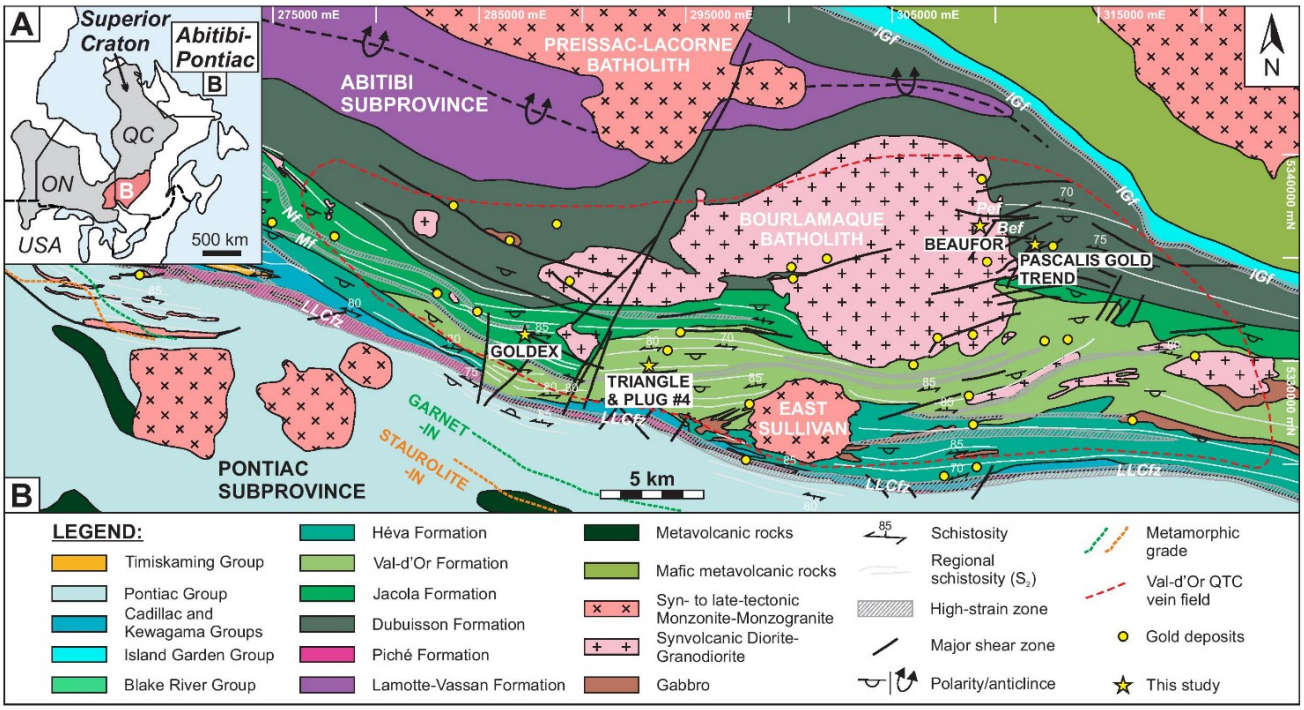

Figure 1A. Schematic map of the Superior Craton showing the Abitibi and Pontiac subprovinces. **1B**. Geological map of the VVF outlining the location of the studied orebodies (modified from Pilote et al. 2000).

3 Methodology

Drill cores from five QTC vein orebodies (Goldex, Triangle, Plug #4, Beaufor, Pascalis Gold Trend), described in detail in Herzog et al. (2022), were investigated. For this study, key cross-cutting relationships between sulfide minerals, texture and paragenesis were determined in thin sections for each orebody.

Based on the paragenesis, 26 representative samples were prepared in five epoxy mounts, containing three to four 6 mm cylindrical rock cores that were drilled out of samples. The mounted samples were characterised for their texture in detail by reflected light microscopy, as well as for their major element composition, internal heterogeneity and zonation by energy dispersive spectroscopy and backscattered electron imaging using a FEI 50 scanning electron microscope. Fe was analysed on a CAMECA SX-100 electron probe micro-analyser.

3.1 Multiple sulfur isotopes

In-situ multiple sulfur isotopes ($\delta^{34}S$, $\Delta^{33}S$) were determined (CAMECA IMS1280 SIMS at UWA) in pyrite (n=91), which contained standard blocks of matrix-matched Sierra pyrite reference material (LaFlamme et al. 2016). Spot analyses used a focused, 10 µm, Gaussian Cs^+ beam at 20 kV and 2.3 nA and measurements of ^{32}S, ^{33}S and ^{34}S followed the protocol outlined in LaFlamme et al. (2016), including absolute propagated $\delta^{34}S$ and $\Delta^{33}S$ error calculations. Matrix-matched reference material was interspersed with unknown sample material measurements and the Sierra pyrite was used to monitor standard repeatability, analytical drift and to correct for instrumental mass fractionation. Secondary pyrite standards 248474 (Isua) and Balmat, located in a separate mount, were used to monitor the accuracy of sulfur isotope data measurements. Calibrated against Sierra, they returned $\delta^{34}S$ and $\Delta^{33}S$ values +2.4±0.6‰, +2.9±0.4‰ (n=10, 2SD), respectively, and +16.1±0.2‰, +0.03±0.05‰ (n=10, 2SD) for $\delta^{33}S$.

3.2 Sulfide trace element compositions

Thirty-four analytes were measured in pyrite in five, uncoated, epoxy mounts comprising 69 spot and line analyses, using a RESOlution 193 nm ArF Excimer laser system coupled to an Agilent 7900 ICPMS, as well as five quantitative maps on the same laser system coupled to a Tofwerk time of flight-ICPMS at UQAC. Spots, lines and maps were analysed at various conditions (beam sizes 7-55 µm, pulse rates 15-120 Hz, scan speeds 10-210 µm/s and fluences of 3-6 J/cm^2), including the following external reference materials: Laflamme, MASS1 and GSE, which were used, with Fe EPMA data as an internal standard, for raw data normalization in Iolite v.4. Averaged values (ppm) for each sulfide domain are reported. UQAC-FeS1, FeS5, MSS5 and GSE reference materials were used to monitor individual laser sessions.

4 Results

4.1 Major sulfide textures and paragenesis

Laminated, m-wide QTC veins of the Goldex, Triangle, Plug #4, Pascalis Gold Trend and Beaufor orebodies are contained within reverse shear zone in chloritized wallrocks, particularly in gabbroic to dioritic intrusions (Figure 2A). These veins host

the bulk of the gold in pyrite-rich (>95 vol%) sulfideassemblages that frequently form cm- to dm-sized vein- and wallrock-hosted sulfide aggregates (Figure 2B). These sub- to euhedral pyrite aggregates display a porous core (Py1) consisting of abundant carbonate and tourmaline inclusions up to several 10s of µm, as well as minor sulfide inclusions including chalcopyrite, sphalerite and galena (Figure2C). Homogeneous pyrite rims (Py2) surround the porous Py1 core and host nm- to µm sized native Au and polymetallic Au-Ag-Te-Bi inclusions, which are primarily calaverite. Minor petztite and metallic BiTeare frequently associated with calaverite and chalcopyrite inclusions (Figure 2D). Texturally late Py2 rims have also been recognized to be associated with the deposition of pyrrhotite (Robert and Brown 1986).

Figure 2A and 2B. Field photographs of QTC orogenic gold mineralization hosted in pyrite-rich aggregates acrossthe VVF. **2C and 2D.** Porous Py1 core domain in

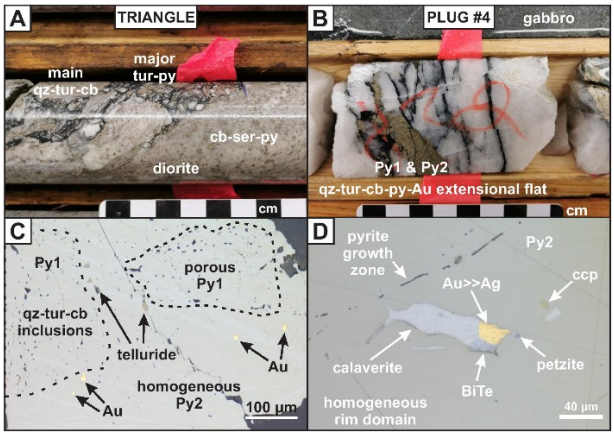

pyrite with a homogeneous Py2 rim overgrowth, which contains bulk of the native Au and polymetallic (Au-Ag-Te-Bi) inclusions. Cb=carbonate, py=pyrite, qz=quartz, ser=sericite, tur=tourmaline.

4.2 Multiple sulfur isotopes

In-situ sulfur isotope analyses of pyrite hosted in the five QTC vein sets define a wide range in $\delta^{34}S$ (from -0.4‰ to +6.3‰), with the lowest and highest values recorded in Py1 and Py2 of the Goldex and Beaufor orebodies, respectively. In all five orebodies, the two pyrite domains display a consistent isotopic shift in $\delta^{34}S$ of up to +3.0‰ (Figure 3), from a slightly lower Py1 domain (n=32) towards a ^{34}S enriched homogeneous Py2 rim (n=59). All orebodies show a small negative $\Delta^{33}S$ from the mass-dependent fractionation field for sulfur for Py1 and Py2 (from - 0.20‰ to +0.01‰).

4.3 Pyrite trace elements

Elemental analyses of Py1 core domains and gold-rich Py2 rims reveal that besides Ag-Te-Bi, commonly associated with gold, only five (Co, Ni, As, Se, Sb) of the 34 elements measured occur at measurable concentrations, while all other analyzed elements are below detection limit. The Py1 cores are enriched in localized Co (4500 ppm) and Ni (635ppm) in the Pascalis Gold Trend and Goldex orebodies, respectively, and yield comparably low As(<67 ppm) and Au (0<<30 ppm) concentrations. The homogeneous Py2 rims of all five orebodies yield low, minor and trace concentrations and displayelevated Au (<1250 ppm) contained in weakly oscillatory-zoned Py2 with Co (<2200 ppm), Ni (<550 ppm) and As (<550 ppm). Native Au and polymetallic inclusions in Py2 are unrelated to the oscillatory-zoned pyrite areas in the five orebodies.

Figure 3. Multiple S isotope data from Py1 and Py2 hostedin

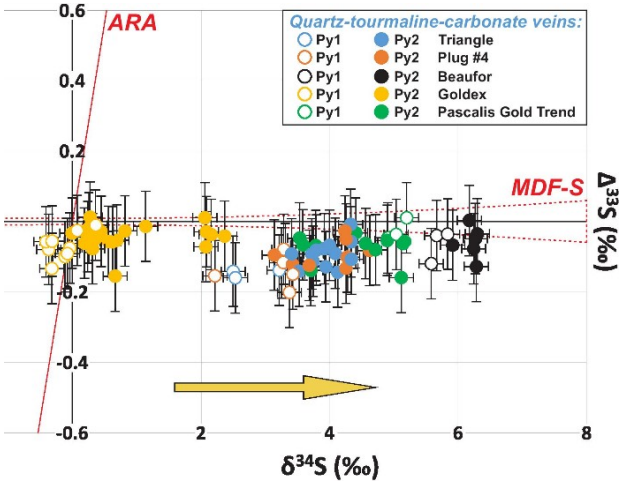

the five QTC vein sets. The golden arrow indicates the observed sulfur isotope evolution of up to +3.0‰ from Py1to Py2. ARA=Archean Reference Array of $\Delta^{33}S \approx 0.89 * \delta^{34}S$ from Ono et al. (2009), MDF-S = mass-dependent fractionation field for sulfur from LaFlamme et al. (2018).

5 Conclusions

The recognition of texturally late pyrrhotiteassociated with QTC vein formation in the VVF implies that the pyrite-rich assemblages deposited native gold in homogeneous Py2 rims under more reducing *f*O2 conditions within the pyrite stabilityfield. A decrease in *f*O2 is also supported by lower Ni and Co concentrations in Py2, both known to have alower solubility at lower *f*O2, compared to the locally enriched Py1 core (Jansson and Liu 2020). The lack of hematite-bearing assemblages in alteration halos also supports a more reducing environment. The consistent isotopic shift in $\delta^{34}S$ values (+3.0‰) observed from Py1 core to Py2 rims in the five orebodies suggests fluid desulfidation (Figure 4A), through the removal of $Au(HS)^-$ complexes, thereby causing a decrease in fluid *f*S2, is the main driver of gold deposition in these orebodies. The consistent, negative $\Delta^{33}S$ values excludes sulfur mixing as a precipitation mechanism. Particularly, the replacement of ilmenite, titanomagnetite and magnetite by pyrite in intrusive wallrocks contributes to efficient gold mineralization. At 300°C, typical for OGD formation (Goldfarb and Groves 2015), these decreases in fluid *f*O2 and *f*S2, induced by pervasive fluid desulfidation-wallrock sulfidation, are also associated with a decrease in fluid *f*Te2 (Figure 4B), resulting in the formation of calaverite related with

Ag-Te-Bi assemblages hosted as inclusions in Py2. Our findings show that in As-poor (<0.1 wt%) pyrite in meta-volcanic orogenic gold districts a coupled decrease in fluid *f*O2, *f*S2 and *f*Te2, as a result of wallrock sulfidation presents a key mechanism leading to efficient OGD formation.

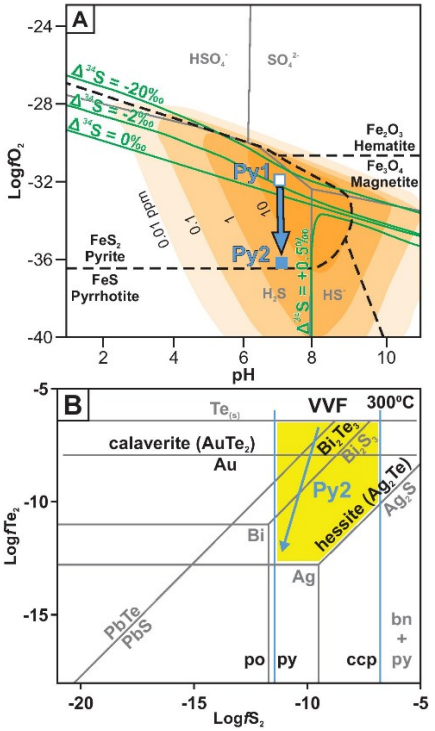

Figure 4A. A pH vs. logfO_2 diagram showing changes in $\delta^{34}S$ values related to gold solubility. Modified from Ohmoto (1972) and Hodkiewicz et al. (2009). **4B.** LogfTe_2- LogfS_2 diagram showing relationship between a decreasein fluid fTe_2 and fS_2 activities and telluride formation during Py2 growth in the VVF. Modified from Afifi et al. (1988).

Acknowledgements

The authors appreciate financial support by the Canada First Research Excellence Fund Metal Earth project. M.H. thanks for support at Agnico Eagle Mines Ltd. by R. Morel, J.A. Marcotte, D. Yergeau, at Eldorado Gold Corp. by J. Thelland, É. Gagnon, M. Le Bacq, B. Gagnon and at Probe Metals Inc. by M. Gagnon, B. Beh.

References

Afifi AM, Kelly WC, Essene EJ (1988) Phase relations among tellurides, sulfides, and oxides: I. Applications to telluride-bearing ore deposits. Econ Geol 83:395-404. https://doi.org/10.2113/gsecongeo.83.2.395

Bedeaux P, Pilote P, Daigneault R, Rafini S (2017) Synthesisof the structural evolution and associated gold mineralization of the Cadillac fault, Abitibi, Canada. Ore Geol Rev 82:49-69. https://doi.org/10.1016/j.oregeorev.2016.11.029

Goldfarb RJ, Groves DI (2015) Orogenic gold: Common or evolving fluid and metal sources through time. Lithos 233:2-26. https://doi.org/10.1016/j.lithos.2015.07.011

Herzog M, LaFlamme C, Beaudoin G, Marsh J, Guilmette C (2022) U-Pb vein xenotime geochronology constraints ontiming and longevity of orogenic gold mineralization in theMalartic-Val-d'Or Camp, Abitibi Subprovince, Canada. Miner Deposita 7:1-29. https://doi.org/10.1007/s00126- 022-01131-1

Hodkiewicz PF, Groves DI, Davidson GJ, Weinberg RF, Hagemann SG (2009) Influence of structural setting on sulphur isotopes in Archean orogenic gold deposits, eastern Goldfields Province, Yilgarn, Western Australia. Miner Deposita 44:129-150. https://doi.org/10.1007/s00126-008-0211-5

Jansson NF, Liu W (2020) Controls on cobalt and nickel distribution in hydrothermal sulphide deposits in Bergslagen, Sweden – constraints from solubility modelling. GFF 142.2:87-95. https://doi.org/10.1080/11035897.2020.1751270

LaFlamme C, Martin L, Jeon H, Reddy SM, Selvaraja V, Caruso S, Bui TH, Roberts MP, Voute F, Hagemann S, Wacey D, Littman S, Wing B, Fiorentint M, Kilburn MR (2016) In situ multiple sulfur isotope analysis by SIMS of pyrite, chalcopyrite, pyrrhotite, and pentlandite to refine magmatic ore genetic models. Chem Geol 444.9:1-15. https://doi.org/10.1016/j.chemgeo.2016.09.032

LaFlamme C, Jamieson JW, Fiorentini ML, Thébaud N, Caruso S, Selvaraja V (2018) Investigating sulfur pathways through the lithosphere by tracing mass independent fractionation of sulfur to the Lady Bountiful orogenic gold deposit, Yilgarn Craton. Gond Res 58:27- 38. https://doi.org/10.1016/j.gr.2018.02.005

Ohmoto H (1972) Systematics of sulfur and carbon isotopes in hydrothermal ore deposits. Econ Geol 67:551-578. https://doi.org/10.2113/gsecongeo.67.5.551

Ono S, Kaufman AJ, Farquhar J, Sumner DY, Beukes NJ (2009) Lithofacies control on multiple-sulfur isotope records and Neoarchean sulfur cycles. Precam Res 169:58-67. https://doi.org/10.1016/j.precamres.2008.10.013

Palin JM, Xu Y (2000) Gilt by Association? Origins of pyritic gold ores in the Victory mesothermal gold deposit, Western Australia. Econ Geol 95.8:1627-1634. https://doi.org/10.2113/gsecongeo.95.8.1627

Pilote P, Moorhead J, Mueller W (2000) Partie A.Développement d'un arc volcanique, La region de Vald'Or, ceinture de l'Abitibi: Volcanologie physique etévolution métallogénique.Québec Ministère des Ressources Naturelles, MB 2000-09, pp 20. https://gq.mines.gouv.qc.ca/documents/examine/MB200009/MB200009.pdf

Pokrovski GS, Escoda C, Blanchard M, Tesyemale D, Hazemann J-L, Gouy S, Kokh MA, Boiron M-C, de Parseval F, Aigouy T, Menjot L, de Parseval P, Proux O, Rovezzi M, Béziat D, Salvi S, Kouzmanov K, Bartsch T, Pttgen R, Doert T (2021) An arsenic-driven pump for invisible gold in hydrothermal systems. Geochem Persp Let 17:39-44. https://doi.org/10.7185/geochemlet.2112

Powell WG, Carmichael DM, Hodgson CJ (1995) Conditions and timing of metamorphism in the southern Abitibi greenstone belt, Quebec. Can J Earth Sci 32:787-805. https://doi.org/10.1139/e95-067

Reich M, Kesler SE, Utsunomyia S, Palenik CS, Chryssoulis SL, Ewing RC (2005) Solubility of gold in arsenian pyrite.Geochim Cosmochim Acta 69.11:2781-2796. https://doi.org/10.1016/j.gca.2005.01.011

Robert F, Brown AC (1986) Archean Gold-Bearing Quartz Veins at the Sigma mine, Abitibi greenstone belt, Quebec: Part II. Vein Paragenesis and Hydrothermal Alteration. Econ Geol 81:593-616. http://dx.doi.org/10.2113/gsecongeo.81.3.593

Sugiono D, LaFlamme C, Thébeaud N, Martin L, Savard D, Fiorentini M (2022) Fault-induced gold saturation of a single auriferous fluid is a key process for orogenic gold deposit formation. Econ Geol 117.6:1405-1414. https://doi.org/10.5382/econgeo.4923

Tooth B, Ciobanu CL, Green L, O'Neill B, Brugger J (2011) Bi-melt formation and gold scavenging from hydrothermal fluids: An experimental study. Geochim Cosmochim Acta 75:5243-5443. https://doi.org/10.1016/j.gca.2011.07.020

Utility of volcanic rock geochemistry in discriminating fertile areas for epithermal gold mineralization: A case study in Japan

Mizuki Ishida[1], Kentaro Nakamura[1], Hikaru Iwamori[2], Takahiro Hosono[3], Yasuhiro Kato[1,4]
[1]*Department of Systems Innovation, School of Engineering, The University of Tokyo, Tokyo, Japan*
[2]*Earthquake Research Institute, The University of Tokyo, Tokyo, Japan*
[3]*Faculty of Advanced Science and Technology, Kumamoto University, Kumamoto, Japan*
[4]*Ocean Resources Research Center for Next Generation, Chiba Institute of Technology, Chiba, Japan*

Abstract. Epithermal gold deposits are formed in shallow crustal environments by precipitation of ore minerals from hydrothermal fluids, associated with magmatic activities. Previous epithermal gold exploration has heavily relied on the presence of hydrothermal alteration zones and geological structures as exploration guides, and the natureof magmas is rarely considered. Here we show from the whole-rock geochemistry of volcanic rocks that ore- forming magmas of large (>200 t Au) Hishikari epithermal gold deposit in Japan is likely to have formed by combination of three geological processes which could have maintained a relatively high sulfur solubility in magmas: (i) oxidized source mantle of primary magmas,
(ii) differentiation in deep crust without significant assimilation of accretionary sediments and (iii) late magnetite saturation relative to the timing of fluid release in shallow crust. In contrast, representative, previously explored areas in Japan (Toyoha, Nansatsu, Iriki) failed to meet more than one of the above criteria, which likely explain the smaller or lack of gold mineralization in these areas. We suggest that elemental source conditions represented by the geochemistry of regional volcanic rocks can be utilized in early stages of epithermal gold exploration in addition to the conventional indicators of elemental transport/precipitation.

1 Introduction

The expanding global population and the transition to a low-carbon society will require a wide range of minerals in increasing quantities for the foreseeable future. The discovery and extraction of new primary resources will continue to play a central role in sustaining mineral supplies (Ali et al. 2017).However, recent years have seen a marked decline in the number of new mineral deposits discovered, despite considerable increases in exploration expenditures (Schodde 2019); exploration efficiencymust therefore be improved to ensure mineral resources remain available to industry. Since near half of the world exploration expenditure is spent for gold, effective methods for gold exploration will be of particular interest.

Many gold deposits are primarily formed in association with magmatic activity. Among them, epithermal deposits, producing more than 10% of world's gold production, are important sources of gold and associated critical metals (Frimmel 2008). Epithermal gold deposits are distributed in subduction zones and formed in shallow (less than 1 km) crustal environments by the precipitation of ore minerals from magmatic-hydrothermal fluids.

Previous epithermal gold exploration, especially in Japan, have heavily relied on the presence of hydrothermal alteration zones (evidence of elemental transport) and geological structures (facilitates elemental precipitation) as exploration guides. Although hydrothermal fluids and ore- forming elements are largely sourced from magmas (Richards 2011), the nature of those magmas is rarely considered in epithermal gold exploration due to a lack of understanding and effective methodologies. This study therefore aims to determine the geochemical features of magmas that are capable of forming large epithermal gold deposits by using case studies in Japan, utilizing syn-mineralization volcanic rocks near deposits as the surface expression of ore-forming magmas. Then we try to establish new exploration guidelines for epithermal gold deposits that incorporate the magmatic processes, using whole-rock geochemistry of volcanic rocks.

2 Case study areas

The study takes place in the Hokusatsu and the Nansatsu regions of south Kyushu and the Toyoha region of southwest Hokkaido, Japan (Figure 1). These regions have been the subject of epithermal gold exploration by the Ministry of International

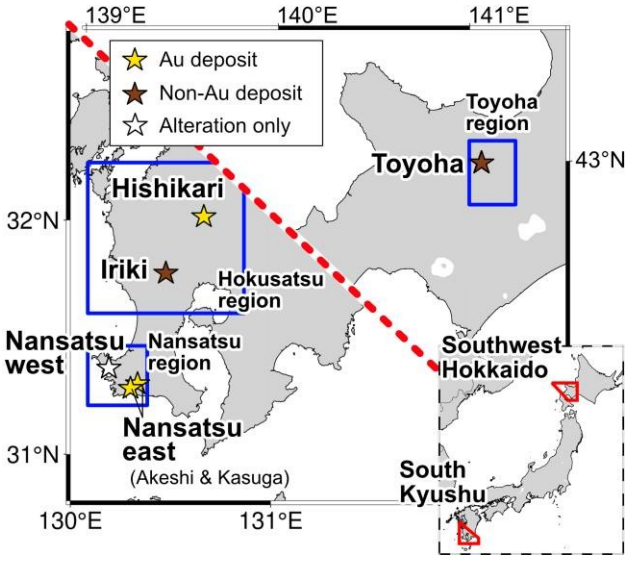

Figure 1. Study areas of this study.

Trade and Industry (MITI, what is now METI) of Japan in 1963–2003 (METI 2004).

2.1 Hokusatsu region

The Hishikari area in Hokusatsu region hosts a large (more than 200 t) gold deposit (Hishikari deposit), which is a low-sulfidation deposit formed in 1.3 – 0.6 Ma (Watanabe 2005). In contrast, the Iriki area hosts a clay deposit (Iriki high- to low-sulfidation deposit) formed at 0.5 Ma, with much smaller (less than 10 t) gold mineralization.

2.2 Nansatsu region

The eastern part of the Nansatsu region (Nansatsu east) hosts high- to low- sulfidation gold deposits formed around 4 Ma. The Akeshi and Kasuga high-sulfidation deposits are medium-sized (more than 10 t) gold deposits (Ishida et al. 2021). In contrast, no gold mineralization is known in the western part of Nansatsu region (Nansatsu west).

2.3 Toyoha region

The Toyoha region is home to an intermediate-sulfidation Pb-Zn deposit (Toyoha deposit) formed in 3 – 0.5 Ma. The Toyoha deposit have produced more than 1.2 Mt Zn and 0.4 Mt Pb, but only endowed with minor (less than 1 t) gold mineralization (Watanabe 2002).

3 Methods

Composition of volcanic rocks in Nansatsu and Toyoha regions were analysed in this study. The major element contents were determined using a Rigaku ZSX Primus II X-ray fluorescence (XRF) spectrometer, and the trace element contents were analysed using an inductively coupled plasma mass spectrometer (ICP-MS; Thermo Fisher Scientific iCAP Q) at the Department of Systems Innovation, the University of Tokyo (Yasukawa et al. 2014). Strontium and Nd isotope analyses were acquired by thermal ionization mass spectrometry (TIMS) with Thermo Finnigan TRITON XT, and the Pb isotopic compositions were measured using a Thermo Finnigan NEPTUNE multiple collector ICP-MS at the Ocean Resources Research Center for Next Generation, Chiba Institute of Technology (Machida et al. 2009; Tanimizu and Ishikawa 2006).

4 Potential geochemical indicators of gold in magmas

Gold-rich fluids that are favorable for gold mineralization require gold-rich magmas (Zajacz et al. 2012). The solubility of gold in magma is controlled by S2-, while the solubility and speciation of sulfur is in turn governed by the magma oxygen fugacity (Jugo et al. 2010). However, gold, sulfur, and oxygen fugacity in magmas are relatively hard to analyze from volcanic rocks, especially in the context of exploration where large number of samples must be processed. We therefore sought alternative geochemical indicators related to magma oxygen fugacity that might allow us to estimate the behavior of gold in magmas and to discriminate between gold-mineralizing and barren areas. We divided the magma evolution process into three stages (mantle, deep crust, and shallow crust) and found indicators corresponding to each stage.

4.1 Mantle

The generation of gold-rich primary magma in the mantle requires relatively high oxygen fugacity in which both S2- and S6+ are stable (Li and Audétat 2013). The V/Yb ratio of high-MgO rocks (more than 6 wt.%) is known as an indicator of oxygen fugacity during mantle melting (Laubier et al. 2014). We found a higher V/Yb ratio (160–220) in the South Kyushu volcanic rocks except for Iriki rocks (Figure 2; denoted as Hishikari and Nansatsu east) than the global average (158; Cottrell et al. 2021), indicating the presence of gold-rich primary magmas in these gold-mineralized areas. In contrast, V/Yb ratio of volcanic rocks in southwest Hokkaido (corresponding to the Toyoha region) are close to the global average, and those in the Iriki area were close to mid-ocean ridge basalt (MORB).

4.2 Deep crust

The assimilation of accretionary sediments in the deep part of the crust is the most prominent process in reducing subduction zone magmas, which can be recognized from the Sr-Nd-Pb isotope ratios of volcanic rocks. When the oxidizing magma is reduced and the sulfur speciation changes, the solubility of sulfur decreases rapidly, precipitating large amounts of sulfide minerals in the magma

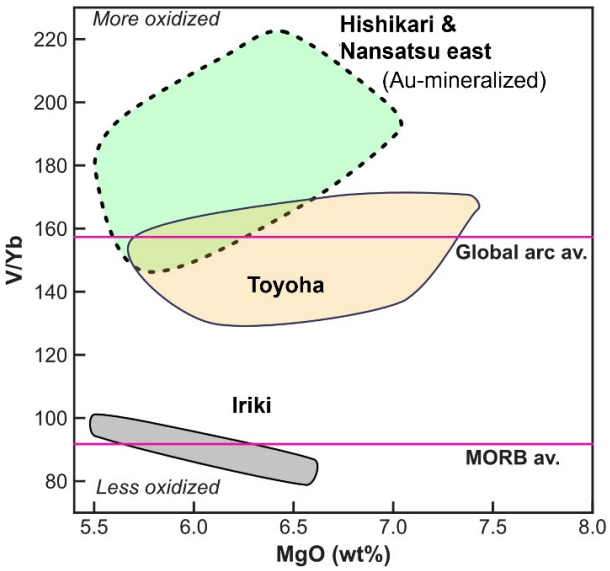

Figure 2. V/Yb ratio of high-MgO volcanic rocks corresponding to the studied area. Data from GEOROC.

(Tomkins et al. 2012). Since sulfide phases precipitate with gold in magma, this process could hinder the formation of gold deposits. In this study, volcanic rocks in the Nansatsu west area (Oldest stage Nansatsu volcanic rocks) had enriched isotope signatures that were close to those of the Shimanto supergroup (accretionary sediments), indicating that the magma reduction resulting from assimilation had inhibited the formation of gold deposits in this area (Figure 3). In other areas, the magmas were likely to have ascended without such reduction processes.

4.3 Shallow crust

In the shallow part of the crust, the timing of magnetite saturation relative to fluid release from the magma can have a profound effect on the gold content of the fluid because magnetite saturation can also reduce magmas (Jenner et al. 2010). The timing of magnetite saturation can be estimated from the MgO content of the volcanic rocks in which total Fe sharply decreases, and this can be compared with the timing of fluid release estimated generally to be <2.5 wt.% MgO (Hao et al. 2022). We found that volcanic rocks in the Hishikari area (except for the oldest unit K-IA) experienced magnetite saturation at around 2 wt.% MgO (Figure 4). We argue that this was likely late enough to enrich the released fluid with gold. Timing of magnetite saturation was close to the global average (MgO 4–5 wt.%; Park et al. 2021) or earlier in other areas, which could have hindered the formation of large gold deposits.

5 Implications for exploration

The above results demonstrated that the following geochemical indicators can be used to identify the presence of magma suitable for gold mineralization:

- V/Yb > 160 for volcanic rocks with MgO > 6 wt.%
- Sr-Nd-Pb isotopic ratios that do not extend toward the isotopic ratio of accretionary sediments
- Total Fe of volcanic rocks sharply declining only when MgO < 2.5 wt.%

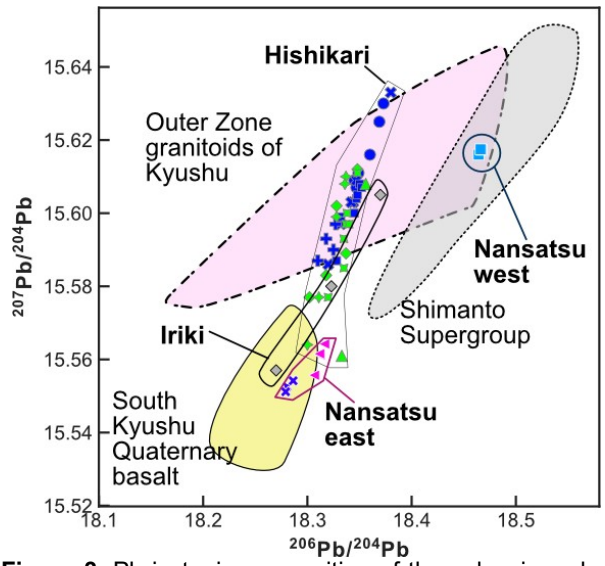

Figure 3. Pb isotopic composition of the volcanic rocks in south Kyushu. Data of Hishikari area from Hosono et al. (2003) and Iriki area from Hosono et al. (2008).

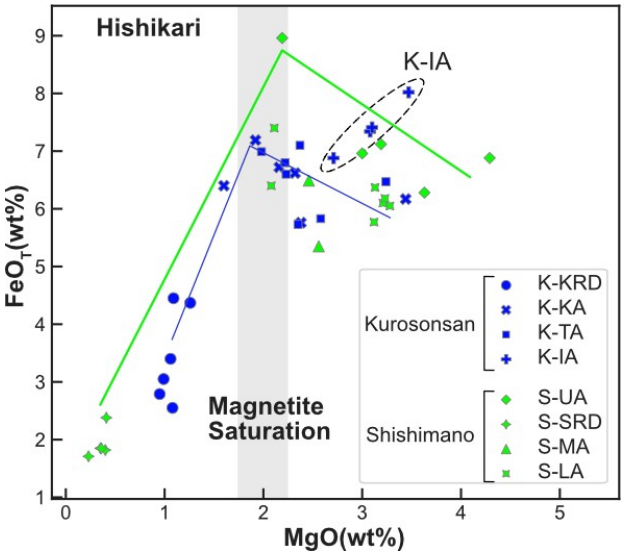

Figure 4. Timing of magnetite saturation for the Hishikari volcanic rocks. Data from Hosono and Nakano (2003).

Transport of Au in magma from mantle to shallow crust

Area	Primary magma fO_2	Assimilation of reducing crustal materials	Timing of magnetite saturation	Result
Hishikari (Except for K-IA)	High	Minor	Late	**Large Au deposit**
Nansatsu east	High	Minor	Average	Middle Au deposit
Iriki	Low	Minor	Average	Minor Au mineralization
Toyoha	Low	Minor	Average	Minor Au mineralization
Nansatsu west	unknown	Significant	unknown	Hydrothermal alteration only

Figure 5. Factors which influenced the epithermal gold mineralization of the studied area. Green: Facilitated gold mineralization; Pink: Hindered gold mineralization

The fact that only the volcanic rocks from the Hishikari area fulfilled all three criteria indicates that all the conditions along magma ascent must be met in order to generate a large gold deposit (Figure 5). The smaller or lack of gold mineralization in the other studied areas can thus be explained by unfavorable magma conditions. We suggest that conventional indicators of elemental transport/precipitation combined with the elemental source conditions (i.e., magma) described here should allow the identification of promising areas for exploration. The collection of additional geochemical data should also allow further refinement of these exploration guidelines.

Acknowledgements

We thank Dr. S. Machida, Ms. K. Ashida, Ms. Y. Itabashi, Ms. R. Tajiri, Prof. M. Nakagawa, Mr. S. Murakami and Mr. Y. Hieda for help in sample preparation and chemical analyses. Discussion with Assoc. Prof. K. Yasukawa, Dr. J. Ohta, Dr. K. Fujinaga, Prof. S. Koshizuka and Prof. A. Nakao improved the quality of the abstract. This research was funded by Japan Society for the Promotion of Science KAKENHI Grant No. JP20J22038 given to the first author.

References

Ali SH, Giurco D, Arndt N, Nickless E, Brown G, DemetriadesA, Durrheim R, Enriquez MA, Kinnaird J, Littleboy A, Meinert LD, Oberhänsli R, Salem J, Schodde R,Schneider G, Vidal O, Yakovleva N (2017) Mineral supply for sustainable development requires resource governance. Nature 543:367-372. doi:10.1038/nature21359.

Cottrell E, Birner SK, Brounce M, Davis FA, Waters LE, KelleyKA (2021) Oxygen Fugacity Across Tectonic Settings. Magma Redox Geochemistry 33-61. doi: 10.1002/9781119473206.ch3

Frimmel HE (2008) Earth's continental crustal gold endowment. Earth and Planetary Science Letters 267:45- 55. doi: 10.1016/j.epsl.2007.11.022.

Hao H, Park J-W, Campbell IH (2022) Role of magma differentiation depth in controlling the Au grade of giant porphyry deposits. Earth and Planetary Science Letters 593:117640.doi: https://doi.org/10.1016/j.epsl.2022.117640.

Hosono T, Nakano T (2003) Petrochemistry of Volcanic Rocksin the Hishikari Mining Area of Southern Japan, with Implications for the Relative Contribution of Lower Crust and Mantle-derived Basalt. Resource Geology 53:239- 259. doi: https://doi.org/10.1111/j.1751-3928.2003.tb00174.x.

Hosono T, Nakano T, Murakami H (2003) Sr–Nd–Pb isotopic compositions of volcanic rocks around the Hishikari gold deposit, southwest Japan: implications for the contributionof a felsic lower crust. Chemical Geology 201:19-36. doi: 10.1016/s0009-2541(03)00205-5.

Hosono T, Nakano T, Shin K, Murakami H (2008) Assimilationof lower to middle crust by high alumina basalt magma asan explanation for the origin of medium-K volcanic rocks in southern Kyushu, Japan. Lithos 105:51-62. doi: 10.1016/j.lithos.2008.02.007.

Ishida M, Romero R, Leisen M, Yasukawa K, Nakamura K, Barra F, Reich M, Kato Y (2021) Auriferous pyrite formed by episodic fluid inputs in the Akeshi and Kasuga high-sulfidation deposits, Southern Kyushu, Japan. Mineralium Deposita. doi: 10.1007/s00126-021-01053-4.

Jenner FE, O'Neill HSTC, Arculus RJ, Mavrogenes JA (2010) The Magnetite Crisis in the Evolution of Arc-related Magmas and the Initial Concentration of Au, Ag and Cu. Journal of Petrology 51:2445-2464. doi: 10.1093/petrology/egq063.

Jugo PJ, Wilke M, Botcharnikov RE (2010) Sulfur K-edge XANES analysis of natural and synthetic basaltic glasses: Implications for S speciation and S content as function of oxygen fugacity. Geochimica et Cosmochimica Acta 74:5926-5938. doi: 10.1016/j.gca.2010.07.022.

Laubier M, Grove TL, Langmuir CH (2014) Trace element mineral/melt partitioning for basaltic and basaltic andesitic melts: An experimental and laser ICP-MS study with application to the oxidation state of mantle source regions. Earth and Planetary Science Letters 392:265-278. doi: 10.1016/j.epsl.2014.01.053.

Li Y, Audétat A (2013) Gold solubility and partitioning between sulfide liquid, monosulfide solid solution and hydrous mantle melts: Implications for the formation of Au-rich magmas and crust–mantle differentiation. Geochimica et Cosmochimica Acta 118:247-262. doi:10.1016/j.gca.2013.05.014.

Machida S, Hirano N, Kimura J-I (2009) Evidence for recycled plate material in Pacific upper mantle unrelated to plumes. Geochimica et Cosmochimica Acta 73:3028-3037. doi: 10.1016/j.gca.2009.01.026.

METI (2003) Report on the regional geological structure survey in the fiscal year Heisei 15: Domestic Survey Overall Evaluation.

Park J-W, Campbell IH, Chiaradia M, Hao H, Lee C-T (2021) Crustal magmatic controls on the formation of porphyry copper deposits. Nature Reviews Earth & Environment 2:542-557. doi: 10.1038/s43017-021-00182-8.

Richards JP (2011) Magmatic to hydrothermal metal fluxes in convergent and collided margins. Ore Geology Reviews 40:1-26. doi: 10.1016/j.oregeorev.2011.05.006.

Schodde R (2019) Trends in Exploration. International Mining and Resources Conference. Melbourne, Australia.

Tanimizu M, Ishikawa T (2006) Development of rapid and precise Pb isotope analytical techniques using MC-ICP-MS and new results for GSJ rock reference samples. Geochemical Journal 40:121-133. doi:10.2343/geochemj.40.121.

Tomkins AG, Rebryna KC, Weinberg RF, Schaefer BF (2012) Magmatic sulfide formation by reduction of oxidized arc basalt. Journal of Petrology 53:1537-1567. doi: 10.1093/petrology/egs025.

Watanabe Y (2002) Late cenozoic metallogeny of southwest Hokkaldo, Japan. Resource Geology 52:191-210. doi: 10.1111/j.1751-3928.2002.tb00130.x.

Watanabe Y (2005) Late Cenozoic evolution of epithermal gold metallogenic provinces in Kyushu, Japan. Mineralium Deposita 40:307-323. doi: 10.1007/s00126-005-0025-7.

Yasukawa K, Liu H, Fujinaga K, Machida S, Haraguchi S, Ishii T, Nakamura K, Kato Y (2014) Geochemistry and mineralogy of REY-rich mud in the eastern Indian Ocean. Journal of Asian Earth Sciences 93:25-36. doi: https://doi.org/10.1016/j.jseaes.2014.07.005.

Zajacz Z, Candela PA, Piccoli PM, Wälle M, Sanchez-Valle C (2012) Gold and copper in volatile saturated mafic to intermediate magmas: Solubilities, partitioning, and implications for ore deposit formation. Geochimica et Cosmochimica Acta 91:140-159. doi:10.1016/j.gca.2012.05.033.

Quantification of hydrothermal alteration associated with gold-antimony mineralization along the Antimony Line, Murchison greenstone belt, South Africa.

Thabo S. Kgarabjang[1], Napoleon Q. Hammond[1]
[1]Department of Geology and Mining, University of Limpopo, South Africa.

Abstract. The Antimony Line in the Archaean Murchison greenstone belt hosts several gold-antimony mineralizations within massive, fractured talcose and quartz-carbonate host rocks. Samples from three orebodies, Athens, Beta and Monarch along the Antimony Line were studied to quantify hydrothermal alteration and characterize the geochemical distribution of the gold-antimony mineralization. Mass-balance studies of the hydrothermally altered assemblage indicated variable degree of enrichment of the trace and pathfinder elements (Au, As, Sb and Ag) in the deposits. In particular, antimony recorded the highest enrichment at Beta while gold enrichment is highest at Monarch. Antimony generally shows an increasing trend of enrichment from 3083% at Monarch to 7167% at Beta, while gold enrichment increases from 67% at Beta to 9761% at Monarch. The arsenic and gold distribution in the orebodies show similar pattern, suggesting a close association with gold mineralization, which can be used as a vector to identify extensions of the mineralization within the belt.

1 Introduction

The Murchison greenstone belt dated 3.0 Ga forms part of the several Archaean volcano-sedimentary belts within the Kaapvaal Craton. It is located in the northeastern portion of the craton approximately 200 km north of the Barberton greenstone belt. The Antimony Line is a 250 m wide shear zone located centrally within this greenstone belt and extends for about 50 km. The sheer zone is characterized by intense semi-brittle deformation and hosts several gold and antimony orebodies within massive fractured talcose and quartz-carbonate host rocks of the Weigel Formation (Fig. 2).

Studies on the chemistry, mineralogical and textural characteristics of the host rocks in three orebodies, Athens, Beta and Monarch deposits along the Antimony Line show extensive hydrothermal alteration. As characterized in most hydrothermal ore deposits, the intensity of the alteration increases towards the mineralized zones from the unaltered sections of the host rocks. In this study, quantitative evaluation of the chemical compositional changes (major and trace elements) of the host rocks linked to the hydrothermal alteration processes was undertaken using the isocon method of Grant (1986). This method is a widely used technique to quantify the changes in mass/volume/concentration of elements associated with alteration processes.

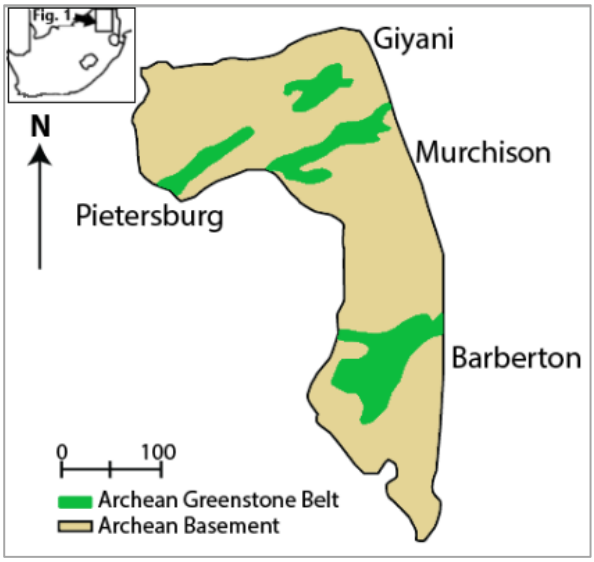

Figure 10. Locality map of the Murchison greenstone belt. Map adapted from Madisha (1996).

1.1 Gold and Antimony Mineralization

Gold Mineralization

The Antimony Line hosts major gold mineralization within massive, fractured talcose and carbonate schist host rocks, with epigenetic gold-antimony occurring along the ENE-trending shear from the Gravelotte, Athens, Beta, and Monarch orebodies along a distance of about 12 km (Fig. 2). Previous studies on gold-antimony mineralization along the Antimony Line in the Murchison greenstone belt (e.g. Davis et al. 1986; Vearncombe et al. 1992; Madisha 1996) have documented that the Au mineralization occurs in close association with the sulphides, and is present either as free gold or occluded in sulphides (Vearncombe et al. 1992; Ward and Wilson 1998). Additionally, gold is associated with the arsenopyrite horizons, which form discrete lenses at or near the antimony mineralization.

Antimony Mineralization

Antimony mineralization occurs as disseminations within the quartz-carbonate schists throughout the Antimony Line. Most of the antimony, often accompanied by gold, occurs as veins of quartz-carbonate-stibnite which occupy tension fractures along the Antimony Line (Davis et al. 1986). Antimony mineralization in the stibnite (Sb_2S_3) form is documented to be the richest in the core of the orebody while the mineralization in berthierite

($FeSb_2S_4$) form is more concentrated towards the margin of the orebody (Davis et al. 1986).

were identified to be Ga and Al_2O_3. Given that, an immobile element has little or no change in

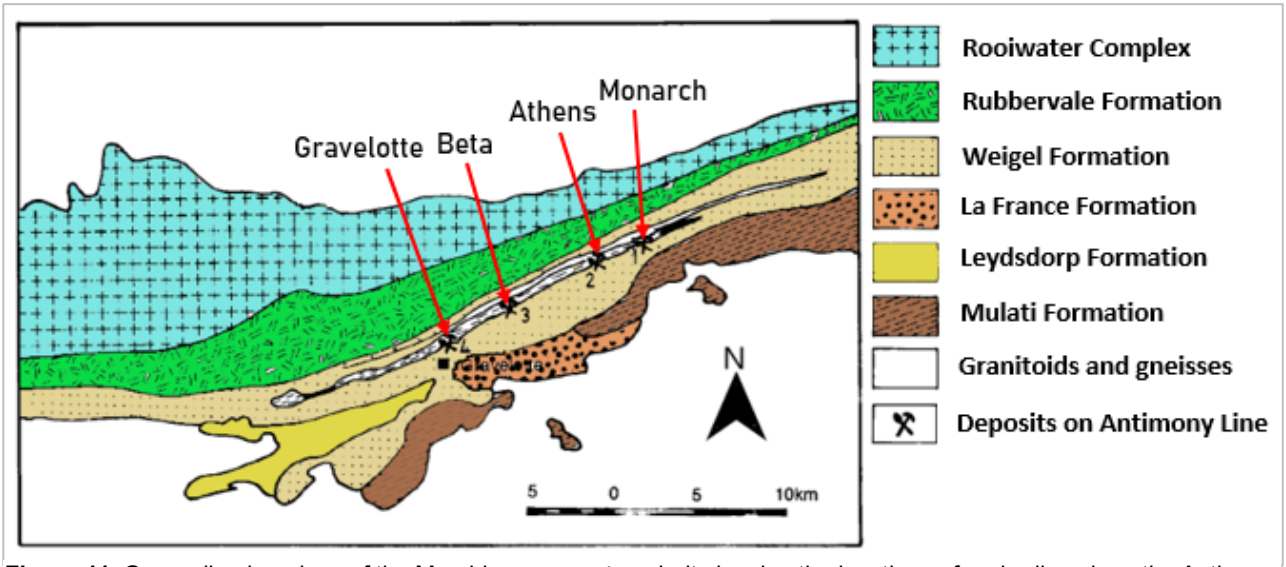

Figure 11. Generalized geology of the Murchison greenstone belt showing the locations of orebodies along the Antimony Line. Map adapted from Maiden and Boocock (1984).

2 Methodology

Two hundred and sixty-six (266) borehole samples were taken from Athens, Beta and Monarch orebodies collectively. Out of this, fifteen (15) samples from Athens, twenty-one (21) samples from Monarch and fifteen (15) samples from Beta orebody were selected and prepared for geochemical analysis. The geochemical analysis was undertaken using X-ray fluorescence (XRF) and inductively coupled plasma mass spectrometry (ICP-MS) to determine major and trace element concentrations including Sb, As, Au and Ag in host rocks respectively. The Grant (1986) mass-balance method was used to plot isocon diagrams to investigate alteration along the Antimony Line. Ore elements and the pathfinders were plotted on ternary diagram to understand their association and distribution across the three deposits, Athens, Beta, and Monarch.

3 Mass-balance calculations

The basic equation used by Grant (1986) for mass balance calculation to quantify changes in mass/volume/concentration of elements associated with alteration processes relates the concentration of element "i" in the altered rock (Ci^A) to its concentration before alteration (Ci^0) is given as follows:

$$Ci^A = M^0/M^A\,[Ci^0 + \Delta Ci] \quad \text{..... (1)}$$

Where M^0 is the mass of the host rock before alteration, M^A is the mass of the host rock after alteration and ΔC_i is the concentration change of element "i" after alteration. Using the method of Maclean and Kranidiotis (1987), the most immobile element in the Athens, Beta and Monarch deposits concentration, that is its concentration before and after alteration is the same, equation (1) can be expressed as follows:

$$Ci^A = M^0/M^A\,[Ci^0] \quad \text{..... (2)}$$

Equation (2) can further be expressed as:

$$y = mx \quad \text{..... (3)}$$

Where: y = Ci^A, m = M^0/M^A, and x = Ci^0

The M^0/M^A for Ga in Athens, Beta, and Monarch were calculated and values are expressed in Table 1.

Table 1. Ga constants for Athens, Beta and Monarch orebodies.

Athens	Beta	Monarch
M^0/M^A = 1.08	M^0/M^A = 0.54	M^0/M^A = 0.53

Ga constants for the Athens, Beta and Monarch deposits are substituted into equation (3) to create best-fit isocons:

Athens: y = 1.08x..... (4)
Beta: y = 0.54x..... (5)
Monarch: y = 0.53x..... (6)

These equations (4), (5) and (6) were used to create isocon diagrams to determine the relative enrichments or depletions of elements in the Athens, Beta and Monarch host rocks during alteration. Elements that were added to the host rocks plot above the reference line (best fit isocon) and elements that were removed from the host rocks during alteration plot below the best fit isocon. The isovolumetric isocon is a line of:

$$y = mx \quad \text{..... (7)}$$

Where: m= M^0/M^A =1

Host rocks that have been reduced in volume/mass as a result of alteration are characterized by best-fit isocon plotting below the isovolumetric isocon, while host rocks that have increased in volume/mass are characterized by the best fit isocon plotting above the isovolumetric isocon. The isocon diagrams for Athens, Beta, and Monarch deposits are shown in Figures 3, 4 and 5 respectively.

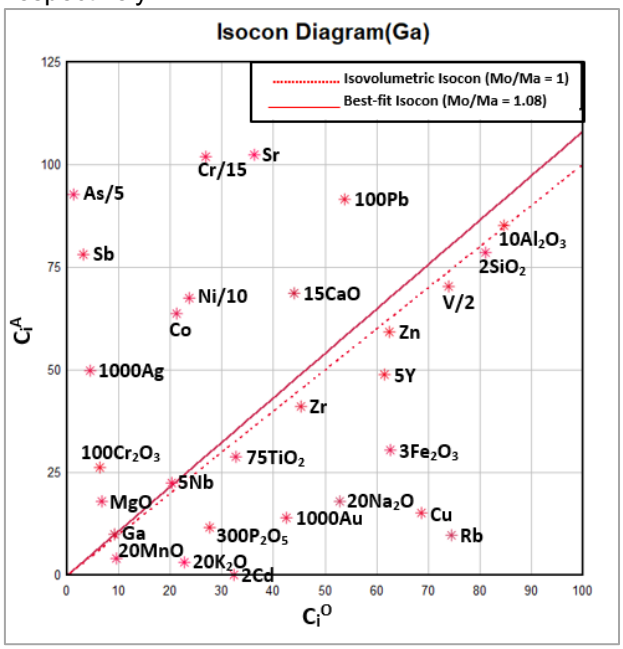

Figure 12. Isocon diagram for major oxides and trace elements to determine mass changes using Ga constant at the Athens Orebody. Isocon diagram adapted from Grant (1986).

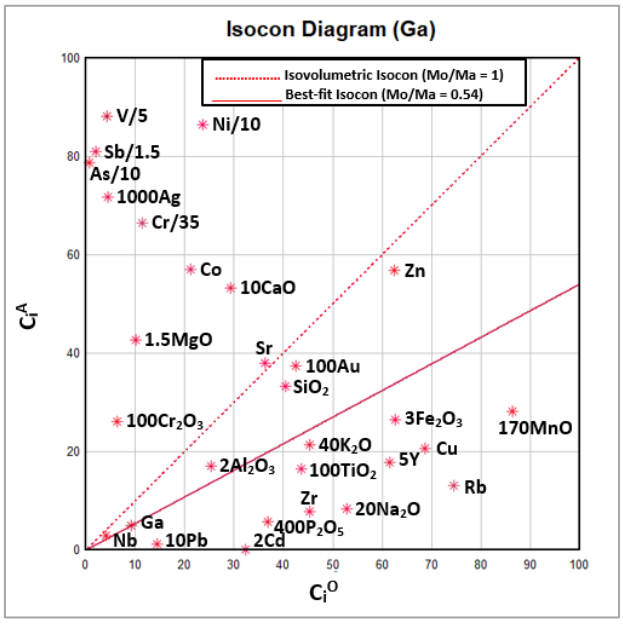

Figure 13. Isocon diagram for major oxides and trace elements to determine mass changes using Ga constant at the Beta Orebody. Isocon diagram adapted from Grant (1986).

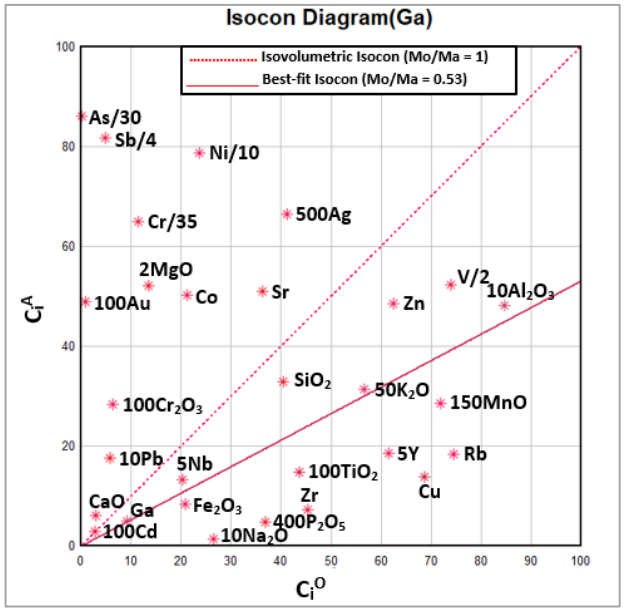

Figure 14. Isocon diagram for major oxides and trace elements to determine mass changes using Ga constant at the Monarch Orebody. Isocon diagram adapted from Grant (1986).

4 Gold, Arsenic and Antimony distribution along the Antimony Line

The distribution of Au, As and Sb in the Athens, Beta, and Monarch deposits varies significantly and shows variable enrichments from one deposit to another (Fig. 6). These variations may be attributed to physicochemical inconsistencies in hydrothermal alteration along the Antimony Line. Gold shows higher concentrations in Monarch than in the Beta and Athens deposits, where Au concentration is relatively low. Antimony shows a scattered distribution across Beta and Monarch. Gold and arsenic show similar distribution patterns in the orebodies, with high As concentrations and high Au concentrations in the Monarch deposit.

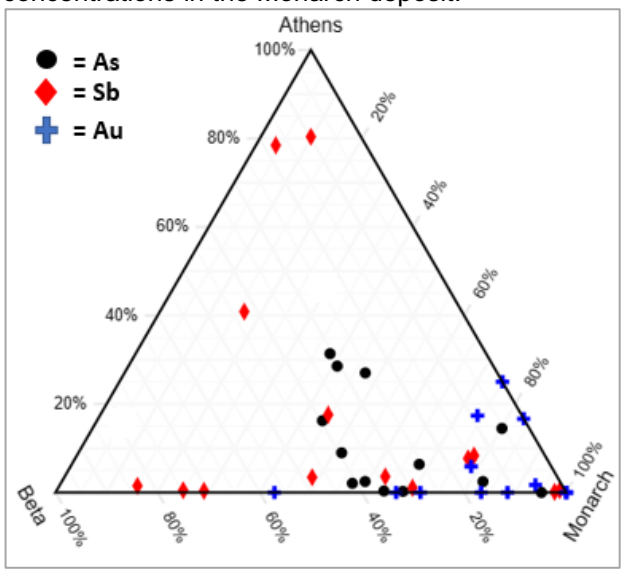

Figure 6. Ternary plot showing the distribution of gold, antimony, and arsenic in the three ore bodies, Athens, Beta and Monarch along the Antimony Line.

5 Conclusions

The mass-balance changes associated with alteration indicate enrichments of SiO_2, MgO, CaO Cr_2O_3, Sb, Au, As, Ag, Cr, Ni, and Co in the host rocks while elements including MnO, P_2O_5, and Rb were removed (Fig. 3-5). There is however variable degree of enrichment of the trace and pathfinder elements (Au, As, Sb and Ag) in each of the orebodies, Athens, Beta and Monarch. In particular, Au enrichment is highest at Monarch, while antimony recorded the highest enrichment at Beta. Thus, antimony shows an increasing trend from Monarch (3083%) to Beta (7167%), while gold enrichment increases from Beta (67%) to Monarch (9761%). In general, The Au enrichment is highest in the Monarch compared to Beta and Athens deposits. There was no significant change in the mass/volume of host rocks at the Athens deposit during hydrothermal alteration (Fig. 3). However, the volume/mass of host rocks in the Beta and Monarch deposits show significant reduction (>50%) as a result of removal of elements (such as MnO, Na_2O, Cu, Rb) (Fig. 4-5). The Au and As distribution pattern in the orebodies shows co-variation (Fig. 6), with highest enrichments of the two elements at the Monarch deposit, suggesting a close association with Au mineralization. The close association between Au and As is consistent with the reported Au and As relationships in many greenstone belts (Boyle and Jonasson 1973) and as such, both Au and As can be useful pathfinder tool for gold exploration in the Murchison greenstone belt.

Acknowledgements

The support of the Department of Science and Innovation through its funding agency, the National Research Foundation, and the Centre of Excellence for Integrated Mineral and Energy Resource Analysis (DSI-NRF CIMERA) towards this research is hereby acknowledged. We are thankful to the geological staff at the Mopani Stibium Mine for their assistance during visits to the site.

References

Boyle, R.W. and Jonasson, I.R. (1973): The geochemistry of arsenic and its use as an indicator element in geochemical prospecting. Journal of Geochemical Exploration, v. 2 (3), p. 251-269.

Davis, D.R., Paterson, D.B., Griffiths, D.H.C. (1986): Antimony in South Africa. Journal of the Southern African Institute of Mining and Metallurgy, v. 86 (6), p.173-193.

Grant, J.A. (1986a): The isocon diagram; a simple solution to Gresens' equation for metasomatic alteration. Economic geology, v. 81 (8), p.1976-1982.

MacLean, W.H. and Kranidiotis, P. (1987): Immobile elements as monitors of mass transfer in hydrothermal alteration; Phelps Dodge massive sulfide deposit, Matagami, Quebec. Economic Geology, v. 82 (4), p. 951-962.

Madisha, M.E. (1996): Carbonate alteration of serpentinite in the Murchison greenstone belt, Kaapvaal Craton: implication for gold mineralization. Unpublished MSc thesis, Rand Afrikaans University, p. 178.

Maiden, K.J. and Boocock, C.N. (1984): Deformational and metamorphic features of antimony ores of the murchison antimony line, north-eastern Transvaal. Transactions of the Geological Society of South Africa, v. 87, p. 327-333.

Vearncombe, J.R., Barton, J.M., Cheshire, P.E., de Beer, J.H., Stettler, E.H., and Brandl, G. (1992): Geology, geophysics and mineralization of the Murchison Schist Belt, Rooiwater Complex and surrounding granitoids. Geological Survey of South Africa, p. 139.

Ward, J.H.W. and Wilson, M.G.C. (1998): Gold outside the Witwatersrand Basin. In: Wilson, M.G.C. and Anhaeusser, C.R. (Eds.). The Mineral Resources of South Africa. Handb. Counc. Geosci., v. 16, p. 350-386.

Complex hydrothermal evolution during retrograde terrane exhumation, Nalunaq gold deposit, South Greenland

Jochen Kolb[1], Robin-Marie Bell[2], Torsten Vennemann[3], Laure Martin[4], Marco L. Fiorentini[4], Tod Waight[5]
[1]*Karlsruhe Institute of Technology*
[2]*Copenhagen*
[3]*University of Lausanne*
[4]*University of Western Australia*
[5]*University of Copenhagen*

Abstract. The Paleoproterozoic orogenic gold deposit of Nalunaq in South Greenland is located in a NW-vergent thrust in an amphibolite facies terrane. Gold mineralization is hosted in a quartz vein system with biotite-arsenopyrite alteration zone. We present the stable isotope characteristics of four hydrothermal alteration assemblages at Nalunaq. The isotopes indicate that a metamorphic fluid of similar composition is responsible for hydrothermal alteration lasting from the ca. 1785 Ma, pre-gold, peak metamorphic stage at ~650°C to the ca. 1765 Ma, post-gold stage at ~500°C. Ca. 1745 Ma, post-gold hydrothermal alteration is contemporaneous with late-orogenic granite. The fluid is most likely derived from Paleoproterozoic rocks. Stable isotopes indicate a meteoric fluid source in equilibrium with the late-stage hydrothermal alteration assemblage at ca. 250°C. The retrograde evolution of the terrane hosting Nalunaq is initially characterized by hydrothermal overprint by a metamorphic fluid. Economic gold mineralization is likely related to focused fluid flow in a thrust. The hydrothermal system drastically changed to meteoric fluids upon further terrane exhumation and development of hydrothermal fluid cells by widespread granite intrusion overprinted the gold mineralization.

1 Introduction

Orogenic gold deposits are structurally controlled hydrothermal deposits that are hosted by metamorphic rocks and are formed by orogenic processes. They are often one of many stages in a complex evolution, involving locally several hydrothermal stages, which may not all be auriferous. This geological setting allows detailed investigation of hydrothermal fluids present during orogeny. Stable isotopes of hydrothermal alteration minerals allow interpretations of T, precipitation mechanisms and fluid source, although stable O, D, C, S isotopes are often equilibrated with the metamorphic host rocks of the gold deposits (Hoefs 2015). Thus, the stable isotope composition of the fluids often is not a direct link to the fluid source, and fluid-rock interaction along the fluid pathway has to be taken into account (Ridley and Diamond 2000). However, detailed investigations of orogenic gold quartz veins in the Val-d'Or vein field (Canada) show that the stable isotope compositions are the result of fluid-rock reaction and mixing between an upper crustal fluid and a metamorphic fluid (Beaudoin and Pitre 2005).

We present stable isotope data from four hydrothermal stages and wall rocks of the Paleoproterozoic orogenic gold mineralization in Nalunaq, South Greenland. The data indicate a complex hydrothermal evolution during the retrograde exhumation of the auriferous terrane in the Paleoproterozoic Ketilidian Orogen.

2 Regional Geology

The Nalunaq gold deposit is an orogenic gold deposit that is situated in the Paleoproterozoic Ketilidian Orogen in South Greenland (Bell et al. 2017a, b; Kaltoft et al. 2000; Steenfelt et al. 2016). The Ketilidian Orogen developed at the southern margin of the Archean North Atlantic Craton (Garde et al. 2002). It is divided into three domains; the Northern, the Central and the Southern domains (Steenfelt et al. 2016). The Northern Domain represents the hinterland, where Archean rocks are unconformably overlain and intruded by Paleoproterozoic rocks, and ca. 1845-1800 Ma, north-vergent nappes are thrust over Archean rocks (Garde et al. 2002; Steenfelt et al. 2016). The wedge-shaped Central Domain consists of variably deformed, ca. 1854-1795 Ma, calc-alkaline monzogranite and granodiorite, with subordinate tonalite, hornblende diorite and gabbro (Julianehåb Igneous Complex; Garde et al. 2002; Steenfelt et al. 2016). Major, NE-trending, near-vertical, ca. 1815-1800 Ma, sinistral shear zones form the contact between the Central and Northern domains and transect the Central Domain (Garde et al. 2002).

The northern part of the Southern Domain consists of < ca. 1800 Ma meta-sedimentary rocks with detritus derived from igneous rocks of the Central Domain (Mueller et al. 2002). The dominantly siliciclastic rocks overly the rocks of the Central Domain tectonically or unconformably. They are interlayered with ca. 1808 Ma meta-volcanic and meta-volcanoclastic rocks (Mueller et al. 2002). Peak metamorphism was estimated at 580 °C and ~3 kbar (Garde et al. 2002).

The southern part of the Southern Domain consists of paragneiss, amphibolite and migmatite, with the PT conditions increasing to the south to > 800°C and ~5 kbar (Garde et al. 2002). Anatectic granite with ages of ca. 1790-1780 Ma constrains the age of peak granulite facies metamorphism (Garde et al. 2002).

Deformation in the Southern Domain is complex with up to five stages and lasted from > 1800 Ma to ca. 1730 Ma (Garde et al. 2002). Early folds are SE-vergent and overprinted by shear zones that indicate NE-directed transport at ca. 1792 Ma. Up to three stages of later folding with initial NW-directed deformation overprinted the shear zones and the associated regional foliation. Late-orogenic granite of the Ilua Plutonic Suite intruded at ca. 1755–1732 Ma (Garde et al. 2002).

3 Geology of the Nalunaq gold deposit

The Nalunaq gold deposit (ca. 11t Au) is located in the NW-vergent Nanortalik Nappe of the Southern Domain close to the contact with the Central Domain (Bell et al. 2017a, b; Kaltoft et al. 2000; Steenfelt et al. 2016). The Nanortalik Nappe consists of meta-pelitic schist, calcareous meta-sedimentary rock, quartz-graphite-sulfide rock, amphibolite and meta-volcanoclastic rocks (Kaltoft et al. 2000). The nappe was intruded by granite of the Ilua Plutonic Suite at ca. 1745 Ma (Bell et al. 2017b).

Gold mineralization is hosted in amphibolite composed of plagioclase, hornblende and clinopyroxene, with minor quartz, biotite and traces of pyrite, chalcopyrite, pyrrhotite and ilmenite (Bell et al. 2017b). Four hydrothermal alteration stages are defined (Bell et al. 2017b):

1. The clinopyroxene-plagioclase-garnet alteration zone is ubiquitous and surrounds quartz-plagioclase veins and rods. Minor constituents are chalcopyrite, pyrite, sphalerite and titanite. The titanite was dated at 1783 ± 9 Ma, which is the age of peak metamorphism in the Southern Domain.
2. The biotite-arsenopyrite alteration is developed around the contemporaneous auriferous quartz veins. The alteration assemblage comprises biotite, quartz, chlorite, sericite, actinolite, arsenopyrite, pyrrhotite, tourmaline, titanite, maldonite, löllingite, pyrite, chalcopyrite, Bi-sulfosalts and gold.
3. The calcite-titanite alteration forms centimetre-scale calcite pockets with minor clinopyroxene, plagioclase and quartz, and a halo of plagioclase, titanite, quartz, pyrrhotite, spinel, chalcopyrite and ilmenite. Titanite was dated at 1766 ± 9 Ma, which is indistinguishable from a zircon age of 1762 ± 9 Ma for an aplite dyke that crosscuts auriferous quartz veins.
4. The epidote-calcite-zoisite alteration consists of calcite, zoisite, epidote, chlorite, titanite, muscovite, prehnite, hematite, microcline, apatite and clay minerals. Titanite was dated at 1745 ± 5 Ma, which is the age of the local granite intrusion.

The auriferous quartz veins have a lateral extent of ~2 km (Bell et al. 2017a). One single vein system, the Main Vein, was mined. It is continuous throughout the deposit, 0.5–2.0 m wide, and surrounded by discontinuous extension veins (Bell et al. 2017a). It is hosted in a reverse, NW-vergent shear zone, with pinch and swell structure, dipping between 25° and 80° to the SE (Bell et al. 2017a). Locally, ~20 cm wide reverse shear zones cross the Main Vein. The Main Vein is further cut by an array of post-mineralization faults, pegmatites and the 1762 Ma aplite.

4 Methods

Stable sulfur isotopes were measured using in situ multi collector SIMS analysis with the CAMECA IMS 1280 ion probe at the Centre for Microscopy and Microanalysis of the University of Western Australia, using methods described in detail by Farquhar et al. (2013). Pyrite and pyrrhotite grains were drilled from polished thin sections and mounted with the standards Sierra (pyrite) and Alexo (pyrrhotite) (LaFlamme et al. 2016). The average standard deviation on standard Alexo is 0.09‰ for ^{33}S, 0.14‰ for ^{34}S and 0.37‰ for ^{36}S. The large uncertainty for ^{36}S makes this data not useful for interpretation. The S-isotope data are expressed in the typical -notation versus the Vienna Canon Diablo meteorite (VCDT) standard in permil (‰) (Ding et al. 2001). The $\Delta^{33}S$ and $\Delta^{36}S$ values were calculated using calibrated ^{33}S and ^{34}S values and the theoretical equation of mass-dependent fractionation for sulfur isotopes.

Stable oxygen, carbon and hydrogen isotope ratios were measured in 24 silicate and carbonate separates from 17 samples of hydrothermal alteration zones and one whole rock sample from an unaltered fine-grained amphibolite using facilities at the University of Lausanne, Switzerland. The O-isotope composition was determined using methods described by Sharp (1990) and Vennemann et al. (2001). The O-isotope ratio is measured by a Finnigan MAT 253 isotope ratio mass spectrometer. Oxygen isotope compositions are given in the standard -notation, expressed relative to VSMOW in permil (‰). Replicate O-isotope analyses of the standard (NBS-28 quartz; n=5) has an average precision of ±0.1‰ for ^{18}O. The accuracy is better than 0.2‰ compared to accepted ^{18}O values for NBS-28 of +9.64‰.

The C- and O-isotope composition of carbonates was measured with a GasBench II connected to a Finnigan MAT DeltaPlus XL mass spectrometer, using a He-carrier gas system according to methods adapted after Spötl and Vennemann (2003). Samples are normalized using an in-house standard calibrated against ^{13}C and ^{18}O values of NBS-19 (+1.95 and –2.20‰, relative to VPDB). External reproducibility for the analyses estimated from replicate analyses of the standard was ±0.04‰ for ^{13}C and ±0.07‰ for ^{18}O.

Measurements of the H-isotope composition of minerals were made using the high-temperature (1450°C) reduction method with He-carrier gas and a TC-EA linked to a Delta Plus XL mass spectrometer from Thermo-Finnigan according to a method adapted after Sharp et al. (2001) and Bauer

and Vennemann (2014). The results are given in the standard □-notation, expressed relative to V-SMOW in permil (‰). The precision of the in-house kaolinite and G1 biotite standards for hydrogen isotope analyses was better than ±2‰ for the method used.

5 Results

Stable isotopes were measured on mineral separates of all hydrothermal alteration stages, the crosscutting aplite dyke and the least altered host rock amphibolite.

5.1 Pre-gold mineralization stable isotope characteristics

The host rock amphibolite yields a ^{18}O of 9.3‰, which is high compared to typical amphibolite or tholeiitic basalt (Hoefs 2015). Garnet (n=2) of the clinopyroxene-plagioclase-garnet alteration zone has a ^{18}O of 8.0‰ and clinopyroxene (n=2) has a value of 8.7‰. Isotopic equilibrium between garnet and clinopyroxene indicates temperatures of ca. 650°C (Zheng 1993) for this hydrothermal alteration stage. Pyrite (n=21) shows a wide variation in ^{34}S between 0.73 and 5.55‰. The $\Delta^{33}S$ values cluster tightly between -0.01 and -0.08‰, which means that all data are within the range of mass-dependent fractionation of ± 0.2‰ (Ohmoto et al. 2006).

5.2 Syn-gold mineralization stable isotope characteristics

The $\delta^{18}O$ values of quartz from the auriferous veins (n=6) and the hydrothermal biotite-arsenopyrite alteration zone (n=6) vary in a narrow range between 12.2 and 13.7‰. Biotite (n=5) yields $\delta^{18}O$ values between 8.3 and 8.7‰ with one value at 6.9‰, and δD values between -68 and -74‰. The compositional range is relatively wide, which is reflected in a wide range of equilibrium temperatures between 460 and 650°C (Bottinga and Javoy 1975). Pyrrhotite (n=16) shows a variation in $\delta^{34}S$ between 2.16 and 4.50‰. The $\Delta^{33}S$ values cluster tightly between 0.01 and 0.09‰ (one at 0.21‰), which means that all data are within the range of mass-dependent fractionation of ± 0.2‰ (Ohmoto et al. 2006).

5.3 Post-gold mineralization stable isotope characteristics

Calcite (n=2) from the calcite-titanite alteration zone has ^{18}O of 12.4‰ and ^{13}C of 2.6‰. Plagioclase of the contemporaneous aplite yields ^{18}O of 8.9‰. Epidote and calcite (n=3) from the epidote-calcite-zoisite alteration zone yield variable isotopic compositions, indicating local disequilibrium. The ^{18}O of epidote ranges between -1.2 and 2.8‰. Calcite has ^{18}O of 5.2-7.7‰ and ^{13}C between -7.0 and -9.4‰. Meaningful equilibrium temperatures are at ~250°C for this hydrothermal overprint.

6 Discussion and interpretation

The stable isotope data of the auriferous stage of the Nalunaq gold deposit are typical of orogenic gold deposits (McCuaig and Kerrich 1998; Ridley and Diamond 2000). Assuming temperatures of ~500°C for the auriferous stage (this paper; Bell et al. 2017b), both, quartz and biotite (Bottinga and Javoy 1975; Zheng 1993) indicate ^{18}O of the water component of the hydrothermal fluid of ~10‰. This is in the general range of orogenic gold deposits (^{18}O=4-15‰) and consistent with the observation that ^{18}O increases with increasing temperature of hydrothermal mineralization in orogenic gold deposits (Ho et al. 1992). The D of the water component of the hydrothermal fluid estimated from biotite compositions (Suzuoki and Epstein 1976) is -33‰ and within the typical range for orogenic gold (D=-80 to -5‰). Also ^{34}S of pyrrhotite overlaps with the typical range for orogenic gold deposits of -3 to +9‰ (McCuaig and Kerrich 1998). Sulfur isotopes lack evidence for mass-independent fractionation, indicating a Paleoproterozoic source. The stable isotope systematics of the auriferous stage indicate a metamorphic fluid that formed during metamorphism of the Paleoproterozoic terrane. In particular, oxygen isotopes are heavier than typical primary magmatic fluids. The D values may be influenced by fractionation during phase separation in the fluid during the mineralization stage (Hoefs 2015).

Estimating the isotopy of water in equilibrium with the pre-gold alteration assemblage (Zheng 1993) yields □^{18}O of ~10‰. A fluid of such an isotopic composition is also in equilibrium with the host rock amphibolite, which is isotopically heavier than similar rocks (Hoefs 2015). This indicates pervasive hydrothermal alteration of the rocks at Nalunaq during the peak metamorphic stage. Hydrothermal gold mineralization has a similar oxygen isotope composition, which is either, explained by continuous evolution from the early hydrothermal stage or by total equilibration of the auriferous hydrothermal fluid. Calcite of the post-gold mineralization calcite-titanite alteration zone is also in equilibrium with □^{18}O of ~10‰, indicating hydrothermal alteration at Nalunaq with metamorphic fluid(s) at ca. 1785-1765 Ma. In contrast, plagioclase from the ca. 1765 Ma aplite dyke is in equilibrium with typical values for primary magmatic waters (Hoefs 2015) that are too low to be in equilibrium with the hydrothermal assemblages, indicating only minor or no magmatic influence on the regional hydrothermal evolution.

Stable isotope systematics of the ca. 1745 Ma alteration stage yield □^{18}O of the water component of ~0‰ and □^{13}C of -6.7‰ (Chacko et al. 2001). Although this alteration stage is contemporaneous with the Ilua Plutonic Suite, these values are outside the typical field of primary magmatic water. They are consistent with the composition of meteoric water and atmospheric CO_2 (Hoefs 2015), indicating the

development of hydrothermal cells of meteoric fluids triggered by the granite intrusions. The Ilua Plutonic Suite is late orogenic, which is consistent with the lower-greenschist facies conditions of the contemporaneous hydrothermal alteration system and the meteoric nature of the fluids. This indicates exhumation of the auriferous terrane to shallow crustal levels by ca. 1745 Ma and a complete change of the hydrothermal system from metamorphic to meteoric fluids.

We can show by careful petrography and fieldwork that the hydrothermal evolution at Nalunaq was complex involving both, metamorphic and meteoric fluids. Starting with peak metamorphism, overprint by metamorphic fluids derived from Paleoproterozoic rocks was accompanied by cooling from ~650 to ~500°C. It is likely that economic gold mineralization was controlled by focusing of fluids into progressively developed discrete shear zones during the retrograde tectonic exhumation. A drastic change of the hydrothermal system to meteoric waters occurs ≥20 m.y. after gold mineralization, when the terrane was at shallow crustal levels and late-orogenic granites intruded the terrane.

References

Bauer K, Vennemann T (2014) Analytical methods for the measurement of hydrogen isotope composition and water content in clay minerals by TC/EA. Chemical Geology 363:229-240.

Beaudoin G, Pitre D (2005) Stable isotope geochemistry of the Archean Val-d'Or (Canada) orogenic gold vein field. Mineralium Deposita 40:59-75.

Bell R-B, Kolb J, Waight TE (2017a) Assessment of lithological, geochemical and structural controls on gold distribution in the Nalunaq gold deposit, South Greenland using three-dimensional implicit modelling In: Gessner K, Blenkinsop TG, Sorjonen-Ward P (eds) Characterization of Ore-Forming Systems from Geological, Geochemical and Geophysical Studies. Geological Society Special Publications, London, pp 385-405.

Bell R-B, Kolb J, Waight TE, Bagas L, Thomsen TB (2017b) A Palaeoproterozoic multi-stage hydrothermal alteration system at Nalunaq gold deposit, South Greenland. Mineralium Deposita 52:383-404. doi: doi:10.1007/s00126-016-0667-7.

Bottinga Y, Javoy M (1975) Oxygen isotope partitioning among minerals and triplets in igneous and metamorphic rocks. Reviews of geophysics and Space Physics 13:401-418.

Chacko T, Cole DR, Horita J (2001) Equilibrium oxygen, hydrogen and carbon isotope fractionation factors applicable to geologic systems In: Valley JW, Cole DR (eds) Stable Isotope Geochemistry. Reviews in Mineralogy and Geochemistry, Mineralogical Society of America, pp 1-82.

Ding T, Valkiers S, Kipphardt H, de Bievre P, Taylor PDB, Gonfiantini R, Krouse HR (2001) Calibrated sulfur isotope abundance ratios of three IAEA sulfur isotope reference materials and V-CDT with a reassessment of the atomic weight of sulfur. Geochimica Cosmochimica Acta 65:2433-2437.

Farquhar J, Cliff J, Zerkle AL, Kamyshny A, Poulton SW, Claire M, Adams D, Harms B (2013) Pathways for Neoarchean pyrite formation constrained by mass-independent sulfur isotopes. Proceedings of the National Academy of Sciences 110:17638-17643. doi: 10.1073/pnas.1218851110.

Garde AA, Hamilton MA, Chadwick B, Grocott J, McCaffrey KJW (2002) The Ketilidian orogen of South Greenland: geochronology, tectonics, magmatism, and fore-arc accretion during Palaeoproterozoic oblique convergence. Canadian Journal of Earth Sciences 39:765-793.

Ho SE, Groves DI, McNaughton NJ, Mikucki EJ (1992) The source of ore fluids and solutes in Archean lode gold deposits of Western Australia. Journal of Volcanology and Geothermal Research 50:173-196.

Hoefs J (2015) Stable Isotope Geochemistry. Springer, Heidelberg.

Kaltoft K, Schlatter DM, Kludt L (2000) Geology and genesis of Nalunaq Palaeoproterozoic shear zone-hosted gold deposit, South Grenland. Transactions of the Institution of Mining and Metallurgy (Section B: Applied Earth Sciences) 109:B23-B33.

LaFlamme C, Martin L, Jeon H, Reddy SM, Selvaraja V, Caruso S, Bui TH, Roberts MP, Voute F, Hagemann S, Wacey D, Littman S, Wing B, Fiorentini M, Kilburn MR (2016) In situ multiple sulfur isotope analysis by SIMS of pyrite, chalcopyrite, pyrrhotite, and pentlandite to refine magmatic ore genetic models. Chemical Geology 444:1-15. doi: https://doi.org/10.1016/j.chemgeo.2016.09.032.

McCuaig TC, Kerrich R (1998) P-T-t deformation fluid characteristics of lode-gold deposits: evidence from alteration systematics. Ore Geology Reviews 12:381-453.

Mueller WU, Dostal J, Stendal H (2002) Inferred Palaeoproterozoic arc rifting along a consuming plate margin: insights from the stratigraphy, volcanology and geochemistry of the Kangerluluk sequence, southeast Greenland. International Journal of Earth Sciences vol.91:209-230.

Ohmoto H, Watanabe Y, Ikemi, Poulsen SR, Taylor BE (2006) Sulphur isotope evidence for an oxic Archaean atmosphere. Nature Letters 442:908-911.

Ridley JR, Diamond LW (2000) Fluid chemistry of orogenic lode gold deposits and implications for genetic models In: Hagemann S, Brown PE (eds) Gold in 2000. Reviews in Economic Geology, pp 141-162.

Sharp ZD (1990) A laser-based microanalytical method for the in-situ determination of oxygen isotope ratios of silicates and oxides. Geochimica et Cosmochimica Acta 54:1353-1357.

Sharp ZD, Atudorei V, Durakiewicz T (2001) A rapid method for determining the hydrogen and oxygen isotope ratios from water and solid hydrous substances. Chemical Geology 178:197-210.

Spötl C, Vennemann TW (2003) Continuous-flow IRMS analysis of carbonate minerals. Rapid Communications in Mass Spectrometry 17:1004-1006.

Steenfelt A, Kolb J, Thrane K (2016) Metallogeny of South Greenland: a review of geological evolution, mineral occurrences and geochemical exploration data. Ore Geology Reviews 77:194-245.

Suzuoki T, Epstein S (1976) Hydrogen isotope fractionation between OH-bearing minerals and water. Geochimica et Cosmochimica Acta 40:1229-1240.

Vennemann TW, Morlok A, von Engelhardt WE, Kyser TK (2001) Stable isotope composition of impact glasses from the Nördlinger Ries impact crater, Germany. Geochimica et Cosmochimica Acta 65:1325-1336.

Zheng Y-F (1993) Calculation of oxygen isotope fractionation in anhydrous silicate minerals. Geochimica et Cosmochimica Acta 57:1079-1091.

Complex hydrothermal evolution during retrograde terrane exhumation, Nalunaq gold deposit, South Greenland

Jochen Kolb[1], Robin-Marie Bell[2], Torsten Vennemann[3], Laure Martin[4], Marco L. Fiorentini[4], Tod Waight[5]
[1]*Karlsruhe Institute of Technology*
[2]*Copenhagen*
[3]*University of Lausanne*
[4]*University of Western Australia*
[5]*University of Copenhagen*

Abstract. The Paleoproterozoic orogenic gold deposit of Nalunaq in South Greenland is located in a NW-vergent thrust in an amphibolite facies terrane. Gold mineralization is hosted in a quartz vein system with biotite-arsenopyrite alteration zone. We present the stable isotope characteristics of four hydrothermal alteration assemblages at Nalunaq. The isotopes indicate that a metamorphic fluid of similar composition is responsible for hydrothermal alteration lasting from the ca. 1785 Ma, pre-gold, peak metamorphic stage at ~650°C to the ca. 1765 Ma, post-gold stage at ~500°C. Ca. 1745 Ma, post-gold hydrothermal alteration is contemporaneous with late-orogenic granite. The fluid is most likely derived from Paleoproterozoic rocks. Stable isotopes indicate a meteoric fluid source in equilibrium with the late-stage hydrothermal alteration assemblage at ca. 250°C. The retrograde evolution of the terrane hosting Nalunaq is initially characterized by hydrothermal overprint by a metamorphic fluid. Economic gold mineralization is likely related to focused fluid flow in a thrust. The hydrothermal system drastically changed to meteoric fluids upon further terrane exhumation and development of hydrothermal fluid cells by widespread granite intrusion overprinted the gold mineralization.

1 Introduction

Orogenic gold deposits are structurally controlled hydrothermal deposits that are hosted by metamorphic rocks and are formed by orogenic processes. They are often one of many stages in a complex evolution, involving locally several hydrothermal stages, which may not all be auriferous. This geological setting allows detailed investigation of hydrothermal fluids present during orogeny. Stable isotopes of hydrothermal alteration minerals allow interpretations of T, precipitation mechanisms and fluid source, although stable O, D, C, S isotopes are often equilibrated with the metamorphic host rocks of the gold deposits (Hoefs 2015). Thus, the stable isotope composition of the fluids often is not a direct link to the fluid source, and fluid-rock interaction along the fluid pathway has to be taken into account (Ridley and Diamond 2000). However, detailed investigations of orogenic gold quartz veins in the Val-d'Or vein field (Canada) show that the stable isotope compositions are the result of fluid-rock reaction and mixing between an upper crustal fluid and a metamorphic fluid (Beaudoin and Pitre 2005).

We present stable isotope data from four hydrothermal stages and wall rocks of the Paleoproterozoic orogenic gold mineralization in Nalunaq, South Greenland. The data indicate a complex hydrothermal evolution during the retrograde exhumation of the auriferous terrane in the Paleoproterozoic Ketilidian Orogen.

2 Regional Geology

The Nalunaq gold deposit is an orogenic gold deposit that is situated in the Paleoproterozoic Ketilidian Orogen in South Greenland (Bell et al. 2017a, b; Kaltoft et al. 2000; Steenfelt et al. 2016). The Ketilidian Orogen developed at the southern margin of the Archean North Atlantic Craton (Garde et al. 2002). It is divided into three domains; the Northern, the Central and the Southern domains (Steenfelt et al. 2016). The Northern Domain represents the hinterland, where Archean rocks are unconformably overlain and intruded by Paleoproterozoic rocks, and ca. 1845-1800 Ma, north-vergent nappes are thrust over Archean rocks (Garde et al. 2002; Steenfelt et al. 2016). The wedge-shaped Central Domain consists of variably deformed, ca. 1854-1795 Ma, calc-alkaline monzogranite and granodiorite, with subordinate tonalite, hornblende diorite and gabbro (Julianehåb Igneous Complex; Garde et al. 2002; Steenfelt et al. 2016). Major, NE-trending, near-vertical, ca. 1815-1800 Ma, sinistral shear zones form the contact between the Central and Northern domains and transect the Central Domain (Garde et al. 2002).

The northern part of the Southern Domain consists of < ca. 1800 Ma meta-sedimentary rocks with detritus derived from igneous rocks of the Central Domain (Mueller et al. 2002). The dominantly siliciclastic rocks overly the rocks of the Central Domain tectonically or unconformably. They are interlayered with ca. 1808 Ma meta-volcanic and meta-volcanoclastic rocks (Mueller et al. 2002). Peak metamorphism was estimated at 580 °C and ~3 kbar (Garde et al. 2002).

The southern part of the Southern Domain consists of paragneiss, amphibolite and migmatite, with the PT conditions increasing to the south to > 800°C and ~5 kbar (Garde et al. 2002). Anatectic granite with ages of ca. 1790-1780 Ma constrains the age of peak granulite facies metamorphism (Garde et al. 2002).

Deformation in the Southern Domain is complex

with up to five stages and lasted from > 1800 Ma to ca. 1730 Ma (Garde et al. 2002). Early folds are SE-vergent and overprinted by shear zones that indicate NE-directed transport at ca. 1792 Ma. Up to three stages of later folding with initial NW-directed deformation overprinted the shear zones and the associated regional foliation. Late-orogenic granite of the Ilua Plutonic Suite intruded at ca. 1755–1732 Ma (Garde et al. 2002).

3 Geology of the Nalunaq gold deposit

The Nalunaq gold deposit (ca. 11t Au) is located in the NW-vergent Nanortalik Nappe of the Southern Domain close to the contact with the Central Domain (Bell et al. 2017a, b; Kaltoft et al. 2000; Steenfelt et al. 2016). The Nanortalik Nappe consists of meta-pelitic schist, calcareous meta-sedimentary rock, quartz-graphite-sulfide rock, amphibolite and meta-volcanoclastic rocks (Kaltoft et al. 2000). The nappe was intruded by granite of the Ilua Plutonic Suite at ca. 1745 Ma (Bell et al. 2017b).

Gold mineralization is hosted in amphibolite composed of plagioclase, hornblende and clinopyroxene, with minor quartz, biotite and traces of pyrite, chalcopyrite, pyrrhotite and ilmenite (Bell et al. 2017b). Four hydrothermal alteration stages are defined (Bell et al. 2017b):

5. The clinopyroxene-plagioclase-garnet alteration zone is ubiquitous and surrounds quartz-plagioclase veins and rods. Minor constituents are chalcopyrite, pyrite, sphalerite and titanite. The titanite was dated at 1783 ± 9 Ma, which is the age of peak metamorphism in the Southern Domain.
6. The biotite-arsenopyrite alteration is developed around the contemporaneous auriferous quartz veins. The alteration assemblage comprises biotite, quartz, chlorite, sericite, actinolite, arsenopyrite, pyrrhotite, tourmaline, titanite, maldonite, löllingite, pyrite, chalcopyrite, Bi-sulfosalts and gold.
7. The calcite-titanite alteration forms centimetre-scale calcite pockets with minor clinopyroxene, plagioclase and quartz, and a halo of plagioclase, titanite, quartz, pyrrhotite, spinel, chalcopyrite and ilmenite. Titanite was dated at 1766 ± 9 Ma, which is indistinguishable from a zircon age of 1762 ± 9 Ma for an aplite dyke that crosscuts auriferous quartz veins.
8. The epidote-calcite-zoisite alteration consists of calcite, zoisite, epidote, chlorite, titanite, muscovite, prehnite, hematite, microcline, apatite and clay minerals. Titanite was dated at 1745 ± 5 Ma, which is the age of the local granite intrusion.

The auriferous quartz veins have a lateral extent of ~2 km (Bell et al. 2017a). One single vein system, the Main Vein, was mined. It is continuous throughout the deposit, 0.5–2.0 m wide, and surrounded by discontinuous extension veins (Bell et al. 2017a). It is hosted in a reverse, NW-vergent shear zone, with pinch and swell structure, dipping between 25° and 80° to the SE (Bell et al. 2017a). Locally, ~20 cm wide reverse shear zones cross the Main Vein. The Main Vein is further cut by an array of post-mineralization faults, pegmatites and the 1762 Ma aplite.

4 Methods

Stable sulfur isotopes were measured using in situ multi collector SIMS analysis with the CAMECA IMS 1280 ion probe at the Centre for Microscopy and Microanalysis of the University of Western Australia, using methods described in detail by Farquhar et al. (2013). Pyrite and pyrrhotite grains were drilled from polished thin sections and mounted with the standards Sierra (pyrite) and Alexo (pyrrhotite) (LaFlamme et al. 2016). The average standard deviation on standard Alexo is 0.09‰ for ^{33}S, 0.14‰ for ^{34}S and 0.37‰ for ^{36}S. The large uncertainty for ^{36}S makes this data not useful for interpretation. The S-isotope data are expressed in the typical -notation versus the Vienna Canon Diablo meteorite (VCDT) standard in permil (‰) (Ding et al. 2001). The $\Delta^{33}S$ and $\Delta^{36}S$ values were calculated using calibrated ^{33}S and ^{34}S values and the theoretical equation of mass-dependent fractionation for sulfur isotopes.

Stable oxygen, carbon and hydrogen isotope ratios were measured in 24 silicate and carbonate separates from 17 samples of hydrothermal alteration zones and one whole rock sample from an unaltered fine-grained amphibolite using facilities at the University of Lausanne, Switzerland. The O-isotope composition was determined using methods described by Sharp (1990) and Vennemann et al. (2001). The O-isotope ratio is measured by a Finnigan MAT 253 isotope ratio mass spectrometer. Oxygen isotope compositions are given in the standard -notation, expressed relative to VSMOW in permil (‰). Replicate O-isotope analyses of the standard (NBS-28 quartz; n=5) has an average precision of ±0.1‰ for ^{18}O. The accuracy is better than 0.2‰ compared to accepted ^{18}O values for NBS-28 of +9.64‰.

The C- and O-isotope composition of carbonates was measured with a GasBench II connected to a Finnigan MAT DeltaPlus XL mass spectrometer, using a He-carrier gas system according to methods adapted after Spötl and Vennemann (2003). Samples are normalized using an in-house standard calibrated against ^{13}C and ^{18}O values of NBS-19 (+1.95 and –2.20‰, relative to VPDB). External reproducibility for the analyses estimated from replicate analyses of the standard was ±0.04‰ for ^{13}C and ±0.07‰ for ^{18}O.

Measurements of the H-isotope composition of minerals were made using the high-temperature (1450°C) reduction method with He-carrier gas and a TC-EA linked to a Delta Plus XL mass spectrometer from Thermo-Finnigan according to a method adapted after Sharp et al. (2001) and Bauer

and Vennemann (2014). The results are given in the standard □-notation, expressed relative to V-SMOW in permil (‰). The precision of the in-house kaolinite and G1 biotite standards for hydrogen isotope analyses was better than ±2‰ for the method used.

5 Results

Stable isotopes were measured on mineral separates of all hydrothermal alteration stages, the crosscutting aplite dyke and the least altered host rock amphibolite.

5.1 Pre-gold mineralization stable isotope characteristics

The host rock amphibolite yields a $\delta^{18}O$ of 9.3‰, which is high compared to typical amphibolite or tholeiitic basalt (Hoefs 2015). Garnet (n=2) of the clinopyroxene-plagioclase-garnet alteration zone has a $\delta^{18}O$ of 8.0‰ and clinopyroxene (n=2) has a value of 8.7‰. Isotopic equilibrium between garnet and clinopyroxene indicates temperatures of ca. 650°C (Zheng 1993) for this hydrothermal alteration stage. Pyrite (n=21) shows a wide variation in $\delta^{34}S$ between 0.73 and 5.55‰. The $\Delta^{33}S$ values cluster tightly between -0.01 and -0.08‰, which means that all data are within the range of mass-dependent fractionation of ± 0.2‰ (Ohmoto et al. 2006).

5.2 Syn-gold mineralization stable isotope characteristics

The $\delta^{18}O$ values of quartz from the auriferous veins (n=6) and the hydrothermal biotite-arsenopyrite alteration zone (n=6) vary in a narrow range between 12.2 and 13.7‰. Biotite (n=5) yields $\delta^{18}O$ values between 8.3 and 8.7‰ with one value at 6.9‰, and δD values between -68 and -74‰. The compositional range is relatively wide, which is reflected in a wide range of equilibrium temperatures between 460 and 650°C (Bottinga and Javoy 1975). Pyrrhotite (n=16) shows a variation in $\delta^{34}S$ between 2.16 and 4.50‰. The $\Delta^{33}S$ values cluster tightly between 0.01 and 0.09‰ (one at 0.21‰), which means that all data are within the range of mass-dependent fractionation of ± 0.2‰ (Ohmoto et al. 2006).

5.3 Post-gold mineralization stable isotope characteristics

Calcite (n=2) from the calcite-titanite alteration zone has $\delta^{18}O$ of 12.4‰ and $\delta^{13}C$ of 2.6‰. Plagioclase of the contemporaneous aplite yields $\delta^{18}O$ of 8.9‰. Epidote and calcite (n=3) from the epidote-calcite-zoisite alteration zone yield variable isotopic compositions, indicating local disequilibrium. The $\delta^{18}O$ of epidote ranges between -1.2 and 2.8‰. Calcite has $\delta^{18}O$ of 5.2-7.7‰ and $\delta^{13}C$ between -7.0 and -9.4‰. Meaningful equilibrium temperatures are at ~250°C for this hydrothermal overprint.

6 Discussion and interpretation

The stable isotope data of the auriferous stage of the Nalunaq gold deposit are typical of orogenic gold deposits (McCuaig and Kerrich 1998; Ridley and Diamond 2000). Assuming temperatures of ~500°C for the auriferous stage (this paper; Bell et al. 2017b), both, quartz and biotite (Bottinga and Javoy 1975; Zheng 1993) indicate $\delta^{18}O$ of the water component of the hydrothermal fluid of ~10‰. This is in the general range of orogenic gold deposits ($\delta^{18}O$=4-15‰) and consistent with the observation that $\delta^{18}O$ increases with increasing temperature of hydrothermal mineralization in orogenic gold deposits (Ho et al. 1992). The δD of the water component of the hydrothermal fluid estimated from biotite compositions (Suzuoki and Epstein 1976) is -33‰ and within the typical range for orogenic gold (δD=-80 to -5‰). Also $\delta^{34}S$ of pyrrhotite overlaps with the typical range for orogenic gold deposits of -3 to +9‰ (McCuaig and Kerrich 1998). Sulfur isotopes lack evidence for mass-independent fractionation, indicating a Paleoproterozoic source. The stable isotope systematics of the auriferous stage indicate a metamorphic fluid that formed during metamorphism of the Paleoproterozoic terrane. In particular, oxygen isotopes are heavier than typical primary magmatic fluids. The δD values may be influenced by fractionation during phase separation in the fluid during the mineralization stage (Hoefs 2015).

Estimating the isotopy of water in equilibrium with the pre-gold alteration assemblage (Zheng 1993) yields $\delta^{18}O$ of ~10‰. A fluid of such an isotopic composition is also in equilibrium with the host rock amphibolite, which is isotopically heavier than similar rocks (Hoefs 2015). This indicates pervasive hydrothermal alteration of the rocks at Nalunaq during the peak metamorphic stage. Hydrothermal gold mineralization has a similar oxygen isotope composition, which is either, explained by continuous evolution from the early hydrothermal stage or by total equilibration of the auriferous hydrothermal fluid. Calcite of the post-gold mineralization calcite-titanite alteration zone is also in equilibrium with $\delta^{18}O$ of ~10‰, indicating hydrothermal alteration at Nalunaq with metamorphic fluid(s) at ca. 1785-1765 Ma. In contrast, plagioclase from the ca. 1765 Ma aplite dyke is in equilibrium with typical values for primary magmatic waters (Hoefs 2015) that are too low to be in equilibrium with the hydrothermal assemblages, indicating only minor or no magmatic influence on the regional hydrothermal evolution.

Stable isotope systematics of the ca. 1745 Ma alteration stage yield $\delta^{18}O$ of the water component of ~0‰ and $\delta^{13}C$ of -6.7‰ (Chacko et al. 2001). Although this alteration stage is contemporaneous with the Ilua Plutonic Suite, these values are outside the typical field of primary magmatic water. They are consistent with the composition of meteoric water and atmospheric CO_2 (Hoefs 2015), indicating the

development of hydrothermal cells of meteoric fluids triggered by the granite intrusions. The Ilua Plutonic Suite is late orogenic, which is consistent with the lower-greenschist facies conditions of the contemporaneous hydrothermal alteration system and the meteoric nature of the fluids. This indicates exhumation of the auriferous terrane to shallow crustal levels by ca. 1745 Ma and a complete change of the hydrothermal system from metamorphic to meteoric fluids.

We can show by careful petrography and fieldwork that the hydrothermal evolution at Nalunaq was complex involving both, metamorphic and meteoric fluids. Starting with peak metamorphism, overprint by metamorphic fluids derived from Paleoproterozoic rocks was accompanied by cooling from ~650 to ~500°C. It is likely that economic gold mineralization was controlled by focusing of fluids into progressively developed discrete shear zones during the retrograde tectonic exhumation. A drastic change of the hydrothermal system to meteoric waters occurs ≥20 m.y. after gold mineralization, when the terrane was at shallow crustal levels and late-orogenic granites intruded the terrane.

References

Bauer K, Vennemann T (2014) Analytical methods for the measurement of hydrogen isotope composition and water content in clay minerals by TC/EA. Chemical Geology 363:229-240.

Beaudoin G, Pitre D (2005) Stable isotope geochemistry of the Archean Val-d'Or (Canada) orogenic gold vein field. Mineralium Deposita 40:59-75.

Bell R-B, Kolb J, Waight TE (2017a) Assessment of lithological, geochemical and structural controls on gold distribution in the Nalunaq gold deposit, South Greenland using three-dimensional implicit modelling In: Gessner K, Blenkinsop TG, Sorjonen-Ward P (eds) Characterization of Ore-Forming Systems from Geological, Geochemical and Geophysical Studies. Geological Society Special Publications, London, pp 385-405.

Bell R-B, Kolb J, Waight TE, Bagas L, Thomsen TB (2017b) A Palaeoproterozoic multi-stage hydrothermal alteration system at Nalunaq gold deposit, South Greenland. Mineralium Deposita 52:383-404. doi: doi:10.1007/s00126-016-0667-7.

Bottinga Y, Javoy M (1975) Oxygen isotope partitioning among minerals and triplets in igneous and metamorphic rocks. Reviews of geophysics and Space Physics 13:401-418.

Chacko T, Cole DR, Horita J (2001) Equilibrium oxygen, hydrogen and carbon isotope fractionation factors applicable to geologic systems In: Valley JW, Cole DR (eds) Stable Isotope Geochemistry. Reviews in Mineralogy and Geochemistry, Mineralogical Society of America, pp 1-82.

Ding T, Valkiers S, Kipphardt H, de Bievre P, Taylor PDB, Gonfiantini R, Krouse HR (2001) Calibrated sulfur isotope abundance ratios of three IAEA sulfur isotope reference materials and V-CDT with a reassessment of the atomic weight of sulfur. Geochimica Cosmochimica Acta 65:2433-2437.

Farquhar J, Cliff J, Zerkle AL, Kamyshny A, Poulton SW, Claire M, Adams D, Harms B (2013) Pathways for Neoarchean pyrite formation constrained by mass-independent sulfur isotopes. Proceedings of the National Academy of Sciences 110:17638-17643. doi: 10.1073/pnas.1218851110.

Garde AA, Hamilton MA, Chadwick B, Grocott J, McCaffrey KJW (2002) The Ketilidian orogen of South Greenland: geochronology, tectonics, magmatism, and fore-arc accretion during Palaeoproterozoic oblique convergence. Canadian Journal of Earth Sciences 39:765-793.

Ho SE, Groves DI, McNaughton NJ, Mikucki EJ (1992) The source of ore fluids and solutes in Archean lode gold deposits of Western Australia. Journal of Volcanology and Geothermal Research 50:173-196.

Hoefs J (2015) Stable Isotope Geochemistry. Springer, Heidelberg.

Kaltoft K, Schlatter DM, Kludt L (2000) Geology and genesis of Nalunaq Palaeoproterozoic shear zone-hosted gold deposit, South Grenland. Transactions of the Institution of Mining and Metallurgy (Section B: Applied Earth Sciences) 109:B23-B33.

LaFlamme C, Martin L, Jeon H, Reddy SM, Selvaraja V, Caruso S, Bui TH, Roberts MP, Voute F, Hagemann S, Wacey D, Littman S, Wing B, Fiorentini M, Kilburn MR (2016) In situ multiple sulfur isotope analysis by SIMS of pyrite, chalcopyrite, pyrrhotite, and pentlandite to refine magmatic ore genetic models. Chemical Geology 444:1-15. doi: https://doi.org/10.1016/j.chemgeo.2016.09.032.

McCuaig TC, Kerrich R (1998) P-T-t deformation fluid characteristics of lode-gold deposits: evidence from alteration systematics. Ore Geology Reviews 12:381-453.

Mueller WU, Dostal J, Stendal H (2002) Inferred Palaeoproterozoic arc rifting along a consuming plate margin: insights from the stratigraphy, volcanology and geochemistry of the Kangerluluk sequence, southeast Greenland. International Journal of Earth Sciences vol.91:209-230.

Ohmoto H, Watanabe Y, Ikemi, Poulsen SR, Taylor BE (2006) Sulphur isotope evidence for an oxic Archaean atmosphere. Nature Letters 442:908-911.

Ridley JR, Diamond LW (2000) Fluid chemistry of orogenic lode gold deposits and implications for genetic models In: Hagemann S, Brown PE (eds) Gold in 2000. Reviews in Economic Geology, pp 141-162.

Sharp ZD (1990) A laser-based microanalytical method for the in-situ determination of oxygen isotope ratios of silicates and oxides. Geochimica et Cosmochimica Acta 54:1353-1357.

Sharp ZD, Atudorei V, Durakiewicz T (2001) A rapid method for determining the hydrogen and oxygen isotope ratios from water and solid hydrous substances. Chemical Geology 178:197-210.

Spötl C, Vennemann TW (2003) Continuous-flow IRMS analysis of carbonate minerals. Rapid Communications in Mass Spectrometry 17:1004-1006.

Steenfelt A, Kolb J, Thrane K (2016) Metallogeny of South Greenland: a review of geological evolution, mineral occurrences and geochemical exploration data. Ore Geology Reviews 77:194-245.

Suzuoki T, Epstein S (1976) Hydrogen isotope fractionation between OH-bearing minerals and water. Geochimica et Cosmochimica Acta 40:1229-1240.

Vennemann TW, Morlok A, von Engelhardt WE, Kyser TK (2001) Stable isotope composition of impact glasses from the Nördlinger Ries impact crater, Germany. Geochimica et Cosmochimica Acta 65:1325-1336.

Zheng Y-F (1993) Calculation of oxygen isotope fractionation in anhydrous silicate minerals. Geochimica et Cosmochimica Acta 57:1079-1091.

Constraints on the Genesis of Au Veins in Interior Alaska: Evidence from Geochronology and Vein Textures

Douglas C Kreiner[1], William Thompson[2], Jonathan S Caine[3], Ashleigh Ball[4], Christopher Holm-Denoma[3], Paul O'Sullivan[5], Holly Stein[6,7]

[1]U.S. Geological Survey, Anchorage, United States, [2]Northern Star Resources, Pogo, United States, [3]U.S. Geological Survey, Denver, United States, [4]Northern Star Resources, Perth, Australia, [5]GeoSep Services, Moscow, United States, [6]AIRIE Program, Fort Collins, United States, [7]University of Oslo, Oslo, Norway

Abstract. Genesis of Au-bearing, low sulfide quartz veins in the Pogo and Tibbs Creek regions of interior Alaska remain enigmatic. New geochronology of igneous and mineralization phases indicates that gold veins post-date regional metamorphism. Re-Os geochronology on arsenopyrite coeval with gold constrains mineralization to ca. 105 Ma, during a magmatic lull. LA-ICP-MS U/Pb zircon constrains a pre-mineral peraluminous granitic event at ca. 114-110 Ma and a post-mineral dioritic event at ca. 99-93 Ma. Petrographic observations of veins show multiple stages of Au-Bi-Te(-As) mineralization in quartz dominant veins. Veins textures are diverse with early, generally barren, plasticly deformed quartz, later granular quartz, and multiple styles of brecciation. The latest event is characterized by bladed carbonate-euhedral quartz veins, indicating boiling and shallow crustal levels of formation. These observations are inconsistent with traditional orogenic and intrusion-related models and require a new genetic model for interior Alaska veins.

1 Introduction

Gold-quartz vein deposits in the Pogo-Tibbs region include the 8 Moz Pogo gold district, including the newly discovered 1 Moz Goodpaster deposit (Northern Star Resources, 2022). Active exploration along a 50 km trend is focused on defining additional resources. Veins are hosted in regionally metamorphosed gneiss and schist intruded by pulses of Cretaceous granitoids.

Previous estimates on the age of mineralization at Pogo are based on a single ~104 Ma molybdenite Re-Os date (Selby et al. 2002). Broadly coeval magmatism documented between 107-105 Ma (Day et al. 2003; Dilworth et al. 2007) in the region has led to the hypothesis that the veins are magmatic hydrothermal in origin. However, molybdenite is not coeval with gold in the veins – and igneous zircon crystallization ages are not well documented. Others have inferred the veins are orogenic, forming at 7-10 km depth (Dilworth, 2003). This study applies new U-Pb zircon crystallization ages of igneous phases with Re-Os geochronology on arsenopyrite coeval with gold in multiple paragenetic events to constrain the age of ore formation. Detailed petrographic observations of vein textures and mineralogy and geochemistry constrain the structural styles and depth of vein formation. New data suggest no temporal relation to magmatism, and shallow depths of ore formation evidenced by boiling textures require a new genetic model that changes the paradigm for new discovery in the region.

2 Geologic Setting of Vein Deposits

Host rocks to the veins include biotite-quartz-feldspar Devonian orthogneiss and Mississippian paragneiss of the Lake George assemblage of Foster et al. (1994) of parautochthonous North American basement (Dusel-Bacon et al. 2006; Fig. 1). Devonian and Mississippian gneisses underwent regional amphibolite facies metamorphism in the Cretaceous (Foster et al., 1994).

Deformation across the region is poorly constrained, with some evidence for mid Paleozoic, Jurassic, and Early Cretaceous pulses of contraction and extension (Dusel-Bacon et al. 2006). Plastic regime contractional deformation ceased by ca. 115 Ma (Day et al., 2003). During the formation of veins, the region is interpreted to have been undergoing extension (Rhys et al. 2003).

Felsic and intermediate plutonic rocks intruded episodically from the Permian, through early Tertiary. In the Pogo and Tibbs Creek region. Mid Cretaceous (114-90 Ma) felsic plutonism is predominant, with sparse early Tertiary felsic intrusions in the district.

3 Igneous Geochronology and chemistry

3.1 U-Pb zircon geochronology

Twelve new LA-ICPMS zircon U-Pb dates combined with existing geochronology highlight three major pulses of mid Cretaceous magmatism. Early unfoliated to weakly foliated and recrystallized two-mica and garnet-bearing granite and granodiorite yield U-Pb zircon crystallization ages of ca. 113-108 Ma. An intermediate age suite, characterized by tonalite to granodiorite, yields U-Pb monazite, zircon, and SHRIMP-RG zircon crystallization ages of ca. 107-105 Ma (Day et al., 2003; Dilworth et al., 2007). The youngest suite is characterized by granodiorite to quartz diorite with LA-ICPMS U-Pb zircon crystallization ages of ca. 98-93 Ma.

3.2 Igneous geochemistry

Secular trends in the geochemistry are pronounced. Early granite is strongly peraluminous and straddles the syn-collisional to volcanic arc fields on a Y+Nb and Yb+Ta versus Rb Pearce plot. Intermediate tonalite is characterized by weakly peraluminous to

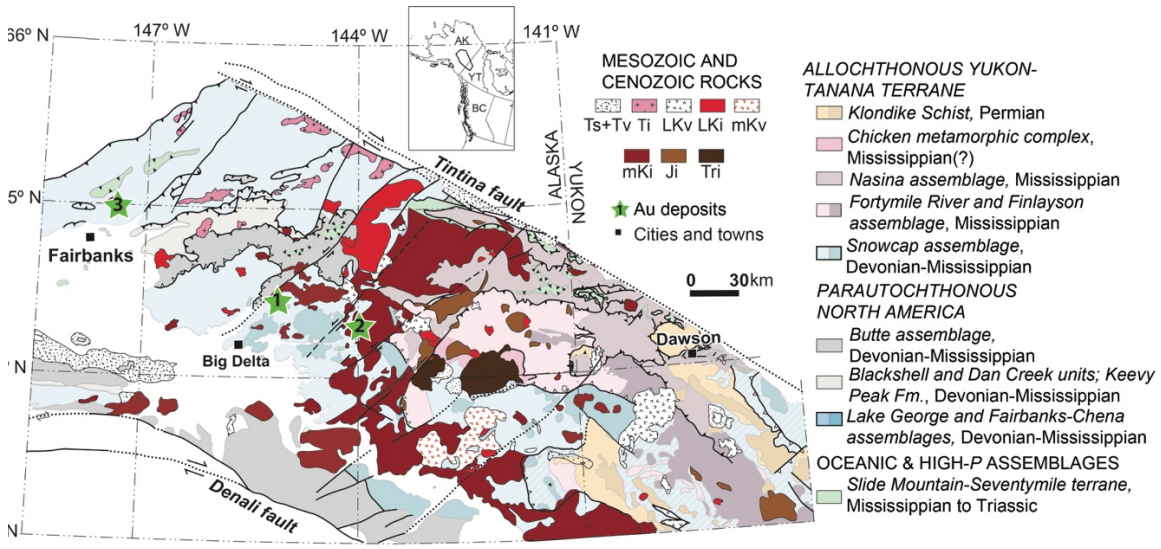

Figure 1. Geologic map of eastern interior Alaska. Gold deposits as green stars: 1: Pogo; 2: Tibbs Creek; 3: Fort Knox. Map modified and nomenclature of all units from Dusel-Bacon et al. (2006).

metaluminous phases. Late diorite to granodiorite plot in the volcanic arc field on the Pearce plot.

Zircon trace elements analyzed on the SHRIMP-RG in all igneous suites exhibit steep light and flat middle to heavy REE patterns. These patterns are consistent with shallow non-garnet residual sources. Ti-in-zircon calculations indicate metaluminous diorite crystallized at higher temperatures than peraluminous granites. All suites exhibit strong negative Eu anomalies with weak to absent Ce anomalies and are strongly depleted in Eu and Ce compared to typical intermediate arcs.

4 Vein Textures

Veins in the Pogo district are quartz dominant; sulfide minerals are sparse, commonly less than 1% of veins. Within individual veins, massive arsenopyrite or pyrrhotite-pyrite occur. Veins exhibit diverse textures ranging from massive quartz with thicknesses ranging from 10s of cms to >10m to pervasive breccias. Quartz is described as milky white and massive, sugary light to dark grey, and granular milky white to grey or brecciated.

4.1 Quartz and carbonate vein textures

Early quartz is recrystallized and is preserved as clasts within brecciated quartz veins, or as massive interlocking quartz veins. Quartz veins are commonly brecciated, cemented by younger generations of granular quartz(±sulfides or sericite and carbonates), sulfides with minor quartz, or extremely fine-grained dark grey cataclastic material. Megascopic breccia textures are often obscured but readily apparent in thin sections.

Wide zones of vein quartz are cut by thin arsenopyrite, pyrite, or pyrrhotite dominant veinlets ranging from mm scale to cm scale. Other crosscutting veinlets include mm-scale sulfide-poor quartz (±sericite) and carbonate assemblages. Sulfide ubiquitously post-dates early quartz.

Brecciation is common across both the Pogo and Tibbs Creek occurrences. Hydrothermal breccias are characterized by angular to sub-angular clasts cemented by varying amounts of quartz, sulfide, carbonate, and sericite (Fig. 2a). Clasts are predominantly broken quartz fragments or polygranular quartz vein. Clasts locally exhibit superimposed secondary strain textures. Sulfide clasts observed are more commonly associated with cataclasite breccias. Cataclasite consists of milled subrounded to rounded clasts commonly composed of arsenopyrite and pyrite cemented by dark, very fine-grained cataclasite that often contains minor arsenopyrite and pyrite (Fig. 2b).

Bladed carbonate veins with terminated euhedral quartz crystals (Fig. 2c) and local open space in the vein are ubiquitous throughout the mineralized occurrences. Carbonates are dolomite throughout the Pogo veins, but pure calcite in the Tibbs Creek occurrences. Terminated quartz crystals show strong growth zoning around the crystal faces demarcated by abundant fluid inclusions (Fig. 2c) with coexisting liquid-vapor and vapor rich assemblages. Associated with the bladed carbonates are open space veins, and strongly silicified sinter-like replacement textures.

4.2 Sulfide mineral textures and paragenesis

Sulfide assemblages in the veins are characterized by abundant pyrite, pyrrhotite, and arsenopyrite with less abundant Au, bismuthinite, native bismuth, loellingite and Bi-telluride. Sulfides can be massive – particularly pyrite-pyrrhotite and arsenopyrite – or disseminated. Where massive, grain size can range from mm- to cm-scale. Bismuthinite, native bismuth, and tellurides are most common as inclusions within arsenopyrite but also occur as principal phases in quartz veins.

Gold is strongly correlated with bismuth and tellurium and shows little correlation with arsenic or antimony. Gold occurs as inclusions within As, Bi,

and Te sulfides and sulfosalts, is intergrown with sulfides, or as free gold interstitial to quartz grains.

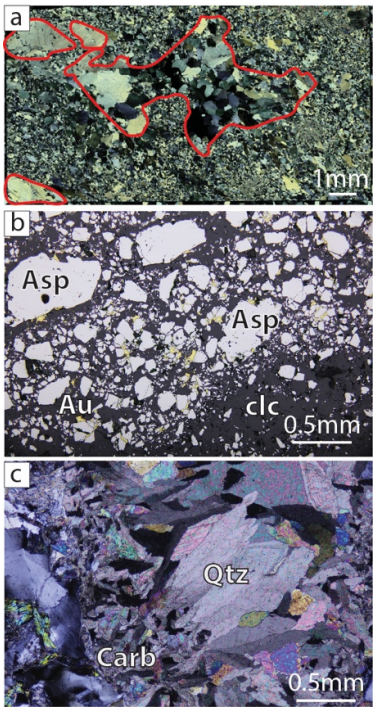

Figure 2. Vein textures. A) hydrothermal breccia with early quartz vein clasts (red) cemented by later granular quartz. B) milled arsenopyrite (Asp) clasts cemented by cataclasite (clc) matrix with gold (Au) growing on clast margins. C) terminated quartz (Qtz) crystals with inclusion rich growth zones and bladed carbonate (Carb).

Gold is present in multiple paragenetic stages in the veins. Early Au-bearing quartz clasts (Fig. 3) represent the earliest stages of gold. Subsequent generations of gold are recorded in quartz-gold, or arsenopyrite-gold matrix or veinlets. Gold is also found in syn- mineral cataclastic breccias (Fig. 3) and locally post-dates the milling event, where it occurs as rims or patchy cement between arsenopyrite grains (Fig. 2b). Sulfide events ubiquitously cut earlier quartz, and are commonly characterized by Au-Bi, or Au-Te assemblages. Gold-bearing carbonate and bladed carbonate-quartz veins that cut the breccias record the latest gold-bearing events.

5 Geochronology of Mineralization

A Re-Os NTIMS age of ca. 104 Ma was determined for molybdenite at the Liese deposit (Selby et al. 2002). New Re-Os NTIMS dating of arsenopyrite coeval with multiple gold-bearing assemblages in the paragenesis at Pogo yields ages ranging from ca. 106-103 Ma for Au mineralization. At Tibbs Creek, direct dating of mineralization via Re-Os is in progress, though veins at Blue Lead and Wolverine, are hosted within the 108-104 Ma granite indicating a similar age of veins across the region.

Preliminary Lu-Hf dating via LA-ICPMS of bladed carbonate vein assemblages that occur within the mineralized zones, and co-precipitate with quartz yield Mesozoic isochron ages of 138 and 110.4 Ma.

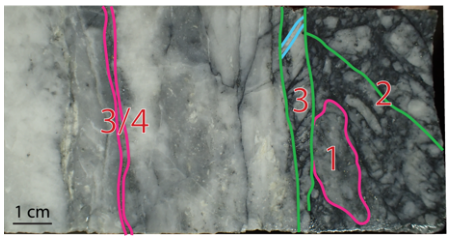

Figure 3. Gold generations at Pogo. 1: early quartz-gold clast cemented by 2: gold-arsenopyrite cataclasite. Events 1 and 2 are cut by 3: second generation of gold-bearing cataclasite that truncates a carbonate vein (blue outline). The latest generation is 3/4: quartz-gold vein.

However, the 2-sigma uncertainties are large, ca. 45 and 53 Ma, respectively. Despite the significant uncertainties, interpreted ages are Mesozoic, and based on relative timing constraints, places the bladed-carbonate event coeval with gold mineralization.

Orthogneiss adjacent to a diorite pluton ~20km east of Pogo hosts a ca. 95 Ma (Re-Os) molybdenite bearing quartz vein that distinctly lacks Au, As, Bi, Te (Dave Selby, pers. communication; Fig. 4).

6 Discussion

Regional synthesis of the igneous geochronology and mineralization ages indicates there is little temporal overlap between Au mineralization and mid Cretaceous magmatism (Fig. 4). Dilworth et al. (2007) documents the ca. 107-106 Ma tonalite suite in a series of small stocks or dikes adjacent to the deposit. This event ceased prior to mineralization (Fig. 4). Tonalite of this age is unmineralized and rarely altered. At Tibbs Creek, gold-bearing quartz veins are locally hosted within the largely unaltered ~108-104 Ma Black Mountain granite of Day et al. (2003). Mapping and field observations indicate sparse alteration of igneous phases younger than 110 Ma, no zoning of hydrothermal assemblages around igneous bodies, and a distinct lack of magmatic hydrothermal alteration. Despite the close temporal relations between emplacement and vein formation, a direct link has not been identified.

Previous studies of Al-in-hornblende barometry from granitoids and fluid inclusions have placed inferred depths of vein formation and gold mineralization at ~5-9km (Dilworth 2003). New observations of vein textures during our study suggest at least four generations of Au mineralization in highly brecciated, cyclical depositional events. Recognition of Au-bearing calcite and associated bladed carbonate-quartz veins with coeval liquid-vapor and vapor rich fluid inclusions across the Pogo and Tibbs Creek occurrences suggest boiling occurred in the veins. Geochronology of bladed carbonate indicates boiling events occurred in the mid Cretaceous. Given the Re-Os arsenopyrite ages in multiple gold-

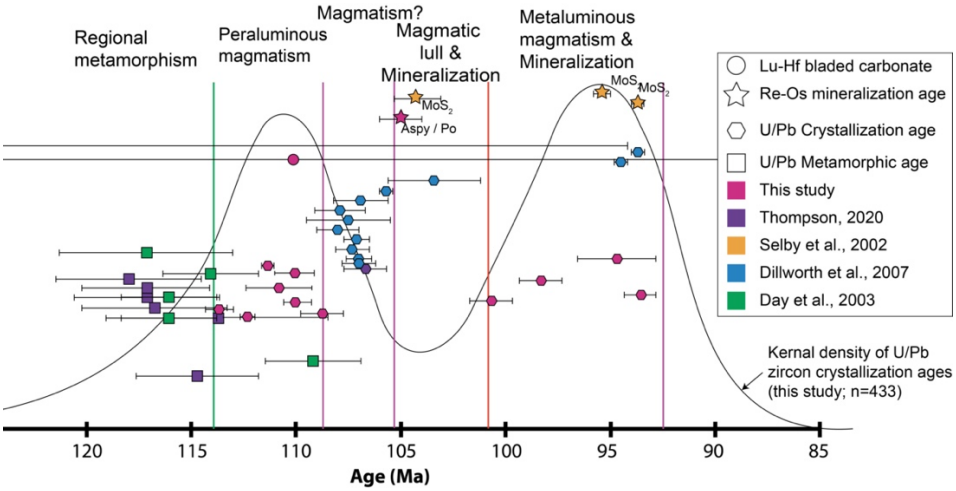

Figure 4. Geochronology summary for the Pogo deposit. Kernel density plot is inclusive of geochronology from this study.

bearing paragenetic stages plot within a span of ~2 My, boiling likely occurred at the same time. These constraints, combined with the observations of cyclic brittle deformation textures in breccias, place the depth of formation for Au-As-Bi veins at <2 km.

Models for typical orogenic gold veins suggest the depth of formation for Au-As mineralization occurs at depths of >6 km, and Hg-Sb assemblages are predominant at shallow depths (Groves et al., 1998), the latter is distinctly lacking in interior Alaska. Therefore, we propose a hybrid model for the formation of Au-As-Bi quartz veins in eastern interior Alaska. Our model invokes the circulation of shallow meteoric waters that mix with CO_2 derived from prograde metamorphic reactions percolating upwards. Metals were stripped from host rocks by the bicarbonate fluid along flow paths and concentrated in upwelling zones where boiling plays a role in deposition of Au, As, and Bi.

Conclusions

New igneous and mineralization geochronology indicate that Au-bearing quartz veins formed at ca. 105 Ma. during a magmatic lull between peraluminous magmatism from ca. 114-110, and metaluminous dioritic magmatism at ca 107-106, and 99-93 Ma. Textural evidence of boiling suggests shallow levels of ore formation. These new observations in the region are incompatible with traditional models invoked for the formation of Au-veins and require a new genetic model. Shallowly circulating fluids stripped metals from wall rocks along the flow path, were concentrated in permeable structural zones where boiling played an important role for deposition of Au, As, Bi, and Te in the veins.

Acknowledgements

The authors would like to thank Northern Star Resources Pogo team for continued support of our research. Any use of trade, firm, or product names is for descriptive purposes only and does not imply endorsement by the U.S. Government.

References

Day WC, Aleinikoff, JN, Roberts P, Smith M, Gamble, BM, Henning, MW, Gough, LP, and Morath, LC (2003) Geologic map of the Big Delta B–2 quadrangle, eastcentral Alaska: U.S. Geological Survey Geologic Investigations Series I–2788.

Dilworth, KM, 2003, Geological setting, nature, and evolution of reduced intrusions and gold bearing quartz veins of the 4021 prospect, Goodpaster District, East-Central Alaska: University of British Columbia, unpublished MS thesis, 192 p.

Dilworth K, Mortensen JK, Ebert S, Tosdal RM, Smith MT and Roberts P (2007) Cretaceous reduced granitoids in the Goodpaster mining district, east-central Alaska. Can J Ear Sci 44:1347–1373.

Dusel-Bacon C, Hopkins MJ, Mortensen JK, Dashevsky SS, Bressler JR and Day WD (2006) Paleozoic tectonic and metallogenic evolution of the pericratonic rocks of east-central Alaska and adjacent Yukon: in Colpron M and Nelson JL (eds), Paleozoic Evolution and Metallogeny of Pericratonic Terranes at the Ancient Pacific Margin of North America, Canadian and Alaskan Cordillera: Geological Society of Canada Special Paper 45: 25-74.

Groves DI, Goldfarb RJ, Gebre-Mariam M, Hagemann SG, Robert F (1998) Orogenic gold deposits: A proposed classification in the context of their crustal distribution and relationship to other gold deposit types. Ore Geol Rev 13:7–27

Foster HL, Keith TE, and Menzie WD (1994) Geology of the Yukon-Tanana terrane of east-central Alaska. in The Geology of Alaska. edited Plafker G and Berg HC. Geol. Soc. Amer. Boulder CO, The Geology of North America, G-1:205-240.

Northern Star Resources (2022) https://www.nsrltd.com/investor-and-media/asx-announcements/2022/may/resources,-reserves-and-exploration-update. Accessed February 8, 2023.

Rhys D, DiMarchi J, Smith M, Friesen R, Rombach C (2003) Structural setting, style, and timing of vein-hosted gold mineralization at the Pogo deposit, east central Alaska. Miner Deposita 38:863–875

Selby D, Creaser RA, Hart CJ, Rombach CS, Thompson JFH, Smith MT, et al. (2002) Timing of sulphide and gold mineralization at Fort Knox and Pogo gold deposits, Tintina Gold Belt: evidence from Re-Os molybdenite dates for distinct gold mineralization episodes. Geology 30:791-794.

Thompson W. (2020) Geochemical, spatial, and temporal relationships of the intrusives and meta-intrusives of the Pogo deposit, Eastern interior AK. University of Alaska, Fairbanks unpub. MS Thesis, 146p

Fluid evolution and carbon-gold systematics at the Fairview Mine, Barberton Greenstone Belt, South Africa

Rutger La Cock[1], Bjorn von der Heyden[1], Long Li[2], Yifan Du[2], Matthew Steele-MacInnes[2]
[1]Department of Earth Sciences, Stellenbosch University, South Africa
[2]Department of Earth & Atmospheric Sciences, University of Alberta, Canada

Abstract. The Fairview mine is one of the most profitable gold mines within the Barberton Greenstone Belt (BGB). Recent work has centred around the structural aspects controlling mineralisation, but little work has been done regarding the chemical controls on mineralisation. With the help of scanning electron microscopy (SEM) and laser ablation inductively coupled plasma mass spectrometry (LA-ICP-MS), this research shows how the variation in carbonate species and sulphide trace element composition can be utilized to track different fluid flow events. Field evidence suggests that graphite has an important role to play in gold deposition as it is frequently found within high-grade shear zones. This graphite is shown to be nanocrystalline in size and have a high degree of structural disorder. Geothermometry calculations based off Raman spectra of graphite show that shear zones were subjected to maximum temperatures of around 400 ºC. Carbon isotope signatures provide insights into the potential source of ore-fluids which led to mineralisation at Fairview. These findings have significant implications for ore-forming models pertaining to Archaean greenstone belts.

1 Introduction

The Barberton Greenstone Belt (Figure 1) represents one of the oldest and best-preserved fragments of continental crust on Earth (Brandl et al. 2006). Like many other greenstone belts, the BGB hosts a number of economically significant gold deposits, with over 350 tons of gold extracted from the belt since 1882 (Agangi et al. 2019). Recent studies have focussed on characterising the structural controls on gold mineralisation within the well-endowed, Sheba-Fairview Complex (Gloyn-Jones & Kisters 2018, 2019; Pintos Cerda et al. 2020; Jones & Kisters 2022). However, the chemical controls on mineralisation are still poorly understood.

To understand the chemical controls on mineralisation it is important to know how the auriferous fluid may have evolved over time. As there is evidence for multiple phases of fluid flow at Fairview (Altigani et al. 2016), SEM and LA-ICP-MS were used to differentiate between temporally separate fluids based on sulphide chemistry. These methods also provided insights into ore textures and mineral composition, allowing for a detailed characterisation of the Fairview gold ore.

A connection between carbon and mineral deposits has long been recognised (Agricola 1556). Specific links between carbon and gold have been a subject of much debate with some authors suggesting that they play a crucial role in the formation of high-grade, orogenic gold deposits (e.g., Gaboury 2021). Gloyn-Jones & Kisters (2019) highlight the importance of carbon in the form of graphite at Fairview and its role in strain localisation.

However, the role of carbon in deposit formation has not been fully assessed. As there is a strong association between Au-bearing sulphides and graphite, the present research focussed strongly on this association. Raman spectroscopy was used to classify the nature of the graphite found in and around high-grade shear zones at Fairview. Carbon isotopes were measured for both carbonates and graphite and serves to provide information on the source of auriferous fluids, the temperatures reached in shear zones and degree of fluid-rock interaction. Knowing how carbon contributes to gold deposition at Fairview will help geologists discern whether or not graphite is a useful parameter to consider during exploration, for example, by utilising graphite's electrically conductive geophysical response as an exploration guide.

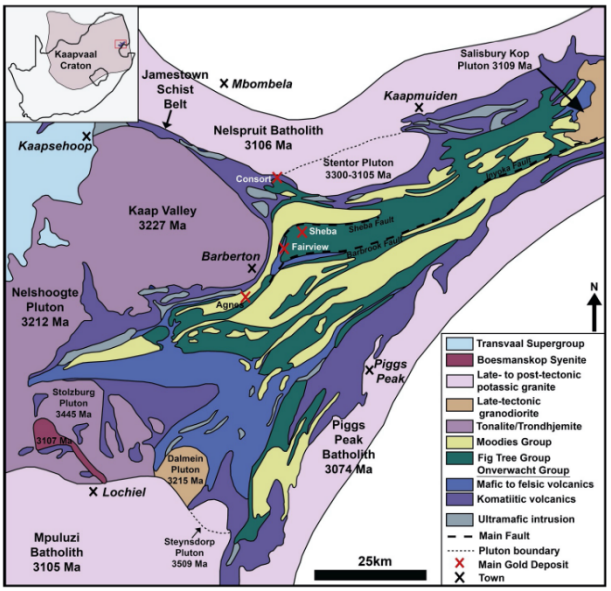

Figure 15: Barberton Greenstone Belt along with the position of economically significant gold mines. The Sheba-Fairview Complex is located within an arcuate corridor in the NW portion of the belt (map taken from Jones 2021, initially adapted from Anhaeusser, 2016). The ages of plutons surrounding the belt are after Robb (2006).

2 Methodology

2.1 Ore classification

Ore classification comprised of reflected/transmitted light microscopy, SEM and LA-ICP-MS, all of which were done at Stellenbosch University at the Central Analytical Facility (CAF). Over 20 thin-sections were available from previous studies for transmitted light

microscopy. Ten thick-sections were prepared for reflected light microscopy with five of these being used for subsequent SEM and LA-ICP-MS.

SEM data were collected using a MERLIN Zeiss with an Energy Dispersive X-ray Spectrometer (EDX) being used to determine major oxide weight percentages and element percentages on each mineral. The beam energy for EDS was set to 20 kV, with a current between 19 and 21 µA, and a set working distance of 8 mm. Standards were set according to the elements expected to be seen in the different sulphide and carbonate phases.

LA-ICP-MS spot analyses were used to decipher whether there were any significant chemical differences between the two pyrite generations. R software was used to generate box plots comparing the trace element distribution between the two different pyrite generations. Line scan data were then collected to augment the spot analyses as line scan data is more effective in detecting uneven trace element distributions within solid phases (Sanborn & Kelmer 2003). The following elements were tested for during LA-ICP-MS analysis: ^{34}S, ^{47}Ti, ^{51}V, ^{53}Cr, ^{55}Mn, ^{57}Fe, ^{59}Co, ^{60}Ni, ^{63}Cu, ^{66}Zn, ^{75}As, ^{77}Se, ^{95}Mo, ^{107}Ag, ^{111}Cd, ^{115}In, ^{118}Sn, ^{121}Sb, ^{125}Te, ^{182}W, ^{197}Au, ^{202}Hg, ^{205}Tl, ^{208}Pb and ^{209}Bi. A spot size of 20 µm was used with laser energy and frequency at 3 J/cm^2 and 6 Hz respectively.

2.2 Raman spectroscopy

Raman spectroscopy data were collected from graphite samples using a HORIBA Scientific LabRAM HR Evolution confocal Raman Spectrometer at the University of Alberta, Canada. This spectrometer is equipped with a 532 nm wide laser and an Olympus MPLN 10 x objective. Laser power was set to 100 % (i.e., no neutral density filter) with the confocal hole size being 200 µm. Acquisition time was set to 40 seconds with three accumulations run per sample. The spectral range over which data was collected was 1000-1800 cm^{-1}. Raman spectra were fitted using the open-source software by Fityk (Wojdyr 2010).

2.3 Carbon isotopes

Carbon isotope analyses were conducted at the University of Alberta, Canada, on three mineral separates: graphite, carbonates and black quartz (which contains very fine-grained graphite). Slightly different protocols were used depending on the mineral separate. The generated CO_2 gas is cryogenically purified and collected into a glass sampler and sent to a Thermo Scientific Delta V Plus isotope-ratio mass spectrometer for isotope measurements at a dual-inlet mode. Isotopic compositions were reported as δ notation relative to the Vienna PeeDee Belemnite standard for $\delta^{13}C$ and the Vienna Standard Mean Ocean Water for $\delta^{18}O$. The analytical uncertainty of 2σ (less than 0.2 ‰) is based on repeated analyses of international reference materials and laboratory internal standards.

3 Fairview gold ore and fluid evolution

The samples analysed during this study originate from the Main Reef Complex at the Fairview mine. Economically significant shear zones show a quartz-carbonate sulphide mineralogy (Gloyn-Jones & Kisters 2019). The major sulphides are pyrite and arsenopyrite, with pyrite having the strongest association with native gold. Two generations of pyrite were identified. The first generation of pyrite (Py_1) occurs as small (< 1 mm), independent, anhedral to subhedral grains or as cores to pyrite generation two (Py_2). Py_2 grains are large (up to 5 mm), euhedral, and occur as independent grains or as rims to Py_1. The LA-ICP-MS analyses served to differentiate between the two generations of pyrite, and thereby document how the ore fluid evolved over time. From the results of the spot analyses (Figure 2), the two generations of pyrite appear fairly similar in terms of their trace element composition. However, grain mapping of large, zoned, pyrite allows for easy discernment between the two pyrite generations (Figure 3). The trace element maps suggest that Py_1 formed from a single fluid flow event, whereas Py_2 formed during a later event which involved multiple pulses of fluids with slight variations in chemistry. The Py_2, which is most closely associated with free gold, shows significant elevations in nickel and arsenic.

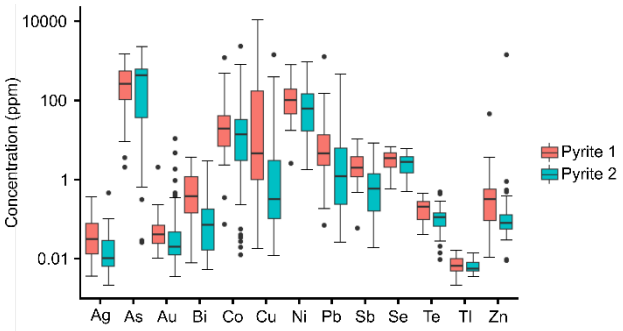

Figure 16: Box and whisker plot comparing the trace element composition of the two different pyrite generations (n = 76).

Changes in carbonate chemistry within shear zones at the Fairview mine document the changes in Ca/Fe/Mg concentrations of different fluids. Changes in carbonate speciation in shear zones is significant as it can influence desulphidation reactions (Goldfarb et al. 2005), which is a primary mechanism by which gold is deposited. When wall rocks contain initial molar ratios of Fe / (Fe + Mg) ≤ 0.5, nearly all Fe is incorporated into the magnesite-siderite series of carbonates. This prevents pyritization of Fe-bearing phases and thereby hinders gold deposition which takes place via desulphidation reactions.

At Fairview, carbonate species were used to track changes in fluid composition in terms of its major and minor elements whereas changes in trace element

compositions of ore fluids were traced using grain maps of zoned pyrite.

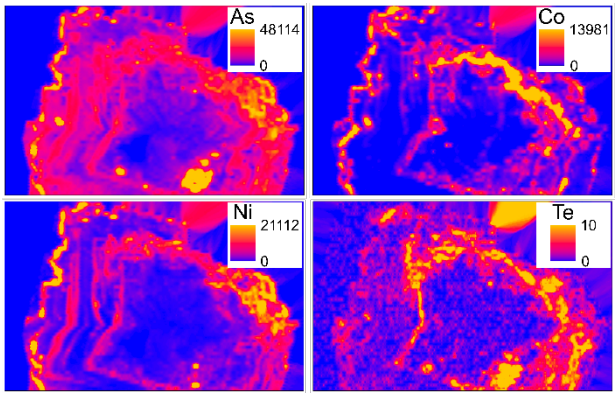

Figure 17: Trace element maps of a zoned pyrite grain illustrating the variability in trace element chemistry between Py_1 in the core and Py_2 towards the rim (concentrations are in parts per thousand).

4 Characterisation of graphite and C isotopes

Seven graphite samples from various levels of the Fairview mine were analysed using Raman spectroscopy. All samples exhibited a strong graphite peak (G band) and disorder peak (D band). The graphite peak wavelength ranged between 1560-1585 cm^{-1} whilst the disorder peak wavelength ranged between 1335-1350 cm^{-1}. Based on the ratio of the peak intensities of the D and G bands, the graphite is interpreted to have a high degree of structural disorder. Tuinstra & Koenig (1970) pointed out the relationship between the ratio of peak intensities (D and G bands) and graphite crystal size. Graphite from Fairview is calculated to have an average crystal size of 16.34 nm. Geothermometry calculations based off the Raman spectra show that graphite experienced an average maximum temperature of 403 ºC (n = 21), which is slightly higher than the average temperature of 320 ºC experienced at the greenstone belt scale (Cloete 1999).

Carbon isotopes were measured primarily to gain insights into the source of the fluids, which formed Fairview's gold deposits. The average value for graphite found in shear zones is -21,7 ‰ and is similar to that of Fig Tree shales which have an average of -23,7 ‰ (Figure 4). This implies that the graphitic carbon found in shear zones may have a genetic relationship with the carbon in the Fig Tree shales, although an externally derived fluid with similar carbon isotopes signatures cannot be discounted. The C isotope signatures of the different carbonate minerals mostly fall within the expected range for carbonate carbon. Although most of the values lean to the boundary between sedimentary carbonate and the mantle range, they can be explained by metamorphic effect rather than involvement of mantle-derived fluids. These carbonates likely derived their carbon from decarbonation/dissolution reactions of pre-existing carbonate-bearing country rocks such as those studied by Toulkeridis et al. (1998). At this stage, the C isotope data on quartz appears to show a mixed signature and is, therefore, not considered a robust interpretation regarding fluid source, and more work is being done to understand the reason for this signature. Carbon isotope compositions of both graphite and carbonates seemingly argue in favour of the ore fluids being sourced from within the greenstone belt. Black shales of the Fig Tree group appear as a likely candidate for the source of auriferous fluids based on the similar isotope values of carbonaceous material in Fig Tree shales and graphite from shear zones. However, black shales from outside the greenstone belt may have similar C isotope signatures (Jaguin et al. 2014) and one can, therefore, not rule out the possibility that fluids were derived from an external subducting slab, outside the BGB.

As this research represents the first instance of carbon isotopes being run on individual carbonate minerals in Barberton, it is useful to look more closely at their C isotope signatures and assess whether they can serve as a tracer for fluid flow events. Slight variations can be seen in the different carbonate species (Fig.4); however, all fall within a fairly narrow range of 2.8 ‰. The minor variations in $\delta^{13}C$ values of different carbonates can be due to: 1) changes in oxygen fugacity and pH of the fluid, 2) variability of country rock, and 3) degree of fluid-rock interaction (Ohmoto, 1972; Sharp, 2007). Changes in fO_2 and pH can alter the $\delta^{13}C$ values of carbon species within the fluids which will impact the $\delta^{13}C$ composition of the carbonates formed from these fluids. Given that the individual carbonates examined in this study are frequently co-occurring, and that no major differences in isotope composition are seen between what are interpreted as temporally separate carbonates, it does not appear viable to utilize C isotopes as a tracer for different fluid pulses. More detailed investigations into carbonate growth textures may reopen the possibility of using C isotopes to trace fluid flow events.

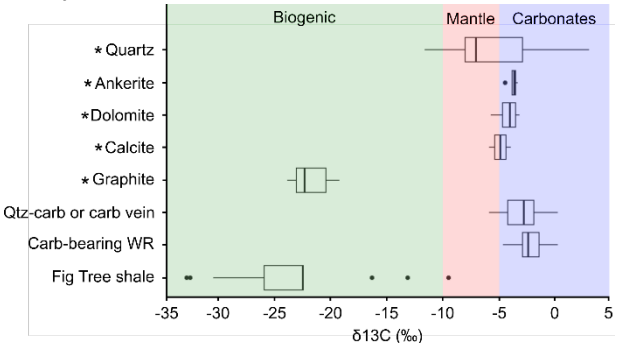

Figure 18: Compilation of carbon isotope work done in the BGB, those box plots marked with an asterisk indicates data which emulated from this study (existing data from Hayes et al. 1983; de Ronde et al. 1992; Strauss & Moore, 1992; de Ronde & Ebbesen 1996; Grassineau et al. 2006). The green, pink and blue background colours correspond to the different carbon sources of biogenic, mantle and carbonates respectively (ranges after Luque et al. 2012).

5 Conclusions

Through use of SEM and LA-ICP-MS it is possible to detect the changes in major, minor and trace compositions of the ore fluid and, thereby, understand how the fluid evolved over time. Nanocrystalline graphite within shear zones that is closely associated with Au-bearing sulphides has a high degree of structural disorder, with Raman geothermometry suggesting that it may have experienced temperatures of up to 400 ºC. Carbon isotope analyses suggest that the ore-forming fluids may have been derived from Fig Tree Group sedimentary rocks from within the greenstone belt. This research shows that carbon has an important role to play in forming high-grade gold deposits in greenstone belts. It is recommended that further investigations be made into the degree of interaction between nanocrystalline graphite and gold/sulphides.

Acknowledgements

The authors' gratitude is extended towards the helpful staff at both Stellenbosch University and the University of Alberta who aided in various analyses. Thank you to the DSI-NRF CIMERA for their generous funding of this research project.

References

Agangi A, Hofmann A, Eickmann B, Marine-Carbonne J (2019) Mesoarchaean Gold Mineralisation in the Barberton Greenstone Belt: A Review. (eds) The Archaean Geology of the Kaapvaal Craton, Southern Africa; Regional Geology Reviews. pp 171-184

Agricola G (1556) De re metallica (Hoover HC, Hoover LH trans., 1950), Dover Publications, New York.

Altigani MAH, Merkle RKW, Dixon RD (2016) Geochemical evidence of episodes of gold mineralisation in the Barberton Greenstone Belt, South Africa. Ore Geology Reviews. 75:186-205

Anhaeusser CR (2016) The Barberton-Makhonjwa mountainland - an ancient landscape yielding clues to the origin of the Earth and life. In: Anhaeusser CR, Viljoen MJ, Viljoen RP (ed) Africa's Top Geological Sites; Struik Nature, Cape Town. pp. 61-66

Brandl G, Cloete M, Anhaeusser CR (2006) Archaean Greenstone Belts. In: Johnson MR, Anhaeusser CR, Thomas RJ (ed) The Geology of South Africa; Geological Society of South Africa., Council for Geoscience, Pretoria. pp 9-56

Cloete M (1999) Aspects of volcanism and metamorphism of the Onverwacht Group lavas in the south-western portion of the Barberton greenstone belt. Geological Survey of South Africa Memoir. 84. 232.

de Ronde CEJ, Ebbesen TW (1996) 3.2 b.y. of organic compound formation near sea-floor hot springs. Geology. 24.9:791-794

de Ronde CEJ, Spooner ETC, de Wit MJ, Bray CJ (1992) Shear Zone-Related, Au Quartz Vein Deposits in the Barberton Greenstone Belt, South Africa: Field and Petrographic Characteristics, Fluid Properties, and Light Stable Isotope Geochemistry. Economic Geology. 87:366-402

Gaboury D (2021) The neglected Involvement of Organic Matter in Forming Large and Rich Hydrothermal Orogenic Gold Deposits. Geosciences. 11.344:1-13

Gloyn-Jones J, Kisters A (2018) Regional folding, low-angle thrusting and permeability networks: Structural controls of gold mineralization in the Hope reef at Fairview Mine, Barberton greenstone belt, South Africa. Ore Geology Reviews. pp 1-56

Gloyn-Jones J, Kisters A (2019) Ore-shoot formation in the Main Reef Complex of the Fairview Mine – multiphase gold mineralization during regional folding, Barberton Greenstone Belt, South Africa. Miner Deposita. 54.8:1157-1178

Goldfarb RJ, Baker T, Dubé B, Groves DI, Hart CJR, Gosselin P (2005) Distribution, Character, and Genesis of Gold Deposits in Metamorphic Terranes. In: Hedenquist JW, Thompson JFH, Goldfarb RJ, Richards JP (ed) Economic Geology 100th Anniversary Volume (1905-2005). pp 407-450

Grassineau NV, Abell P, Appel PWU, Lowry D, Nisbet EG (2006) Early life signatures in sulfur and carbon isotopes from Isua, Barberton, Wabigoon (Steep Rock), and Belingwe Greenstone Belts (3.8 to 2.7 Ga). Geological Society of America Memoirs. 198:33-52

Hayes JM, Kaplan IR, Wedeking KW (1983) Precambrian organic geochemistry: Preservation of the record. In: Schopf JW (ed) Earth's Earliest Biosphere: Its Origin and Evolution; Princeton University Press, New Jersey. pp 93-134

Jaguin J, Boulvais P, Boiron M-C, Poujol M, Gapais D, Ruffet G, Briant N (2014) Stable isotopes (O, C) and fluid inclusion study of quartz-carbonate veins from the antimony line, Murchison Greenstone Belt. American Journal of Science. 314:1140-1170

Jones C & Kisters A (2022) Regional and local controls of hydrothermal fluid flow and gold mineralization in the Sheba and Fairview mines, Barberton Greenstone Belt, South Africa. Ore Geology Reviews. 104805:1-20

Luque FJ, Crespo-Feo E, Barrenechea JF, Ortega L (2012) Carbon isotopes of graphite: Implications on fluid history. Geoscience Frontiers. 3.2:197-207

Ohmoto H (1972) Systematics of Sulfur and Carbon Isotopes in Hydrothermal Ore Deposits. Economic Geology. 67.5:551-578

Pintos Cerda LP, Jones C & Kisters A (2020) Multi-stage alteration, rheological switches and high-grade gold mineralization at Sheba Mine, Barberton Greenstone Belt, South Africa. Ore Geology Reviews. pp 1-73

Robb LJ, Brandl G, Anhaeusser CR, Poujol M (2006) Archaean granitoid intrusions. In: Johnson MR, Anhaeusser CR, Thomas RJ (ed) The Geology of South Africa; Geological Society of South Africa. Council for Geoscience, Pretoria. pp 57-94

Sanborn M, Telmer K (2003) The spatial resolution of LA-ICP-MS line scans across heterogeneous materials such as fish otoliths and zoned minerals. Journal of Analytical Atomic Spectrometry. 10:1231-1237

Sharp S (2007) Principles of Stable Isotope Geochemistry (2nd edition). Chapter 12: Metamorphic Petrology. Pearson, Michigan.

Strauss H, Moore TB (1992) Abundances and Isotopic Compositions of Carbon and Sulfur Species in Whole Rock and Kerogen Samples. In: Schopf JW, Klein C (ed) The Proterozoic Biosphere: A Multidisciplinary Study; Cambridge University Press. pp 709-797

Toulkeridis T, Goldstein SL, Clauer N, Kroner A, Todt W, Schdlowski M (1998) Sm–Nd, Rb–Sr and Pb–Pb dating of silicic carbonates from the early Archaean Barberton Greenstone Belt, South Africa Evidence for post-depositional isotopic resetting at low temperature. Precambrian Research. 92:129-144

Tuinstra F, Koenig JL (1970) Raman Spectrum of Graphite. Journal of Chemical Physics. 53:1126-1130

Wojdyr M (2010) Fityk: a general-purpose peak fitting program. Journal of Applied Crystallography. 43:1126-1128

The Control of Sulfur Fugacity on Metal Melts and Gold Mineralization: A Case Study of the Jinjingzui Au Deposit

Xinhao Li[1,2,3], Guiqing Xie[1,2], Sarah A. Gleeson[3,4], Jingwen Mao[1,2]
[1]*School of Earth Sciences and Resources, China University of Geosciences, Beijing, China*
[2]*MNR Key Laboratory for Exploration Theory & Technology of Critical Mineral Resources, China University of Geosciences, Beijing, China*
[3]*GFZ German Research Centre for Geosciences, Potsdam, Germany*
[4]*Institute of Geological Sciences, Freie Universität Berlin, Berlin, Germany*

Abstract. Bismuth and Te melts are thought to collect Au from hydrothermal fluids based on previous experimental and modelling studies. This study documents an early phase of Bi-Te-Au formed at low sulfidation states (pyrrhotite stability) and a Te-Au association under higher sulfidation states (pyrite stability) in the Jinjingzui Au deposit. Here, we present EPMA data on bismuth tellurides and LA-ICP-MS data of sulfide minerals. We propose that low sulfidation states can keep Bi in the melt phase by preventing the formation of bismuth sulfide (solid), whereas the stability of the Te-melts may not be affected by sulfidation.

1 Introduction

Metal melts have long been inferred to contribute to mineralization because of the mosaic and droplet derived textures of certain minerals, some of which intimately coexist with gold. Bismuth-Te(-Se) minerals widely occur in Au-rich systems of different origins (Ciobanu and Cook 2005; Li et al 2023). The capability of Bi to form a melt phase and efficiently collect Au in hydrothermal conditions without Au saturation has been proven by experimental and modelling studies (Douglas et al. 2000; Tooth et al. 2008). This model has been applied to Au mineralization in different systems; most of the studies emphasize the low oxidation state as a major factor in Bi melt generation. Recent petrographic and microthermometric studies in vein-type deposit indicate that metal melts collecting gold mechanism can also be applied to Te-rich systems (Jian et al. 2021).

The Jinjingzui Au deposit has early Bi-Te-Au associations and late Te-Au associations. The early Bi-Te-Au association occurs in quartz with pyrrhotite mineral inclusions indicating low sulfidation states. The Te-Au association occurs with late pyrite indicating higher sulfidation states. With in-situ major and minor element contents of bismuth tellurides, and trace element concentrations of sulfide minerals from the deposit, this study explores the role of sulfidation state upon the Bi-Te melts stability and their Au collecting mechanism.

2 Deposit geology and Au occurrence

Located in Edong ore cluster, Middle–Lower Yangtze River metallogenic belt, China, the Jinjingzui Au deposit contains 7.6 metric tons of Au at an estimated 7.4 g/t average grade with no economic Cu (Li et al. 2007). Despite the skarn alteration in the contact zones between the diorite intrusion and the limestone host rock, Au mineralization occurs in veins inside the intrusion. Field studies indicate a sequence of early thin quartz ± K-spar ± pyrite I veins, intermediate thick quartz + pyrite ± chalcopyrite ± bornite II veins and late calcite ± pyrite III veins (Figure 1). The III veins are barren. Some I and II veins can be divided into a quartz dominated domain and a sulfide dominated domain (Figure 2a). Sulfide minerals are interstitial between quartz crystals, indicating they formed later than the quartz (Figure 2b c d).

Figure 1. Field pictures showing vein sequence of the Jinjingzui deposit

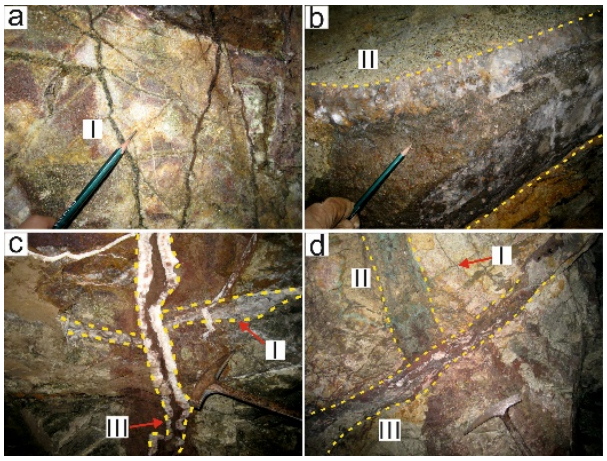

Microscopic observations indicate that abundant Bi-Te-Au associations (bismuth tellurides coexisting with native Au) occur in the quartz dominated domains of the I and II veins (Figure 3a b); the quartz crystals contain small pyrrhotite inclusions (Figure 3c). The sulfide dominated domains contain minor Te-Au association (native Au + calaverite; Figure 3d).

3 Methodology

The compositions of native Au, Bi- and Te- bearing minerals were determined using a JOEL JXA–8230 electron microprobe at the Key Laboratory of Metallogeny and Mineral Assessment, Institute of Mineral Resources, Chinese Academy of

Geological Sciences (CAGS), Beijing. The operating conditions are: accelerating voltage of 20 kV, beam current of 20 nA, and beam diameter of 1 μm. The counting time was 10 s on the peak, and 5 s each on left–hand and right–hand background position for each element. ZAF corrections were made with proprietary JEOL software.

Figure 2. a The quartz dominated domain and sulfide dominated domain of II vein; **b, c, d** hand-specimen and photomicrographs showing sulfides infilling the interstitial spaces of quartz crystals. Cal-calcite; Py-pyrite; Qz-quartz.

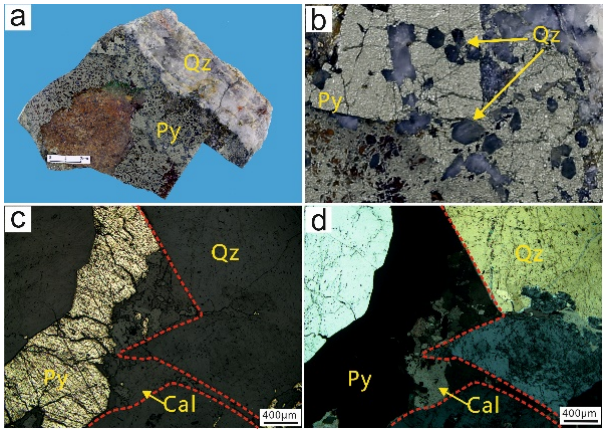

Trace element analysis of pyrite, chalcopyrite, bornite and pyrrhotite was carried out using LA-ICP-MS at the Beijing Createch Testing Technology Co., Ltd., Beijing, China, adopting a RESOlution 193 nm laser ablation system that consists of a COMPex Pro 102 ArF excimer laser and a Micro Las optical system. The chemical composition of the sulfides was corrected using the USGS MASS-1 sulfide standard value. The offline concentration calculation was carried out using the ICPMS Data Cal program.

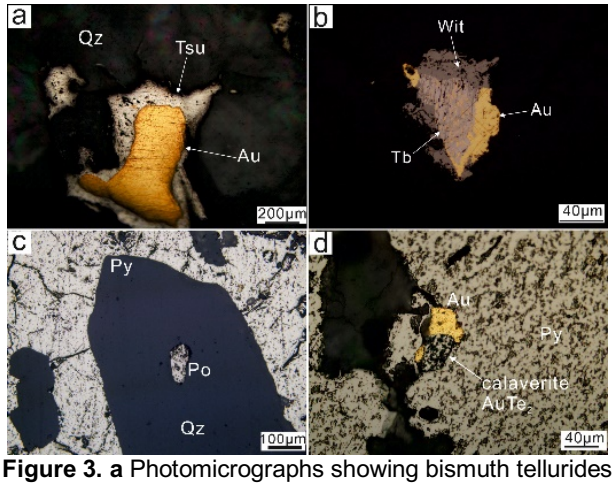

Figure 3. a Photomicrographs showing bismuth tellurides coexisting with native Au in quartz dominate domains; **b** Bi-Te-Au association is typically coated by later bismuth sulfides (wittichenite in this picture); **c** pyrrhotite inclusions occur in the early quartz crystals; **d** calaverite coexisting with native gold and pyrite occur in sulfide dominate domains. Au-native Au; Po-pyrrhotite; Py-pyrite; Qz-quartz; Tb-tellurobismuthite; Tsu-tsumoite; Wit-wittichenite (Cu_3BiS_3).

4 Results and interpretation

A ternary plot of bismuth telluride contents from I veins and II veins shows that the bismuth tellurides from II veins generally have higher Te and S contents (Figure 4). The Au concentrations are low in all sulfide minerals (Figure 5), including the As-rich pyrites in III veins, which means that native Au is the major form of Au mineralization in the deposit.

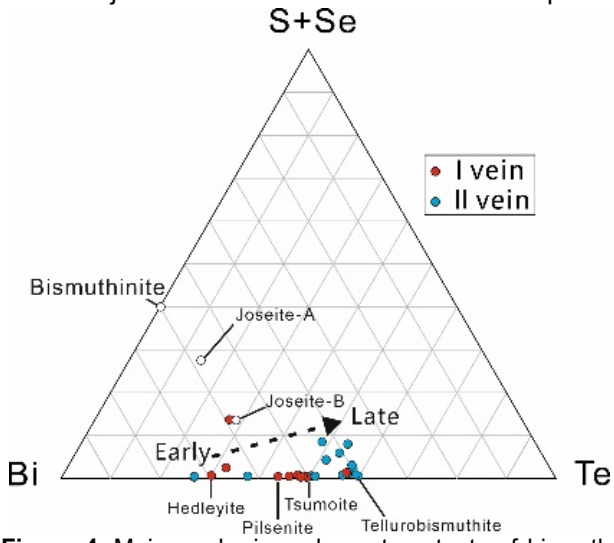

Figure 4. Major and minor element contents of bismuth tellurides showing that bismuth tellurides from the II veins are S- and Te- rich.

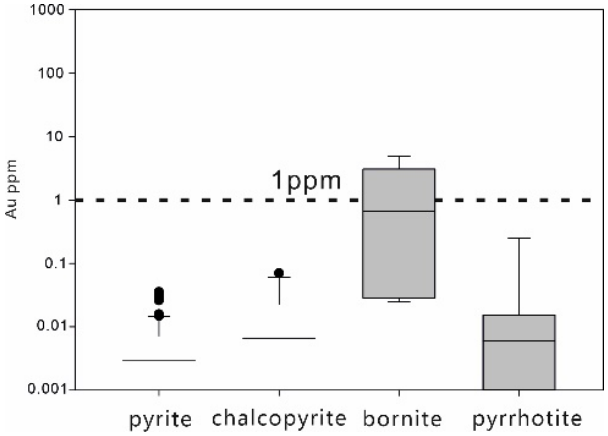

Figure 5. Trace element concentrations showing sulfide minerals generally do not contain Au in the Jinjingzui deposit.

The intimate coexistence of bismuth telluride and native Au in early stages can be explained by Bi-Te melts scavenging Au. The higher S contents of bismuth tellurides from the later II vein imply an increase in sulfidation state probably due to the declining temperature (Einaudi et al. 2003, Fig 4; Ciobanu et al. 2010). This higher sulfidation state stabilizes Bi sulfide and prevents the formation of Bi melts (Tooth et al. 2008, Fig 2b). Tellurium, however, does not react with sulfur (Snelling, 1912; Aravamudan et al. 1973), thus, it remains in the melt phase. This is supported by the late Te-Au association observed in the sulfide dominated stage. The early Au mineralization (in I and II veins) caused by Bi-Te melt collection may have depleted the Au in the hydrothermal fluid, therefore, no Au is

incorporated into the late As-rich pyrites from the late III veins.

5 Conclusions

The early Au mineralization at Jinjingzui is caused by the Bi-Te melts collecting Au under low sulfidation states. Later high sulfidation states result in Bi sulfide formation at the expense of the Bi-melts, yet Te-melts may still exist. Sulfidation state is an important parameter controlling the geochemical behaviour of Bi and Te in hydrothermal fluids, which can affect the mechanism of efficient Au mineralization.

Acknowledgements

We thank Xiaodan Chen and Zhenyu Chen for their assistance in the electron microprobe analysis. This study is financially supported by the National Science Foundation of China (41925011 and 92162217).

References

Aravamudan G, Sethuraman PR, Udupa MR (1973) Complexation of tellurium(II) with thioglycolic acid and reactivity patterns of the system. J inorg nucl Chem 35:3291–3298

Ciobanu CL, Birch WD, Cook NJ, Pring A, Grundler PV (2010) Petrogenetic significance of Au-Bi-Te-S associations: The example of Maldon, Central Victorian gold province, Australia. Lithos 116:1–17

Ciobanu CL, Cook NJ, Pring A (2005) Bismuth tellurides as gold scavengers. In: Mao JW, Bierlein FP (eds) Mineral deposit research: meeting the global challenge. Springer, Berlin, pp 1383–1386

Douglas N, Mavrogenes J, Hack A, England R (2000) The liquid bismuth collector model: An alternative gold deposition mechanism. 15th Austral Geol Conv Abstr 59:135

Einaudi MT, Hedenquist JW, Inan EE (2003) Sulfidation state of fluids in active and extinct hydrothermal systems: transitions from porphyry to epithermal environments. In: Simmons SF, Graham I (eds), Volcanic, Geothermal, and Ore-Forming Fluids: Rulers and Witnesses of Processes within the Earth. Soc Econ Geol Spec Publ 10:285–313

Jian W, Mao JW, Lehmann B, Cook NJ, Xie GQ, Liu P, Duan C, Alles J, Niu ZJ (2021) Au-Ag-Te-rich melt inclusions in hydrothermal gold-quartz veins, Xiaoqinling lode gold district, central China. Econ Geol 116:1239–1248

Li J, Jiang ZG, Chen MS, Yuan HW (2007) Detailed Investigation Report of Gold Mine in Jinjingzui Mining Area, Daye City, Hubei Province. 1–120 (In Chinese)

Li XH, Xie GQ, Gleeson SA, Mao JW, Ye ZC, Jin YL (2023) Palladium, platinum, selenium and tellurium enrichment in the Jiguanzui-Taohuazui Cu-Au deposit, Edong ore district: Distribution and comparison with Cu-Mo deposits. Ore Geol Rev 154:105335

Snelling WO (1912) Sulfide of tellurium. J Am Chem Soc 34:802–811

Tooth B, Brugger J, Ciobanu CL, Liu WH (2008) Modeling of gold scavenging by bismuth melts coexisting with hydrothermal fluids. Geol 36:815–818

Metallogenic Fingerprinting of Gold Endowment in Magmatic Hydrothermal Deposits

Carolina N. Mafra[1], Hoi Ian Kong[1], Robert R. Loucks[1], Marco Fiorentini[1]
[1]The University of Western Australia, Perth, Australia

Abstract. The variable gold endowment in magmatic-hydrothermal deposits has been ascribed to the nature of the underlying lithospheric mantle, geodynamic settings, K_2O/SiO_2 in parental melts, and depth of hydrothermal fluid exsolution. However, the ultimate parameters affecting gold magmatic fertility are still largely unconstrained. The distinction in chemical composition of primitive melts temporally and spatially associated with gold-fertile arc segments and unmineralised arc segments constrain differences in sources of gold-rich and gold-poor mantle-derived melts. Furthermore, it suggests that gold fertility is a primary feature acquired at the mantle source. Gold-rich mantle-derived melts are consistently enriched in Nb, Ta, and Zr— evidence for lithospheric mantle metasomatism by low-degree partial melts from deeper asthenospheric mantle. In this framework, magmatic-tectonic triggers capable of selectively melting metasomatic enriched zones of the lithospheric mantle would play a first-order genetic control on gold fertility. Calc-alkalic and shoshonitic magmas that exsolved the hydrothermal fluid that formed gold-rich magmatic-hydrothermal deposits display distinct lithophile trace element compositions, that is a proxy of the degree to which the lithospheric mantle source was previously refertilised. We have defined a series of trace element ratios reflecting the participation of an enriched source in the generation of fertile magmas that are effective in discriminating them from ordinary, barren systems.

1 Introduction

Magmatic processes control the metallogenic potential of magmatic-hydrothermal Cu and Au districts. Magmatic fertility represents the potential of a melt to exsolve hydrothermal fluids capable of forming ore deposits. It is controlled by source and magmatic differentiation processes. The former corresponds to primary features favouring the generation of metallogenic camps, whereas the latter modifies the physiochemical properties of the intruding magmas, affecting their potential to form distinct ore deposits.

It is well recognised that copper fertility is an emerging property of the melt, developed under compressive stress by the intermittent replenishment of magma chambers at Moho depths (Loucks 2014; 2021). In such conditions, amphibole is an early phase to crystallise, whereas plagioclase crystallisation is delayed. Consequently, ore-forming intrusions have higher Sr/Y ratios compared to Cu-infertile intrusions.

Conversely, the origin of gold fertility is poorly understood, and formulating trustworthy petrochemical indicators for gold-rich deposits is still needed. Comparing the lithophile element chemical composition of gold-ore-forming magmas with barren reference suites is expected to lead to the recognition of trace element ratios that may be interpreted to represent petrogenetic processes responsible for the observed variable gold endowment in magmatic-hydrothermal deposits. Additionally, it should shed light on tectono-magmatic settings favourable for gold mineralisation. This research shows that moderate-to-high-potassium calc-alkalic magmas that exsolved hydrothermal fluid that formed gold-rich magmatic-hydrothermal deposits have distinct incompatible lithophile element compositions. Trace element ratios representing incipient melting of an enriched source can sort gold-fertile from gold-infertile intrusions on a province scale.

1.1 First-order controls on gold fertility in magmatic-related gold deposits

Magmatic-related gold-rich mineral systems form a wide range of deposit types globally (Sillitoe 2020). It has been proposed that a key ingredient common to all these mineral systems is that gold fertility is controlled by the nature of the underlying metasomatised lithospheric mantle (Hronsky et al. 2012; Loucks 2012; Tassara et al. 2017, 2018; Saunders et al. 2018; Holwell et al. 2019; Rielli et al. 2022; Wang et al. 2022). Contrarily, gold-rich magmatic-hydrothermal systems have also been attributed to magmatic fractionation processes (Murakami et al. 2010; Chiaradia 2020, 2021, 2022; Park et al. 2021; Hao et al. 2022), post-subduction and extensional settings and alkaline magmatism. However, although magmatic differentiation may favour gold enrichment in magmatic-hydrothermal systems, these aspects seem to exert a second-order influence on gold metallogenic fertility (Rielli et al. 2022).

Primitive melts in gold-bearing arc segments have distinctive incompatible element compositions compared to unmineralised arc segments (Figure 1) (Loucks and Ballard 2003; Loucks 2012; Hronsky et al. 2012). Interestingly, primitive melts spatially and temporally associated with gold deposits are consistently enriched in high-field-strength elements (HFSEs: Nb, Ta, Zr, etc.) compared to primitive basalts unrelated to mineralisation (Arima and Kerrich 1988; Loucks 2012; Saunders et al. 2018). The association between Au enrichment simultaneously with Nb indicates participation of an enriched source. Niobium is the most incompatible of the HFSEs in mantle minerals and metamorphic fluids, and its concentration in the mantle source is very sensitive to melt addition and extraction. Nevertheless, the fact that Nb, Ta, and Zr have negligible solubilities in slab-derived hydrothermal fluids (Ayres 1998; Keppler 2017; Rustioni et al.

2019) precludes aqueous fluids as the agents of relevant refertilisation, favouring low degree partial melts of underlying mantle as the fertilising agent.

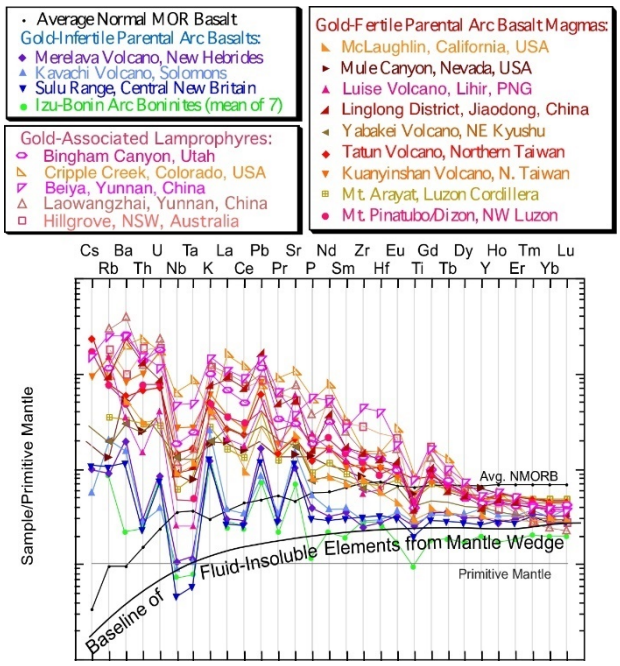

Figure 1. Incompatible lithophile trace element series, ordered by melt/restite partition coefficients, comparing primitive basalts from unmineralised arc segments with basalts and lamprophyres (6 to 12 wt.% MgO, Mg# > 60) that are spatially and temporally associated with major gold districts of late Neogene-Quaternary age. The elements are normalised to abundances in primordial mantle (McDonough and Sun 1995). Modified from (Loucks 2012; Hronsky et al. 2012).

Therefore, gold fertility seems to be a multi-stage petrogenetic process. In this framework, in a first stage, a geodynamic setting conducive to fertilisation of the lithospheric mantle is necessary. Accordingly, magmatic-tectonic triggers capable of selectively melting these metasomatic enriched domains are required in order to form any gold mineralised camp in the mid-to-upper crust.

2 Methodology

In order to have a meaningful perspective on petrochemical processes that control gold endowment in magmatic-hydrothermal deposits, it is required to acquire and investigate a representative sample set with a diverse compositional range as well as broad coverage of geodynamic settings. The most efficient approach to accomplish the extensive amount of data required to fully understand the origin of gold metallogenic fertility is compilation of existing analytical data from literature.

This work relies primarily on geochemical data from the north and south American Cordillera, the western Tethyan Orogenic belt, and the western Pacific Rim compiled into an extensive database. The compiled data was combined with new data from the Western USA. Figure 2 summarises sample localities covered by this project.

Magmatic rocks associated with magmatic-hydrothermal deposits are inevitably affected by post-magmatic processes. Consequently, petrographic and chemical filters were applied to consider only magmatic features in the whole rock.

Only samples described to best represent the magma composition that exsolved the mineralising hydrothermal fluids were considered. The compilation did not include passively mineralised rocks, extrusive rocks, nor crystal cumulates to a noticeable degree (whole-rock analyses having Al_2O_3 > 20 wt. % or Eu/Eu* > 1.3). All the analyses from altered or weathered samples, yielding a total volatile content (LOI) greater than 3.5 wt. %, analytical totals outside the 97.5 – 101.5 wt.% range (volatile-free basis), Na_2O and CaO content plotting outside the magmatic range for continental arc magmas, or samples containing altered plagioclase and amphibole grains were eliminated.

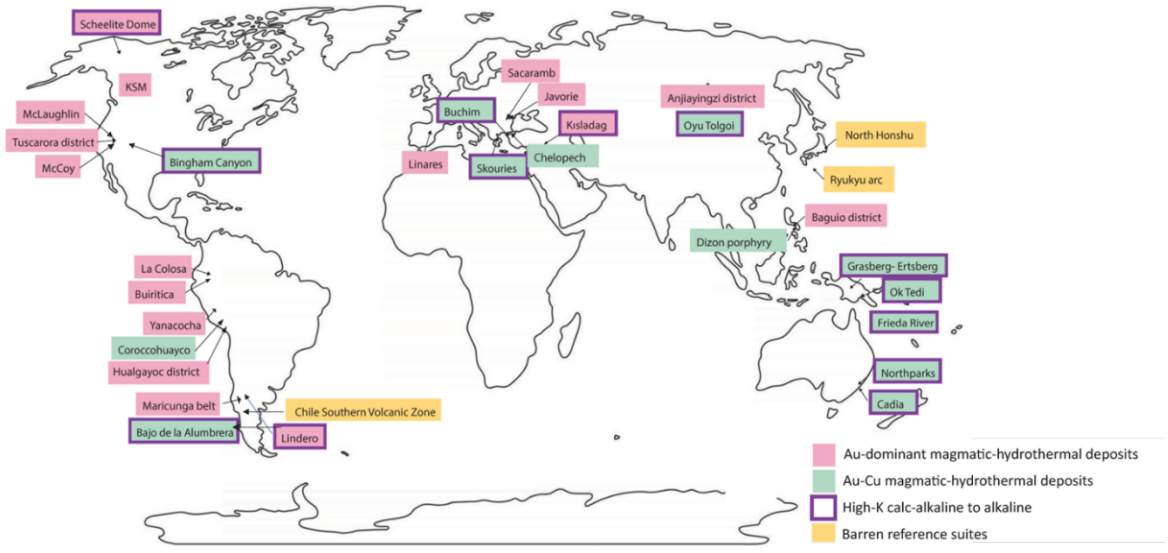

Figure 19. Locations of the samples considered in this study. Least-altered samples of ore-forming intrusions parental to major Au and Cu-Au deposits of Phanerozoic age worldwide are compared with barren reference suites from unmineralised arc segments and time intervals.

4 Results

The degree to which the lithospheric mantle has been refertilised can be represented by element ratios having highly incompatible elements in the numerator and mildly incompatible elements in the denominator. In Figure 3, an element from the left-hand side of the spidergram (Figure 1) is divided by an element on the right side to represent its general slope. These trace element ratios efficiently sort gold-fertile from gold-infertile intrusions. Ratios containing Nb in the numerator are particularly efficient in sorting gold-fertile from gold-infertile intrusions.

5 Discussion

Au-rich magmatic-hydrothermal deposits have distinct chemical characteristics compared to magmas from unmineralised arc segments and time intervals. These distinctions can be recognised in primitive mafic rocks contemporaneous to ore-forming intrusions (Figure 1) and in the ore-forming intrusions themselves (Figure 3). The fact that gold-fertile magmas are compositionally distinct from gold-infertile magmas across the whole magmatic differentiation series (low- to high SiO_2) is strong evidence that Au fertility is a primary property acquired at the magma source and not an emergent property developed during atypical chemical evolution within the crust.

The plots in Figure 3 show that the chemical distinction characteristic of gold fertility is shared by ore-forming magmas that generated Au-dominant and Cu-Au deposits, meaning that they may share a similar enriched source, whereas magmas from barren arc segments plot in the bottom left part of the diagrams. The lower trace element ratios from ordinary arc magmas are consistent with their source being the depleted upper asthenospheric mantle.

These trace element ratios suggest that gold-ore-forming intrusions have consistently higher HFSEs, and other highly incompatible lithophile elements concentrations than barren arc magmas. Interestingly, Nb is the most incompatible of the wedge-controlled HFSEs and is a proxy for source enrichment by low degree partial melts. Thus, the results show that gold-fertile magmas are formed by incipient melting of a source that was previously enriched in these elements.

6 Conclusions

Plots of U/Hf vs. Nb/Lu, Nb/Yb vs. U/Y, and Nb/Y vs. Nb/Zr are efficient in sorting gold-ore-forming from gold-infertile intrusions at convergent margins and post-subduction settings throughout the Phanerozoic. These plots aid in screening terrains and geodynamic settings favourable for hosting gold-rich magmatic-hydrothermal deposits. Using Nb as a proxy for gold fertility in whole rock is advantageous because Nb is relatively resistant to post-magmatic alteration. The systematic enrichment of gold-fertile magmas in Nb also provides reliable indications about the origin of gold fertility.

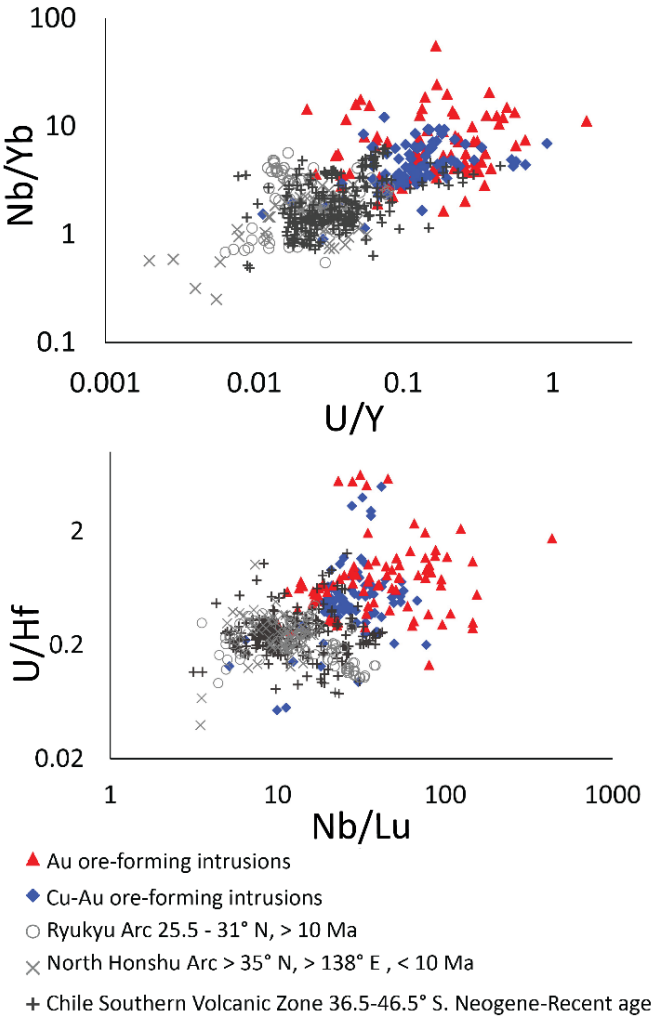

Figure 3. Trace element ratios having a highly incompatible element in the numerator and a mildly incompatible element in the denominator are efficient in sorting gold-fertile ore-forming intrusions from barren reference suites.

Acknowledgements

This study is part of the Australian Research Council-Industry Linkage Project 190100785 to develop exploration guides to magmatic-hydrothermal gold-rich ore deposits. The authors are grateful to the sponsoring companies and support institutions of the project who provided samples and data.

References

Ayers J (1998) Trace element modeling of aqueous fluid–peridotite interaction in the mantle wedge of subduction zones. Contrib Mineral and Petrol 132: 390-404.

Arima M, Kerrien R (1988) Jurassic kimberlites from Picton and Varty Lake, Ontario: Geochemical and stable isotopic characteristics. Contrib Mineral and Petrol 99: 385-391.

Chiaradia M (2020) Gold endowments of porphyry deposits controlled by precipitation efficiency. Nat Commun 11:1-10.
Chiaradia M (2022) Distinct magma evolution processes control the formation of porphyry Cu–Au deposits in thin and thick arcs. Earth Planet Sci Lett 599: 117864.
Hao H, Park J W, Campbell I H (2022) Role of magma differentiation depth in controlling the Au grade of giant porphyry deposits. Earth Planet Sci Lett 593: 117640.
Holwell D A, Fiorentini M, McDonald I et al (2019) A metasomatized lithospheric mantle control on the metallogenic signature of post-subduction magmatism. Nat Commun 10: 3511.
Hronsky J, Groves D I, Loucks R R, Begg G C (2012) A unified model for gold mineralisation in accretionary orogens and implications for regional-scale exploration targeting methods. Mineral Deposita 47: 339-358.
Keppler H (2017) Fluids and trace element transport in subduction zones. Am Mineral 102: 5-20.
Loucks R R, Ballard J R (2003) Report 2C: Petrochemical characteristics, petrogenesis and tectonic habits of gold-ore-forming arc magmas. Unpublished report for industry-sponsored research project: Predictive Guides to Copper and Gold Mineralization at Circum-Pacific Convergent Plate Margins. 69p
Loucks R R (2012) Chemical characteristics, geodynamic settings, and petrogenesis of gold ore-forming arc magmas. CET Quarterly News, issue 20.
Loucks R R (2014) Distinctive composition of copper-ore-forming arcmagmas. Aust J Earth Sci 61: 5-16.
Loucks R R (2021) Deep entrapment of buoyant magmas by orogenic tectonic stress: Its role in producing continental crust, adakites, and porphyry copper deposits. Earth-Sci Rev 220: 103744.
Murakami H, Seo J H, Heinrich C A (2010) The relation between Cu/Au ratio and formation depth of porphyry-style Cu–Au±Mo deposits. Mineral Deposita 45: 11-21.
Park J W, Campbell I H, Chiaradia M, Hao H, Lee C T (2021) Crustal magmatic controls on the formation of porphyry copper deposits. Nat Rev Earth Environ 2: 542-557.
Rielli A, Tomkins A G, Nebel O et al (2022) Incipient metal and sulfur extraction during melting of metasomatised mantle. Earth Planet Sci Lett 599: 117850.
Rustioni G, Audétat A, Keppler H (2019) Experimental evidence for fluid-induced melting in subduction zones. Geochem Perspect Lett 11: 49-54.
Saunders J E, Pearson N J, O'Reilly S Y, Griffin W L (2018) Gold in the mantle: A global assessment of abundance and redistribution processes. Lithos 322: 376-391.
Sillitoe R H (2020) Gold deposit types: An overview. Society of Econ Geol Spec Pub 23: 1–28.
Tassara S, González-Jiménez J M, Reich M et al (2017) Plume-subduction interaction forms large auriferous provinces. Nat Commun 8: 1-7.
Tassara S, González-Jiménez J M, Reich M et al (2018) Highly siderophile elements mobility in the subcontinental lithospheric mantle beneath southern Patagonia. Lithos 314: 579-596.
Wang X, Wang Z, Cheng H et al (2022). Gold endowment of the metasomatized lithospheric mantle for giant gold deposits: Insights from lamprophyre dykes. Geochi et Cosmochim Acta 316: 21-40.

Overprinted mineralizing gold events at the Paleoproterozoic Alta Floresta Mineral Province, Brazil

Maria José Mesquita[1]; Márcia Elisa Boscato Gomes[2]; Igor de Camargo Moreira[1]; Renata Augusta Sampaio Paes[1]; Hevelyn Eduarda da Silva Martins[1]; José Henrique Matos[1]; Alberto Ruggiero[1]; Guilherme Primo[1]; Diego Fernando Ducart[1]; João Gabriel da Silva[1]; Luciano Poggi[1]; André Massanobu Ueno Kunifoshita[1], Leonardo Zanchetta de Laurentis[1].
[1]Universidade Estadual de Campinas -Unicamp
[2]Universidade Federal do Rio Grande do Sul - UFRGS

Abstract. The Large gold provinces commonly show complicated mineralization histories, and the Paleoproterozoic Alta Floresta Mineral Province is a good example. The current models defined three deposit types, all connected to a single (1.88–1.75 Ga) magmatic-hydrothermal event. However, diverse geodynamic environments and older ages of Type-1 mineralization weaken the single metallogenic event. By scale-integrated analyses, we revise tectonic-geological context, structural-hydrothermal alterations, and chlorite-white mica geothermobarometer and propose the type-1 as granitoid-hosted orogenic gold deposits and the overprinting of the two events. The older orogenic-gold event developed orogenic gold deposits on WNW-trending shear zones in Peixoto de Azevedo inlier granitic-gneiss rocks. Phengite, biotite, chlorite-carbonate phyllonite (3.3-6.1kbar, 300º-420ºC) host fault-fill quartz veins (pyrite-chalcopyrite-magnetite-pyrrhotite-gold-Bi-Ag tellurides). Mg-rich chlorite-phengite is a footprint. A younger magmatic-hydrothermal event in Juruena magmatic-arc rocks produced Fe-rich chlorite-white mica alteration zones (0.6-4.6kbar, 120º-380ºC), and stockwork-breccia ore (pyrite-chalcopyrite-gold-Ti minerals-molybdenite-allanite) in porphyry-epithermal deposits. Phyllic alteration destroyed the phengite phyllonite foliation. The ages of two pyrite populations (1.98 and 1.84 Ga) in fault-fill veins and molybdenite in late fractures (1.81-1.78 Ga) or disseminated in ca. 1.79 Ga syenogranite porphyry distinguish two episodes. The AFMP multi-scale approach enlightens the two ore events overprint, allowing a new explorational potential.

1 Introduction

The world's largest hydrothermal deposits and metallogenic provinces have shown complex events superposition. Multistage mineralization events are mandatory to enrich most giant deposits (Meffre et al. 2012; Augustin and Gaboury 2018). Especially in Archean and Paleoproterozoic provinces, the literature describes many deposits with two or more stages of mineralization, magmatic activity, and multiple deformation histories (Fougerouse et al. 2017; Le Mignot et al. 2017; Augustin and Gaboury 2018).

However, in many mineral provinces, the possibility and implications of multiple mineralizing episodes are yet to be appropriately recognized, and the Alta Floresta Mineral Province (AFMP) is an example of this. AFMP is one of the promising Brazilian provinces for gold and copper.

The AFMP has an inlier nucleus, called Peixoto de Azevedo domain (PdA inlier), of the older Tapajos-Parima Geochronological Province (ca. 2.05 to 1.97 Ga volcanic arc-related rocks) surrounded and cut by younger rocks of the Rio Negro-Juruena Geochronological Province (arc-related or rifting-related environment of ca.1.82 to 1.52 Ma; Santos et al. 2001). Type-1 (Au ± Cu shear zone-hosted veins) are entirely hosted in the older granitic, granitic-gneiss, and metamafic rocks of the PdA inlier, while Type-2 (Au-Cu porphyry deposits) and Type-3 (Au ± Ag ± base metals epithermal deposits) are in the younger rocks of the Rio Negro-Juruena Province.

The current AFMP metallogenic models connect the three deposit types as part of a single magmatic-hydrothermal system restricted to a ca. 1.88–1.75 Ga event but at different crustal levels (Acevedo 2014; Assis et al. 2017; Rocha et al. 2020). They constrained it to the last stages of the Statherian magmatic arc evolution in the Rio Negro-Juruena Province. However, the mineralization ages are restricted to porphyry and epithermal deposits (Type-2 and Type-3), while two ages for Type-1 Paraiba deposit's pyrite yielded ca. 1.98 and 1.84 Ga (Paes de Barros 2007; Santos 2011 respectively), open for older mineralization events. Motivated by the tectonic position in older metamorphic rocks, the ore structural control in all scales, the older ages of Type-1 deposits' mineralization, and gaps between the reported productions, the present text presents some of the published AFMP data and new data to propose the type-1 deposits as granitoid-hosted orogenic gold and search for an alternative to a single-episode mineralization scenario.

2 Results

The results are based on mostly new data on structural control, hydrothermal alteration, and mineralization of the Paraiba, Peteca, and Serrinha do Guarantã deposits, and Luiz Bastos target of the Type-1, União do Norte District of Type-2, and Juruena District of Type-3. In addition, the overprinted characteristics of Type-2 and -3 of Peteca and Paraiba deposits and Luiz Bastos targets and reviewed chlorite and muscovite mineral chemistry from the literature are also presented. For complete results, consult Mesquita et al. (2022).

2.1 Type-1 deposits

The Type-1 deposits are entirely developed in the 2.04-1.98 Ga PdA inlier of the Tapajos-Parima Province, hosted within ductile shear zones.

Granitoids, quartz-feldspathic gneiss, mafic and ultramafic amphibolites are the primary host rocks, which show two foliations (S_n and S_{n+1}). S_n is a well-developed spaced foliation trends 00-050º and dips 70-90 º WNW (Fig. 1).

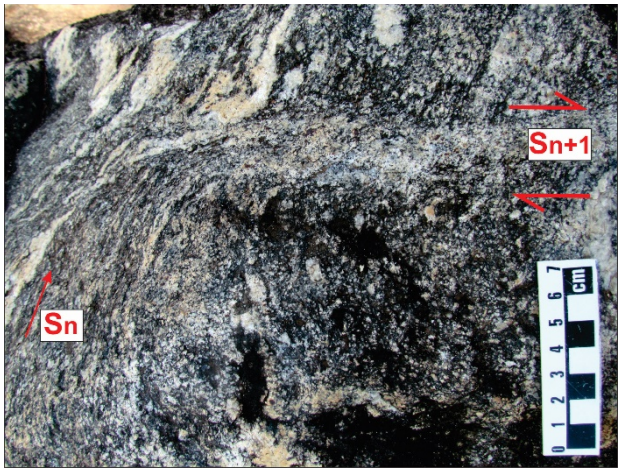

Figure 1. Type-1 deposit host rock: S_n (040/80SE) banding transposed by S_{n+1} (340/88SW) discrete shear band in 1.98 Ga (Miguel Jr. 2011) metagranodiorite.

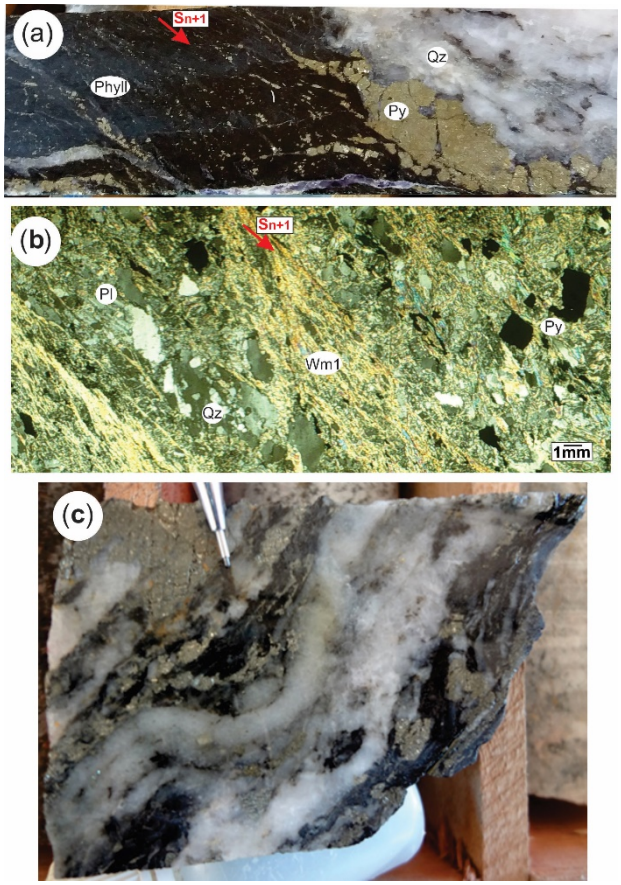

Figure 2. (a) phlogopite-carbonate phyllonite (Phyill) host the quartz vein (Qz) (Paraiba deposit); (b) phyllonite fabric with strong muscovite alteration defining S_{n+1} foliation. Plagioclase replaced by mica; (c) Anastomosed ore quartz vein with laminated texture (quartz bands alternate phlogopite-carbonate phyllonite bands (black) and sulphide films).

A WNW-trending first-order shear zone system develops a mylonitic S_{n+1}, which deflects S_n (Fig. 1). The high-strain zones are composed of phyllonite hosting the quartz veins (Fig. 2a). In the phyllonite, S_{n+1} is a continuous schistosity defined by muscovite, biotite, and chlorite bands alternated with quartz bands (Fig. 2b).

The Type-1 gold-quartz veins concentrate in shear zones subsidiary to the transcurrent first-order shear zones: either N-trending (Paraíba, Luiz Bastos, and Buriti-Porteira deposits) or E-trending (Peteca, João Fidelis, and Queiroz deposits). The Serrinha do Guarantã vein deposit is the only one in a first-order shear zone.

Hydrothermal alteration and phyllonite formation are concomitant and restricted to the shear zones. The alteration sequence varies from distal (from the ore vein) muscovite alteration (muscovite Wm-1, quartz, pyrite, and chlorite) to proximal biotite-carbonate (biotite-phlogopite, quartz, calcite, chlorite Chl-1, pyrite and traces of gold), and chlorite-carbonate alteration (Chlorite Chl-2, calcite, muscovite Wm-2, pyrite, chalcopyrite and traces of gold). Quartz-calcite veinlets with pyrite, chalcopyrite, and traces of gold cut the phyllonite rocks. The veinlets are sub-horizontal to low angle (<30º), and the internal mineral growth indicates dilational veinlets.

The fault-fill veins are steeply dipping and oblique to parallel to the shear zone S_{n+1} foliation. Internal vein textures vary from massive-milky in the center and towards the vein walls, a characteristic laminated texture, as in the Peteca deposit. The Paraíba and Serrinha de Guarantã veins are laminated (Fig. 2c). The veins show a strong oblique quartz lineation along the shear margins, characteristic of an L-tectonite, with gold filling the space between the quartz rods. Under the microscope, the vein quartz is heterogeneously deformed, showing different microstructural domains (Fig. 3). Early relict quartz (Qz1) occurs with large pyrite (Py-1) grains surrounded by sizeable recrystallized quartz (Qz2) grains. Discrete anastomosed shear bands and fractures, subparallel to the vein walls, cut the previous quartz domains, developing bands of small recrystallized quartz grains (Qz3), chlorite, and pyrite (Py2) (Fig.3).

The ore mineralization is restricted to the quartz veins and rare in phyllonites. The gold orebodies in the Paraiba and Peteca deposits are massive in irregular long stripes and lenses or as free-gold.

Gold also occurs as inclusions and infilling fractures in pyrite Py1 (Fig.3). The fractures are filled by chalcopyrite altered to covellite, galena and sphalerite, and Bi-Ag tellurides. At the Paraiba deposit, fractures with molybdenite cut the phyllonite. In the Serrinha de Guarantã orebodies, gold occurs with bornite-chalcopyrite aggregates.

2.2 Type-2 and -3 deposits

All Type-2 and -3 deposits and occurrences lie in a corridor up to 400 km from União do Norte District (Type-2 Jaca deposit) to beyond Apiacás town (Type-3 Juruena deposit), forming in various tectonic environments.

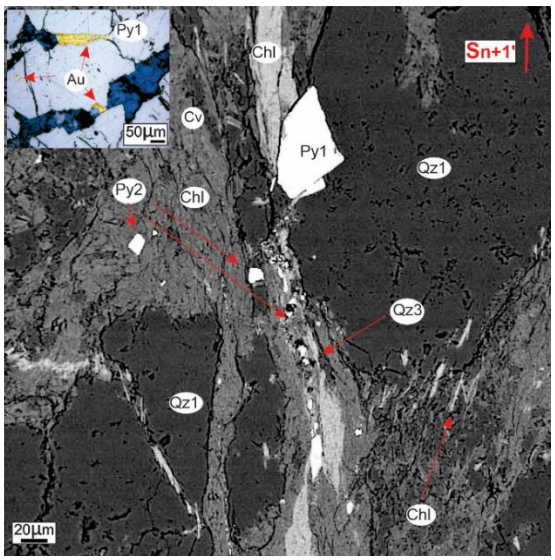

Figure 3. Gold-quartz vein textures: quartz (Qz1) and pyrite (Py1) cut and deformed by discrete, anastomosed shear bands ($S_{n+1'}$) defined by chlorite (Chl), Qz2, and a new generation of fine pyrite grains (Py-2) (EMP back-scattered electron image). In cart image: pyrite (Py1) with gold inclusions and in fractures with chalcopyrite altered to covellite (red arrows) (Peteca ore).

These deposits occur within the 1.80 to 1.75 Ga Juruena Magmatic arc and the 1.90–1.85 Ga post-orogenic rocks of the Cuiu-Cuiu magmatic arc. NE-trending faults and fractures crosscut and dislocate the WNW first-order shear zones and the S_{n+1} foliation (hosting the Type-1 deposits) and control most of the Type-2 and -3 deposits (Paes et al. in this volume).

The União do Norte District consists of an epiclastic volcaniclastic sequence intruded by several mostly alkaline quartz-feldspar porphyries and rare plagioclase porphyries (Fig. 4a, b). Additionally, several mafic dykes of unknown ages cut all the rocks and hosted many gold occurrences. The mineralization is intimately related to a sericite alteration, mainly associated with stockworks composed of Type-D pyrite veinlets with well-developed sericite or sericite-quartz halo (Fig. 4b). A-type or EM-type veinlets are absent at the moment of research.

In the Juruena District, the main host rocks are 1.82-1.77 Ga high K calc-alkaline to alkaline volcanic rocks and 1.84-1.78 Ga granitoids and lamprophyre dikes (Fig. 2). A pervasive K-feldspar-hematite alteration is overprinted by quartz-sericite alteration, cut by several hydrothermal breccias and veinlets. There are sericite polymictic breccia, chlorite cement-supported carbonate breccia, and sulphide-silica breccia, mostly chalcopyrite cement. There are three populations of silica veinlets, named vl 1, 2, and 3. Vl 1 is a banded quartz-sericite veinlet. The sulphide-quartz vl 2 has a wavy morphology, composed of milky quartz, chalcopyrite, pyrite, minor galena, and sphalerite (Fig. 4c, d). The silica-calcite-fluorite vl 3 has straight, well-defined walls and cut the sulphite-quartz vl 2. Coarse grain idiomorphic calcite has a massive or zonal growth texture (Fig. 4d).

In other respects, the Paraiba and Peteca deposits also show Type-2 and -3 characteristics. Distal from the pair phyllonite/fault-fill ore veins, non-foliated potassic (K-feldspar-hematite, quartz, biotite, and molybdenite), sericitic (Wm-3 muscovite, quartz, calcite, pyrite, rutile, ilmenite, and titanite), propylitic, and epidote-carbonate (epidote, allanite, calcite, Mn-calcite, chalcopyrite, molybdenite, pyrite, rutile, ilmenite, titanite, gold) alterations are observed, pervasive or in veinlets. Sericitic alteration veinlets are mineralized and composed of quartz, pyrite, molybdenite, and chalcopyrite with sericite halos (Paraiba deposit). A pervasive sericitic alteration cuts and obliterates the muscovite phyllonite S_{n+1}. The propylitic alteration evolved into an epidote-carbonate-stockwork. In the Paraíba deposit, epidote-carbonate breccia is high-grade copper and gold and one of the orebodies (Poggi et al. 2022).

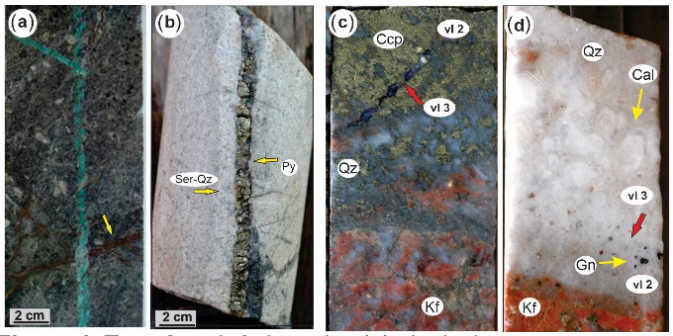

Figure 4. Type-2 and -3 deposits: (a) plagioclase porphyric intrusions strongly sericitized and affected by pyrite veinlets (arrow). Phenocrysts of polymorphic plagioclase and biotite; (b) typical Type-D pyrite veinlet (in the sense of Gustafson and Hunt 1975) with sericite-quartz or sericite halo host in arkose of the epiclastic-volcaniclastic sequence; (c) 6 cm thick quartz-sulphide (in the walls) to massive sulphide (in the centre) vl 2 cut by millimetric quartz-fluorite vl 3 in a K-feldspar-hematite altered granite. Note the absence of alteration halo in the vl 2 wall; (d)) quartz-sulphide vl 2 with disseminated galena evolved to calcite vl 3. Calcite shows a zonal growth texture (yellow arrow). Sílica halo in the K-feldspar-hematite altered rock.

2.3 Chlorite and white mica

The available chlorite and white mica chemical composition of Type-1, -2, and -3 deposits are presented in Gomes et al. (in this volume). The main results suggest the Type-1 deposits show Mg-rich chlorite and Mg- and Si-rich muscovite-phengite footprints. The consistently high crystallization temperature (above 350ºC) and almost zero vacancies suggest metamorphic chlorite. Chlorite-white mica thermobarometers show a limited temperature variation (420-300ºC) and significant high-pressure variation (3-7 kbar) attributed to supralithostatic fluid pressure regimes.

In contrast, Fe-rich and Al-Fe-rich alterations are the main footprints for the porphyry (Type-2) and epithermal (Type-3) deposits, respectively. The P-T evolution has more substantial temperature

variation (380-120ºC) and lower pressure (4.6-0.6 kbar), coherent with the cooling of a shallow hydrothermal-magmatic system.

3 Discussion and conclusions

Many authors have already interpreted the Type-2 and Type-3 deposits as Au-Cu-Mo porphyry and intermediated Au-Pb-Zn-Cu epithermal, respectively, developed due to the same evolved magmatic-hydrothermal event, together with the Type-1 Au-Cu veins in shear zones (Paes de Barros 2007; Moura et al. 2006; Assis 2011, 2015; Miguel Jr. 2011; Rodrigues 2012; Acevedo 2014; Trevisan 2015; Assis et al. 2017; Galé 2018; Rocha 2016). However, our findings based on new and reinterpreted data suggest that a distinct hydrothermal event during active shearing created the Type-1 deposits.

The main Type-1 deposits' characteristics such as (a) hosted in deformed and metamorphosed metagranitoids of the Paleoproterozoic PdA inlier; (b) compressional to transpressional regimes of post-orogenic environments related to the NW-trending shear zone system; (c) hydrothermal alteration associated with ore mineralization is restricted to the shear zones; (d) and fault-fill quartz veins in phyllonites of the subsidiary structures suggest the Type-1 deposits are consistent with the orogenic gold model, as stated by many authors, as the seminal Groves et al. (1998).

At the Type-2 deposit, the large and undeformed hydrothermal alteration zones and the widespread sericitic zone hosting the D-type pyrite veinlets in stockworks, suggest porphyry deposits (Sillitoe 2010). At the Type-3 deposits in the Juruena District, several generations of hydrothermal breccias (sericitic, chloritic, carbonatic, and quartz-sulphide) and veinlets (vl-1, vl-2, and vl-3) suggest epithermal deposits (Hedenquist et al. 2020; Wang et al. 2019). The Type-3 relationship with the porphyry deposits (Type-2), both hosted in oxidized calc-alkaline granitic and volcanic rocks of the Juruena magmatic arc, are common features of intermediate-sulphidation (IS) epithermal deposits (Wang et al. 2019).

The mineral assemblages point to hydrated minerals of the orogenic event in phyllonite, defining S_{n+1} foliation (Fig. 2). Contrastingly, the magmatic-hydrothermal event that created the Type-2 and Type-3 deposits formed minerals in a lower rock-fluid ratio (r/w) and variable accessory minerals. The sericite (Wm-3) in the sericitic zone, the Wm-4 in the sericitic ore veinlets and their halos, and the chlorite (Chl-3) in the propylitic alterations are characteristic non-foliated.

The main ore assemblage also shows differences between the two events. The orogenic gold deposit fault-fill quartz veins are composed of pyrite, chalcopyrite, pyrrhotite, magnetite, gold, and Bi-Ag tellurides. In contrast, the quartz veinlets and halos of phyllic/sericitic alteration consist of pyrite, molybdenite, chalcopyrite, rutile, ilmenite, and titanite, and the epidote-carbonate stockworks consist of epidote, allanite, calcite, Mn-calcite, chalcopyrite, molybdenite, pyrite, rutile, and gold.

Recognizing the granitoid-hosted orogenic gold deposits as a distinct ore-hydrothermal event, separate from the magmatic-hydrothermal one, and recognizing their overprint relationships will assist exploration within the Alta Floresta Mineral Province.

References

Alves, C. L., et al. 2020. The Orosirian Cuiú-Cuiú magmatic arc in Peixoto de Azevedo domain, Southern of Amazonian craton. Journal of South American Earth Sciences, 102, 102648. https://doi.org/10.1016/j.jsames.2020.102648

Assis R.R., et al. 2017. Linking the Timing of Disseminated Granite-Hosted Gold-Rich Deposits to Paleoproterozoic Felsic Magmatism at Alta Floresta Gold Province, Amazon Craton, Brazil: Insights from Pyrite and Molybdenite Re-Os Geochronology. Economic Geology, 112: 1937–1957. https://doi.org/10.5382/econgeo.2017.4535

Augustin, J. and Gaboury, D. 2018. Multistage and multi-sourced fluid and gold in the formation of orogenic gold deposits in the world-class Mana district of Burkina Faso – Revealed by LA-ICP-MS analysis of pyrites and arsenopyrites. Ore Geology Reviews, 104, 495–521. https://doi.org/10.1016/j.oregeorev.2018.11.011

Fougerouse, D. et al. 2017. Evidence for two stages of mineralization in West Africa's largest gold deposit: Obuasi, Ghana. Economic Geology, 112, 3–22. https://doi.org/10.2113/econgeo.112.1.3

Le Mignot, E. et al. 2017. The Paleoproterozoic copper-gold deposits of the Gaoua district, Burkina Faso: Superposition of orogenic gold on a porphyry copper occurrence?. Economic Geology, 112(1), 99-122. https://doi.org/10.2113/econgeo.112.1.99

Meffre, S. et al. 2016. Multistage enrichment processes for large gold-bearing ore deposits. Ore Geology Reviews, 76, 268-279. https://doi.org/10.1016/j.oregeorev.2015.09.002

Mesquita et al. 2022. Paleoproterozoic gold deposits at AFMP, Brazil: two overprinted mineralizing events? From: Torvela, T., Lambert-Smith, J. S. and Chapman, R. J. (eds). Recent Advances in Understanding Gold Deposits: from Orogeny to Alluvium. Geological Society, London, Special Publications, 516. https://doi.org/10.1144/SP516-2021-64

Moura, M.A. et al. 2006. Granite-related Paleoproterozoic, Serrinha gold deposit, Southern Amazonia, Brazil: hydrothermal alteration, fluid inclusion and stable isotope constraints on genesis and evolution. Economic Geology, 101, 585-605. https://doi.org/10.2113/gsecongeo.101.3.585

Pogi et al. 2022. New Insights into the Evolution and Footprints of the Paraíba Au-Cu-Mo Deposit, Alta Floresta Mineral Province (Brazil), through Integration of Spectral and Conventional Methods. Minerals 2022, 12, 1327. https://doi.org/10.3390/min12101327

Santos, J.O.S. et al. 2001. Gold deposits of the Tapajós and Alta Floresta domains, Tapajós-Parima orogenic belt, Amazon Craton, Brazil. Mineralium Deposita, 36, 278-299. https://doi.org/10.1007/s001260100172

Groves, D.I. et al. 1998. Orogenic gold deposits: A proposed classification in the context of their crustal distribution and relationship to other gold deposit types. Ore Geology Reviews, 13, 7–27. https://doi.org/10.1016/S0169-1368(97)00012-7

Sillitoe, R.H. 2010. Porphyry copper systems. Economic Geology, 105, 3–41. https://doi.org/10.2113/gsecongeo.105.1.3

Wang, L. et al. 2019. A review of intermediate sulfidation epithermal deposits and subclassification. Ore Geology Reviews, 107, 434-456. https://doi.org/10.1016/j.oregeorev.2019.02.023

Geophysical VLF prospecting for orogenic gold in the historic mining area in the Sudetes (SW Poland)

Stanisław Z. Mikulski[1], **Szymon Ostrowski**[1]
[1]*Polish Geological Institute-National Research Institute*

Abstract. The abandoned historic gold mining areas in the Sudetes are prospective for vein-type gold deposits. The applied VLF geophysical survey showed a number of linear anomalies indicating the possibility of occurrence of the new ore veins between the areas of former mining exploitation. In the light of the obtained VLF results as well as previous bulk-rock geochemistry and mineralogical study, which showed high gold content in the ores from mining wastes, this area is very promising for successful gold prospecting.

1 Introduction

The application of geophysical methods such as VLF (very low frequency electromagnetic technique) in the fast mapping of the structural features (Gnaneshwar et al. 2011; Ramesh Babu et al. 2007), and search for vein-type deposits (Ostrowski 2014) in former metal ore mining areas has been used for a long time and in many places it has enabled the recognition of the continuation of the course of already known ore veins or indicated their completely new occurrences.

VLF is the geophysical technique known and widely used for decades, although its applications are diminishing nowadays due to mostly to the fact that obtained results are usually qualitative. The full description of the technique basics can be found in (Paterson and Ronka 1971; Phillips and Richards 1975; Sharma et al. 2014), and attempts of more quantitative approach to the VLF results has been made recently (Singh and Sharma 2016). The VLF surveying technique is one of the techniques based on the electromagnetic induction phenomena. The electromagnetic fields effecting from the phenomena and generated by some geological features might be measured from surface and translated to the geological model.

Polish Geological Institute conducted a geophysical survey with VLF technique in a former gold mining area in the Klecza-Radomice Ore District (KROD), (Mikulski et al. 2021). In KROD during the years 1922-33, small-scale mining of arsenic and gold ores was carried out there, from quartz veins intersecting Lower Paleozoic shales.

2 Geological background and gold mineralization

The Klecza-Radomice Ore District KROD is hosted by rocks of to the Kaczawa Metamorphic Complex (KMC) that belongs to the basement of the Western Sudetes unit considered as a continuation of the Saxothuringian Zone of the European Variscides in the north-eastern part of the Bohemian Massif. KMC is representing there by flysch-like sediments of Ordovician-Devonian age that were deformed and metamorphosed to lower green schist facies (Kryza and Muszyński 1992). In the KROD the gold bearing quartz-sulfide mineralization consist of 8 main and more than 9 smaller veins (Mikulski 2007). Veins have major NE-SW and minor NW-SE strike directions, and are steep dipping (65-85°) to W. They were explored on a length of about 90-150m and down dip to 100m below surface, showing different thickness from 0.25 to 1.5m. Most frequently veins cut host rocks but locally may appear as saddle reefs. Bigger veins are preferentially located in fractured zones discordant to the bedding and run close to, or along the axial planes of F_1 anticlines. Several veins run oblique in direct surroundings of the Pławna fault zone of inverse character (Figure 1).

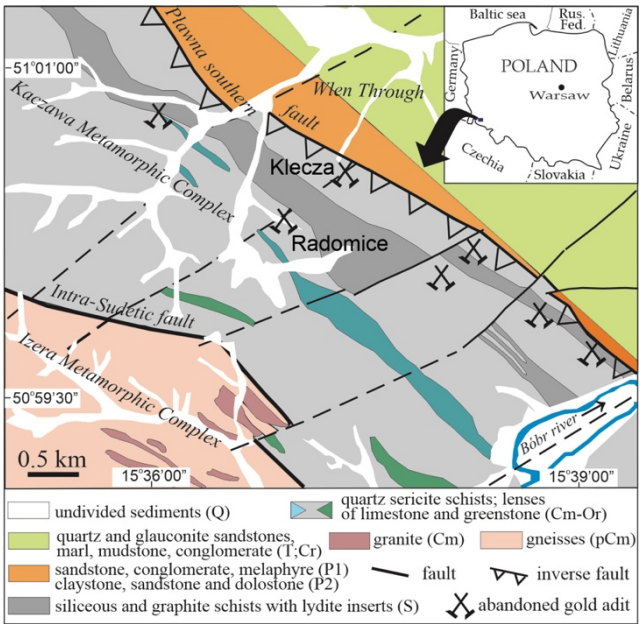

Figure 1. Location of the Klecza-Radomice Ore District (KROD; after Mikulski 2007) on the schematic geological map (modified from Milewicz 1962; Milewicz and Frączkiewicz 1983; Milewicz and Kozdrój 1994)

The richest in gold ore mineralization is of a massive type and dominated by arsenopyrite and in places by pyrite. The content of gold and arsenic in ore veins was in the range of 3-40ppm Au and 2-12% As. Sericite and graphitic schists are favourable host of sulfides mineralization. These rocks are strongly altered due to silicification, sericitization,

carbonatization, chloritization, feldspathization and sulfidization. The ore massive mineralization is fractured and overprinted by rare base metal sulfide (chalcopyrite galena and sphalerite) associated with common carbonates (mainly ankerite and dolomite). Gold occurs as refractory and microscopic gold. Separated pyrite and arsenopyrite contained up to 68.5ppm and 15ppm of gold, respectively (Mikulski 2007). Fineness of the microscopic gold is variable from very low (630) to very high (940) (Paulo and Salomon 1973; Olszyński and Mikulski 1997; Mikulski 2007). The mineralization in KROD has been classified as an orogenic gold deposit due to geological setting between metamorphic terranes, strong structural control of ores, low Au/Ag ratios, not significant base-metal contents, and low salinity of mineralizing fluids (<7 wt% NaCl equivalent), (Mikulski 2003). The Re-Os isotopic age obtained for Co-arsenopyrite from the northern ore field in Klecza revealed an age value of 316.6±0.4 Ma (Mikulski et al. 2005).

3 Geophysical prospecting with application of the VLF methods

Geophysical survey was carried in 2017-2018 in two sites, in radius of approximately 1 km from two historic mines. The survey was done with VLF technique. Measurements were acquired along 30 acquisition lines of 0,3 to nearly 1,5 km long and of total length of more than 30 km, covering the area of ca. 3 km^2 - virtually entire area of interest. The field measurements were performed along parallel traverses spaced ca. 100 m in between. Primary field intensity, in-phase (IP) and quadrature (QUAD) components of phase shift were measured for three different frequencies generated by three far-field transmitters. The Fraser filtration (Fraser 1969) was applied to all obtained datasets of phase shift components, and the results (both unfiltered and filtered) were compiled to the series of point-maps (Figure 2). Hand interpretation of the resulting maps by connecting VLF anomalies on subsequent traverses yielded linear anomalies that can be regarded as probable course of ore veins (Figure 3).

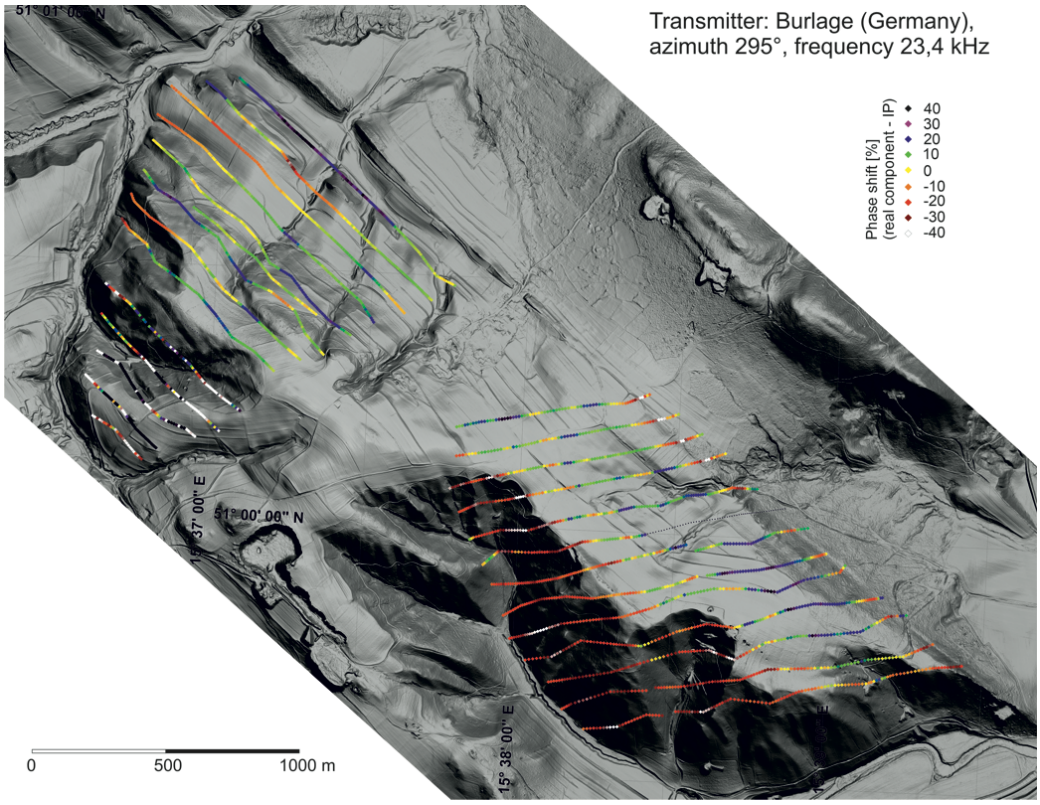

Figure 2. Point-map of in-phase component of induced VLF field. Illustration of the survey setting and one of the unfiltered phase shift components.

4 Final remarks

On the basis of prepared maps of Fraser-filtered VLF datasets the course of linear anomalies were identified. Four lineament populations (or modes) are present (Figure 3). The lineaments can be attributed to different structural elements and different stages of deformations. In our opinion the most promising places for further ore investigations (including drilling locations) are nexuses where lineaments of mode (7) and mode (10) and (9) are intersecting and ore enrichment might take place.

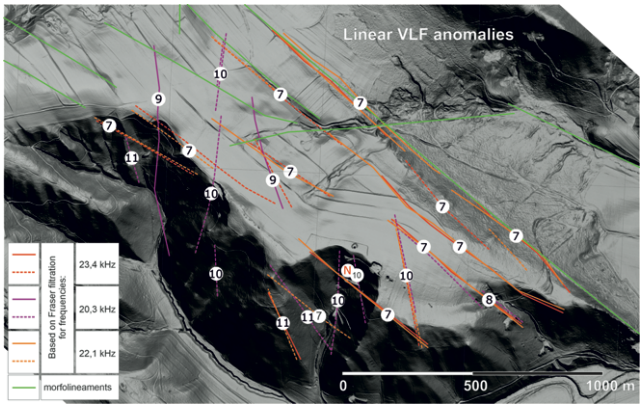

Figure 3. A fragment of the map of interpreted linear VLF anomalies. The anomalies are results of linear structural features with conductivity contrasting to the surrounding medium.

Acknowledgements

The presented results were obtained in PGI-NRI during performing the project financed by the National Fund for Environmental Protection and Water Management, in accordance with the grant agreement No. 289/2018.

References

Fraser DC (1969) Contouring of VLF-EM data. Geophysics 34:958–967

Gnaneshwar P, Shivaji A, Srinivas Y, Jettaiah P, Sundararajan N (2011) Very-low-frequency electromagnetic (VLF-EM) measurements in the Schirmacheroasen area, East Antarctica. Polar Science 5:11–19

Groves DI, Goldfarb RJ, Gebre-Mariam M, Hagemann SG, Robert F (1998) Orogenic gold deposits: A proposed classification in the context of their crustal distribution on relationship to other gold deposit types. Ore Geol Rev 13:7–27

Kryza R, Muszyński A (1992) Pre-Variscan volcanic-sedimentary succession of the central southern Góry Kaczawskie, SW Poland: outline geology. Annales Societatis Geologorum Poloniae 62:117–140

Mikulski SZ (2003) Orogenic quartz-sulfide-gold veins from the Klecza-Radomice ore district in the Kaczawa Mountains (W Sudetes). In: Eliopoulos et al. (eds) Mineral Exploration and Sustainable Development. Millpress, Rotterdam: 787–790

Mikulski SZ (2007) The late-Variscan gold mineralization in the Kaczawa Mountains, Western Sudetes. Polish Geological Institute Special Papers 22: 1–162. PGI Warszawa

Mikulski SZ, Markey RJ, Stein HJ (2005) Re-Os ages for auriferous sulfides from the gold deposits in the Kaczawa Mountains (SW Poland). In: Mao J and Bierlein FP (eds) Mineral Deposit Research: Meeting the Global Challenge, Springer-Verlag Berlin, Germany: 793–796

Mikulski SZ, Ostrowski S, Cymerman Z, Małek R, Sadłowska K, Handke B, et al. (2021, unpublished) Evaluation of the possibility of obtaining rare raw materials (especially some metals) from areas and deposits not yet explored in this respect. Task 4.1. NGA no 1955/2021. Warszawa (In Polish)

Milewicz J (1962) Detailed geological map of the Sudety Mountains in the scale of 1:25,000. Lubomierz sheet. Wydawnictwa Geologiczne Warszawa

Milewicz J, Frąckiewicz W (1983) Detailed geological map of the Sudety Mountains in the scale of 1:25,000. Wleń sheet. Wydawnictwa Geologiczne Warszawa

Milewicz J, Kozdrój W (1994) Detailed geological map of the Sudety Mountains in the scale of 1:25,000. Proboszczów sheet. Państwowy Instytut Geologiczny Warszawa

Olszyński W, Mikulski SZ (1997) Native gold in crystalline schists from Radomice near Wleń: Noble metals in NE part of Bohemian Massif and its surroundings, genesis, occurrence, perspectives. Jarnoltowek 19-21.06.1997. Wrocław: 86–90 (In Polish)

Ostrowski S (2014) Mapping with VLF tool - gold investigation case study that yielded unexpected structural minutiae. Geologia Sudetica 42:68

Paterson NR, Ronka V (1971) Five years of surveying with the very low frequency electromagnetic method. Geoexploration 9:7–26

Paulo A, Salamon W (1973) Native gold in ore veins of the Western part of Góry Kaczawskie Mts. (West Sudetes). Mineralogia Polonica 4(2):85-91

Phillips WJ, Richards WE (1975) A study of the effectiveness of the VLF method for the location of narrow mineralized zones. Geoexploration 13:215–226

Ramesh Babu V, Ram S, Sundararajan N (2007) Modeling of magnetic and VLF-EM with an application to basement fractures - a case study from Raigad, India. Geophysics 71:133–140

Sharma S, Biswas A, Baranwal V (2014) Very Low-Frequency Electromagnetic Method: A Shallow Subsurface Investigation Technique for Geophysical Applications. In: Sengupta D (ed) Recent Trends in Modelling of Environmental Contaminants. Springer, New Delhi, pp 119–141

Singh A, Sharma SP (2016) Interpretation of very low frequency electromagnetic measurements in terms of normalized current density over variable topography. Journal of Applied Geophysics 133 (2016):82–91

Multiple sulfur isotope analyses identify an Archean sulfur source for the auriferous fluids at the Meliadine gold district, Nunavut, Canada

Philippe Mongeau[1], Crystal LaFlamme[1], Patrick Mercier-Langevin[2], Guillaume Barré[1], Olivier Côté-Mantha[3], Pierre de Cartigny[4], Laure Martin[5]
[1]Département de Géologie et de Génie Géologique, Université Laval, Québec, Québec
[2]Geological Survey of Canada, Québec, Québec
[3]Agnico Eagle Mines Limited, Exploration Division, Val-d'Or, Québec
[4]Institut de Physique du Globe de Paris, Université Paris Cité, Paris, France
[5]Centre for Microscopy, Characterisation & Analysis, University of Western Australia, Western Australia, Australia

Abstract. In Canada, orogenic gold deposits are the main source of gold, but the origin of hydrothermal fluids remains equivocal. The Meliadine gold district (3.7 Moz Au), located in the Churchill Province in Nunavut, contains a series of deposits emplaced during the Paleoproterozoic Trans-Hudson orogenesis, hosted in Archean metavolcanic and metasedimentary rocks of the Rankin Inlet greenstone belt. This project aims to document the multiple sulfur isotope signature ($\delta^{34}S$, $\Delta^{33}S$, $\Delta^{36}S$) of gold-associated sulfides in quartz-carbonate veins through the paragenetic sequence, and to track the source and evolution of auriferous fluids. Samples containing arsenopyrite+pyrrhotite±(pyrite, galena, chalcopyrite) were collected across unmineralized host-rock, intermediate alteration zones and gold-rich vein-related mineralization. In-situ (SIMS) and bulk (IRMS) isotope analyses show that $\delta^{34}S$ does not vary much across the paragenetic sequence and at the sample, drillhole and deposit scale with an average $\delta^{34}S$=3.1±2.8 ‰ (2SD; n=238). Sulfur mass-independent fractionation (S-MIF) is present in all samples, yielding average values of $\Delta^{33}S$=0.32±0.24 ‰ (2SD; n=129) and $\Delta^{36}S$=-0.70±0.56 ‰ (2SD; n=58). This new dataset shows that the devolatilization of deep-seated metasedimentary and metavolcanic units during prograde metamorphism may play an important role in sourcing sulfur, a key ligand for gold.

1 Introduction

The importance of multiple fluid generations and/or long-lived fluid flow for orogenic gold deposits is well established (e.g. Robert et al. 2005; Dubé and Mercier-Langevin, 2020). However, the source of the mineralizing auriferous hydrothermal fluids remains equivocal (Goldfarb and Pitcairn, 2023). Recent studies demonstrate that sulfur isotopes represent an additional tool for gold exploration (e.g., LaFlamme et al. 2018a). It is possible to gain insight into the source and the evolution of the mineralizing fluid chemistry through space and time by multiple sulfur isotope analysis on gold-hosting sulfide grains. Changes in the oxygen fugacity (fO_2) of the fluid largely control the behavior of gold in the fluid, i.e., its transport or precipitation (Williams-Jones et al. 2009). Because $\delta^{34}S$ is highly sensitive to fO_2 variation (Ohmoto and Rye, 1979), $\delta^{34}S$ can serve as a marker of the change (redox conditions) responsible for destabilizing gold-sulfides complexes (LaFlamme et al. 2018a). Therefore, isotopic signatures representing prospective areas for exploration can be identified by characterizing the $\delta^{34}S$ of gold-associated sulfides and by comparing gold-rich and gold-poor zones.

Moreover, Archean sulfur mass-independent fractionation (S-MIF), as $\Delta^{33}S$ and $\Delta^{36}S$ values, can help distinguish between magmatic and sedimentary sources or reservoirs of sulfur from auriferous hydrothermal fluids further helping assess ore-forming processes and area fertility.

The Paleoproterozoic Meliadine gold district (MGD) is hosted in the Archean Rankin Inlet greenstone belt of Nunavut. It is host to orogenic gold deposits within typical structurally controlled quartz-carbonate (calcite ± ankerite) veins. These veins contain multiple arsenopyrite generations that host gold, and thus represents an excellent opportunity to explore the chemical controls on sulfide-related orogenic gold in an Archean greenstone belt. Here, we aim to define the source of sulfur for the mineralizing fluids and test the hypothesis that the multiple sulfur isotope signatures and their variations in space and time (through the paragenetic sequence of sulfides) can help define vectors between poor and rich zones at the deposit and district scale.

2 Geological setting

The MGD, located in the western Churchill Province in northern Canada (Figure 1), hosts 3.7 million ounces of gold in proven and probable reserves (Agnico Eagle Mines Ltd., 2022). This gold district is thought to have been emplaced during the Paleoproterozoic Trans-Hudson orogenesis (THO: Carpenter et al. 2005; Lawley et al. 2015). The MGD comprises multiple deposits that are hosted in the Archean meta-volcanic (e.g., Wesmeg, Normeg and Pump) and meta-sedimentary (e.g., Tiriganiaq and Discovery) rocks of the Rankin Inlet greenstone belt and are associated with the Pyke and Lower faults (Figure 1).

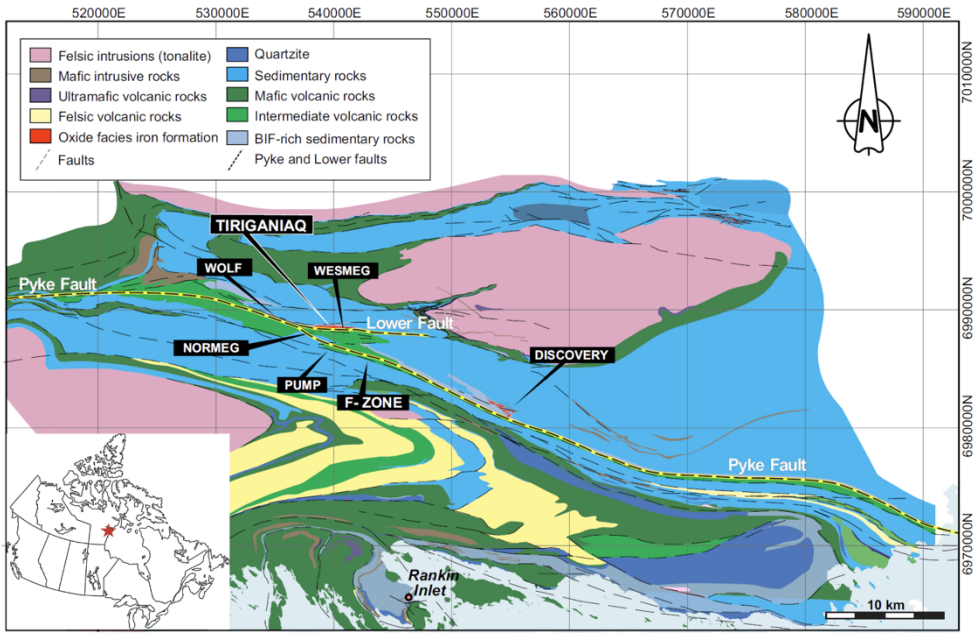

Figure 1. Geology map of the Meliadine Gold District highlighting the geological context and location of the various deposits, modified after St. Pierre et al. (2020).

2.1 Tiriganiaq deposit

The Tiriganiaq deposit is located in the hanging wall of the Lower Fault within an overturned turbiditic succession, located in the central part of the district. The deposit is hosted within several formations that include: 1) the mineralized Tiriganiaq Formation, which is composed of laminated siltstones and graphitic argillite; 2) the Upper Oxide Formation, a package of iron rich turbidites and silicate-oxide-facies iron formations that hosts the majority of the ore, and 3) the Sam Formation, composed of sub-economic greywackes and laminated siltstones, (St. Pierre et al. 2020). These formations have undergone several deformation episodes between 2.56 and 1.8 Ga (MacQuoid, Arrowsmith, Taltson-Thelon, and Trans-Hudson orogenies: Lawley et al. 2015). Gold lodes form as stacked, semicontinuous, gold-rich intervals of quartz-carbonate veins, where replacement style mineralization occurs in sulfidized iron-rich lithologies subparallel to the Lower Fault. Gold is often found in microtextural sites of low deformation (e.g. pressure shadows) and as inclusions in recrystallized and idioblastic arsenopyrite crystals but is also found in the absence of arsenopyrite. Re-Os dating also shows that while the most gold-rich arsenopyrite crystals are associated with the THO (~1.9 Ga), older generations of gold-associated, lower grade, arsenopyrite (~2.27 Ga) are also recognized (Lawley et al. 2015).

2.2 Wesmeg, Normeg and Pump deposits

The Wesmeg, Normeg, and Pump deposits, are all found in the Wesmeg Formation, forming the footwall of the Lower Fault. The Wesmeg Formation consists of mafic volcanic rocks that are interbedded with narrow oxide-facies iron formations cut by gabbro and lamprophyre dykes (St. Pierre et al. 2020). Similar to the Tiriganiaq deposit, gold-rich intervals occur as stacked lodes of quartz-carbonate veins and replacement-style mineralization that are subparallel to the Lower Fault, but are mainly spatially constrained to iron formations (Lawley et al. 2015). Gold is often found microtextural sites of low deformation and as inclusions in idioblastic arsenopyrite crystals, along with a sulfide assemblage consisting of arsenopyrite + pyrrhotite ± (pyrite - chalcopyrite - galena - sphalerite), and oxides (magnetite and ilmenite; Lawley et al. 2015).

3 Methodology

3.1 Sampling strategy

Samples were collected from underground stopes and drill-core from the unmineralized zones towards the high-grade zones, considering the location of the zones, grades, depths, alteration, etc. Samples considered altered are near the main ore zones, whereas unaltered samples are collected as far as possible from the alteration associated with the mineralized zones. Samples from the intermediate alteration zones were collected between the mineralized and unmineralized zones.

3.2 Textural and chemical composition of sulfides

Micro-analytical characterisation was completed on selected sulfides in thin-section at Université Laval. Major and minor elemental analyses were carried out by wavelength dispersive spectrometry using a CAMECA SX-100 EPMA with a beam size of 5 µm at 15 kV and 20 nA. To gain insight into the microtextural characteristics of the various sulfide assemblages and their relationship to gold, back-scatter electron imaging was completed on a FEI Inspect F50 Scanning Electron Microscope using a

beam at 50 kV and 600 µA with a step-size of 20 µm and a 10 ms acquisition time.

3.3 Bulk sulfur isotope analyses

High precision multiple sulfur isotopes measurements ($\delta^{34}S$, $\Delta^{33}S$, $\Delta^{36}S$) were completed on a total of 58 samples of pyrrhotite, arsenopyrite, pyrite and galena (including duplicates). For this purpose, sulfide powders were collected from targeted sulfides within selected samples using a Dremel rotary tool. The extraction of sulfur from the sulfide phases was completed at Université Laval by wet chemistry. Powdered sulfides were dissolved in HCl for pyrrhotite and galena, and with chromium reduced sulfides (CRS) solution following the protocol established by Canfield et al. (1986) for pyrite. In both cases, the produced H_2S was then converted to Ag_2S by reacting with a $AgNO_3$ solution. The measurements of ^{32}S, ^{33}S, ^{34}S and ^{36}S on Ag_2S and arsenopyrite samples were then carried out at the *Institut de Physique du Globe de Paris* using a fluorination line (SF_6^+) coupled to a ThermoFinnigan MAT253 dual inlet gas-source mass spectrometer. The recovered Ag_2S were fluorinated overnight to produce SF_6 in nickel reaction bombs by reaction with F_2 in excess at 250 ºC. As arsenopyrite does not react with acid solutions, the powders were introduced directly into the nickel reaction bombs to react with F_2. The produced SF_6^+ was sequentially purified using cryogenic traps and gas chromatography, then introduced into the mass spectrometer. Measurement accuracy and reliability was monitored by introducing samples of International Atomic Energy Agency (IAEA-S1) Ag_2S standard over the course of the analyses.

3.4 In-situ sulfur isotope analyses

In situ multiple sulfur isotopes ($\delta^{34}S$, $\Delta^{33}S$) of pyrrhotite (n=53), pyrite (n=8) and chalcopyrite (n=7) were completed by a CAMECA IMS 1280 secondary ion mass spectrometry (SIMS) analyses that were carried out at the University of Western Australia, allowing to get spatial resolution of individual sulfide analyses. Small pucks (n=10) of a few millimetres in diameter containing sulfides were extracted from the samples selected for analysis, placed in an epoxy mount and polished and paired with standard blocks of matrix-matched Alexo pyrrhotite, Sierra pyrite and Nifty-b chalcopyrite (LaFlamme et al. 2016). To ensure standard repeatability and to account for analytical drift and instrumental mass fractionation, unknown samples were interspersed with matrix-matched reference materials and analyses monitored using respective standards. Measurements of ^{32}S, ^{33}S, ^{34}S and by spot analyses were carried out following the protocol as defined by LaFlamme et al. (2016) with slight modifications, with the ion microprobe operating in multicollection mode using a focussed, 10 µm Cs^+ beam with impact energy of 20 kV and intensity 2.3 nA.

4 Results

4.1 Sulfide paragenesis

The paragenesis of sulfides was established for the Tiriganiaq deposit, where multiple generations of sulfides have been categorized as generations 1, 2a and 2b (Figure 2). Generation 1 pre-dates gold and is characterized by pyrrhotite ± pyrite that is deformed and oriented within the host-rock foliation (Figure 2A) of laminated siltstones, argillites, iron-rich turbidites, silicate-oxide-facies iron formations and greywackes, but is less abundant in areas rich in veining and gold. Generation 2a is formed of arsenopyrite and 2b is formed of arsenopyrite+pyrrhotite±pyrite and both are discernible from Generation 1 based on texture and major/minor chemical composition, showing As enrichments in generations 2a and b. Pyrrhotite 2b displays elevated arsenic contents correlating sample with gold grade. The differences between 2a and 2b arsenopyrite are based on the different textures, relationship to gold, alteration and recrystallisation haloes observed with the SEM. Generation 2b arsenopyrite and pyrrhotite are commonly related to gold (Figure 2B/C). Pyrrhotite and arsenic-rich recrystallisation haloes of arsenopyrite are associated with free gold. Figure 2D shows an example of the complex sulfide paragenesis, where textural relationships between different phases can be equivocal.

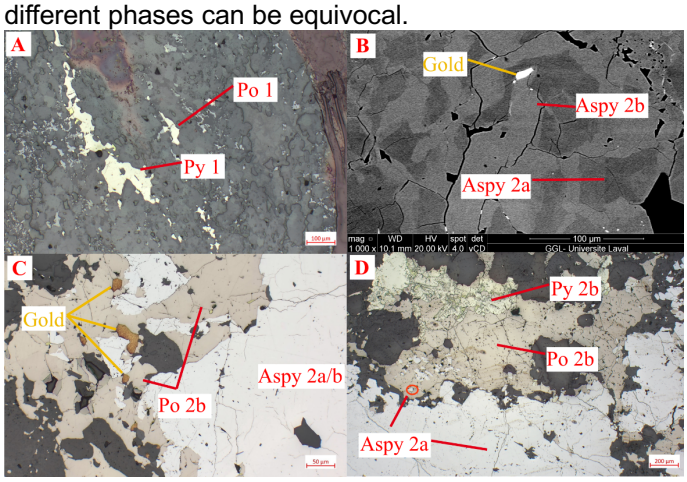

Figures 2A, 2C, 2D: Reflected light photomicrographs of various sulfide generations, textural relationships, and association with gold. **Figure 2B:** Backscatter electron image of gold-rich arsenopyrite, highlighting the arsenic-rich recrystallisation haloes and their relationship to gold.

4.2 Multiple sulfur isotope analyses

Multiple sulfur isotope analyses completed both in situ (SIMS) and in bulk (IRMS) show that $\delta^{34}S$ sees little variation at the sample, drillhole and deposit scale with an average $\delta^{34}S$ = 3.00 ± 2.85 ‰ (2SD; n = 129) and does not correlate with gold grade. Mass-independent fractionation of sulfur (MIF-S) is present in all the in situ and bulk samples yielding average values of $\Delta^{33}S$ = 0.32 ± 0.24 ‰ (2SD; n=129) and $\Delta^{36}S$ = -0.70 ‰ ± 0.56 (2SD; n=58). Plotted $\delta^{34}S$ versus $\Delta^{33}S$ in Figure 3 shows that the $\Delta^{33}S$ values

remain stable across all samples but plot outside of the mass-dependent fractionation array (MDF-S). Sulfide generations from older to most recent also show a shift towards enriched $\delta^{34}S$ values, consistent between all phases and analytical methods (in bulk and in situ) while the $\Delta^{33}S$ remains stable.

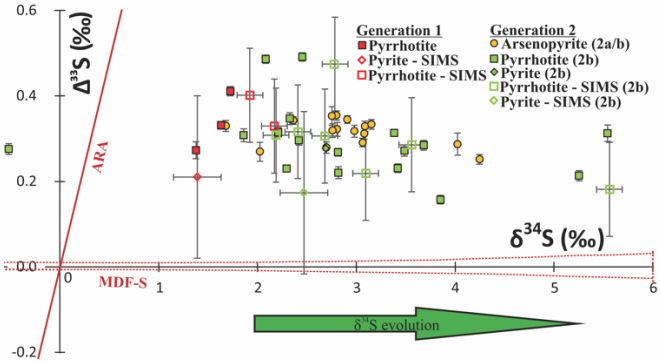

Figure 3. Multiple sulfur isotopes values ($\delta^{34}S$ and $\Delta^{33}S$) of various sulfide phases and generations obtained from SIMS and bulk analyses. Archean Reference Array (ARA, $\Delta^{33}S=0.89*\delta^{34}S$) after Ono et al. (2009). Mass-dependent fractionation of sulfur (MDF-S) after LaFlamme et al. (2018b). The green arrow represents the evolution between relict sulfides (1) and gold-associated sulfide generations (2a/2b). Note the homogeneous $\Delta^{33}S$ during this evolution, a sign of a single source of sulfur.

5 Conclusions

Monitoring fluid-rock reactions is essential to understand gold precipitation mechanisms. While the timing of generation 1 of sulfides remains uncertain, the homogeneous $\Delta^{33}S$ signature with generations 2a and 2b supports the idea of a common local source of fluid (i.e. metavolcanics and metasediments of the host-rock) that has been recycled by subsequent sulfur-poor hydrothermal fluids through fluid-rock reactions. It implies that gold could have been introduced much earlier than previously postulated and have undergone multiple stages of remobilization along with the recycling of sulfur at the district scale (e.g. Lawley et al. 2015). The evolution of the $\Delta^{33}S$ and $\delta^{34}S$ through the paragenetic sequence (Figure 3) shows that the samples remain outside of the MDF-S array, but don't follow the Archean trend either. This suggests a mixing source of sulfur from meta-sedimentary with positive S-MIF $\Delta^{33}S$ values and meta-volcanic rocks with likely near-zero $\Delta^{33}S$ values (i.e., magmatic origin, Siedenberg et al. 2016) that would buffer the overall $\Delta^{33}S$ signature of the mineralization, and/or the remobilization of sulfur and gold at the deposit scale through mass-dependant processes. This new dataset shows that the source of these auriferous fluids clearly recorded an influence of Archean metasedimentary rock, and that the devolatilization of deep-seated metasedimentary and metavolcanic units during prograde metamorphism plays an important role in sourcing sulfur, key to the transportation of gold at the crustal scale.

Acknowledgements

This study is financially supported by Mitacs, Agnico Eagle Mines Ltd., and the TGI 6. Thanks to Marc Choquette, Suzie Côté, Karine Lavallée and Edmond Rousseau at Université Laval, to Matvei Aleshin at the University of Western Australia and to Agnico Eagle Mines Ltd. Staff for technical and scientific support.

References

Canfield D, Raiswell R, Westrich J, Reaves C, Berner R (1986) The use of chromium reduction in the analysis of reduced inorganic sulfur in sediments and shales. Chem. Geol. 54:149-155. https://doi.org/10.1016/0009-2541(86)90078-1,

Dubé B, Mercier-Langevin P (2020) Gold deposits of the Archean Abitibi Greenstone Belt, Canada. Geology of the World's Major Gold Deposits and Provinces. Soc. Econ. Geol. Special Publication 23. https://doi.org/10.5382/SP.23.32,

Goldfarb R.J, Pitcairn I (2023) Orogenic gold: is a genetic association with magmatism realistic? Miner. Depos. 58:5–35. https://doi.org/10.1007/s00126-022-01146-8,

LaFlamme C, Martin L, Jeon H, Reddy S.M, Selvaraja V, Caruso S et al. (2016) In situ multiple sulfur isotope analysis by SIMS of pyrite, chalcopyrite, pyrrhotite, and pentlandite to refine magmatic ore genetic models. Chem. Geol. 444:1-15. https://doi.org/10.1016/j.chemgeo.2016.09.032,

LaFlamme C, Sugiono D, Thébaud N, Caruso S, Fiorentini M, Selvaraja V, et al. (2018a) Multiple sulfur isotopes monitor fluid evolution of an Archean orogenic gold deposit. Geochim. Cosmochim. Acta 222:436-446. https://doi.org/10.1016/j.gca.2017.11.003,

LaFlamme C, Jamieson JW, Fiorentini ML, Thébaud N, Caruso S, Selvaraja V (2018b) Investigating sulfur pathways through the lithosphere by tracing mass independent fractionation of sulfur to the Lady Bountiful orogenic gold deposit, Yilgarn Craton. Gondwana Res. 58:27-38. https://doi.org/10.1016/j.gr.2018.02.005,

Lawley C.J.M, Creaser R.A, Jackson S, Yang Z, Davis B, Pehrsson S, Dubé B, Mercier-Langevin P, Vaillancourt D. (2015) Unraveling the Western Churchill Province Paleoproterozoic gold metallotect: constraints from Re-Os arsenopyrite and U-Pb xenotime geochronology and LA-ICP-MS arsenopyrite trace element chemistry at the BIF-hosted Meliadine gold district, Nunavut, Canada. Econ. Geol. 110:1425-1454. https://doi.org/10.2113/econgeo.110.6.1425,

Ohmoto H and Rye R.O (1979) Isotopes of sulfur and carbon, in Barnes, H.L., ed., Geochemistry of hydrothermal ore deposits, second edition. New York, John Wiley and Sons, Inc., pp. 509-567,

Robert RK, Poulsen KH, Cassidy KF, Hodgson CJ (2005) Gold metallogeny of the Superior and Yilgarn Cratons. Econ. Geol. 100th anniversary volume. https://doi.org/10.5382/AV100.30,

Siedenberg K, Strauss H, Hoffman E.J (2016) Multiple sulfur isotope signature of early Archean oceanic crust, Isua (SW-Greenland). Precambrian Res. 283:1-12 https://doi.org/10.1016/j.precamres.2016.07.002

St. Pierre B, Mercier-Langevin P, Blais J-C, Servelle G, Simard M, Côté-Mantha O, Malo M (2020) Structural controls and relative timing of gold mineralization of the banded iron formation associated Tiriganiaq deposit, Meliadine district, Rankin Inlet greenstone belt, Nunavut. Geol. Surv. Can. 8712:237-250. https://doi.org/10.4095/326041,

William-Jones A.E, Bowell R, Migdisov A (2009) Gold in Solution. Elements 5(5):281-287. http://dx.doi.org/10.2113/gselements.5.5.281.

Revisiting the Kundarkocha gold mine: A rare Paleoarchean greenstone-hosted gold deposit, eastern India

Dhruv Pathania[1], Rajarshi Chakravarti[1], Abdul Latheef T P[1]
[1]Department of Earth Sciences, Indian Institute of Technology, Roorkee, India

Abstract. The Kundarkocha mine is a rare example of a Paleoarchean greenstone-hosted gold deposit. The deposit is situated in the ~ 3.25 Ga (Ghosh et al. 2019) Gorumahisani-Badampahar greenstone belt in Singhbhum Craton of eastern India. Mining operations at Kundarkocha were put to a halt in 2018, owing to inefficient exploration strategies and subsequent low productivity. Gold mineralization at Kundarkocha is hosted predominantly within carbonaceous phyllites and graphitic schists. Native gold grains are recorded in the smoky quartz veins emplaced along the S_2 axial planar foliations and in close spatial association with syn-deformational hydrothermal pyrite, referred to as Pyrite-3 here. Occasionally, native gold occurrences are also noted along brittle-ductile deformed metamorphic pyrite (Pyrite-2). However, this second mode of occurrence is volumetrically less significant and was possibly sourced from pre-existing diagenetic pyrite (Pyrite-1) during metamorphism. Our new textural and mineralogical data reveals that the main gold mineralizing event was coeval with D_2 deformation (shearing) and is hosted in second or third-order brittle structures, possibly associated with a crustal-scale shear zone. Combining our new results with known tectono-thermal events in the area provides useful insights into the nature, controls, and possible timing of gold mineralization at the Kundarkocha.

1 Introduction

Neoarchean greenstone belts dated at ca. 2.8 – 2.5 Ga stand out as the most fertile environments for the formation of orogenic gold deposits. Thus, logically, it may be speculated that significant proportions of gold had already accumulated in the Earth's crust before 2.8 Ga, which was redistributed and concentrated to economic levels with the advent of plate tectonics in the Neoarchean (Frimmel 2018). However, before ~ 3 Ga, there is an apparent dearth of economic orogenic gold deposits, the reasons for which remain unclear. The study related to the gold mobility and possible Paleoarchean gold sink was published by Hoffmann et al. (2017) where the author put forward pervasive seafloor silicification, the rarity of black shales, and low gold content in the ultramafic rocks to be the potential causes behind the low mineralization potential of Paleoarchean greenstone belts for orogenic gold formation. To this end, here we investigate a rare Paleoarchean greenstone-hosted gold deposit, i.e., Kundarkocha, situated in the Singhbhum Craton in eastern India.

The Kundarkocha deposit is situated within the ~ 3.25 Ga Gorumahisani-Badampahar greenstone belt in the Singhbhum Craton. The mine was operated for a short span of 12 years, having an annual gold production of ~ 15 kg at an average grade of 3 g/ton (India Minerals Yearbook 2018), before being de-commissioned in 2018. Previous studies in the Kundarkocha deposit recognize a close spatial association of gold with pyrite, along second or third-order brittle-ductile structures (Hazarika et al. 2013; Sahoo and Venkatesh 2015). Those studies, however, provide contrasting views on the origin of gold at Kundarkocha, i.e., a sedimentary pyrite-hosted origin vs an arsenopyrite proto-ore possibly derived from the alteration of ultramafic rocks. Moreover, the paragenetic position of gold remains unclear. To this end, here we revisit the Kundarkocha mine and present detailed textural observations and mineralogical data, which enhance our understanding of the nature and control of gold mineralization at the Kundarkocha.

2 Geological setting

The current study area, i.e., the Kundarkocha deposit lies in the Gorumahisani-Badampahar greenstone belt (GBG) in the Singhbhum Craton. The arcuate GBG belt in eastern Singhbhum has two arms with curvilinear outcrops of volcano-sedimentary successions moulded against plutons of the Singhbhum granite batholith (Saha et al. 2021). The GBG is divided into lower and upper sequences, with the lower sequence comprising komatiite with the pillow to massive basalts with subordinate chemical sediments and the upper sequence consisting of mafic volcanic rocks overlain by clastic sediments (Saha et al. 2021). The region has undergone polyphase deformation with at least three phases that have been well documented (Ghosh et al. 2019). The first phase (D_1) led to the development of the regional isoclinal fold (F_1) plunging NNE. The second phase (D_2) caused extensive shearing and tight folding (F_2) plunging NE-SW with the development of S_2 foliation. The third phase (D_3) caused open folds (F_3) plunging NW.

2.1 Deposit Geology

Kundarkocha deposits belong to the lower sequence of the GBG and consist of basal altered ultramafic rocks and deformed ocelli pillow basalts overlain by green chert, massive black chert, carbonaceous phyllites, graphitic schists, Cr-bearing mica schists and talc-chlorite-serpentinite schists with abundant fuchsite (Jodder et al. 2021).

The major lithologies with which gold is associated are carbonaceous phyllites and graphitic schists. Gold bearing smoky quartz veins are present along the interface between the carbonaceous phyllites and chlorite-fuchsite-serpentine schist and are emplaced parallel to the axial planar foliations (Sahoo and Venkatesh 2015).

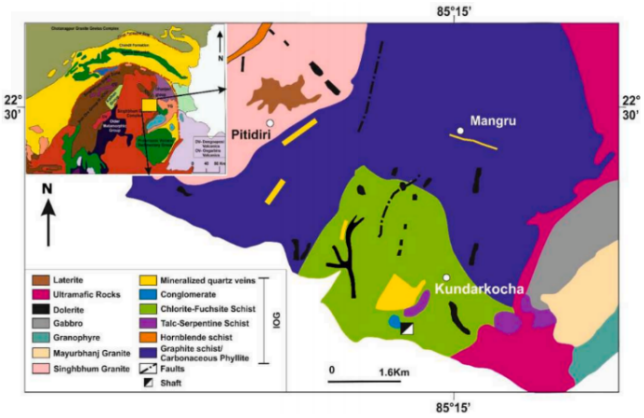

Figure 1. Geological map of Kundarkocha area (Modified after Banerjee and Thiagarajan 1965).

3 Pyrite morphology and paragenesis

Pyrite is the most ubiquitous sulfide in the studied samples and shows a close spatial association with gold. The following genetic varieties of pyrite have been identified based on textural analysis.

Diagenetic pyrite, containing numerous inclusions of aluminosilicates and carbonaceous material, is designated as Pyrite-I. These grains are rarely preserved and have been overprinted by metamorphic and hydrothermal pyrite. This pyrite variety often forms the core of late-stage pyrite.

Metamorphic pyrite containing inclusions of aluminosilicates and silicates, designated as Pyrite-2. It is coarse-grained showing rotation of inclusions and brittle-ductile deformation with secondary foliations cutting across (Figure 4. b), suggestive of its formation during early regional metamorphism.

Pyrite-3 is interpreted to be hydrothermal in nature and is represented by two morphological types, Pyrite-3a and Pyrite-3b. Pyrite-3a occurs as euhedral overgrowths around metamorphic Pyrite-2. Pyrite-3b occurs as fracture free subhedral to euhedral grains in the veins interacting with carbonaceous matter. Both Pyrite-3a and Pyrite-3b have formed during the emplacement of syn-deformational hydrothermal veins and contain inclusions of sphalerite, chalcopyrite, galena, and monazite.

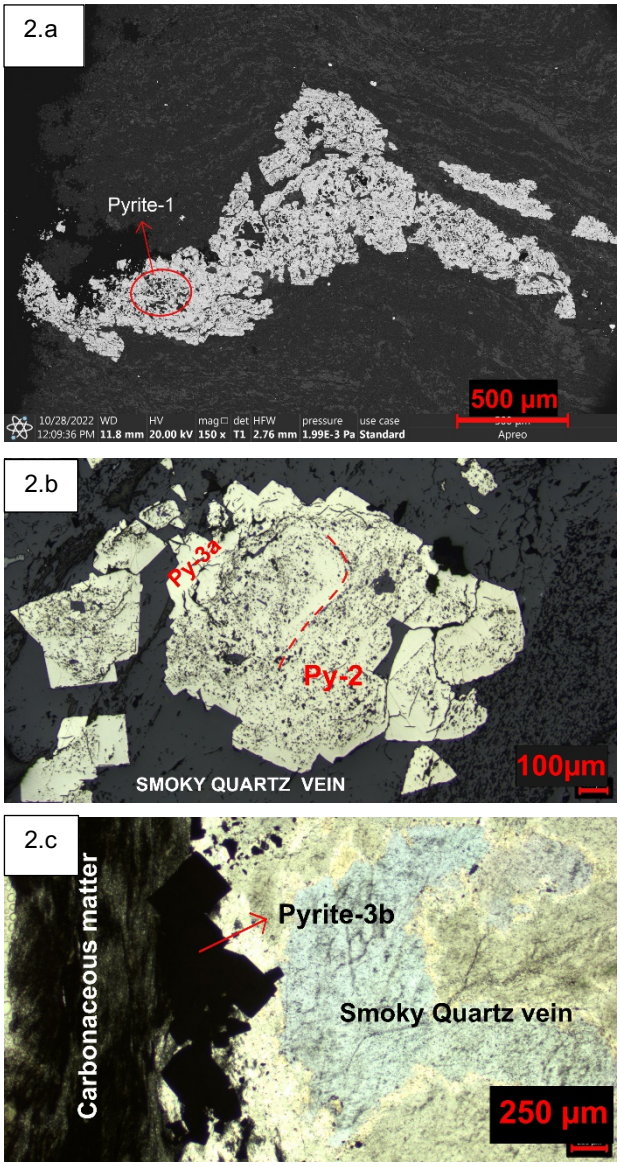

Figure 2. a SEM backscattered electron (BSE) image of folded and fractured metamorphic Pyrite-2 with the inclusion rich core of diagenetic Pyrite-1 (marked by the red circle). **b** Reflected light petrographic image of Pyrite-2 which is of metamorphic nature (rotated inclusions marked by a curved red line) indicating syn-metamorphic nature with overgrowth of hydrothermal Pyrite-3a. **c** Transmitted light petrographic image of Pyrite-3b forming along interaction between the carbonaceous matter and smoky quartz veins.

4 Nature of gold mineralization

Gold mineralization at Kundarkocha exhibits structural as well as lithological control. Our study reveals two modes of occurrence of gold. Native gold on euhedral overgrowths around metamorphic Pyrite-2 and gold mineralization in dilatational smoky quartz veins in spatial association with carbonaceous matter. The latter mode of occurrence, however, is more abundant throughout the deposit. These Au-bearing smoky quartz veins have been sheared and emplaced parallel to the foliation planes (S_2) along the axial planar folds and

show bulging recrystallization texture indicating the depth of emplacement to be 10-15 km which is the characteristic depth of brittle-ductile transition zone.

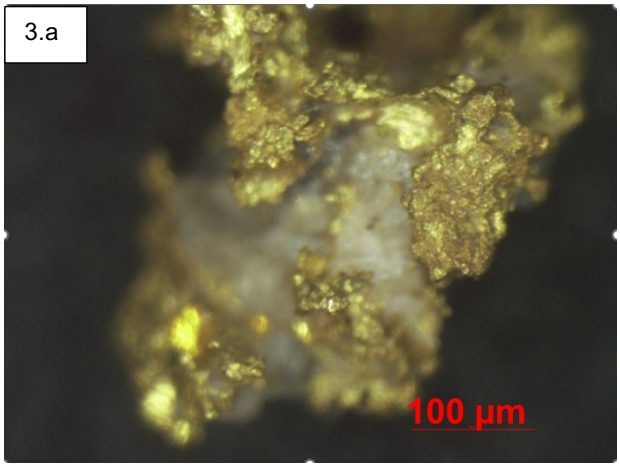

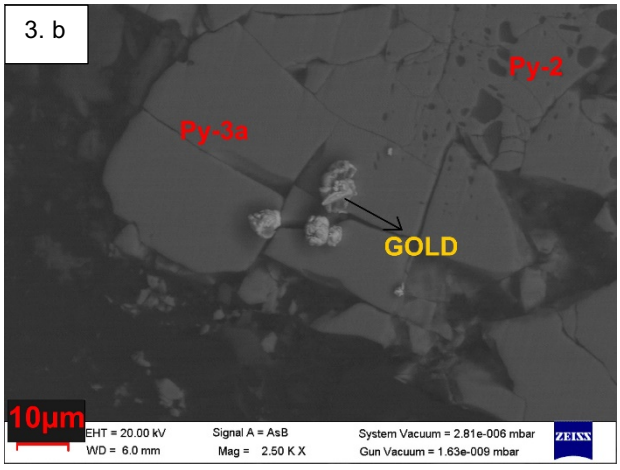

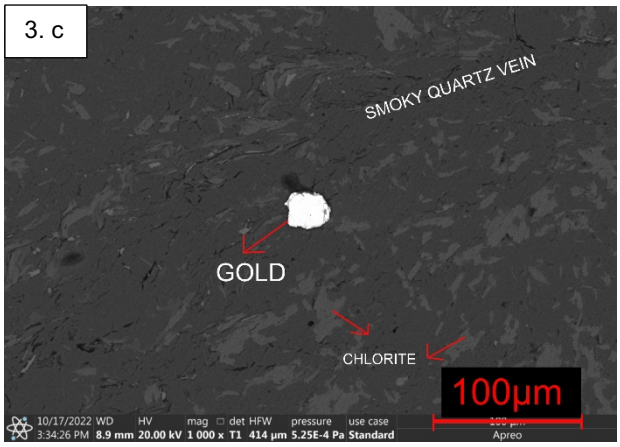

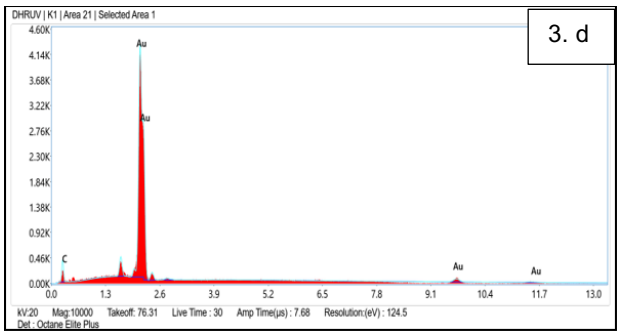

Figure 3. a Stereomicroscopic image of gold in association with the smoky quartz vein. **b** SEM (BSE) image of gold on the euhedral edges of metamorphic Pyrite-2 (inclusion rich). **c** SEM (BSE) image of native gold grain encountered in the carbonaceous phyllites intruded by smoky quartz vein. **d** Representative peak of gold grain obtained from SEM-EDS analysis.

5 Discussion and conclusion

Microstructures encountered in the petrographic study indicate atleast two phases of deformation in the Kundarkocha area (Figure 4. a). The auriferous smoky quartz veins are shear-controlled and emplaced parallel to the S_2 axial foliation planes. The S_2 foliations cut across the folded and fractured metamorphic Pyrite-2 (Figure 4. b). Native gold grains are encountered at the hinge of axial planar microfolds formed during D_2 deformation in close association with these Pyrite-2 grains (Figure 4. c). Hence, it can be deduced that the D_2 deformation event not only led to the emplacement of auriferous smoky quartz veins along S_2 axial foliations but also aided in the mobilization of gold from earlier generation pyrite. The gold grains encountered at the euhedral edges of Pyrite-2 are the remnant grains left over during the process.

The gold mineralization as already discussed, is associated with the smoky quartz veins paralleling the axial planar foliations (S_2). The close association of gold with carbonaceous rocks indicates the possible destabilization of the gold-ligand complex by carbon-induced Eh change. The occurrence of native gold grains showing close spatial association to pyrite and within the fractures in euhedral edges overgrowing metamorphic Pyrite-2 indicate possible mobilization of the lattice-bound gold from diagenetic Pyrite-1during subsequent progressive deformation and hydrothermal events (Figure 3. b).

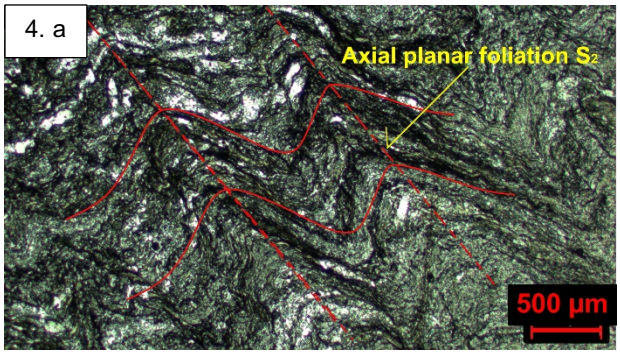

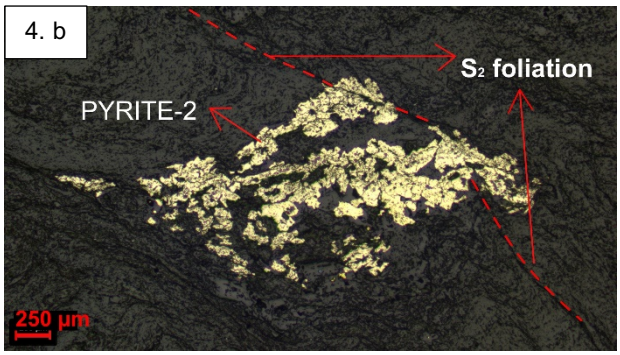

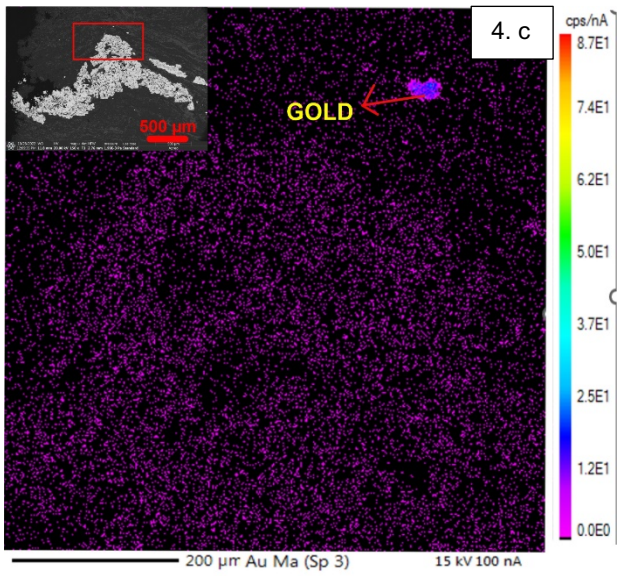

Figure 4. a Transmitted light petrographic image of carbonaceous phyllite indicating atleast two stages of deformation (S_2 foliation marked by the dotted straight red line). **b** Reflected light petrographic image of metamorphic Pyrite-2 cut by S_2 foliation (marked by the dotted curved red line). **c** X-ray elemental map of pyrite-2 for Au, showing gold grain at the hinge of the fold (top left is the SEM (BSE) image of Pyrite-2 with a red box indicating the area of analysis)

The mineralization event and the occurrence of gold either in association with pyrite or with smoky quartz veins can be summarised by the following steps:

1. Regional progressive deformation D_1, at ~ 3.3 Ga to 3.25 Ga (Saha et al. 2021) led to the folding and metamorphism of the host rock. Diagenetic Pyrite-1 present got metamorphosed and underwent ductile deformation producing metamorphic Pyrite-2.
2. D_2 deformation event, at ~ 3.1 Ga to 3.0 Ga (Saha et al. 2021) is related to the shearing event that led to the emplacement of gold-bearing smoky quartz veins along the secondary foliations. This deformation event led to the fracturing of the metamorphic Pyrite-2 (Figure 2. a, Figure 4. b). During this event, late-stage hydrothermal fluids overprinted the metamorphic pyrite and also precipitated individual grains of Pyrite-3b (Figure 2. b, Figure 2. c). This event led to the mobilization and concentration of gold in the form of native gold grains in close vicinity to Pyrite-2 along structurally favourable sites (Figure 4. c).

The source of gold at Kundarkocha, however, remains debatable. Gold could have been sourced from diagenetic pyrite hosted in the protolith of the carbonaceous phyllites, i.e., black shales. However, given the Paleoarchean age, organic-rich black shales were possibly volumetrically insignificant as a gold source, which could explain the small deposit size of Kundarkocha. Alternatively, sub-seafloor hydrothermal alteration of the mafic-ultramafic rocks of the lower GBG belt could have also led to the mobilization and precipitation of Au in structurally and chemically favourable sites. To this effect, this study also highlights the importance of industry-academia collaboration in India for better understanding and effective exploration of mineral deposits.

Acknowledgements

Authors are thankful to director, IIT Roorkee for necessary permissions to carry out the work. IIC, IIT Roorkee is thanked for SEM-EDS analysis. Manmohan minerals private limited is thanked for providing the samples for this work. Prof. Sajeev Krishnan, IISC Bangalore is thanked for help with EPMA analysis. Dr. Rohit Pandey, BHU Varanasi is thanked for help with the X-ray elemental mapping of the sulphides. RC acknowledges a Faculty Initiation Grant (FIG 100930), for funding the research work.

References

Frimmel HE (2018) Episodic concentration of gold to ore grade through Earth's history. Earth-Science Reviews 180:148-158

Ghosh R, Vermeesch P, Gain D, Mondal R, (2019). Genetic relationship among komatiites and associated basalts in the Badampahar greenstone belt (3.25–3.10 Ga), Singhbhum Craton, Eastern India. Precambrian Research 327:196–211

Hazarika P, Mishra M, Chinnasamy SS, Bernhardt (2013) Multi-stage growth and invisible gold distribution in pyrite from the Kundarkocha sediment-hosted gold deposit, eastern India. Ore Geology Reviews 55:134-145

Hofmann A, Pitcairn I, Wilson A (2017) Gold mobility during Paleoarchean submarine alteration. Earth and Planetary Science Letters 462:47-54

Indian Minerals Yearbook 2018 (2019). In: Part-I General Reviews Indian Bureau of Mines 57:1-8

Jodder J, Hofmann A, Ueckermann H (2021) 3.51 Ga old felsic volcanic rocks and carbonaceous cherts from the Gorumahisani Greenstone Belt – Insights into the Palaeoarchaean record of the Singhbhum Craton, India. Precambrian Research 357:106109

Sahoo PR, Venkatesh AS (2014) 'Indicator' carbonaceous phyllite/graphitic schist in the Archean Kundarkocha gold deposit, Singhbhum orogenic belt, eastern India: Implications for gold mineralization vis-à-vis organic matter. Journal of Earth System Science 123 (7):1693-1703

Sahoo PR, Venkatesh AS (2015) Constrains of mineralogical characterisation of gold ore: Implications for genesis, controls and evolution of gold from Kundarkocha gold deposit, eastern India. Journal of Asian Earth Sciences 97:136-149

Saha D, Bachhar P, Deb GK, Deb SP, Banerjee A (2021) Tectonic evolution of the Paleoarchean to Mesoarchean Badampahar-Gorumahisani belt, Singhbhum Craton, India- Implications for coexisting arc and plume signatures in a granite-greenstone terrain. Precambrian Research 357:106094

Singh S, Chakravarti R, Barla A, Behera RC, Neogi S (2021) A holistic approach on the gold metallogeny of the Singhbhum crustal province: Implications from tectono-metamorphic events during the Archean-Proterozoic regime. Precambrian Research 365:106376

Record of the oldest vein-type gold mineralization throughout the Neoproterozoic Nubian shield: the Galat Sufar South gold deposit, NE Sudan

Julien Perret[1,2,3], Aurélien Eglinger[2], Anne-Sylvie André-Mayer[2], Julien Feneyrol[3], Jérôme Ganne[4], Marc Poujol[5]
[1]present address: Centre for Exploration Targeting, School of Earth Sciences, University of Western Australia, 35 Stirling Highway, Crawley, WA 6009, Australia
[2]GeoRessources, Université de Lorraine, CNRS, 54000 Nancy, France
[3]Arethuse Geology SARL, 29 Allée St Jean, ZAC La Barque, 13170 Fuveau, France
[4]IRD, UR234, GET, Université Toulouse III, 14 Avenue Edouard Belin, 31400 Toulouse, France
[5]Géosciences Rennes, UMR CNRS 6118, OSUR, Université Rennes 1, 35042 Rennes Cedex, France

Abstract. Despite the booming interest in Nubian shield for gold exploration, much more remains to be done to constrain geodynamical settings favorable for gold mineralization in a mineral system approach. Constraining pressure-temperature-timing-deformation (*P-T-t-d*) conditions relative to the formation of the structurally controlled Galat Sufar South (GSS) deposit is a case in point and represents a step forward in the understanding of the Pan-African gold mineral system along the westernmost Atmur-Delgo suture. The formation of the GSS gold deposit, hosted in an arc-related volcanosedimentary sequence metamorphosed and deformed by sheath folding, occurred at 738±16 Ma (*in situ* laser ablation inductively coupled plasma mass spectrometry (LA-ICP-MS) U-Pb dating of hydrothermal apatite coeval to gold mineralization). Additional chlorite-phengite-quartz-water multi-equilibria calculations in ore-hosting meta-volcanosediments suggest that the gold event occurred under lower amphibolite facies conditions (~7.2 kbar - 420 °C), probably during the tectonic accretion of the sedimentary wedge formed during Atmur-Delgo intra-oceanic subduction. To date, the GSS deposit is the oldest lode gold occurrence documented throughout the Nubian shield and the only one formed at regional peak metamorphism conditions in such a setting.

1 Geological setting

The Galat Sufar South (GSS) gold deposit (indicated resources of 75.6 Mt @ 1.27 g/t Au for a total of 3.08 Moz Au with a 0.6 g/t Au cut-off; Duckworth 2020) lies in NE Sudan, within the western portion of the Neoproterozoic Arabian–Nubian shield (ANS). The ANS belongs to the East-African-Antarctica orogen and results from the tectonic accretion and collision between terranes that accreted onto the Saharan meta-craton during a ~850–550 Ma 'Supercontinent Cycle', (*e.g.,* Johnson et al. 2011; Fritz et al. 2013).

GSS is encompassed within a complexly deformed zone at the junction between the Atmur–Delgo and Keraf sutures, both structures hosting gold occurrences (Johnson et al. 2017; Perret et al. 2020; Gaboury et al. 2020; Perret et al. 2021a). The mineralization is hosted by a strongly deformed meta-volcanosedimentary unit enclosed within interleaved lava flows, pyroclastic horizons and primary volcanic breccia (Perret et al. 2020). This assemblage is surrounded by meta-pelites interlayered with marbles.

The deposit-scale structural framework is dominated by a high-strain ductile D_{2GSS} deformation stage, expressed by the main penetrative L_2 stretching lineation and S_2 penetrative fabric throughout the GSS area (Perret et al. 2020). These structures are contemporaneous to gold mineralization and control the ore-shoot geometry from the hundreds of kilometers up to the micrometer scales (Perret et al. 2021b). They likely relate to Atmur-Delgo suturing, *i.e.*, intra-oceanic subduction and arc-continent collision (Perret et al. 2020).

2 Sampling and analytical techniques

2.1 Sampling

The studied samples are part of the ore-bearing meta-volcanosedimentary sequence dominating the local lithological framework. The two samples analysed in this study (GS-55-02 and -04) have been collected along a diamond drill core crosscutting the GSS ore zone.

2.2 U-Pb dating of apatite

Prior to dating, apatite grains were imaged by cathodoluminescence at the GeoRessources laboratory (Université de Lorraine-CNRS, Nancy, France). *In situ* LA-ICP-MS U-Pb dating on apatite was conducted at Géosciences Rennes (Université de Rennes-CNRS, France).

2.3 Chlorite-phengite-quartz-water multi-equilibria calculations

The D_{2GSS}-related GSS mineral assemblage displays textural association between chlorite - a geothermometer -, phengite - a geobarometer - and quartz. Inferring geochemical equilibria between these mineral phases enables to carry out multi-equilibria calculations (*e.g.,* Vidal and Parra 2000), following the procedure detailed in Ganne et al. (2012). Calculations are completed from electron microprobe analyses (EMPA) of coexisting chlorite and phengite coeval to gold mineralization, carried out at the GeoRessources laboratory (Université de Lorraine-CNRS, Nancy, France).

3 Results

3.1 Petrography

Chlorite, phengite and quartz form most of the mineralizing D_{2GSS} deformation stage-related silicate mineral assemblage in the ore-bearing tuffaceous horizon (Fig. 1; Perret et al. 2020).

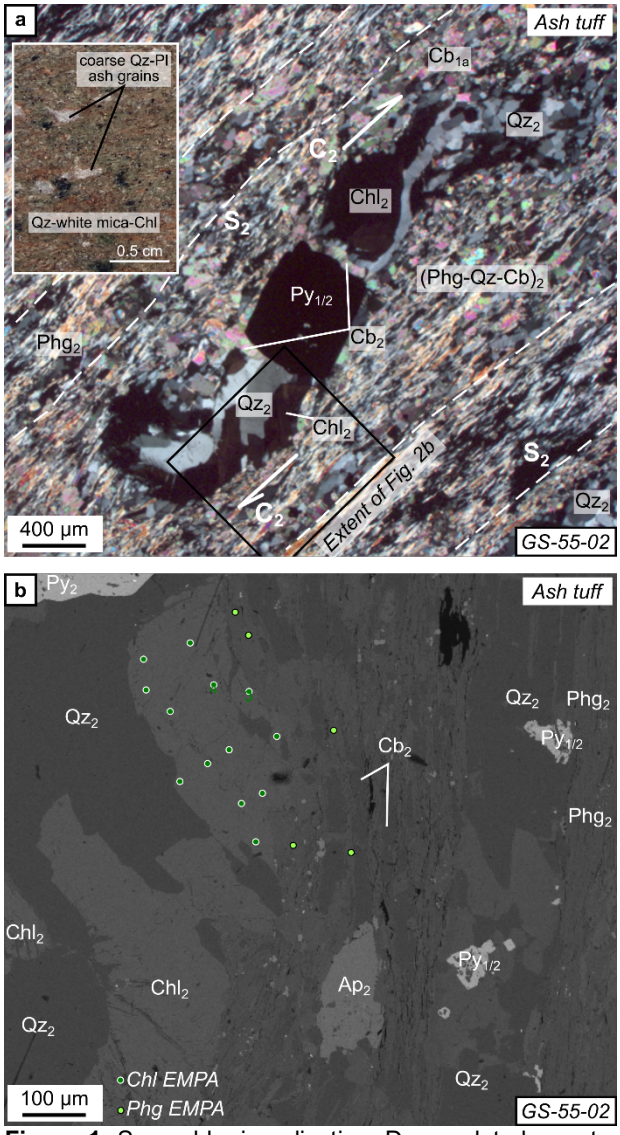

Figure 1. Syn-gold mineralization, D_{2GSS}-related, quartz-chlorite-phengite-apatite-pyrite mineral assemblage in ash tuffs**. a** D_{2GSS}-related quartz-chlorite asymmetrical strain fringes formed around $Py_{1/2}$ grains in the phengite-dominated schistose mineral gangue (cross-polarized, transmitted light). **b** Chlorite-phengite-apatite textural association and position of EMPA dataspots (BSE-SEM)

These mineral phases are in textural equilibrium (i) in the mineral gangue and (ii) between quartz-chlorite strain fringes around ore-related pyrite grains and the surrounding phengite-dominated matrix (Fig. 1a). Besides, apatite forms up to 500 µm-long, subhedral grains intergrown and elongated in the phengite-chlorite mineral gangue affected by the S_2 fabric in these pyroclastics (Fig. 1b). Scarcer apatite also consists of mineral inclusions in altered pyrite cores where overgrown by a mineral inclusion-free pyrite rim.

3.2 U-Pb dating of apatite

Dated apatite typically shows a rounded bright core and a large subhedral darker rim overgrown by a late, thin and brighter apatite external rim. Apatite rims are almost not radiogenic (<1.1 ppm U except for two datapoints with 2.5 and 2.7 ppm U) whereas cores are slightly U-enriched (~1.5-6.5 ppm U) but U/Th ratio is almost systematically <1.

Despite their low radiogenic content, plotting U-Pb isotopic compositions of apatite in a Tera-Wasserburg diagram enables to draw a *Discordia* line with a lower intercept at 738±16 Ma (*n*=76 on thirty grains, MSWD=1.2, Fig. 2). The 738±16 Ma date is considered as a reliable hydrothermal crystallization age as the initial $^{207}Pb/^{206}Pb$ value obtained is ~0.88, which is close to the expected common Pb ratio at this age following the Pb evolution model of Stacey and Kramers (1975).

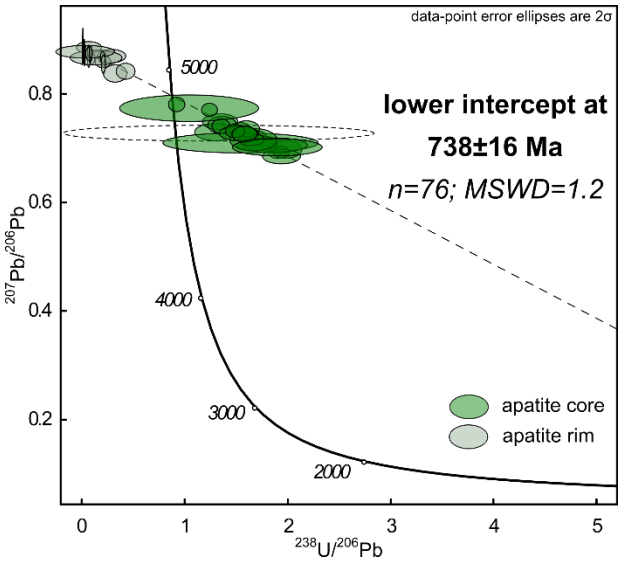

Figure 2. Tera-Wasserburg diagram for U-Pb dating of apatite coeval to Galat Sufar South gold mineralization produced using the Isoplot program

3.3 Chlorite-phengite-quartz-water multi-equilibria calculations

Approximately half of chlorite compositions measured involve elemental exchanges between the (Fe, Mg)-amesite-sudoite-(clinochore-daphnite) end-members. Phengite compositions are mostly muscovite- and celadonite-enriched although some datapoints are up to 20% pyrophyllite-rich where celadonite proportion is below 10%. Both chlorite and phengite compositions highlight the predominance of the Tschermak substitution ($Al^{VI}Al^{IV} \leftrightarrow (Fe^{2+},Mg)^{VI}Si^{IV}$) with little contribution of the pyrophyllitic substitution ($K^{XII}Al^{IV} \leftrightarrow \square^{XII}Si^{IV}$ where $\square^{XII}$ represents a vacancy in the A1 site of a white mica) for phengite.

Prior to multi-equilibria calculations, data were filtered on the basis of the compositional criteria

detailed in Vidal and Parra (2000). Eighteen out of forty-one chlorite analyses and one out of forty-five phengite analyses were removed from the original dataset. Multi-equilibria calculations then lead to consider multiple *P-T* couples associated to a $\sqrt{\Sigma\Delta G^2}$ free Gibbs energy. If several *P-T* equilibria are calculated from a given phengite composition and distinct chlorite compositions, they are classified as redundant, except for the one associated to the lower $\sqrt{\Sigma\Delta G^2}$ value, *i.e.*, the non-redundant equilibrium.

The statistical processing of calculated equilibria demonstrates the existence of two stability gaps, *i.e., P-T* windows where equilibria with relatively low $\sqrt{\Sigma\Delta G^2}$ are clustered: ~2.6 kbar - 330°C and ~7.2 kbar - 420 °C (Fig. 3).

4 Discussion

4.1. Timing of the Galat Sufar South gold mineralization

The GSS petrographic-structural model suggests that (i) the pervasive chlorite-phengite mineral gangue, (ii) the main penetrative fabric, (iii) dissolution-reprecipitation of pyrite and (iv) core-hosted mineral inclusions all relate to the deformation stage when the economic gold mineralization occurred (Perret et al. 2020, 2021b). As apatite either occurs as intergrown with chlorite and phengite or as mineral inclusion in pyrite cores, it leads to infer that it likely records the main gold event forming the GSS deposit. The obtained 738±16 Ma date is therefore interpreted as the age of D_{2GSS} deformation and concomitant GSS gold mineralization. The obtained age is consistent with the timing of intra-oceanic subduction initiating Atmur-Delgo suturing (~750-650 Ma; Harms et al. 1994), in agreement with the mineralization timing inferred from tectonic-mineralization relationships (Perret et al. 2020, 2021b).

Despite the apparent spatial relationship between the GSS deposit and the Keraf shear zone, dating of the GSS gold deposit confirms that it is not genetically associated to late orogenic Keraf strike-slip shearing (~650-550 Ma; Abdelsalam et al. 1998; Bailo et al. 2003; Perret 2021). GSS should therefore not be interpreted as orogenic gold *sensu stricto* anymore (*e.g.,* Johnson et al. 2017) as it rather relates to early Atmur-Delgo suturing, as previously inferred (Perret et al. 2020).

4.2. Geodynamical setting associated to the Galat Sufar South gold mineralization

On one hand, the syn-D_{2GSS} chlorite-phengite-quartz assemblage records ~7.2 kbar - 420 °C stability conditions corresponding to lower amphibolite facies conditions. Such conditions, corresponding to regional peak metamorphism (Johnson et al. 2011; Fritz et al. 2013) are interpreted as the mineral assemblage crystallization conditions, *i.e.,* related to the D_{2GSS} deformation stage and concomitant GSS gold mineralization, for several reasons.

First, they are consistent with the trace element evolution pattern in pyrite observed at the GSS deposit, indicative of syn-gold mineralization pyrite recrystallization under amphibolite facies metamorphism (Perret et al. 2021b). Second, the obtained *P-T* constraints are in line with the structural patterns observed throughout the studied area, *e.g.*, sheath folding and non-coaxial ductile flow of pyroclastics and marbles (Perret et al. 2020). We thus suggest that the ore-related mineral gangue recorded lower amphibolite facies conditions coeval to gold mineralization and consistent with regional-scale deformation regime. Last but not least, mineralization likely occurred within the sedimentary wedge formed during Atmur-Delgo intra-oceanic subduction, supported by the record of comparable *P-T* conditions in wedges at accretionary-type subduction settings (Guillot et al. 2009).

On the other hand, the *P-T* field of stability at ~2.6 kbar - 330°C corresponds to the most stable calculated thermodynamic equilibria with $\sqrt{\sum\Delta G^2}$<500 J. It more likely relates to resetting of the chlorite-phengite-quartz compositions and greenschist-facies retrograde metamorphism during exhumation of rocks within the sedimentary wedge.

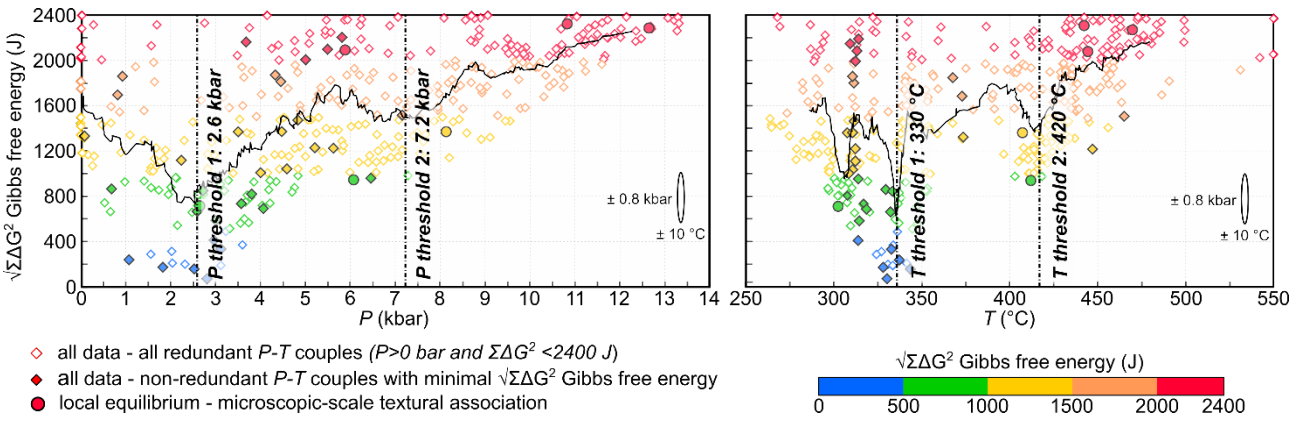

Figure 3. Statistical processing of *P-T* conditions estimated from chlorite-phengite-quartz-water multi-equilibria calculations for the syn-gold mineralization D_{2GSS} deformation stage at the Galat Sufar South deposit. *P* (left) and *T* (right) are sorted by increasing values and plotted against $\sqrt{\Sigma\Delta G^2}$ Gibbs free energy. The black line gives the Gibbs free energy running mean over 21 points

4.3. Insights into the Pan-African gold mineral system in the Nubian shield

The synchronism between Atmur-Delgo intra-oceanic subduction and GSS gold mineralization suggests that mineralizing fluids may be derived from prograde to peak metamorphism devolatilization during early Atmur-Delgo suturing. The timing of the mineralizing event (738±16 Ma) thus strongly differs from the typical ~650-600 Ma age of late tectonic, crustal shear zone-hosted, orogenic and intrusion-related gold deposits described throughout the Arabian-Nubian shield, formed under retrograde greenschist facies metamorphic conditions (*e.g.,* Zoheir et al. 2019).

To date, the new *P-T-t-d* constraints on GSS gold mineralization make it (i) the oldest lode gold occurrence documented throughout the Nubian shield and (ii) the only one to occur at regional peak metamorphism conditions at a intra-oceanic subduction site. In terms of timing, the tectonic accretion-related GSS therefore formed in a similar geodynamical setting as porphyry copper deposits described in the Nubian shield (*e.g.,* Bierlein et al. 2020). It is thus strongly disconnected from late collisional orogenic gold *sensu stricto*. The GSS gold deposit therefore brings critical insights into the understanding of the Pan-African gold mineral system of the Nubian shield as it exemplifies the existence of syn-tectonic accretion lode gold mineralization in the region.

5 Conclusions

The Galat Sufar South gold deposit formed at 738±16 Ma (*in situ* LA-ICP-MS U-Pb dating of hydrothermal apatite coeval to mineralization) under ~7.2 kbar - 420 °C lower amphibolite facies conditions (syn-mineralization chlorite-phengite-quartz-water multi-equilibria calculations). In agreement with the nature of host rocks and deformation style already documented, these data support that the Galat Sufar South mineralization occurred within the sedimentary wedge formed during Atmur-Delgo intra-oceanic subduction, rather than during late tectonic Keraf strike-slip shearing as previously thought. The GSS deposit is (i) the oldest lode gold occurrence documented throughout the Nubian shield to date and (ii) the first evidence of lode gold mineralization related to tectonic accretion and formed under regional peak metamorphism conditions in the province.

Acknowledgements

The authors are grateful to Orca Gold Inc., which used to operate the GSS deposit back in 2019-2020 when we conducted field work, for its welcome on site and its substantial logistical support. This work is part of Julien Perret's PhD project which benefited of a CIFRE funding, reference CIFRE N°2017/1737, attributed by the French National Research and Technology Agency (ANRT).

References

Abdelsalam MG, Stern RJ, Copeland P, et al (1998) The Neoproterozoic Keraf Suture in Ne Sudan: Sinistral Transpression Along the Eastern Margin of West Gondwana. J Geol 106:133–148.

Bailo T, Schandelmeier H, Franz G, et al (2003) Plutonic and metamorphic rocks from the Keraf Suture (NE Sudan): a glimpse of Neoproterozoic tectonic evolution on the NE margin of W. Gondwana. Precambrian Res 123:67–80

Bierlein FP, Potma W, Cernuschi F, et al (2020) New Insights into the Evolution and Age of the Neoproterozoic Jebel Ohier Porphyry Copper Deposit, Red Sea Hills, Northeastern Sudan. Econ Geol 115:1–31.

Duckworth G (2020) Feasibility study - NI 43-101 TECHNICAL REPORT - Block 14 gold project. Lycopodium Minerals Pty Ltd

Fritz H, Abdelsalam M, Ali KA, et al (2013) Orogen styles in the East African Orogen: A review of the Neoproterozoic to Cambrian tectonic evolution. J Afr Earth Sci 86:65–106.

Gaboury D, Nabil H, Ennaciri A, Maacha L (2020) Structural setting and fluid composition of gold mineralization along the central segment of the Keraf suture, Neoproterozoic Nubian Shield, Sudan: implications for the source of gold. Int Geol Rev 1–27.

Ganne J, De Andrade V, Weinberg RF, et al (2012) Modern-style plate subduction preserved in the Palaeoproterozoic West African craton. Nat Geosci 5:60–65.

Guillot S, Hattori K, Agard P, et al (2009) Exhumation Processes in Oceanic and Continental Subduction Contexts: A Review. In: Lallemand S, Funiciello F (eds) Subduction Zone Geodynamics. Springer Berlin Heidelberg, Berlin, Heidelberg, pp 175–205

Harms U, Darbyshire DPF, Denkler T, et al (1994) Evolution of the Neoproterozoic Delgo suture zone and crustal growth in northern Sudan: geochemical and radiogenic isotope constraints. Geol Rundsch 83:591–603

Johnson PR, Andresen A, Collins AS, et al (2011) Late Cryogenian–Ediacaran history of the Arabian–Nubian Shield: A review of depositional, plutonic, structural, and tectonic events in the closing stages of the northern East African Orogen. J Afr Earth Sci 61:167–232.

Johnson PR, Zoheir BA, Ghebreab W, et al (2017) Gold-bearing volcanogenic massive sulfides and orogenic-gold deposits in the Nubian Shield. South Afr J Geol 120:63–76

Perret J (2021) Répartition spatio-temporelle du système métallogénique de l'or panafricain au sein du bouclier arabo-nubien: étude multiscalaire le long de la suture de Keraf (Soudan). PhD Thesis, Université de Lorraine

Perret J, André-Mayer A-S, Eglinger A, et al (2021a) Structural and geochemical ore-forming processes in deformed gold deposits: towards a multi-scale and -method approach. Geol Soc Lond Spec Publ SP516-2021–37.

Perret J, Eglinger A, André-Mayer A-S, et al (2020) Subvertical, linear and progressive deformation related to gold mineralization at the Galat Sufar South deposit, Nubian Shield, NE Sudan. J Struct Geol 135:.

Perret J, Feneyrol J, Eglinger A, et al (2021b) Tectonic record and gold mineralization in the central part of the Neoproterozoic Keraf suture, Gabgaba district, NE Sudan. J Afr Earth Sci 181:104248.

Stacey J t, Kramers 1JD (1975) Approximation of terrestrial lead isotope evolution by a two-stage model. Earth Planet Sci Lett 26:207–221

Vidal O, Parra T (2000) Exhumation paths of high-pressure metapelites obtained from local equilibria for chlorite-phengite assemblages. Geol J 35:139–161.

Zoheir B, Emam A, Soliman N, Holzheid A (2019) Gold Metallogeny of the Egyptian South Eastern Desert. In: Doronzo D, Schingaro E, Armstrong-Altrin Z, Zoheir B (eds) Petrogenesis and Exploration of the Earth's Interior. Springer Berlin Heidelberg, Berlin, Heidelberg, pp 261–263

Mineralogical controls on the generation of gold-rich metamorphic fluids

Iain Pitcairn[1], Thomas Zack[2], Georges Beaudoin[3], Carl Guilmette[3]
[1]*Department of Geological Sciences, Stockholm University, Stockholm Sweden*
[2]*Department of Earth Sciences, University of Gothenburg, Gothenburg, Sweden*
[3] *Département de géologie et de génie géologique, Université Laval, Québec, Canada*

Abstract. Gold becomes enriched in metamorphic fluids produced by chlorite breakdown through liberation during transition of pyrite (Py) to pyrrhotite (Po). However, in some terranes the metamorphic window where the Py to Po transition occurs doesn't match the window of metamorphic fluid production. We describe the sulfide mineral evolution in metasedimentary rocks from the Pontiac subprovince, Abitibi Greenstone Belt, Canada. Samples from the biotite and garnet zones are particularly interesting as they have undergone the transition from Py to Po but still have high whole rock Au and H2O content. We have identified 3 potential occurrences of Au in these samples; within cobaltite and rarely other sulfides, as micro or nano scale particles along sulfide and silicate grain boundaries and within the background silicate minerals. The micro or nano scale Au particles were identified through LA-ICP-MS line scans across samples where Au peaks do not coincide with sulfide minerals. Gold particles along grain boundaries would very easily become dissolved in metamorphic fluids and this set of mineral changes may be an important control on the production of strongly Au enriched metamorphic fluids.

1 Introduction

A critical step in the development of world-class orogenic gold terranes is the generation of gold-rich metamorphic fluids. The model for the enrichment of gold in metamorphic fluids is through the release of gold during the transition of pyrite (Py) to pyrrhotite (Po) during prograde metamorphism in the presence of metamorphic fluid produced dominantly by the breakdown of chlorite (Pitcairn et al. 2006; Large et al. 2007; Tomkins 2010). Maximising the gold enrichment in the metamorphic fluid requires 1) that the metamorphic window of fluid production matches that of the Py-Po transition, 2) that the gold released by the Py-Po transition is easily available for dissolution within the fluid and 3) that the fluid has the appropriate composition to take the gold into solution. Tomkins (2010) suggests that chlorite breakdown drives the Py-Po transition as increased H_2S is required to maintain equilibrium fluid conditions as H_2O is released from chlorite.

In a number of metamorphic belts however, it is clear that the window of metamorphic fluid release does not always perfectly match the timing of gold mobility from the rock or the window of the Py-Po transition. In the Otago and Alpine Schists in New Zealand for example, whole-rock gold concentrations decrease between 300°C and 550°C whereas the main temperature of fluid release is 500°C to 550°C (Pitcairn et al. 2006). Another example is the Pontiac metasedimentary rocks from the Abitibi Greenstone Belt, Canada. Here the gold mobility occurs between biotite and staurolite zones equivalent to between 450°C and 550°C, which matches the window of metamorphic fluid release (Pitcairn et al. 2021). However, the Py-Po transition is more diffuse with both Py and Po occurring in some samples from chlorite to the sillimanite zones. Of particular interest are samples from the biotite and garnet zones that contain high whole-rock gold contents and abundant chlorite yet the dominant sulfide is Po. If the Py-Po transition is driven by fluid released from breakdown of chlorite then these Po bearing rocks should have no chlorite and depleted gold concentrations. It is clear on a local-scale at least, that there are more factors involved in the release of gold from pyrite during metamorphism.

In this study we present in-situ analyses of sulfide minerals from the Pontiac metasedimentary rocks, Abitibi Greenstone Belt, Canada. We focus specifically on samples from the biotite and garnet zones that have yet to lose their gold during metamorphic dewatering as these samples provide a window into the mineral processes involved in removal of the gold from pyrite.

2 Geological Setting

The Abitibi belt is the world's most well mineralised Archean greenstone belts with a total gold endowment of over 9000t (Dubé and Mercier-Langevin, 2020). The belt comprises E-W trending successions of metamorphosed volcano-sedimentary rocks deposited 2795 to 2669 Ma (Ayer et al., 2002; Daigneault et al., 2002; Thurston et al., 2008) with intervening bodies of intrusive rock. Linear belts of sedimentary rocks including graywacke- and mudstone-dominated turbidites are spatially associated with major fault zones such as the Porcupine-Destor fault zone and the Larder Lake–Cadillac fault zone. Metamorphism in the southern Abitibi occurred between 2669 ± 1 Ma and 2643 ± 4 Ma (Dubé and Mercier Langevin, 2020).

The orogenic gold deposits of the Abitibi belt occur as arrays of quartz-carbonate veins containing native gold and enrichments in As and Sb ± W, Se, Te, Bi, and Mo (Robert et al., 2005; Dubé and Mercier-Langevin, 2020). Orogenic gold deposits of the southern Abitibi belt and northern Pontiac subprovince formed between ca. 2670 and 2640 ± 10 Ma, with the bulk of deposits formed during the D3 deformational event between 2660 and 2640 Ma (Dubé and Mercier Langevin, 2020).

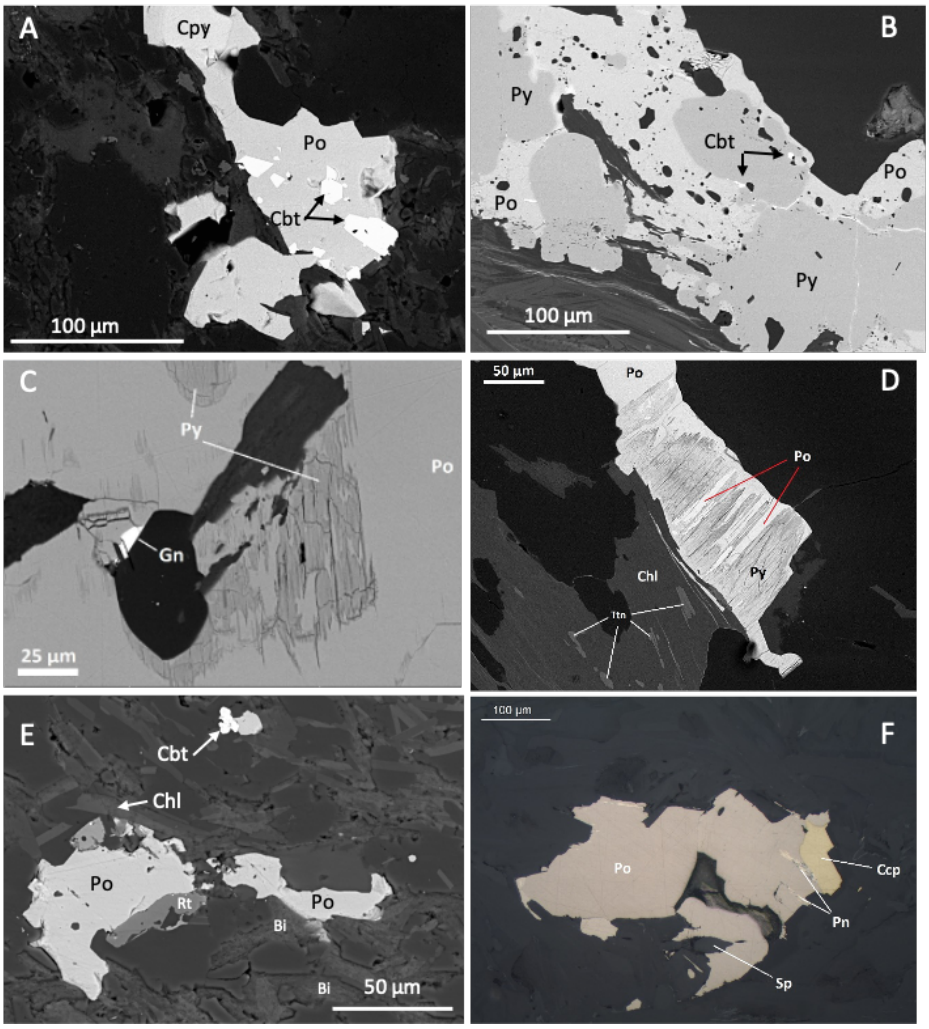

Figure 20. Electron backscatter and reflected light images of sulfide minerals from the Pontiac subprovince and Abitibi belt metasedimentary rocks, Canada. A: Porcupine group chlorite zone sample AB115 (1.5ppb Au) showing Cbt inclusions within Po. B – Pontiac biotite zone sample AB97 (22.7ppb Au) showing a large Py undergoing transition to Po with Cbt inclusions on grain boundaries. C - Pontiac biotite zone sample AB65 (2.8ppb Au) showing relicts of Py within Po. D – Pontiac garnet zone sample AB28 (1.1ppb Au) showing transition of Py to Po along preferential crystallographic orientations. E – Pontiac garnet zone sample AB34 (5.9ppb Au) with irregular Po and associated Cbt. F – Pontiac Kyanite zone sample AB43 (0.45ppb Au) showing Po with Pn inclusions and Ccp. Abbreviations: Bi – biotite Cbt – cobaltite, Ccp – chalcopyrite, Chl – chlorite, Gn – galena, Ilm – ilmenite, Pn – pentlandite, Po – Pyrrhotite, Py – Pyrite, Rt – rutile.

3 Sampling and analytical methods

Metasedimentary rock samples were collected in 2016 from the Abitibi belt and Pontiac subprovince which exposes a metamorphic transition from biotite-zone in the north to sillimanite-zone in the south (Benn et al., 1994). Whole-rock gold concentrations and their variations with metamorphic grade are reported in Pitcairn et al. (2021). The sulfide mineralogy was characterised using the polarising microscope and the scanning electron microscope at the Natural History Museum, Stockholm, Sweden.

In-situ mineral analyses were carried out at the Department of Earth Sciences, University of Gothenburg, Sweden in two separate batches, one in 2017 , one in 2023 using an Agilent 8800QQQ triple Quadrupole ICP-MS coupled to a New Wave NWR 213 laser ablation system. Spot analyses used spot-sizes of 30µm and 15µm, and energy output and the repetition rate were 4.3 J/cm2 and 10Hz respectively. Line scans were performed using a 50 µm spot size, and energy output and the repetition rate were 5.5 J/cm2 and 10Hz respectively. The following isotopes were measured for spot analyses: ^{27}Al, ^{29}Si, ^{34}S, ^{57}Fe, ^{59}Co, ^{60}Ni, ^{63}Cu, ^{66}Zn, ^{75}As, ^{77}Se, ^{95}Mo, ^{107}Ag, ^{121}Sb, ^{125}Te, ^{197}Au, ^{202}Hg, ^{208}Pb and ^{209}Bi. Line scans included also the following; 31P, 39K, 44Ca, 49Ti, 181Ta and 205Tl. Instrument calibration was performed using glass reference materials NIST-SRM-610 and GSD-1G. Accuracy, precision and fractionation effects due to matrix differences

between the glass standard and the sulphide minerals were controlled using sulphide reference materials MASS-1 and Po-725. Data processing and reduction were carried out using Glitter with ^{57}Fe used as internal standard to convert counts per seconds (CPS) to concentrations for each element in the case of the spot analyses.

4 Results and discussion

As reported in Pitcairn et al. (2021) the dominant Fe sulfide in the Pontiac and Abitibi sedimentary

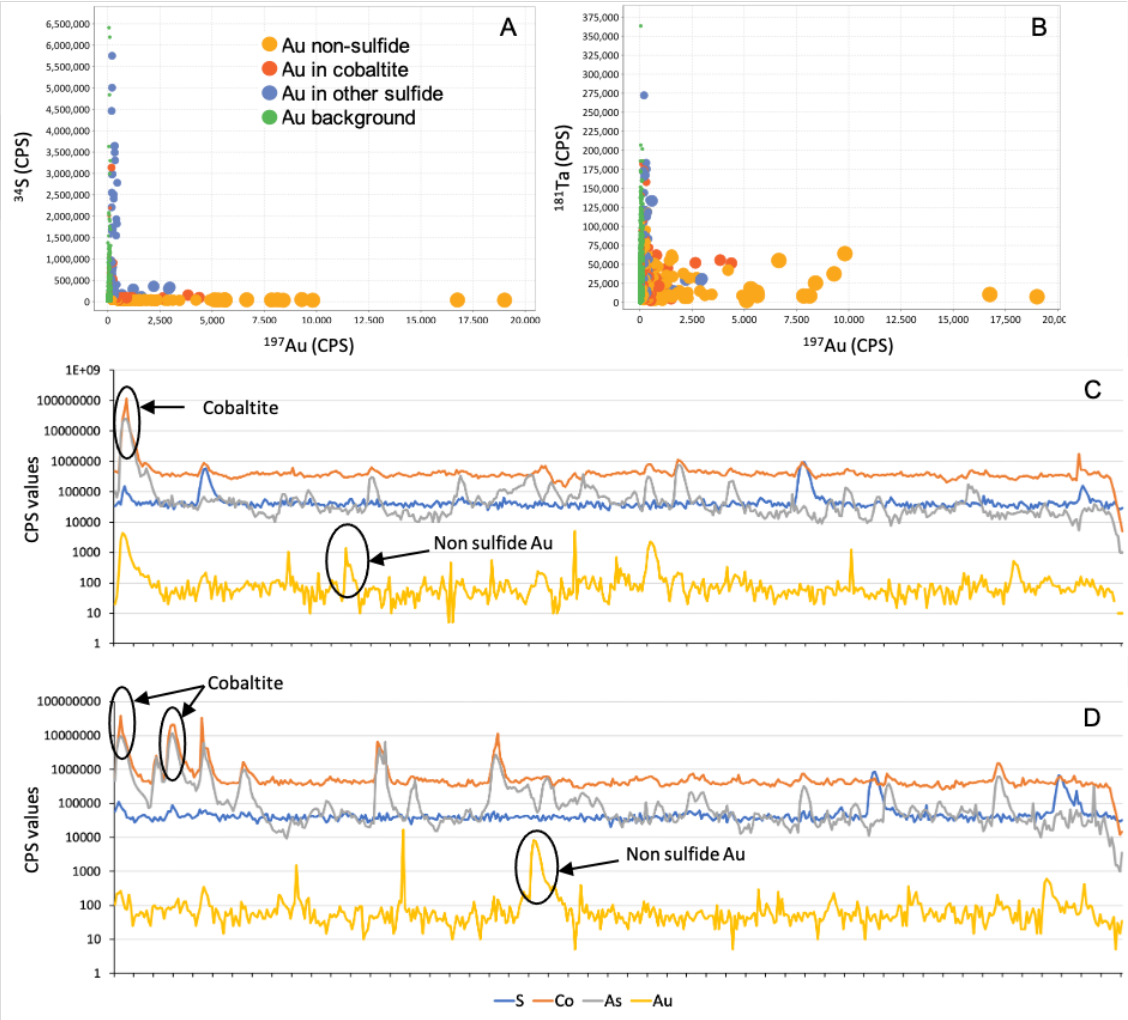

Figure 21 LA-ICP-MS line scan data from Pontiac garnet zone sample AB34 (5.9ppb Au). A: CPS values of ^{34}S vs ^{197}Au showing the different Au occurrences in the sample. B: CPS values of ^{181}Ta vs ^{197}Au showing the lack of correlation between Ta and Au. In images A and B sample point size increases with increasing Au content. C and D: CPS values for S, Co, As and Au showing the different occurrences of Au such as within cobaltite and as non-sulfide Au.

rocks changes from Py at lower metamorphic grades to Po at higher grades (Fig. 1). Pyrrhotite occurs locally in chlorite zone samples and Py is also observed in some kyanite and sillimanite zone samples indicating that the transition is not driven solely by PT conditions but by the composition and availability of metamorphic fluid (e.g., Ferry 1981). Pitcairn et al (2021) estimates that the Py:Po ratio changes from 0.7 to 0.25 between chlorite and sillimanite zones. Abundances of the minor sulfides such as cobaltite are currently being determined. Cobaltite is most abundant in samples from the biotite-garnet zones (Fig. 1), and is not observed in any sample from staurolite, kyanite and sillimanite zones. An interesting textural observation is the occurrence of porus Po in the chlorite-biotite zone samples. This is an intermediary stage of the Py-Po transition as this texture is not observed at the higher metamorphic grades such as the kyanite and sillimanite zones where Po textures are more compact, subhedral and blocky (Fig. 1F)

Gold concentrations in the sulfide phases are shown in Table 1. Samples are grouped into 3 metamorphic facies groups; chlorite-biotite (which includes samples from the Porcupine and Pontiac groups), garnet-staurolite and kyanite sillimanite. The most consistently gold enriched mineral is cobaltite with mean concentrations of 0.43 +/- 0.35 ppm Au. Only 2 in 109 individual spot analyses of Po contain gold above detection limit (Table 1). Porus Po which occurs on the margins and relict grain boundaries of Po aggregates (Fig. 1B)

Table 2: Gold concentrations in ppm in different sulfide minerals from the Pontiac and Abitibi. The data combine analyses carried out in 2017 and 2023 which had different detection limits (d.l.) - 0.01 in the 2017 analyses and 0.003 in 2022. Abbreviations as Figure 1.

	Py	Po	Porus Po	Cbt	Cpy
Chlorite-biotite zones					
Mean	0.14	0.04	0.23	0.43	0.07
SD	0.73	0.12	0.61	0.35	0.04
MAX	5.84	0.76	2.46	1.05	0.11
MIN	d.l.	d.l.	d.l.	d.l.	d.l.
n	*63*	*38*	*16*	*9*	*5*
Garnet-staurolite zones					
Mean	0.03	d.l.			0.04
SD	0.01				0.02
MAX	0.06	d.l.			0.08
MIN	d.l.	d.l.			d.l.
n	*9*	*45*			*8*
Kyanite sillimanite zones					
Mean	d.l.	d.l.			0.04
SD					0.04
MAX	d.l.	d.l.			0.11
MIN	d.l.	d.l.			d.l.
n	*10*	*26*			*6*

contains much higher Au contents of up to 2.4 ppm (Table 1). Pyrite contains average Au concentrations of 0.14 ppm with individual analyses as high as 5.8 ppm (Table 1). The high variability indicates the Au is heterogeneously distributed in the Py.

In samples from the biotite and garnet zones the whole rock gold concentration is high despite the majority of sulfide being essentially gold-free Po. In these samples we carried out line scan analyses in order to identify the host of the gold. The data clearly show an association of gold within cobaltite but not all cobaltite is gold-enriched (Fig. 2), and enrichments are patchy with gold peaks occurring on the margins of As-Co peaks. The line scans also show a large number of gold peaks not associated with cobaltite or any other sulfide. These peaks are often narrower than those associated with cobaltite but are more abundant. We interpret these peaks to represent micro particles of gold within the rock most likely occurring on silicate grain boundaries.

In sample AB34 (garnet zone with gold concentration of 5.9ppb), 17 separate line scans were carried out with a total of 7145 individual spot analyses. 88% of the spots represent "background gold" (CPS values between 60 and 150), 7% are non-sulfide gold with CPS values up to 19000, 3.5% are cobaltite gold and 1.5% gold in other sulfide (Fig. 2A). The lack of correlation between gold and tantalum (Fig. 2B) indicates that interference by $^{181}Ta^{16}O$ is not occurring.

The line scan results indicate that gold micro particles may be an important form of gold in biotite and garnet zone samples. We interpret these microparticles to be the product of the Py-Po transition where gold is liberated from Py, not incorporated into Po but not yet removed from the rock until the major flush of metamorphic fluid. The occurrence of non-sulfide gold at other metamorphic grades is currently being investigated but it is assumed that they are less abundant in rocks that have produced their major pulse of metamorphic fluid. These results may have considerable importance for the production of gold-rich metamorphic fluids as the gold micro particles will most likely be easily dissolved in H_2S-bearing metamorphic fluids.

Acknowledgements

We thank Natural Resources Canada (NRCAN) for a TGI5 research grant and Stockholm University for research funding. We also acknowledge Nikolaos Leventis for data produced during his MSc thesis at Stockholm University.

References

Ayer J, Amelin Y, Corfu F, Kamo S, Ketchum JF, Kwok K, Trowell NF (2002) Evolution of the Abitibi greenstone belt based on U-Pb geochronology: Autochthonous volcanic construction followed by plutonism, regional deformation and sedimentation. Precamb Res 115:63–95

Benn K, Miles W, Ghassemi MR, Gillett J (1994) Crustal structure and kinematic framework of the northwestern Pontiac subprovince, Quebec: An integrated structural and geophysical study. Can J Earth Sci 31:271–281

Daigneault R, Mueller W, Chown EH (2002) Oblique Archean subduction: Accretion and exhumation of an oceanic arc during dextral transpression, Southern volcanic zone, Abitibi subprovince, Canada. Precamb Res 15:261–290

Dubé B, Mercier-Langevin P (2020) Gold deposits of the Archean Abitibi greenstone belt, Canada. In Sillitoe, RH et al. eds, Geology of the World's Major Gold Deposits and Provinces:
Soc Econ Geol Spec Pub 23:669–708

Ferry J (1981) Petrology of graphitic sulfide-rich schists from south-central Maine: an example of desulfidation during prograde regional metamorphism. Am Min 66:908-930 Large RR, Maslennikov V, Robert F, Danyushevsky LV,

Chang, Z (2007) Multistage sedimentary and metamorphic origin of pyrite and gold in the giant Sukhoi Log deposit, Lena gold province, Russia. Econ Geol 102:1232−1267 Pitcairn IK, Teagle DAH, Craw D, Olivo GR, Kerrich R,

Brewer TS (2006) Sources of metals in orogenic gold deposits: insights from the Otago and Alpine Schists, New Zealand. Econ Geol 101:1525-1546

Pitcairn IK, Leventis N, Beaudoin G, Faure S, Guilmette C. Dubé B. (2021) A metasedimentary source of gold in Archean orogenic gold deposits? Geology 49:862-866

Robert F, Poulsen KH, Cassidy KF, Hodgson CJ (2005) Gold metallogeny of the Yilgarn and Superior cratons. Econ Geol 100th Ann Vol:1001–1033

Tomkins AG (2010) Windows of metamorphic sulphur liberation in the crust: Implications for gold deposit genesis. Geochim Cosmochim Acta 74:3246-3259

Thurston PC, Ayer JA, Goutier J, Hamilton MA (2008) Depositional gaps in Abitibi greenstone belt stratigraphy: A key to exploration for syngenetic mineralization. Econ Geol Bull Soc Econ Geol 103:1097–1134

Metal and ligand mobility during prograde metamorphism of metasedimentary belts in the Superior Province: Implications for gold endowment

Diogo Ribeiro[1,2], Bertrand Rottier[1,2], Antoine Godet[1,2], Georges Beaudoin[1,2], Carl Guilmette[1,2], Clifford Patten[3], Jochen Kolb[3], Iain Pitcairn[4]

[1] *Département de Géologie et Génie Géologique, Faculté des Sciences et de Génie, Université Laval, Canada*

[2] *Centre de Recherche sur la Géologie et l'Ingénierie de Ressources Minérales (E4m), Université Laval, Canada*

[2] *Institut für Angewandte Geowissenschaften, Karlsruher Institut für Technologie, Germany*

[3] *Institutionen för Geologiska Vetenskaper, Stockholms Universitet, Sweden*

Abstract. The metasedimentary subprovinces of the Superior craton are exposed in the vicinity of, and are overthrust by, Au-endowed greenstone belts, suggesting that they could have sourced significant volumes of metals (e.g. Au, As, Sb) and ligands (Cl and S) to the overlying orogenic gold deposits. We track metal and ligand concentrations in the metasedimentary rocks, and the textural and chemical evolution of sulfides during prograde metamorphism. Representative samples were collected across different metamorphic zones along three transects featuring contrasting Au endowment: well-endowed (Rouyn-Noranda, Pontiac), moderately-endowed (Geraldton, Quetico), and poorly-endowed (Thunder Bay, Quetico) areas. In the three areas, Au, As and Sb concentrations are identical in low-grade metamorphic rocks, and As and Sb contents decrease with increasing metamorphic grade. However, decrease of Au concentration with increasing metamorphic grade is only observed in the well- and moderately-endowed areas, suggesting that gold was mobilized during prograde metamorphism. At Geraldton, sulfide textural and in-situ analysis suggest two main prograde continuous reactions: (1) pyrite I, the main host for Au, As, and Sb, to pyrrhotite; and (2) pyrrhotite to pyrite II. Our results show that Au, As, and Sb were mobilized during prograde metamorphism and may have migrated to the overlying mineralized systems.

1 Introduction

It is generally accepted that the majority of the fluids involved in orogenic gold deposits result from metamorphic devolatilization (Goldfarb and Pitcairn 2022). The breakdown reactions of chlorite and pyrite at the greenschists to amphibolite facies transition are seen as major contributors of fluid, metals, and sulfur (Phillips and Powell 2010; Tomkins 2010). Previous studies have shown that metasedimentary rocks release orogenic Au-related elements (e.g., S, Au, As, and Sb) during prograde metamorphism, indicating that they may represent a viable source of metals and ligands for orogenic gold deposits (Pitcairn et al. 2006; Tomkins, 2010; Zhong et al. 2015). Although metasedimentary rocks are generally recognized as a source of metals in Phanerozoic deposits, they have been often overlooked in Archean greenstone belts, given their low abundance. However, in the Superior Province, high-grade metasedimentary belts (up to granulite facies) occur adjacent to and are commonly overthrust by low- to medium-grade greenstone belts (up to lower amphibolite facies). This tectonometamorphic setting suggests that the devolatilization of the metasedimentary belts may have sourced significant volumes of metals and ligands to the overlaying greenstone belts. This is the case in the Pontiac and Quetico subprovinces exposed in the vicinity of the world-class Abitibi gold camp and the Beardmore-Geraldton belt, respectively. They consist of a sequence of metamorphosed turbiditic graywacke and mudstone interlayered with minor basaltic and komatiitic volcanic units, intruded by abundant felsic plutonic series of various geochemical affinities. These sequences expose apparently continuous metamorphic gradients and field isograds from the biotite to the sillimanite zone toward the south in the Pontiac subprovince, and from the chlorite zone to the partial melting zone inward in the Quetico subprovince.

While a systematic decrease of Au, As, and Sb concentrations with increasing metamorphic grade was recently documented in the Pontiac subprovince (Pitcairn et al. 2021), which is consistent with their mobilization during prograde metamorphism, their mobility at the mineral scale and the metal mobility in the Quetico subprovince at the basin scale are still unknown.

We report whole-rock geochemistry data for trace elements, and whole-rock ultra-low detection limit data for Au acquired by pressed powder pellet (PPP)-LA-ICP-MS from a suite of representative metasedimentary and subordinate interlayered mafic volcanic rocks across three transects featuring contrasting gold endowment, as well as textural and in-situ geochemical analysis of sulfides in metasedimentary rocks from a transect located in the Quetico subprovince.

2 Sampling and analytical methods

Sampling was carried out in three different areas across the Pontiac and Quetico subprovinces, representing well-endowed (Rouyn-Noranda, Pontiac), moderately endowed (Geraldton, Quetico), and poorly endowed (Thunder Bay, Quetico) sectors. The classification of each area regarding its endowment is based on the abundance of nearby orogenic gold deposits in the adjacent greenstone

belts. Representative samples of metasedimentary and subordinate interlayered mafic volcanic rocks were collected from all the metamorphic zones and 143 samples were selected for whole-rock trace element and ultra-low detection limit Au analysis.

Whole-rock analysis was performed at ALS laboratories (Sudbury, Canada). The samples were crushed and pulverized, followed by 4-acid digestion. Major elements were analysed by ICP-AES; Ba, Ce, Cr, Cs, Dy, Er, Eu, Ga, Gd, Ge, Hf, Ho, La, Lu, Nb, Nd, Pr, Rb, Sm, Sn, Sr, Ta, Tb, Th, Tm, U, V, W, Y, Yb, Zr were acquired by ICP-MS after lithium borate fusion; Ag, Cd, Co, Cu, Li, Mo, Ni, Pb, Sc, Zn were analysed by ICP-MS; S and C were acquired by IR spectroscopy; and Cl and F were analysed by IC after KOH fusion.

The ultra-low detection limit analysis for Au were acquired by Pressed Pellet Powder (PPP)-LA-ICP-MS in the Laboratory for Environmental and Raw Materials Analysis (LERA, Institute of Applied Geosciences, KIT). The production of nano-powders and pellets followed a procedure adapted from Peters and Pettke (2016) and Belgrano et al. (2022). The ultra-low detection limit analysis for Au was acquired using a Teledyne 193 nm Excimer Laser coupled to a ThermoFisher Scientific Element XR Sectorfield ICP-MS. The instrumental set up, oxide interference corrections, and data reduction followed the method developed by Patten et al. (2023).

Electron probe microanalysis of sulfides was done using a CAMECA SX-100 five-spectrometer electron probe micro-analyzer at Laval University. Analytical conditions for spot analyses were 15 kV, 20 nA with 20 s counting time on peaks and 10 s on background.

Sulfide LA-ICP-MS analyses were acquired using a RESOlution-SE 193nm Excimer laser coupled to an Agilent 8900 ICP-MS at Laval University. Laser pulse frequency and laser energy density were set to 10 Hz and 2.5 J cm^{-2}, respectively. The list of isotopes monitored for quantitative analyses included ^{23}Na, ^{27}Al, ^{28}Si, ^{32}S, ^{34}S, ^{43}Ca, ^{44}Ca, ^{47}Ti, ^{55}Mn, ^{59}Co, ^{60}Ni, ^{63}Cu, ^{66}Zn, ^{75}As, ^{78}Se, ^{95}Mo, ^{107}Ag, ^{111}Cd, ^{115}In, ^{118}Sn, ^{121}Sb, ^{125}Te, ^{178}Hf, ^{181}Ta, ^{182}W, ^{197}Au, ^{205}Tl, ^{208}Pb, ^{209}Bi. The beam diameters varied among 24, 30, and 38 µm according to the size of the targeted grains. The analyses were performed for 30 s followed by 45 s blanks.

3 Results

3.1 Whole-rock geochemistry

Across the three areas, the low-grade metasedimentary rocks display similar mean concentration values for Au (~1 ppb), As (12.8 – 22.4 ppm), and Sb (0.16 – 1.02 ppm). A systematic decrease of the mean concentrations of As and Sb towards higher metamorphic grade rocks is observed for all the transects: (1) 12.82 to 0.25 ppm As and 0.16 to 0.08 ppm Sb from the biotite to the sillimanite zone in Rouyn Noranda, (2) 22.44 to 0.44 ppm As and 1.02 to 0.06 ppm Sb from the chlorite to the melt zone in Geraldton, and (3) 13.73 to 0.33 ppm As and 0.23 to 0.03 ppm Sb from the chlorite to the melt zone in Thunder Bay. In contrast, the decrease of gold concentrations with increasing metamorphic grade is only detected in the well- and moderately-endowed areas (from 1.03 to 0.16 ppb from the biotite to the sillimanite zone in Rouyn Noranda and from 1.04 to 0.25 ppb from the chlorite to the melt zone in Geraldton), whilst no consistent Au depletion is observed in Thunder Bay (Figure 1).

Carbon and H_2O mean contents also decrease consistently with increasing metamorphic grade in the three areas: (1) 0.12 to 0.02 wt% C and 2.45 to 1.57 wt% H_2O from the biotite to the sillimanite zone in Rouyn Noranda, (2) 0.46 to 0.02 wt% C and 2.73 to 1.32 wt% H_2O from the chlorite to the melt zone in Geraldton, and (3) 0.17 to 0.03 wt% C and 2.37 to 1.00 wt% H_2O from the chlorite to the melt zone in Thunder Bay. However, the mean concentration of S and Cl, as well as Se, Bi, Te, and Hg, show no systematic variation (Figure 1).

The suite of mafic volcanic rocks yields similar trends to the metasedimentary rocks regarding the variation of their Au, As, and Sb contents (Figure 1), which is consistent with Patten et al. (2020), however, the limited dataset is not robust enough to accurately access the mobility of these elements in these protoliths across the full spectrum of metamorphic conditions.

3.2 Textural and chemical evolution of sulfides

In the Geraldton area, on average the sulfides represent around 0.5 vol.% of the metasedimentary rocks. The textural and chemical evolution of the sulfides across different metamorphic grades was accessed to evaluate their role on Au, As, and Sb mobilities. The sulfide evolution features two main continuous reactions: (1) the pyrite I to pyrrhotite transition occurred from the biotite to the cordierite zones and produced transitional sulfide phases with an intermediate composition between pyrite and pyrrhotite; (2) the pyrrhotite to pyrite II transition took place in the sillimanite and melt zones and is expressed by the growth of euhedral pyrite inside pyrrhotite.

Pyrite I is present from the chlorite to the staurolite zones. It often displays subhedral and inclusion-poor cores surrounded by anhedral and inclusion-rich rims. The relative abundance of inclusions gradually decreases toward higher metamorphic grades, resulting in increasingly homogeneous pyrite grains. The Au, As, and Sb median concentrations of pyrite I decrease progressively with increasing metamorphic grade: 33.6 ppb Au, 410.3 ppm As, 17.4 ppm Sb in the chlorite zone (n = 34); 22.3 ppb Au, 127.2 ppm As, 12.7 ppm Sb in the biotite zone (n = 26); and 18.2 ppb Au, 93.5 ppm As, 2.2 ppm Sb in the garnet zone (n = 29).

The transitional sulfide phases produced during the breakdown of pyrite I show linear replacement textures of pyrite gradually transitioning into

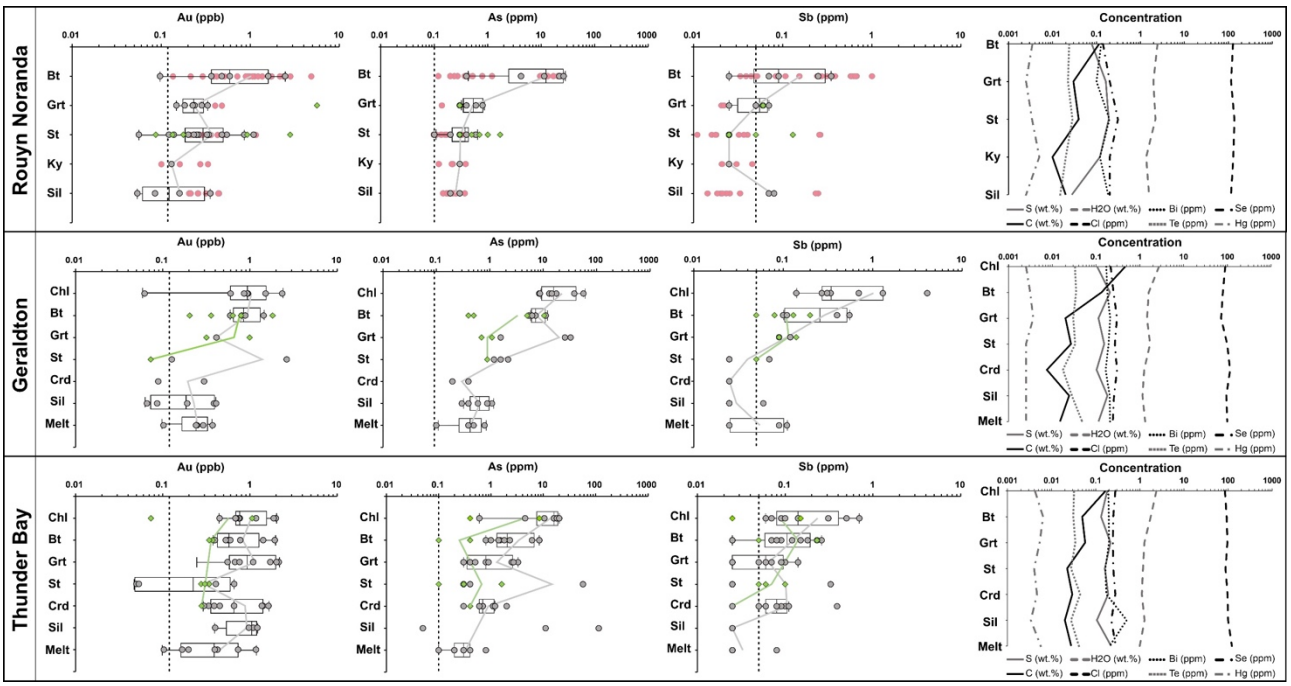

Figure 1. Concentrations of Au, As, and Sb for metasedimentary rocks (gray circles) and mafic volcanic rocks (green diamonds) from Rouyn Noranda, Geraldton and Thunder Bay. Gray and green lines connect the mean concentrations of metasedimentary and volcanic rocks, respectively, in each metamorphic zone. Vertical dashed black lines are the limits of detection. Red circles represent data for metasedimentary rocks from Pitcairn et al. (2021). Diagrams on the right show lines connecting mean concentrations for S, C, H_2O, Cl, Bi, Te, Se, Hg of metasedimentary rocks.

pyrrhotite. These also record a general decrease of mean Au, As, and Sb concentrations with increasing metamorphic grade: 17 ppb Au, 27.3 ppm As, 42.35 ppm Sb in the biotite zone (n = 4); 4 ppb Au, 1.9 ppm As, 0.59 ppm Sb in the garnet zone (n = 2); and 3 ppb Au, 104.3 ppm As, 0.24 ppm Sb in the staurolite zone (n = 8); these concentrations are within the range of values measured for pyrite I and pyrrhotite coexisting in the same metamorphic zone (Figure 2).

Pyrrhotite is present from the biotite to the melt zone, becoming significantly more abundant from the staurolite zone. It commonly displays flames of pentlandite and the grains become more rounded towards higher grades. The median Au, As, and Sb concentrations in pyrrhotite (Figure 2) decrease continuously from 16 ppb Au, 3.64 ppm As, 2.62 ppm Sb in the biotite zone (n = 6); 6 ppb Au, 1.10 ppm As, 0.18 ppm Sb in the garnet zone (n = 8); 5 ppb Au, 11 ppm As, 0.03 ppm Sb in the staurolite zone (n = 10), to 3 ppb Au, 0.07 ppm As, 0.02 ppm Sb in the cordierite zone (n = 25).

Pyrite II grows as euhedral crystals inside pyrrhotite. Their size and distribution are controlled by the pre-existent pyrrhotite grains. Eventually, pyrite II completely consumes pyrrhotite forming clusters of intergrown euhedral pyrite grains, whose shape mimics the boundaries of the precursor pyrrhotite grains. A slight increase of the median Au, As, and Sb contents is observed from pyrrhotite to pyrite II, from 3 ppb Au, 0.11 As, 0.02 Sb in pyrrhotite (n = 40) to 2 ppb Au, 1.49 ppm As, 0.22 ppm Sb in pyrite II (n = 23) in the sillimanite zone; and from 3 ppb Au, 0.24 As, 0.02 Sb in pyrrhotite (n = 28) to 13 ppb Au, 1.80 ppm As, 0.01 ppm Sb in pyrite II (n = 29) in the melt zone. In the melt zone, eventually all sulfides become unstable, remaining preserved only inside porphyroblasts.

4 Discussion and conclusions

Identical Au, As, and Sb contents at low-grade conditions and a systematic decrease of As and Sb concentrations with increasing metamorphic grade are observed in the metasedimentary sequences across the three areas. However, Au depletion toward higher metamorphic grades was not detected in the Thunder Bay area. This indicates that, even though As and Sb were mobilized during prograde metamorphism in all areas, Au release was more efficient in metasedimentary rocks from the endowed areas (Rouyn Noranda and Geraldton) compared to the poorly endowed area (Thunder Bay). The parameters influencing the contrasting gold mobility across the different transects are currently under evaluation.

The Au, As, and Sb concentrations of sulfides in the Geraldton yield similar decreasing trends. The gradual removal of inclusions and trace element depletion in pyrite I with increasing metamorphic grade is interpreted as a continuous structural reorganization, which seems to be an important mechanism for metal mobilization. The pyrite I to pyrrhotite transition is accompanied by a substantial decrease of Au, As, and Sb concentrations, and is likely the main reaction responsible for the release of significant amounts of these elements from the metasedimentary rocks. Similar to pyrite I, the trace element depletion and rounding of pyrrhotite grains toward higher metamorphic grade should be related to its gradual structural reorganization, however, the

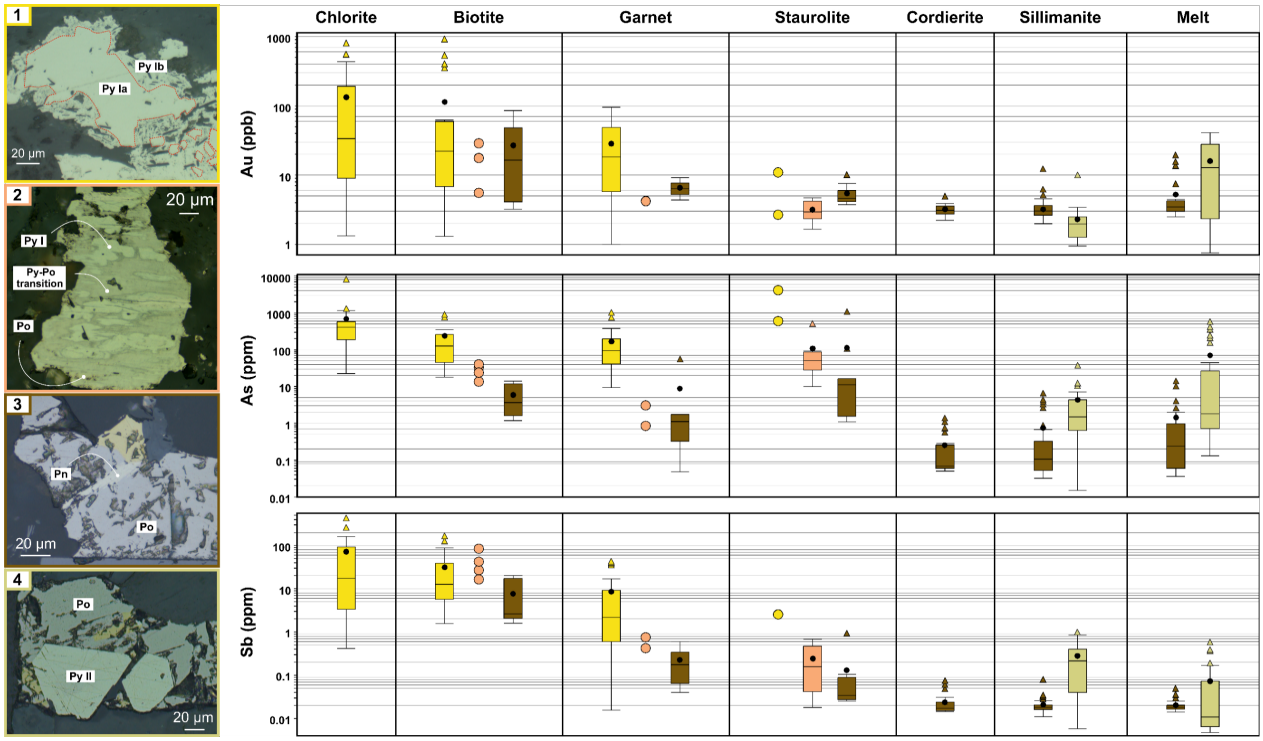

Figure 2. Textures (left) and Au, As, and Sb concentrations (right) of sulfides from metasedimentary rocks in the Geraldton transect. 1 – Pyrite I featuring subhedral and inclusion-poor cores and anhedral and inclusion-rich overgrowths; 2 – Transitional sulfide phases displaying linear replacement textures; 3 – Pyrrhotite with pentlandite flame; 4 – Euhedral pyrite II crystals growing in pyrrhotite. Box-plots (n > 5; black circles are mean values) and circles (n ≤ 5) represent data for pyrite I (yellow), transitional sulfide phases (orange), pyrrhotite (brown), and pyrite II (green) in each metamorphic zone.

volume of metals released should be significantly lower, given its lower metal content.

Although pyrrhotite is present up to the melt zone, the transition to pyrite II indicates that, from the sillimanite zone, pyrrhotite is no longer the main stable sulfide species. The slightly higher Au, As, and Sb of pyrite II compared to coexisting pyrrhotite suggest that these elements were reconcentrated during the transition from pyrrhotite to pyrite II. Nonetheless this reaction should have had limited impact on the mobilization of these elements, given their low concentrations and the low volume percentage of sulfides, which is consistent with the whole-rock data.

Even though the transition from pyrite I to pyrrhotite should release sulfur, no significant sulfur loss during prograde metamorphism is recorded by the whole-rock data, which suggests that sulfur was not significantly mobilized. The sulfur liberated from pyrite may have reacted with Fe released upon the breakdown silicate minerals, such as chlorite, to form pyrrhotite (Zhong et al. 2015).

Both the whole-rock and the sulfide in-situ data record a systematic decrease of Au, As, and Sb concentrations with increasing metamorphic grade. Moreover, there seems to be a correlation between Au mobility in the metasedimentary belts and the Au endowment in the overlying greenstone belts. This suggests that devolatilization of the metasedimentary belts may have sourced significant volumes of these metals to the orogenic gold deposits in the greenstone belts and may be a key factor controlling Au endowment.

Acknowledgements

The authors would like to thank Adrian Rhem, Isaac Malta, and Doug Tinkman for discussion, Marc Choquette and Guillaume Barré for the analytical work, and Metal Earth for founding this project.

References

Goldfarb RJ, Pitcairn IK (2023) Orogenic gold: is a genetic association with magmatism realistic? Mineralium Deposita, 58(1), 5-35.

Patten CGC, Beranoaguirre A, Hector S, Gudelius D, Kolb J, Eiche E (2023) Improved whole rock low detection limit gold analysis by LA-ICP-MS utilizing pressed-powder-pellets. International Journal of Mass Spectrometry, 488, 117039.

Patten CGC, Pitcairn IK, Molnár, Kolb J, Beaudoin G, Guilmette C, Peilod A (2020) Gold mobilization during metamorphic devolatilization of Archean and Paleoproterozoic metavolcanics rocks. Geology, 48(11), 1110-1114.

Phillips GN, Powell R (2010) Formation of gold deposits: a metamorphic devolatilization model. Journal of Metamorphic Geology, 28(6), 689-718.

Pitcairn IK, Leventis N, Beaudoin G, Faure S, Guilmette C, Dubé B (2021) A metasedimentary source of gold in Archean orogenic gold deposits. Geology, 49(7), 862-866.

Pitcairn IK, Teagle DAH, Craw D, Olivo GR, Kerrich R, Brewer TS (2006) Sources of Metals and Fluids in Orogenic Gold Deposits: Insights from the Otago and Alpine Schists, New Zealand. Economic Geology, 101(8), 1525-1546.

Tomkins AG (2010) Windows of metamorphic sulfur liberation in the crust: Implications for gold deposit genesis. Geochimica et Cosmochimica Acta, 74(11), 3246-3259.

Zhong R, Brugger J, Tomkins AG, Chen Y, Li W (2015) Fate of gold and base metals during metamorphic devolatilization of a pelite. Geochimica et Cosmochimica Acta, 171, 338-352.

Petrographic and chemical characterization of superimposed Au-bearing events at the Augmitto-Bouzan deposit (Abitibi)

Rita Rodrigues[1], Georges Beaudoin[1], Bertrand Rottier[1], Guillaume Raymond[1], Baptiste Chapon[2]
[1]Departement de génie et génie géologique, Université Laval, Québec, Canada
[2]CEGEP de l'Abitibi-Témiscamingue, Rouyn-Noranda, Québec, Canada

Abstract. At the Augmitto-Bouzan deposit, gold endowment is the result of syn- and post-shear mineralization events. Syn-shear quartz-carbonate-tourmaline (QCT) veins and associated alteration halos represent orogenic gold-type mineralization and constitute the most important hydrothermal event, yet account for minor gold contents. Nevertheless, these structures still constitute primary exploration targets as they host two superimposed mineralization events responsible for most gold endowment at the deposit. The first occurs as reopening of QCT veins and consists of carbonate precipitation accompanied by free gold. The second is characterized by carbonate-chlorite-pyrite/pyrrhotite (CCP) veinlets and accounts for major gold contributions, particularly when spatially associated with arsenopyrite. To understand the spatial and temporal controls on the mineralization at the Augmitto-Bouzan deposit, in situ chemical analyses were performed on gold-related sulfides. Arsenopyrite from QCT vein selvages and alteration halos and pyrite from CCP veinlets show variable Ni+Co contents yielding a trend towards the Astoria orebody. This pattern is consistent with observed changes in mineral associations from CCP veinlets. Given that the Astoria segment hosts late Proterozoic gabbro dykes, this spatial relationship raises questions regarding the influence of the dykes on the formation of CCP veinlets and, thus, their role in gold remobilization and/or as a late gold source.

1 Introduction

Orogenic Gold Deposits (OGD) usually consist of gold-rich veins spatially constrained to major crustal compressional to transpressional discontinuities and their subsidiary structures (Groves et al. 2003). At the deposit scale, these systems are often characterized by irregular distribution of gold grades. This feature is commonly the product of multiple vein generations with contrasting gold contents, illustrating a sequence of superimposing hydrothermal events that have taken place in areas marked by long-lived deformation. Recognizing such processes is fundamental to understand gold distribution and therefore to: (**i**) interpret gold grade patterns; (**ii**) accurately assess the prospectivity of exploration targets; and (**iii**) identify ore shoots. Straddling the Cadillac-Larder Lake Tectonic zone (CLLTz), the Augmitto-Bouzan deposit is a prime example of the irregular gold distribution patterns amongst OGD. At the property, gold grades vary significantly along strike of the fault and economic grades are mostly restricted to the western sector, in several steeply east-plunging orebodies (Fig.1). In the eastern sector of the deposit, equivalent veins are largely barren.

Here we provide textural, mineralogical, and chemical data on the mineralization events responsible for gold endowment at the Augmitto-Bouzan deposit in order to better understand gold grade patterns.

2 Geological context

The Cadillac-Larder Lake Tectonic zone is an east-west trending first-order structure at the southeastern limit of the Abitibi greenstone belt, at the contact with the Pontiac Subprovince to the south (Card and Ciesielski 1986). This crustal-scale shear zone is known as an important metallotect for gold mineralization in the region (Poulsen 2017).

The Augmitto-Bouzan deposit covers 12 km along strike of the CLLTz and comprises 8 contiguous segments where mineralization is associated with the main deformation zone (Fig.1). From west to east, these are: Augmitto, Cinderella, Lake Gamble, Astoria, East-Bay, and Bouzan (Fig.1). Gold mineralization is preferentially hosted in the altered mafic and ultramafic metavolcanic rocks of the Piché Group, with higher grades being confined to its contact with the metasedimentary rocks of the Timiskaming Group. Across the property, albitic dykes intrude the Piché Group and may locally host mineralization. In the Astoria segment, two late Proterozoic gabbro dykes (metric to hectometric) intrude both the metavolcanic and metasedimentary units (Fig.1). These two bodies are part of the regional scale Abitibi Dyke swarm event and result in a contact metamorphic aureole of approximately 50m in width (Powell et al. 1995).

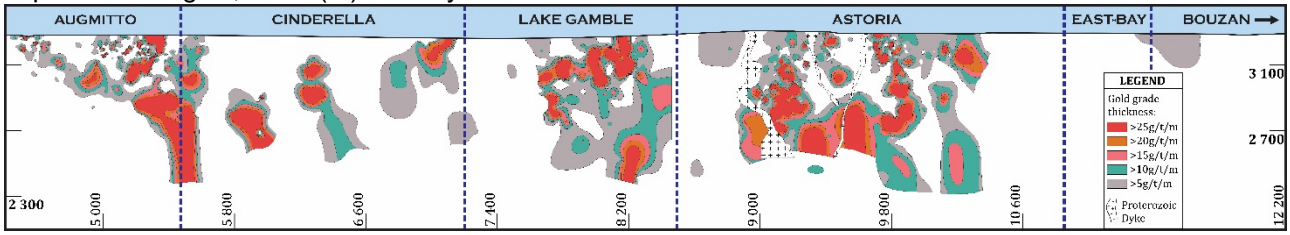

Figure 1. Spatial distribution of gold grade grades in the Piché Group across the different segments of the deposit. The Bouzan segment extends for more 3km to east and is barren. Coordinates are in UTM Zone 17 NAD83.

3 Methods

Core logging was performed on 93 drillholes spatially distributed across the 12 km of the deposit. Transmitted- and reflected-light microscopy was carried out on 99 polished thick sections aiming spatial coverage of the deposit.

Quantitative micro-XRF data were obtain from polished thick sections using an M4 Tornado Micro X-Ray Fluorescence instrument at Université Laval (Québec, Canada). Analytical conditions were 20 µm step size, 50 kV acceleration voltage, 600 µA field intensity, and 5 ms dwell time. Geochemical maps were produced using the AMICS software.

Major and minor elements analyses were performed on (**i**) arsenopyrite from QCT alteration halos and selvages, (**ii**) pyrite from CCP veinlets, and (**iii**) gold from different mineralization stages. Analyses were obtained using a CAMECA SX-100 Electron Probe Micro-analyser equipped with 5 WDS spectrometers at Université Laval (Québec, Canada). For sulfides, S, Cd, Sb, Zn, Cu, Mn, Fe, Co, Ni, and As were analysed using a 5 µm beam size, 15 kV acceleration voltage, and 20 nA beam current. For gold analyses, Au, Ag, and Te concentrations were obtain under the same conditions. Data processing included the imputation of censored values (values below detection limit) using the lrEM (log-ratio Expectation-Maximization) algorithm (Palarea-Albaladejo and Martín-Fernández 2015). Elements with more than 40% of censored values were not considered in the interpretation of the dataset.

4 Results

4.1 Paragenesis of hydrothermal episodes

Six hydrothermal episodes, associated with both barren and gold-bearing events, have been identified at the Augmitto-Bouzan deposit (Fig.2).

The first hydrothermal episode is recorded by barren, deformed, early carbonate ± quartz (ECQ) veins located along the main deformation fabric. The development of microcrystalline quartz-chlorite (MQC) veins (2nd hydrothermal episode, Fig.2) is synchronous to the main shear and marks the earliest gold event identified, where mineralization occurs as free gold in the quartz-chlorite matrix.

The second gold event consists of micrometric gold inclusions in arsenopyrite from vein selvages and mica-rutile-tourmaline-sulfide alteration halos associated with the emplacement of syn-shear quartz-carbonate-tourmaline (QCT) veins (3rd hydrothermal episode, Fig.2). In mafic and ultramafic units, the presence of arsenopyrite is mostly restricted to QCT vein selvages whereas the alteration halos are dominated by gersdorffite. In sedimentary units, arsenopyrite occurs both in QCT vein selvages and in proximal alteration halos (Fig.3c). Both MQC and QCT hydrothermal episodes appear to account for a small percentage of the overall gold budget of the deposit.

The third gold event is spatially constrained to QCT veins from endowed areas between Augmitto and Astoria. Petrography combined with micro-XRF multi-element maps revealed that free gold within these structures is associated with late carbonate infillings (CI) overprinting the QCT veins (Fig.3a,b).

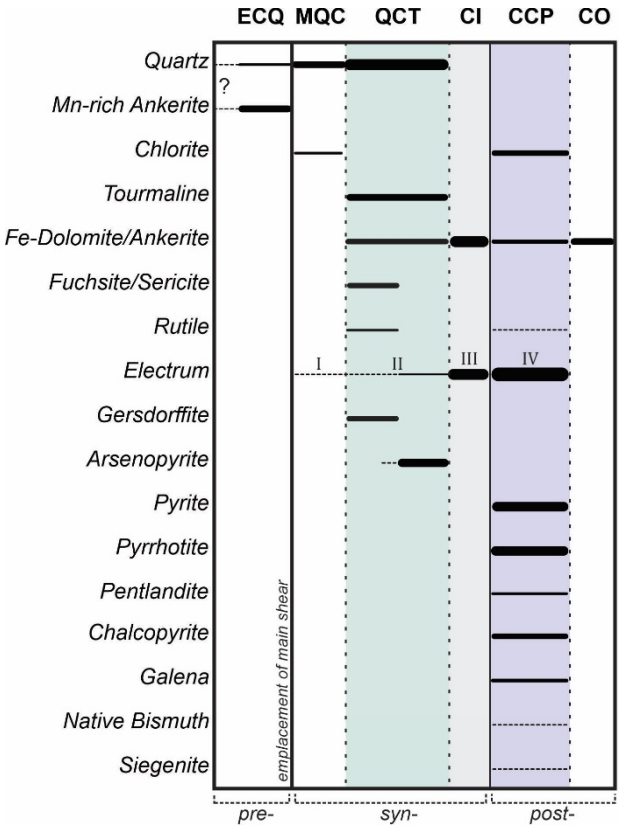

Figure 2. Paragenetic sequence of hydrothermal episodes at the Augmitto-Bouzan deposit.

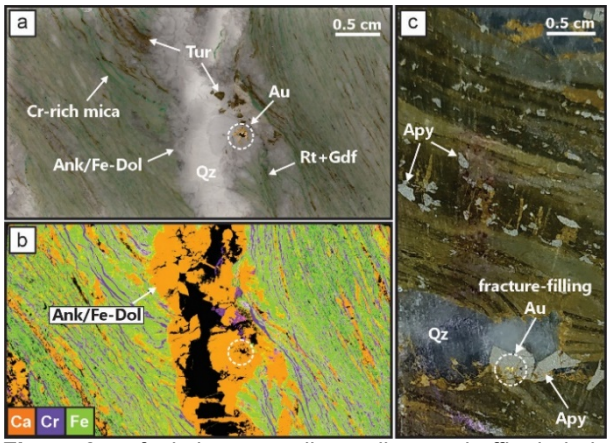

Figure 3. a, fuchsite-tourmaline-rutile-gersdorffite halo in ultramafic unit and associated QCT vein; **b**, micro-XRF Ca-Cr-Fe geochemical map of **a** illustrating the superimposition of a late gold-bearing carbonate infilling (CI); **c**, sericite-tourmaline-rutile-arsenopyrite alteration halo in sedimentary rock and associated QCT vein.

The last gold event is associated with the fifth hydrothermal episode (Fig.2) and is characterized by carbonate-chlorite-pyrite/pyrrhotite (CCP) millimetric to centimetric veinlets, commonly associated with minor chalcopyrite, galena, and native bismuth (Fig.4), that crosscut all previous vein generations. The prevalence of pyrite over pyrrhotite in CCP veinlets seems to be closely related with increased

distance from the Astoria orebody. In Astoria, pyrrhotite is predominant, and minor phases such as chalcopyrite and galena are more abundant, with locally siegenite. Additionally, pentlandite is common as exsolution "flames" in pyrrhotite (Fig.4e). Gold mineralization linked with this episode is particularly important when spatially associated with arsenopyrite from QCT vein selvages and alteration halos, where micrometric free gold is observed filling fractures in arsenopyrite (Fig.4b-f).

When arsenopyrite is absent from QCT halos and selvages, CCP veinlets tend to be barren of gold. Less commonly, mineralization associated with this event can also occur as micrometric free gold inclusions in pyrite or inside the veinlets (Fig.4a). Together, CI and CCP account for most of the gold endowment of the deposit.

The latest hydrothermal episode recorded is marked by barren carbonate-only veins that crosscut all previous assemblages (Fig.2).

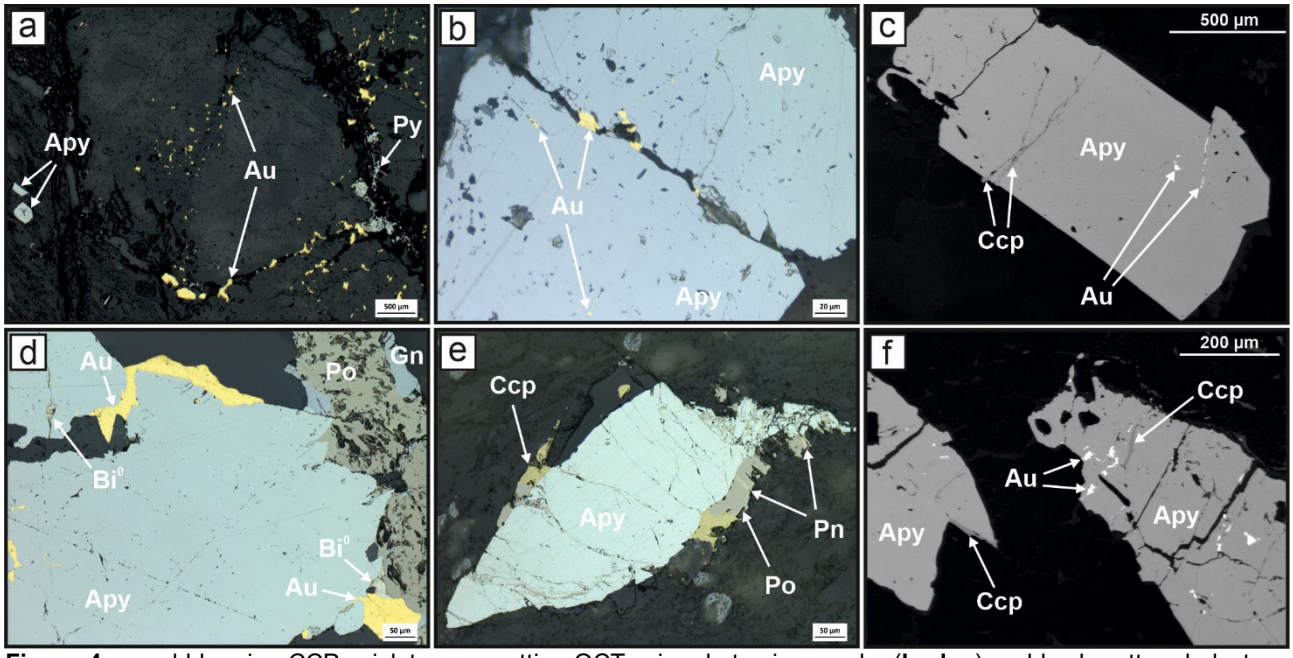

Figure 4. a, gold-bearing CCP veinlets crosscutting QCT vein; photomicrographs (**b**, **d**, **e**) and backscattered electron images (**c**, **f**) of CCP assemblages filling fractures in arsenopyrite from QCT selvages and alteration halos.

4.2 Mineral chemistry of Au and Au-associated sulfides

Gold mineralization associated with CI and CCP mineralization events occurs as electrum with variable Au and Ag contents. Electrum associated with CCP veinlets presents lower average Au contents (±91 wt%) when compared to the CI event (±93 wt%). No clear relationship was observed between electrum composition and the different segments of the deposit, or its textural context (pyrite inclusions, veinlets, or arsenopyrite fracture-filling).

There is a significant compositional variation of Ni+Co in arsenopyrite (Fig.5a).

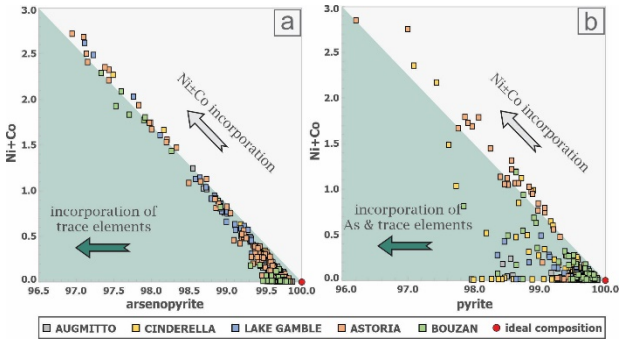

Figure 5. Arsenopyrite (**a**) and pyrite (**b**) deviation from ideal compositions by incorporation of Ni+Co (wt%) from the different segments of the deposit. Vectors for As and trace-elements incorporation are shown.

This variation yields a trend marked by increasing Ni+Co values from the western end of the property towards the Astoria orebody (Fig.6a). In the eastern sector of the property (Bouzan), Ni+Co contents in arsenopyrite decrease considerably, except for one sample, where significant Co±Ni enrichment (up to 2.11 wt% Co and 0.35 wt% Ni) is documented in arsenopyrite rims (Fig.4e). An identical trend is shown by pyrite, in which Ni+Co concentrations progressively increase towards the Astoria orebody (Fig.6b), where considerably higher Ni+Co values are documented (up to 2.85 wt%).

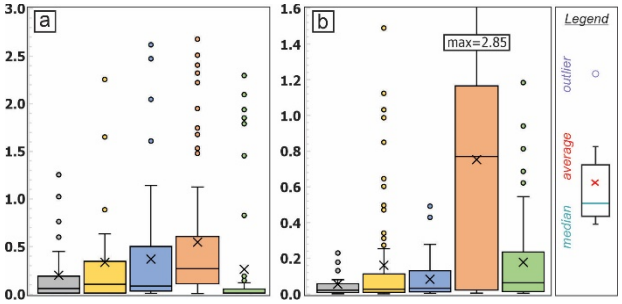

Figure 6. Arsenopyrite (**a**) and pyrite (**b**) Ni+Co contents (in wt%) from the different segments of the deposit, from left to right: Augmitto, Cinderella, Lake Gamble, Astoria, and Bouzan.

East of this segment, Ni+Co contents in pyrite drop significantly (Fig.6b). Pyrite analyses also

register considerable compositional deviation marked by As incorporation (Fig.5b). Arsenic content in pyrite displays an opposite trend to that of Ni+Co, in which As values tend to progressively decrease towards the Astoria orebody; from approximately 388 to 266 ppm from Augmitto to Lake Gamble, reaching below detection limit in Astoria.

5 Discussion and conclusions

A detailed study of samples regularly distributed across the Augmitto-Bouzan deposit allowed the identification of six hydrothermal episodes, four of which contain gold mineralization.

Of all gold-bearing episodes, MQC veins appear to be responsible for the smallest percentage of the overall gold budget of the deposit, and QCT veins for slightly higher gold contributions. Given the timing of emplacement, mineralogy, and regional context, QCT veins have been interpreted as classical OGD-type veins. During the initial stages, the development of mica-tourmaline-rutile-sulfide alteration halos is probably related to fluid infiltration along the main deformation fabric. In the mafic and ultramafic units of the Piché Group, gersdorffite is the main sulfide phase in the alteration halos and occurs as abundant, small (<25µm), euhedral crystals. The fracturing stage of this episode is marked by the precipitation of large euhedral arsenopyrite in vein selvages. In contrast, in the sedimentary units of the Timiskaming Group, where Ni+Co contents of the host rocks are significantly lower, arsenopyrite is the main sulfide phase in both the alteration halos and selvages of QCT veins. Although observation shows that the most significant gold contributions are late relative to QCT veins, these still constitute primary exploration targets. QCT veins and associated selvages and alteration halos host later mineralization events which account for most of the overall gold budget of the deposit, such as the CI and CCP hydrothermal episodes. The presence of CI was only observed in the western sector of the deposit, between the Augmitto and Astoria segments (Fig.1). This gold-bearing episode occurs exclusively as reopening of QCT veins along host rock contacts. This observation, together with the recurrent development of associated extensional veins, both filled by undeformed euhedral carbonate, suggests that the emplacement of these structures occurred during the seismic failure periods of the shear.

The latest gold event corresponds to CCP veinlets, which can be found across the entire property crosscutting all previous assemblages. In the gold-poor eastern sector of the deposit (Bouzan segment), these veinlets represent the only evidence of gold mineralization. Petrography shows that gold contents linked with this episode are particularly relevant when spatially associated with arsenopyrite from QCT selvages and alteration halos. This observation suggests that arsenopyrite constitutes an important geochemical trap enabling gold deposition and therefore its presence played a major role during the CCP mineralization stage. These findings are consistent with gold grades at the deposit, where higher values are associated with the ultramafic and mafic units of the Piché Group at its contact with sedimentary units of the Timiskaming Group where arsenopyrite is more abundant. A particularity of CCP veinlets is that they show variable mineralogical associations with the relative distance towards the Astoria segment. For example, the predominance of pyrrhotite over pyrite as the main Fe-sulfide gradually increases with decreased distance from the Astoria orebody. This pattern is also accompanied by higher abundance of minor phases, including pentlandite as exsolutions in pyrrhotite, and the occurrence of siegenite in Astoria. This data is consistent with the Ni+Co trend documented in pyrite from CCP veinlets. An identical pattern is registered in arsenopyrite from QCT vein selvages and alteration halos.

Thus, a clear change in CCP mineral associations and chemical signature of gold-related sulfides occurs towards the Astoria segment. Given that this segment is also host of late Proterozoic gabbro dykes, this spatial relationship brings into question the plausible influence of the emplacement of the dykes on the formation of the CCP veinlets; either solely acting as a thermal source responsible for remobilization and reconcentration of previously established gold contents, or as a direct source of a late gold input. In order to better comprehend these chemical and mineralogical modifications and overcome censored data, major and minor elements data will be completed with LA-ICP-MS analyses on arsenopyrite and pyrite.

This study shows that mineralization at the Augmitto-Bouzan deposit results from superimposed syn- and post-shear gold events. These findings provide new exploration targets for the segment and, thus, revaluation of barren areas could prove significant.

Acknowledgements

This research is supported by the FRQNT (grant #FT130375). The authors would like to thank Yorbeau Inc. and IamGold for allowing access to the property and support during logging and sampling.

References

Card KD, Ciesielski A (1986) DNAG#1. Subdivisions of the Superior Province of the Canadian Shield. Geoscience Canada 13(1), 5-13

Groves DI, Goldfarb EJ, Robert F, Hart CJR (2003) Gold deposits in metamorphic belts: overview of current understanding, outstanding problems, future research, and exploration significance. Econ. Geology 98(1), 1-29

Palarea-Albaladejo J, Martín-Fernández JA (2015) zCompositions – R package for multivariate imputation of left-censored data under a compositional approach. Chemometr Intell Lab Syst 143:85-96

Poulsen KH (2017) The Larder Lake-Cadillac Break and its gold districts. Reviews in Econ. Geology 19(1), 133-167

Powell W, Carmichael D, Hodgson C (1995) Conditions and timing of metamorphism in the southern Abitibi greenstone belt, Quebec. Canadian Journal. of Earth Sciences 32(6), 787-805

The trace element composition of pyrite through metamorphism at the Yukon-Tanana Terrane, Yukon

Nelson Román[1], Daniel D. Gregory[1], Nathan R. Cleven[2], James J. Ryan[2]
[1] *Department of Earth Sciences, University of Toronto, Ontario, Canada*
[2] *Geological Survey of Canada, British Columbia, Canada*

Abstract. This study aims to constrain how the composition of pyrite changes through metamorphism prior to its transition to pyrrhotite. For this, we used metasedimentary rock samples with different metamorphic grades from the Yukon-Tanana terrane, Yukon. Sulfide composition was analyzed by LA-ICP-MS, and metamorphic grades were constrained by Raman spectroscopy analyses of carbonaceous matter. Peak metamorphic temperatures in the sample suite range from 347 ± 9°C to 598 ± 34°C, consistent with a variation from greenschist to amphibolite metamorphic facies. Compositional changes in pyrite were observed as a function of increasing metamorphic grades. Manganese, Cu, Mo, Ag, As, Sb and Tl show consistent decreasing trends, while Co and Ni concentrations increase with prograde metamorphism. The magnitude of these changes is smaller than the element release associated with the transformation of pyrite into pyrrhotite.

1 Introduction

The trace element chemistry of sedimentary-diagenetic pyrite has been used to understand its parental fluids, and its application ranges from determination of past ocean chemistry (e.g.: Large et al. 2014, 2017; Gregory et al. 2017) to mineral deposit formation (e.g.: Large et al. 2011; Gregory et al. 2015). Moreover, pyrite chemistry has been used to evaluate the metallogenic fertility of sedimentary rock units in orogenic Au deposit districts, considering its potential role as a source of Au in metamorphic devolatilization genetic models (Pitcairn et al. 2006; Large et al. 2011). However, it is not well understood how pyrite trace element content is retained prior to the pyrite–pyrrhotite transition. For evaluating this, we studied samples with variable metamorphic grade from the Yukon-Tanana terrane, Yukon. This study provides some of the first empirical data testing how well pyrite trace element content is retained through metamorphism, expanding on the studies of Pitcairn et al. (2010) and Finch and Tomkins (2017).

2 Geological Background

The Yukon-Tanana terrane (YTT) is one of the pericratonic terranes that constitute the North American Cordillera accretionary orogen in Yukon, Canada (Fig. 1). The YTT formed as an independent crustal fragment in the Late Devonian when it rifted from the western Laurentian continental margin, and it evolved as a pericratonic continental- to island-arc terrane during the Paleozoic (Colpron et al. 2006; Nelson et al. 2013). Its evolution during this period is recorded by four main tectonic assemblages: (1) the Snowcap assemblage, a basal assemblage of siliciclastic rocks with continental margin affinity; and the (2) Finlayson, (3) Klinkit and (4) Klondike assemblages, all younger volcano-sedimentary assemblages with arc and back-arc affinity (Colpron et al. 2006; Nelson et al. 2013).

Widespread regional metamorphism occurred in YTT, mostly driven by its accretion to the western margin of Laurentia and starting as early as the Early Mississippian and continuing, intermittently, to the mid-Cretaceous (Staples et al. 2016). Metamorphism in the YTT reached amphibolite facies metamorphic grade (Staples et al. 2016), but lower metamorphic grades have been reported in southeastern Yukon (Read et al. 1991).

The YTT hosts orogenic Au mineralization in the Klondike, White Gold and Dawson Range mineral districts (Fig. 1; Allan et al. 2013). It has been suggested that coeval metamorphism and associated rock dehydration of an underplated portion of the YTT could have provided mineralizing metamorphic fluids for orogenic Au mineralization in some of these districts (Staples et al. 2016).

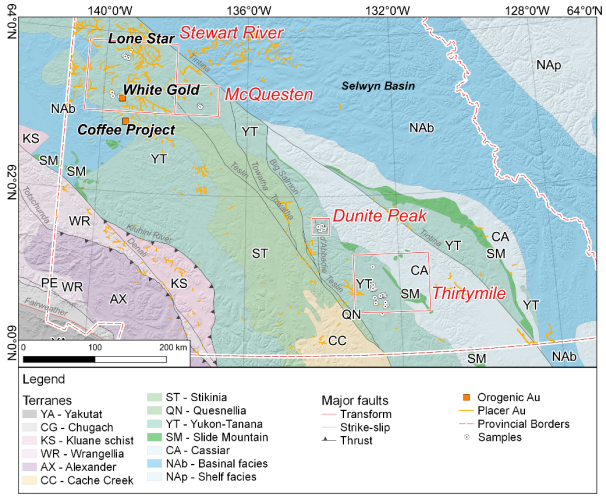

Figure 1. Terrane map of Yukon, showing the location of the YTT (YT in the map; Nelson et al. 2013). The regions considered for sampling are indicated with red rectangles.

3 Samples and Methods

Seventeen metasedimentary samples from the Finlayson and Snowcap assemblages were used for this study. The sample suite includes micaceous quartzite and metapelite with variable content of carbonaceous matter. To represent different metamorphic grades, rock samples from the Thirtymile and Dunite Peak regions, in southeast Yukon, and from the Stewart River and McQuesten regions in west-central Yukon were utilized (Fig. 1).

The trace element composition of pyrite and pyrrhotite was analyzed using laser ablation inductively coupled plasma mass spectrometry (LA-ICP-MS), at the Department of Earth Sciences, University of Toronto (UofT), and at the Geological Survey of Canada (GSC) in Ottawa, Ontario. The following isotopes were measured: ^{23}Na, ^{25}Mg, ^{27}Al, ^{29}Si, ^{34}S, ^{39}K, ^{42}Ca, ^{47}Ti, ^{51}V, ^{55}Mn, ^{57}Fe, ^{59}Co, ^{60}Ni, ^{65}Cu, ^{66}Zn, ^{75}As, ^{77}Se, ^{95}Mo, ^{109}Ag, ^{121}Sb, ^{125}Te, ^{181}Ta, ^{182}W, ^{197}Au, ^{205}Tl, ^{206}Pb, ^{207}Pb, ^{208}Pb and ^{209}Bi. Calibration was done using matrix-matched reference materials. After data reduction, data were normalized to account for the matrix material ablated together with the target sulfide grain during analysis. Spots with more than 30% matrix were discarded. Additionally, only spots with a S measured/S expected ratio between 0.75-1.25 were considered. Using this scheme, 78 pyrite and 28 pyrrhotite spot analyses of a total of 203 spots comply with these quality control criteria.

The degree of graphitization of carbonaceous matter in the samples was used as a proxy for the peak metamorphic temperature, and this, in turn, as an indication of the metamorphic grade of the samples (Beyssac et al. 2002, Aoya et al. 2010). This was studied through Raman spectroscopy on carbonaceous materials (RSCM), at the Royal Ontario Museum, Toronto, Canada, following the analytical conditions recommended by Aoya et al. (2010). Each sample was characterized by the acquisition of at least 20 spot analyses. The RSCM temperatures reported here were calculated following the Aoya et al. (2010) procedures, with one standard deviation as the associated error.

4 Results

4.1 Sulfide occurrence

The main sulfides occurring in the samples are pyrite and pyrrhotite (Fig. 2). Chalcopyrite, galena and sphalerite were also found in some samples.

Pyrite occurs in most samples, but with low abundance (<0.5% modal). It occurs primarily as small (<20 µm) euhedral to subhedral grains, between recrystallized quartz grains or included in them (Fig. 2A, B). Pyrrhotite is present in the four YTT regions and it is less common than pyrite. Its main occurrence mode is as inclusions in quartz as small grains (<20 µm) associated with pyrite (Fig. 2C), or also it can be present as larger grains (>500 µm) associated with chalcopyrite (Fig. 2D).

4.2 Pyrite and pyrrhotite LA-ICP-MS analyses

The trace element composition of pyrite and pyrrhotite in the YTT samples is presented in Figure 3. The most abundant element in the analyzed pyrite grains is Ni, with a median concentration of 656 ppm. Other elements with median concentrations above 100 ppm are Co, As, Se and Pb. Gold was above the detection limit only in 22 of the 78 pyrite spot analyses, with a median concentration of 0.18 ppm after matrix correction. The most abundant elements in pyrrhotite are Ni and Co, with medians of 1359 and 653 ppm, respectively. Other elements detected and quantified in most spots were Mn, Se, Ag, Pb and Bi. Conversely, As and Au concentrations were mostly below the detection limit.

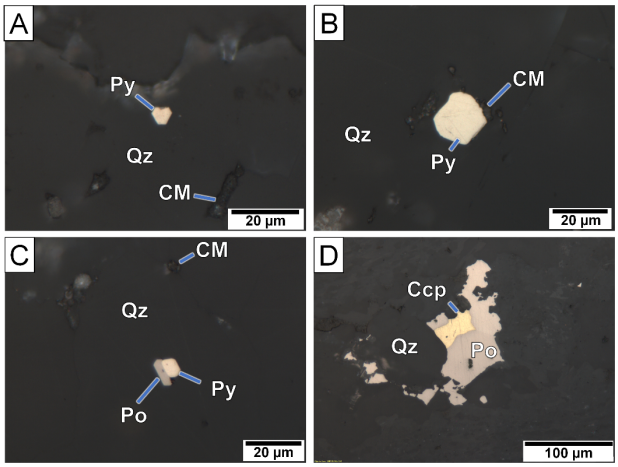

Figure 2. Reflected light microphotographs of the sulfides in YTT samples. A: euhedral pyrite grain between quartz grains; B: euhedral pyrite grain included in quartz and associated with carbonaceous matter. C: pyrite and pyrrhotite grains included in quartz. D: Composite pyrrhotite-chalcopyrite grain between quartz crystals. Abbreviations: CM: carbonaceous matter, Ccp: chalcopyrite, Po: pyrrhotite, Py: pyrite, Qz: quartz.

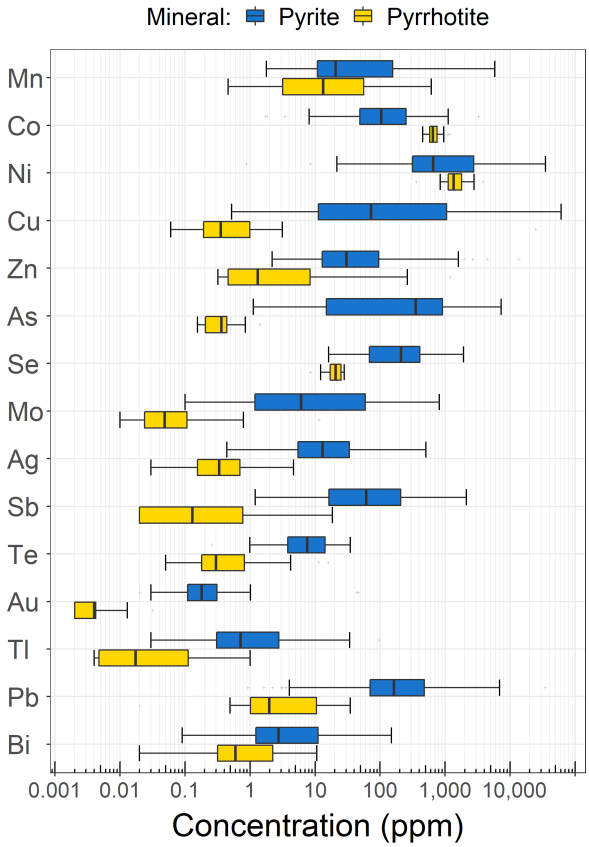

Figure 3. LA-ICP-MS trace element concentrations in pyrite and pyrrhotite in the YTT samples.

Most trace elements are depleted in pyrrhotite compared to pyrite, except Co and Ni (Fig. 3). The most notable differences between both minerals are their Cu, As, Mo and Sb concentrations, where pyrrhotite has concentrations of at least two orders of magnitude less than pyrite.

4.3 RSCM Temperatures

RSCM temperatures range from 347 ± 9°C to 598 ± 34°C in the analyzed samples (Table 1). The temperatures vary across regions and the lowest temperatures are found in the Thirtymile region. Two distinct RSCM temperature groups occur in the Thirtymile region: one ~340-360°C and another group with higher temperatures (~400-500°C). Similar temperatures were obtained for samples in proximity to each other, denoting spatial consistency in the RSCM results.

Table 1: RSCM temperatures of the YTT samples.

Region	Sample	RSCM (°C)	
		Temp.	St.Dev.
Stewart River	03RAY052B1	598	35
	00RAY271A	578	30
	03GGA028A01	576	33
McQuesten	09RAYEK010A01	583	27
	09RAYEK002A01	526	28
Dunite Peak	16RAYAP072A	510	32
	16RAYAP192A	492	17
Thirtymile	18RAYNC128A	509	30
	18RAYNC030B	476	17
	18RAYNC091A	472	23
	18RAYNC024A	460	17
	18RAYNC057A	355	10
	18RAYNC070A	351	3
	18RAYNC062A	347	9

5 Discussion

5.1 The origin of pyrite in the YTT

The Co/Ni ratios of pyrite in YTT is <2 for most analyzed spots (Fig. 4), suggestive of a sedimentary or diagenetic origin (e.g.: Gregory et al. 2015). In addition, Co and Ni concentrations of pyrite in YTT are similar to the pyrite in the Road River and Earn groups of the Selwyn basin (Fig. 4), interpreted as sedimentary to diagenetic (Sack et al. 2018). Further, the pyrite textures in the YYT samples (Fig. 2) resemble the small euhedral pyrite textures reported by Gregory et al. (2015) in black shales, also interpreted as early diagenetic. Considering this, pyrite in YTT could have a sedimentary-diagenetic origin, justifying the use of it to study how sedimentary pyrite composition evolves through metamorphism.

5.2 Peak temperatures of metamorphism

Based on their peak metamorphic temperatures, the samples used for pyrite compositional analyses can be subdivided in three groups, with generalized temperature in the following ranges: 340-360°C (Group 1), 450-500°C (Group 2) and 500-600°C (Group 3). These groups broadly represent greenschist, upper greenschist to lower amphibolite and amphibolite facies, respectively.

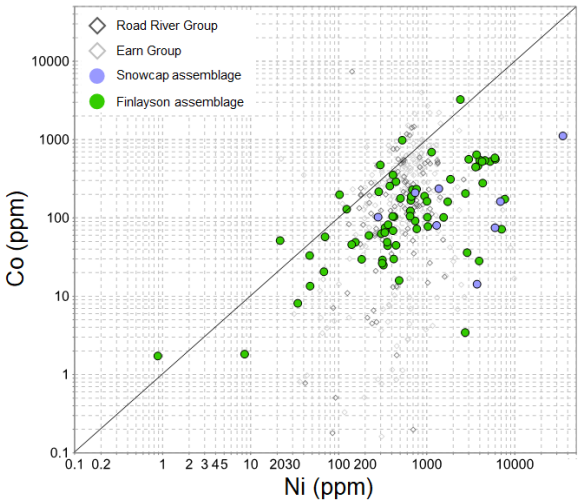

Figure 4. Co vs. Ni concentrations in pyrite of YTT, compared with pyrite of the Road River and Earn Groups of the Selwyn Basin (from Sack et al. 2018).

5.3 Trace element composition in pyrite and metamorphic grade

Clear decreasing concentration trends with higher metamorphic grades are observed for Mn, Cu, Mo, Ag, As, Sb and Tl in YTT pyrite (Fig. 5). Conversely, the concentrations of Co and Ni increase with higher metamorphic grades. Other elements, such as Zn, Se, Te, Au, Pb and Bi, do not show obvious trends.

The enrichment of Co and Ni could be caused by a relative enrichment caused by the loss of other elements (S). The loss of Cu could be linked to the formation of chalcopyrite. Similarly, the loss of Ag and Sb could be due to remobilization to galena, a process suggested by Pitcairn et al. (2010) during prograde metamorphism. The same process could be acting on Tl, an element commonly enriched in galena (George et al. 2018). More data is required to accurately evaluate the loss of Au and Te, especially considering that most analyses were below the detection limit for these elements.

The remobilization trends shown in Figure 5 do not reflect how elements are lost during breakdown of pyrite into pyrrhotite, one of the main mechanisms proposed for explaining release of metals to form orogenic Au deposits (Tomkins 2010). The data compiled by this study suggests that the magnitude of the compositional variation of pyrite through metamorphism (Fig. 5) is smaller than the change provoked by the breakdown of pyrite into pyrrhotite (Fig. 3), supporting the fundamental role of this process for metal release.

Since some elements show the same trends with metamorphism, concentration ratios between them might constitute robust source trackers that could be preserved through metamorphism. This seems to be the case for Co/Ni ratios. Conversely, the results

here suggest that caution must be exerted for the use of single element thresholds as paleo-chemical proxies or gold fertility indicators.

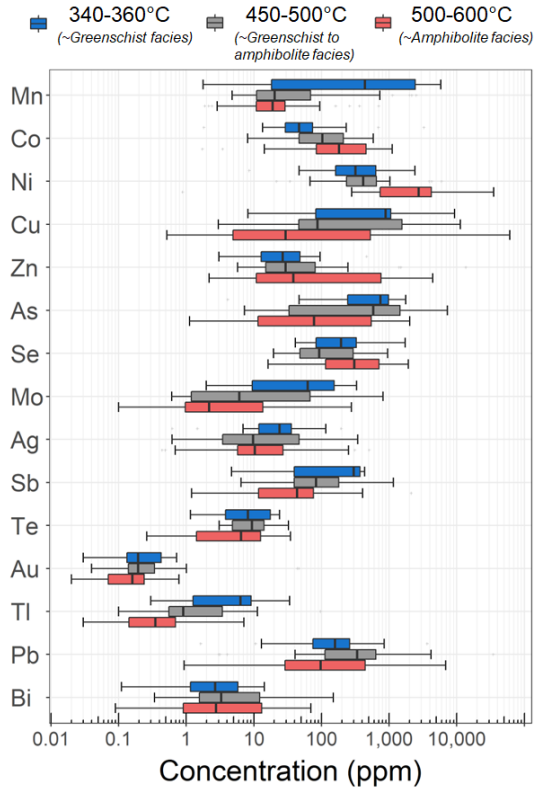

Figure 5. LA-ICP-MS trace element concentrations in pyrite, subdivided by metamorphic grade.

6 Concluding remarks

This study suggests that the trace element composition of pyrite changes through metamorphism, however, the magnitude of this change is less than the change associated with pyrite-pyrrhotite transformation. Ratios between elements with similar behavior during metamorphism could constitute robust trackers of the original trace element composition of pyrite.

Acknowledgements

This study was funded by the Geological Survey of Canada, through the Research Affiliate Program. Additional funding was provided through a NSERC Discovery Grant to D. Gregory. N. Román thanks financial support provided by the Hugh Snyder International Scholarship in Earth Sciences (Ph.D. scholarship). We thank Xu Chu, Veronica Di Cecco and Ivano Gennaro for their help with RSCM analyses, and Hehe Jiang and Colin Bray for their help with LA-ICP-MS analyses.

References

Allan MM, Mortensen JK, Hart CJR, et al (2013) Magmatic and Metallogenic Framework of West-Central Yukon and Eastern Alaska. In: Colpron M, Bissig T, Rusk BG, Thompson JFH (eds) Tectonics, Metallogeny, and Discovery: The North American Cordillera and Similar Accretionary Settings. Society of Economic Geologists, pp 111–168

Aoya M, Kouketsu Y, Endo S, et al (2010) Extending the applicability of the Raman carbonaceous-material geothermometer using data from contact metamorphic rocks. Journal of Metamorphic Geology 28:895–914

Beyssac O, Goffé B, Chopin C, Rouzaud JN (2002) Raman spectra of carbonaceous material in metasediments: a new geothermometer. Journal of Metamorphic Geology 20:859–871

Colpron M, Nelson JL, Murphy DC (2006) A tectonostratigraphic framework for the pericratonic terranes of the northern Canadian Cordillera. In: Colpron, M. and Nelson, J.L., eds., Paleozoic Evolution and Metallogeny of Pericratonic Terranes at the Ancient Pacific Margin of North America, Canadian and Alaskan Cordillera: Geological Association of Canada, Special Paper 45. pp 1–23

Finch EG, Tomkins AG (2017) Pyrite-Pyrrhotite Stability in a Metamorphic Aureole: Implications for Orogenic Gold Genesis. Economic Geology 112:661–674

George LL, Biagioni C, D'Orazio M, Cook NJ (2018) Textural and trace element evolution of pyrite during greenschist facies metamorphic recrystallization in the southern Apuan Alps (Tuscany, Italy): Influence on the formation of Tl-rich sulfosalt melt. Ore Geology Reviews 102:59–105

Gregory DD, Large RR, Halpin JA, et al (2015) Trace Element Content of Sedimentary Pyrite in Black Shales. Economic Geology 110:1389–1410

Gregory DD, Lyons TW, Large RR, et al (2017) Whole rock and discrete pyrite geochemistry as complementary tracers of ancient ocean chemistry: An example from the Neoproterozoic Doushantuo Formation, China. Geochimica et Cosmochimica Acta 216:201–220

Large RR, Bull SW, Maslennikov VV (2011) A Carbonaceous Sedimentary Source-Rock Model for Carlin-Type and Orogenic Gold Deposits. Economic Geology 106:331–358

Large RR, Halpin JA, Danyushevsky LV, et al (2014) Trace element content of sedimentary pyrite as a new proxy for deep-time ocean–atmosphere evolution. Earth and Planetary Science Letters 389:209–220

Large RR, Mukherjee I, Gregory DD, et al (2017) Ocean and Atmosphere Geochemical Proxies Derived from Trace Elements in Marine Pyrite: Implications for Ore Genesis in Sedimentary Basins. Economic Geology 112:423–450

Nelson JL, Colpron M, Israel S (2013) The Cordillera of British Columbia, Yukon, and Alaska: Tectonics and Metallogeny. In: Colpron M, Bissig T, Rusk BG, Thompson JFH (eds) Tectonics, Metallogeny, and Discovery: The North American Cordillera and Similar Accretionary Settings. Society of Economic Geologists, pp 53–109

Pitcairn IK, Teagle DAH, Craw D, et al (2006) Sources of metals and fluids in orogenic gold deposits: Insights from the Otago and Alpine schists, New Zealand. Economic Geology 101:1525–1546

Pitcairn IK, Olivo GR, Teagle DAH, Craw D (2010) Sulfide evolution during prograde metamorphism of the Otago and Alpine schists, New Zealand. Canadian Mineralogist 48:1267–1295

Read PB, Woodsworth GJ, Greenwood HJ, et al (1991) Metamorphic map of the Canadian Cordillera: map 1714A. Geological Survey of Canada

Sack PJ, Large RR, Gregory DD (2018) Geochemistry of shale and sedimentary pyrite as a proxy for gold fertility in the Selwyn basin area, Yukon. Mineralium Deposita 53:997–1018

Staples RD, Gibson HD, Colpron M, Ryan JJ (2016) An orogenic wedge model for diachronous deformation, metamorphism, and exhumation in the hinterland of the northern Canadian Cordillera. Lithosphere 8:165–184

Tomkins AG (2010) Windows of metamorphic sulfur liberation in the crust: Implications for gold deposit genesis. Geochimica et Cosmochimica Acta 74:3246–3259

Structural control of gold deposits at Eastern Alta Floresta Mineral Province Brazil, preliminary results

Renata Augusta Sampaio Paes' Maria José Mesquita', Márcia Elisa Boscato Gomes[2], Igor de Camargo Moreira', Hevelyn Eduarda da Silva Martins', José Henrique Matos', Alberto Ruggiero', Guilherme Primo', Diego Fernando Ducart', Luciano Poggi', André Massanobu Ueno Kunifoshita' Leonardo Zanchetta de Laurentis' and João Gabriel da Silva'

[1]Campinas University, Campinas, São Paulo, Brazil

[2]The Rio Grande do Sul Federal University, Porto Alegre, RS, Brazil

Abstract. The linear features acquired through satellite and aerogeophysics data, in association with structural measures of foliation and mineralised veins orientation in field mapping, provide a previous analysis from the area's structural framework, a routine suitable for the Alta Floresta Mineral Province, a high areal extension, important and weakly understood Brazilian mineral province. This work points out the existing correlation between the primary gold deposits hosted in rocks of calcium-alkaline to the alkaline composition of the province to the presence of NW first-order shear zones, NS and EW secondary shear zones, as well as relatively more recent NS and NE faults and fractures.

1 Introduction

The Alta Floresta Mineral Province (AFMP) has an extensive and productive history of artisanal and small-scale mining and is currently one of the most promising regions for gold and copper exploration in Brazil. Consequently, research projects and investments have increased exponentially, particularly following the discovery of significant copper and gold occurrences in 2018 (Bloomberg 2018.).

Located at northern Mato Grosso State, the AFMP presents an approximately 500 km² areal extension, with dozens of primary gold mineralisations that can be grouped into three major types according to the ore typology (Mesquita et al. 2022): (i) Au ± Cu in shear zone veins, following the example of the Edu, Paraíba, Basilio, Peteca, Porteira-Buriti, Viúva, Serrinha de Guarantã (and Luiz Bastos; (ii) Cu + Au ± Mo deposits disseminated in breccias or in stockworks, for example the Pé Quente, X1, Luizão, Serrinha and Jaca and (iii) Au + base metal deposits in veins developed on faults as for example the Francisco Bigode, and Luiz Bastos deposits. The detailed set of work carried out on these deposits is available at Mesquita et al (2022).

There are several metallogenetic models described for the mineralisation, such as porphyry (Moura et al. 2006; Assis 2015) and intermediate sulfidation epithermal (Assis et al. 2017), orogenic type (Paes de Barros 1994; Siqueira 1997; Silva Abram 2008; Moreton and Martins 2005) and Intrusion related gold system - IRGS (Santos et al. 2001). However, the spatial relationships between mineralisation and the structural framework remain poorly understood, and a lack of integration, data is necessary to construct of robust exploratory models that make exploration in the area feasible and more dynamic.

2 Geological context

The PMAF is in the southwestern Amazon Craton in northern Mato Grosso state (Projeto Radambrasil - Brazil, 1980), between Tapajós-Parima (2.03-1.88 Ga) and Rondônia-Juruena (1.82-1.54 Ga) provinces (Santos et al. 2000).

The PMAF is elongated in a WNW-ESE direction, bordered to the north by the Cachimbo Graben and to the south by the Caiabis Graben. In simplified form, it is composed of an older core, called the Peixoto de Azevedo domain (Figure 2), of the former Tapajós-Parima Province (c. 2,05-1,97 Ga, rocks related to the Cuiú-Cuiú volcanic arc) surrounded and cut by younger rocks of the Rondônia-Juruena Province (c.1,82-1,52 Ma, rocks related to the Rondônia-Juruena volcanic arc) (Santos et al. 2000, 2015; Duarte et al. 2012, 2019) (Figure 1).

Some authors point to the origin of the deposits as a single hydrothermal magmatic event developed at different crustal levels in the Estatherian period (Trevisan 2015; Assis 2015; Assis et al. 2017). While for others, the deposits are differentiated into two mineralizing hydrothermal events, one hydrothermal-shear, generating orogenic gold deposits, and another magmatic-hydrothermal generating porphyry-epithermal deposits (Pimenta 2018; Poggi 2019; Mesquita et al. 2022; Poggi et al. 2022).

3 Mineralisation's structural analysis, an overview

The mineralisation's host rocks are 2.04-1.98 Ga granitoids, quartz-feldspathic gneiss, and ultramafic amphibolites, they present at least two deformations episodes. The first one, Dn presents foliation Sn trending to 00-50° and dips 70-90 WNW (Fig 2), that progress from millimeter-scale alternating feldspar-quartz-rich and phyllosilicate-rich domain in orthogneiss to a well-developed spaced foliation in metagranitoids and metamafic rocks (Fig. 3a)

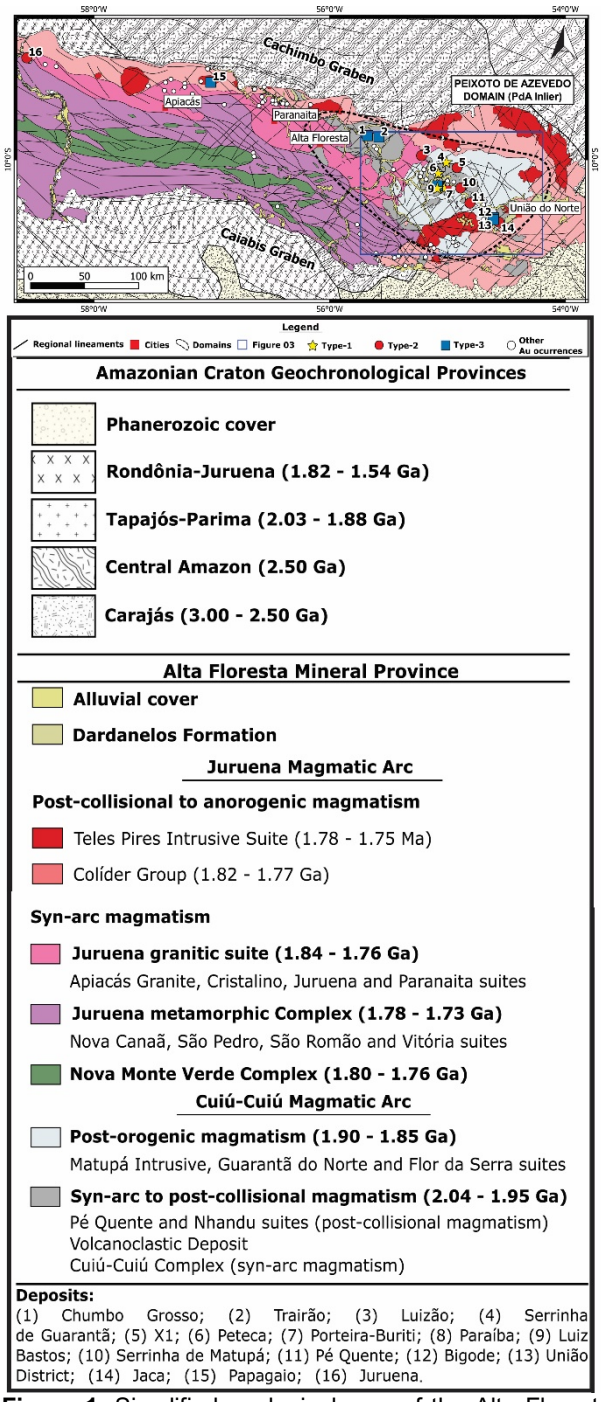

Figure 1. Simplified geological map of the Alta Floresta Mineral Province, highlighting the Peixoto de Azevedo Domain (contour dotted in black.). modified from Lacerda Filho et al. 2004.

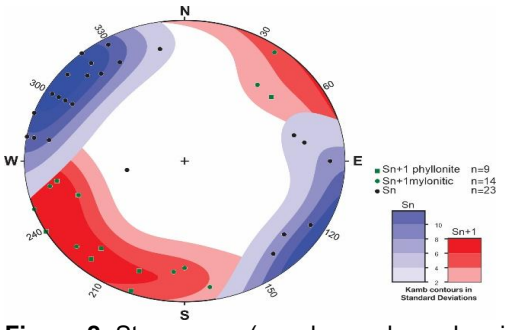

Figure 2. Stereogram (equal area, lower hemisphere) of Sn foliation poles in the host rocks and Sn+1 foliation mylonite and phyllonite.

A second deformation episode (Dn+1) developed several WNW-trending first-order shear zones (Fig. 2). They are transpressional to strike-slip, mostly with dextral movements. Dn+1 develops tens of meters of mylonites (Fig. 3b) transposed to the previous granitoids' Sn. Feldspars porphyroclasts wrapped by an anastomosed mafic matrix (biotite-magnetite/ilmenite-pyrite) define the mylonitic foliation Sn+1 (Fig. 3c). Sn+1 displays an average N20-40W dipping 50-70°SW (Fig. 2). There is a metric to centimetric gradation between mylonites and phyllonites. In the phyllonite, Sn+1 is a continuous schistosity defined by muscovite, biotite and chlorite bands alternating with quartz bands. The feldspars are partially or entirely substituted by micas (Fig. 3d).

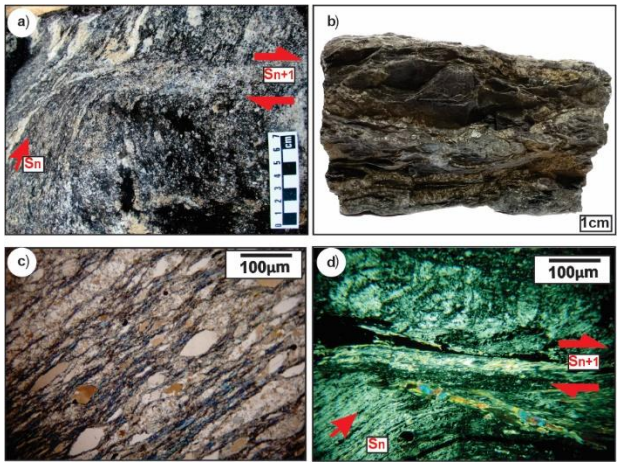

Figure 3. (a) Sn banding transposed by Sn+1 (discrete shear band in 1.98 Ga (Miguel 2011) metagranodiorite (Mesquita et al. 2022); (b) Banded ultramafic amphibolites, with pyrite veinlets associated to the Sn+1 banding; (c) mylonitic foliation defined by tremolite-actinolite associated with white mica chlorite, and quartz ribbon microlithon; (d) Sn banding intercepted by Sn+1.

4 Interpretation

Through the integration of aero-geophysics data, available from the Brazil Geological Service (Alves et al. 2019), and shuttle radar topography (SRTM), used free of charge from the SRTM image catalog on the United States Geological Survey website, in association with field mapping, linear features were interpreted.

Flat topography with a few rocks outcrops characterizes the eastern part of Alta Floresta Mineral Province. We identify different linear features orientations in which the WNW family direction is highlighted, associated with NE continuous structures and NS and NE discontinuous structures (Fig. 4) There are some NW structures already described in the literature as first-order shear zones (Paes de Barros 2007; Miguel Jr. 2011 and Quispe 2016), associated with mineralised veins.

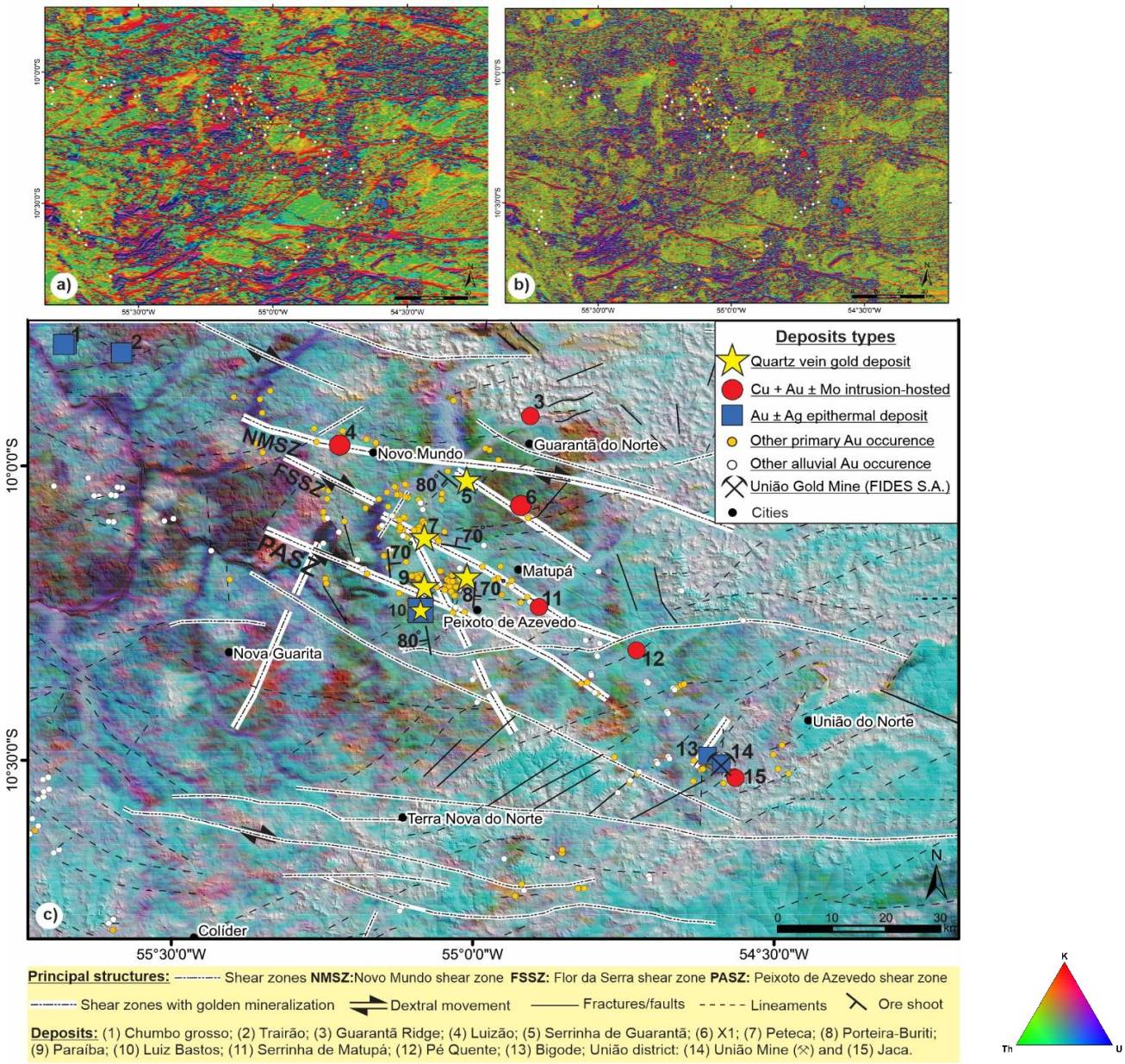

Figure 4. The eastern part of the Alta Floresta Mineral Province aero-geophysics and SRTM images: (a) First vertical derivative from the total magnetic field; (b) Second vertical derivative; (c) Eastmost Alta Floresta Mineral Province geological map, with the main mineral deposits and structures from structural interpretation, with SRTM and ternary aero-gamma spectrometric. Modified from Alves et al. (2019)

Parallel to the first-order shear-zones is found high-grade and low tonnage deposits, restricted to the principal structure, as the Serrinha de Guarantã deposit (Fig 5), the thickest gold quartz vein at the area (1-5m) (Fig. 6c). The mineral assemblage is phlogopite, calcite, quartz, bornite, chalcocite, and chalcopyrite (Fig. 6d) (Rios 2019).

Most gold-quartz veins concentrate in subsidiaries to the first-order shear zones (Fig. 5). These subsidiary shear zones are north-trending, controlling the Paraíba mine (Fig. 6a), Luiz Bastos and Buriti–Porteira deposits, or east-trending, controlling the Peteca mine (Fig. 6e), João Fidelis and Queiroz deposits. The ore is ccp+py, and gold occurs as inclusions, infilling fractures in pyrite and as free gold (Fig. 6b and 6f).

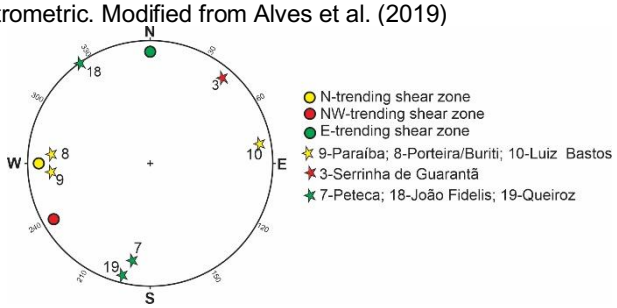

Figure 5. Stereogram (equal area, lower hemisphere) of poles of phyllonite foliation Sn+1 and respectively quartz vein orientations in the shear zone system.

NE-trending faults and fractures crosscut and dislocate the first-order shear zones.

These NE-trending faults appear as discontinuous and discrete lineaments, shallow

structures which draw the landscape. These structures controlled mafic dykes (Rios 2019) and most of the magmatic-hydrothermal deposits, notably the epithermal ones as Trairão, Luiz Bastos, and Francisco-Bigode and União Gold Mine (União do Norte District).

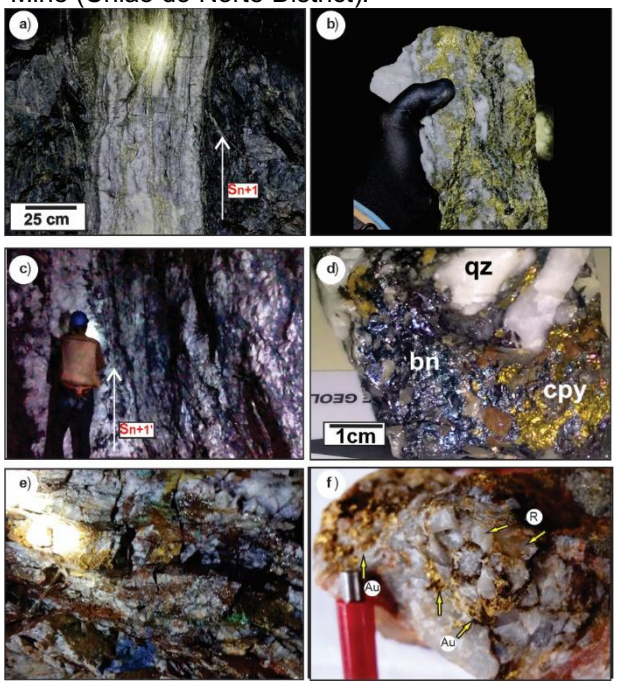

Figure 6. Characteristics of structural controlled ore bodies. Paraiba Mine: a) Mineralised laminated quartz vein at (b) Anastomosed ore vein (Caption from the company public website); Serrinha de Guarantã deposit: (c) Four meters thick mineralised quartz vein and (d) Ore sample; Peteca mine: (e) intensively fractured quartz vein (Caption from the company public website), (f) Free-gold sample (Mesquita et al. 2022).

There is a close relationship between the presence of structurally controlled deposits and the presence of shear zones, fractures, and faults. But the relationship between these requires geochronological studies to establish their temporal evolution. Research that is in progress.

5 Conclusions

The Type-1 gold-quartz veins concentrate along the anastomosing NW lineaments defined by the first-order shear zones. Most of them concentrate in the subsidiary shear zones as N-trending (Paraíba, Luiz Bastos, and Buriti-Porteira deposits) and E-trending (Peteca, João Fidelis, and Queiroz deposits).

NE-trending faults and fractures control most of the Type-2 and -3 deposits. The NE faults crosscut and dislocate the WNW first-order shear zones and the Sn+1 foliation (hosting the Type-1 deposits). The NE-trending faults appear as discontinuous and discrete lineaments. Many Type-3 veinlets are within these NE faults and fractures and their subsidiaries, or in the intersection between the older WNW-trending shear zones and the NE-trending faults.

Acknowledgements

The authors are thanked to the Institute of Geosciences of the University of Campinas, PA Gold Mineração e Metalurgica LTDA, FIDES Mining and METAMAT - Companhia Matogrossense de Mineração. This research has been financially supported by the CAPES - Coordination of Superior Level Staff Improvement through student grant number 88887.481707/2020-00 and SEG -The Society of Economic Geologists, with the Student Research Grant program 20-110 provided by the Hugh E. Mckinstry Fund.

References

Alves CL, et al (2020) The Orosirian Cuiú-Cuiú magmatic arc in Peixoto de Azevedo domain, Southern of Amazonian craton. Journal of South American Earth Sciences, 102, 102648. https://doi.org/10.1016/j.jsames.2020.102648

Assis RR et al (2017) Linking the Timing of Disseminated Granite-Hosted Gold-Rich Deposits to Paleoproterozoic Felsic Magmatism at Alta Floresta Gold Province, Amazon Craton, Brazil: Insights from Pyrite and Molybdenite Re-Os Geochronology. Economic Geology, 112: 1937–1957. https://doi.org/10.5382/econgeo.2017.4535

Bloomberg (2018) Has Anglo American found something big in Brazil?. http://www.bloomberg.com/news/articles/2018-07-26/has-anglo-american-found-something-big-in-brazil

Lacerda Filho JV et al (2004) Geologia e Recursos Minerais do Estado de Mato Grosso: texto explicativo dos mapas geológicos e de recursos minerais do Estado de Mato Grosso. MME/CPRM/ SICME-MT. Programa Integração, Atualização e Difusão de Dados da Geologia do Brasil e Subprograma Mapas Geológicos estaduais, escala (1:1.000.000). Cuiabá: MME/CPRM/SICME-MT. v. 1. 235 [in Portuguese].

Mesquita MJ et al (2022) Paleoproterozoic gold deposits at AFMP, Brazil: two overprinted mineralizing events? From: Torvela, T., Lambert-Smith, J. S. and Chapman, R. J. (eds). Recent Advances in Understanding Gold Deposits: from Orogeny to Alluvium. Geological Society, London, Special Publications, 516. https://doi.org/10.1144/SP516-2021-64

Moura MA et al (2006) Granite-related Paleoproterozoic, Serrinha gold deposit, Southern Amazonia, Brazil: hydrothermal alteration, fluid inclusion and stable isotope constraints on genesis and evolution. Economic Geology, 101, 585-605. https://doi.org/10.2113/gsecongeo.101.3.585

Pogi L et al (2022) New Insights into the Evolution and Footprints of the Paraíba Au-Cu-Mo Deposit, Alta Floresta Mineral Province (Brazil), through Integration of Spectral and Conventional Methods. Minerals 2022, 12, 1327. https://doi.org/10.3390/min12101327

Santos JOS et al (2001) Gold deposits of the Tapajós and Alta Floresta domains, Tapajós-Parima orogenic belt, Amazon Craton, Brazil. Mineralium Deposita, 36, 278-299. https://doi.org/10.1007/s001260100172

Santos JOS, et al (2000) A new understanding of the provinces of the Amazon Craton based on integration of field mapping and U–Pb and Sm–Nd geochronology. Gondwana Research, 3,453–488, https://doi.org/10.1016/S1342-937X(05)70755-3

Trevisan VG (2015) Estudo comparativo entre mineralizações filonares de Au+Cu e Au + metais de base do setor leste da Província de Alta Floresta (MT), Cráton Amazônico. Master's thesis, Institute of Geosciences, University of Campinas, Brazil.

Metallogeny of gold (from in-situ to placer) in the Loch Tay area of Central Scotland

Lucia Savastano[1], Robert J. Chapman[1], Taija M. Torvela[1]
[1]School of Earth and Environment, University of Leeds, United Kingdom

Abstract. The Loch Tay area of Central Scotland hosts gold mineralisation in the form of both vein-sited and widespread placer occurrences. This work seeks to elucidate the unresolved genetic relationships between these two gold occurrence types and to provide insights into the local mineralisation styles. Assessing the compositional features of in-situ gold against those of their proximal eluvial and placer expressions provides: i) a template to investigate the origins of placer gold for which the hypogene source is unknown; ii) insights into the compositional variations of gold between paragenetic stages where the hypogene source is known. The microchemical signature (alloy composition and inclusion mineralogy) of gold has quantitatively been determined on a particle basis and detailed paragenetic sequences have been established for nearby, gold-bearing hydrothermal veins. Gold precipitates at least twice in the Calliachar Burn, River Almond and Lead Trial hydrothermal systems, which have ultimately resulted in distinguished genetic features. Although wider, the range of signatures exhibited by placer gold populations is compatible with that of local eluvial and in situ gold samples, suggesting subtle mineralogical variations within geographically proximal and genetically related vein systems.

1 Introduction and geological background

Particulate gold is highly stable in most surface settings, retaining compositional features that can be representative of the environment of gold precipitation. The intrinsic gold/silver ratios of the particles are controlled by the chemical and physical conditions at the point of precipitation from a hydrothermal fluid (Gammons and Williams Jones, 1995). Natural gold alloy may also contain minor amounts of Cu, Pd or Hg, which may form useful complementary discriminants (e.g., Leake et al., 1997; Chapman et al., 2000a). Alluvial gold populations are generally the product of relatively large volumes of mineralised material, therefore exhibit wider ranges in silver content than vein-hosted gold due to greater variations in the conditions of gold precipitation (Chapman et al., 2000a). Consequently, a detailed evaluation of the particle gold/silver ratios yields the potential to inform on the (evolving) mineralising conditions within the related ore body.

Consideration of the gold alloy composition has contributed to the definition of detailed paragenetic sequences in various hydrothermal systems (e.g., Parnell et al., 2000; Arif and Baker., 2004; Spence-Jones et al., 2018). Because an increased Ag content derives from lower temperatures and/or the lower Au/Ag ratio of the modifying fluids, with respect to the initial mineralizing fluids (Gammons and William Jones, 1995), it can be deduced that silver-rich gold alloys generally form later in the paragenesis. Mineral inclusions in placer gold can inform on the nature and proximity of the in-situ mineralisation, if similar species and assemblages are found in the hypogene environment (e.g., Leake et al., 1997; Chapman et al., 2010b).

Our methodology allows the correlation of compositional features of gold from specific paragenetic stages with that of nearby eluvial and gossan-derived gold, to inform on the potential source of proximal placer gold.

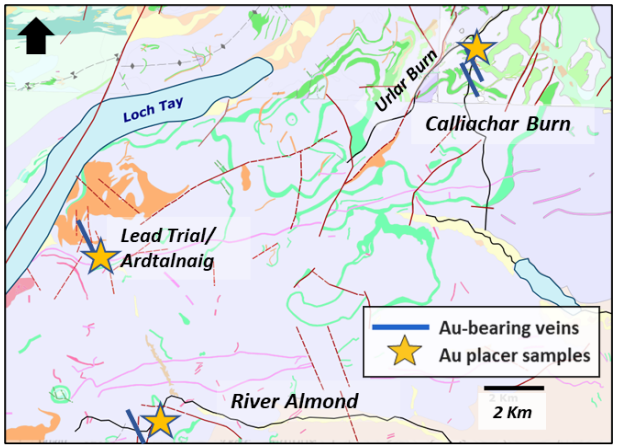

Figure 1. Map with locations of the sites of interest (after the geological map from https://digimap.edina.ac.uk/).

Near Loch Tay (Perthshire, Central Scotland), NNW-SSE-striking vein arrays outcrop across the Southern Highland Group of the Grampian Highlands. At Calliachar-Urlar Burn, River Almond and the 'Lead Trial' (Green Glen Minerals, 2023), some of these veins have been identified as high-grade, gold-bearing ones (Figure 1; e.g., Mason 1990, Ixer et al. 1997). Their mineralogy mainly consists of quartz plus sulphide assemblages which partially vary upon location (commonly pyrite, galena and chalcopyrite). The whole area is generally overgrown by vegetation, and gold can more frequently be recovered as placer particles in stream sediments, particularly at Calliachar Burn and River Almond (e.g., Chapman et al. 2023).

2 Methodology

2.1 Hydrothermal vein sampling and analysis

Sulphide/gold-bearing veins were sampled at the main localities indicated in Figure 1. Samples of six different veins from the Calliachar-Urlar system and of five veins from Lead Trial/Ardtalnaig were

analysed to reconstruct overarching vein parageneses for both localities; a vein paragenetic history at River Almond was established by extensive analysis of a single gold-bearing vein. The analytical protocol consists of the application of SEM-CL (cathodoluminescence) on quartz and SEM-EDS detection of mineral phases in the BSE (Back-Scatter) mode.

2.2 Gold particle sampling and analysis

The gold sample suite analysed for this study is indicated in Table 1. The in-situ gold samples (Calliachar_6V and Almond_6V) are located in the same veins from which the gossan-related (Calliachar_6G) and the crushed-ore (Almond_6H) gold samples were respectively retrieved. Placer gold populations were recovered downstream in Calliachar Burn, upstream in River Almond and in the Ardtalnaig Burn, in proximity to the ore-bearing veins. Gold compositional signatures (e.g., Chapman et al., 2000a) were determined on a particle basis by the application of i) EPMA on gold alloy; ii) SEM-EDS on mineral inclusions.

Table 1. Gold samples used for this study, with details on sample types/sizes and respective localities.

Sample ID	Locality/sample type	No of particles
Calliachar_1	*Calliachar Burn_placer*	333
Calliachar_6G	*Calliachar Burn_gossan*	77
Calliachar_6V	*Calliachar Burn_in situ*	16
Almond_5	*River Almond_placer*	605
Almond_6H	*River Almond_crushed ore*	104
Almond_6V	*River Almond_in situ*	18
Lead Trial	*Lead Trial_crushed ore*	204
Ardaltnaig	*Ardtalnaig Burn_placer*	58

3 Parageneses of the Au-bearing veins

The paragenetic histories of the Calliachar-Urlar Veins (overarching) and of the Almond Vein (individual) are reported in Table 2. Vein paragenetic analysis at the Lead Trial has revealed a higher degree of textural complexity and it is here illustrated by a slightly expanded text description.

3.1 Calliachar Burn and River Almond

Two main paragenetic stages are associated with gold mineralisation at Calliachar Burn (S1 and S3, Table 2a). S1 comprises euhedral/mottled quartz (Q1) enveloping euhedral pyrite (Py1, Figure 2a) which, in turn, hosts a relatively low amount of visible gold (Au1) as ~10µm size inclusions. The S3 is initiated by fractures in which quartz precipitates to form open-space textures (Q3) and is characterised by the greatest variety in sulphide mineralogy (especially cataclastic pyrite and galena). The dominant, coarser and more silver-rich gold input in the vein paragenetic history occurs within fractures (Au3) in shattered pyrite grains.

At River Almond, the assemblage of pyrite-galena-chalcopyrite-sphalerite is located alongside the second quartz event (Q2_av; CL-dark bands). Gold mineralisation entirely takes place over this paragenetic stage (S2; Table 2b), in the form of both inclusions (earlier) and fracture-fills (later) in sulphides. It is found as inclusions (Au2_a) in pyrite and chalcopyrite; and as fracture-fills (Au2_b) in pyrite, chalcopyrite and sphalerite (Figure 2e). The sample Au2_b shows a higher Ag content and is overall coarser (up to ~80µm size) than Au2_a. (e.g., Webb et al. 2023, under revision).

Table 2. Paragenetic tables for a) Calliachar-Urlar Veins; b) River Almond Vein.

	S1	S2	S3	S4	S5
a)	*Q1 (mottled)*	*Q2 (overprint)*	*Q3 (fractures)*	*Q4 (fractures)*	*Dol/Calcite*
Pyrite			cataclastic		cataclastic
Arsenopyrite			cataclastic		
Chalcopyrite					inclusions
Galena					inclusions
Sphalerite					
Gold	inclusions		in-cracks		

b)	*Q1 (mottled)*	*Q2 (overprint)*	*Dolomite*	*Q3 (fractures)*
Pyrite				
Chalcopyrite				
Galena				
Sphalerite				
Gold		in-cracks		

3.2 Lead Trial

Detailed SEM-CL analyses of hydrothermal quartz from the Lead Trial revealed a variety of internal textural features. The second paragenetic stage (S2) has been classified as the ore-bearing one. This corresponds to an evolution of precursors comb crystal into well-defined euhedral crystals (Q1_LTb) as a result of gradual cooling. Sphalerite and galena systematically overgrow the euhedral quartz (Q1_LTb), thence co-precipitate at this point; in hand specimen, gold mineralisation is consistently found in association with this (dominant) sulphide assemblage and, when rarely observed in thin section, on the surface of CL-bright euhedral crystals (Figure 2c). Therefore, it is assumed to have been introduced in the system at or immediately after this stage. From thin section analysis, sub-spheric and plumose crystals in a moss texture (Q1_LTc, Figure 2b) appear embedded in the Q1_LTb texture. The galena-sphalerite agglomerates that overgrow Q1_LTb become more densely distributed towards the Q1_LTc patterns, where gold is no longer observed. Quartz dissolution and recrystallisation, represented by CL-darker, microcrystalline bands (Q2_LT) that brecciate the CL-bright euhedral cores, constitute a later paragenetic stage.

The internal compositional heterogeneity observed in several gold particles (Figure 2d, 'Lead Trial' sample), can be attributed to evolving/cooling (>Ag) conditions of the same hydrothermal fluid. Furthermore, based on hand-specimen observations, the frequency of gold mineralisation appears to decrease from the margins (coarser quartz, vein breccia) towards the inner parts of the veins. Both pieces of evidence support a hypothesis

of i) gold precipitation during earlier/intermediate stages of the paragenesis; ii) two gold mineralising pulses, with a later one taking place at shallower (lower-T) crustal levels of the system. The paragenetic (textural and mineralogical) associations at this locality suggest a low-sulphidation epithermal mineralisation style.

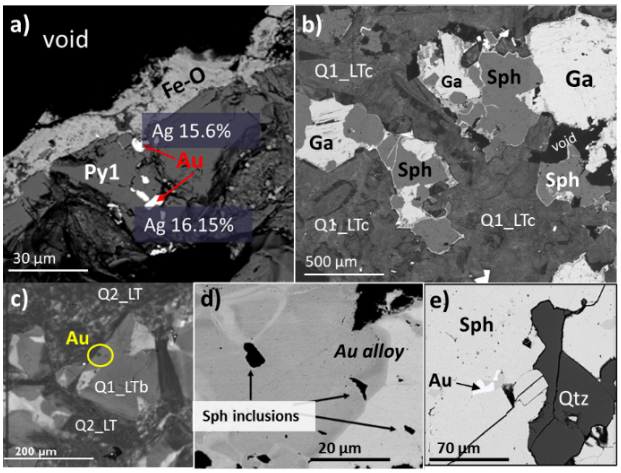

Figure 2. Mineral assemblages and textures from vein paragenetic analyses: a) Calliachar Burn; b) Lead Trial; c) Lead Trial; d) Lead Trial; e) River Almond.

4 Gold alloy analysis

Results are presented in Figure 3, where each data point on the plots corresponds to the silver content of a single gold particle from the respective population. The 'Calliachar_6V' (in-situ) gold is hosted in pyrite, in the form of both inclusions and fracture-fills; the lowest silver contents (~16 to ~18 wt.%) have been observed for the few gold inclusions, which broadly correspond to the smallest (~10µm) particles of the sample, as opposed to the more abundant (and richer in silver) fracture-fills. Similarly, most of the gold forming the 'Almond_6V' (in-situ) sample has been found as coarser particles filling fractures in sulphides (i.e., py, cpy and sph), which record the highest silver contents (~34 to ~42 wt.%) in the alloy. As per both the Calliachar_6V and Almond_6V samples, the generally coarser, silver-rich gold can be attributed to a later or separate mineralising event than the gold observed as inclusions in sulphides.

Callichar_6G and Almond_6H (Ag plots in Figure 3) are gold populations derived from gossan-related and crushed-ore material, respectively. As these were both mechanically recovered through panning procedures, the smallest, generally low-silver particles (≤50 µm) could hardly be retained. Evidence of this can be found in the 'Calliachar_6G' silver profile, which does not appear to be coincident with the 'Calliachar_6V' one, despite having been obtained from the same vein material. On the other hand, the dominant silver-rich trend displayed by the Almond_6V plot (Figure 3) is hardly reflected in the Almond_6H plot (Figure 3), hinting at notable variations in the silver content distribution across gold from the same hypogene environment. In addition, the sub-horizontal Ag distribution in the 'Calliachar_6G' (gossan-derived gold) plot suggests mainly stationary physicochemical conditions of the hydrothermal fluid responsible for the local gold precipitation, in contrast to the 'Calliachar_1' profile (representative of placer gold).

The 'Lead Trial' silver profile (Figure 3) displays a clear partitioning of the population into two main classes, which respectively show steady (median of ~27 wt.%) and increasing (from ~29 to ~57 wt.%) silver values in the gold particle alloys. These trends were confirmed by SEM-BSE imaging of the same set of particles, indicating the co-existence of two different alloy phases (in the form of Ag-rich patches or tracks) internally to many of the grains. Modified conditions of the fluid(s) responsible for gold precipitation are invoked to explain this evidence (e.g., Chapman et al. 2021b).

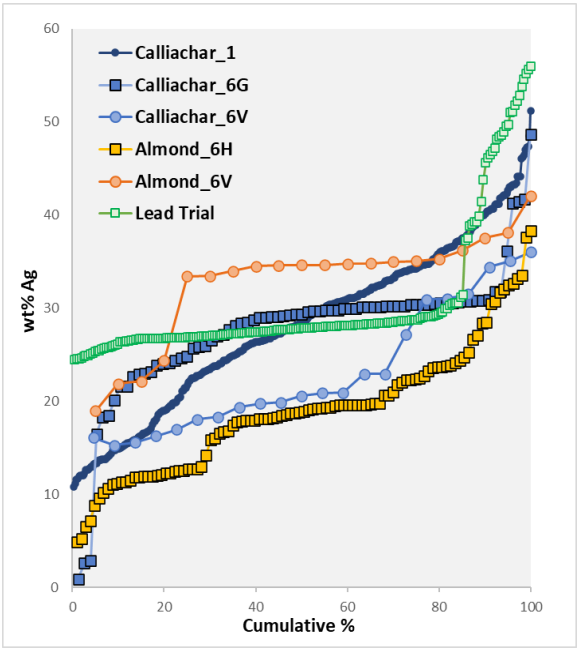

Figure 3. Cumulative percentile of the number of particles vs increasing wt.% Ag plots, for the studied gold samples.

5 Paragenetic constraints inferred frommineral inclusions in gold

Mineral inclusions were found in eluvial and placer gold samples from sites adjacent/proximal to the veins. The inclusion assemblages in the eluvial samples were evaluated in parallel with the silver contents of their hosting gold particles, to complement the gold-bearing vein parageneses.

At Calliachar Burn, the mineral inclusions in gossan-related gold can be used to underpin the sulphide mineralogy coeval with the auriferous stage of mineralisation, as it would be reflected in the associated hydrothermal vein(s). Figure 4 illustrates the distribution of the identified inclusion species across the two 'Calliachar_6G' alloy classes (by wt.% Ag). A distinct compositional signature (i.e., Ag content in the alloy and associated sulphide

assemblage in vein) has been deduced for Au3 in Calliachar_6V, which is perfectly consistent with the signature (Ag content and mineral inclusions) of Calliachar_6G. The placer gold (Calliachar_1) signature (Py-dominated) has also appeared to be broadly compatible with the 'Au3' signature.

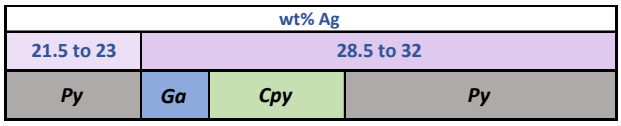

Figure 4. Relative abundance of inclusion species by gold particle (wt.% Ag) classes (Calliachar_6G).

The inclusion mineralogy of the placer sample from Upper River Almond (Almond_5), used for comparison with the respective vein-sited assemblage (Au-Py-Ga-Sph-Cpy), is indicated in Figure 5a. The in-situ mineral associations are more effectively reflected in the first alloy class (up to ~27 wt.% Ag), where Py, Ga and Sph were observed.

Galena, sphalerite and molybdenite inclusions are located in both the gold alloy classes (Figure 5b; wt.% Ag <29.5 and >29.5) distinguished from the analysis of the Lead Trial gold (from crushed-ore). Therefore, they are deemed coeval with the earlier (in-situ) gold paragenetic stage. The inclusion species recorded in the proximal Ardtalnaig (placer) sample revealed higher Mo and Cu and lower Zn and Pb relative abundancies (e.g., Webb et al., SGA 2023), suggesting a linkage with a different phase of mineralisation and subsequent variability in the silver content of the gold alloy.

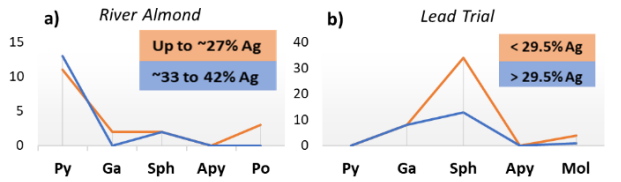

Figure 5. Mineral inclusions in a) Almond_5 (placer gold sample) and b) Lead Trial (crushed-ore gold sample)

5 Conclusions

Our results demonstrate that paragenetic histories of gold-bearing veins from a given locality can be firmed up by assessing the in-situ mineralogical assemblages against the microchemical signatures of adjacent eluvial gold. At least two separate gold mineralising episodes have been identified at Calliachar Burn, River Almond and Lead Trial/Ardtalnaig; the gold signatures combined with the vein parageneses indicate i) the overlap of multiple fluid sources at the first two localities and ii) an evolving hydrothermal fluid responsible for gold precipitation at the Lead Trial. Placer gold can be used to underpin the associated mineralisation styles on a broader scale; a genetic mineralogical linkage can be drawn between the Calliachar Burn and River Almond hydrothermal systems, whereas the Lead Trial system is suggestive of a dominant low-sulphidation epithermal style with variations in the mineralogical assemblage towards Ardtalnaig.

Acknowledgements

L.S. PhD work has been supported by a NERC-DTP scholarship (no 2114866) and an IOM3 grant (2020). Thanks to Green Glen Minerals for having provided access to the field area and rock samples, and to Dr R. Walshaw for assistance with EPMA.

References

Arif J, Baker T (2004) Gold paragenesis and chemistry at Batu Hijau, Indoneisa: implications for gold-rich porphyry copper deposits. Mineral Deposita 39:523–535

Chapman RJ, Leake R, Moles NR, Earls G, Cooper C, Harrington K, Berzins R (2000a) The application of microchemical analysis of alluvial gold grains to the understanding of complex local and regional gold mineralization: a case study in the Irish and Scottish Caledonides. Econ Geol 95:1753–1773

Chapman RJ, Mortensen JK, Crawford EC, Lebarge WP (2010b) Microchemical studies of placer and lode gold in the Klondike District, Yukon, Canada: 2. Constraints on the nature and location of regional lode sources. Econ Geol 105:1393–1410. https://doi.org/10.2113/econgeo.105.8.1393

Chapman RJ, Banks DA, Styles MT, Walshaw RD, Piazolo S., Morgan DJ, Grimshaw MR, Spence-Jones CP, Matthews TJ, Borovinskaya O. (2021b) Chemical and physical heterogeneity within native gold: implications for the design of gold particle studies. *Miner Deposita* 56, 1563–1588 https://doi.org/10.1007/s00126-020-01036-x

Chapman RJ, Torvela TM, Savastano L. (2023) Insights into Regional Metallogeny from Detailed Compositional Studies of Alluvial Gold: An Example from the Loch Tay Area, Central Scotland. Minerals 2023, 13, 140. https://doi.org/10.3390/min13020140

Gammons CH, Williams-Jones AE (1995) Hydrothermal geochemistry of electrum; thermodynamic constraints. Econ Geol 90:420–432. https://doi.org/10.2113/gsecongeo.90.2.420

Hancock EA, Thorne AM (2011) Mineralogy of lode and alluvial gold from the western Capricorn Orogen, Western Australia. Aus J Earth Sci 58:793–801

Ixer, R., Pattrick, R. and Stanley, C. (1997) Geology, mineralogy and genesis of gold mineralization at Calliachar-Urlar Burn, Scotland; Transactions of the Institution of Mining and Metallurgy Section B-Applied Earth Science, 106, p.99-108.

Leake RC, Chapman RJ, Bland DJ, Condliffe E, Styles MT (1997) Microchemical characterization of gold from Scotland. T I Min Metall B 102:65–82.

Parnell J, Earls G, Wilkinson JJ, Hutton DHW, Boyce AJ, Fallick AE, Ellam RM, Gleeson SA, Moles NR, Carey PF, Legg I (2000) Regional fluid flow and gold mineralization in the Dalradian of the Sperrin Mountains, Northern Ireland. Econ Geol 95:1389–1416

Spence-Jones CP, Jenkin GRT, Boyce AJ, Hill NJ, Sangster CJS (2018) Tellurium, magmatic fluids and orogenic gold: an early magmatic fluid pulse at Cononish gold deposit, Scotland. Ore Geol Rev 102: 894–905

Webb S, Torvela TM, Chapman RJ, Jamieson R, Selby D (2023) An integrated approach towards unravelling the gold mineralisation processes around Ardtalnaig, Scotland; 17th SGA Biennial Meeting.

Webb S, Torvela TM, Chapman RJ, Savastano L (2023) Textural mapping and building a paragenetic interpretation of hydrothermal veins, with a case study from an Au-Cu-Zn-Pb vein in Glen Almond, Loch Tay, Scotland.

Alkalic epithermal Au deposits: Insights into magma evolution and ore fertility using silicate melt inclusions from Lihir Island, Papua New Guinea

Michael Schirra[1], Daniel Müller[2], Zoltan Zajacz[1]
[1]*University of Geneva, Switzerland*
[2]*Consulting Geologist, Las Condes, Santiago, Chile*

Abstract. The fundamental controls on the ore fertility of alkaline high-K melts for the formation of epithermal Au deposits are not well understood. Silicate melt inclusion (SMI) LA-ICP-MS analyses from mafic rocks genetically linked to the formation of the giant Ladolam Au deposit on Lihir Island provide unique insights into magma evolution and its consequences for ore formation. Based on compositional variations in SMIs, textural and geochemical information from mafic phenocrysts and thermobarometric considerations, melting within a variably metasomatized mantle wedge and subsequent deep and shallow crustal magma storage were essential steps in the evolution of Lihir Island and its Au mineralization. Melts that have been extracted from a long-lived, deep (4-7 kbar) magma reservoir can be anomalously Au-rich, whereas melts without evidence for deep storage do not show such an enrichment. Therefore, open-system magma chamber processes in the lower crust appear to be decisive for the ore-forming potential of alkaline melts. Mass balance predict that melt volumes on the order of few tens of km^3 were sufficient to provide the required amount of Au.

1 Introduction

Potassic alkaline magmas formed in extensional tectonic settings (e.g., post-collisional arcs or intra-plate rift systems) have the potential to give birth to world-class porphyry and epithermal Au(-Cu-Ag-Te) deposits (Jensen and Barton 2000). Prominent examples are Cripple Creek (Colorado, USA), Vatukoula (Viti Levu, Fiji), and Ladolam (Lihir Island, Papua New Guinea). Although the association of alkaline magmas with these deposits is well established, the fundamental igneous processes that lead to ore formation remain enigmatic.

Different models have been proposed to explain the geochemical character of high-K alkaline melts and their potential for mineralization (e.g., Richards 2009; Fiorentini et al. 2018). All models have in common that alkaline melts are produced by low-degree partial melting resulting in small volumes of magma. Consequently, the alkaline melts are supposed to be anomalously Au-rich to account for high-grade and high-tonnage mineralization (e.g., > 1500 tons of Au at Ladolam). Although experimental studies indicate that volatile-rich, alkaline, ultramafic to intermediate melts can be Au-rich (Botcharnikov et al., 2011; Zajacz et al., 2012), Au contents of natural melts associated with economic mineralization have never been determined.

Primitive melt compositions are difficult to obtain due to late-stage AFC processes, fluid exsolution, and hydrothermal alteration. A promising approach to investigate primary magmatic processes and their implications for subsequent ore formation are silicate melt inclusions (SMIs) hosted in mafic phenocrysts. They represent melt droplets entrapped during crystal growth and hence provide insights into magmatic processes at depth. LA-ICP-MS analysis allows for the adequate determination of melt compositions from SMIs, including the concentrations of ore-relevant elements such as S, Cl, Cu and Au (Chang and Audétat 2021 and references therein).

This study focuses on the alkaline magmatism that created Lihir Island, Papua Guinea, which hosts the world-class Ladolam epithermal Au deposit in the partially collapsed Luise volcano (Figure 1). Based on SMI and mineral compositions, we reconstruct the magmatic evolution of the system and identify the key parameters and processes that may influence ore fertility. In addition to the subaerial volcanoes on the island itself we also include samples from the Conical Seamount (Figure 1), a small submarine volcano associated with Au mineralization close to Lihir (Petersen et al. 2002).

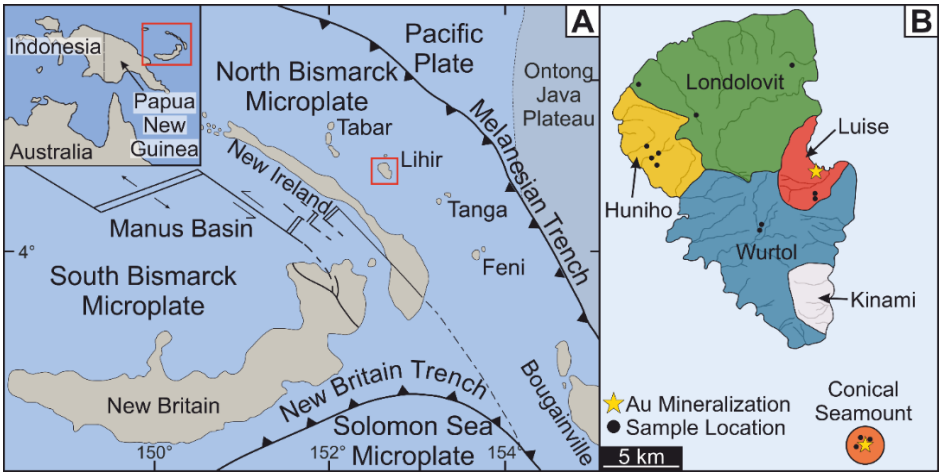

Figure 22: Location of Lihir Island in Papua New Guinea (inset). A) Overview of the Bismarck archipelago showing non-active and active subduction zones along the Melanesian and New Britain Trech, respectively, as well as back-arc spreading within the Manus Basin. B) Geological overview of Lihir Island showing the main volcanic edifices on the Island, including the submarine Conical Seamount volcano (modified from Müller et al. 2001).

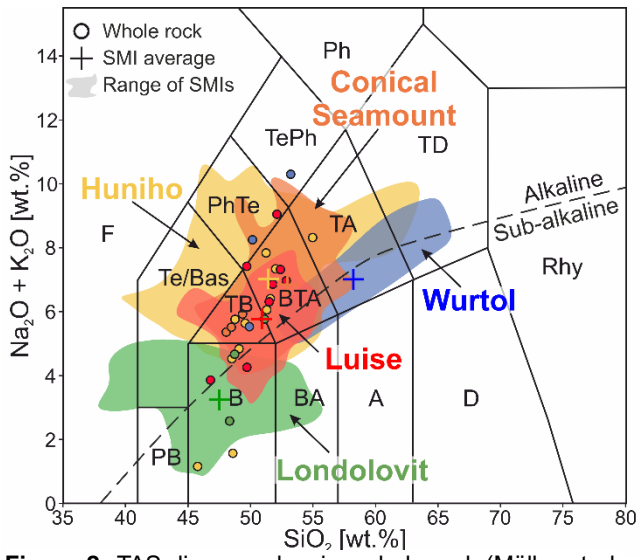

Figure 2: TAS diagram showing whole rock (Müller et al. 2001) and SMI compositions.

2 Geologic setting

Lihir Island is located within the fore-arc region of New Ireland and part of the Tabar-Lihir-Tanga-Feni (TLTF) island chain (Figure 1A). It consists of five Pliocene to Pleistocene volcanic centres, namely Huniho, Wurtol, Luise, Londolovit and Kinami (Figure 1B; Müller et al. 2001). The volcanoes erupted porphyritic, clinopyroxene (cpx)-rich alkali basalts, trachybasalts and basaltic trachyandesites (Figure 2; Müller et al. 2001). Despite the location within the fore-arc of the Kilinailau subduction zone, alkaline magmatism is not related to subduction but to post-collisional extension after cessation of SW-ward subduction due to the collision of the Ontong Java Plateau with the Melanesian trench (Figure 1A; McInnes and Cameron 1994; McInnes et al. 2001). Magmatism in the TLTF island chain is explained by adiabatic decompressional melting of metasomatised mantle along deep, extensional structures which facilitated rapid magma ascent (McInnes and Cameron 1994; Lindley 2016).

Conical Seamount is a small and pristine submarine volcano towards the SE of Lihir (Figure 1B), which erupted high-K cpx-rich trachybasalt similar to rocks from Lihir (Petersen et al. 2002).

Geochronologic data from Lihir is scarce. Biotite K-Ar dating indicate that volcanism may have lasted from 0.9 to 0.3 Ma whereas Conical Seamount is slightly younger with an Ar-Ar biotite age of 0.29 Ma (Brandl et al. 2020 and references therein).

Economic Au mineralization has been discovered within the Luise crater (Ladolam deposit, Müller et al. 2001) and the on top of Conical Seamount (Petersen et al. 2002). Mineralization style differs between the two locations: at Ladolam ore occurs as hydrothermal breccias overprinted by fine-grained auriferous pyrite whereas at Conical Seamount polymetallic quartz-feldspar-sericite veins host most of the Au (Petersen et al. 2002; Müller et al. 2003).

3 Petrography and Mineral Geochemistry

Petrographically, the samples from Lihir Island and Conical Seamount are cpx-dominated, porphyritic rocks with aphanitic to fine-grained, plagioclase-dominated matrix. Olivine and plagioclase phenocrysts can be present but are less abundant than cpx. In addition, magnetite and apatite occur as micro-phenocrysts in some samples. Rare and intensively altered amphibole phenocrysts are present in evolved samples from the Luise volcano.

Texturally, cpx grains can be colourless and largely unzoned (Londolovit), contain colourless cores with intensive green overgrowths (Huniho and Luise, Figure 3) or exhibit oscillatory (Conical Seamount) or sector zoning (Wurtol). Colourless cores often display wavy and diffusive contacts with coloured overgrowth zones, indicating partial dissolution during open-system magma chamber processes. Normal zonation (Mg-rich cores (Mg# 80-93), Fe-rich rims (Mg# 65-80); Figure 3b) indicate replenishment of more evolved by primitive magmas. Chondrite-normalized REE patterns (Sun and McDonough, 1989) show a general REE enrichment from the most primitive (Londolovit) to more evolved cpx compositions (Wurtol). Slightly negative Eu anomalies are only visible in cpx from Wurtol, indicating co-crystallization with plagioclase.

Olivine phenocrysts are usually altered along the rims, but pristine, clear and colourless cores have

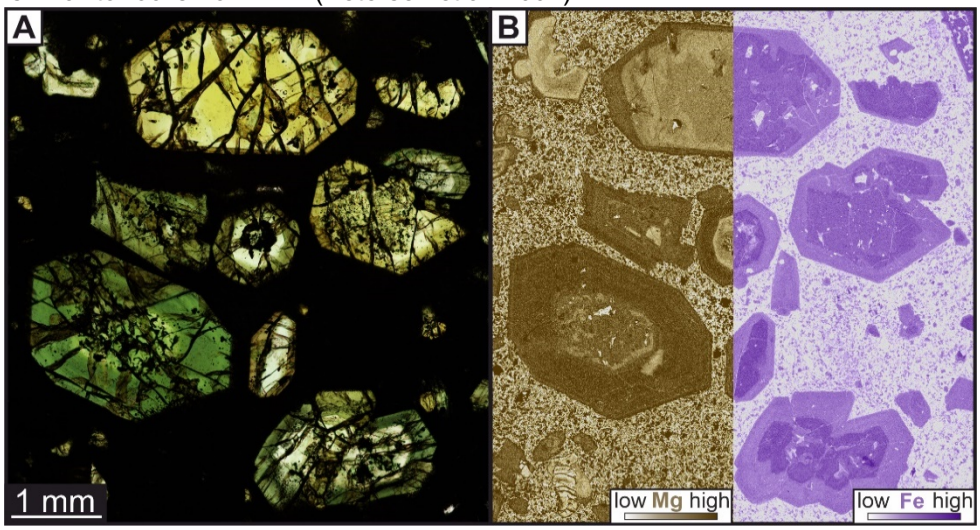

Figure 3: A) Transmitted light image of thick section for SMI petrography showing zoned cpx phenocrysts from the Luise volcano with inherited, colourless cores and concentrically zoned green rims. B) Qualitative QEMSCAN images of the same section shown in A), highlighting the remarkable difference between cores and rims regarding Mg and Fe content of cpx. Note the wavy and irregular boundary between core and rim, indicating dissolution.

been preserved. Most olivine grains have high Mg# (85-90) with relatively high CaO (0.35-0.55 wt.%) and low NiO (< 0.15 wt.%) contents. Olivine from Wurtol contains low CaO (0.15-0.20 wt.%) and high NiO (0.20-0.25 wt.%) at similar Mg# and hosts abundant Cr-rich spinel inclusions, which are absent in olivine from other volcanoes. No olivine has been found in the samples from Conical Seamount.

Plagioclase phenocrysts are anorthite-rich (Bytownite), normally zoned with more evolved rims (Labradorite) and typically exhibit sieve textures.

4 Melt Compositions

Fully enclosed SMIs in olivine and cpx were entirely ablated and the host-mineral contribution was subtracted from mixed signals to derive original melt compositions. Figure 4 shows a typical SMI and the corresponding time-integrated LA-ICP-MS signal.

Analysed SMI compositions overlap with whole rock data (Figure 2 and 5). Slightly wider and overlapping ranges of major oxide compositions (Figure 2) indicate that interaction of different melts produced whole rocks. Primitive mantle-normalized trace element arrays (Sun and McDonough, 1989) display enrichment in fluid-mobile and depletion in fluid-immobile elements, typical for subduction-related melts (Figure 5). High Ba/Th and Pb/Ce ratios indicate the involvement of subduction-derived fluids, while MORB-like Cs/Rb ratios suggest negligible contribution from sediment melts. Trace element systematics are inherited from previous subduction that caused metasomatism of the mantle wedge (McInnes and Cameron 1994; McInnes et al. 2001). Differences between the melts might stem from melting of variously metasomatized regions in the mantle (Londolovit and Conical Seamount SMIs display the lowest and highest Ba/Th ratios, respectively). Strong depletions in Nb and Ta are indicative for flux melting of the mantle source and constant Nb/Zr suggests similar degrees of melting for the different volcanoes. Wurtol is an exception with higher Nb, Ta contents and Nb/Zr ratios pointing towards lower degrees of partial melting, which might also explain the difference of SMI and whole rock compositions (Figure 2 and 5).

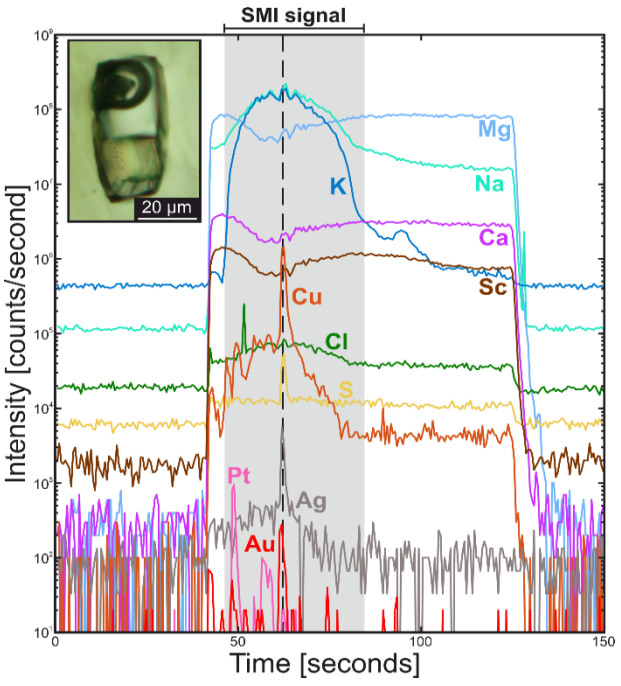

Figure 4: Time-integrated LA-ICP-MS signal of SMI (upper left corner) with a well visible Au peak, overlapping with increased Cu, S and Ag intensities (marked by dashed

Concentrations of S and Cl in the SMIs vary between 500 to 3000 and 1000 to 4000 µg/g, respectively, and show no correlation with proxies for fractional crystallization. With mean Au contents between 3 (Londolovit) and 10 ng/g (Conical Seamount), SMIs are slightly more enriched than melts reported from porphyry Cu deposits (≤ 4 ng/g, Grondahl and Zajacz, 2017) and back-arc basins (≤ 7 ng/g, Jenner et al. 2010). However, few SMIs from Huniho, Wurtol and Conical Seamount contain significantly more Au, up to 100 ng/g. In time-integrated LA-ICP-MS signals elevated Au coincides with S, Cu, and Ag peaks (Figure 4).

5 Thermobarometry and Oxygen Fugacity

Temperature and pressure were estimated from SMI-cpx pairs by applying the thermometer of Scarlato et al. (2021) and the barometer of Masotta et al. (2013). Temperatures range from 1300°C for the most primitive melt (Londolovit) down to 1050°C for the more evolved compositions (Wurtol). Pressure estimates scatter between 1 and 10 kbar, with two distinctive clusters at 1-2 and 4-7 kbar. Oxygen fugacity has been calculated from V partitioning between SMIs and olivine using the method of Shishkina et al. (2018), yielding highly oxidized values of +3 (±1) relative to the FMQ buffer.

6 Magma Evolution and Implications for Ore Formation

High-K alkaline magmatism on Lihir Island and Conical Seamount produced epithermal Au mineralization. Trace element signatures of SMIs indicate that magma generation occurred within a heterogeneously metasomatized mantle wedge by variable degrees of melting. Major element data show that whole rock compositions represent an amalgamation of compositionally variable melt batches which are preserved as SMIs (Figure 2). The metasomatized and refertilized lithospheric mantle is probably the source of Au. Anomalously Au-rich SMIs (≥ 10 ng/g) originate from the deeper crust (4-7 kbar) and are absent in samples from Londolovit, which ascended to and fractionated in the shallower crust (1-2 kbar). This suggests a lower crustal control on the ore fertility of the alkaline melts. Furthermore, the clustering of melts from the Huniho, Luise and Conical Seamount volcanoes within the same high-pressure interval indicates the presence of a long-lived (≥ 0.5 Myrs), frequently replenished magma reservoir in the lower crust.

Conical Seamount is presumably the youngest volcano (0.29 Ma, Brandl et al. 2020) and is the

closest in age to the flank collapse of the Luise

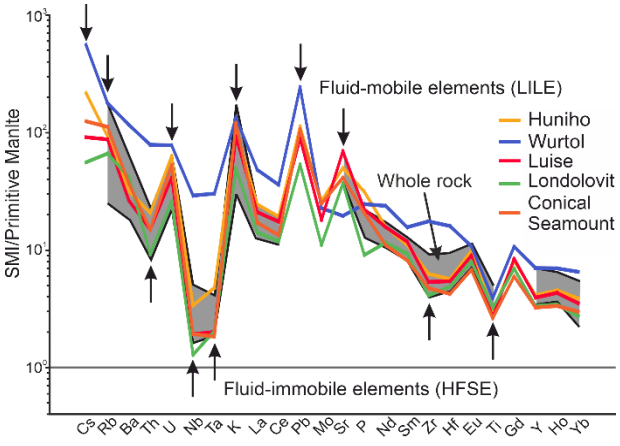

Figure 5: Primitive mantle-normalized (Sun and McDonough, 1989) trace element signature of SMIs and whole rock data from Müller et al. (2001).

volcano (0.19 Ma, Blackwell, 2010), which triggered Au deposition at Ladolam (Müller et al. 2001). Accordingly, the latest melts extracted from the lower crustal magma reservoir appear to be linked to the known Au deposits. The concentric zonation pattern and the scarcity of more mafic (inherited) cores in cop from Conical Seamount suggest longer storage times in the lower crust, which resulted in enhanced ore fertility. Alternatively, high Au contents of SMIs from Huniho and Wurtol could also indicate the presence of not yet discovered Au deposits.

Assuming 10 ng/g Au in the initial melt, simple mass balance predicts that approximately 50 km^3 of melt is required to account for the 1500 t of Au at Ladolam. If the few exceptionally Au-rich SMIs are representative for the ore-related melt, only 5 km^3 would be sufficient. Such small amounts of melt could be extracted from the deeper magma reservoir during periods of extension that facilitate magma ascent from depth to the surface without accumulation at shallower crustal levels. Melts that raise directly to shallower depths (≤ 2 kbar) without significant fractionation are not enriched in Au. Consequently, deep open-system magma chamber processes enhance ore fertility of small melt batches for the generation of alkalic-type epithermal Au deposits. Which processes are decisive for ore fertility is still in the focus of ongoing research.

References

Blackwell, J.L. (2010): Characteristics and origins of breccias in a volcanic-hosted alkalic epithermal gold deposit, Ladolam, Lihir Island, Papua New Guinea; PhD thesis, University of Tasmania.

Botcharnikov, R.E., Linnen, R.L., Wilke, M., Holtz, F., Jugo, P.J., and Berndt, J. (2011): High gold concentrations in sulphide-bearing magma under oxidizing conditions; Nature Geoscience, v. 4, p. 112-115.

Brandl, P.A., Hannington, M.D., Geersen, J., Petersen, S., and Gennerich, H.H. (2020): The submarine tectono-magmatic framework of Cu-Au endowment in the Tabar-to-Feni island chain, PNG; Ore Geology Reviews, v. 121, 103491.

Chang, J., and Audétat, A. (2021): LA-ICP-MS analysis of crystallized melt inclusions in olivine, plagioclase, apatite and pyroxene: quantification strategies and effects on post-entrapment modifications; Journal of Petrology, v. 62, egaa085.

Fiorentini, M.L., LaFlamme, C., Denyszyn, S., Mole, D., Maas, R., Locmelis, M., Caruso, S., and Bui, T.H. (2018): Post-collisional alkaline magmatism as gateway for metal and sulfur enrichment of the continental lower crust; Geochimica et Cosmochimica Acta, v. 223, p. 175-197.

Grondahl, C., and Zajacz, Z. (2017): Magmatic controls on the genesis of porphyry Cu-Mo-Au deposits: The Bingham Canyon example; Earth and Planetary Science Letters, v. 480, p. 53-65.

Jenner, F.E., O´Neill, H.St.C., Arculus, R.J., and Mavrogenes, J.A. (2010): The magnetite crisis in the evolution of arc-related magmas and the initial concentrations of Au, Ag, and Cu; Journal of Petrology, v. 51, p. 2445-2464.

Jensen, E.P., and Barton, M.D. (2000): Gold deposits related to alkaline magmatism; Reviews in Economic Geology, v. 13, p. 279-314.

Lindley, I.D. (2016): Plate flexure and volcanism: Late Cenozoic tectonics of the Tabar-Lihir-Tanga-Feni alkalic province, New Ireland Basin, Papua New Guinea; Tectonophysics, v. 677, p. 312-323.

Masotta, M., Mollo, S., Freda, C., Gaeta, M., and Moore, G. (2013): Clinopyroxene-liquid thermometers and barometers specific to alkaline differentiated magmas; Contributions to Mineralogy and Petrology, v. 166, p. 1545-1561.

McInnes, B.I.A., and Cameron, E.M. (1994): Carbonated, alkaline hybridizing melts from a sub-arc environment: Mantle wedge samples from the Tabar-Lihir-Tanga-Feni arc, Papua New Guinea; Earth and Planetary Science Letters, v. 122, p. 125-141.

McInnes, B.I.A., Gregoire, M., Binns, R.A., Herzig, P.M., and Hannington, M.D. (2001): Hydrous metasomatism of oceanic sub-arc mantle, Lihir, Papua New Guinea: petrology and geochemistry of fluid-metasomatized mantle wedge xenoliths; Earth and Planetary Science Letters, v. 188, p. 169-183.

Müller, D., Franz, L., Herzig, P.M., and Hunt, S. (2001): Potassic igneous rocks from the vicinity of epithermal gold mineralization, Lihir Island, Papua New Guinea; Lithos, v. 57, p. 163-186.

Müller, D., Franz, L., Petersen, S., Herzig, P.M., and Hannington, M.D. (2003): Comparison between magmatic activity and gold mineralization at Conical Seamount and Lihir Island, Papua New Guinea; Mineralogy and Petrology, v. 79; p. 259-283.

Petersen, S., Herzig, P.M., Hannington, M.D., Jonasson, I.R., and Arribas, A. (2002): Submarine gold mineralization near Lihir Island, New Ireland fore-arc, Papua New Guinea; Economic Geology, v. 97, p. 1795-1813.

Scarlato P., Mollo, S., Petrone, C.M., Ubide, T., and Di Stefano, F. (2021): Interpreting magma dynamics through a statistically refined thermometer: Implications for clinopyroxene Fe-Mg diffusion modelling and sector zoning at Stromboli; In - Crustal Magmatic System Evolution: Anatomy, Architecture, and Physico-Chemical Processes, Geophysical Monograph 264, First Edition.

Shishkina, T.A., Portnyagin, M.V., Botcharnikov, R.E., Almeev, R.R., Simonyan, A.V., Garbe-Schönberg, D., Schuth, S., Oeser, M., and Holtz, F. (2018): Experimental calibration and implications of olivine-melt vanadium oxybarometery for hydrous arc magmas; American Mineralogist, v. 103, p. 369-383.

Sun, S.S., and McDonough, W.F. (1989): Chemical and isotopic systematics of oceanic basalts: implications for mantle composition and processes; Geological Society, Lodon, Special Publications, v. 42, p. 313-345.

Zajacz, Z., Candela, P.A., Piccoli, P.M., Wälle, M., and Sanchez-Valle, C. (2012): Gold and copper in volatile saturated mafic to intermediate magmas: Solubilities, partitioning, and implications for ore deposit formation; Geochimica et Cosmochimica Acta, v. 91, p. 140-159.

Granitoid-hosted, orogenic gold mineralization: Genetic constraints on the world-class Archean Gruyere gold deposit, Yilgarn Craton, Western Australia

Ravi Schreefel[1], Steffen G. Hagemann[1], Clayton Davy's[2], Jamie A. Robinson[3], Malcolm P. Roberts[4], Christopher M. Fisher[1], Nicolas Thébaud[1], Robert A. Creaser[5]

[1]Centre for Exploration Targeting, School of Earth Sciences, The University of Western Australia, Perth, Australia
[2]Hamelin Gold Ltd, Perth, Australia
[3] Gold Road Resources Ltd, Perth, Australia
[4] Centre for Microscopy, Characterisation and Analysis, The University of Western Australia, Perth, Australia
[5] Department of Earth and Atmospheric Sciences, University of Alberta, Edmonton, Canada

Abstract. In 2013, the 6.8 Moz Gruyere gold deposit was discovered at the eastern margin of the Yilgarn Craton in Western Australia. Gold mineralization at Gruyere is hosted by the 2830 ± 4 Ma Gruyere monzogranite. Mineralizationis related to contemporaneous chlorite-rich veinlets and sheeted quartz veins crosscutting the foliation, with pervasive wall rock alteration characterized by quartz- sericite-albite-calcite-chlorite ± pyrite-pyrrhotite-arsenopyrite
-gold-telluride assemblages. Chlorite and arsenopyrite geothermometry indicate temperatures between 304-365°Cand 360-425°C, respectively. Arsenopyrite Re-Os geochronology yield a single-analysis model age of 2675 ± 66 Ma. On the basis of these results, gold mineralization at Gruyere is interpreted to reflect a late-Archean, granitoid- hosted, orogenic gold mineral system, with the granitic intrusion behaving as a brittle, rigid body within more ductile, soft supracrustal rocks during mineralization. This implies that the 2675-2630 Ma orogenic gold mineralization event in the Yilgarn Craton was widespread and extends into the easternmost exposed part of the craton.

1 Granitoid-hosted gold deposits

The close spatial relationship between granitic rocks and gold ores have been long recognized (Niggli 1929). Although this invokes a link between intrusions and gold mineralization, their genetic association is highly debated (Duuring et al. 2007; Goldfarb and Pitcairn 2023). Difficulties arise especially in classifying granitoid-hosted, gold-only deposits. Granitic intrusions are suggested to be the source of fluids and metals, implying a similar timing of the intrusion and mineralization (e.g., Robert 2001). The host granitic intrusions may, however, also act as favourable rigid structural sites for fluid flow and/or as geochemical traps for gold mineralization (e.g., Cassidy et al. 1998). Multiple overprinting styles of gold mineralization within a granitic intrusion have also been demonstrated (e.g., Bucci et al. 2002). This has led to debates of the genetic role of the granitic intrusions in the gold mineralization process, with granitoid-hosted gold deposits in different Archean regions classified as 'orogenic', 'intrusion-related', 'skarn', or 'porphyry' (Sillitoe and Thompson 1998; Duuring et al. 2007).

In the well-endowed Archean Yilgarn Craton in Western Australia (Fig. 1), the majority of gold deposits are classified as 'orogenic' (Groves 1993), with most of these deposits hosted by greenschist- facies, meta-volcanic rocks. Although granitic rocks are the dominant lithology in the Yilgarn Craton, only minor orogenic gold deposits are hosted by granitoids. These granitoid-hosted orogenic deposits generally have smaller mineral resources compared to the meta-volcanic hosted deposits, and historically represent a minor fraction of the total gold resource in the Yilgarn Craton (Cassidy et al. 1998). A few Archean intrusion-related and porphyry gold systems are documented in the Yilgarn Craton and, with the possible exception of the Boddington deposit, are generally small (<0.5 Moz Au). The 6.8 Moz Gruyere gold deposit was discovered in 2013 with gold mineralization solely confined within an Archean granitic intrusion, making it one of the largest Archean granitoid-hosted, gold-only systems globally.

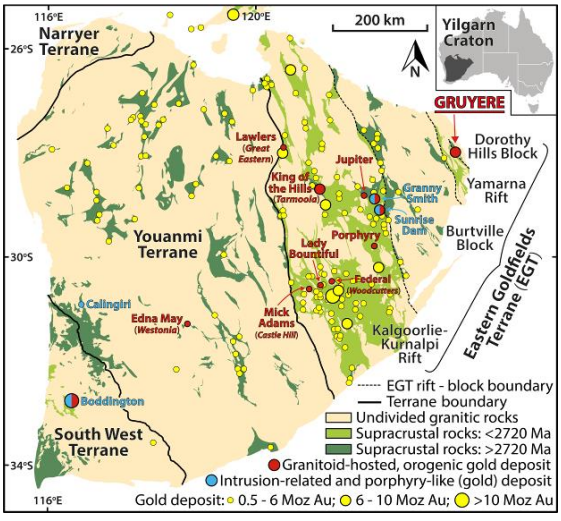

Figure 1. Simplified geological map of the Yilgarn Craton showing gold resource estimates by project (data from DMRIS 2022). In addition, (partially) granitoid-hosted lode gold deposits as well as intrusion-related and porphyry-like systems are shown. The current subdivision of the Yilgarn Craton and the age of supracrustal rocks is also illustrated (modified after Cassidy et al. 2006; Masurel et al. 2022; Schreefel et al. 2023).

This study focuses on the world-class, granitoid-hosted Gruyere gold deposit located at the north-eastern margin of the Yilgarn Craton in West Australia (Fig. 1). As gold mineralization is solely restricted to the Gruyere monzogranite, it provides anexcellent opportunity to examine the genetic link, if any, between a granitoid host and gold mineralization. In this contribution, we present preliminary results from an ongoing study of the lithostratigraphical, structural, and hydrothermal architecture related to gold mineralization at Gruyere.

2 Geological setting

2.1 Lithostratigraphy

The Gruyere intrusion (GYI) is a small monzogranitic body (2,500x200 m; Fig. 2) of predominantly medium-to coarse-grained albitised feldspar and quartz with medium-grained biotite. The GYI is geochemically consistent with the 'high-HFSE' granitic group in the Yilgarn Craton (Champion and Sheraton 1997; Schreefel et al. 2023), which is a rare component (<5%) of all the granitic rocks in the Yilgarn Craton. Furthermore, the GYI yields a magmatic crystallization age of 2830 ± 4 Ma (Schreefel et al. 2023), which is relatively old compared to other lithologies in the Eastern Goldfields Terrane.

Low-Th basalts (Kansas basalt) are present in the south-eastern hanging wall of the GYI, and fine-grained, folded, intermediate to mafic volcanoclastic sedimentary rocks (Wizard Formation - 2840 ± 13 Ma; Tunjic 2019) in the north-eastern hanging wall and western footwall. Several variably deformed felsic to mafic dykes (<1m wide) crosscut the lithostratigraphic sequence, with a massive basaltic dyke (up to 5m wide) present along strike within the GYI proximal to the hanging wall.

2.2 Structural setting

The GYI is located at a major change in the geometryof the Dorothy Hills Shear Zone, where the strikechanges from the regional NW-SE trend to ~N-S,based on aeromagnetic imagery. The cryptic NW-striking, arcuate Alpenhorn and Northern faults (Fig. 2) have been interpreted from aeromagnetics, but appear to not offset the GYI (Osborne et al. 2017).

The GYI displays sharp lithological contacts with the supracrustal lithologies and is steeply (65 - 80°) NE to ENE-dipping, which is similar to the strike of the shear zone. Non-coaxial deformation is variably developed in the GYI and country rocks, with the shear intensity higher at the lithological contacts. Crosscutting dykes trend generally subparallel to the orientation of the GYI. Furthermore, the dominant fabric throughout the entire lithostratigraphy is a pervasive steeply ENE-dipping foliation, with the orientation of biotite S-C fabrics indicating a predominantly sinistral reverse movement, although the orientation of a minor amount of kinematic indicators also indicate dextral movement. Auriferous veins generally dip steeply to the ESE to SE and crosscut the foliation.

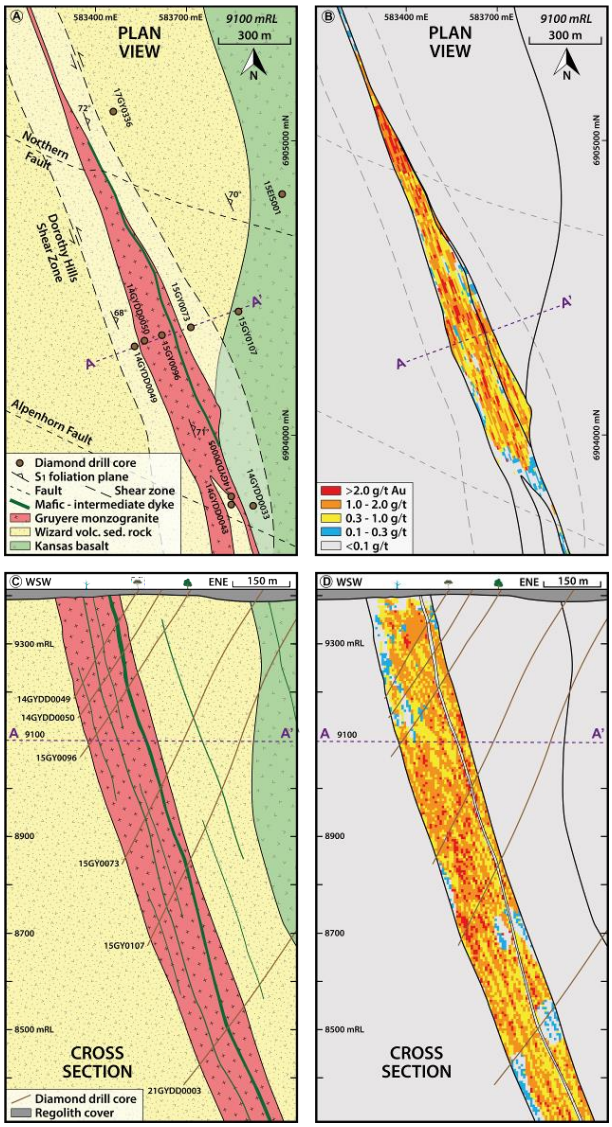

Figure 2. Simplified geological map and cross section of the Gruyere gold deposit; modified after Bath and Walshe (2015) and Gold Road Resources (Written Comm.). A) Map showing the main (metamorphosed) lithostratigraphic units and structures including logged diamond drill holes mostly displayed at 9200 mRL. B) Plan view block model of the gold assay data at 9100 mRL after Gold Road Resources (Written Comm.). C) Cross section including drill traces. D) Block model in cross section. mRL: metres relative level.

3 Hydrothermal alteration and mineralization

3.1 Vein types

Four main groups of veins can be distinguished within the GYI at Gruyere: (1) early, unmineralized V_1 quartz ± feldspar veins, (2) V_2 quartz-chlorite-magnetite veins, (3) gold mineralized V_{3A} to V_{3D} quartz-chlorite-

carbonate veins (Fig. 3), and (4) late, unmineralized V_4 carbonate veins. Gold mineralization at Gruyere is associated with the V_3 veins within the GYI, therefore, this study is mostly focused on these auriferous veinsand related hydrothermal alteration assemblages.

Thin chlorite-pyrite ± pyrrhotite stringer veins (2 - 4 mm; V_{3A}) are abundant and occur in a discontinuous, subparallel sheeted to stockwork-like pattern. Massive, sheeted quartz-rich veins (1 - 20 cm; V_{3B}) are common throughout the GYI, and often have a chlorite-rich vein margin (1 mm - 1 cm). These planar,tabular quartz veins comprise variable amounts offine- to coarse-grained calcite, albite, chlorite, and sub- to euhedral pyrite-pyrrhotite ± arsenopyrite. Locally, quartz veins have a more laminated texture (V_{3B-1}) or massive biotite-chlorite margins (V_{3B-2}) with minor coarse-grained magnetite altered to pyrite ±chlorite. Massive quartz veins (2 - 30 cm; V_{3C}) with narrow slivers of the granitic wall rock are characteristic for the higher gold grade zones (>2.0 g/t). These irregular to sheeted quartz veins havegenerally the same mineral assemblages as the V_{3B} quartz veins, although they locally contain very coarse-grained arsenopyrite, pyrite, and/or pyrrhotite. Coarse-grained arsenopyrite-rich trails (V_{3D}) with minor quartz, pyrite, and chlorite are observed locally.

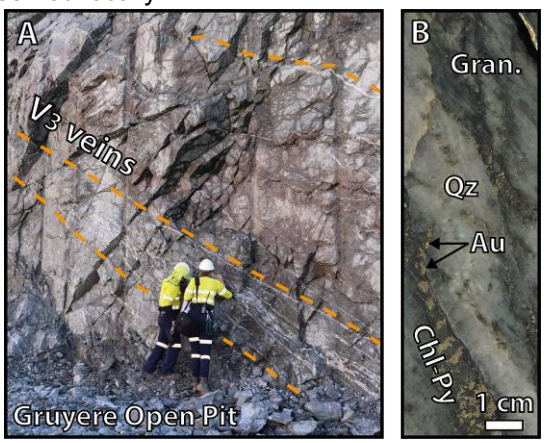

Figure 3. A) Gruyere open pit exposure (looking ENE)illustrating the high frequency of SE-ESE dipping V3B and V3C quartz vein sets within GYI (photo by Kyle Prentice). B) Granitic rock crosscut by a V3C vein consisting of quartz (Qz) with a chlorite-pyrite-gold (Chl-Py-Au) vein margin.

3.2 Proximal wall rock alteration related to V_3

The auriferous V_3 quartz veins in the GYI are typically characterized by semi-concentric zones of hydrothermal alteration assemblages. As multiple V_3 veins are located throughout the GYI, it is interpreted that extensive metasomatic fluid rock interactions (i.e., high fluid-rock ratios) resulted in pervasive hydrothermal alteration of the entire GYI, with a progressive decrease in alteration intensity away from the V_3 veins. The proximal alteration zones (>2.0 g/t Au; 0.5 cm to 10 m wide) are characterized by a 'bleached', beige appearance of the granitic wall rock with pervasive destruction of igneous and metamorphic minerals and textures. The wall rock alteration is characterized by quartz-sericite-albite-calcite ± chlorite ± Fe-Ti oxides ± arsenopyrite-pyrite-pyrrhotite-gold assemblages.

Quantitative micro-analyses (EPMA) were conducted to characterize and classify hydrothermal alteration minerals associated with the V_3 veins. Analyses on gold and telluride show that most grains represent native gold (i.e., >80 wt. % Au) with minor petzite, altaite, and rucklidgeite. Analyzed carbonate grains indicate that calcite is the main carbonate species. The arsenopyrite geothermometer from Kretschmar and Scott (1976) was applied to the arsenopyrite-bearing assemblages, which are all in textural equilibrium with pyrite. The mineralization temperature of arsenopyrite from V_{3C} and V_{3D} veins (n = 295 from 11 samples) ranges from 360°C to 425°C with an average of 395 ± 41°C (31.5 ± 0.7 at. % As; 1SD; Fig. 4A). The sulfur fugacity ranges from -6.4 to -8.4 log f_{S2}, with an average log f_{S2} of -7.3 ± 1.2 (1SD). Chlorite from V_3 veins and associated proximal alteration zones (n = 161 from 11 samples) are Fe-rich and can be classified as chamosite (Bailey 1980). The chlorite geothermometer from Kranidiotis and MacLean (1987) yields temperatures ranging from 304 ± 34°C to 365 ± 28°C (Fig. 4B; 1SD). The average temperature of all chlorites associated with auriferous V_3 veins is 328 ± 51°C (n = 226; 1SD).

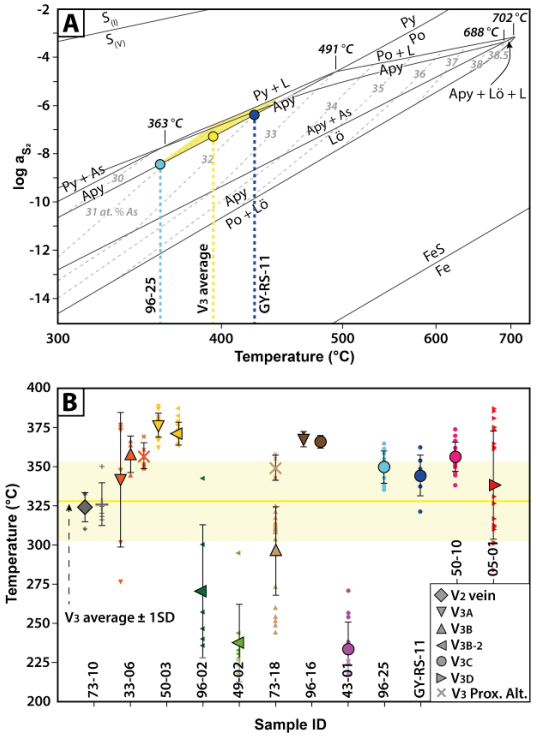

Figure 4. A) Log f_{S2} – T projection of the stability of arsenopyrite contoured in at. % of As, including the lowest (96-25) and highest (GY-RS-11) sample (Kretschmar and Scott 1976). B) Chlorite temperature estimates for V2 andV3 vein samples (Kranidiotis and MacLean 1987).

3.4 Absolute timing of gold mineralization

Four samples with visible arsenopyrite associated with gold (i.e., in equilibrium or in micro-fractures) were selected for rhenium-osmium (Re-Os) geochronology. Initial testing showed, however, that all samples yield very low Re contents (ca. 0.1 - 0.3 ppb Re), therefore, a complete Re-Os analysis by N- TIMS was only performed on sample GY-RS-11. Thisis a massive arsenopyrite-bearing sample with a higher Re content (0.3 ppb Re). The Re-Os analysis yielded a single-analysis mantle model age of 2675 ±
66 Ma. Despite the large error, interpreted to be mainly caused by the low Re and Os contents, this date provides currently the best geochronological constraint for the age of mineralization at Gruyere.

4 Discussion and implications

The auriferous V_3 veins exhibit similar orientations, have mutual cross-cutting relationships and similar hydrothermal alteration halos. This implies that these veins formed progressively during the same deformation and mineralization event (Bath and Walshe 2015; Osborne et al. 2017). Based on field observations, V_3 veins are interpreted to overprint regional metamorphic foliation assemblages (ca. 2663-2649 Ma; Fielding et al. Written Comm.). In addition, constraints from U-Pb and Re-Os geochronology show that gold mineralization must have occurred ca. 150 Myr after the emplacement of the GYI. Furthermore, alteration assemblages related to V_3 veins at Gruyere are common for granitoid- hosted, orogenic gold deposits formed under P-T conditions of 250-400°C and <1-2 kbars at a paleo- depth of <5-8 km (Cassidy et al. 1998).
The GYI is interpreted to have behaved as a brittle, dilatant granitic body within more ductile supracrustal rocks during high fluid pressure and shear zone reactivation with associated hydrothermal alteration and gold mineralization. Fluids were focused within a broad shear zone well after the crystallisation of the GYI; i.e., the intrusion had no genetic relationship with the gold mineralization. For these reasons, gold mineralization at Gruyere is, interpreted to reflect a late-Archean, granitoid-hosted, orogenic gold mineral system. Despite the broad Re-Os age constraint, Gruyere is suggested to be part of the 2675-2630 Ma orogenic gold mineralization event in the Yilgarn Craton (e.g., Groves 1993). This implies that the 2675-2630 Ma event, known to be widespread in the Yilgarn Craton (e.g., Vielreicher et al. 2015), extends into the easternmost exposed greenstone belt, and nearly 385 km from the giant Golden Mile deposit.
Further work (e.g., sulfur isotopes and trace elements on pyrite) is conducted to more precisely constrain the nature of gold mineralization in order to form a robust genetic model that can be used for exploration targeting, particularly in the search of concealed gold ore bodies in the Yilgarn Craton.

Acknowledgements

This work is part of the Yilgarn 2020 research project,which is funded by multiple industry sponsors,MRIWA (M530), GSWA and UWA. SIRF funding fromUWA and assistance from CMCA is acknowledged. We are very thankful for the logistical support and geological input from Gold Road Resources Ltd. G. Beaudoin is thanked for the review of this abstract.

References

Bailey SW (1980) Summary of recommendations of AIPEA nomenclature committee on clay minerals. Am Mineral 65:1–7
Bath AB, Walshe JL (2015) Mineral systems study of the world-class Gruyere gold deposit. CSIRO, pp 1–27
Bucci LA, Hagemann SG, Groves DI, Standing JG (2002) The Archean Chalice gold deposit: A record of complex, multistage, high-temperature hydrothermal activity and gold mineralisation associated with granitic rocks in the Yilgarn Craton, Western Australia. Ore Geol Rev 19:23–67
Cassidy KF, Champion DC, Krapež B, Barley ME, Brown SJA, Blewett RS, Groenewald PB, Tyler IM (2006) A revised geological framework for the Yilgarn Craton, Western Australia. Geol Surv West Aust Rec 2006/8 1–8
Cassidy KF, Groves DI, McNaughton NJ (1998) Late-Archean granitoid-hosted lode-gold deposits, Yilgarn Craton, Western Australia: deposit characteristics, crustal architecture and implications for ore genesis. Ore Geol Rev 13:65–102
Champion DC, Sheraton JW (1997) Geochemistry and Nd isotope systematics of Archaean granites of the Eastern Goldfields, Yilgarn Craton, Australia: Implications for crustal growth processes. Precambrian Res 83:109–132
DMRIS (2022) MINEDEX resource estimates by project - gold. Dep Mines, Ind Regul Safety, Gov West Aust
Duuring P, Cassidy KF, Hagemann SG (2007) Granitoid-associated orogenic, intrusion-related, and porphyry style metal deposits in the Archean Yilgarn craton, WA. Ore Geol Rev 32:157–186
Goldfarb RJ, Pitcairn I (2023) Orogenic gold: Is a genetic association with magmatism realistic? Miner Depos 58:5–35
Groves DI (1993) The crustal continuum model for late-Archaean lode-gold deposits of the Yilgarn Block, Western Australia. Miner Depos 28:366–374
Kranidiotis P, MacLean WH (1987) Systematics of chlorite alteration at the Phelps Dodge massive sulfide deposit, Matagami, Quebec. Econ Geol 82:1898–1911
Kretschmar UH, Scott SD (1976) Phase relations involving Apy in the system Fe-As-S and their application. Can Mineral 14:364–386
Masurel Q, Thébaud N, Sapkota J, De Paoli MC, Drummond M, Smithies RH (2022) Stratigraphy of the Agnew-Wiluna Greenstone Belt: Review, synopsis and implications for the late Mesoarchean to Neoarchean geological evolution of the Yilgarn Craton. Aust J Earth Sci 1–28
Niggli P (1929) Ore Deposits of Magmatic Origin: Their Genesis and Natural Classification. Thomas Murby & Co, London
Osborne JP, Levett J, Donaldson J, Berg R, Davy's C, Prentice K, Tullberg D, Lubieniecki LZ, Tunjic JA, Bath AB, Libby JW (2017) Gruyere gold deposit, Yamarna. In: Philips GN (ed) Australian Ore Deposits, 6th edn. The Australasian Institute of Mining and Metallurgy: Melbourne, pp 267–272
Robert F (2001) Syenite-associated disseminated gold deposits in the Abitibi greenstone belt, Canada. Miner Depos 36:503–516
Schreefel R, Fisher CM, Kemp AIS, Hagemann SG, Masurel Q, Thebaud N, Davy's C, Martin LAJ, Lowrey JR, Lu Y, Cassidy KF (2023) Crustal growth in the Archaean: Insights from zircon petrochronology of the far east Yilgarn Craton, WesternAustralia. Precambrian Res - In Review Sillitoe RH,
Thompson JFH (1998) Intrusion-related vein gold deposits: Types, tectono-magmatic settings and difficulties of distinction from orogenic gold deposits. Resour Geol 48:237–250
Tunjic JA (2019) Laying the foundations of geology for further discoveries. In: AEGC Conference Presentation. Perth, Australia Vielreicher N, Groves DI, McNaughton
NJ, Fletcher IR (2015) Thetiming of gold mineralization across the eastern Yilgarn Craton using U–Pb geochronology of hydrothermal phosphate minerals.Miner Depos 50:391–428

The Geological Setting and Hydrothermal Alteration at the Tucano Gold Deposit, Guiana Shield, Brazil

Gabriel A. R. Soares[1], Rosaline C. Figueiredo e Silva[1], Steffen G. Hagemann[2], Lydia M. Lobato[1,3], Rogério A. Lucena[4]
[1]Geology Graduate Program, Institute of Geosciences, Federal University of Minas Gerais, Belo Horizonte, MG, Brazil
[2]Centre for Exploration Targeting, University of Western Australia, Crawley, WA, Australia
[3]Hydro Fluids & Minerals, Rio de Janeiro, RJ, Brazil
[4]Great Panther Mining Limited, Pedra Branca do Amapari, AP, Brazil

Abstract. The Tucano gold deposit, located in northern Brazil, is an open-pit gold mine that produced 1.4 Moz Au as of 2021. The Tucano deposit is located and controlled by the N-S-striking and steeply W-dipping Urucum Shear Zone. This shear zone is characterized by intense hydrothermal alteration and gold mineralization, and located in chemical metasedimentary rocks – marble and banded iron formation (BIF). Alteration assemblage comprises first stage quartz-clinopyroxene-garnet ± biotite and second stage amphiboles-phlogopite-biotite-magnetite-sulfides. Locally, Na-bearing amphiboles and phlogopite vector proximal alteration zones. Visible gold shows textural relationship with sulfides (pyrrhotite, arsenopyrite), loellingite, silicates (mainly amphibole) and magnetite. Arsenopyrite geothermometry yields temperature estimates of 500 ± 17 °C (1σ, n = 6). Current data support that Tucano is an orogenic, hypozonal hydrothermal deposit developed post-metamorphic peak at amphibolite facies conditions.

1 Introduction

Gold-only deposits in metamorphic belts are structurally controlled and typically found in greenschist metamorphic facies terranes formed at mesozonal crustal levels (Groves et al. 1998). This setting largely complies with the metamorphic model for orogenic fluid source as the bulk of such fluids is produced by chlorite breakdown at the greenschist-amphibolite facies transition (Tomkins 2010). High-temperature hypozonal orogenic gold deposits pose a challenge as metamorphic fluids formed at temperatures of mid-amphibolite facies or higher are thought to be of limited volume and devoid of much S and Au (Tomkins 2010). Thus, the reporting of orogenic gold deposits generated at high grade metamorphic conditions brings forth the need for review of the classic crustal continuum model (Groves et al. 1998). This would require either a different fluid source (magmatic- or mantle-derived) or more complex tectonic settings where high-grade metamorphic terranes are juxtaposed on top of still fertile low-grade rocks (Kolb et al. 2015).

2 Deposit geology

The Tucano gold deposit is located in the north-eastern segment of the Amazon Craton, within a Paleoproterozoic belt stretching from northern Brazil to eastern Venezuela (Rosa-Costa et al., 2006). This tectonic province comprises granulite-migmatite-gneiss complexes, greenstone belts and granitoid plutons assembled in a NE-SW structural architecture and recording several episodes of juvenile crustal accretion followed by crustal reworking (Rosa-Costa et al. 2006).

The Tucano deposit is hosted in the NE-SW trending Serra do Navio greenstone belt, which lies unconformably on a reworked Archean continental landmass (Rosa-Costa et al., 2006). The greenstone belt stratigraphy consists of a lower mafic-dominated volcanic unit, an intermediate chemical-exhalative interval, and an upper siliciclastic package, with metamorphic conditions ranging from greenschist to upper amphibolite facies (Scarpelli and Horikava 2017).

The deposit area features mainly chemical-exhalative and siliciclastic rocks, with restricted metavolcanic rocks (Figure 1). The regional structural architecture is locally affected by a N-S deflection associated with the development of the north-south striking, steeply dipping Urucum Shear Zone. Granitic stocks and dikes crosscut the supracrustal rocks and the variable strain record across intrusions indicate more than one magmatic episode. In this contribution, we present preliminary results from an ongoing study of the lithostratigraphic, structural and hydrothermal control related to gold mineralization at the Tucano gold deposit. This study provides an excellent opportunity to examine the hydrothermal alteration and gold mineralization in amphibolite facies metasedimentary host rocks and test the hypothesis of high temperature orogenic gold mineralization. This is relevant once a significant number of orogenic gold deposits hosted in high metamorphic grade terranes are indeed overprinted mesothermal deposits rather than systems originally formed at high-temperature settings (Kolb et al., 2015).

3 Methodology

Open pit mapping and drill core logging of selected diamond drill cores were carried out and enabled a comprehensive sampling strategy. Analytical work comprised petrographic investigations, SEM-BSE imaging and electron microprobe (EPMA) analyses (at the Federal University of Minas Gerais) of silicate, carbonate, oxide and sulfide minerals.

4 Results

4.1 Regional metamorphic P-T conditions

Gold mineralization at the Tucano deposit is located in a sequence of chemical metasedimentary rocks that consists of a lower BIF package, overlain by marble, which is in turn succeeded by metapelites and quartzites. The BIF is an oxide-type magnetite-quartz banded rock, with ubiquitously disseminated, fine-grained amphiboles (grunerite > actinolite). The marble is a fine- to medium-grained isotropic grey rock consisting of abundant olivine, locally featuring phlogopite and more rarely tremolite. Temperature estimates of 592 ± 25 °C (1σ, n = 5) and 612 ± 28 °C (1σ, n = 5) were obtained via garnet-biotite (Holdaway 2000) and Ti-in-biotite (Henry et al. 2005) geothermometry for peak metamorphic conditions in nearby metapelitic rocks. In addition, pressure estimates at 4.1 ± 0.6 kbars (1σ, n = 5) were obtained via application of the garnet geobarometer calibrated by Wu (2019).

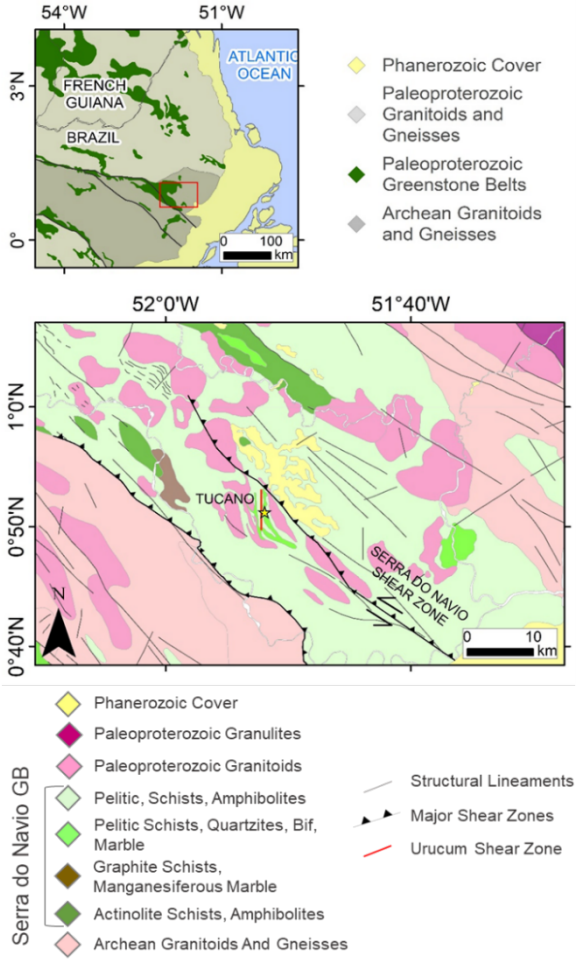

Figure 1. Simplified geologic map of the study area (after Barbosa et al. 2015).

4.2 Hydrothermal alteration assemblages and P-T conditions at the time of gold mineralization

The hydrothermal alteration event can be subdivided in two major stages. The early stage is represented by deformed quartz-clinopyroxene and clinopyroxene veins, as well as clinopyroxene ± garnet nodules and lenses. Locally, hydrothermal biotite was formed in equilibrium with garnet, allowing for temperature estimates using the garnet-biotite geothermometer (578 ± 26 °C - 1σ, n = 4) (Holdaway 2000). Similar values were obtained using the Ti-in-biotite approach (568 ± 23 °C - 1σ, n = 4) (Henry et al. 2005). The second and main stage of hydrothermal alteration is marked by distinct distal and proximal hydrothermal alteration zones in marble and BIF. Distal alteration in marble is characterized by hydrothermal amphibole (tremolite-actinolite) replacement after metamorphic olivine, hydrothermal phlogopite and locally biotite, with traces of sulfides and magnetite. Proximal zone features abundant amphibole (tremolite-actinolite and/or hornblende ± cummingtonite) ± phlogopite/biotite commonly with altered early-stage hydrothermal diopside ± garnet. Magnetite and pyrrhotite are common. Locally, proximal zones are centred about early quartz-clinopyroxene veins superimposed by stringers of amphibole ± sulfides, with no magnetite. Distal alteration zone in BIF is typically characterized by grunerite ± ferroactinolite, and locally, commonly corroded, hedenbergite, concordantly replacing metamorphic quartz-magnetite, but preserving the precursor fabric. The proximal zone is characterized by ferroactinolite-grunerite-pyrrhotite-magnetite but lack metamorphic quartz. The original fabric is partially to totally destroyed. Ti-in-biotite geothermometry (Henry et al. 2005) for stage 2 biotite yielded temperature estimates of only two grains, 550° and 577 °C.

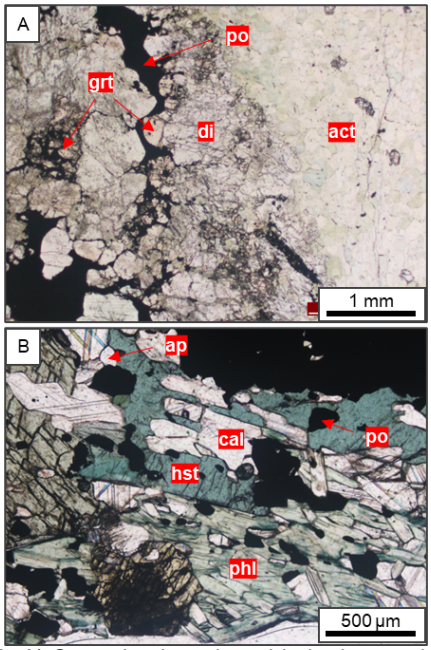

Figure 2. A) Strongly altered marble in the proximal zone showing a characteristic calc-silicate mineral assemblage (grt - garnet, di – diopside) with interstitial pyrrhotite (po). B) Strongly altered marble in a proximal zone displaying Na-bearing amphibole (hst - hastingsite) and phlogopite (phl – phlogopite-aspidolite). Except for the highlighted pyrrhotite, all other opaque grains are magnetite. All photomicrographs are taken under plane polarized transmitted light.

Pyrrhotite is the main sulfide species and can be largely ascribed to the main stage of hydrothermal alteration. It can be found as: (i) lenses and stringers subparallel to the shear zone foliation; (ii) tension gash infill in altered marble; (iii) shear zones that contain networks of anastomosing veinlets, and; (iv) disseminated grains locally showing preferred growth directions parallel to shear zone foliation. The textural relationship between pyrrhotite and magnetite indicates a period of synchronous crystallization, followed by pyrrhotite-only precipitation. Other sulfides such as chalcopyrite, arsenopyrite, pyrite and the arsenide loellingite are rare.

Integration of petrographic observations, gold grade distribution and mineral chemistry data show a direct correlation between Na content in amphibole and Na/K ratio in phlogopite with gold distribution (Figure 3). Thus, calcic-sodic amphiboles (pargasite and hastingsite) and micas from the phlogopite-aspidolite series (Figure 2B) are observed almost exclusively in the proximal alteration zone. In contrast, sodium-poor amphiboles and biotite/phlogopite are featured in both unmineralized and proximal alteration zones.

Visible gold (Figure 4) is locally in equilibrium with pyrrhotite and loellingite, Moreover, gold is also documented in equilibrium with silicates, including amphibole, and magnetite.

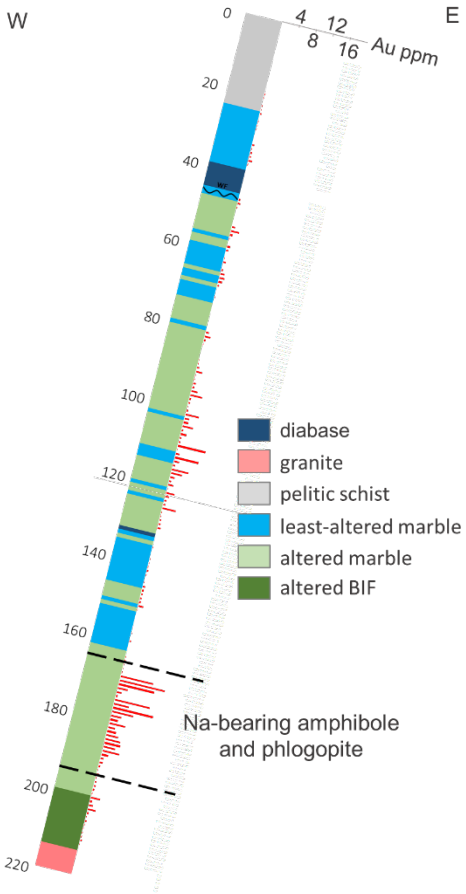

Figure 3. Graphic log of drillhole DDH A29 displaying major lithologies, altered equivalents and gold grades in ppm. Note the interval where Na-bearing amphibole and phlogopite are reported.

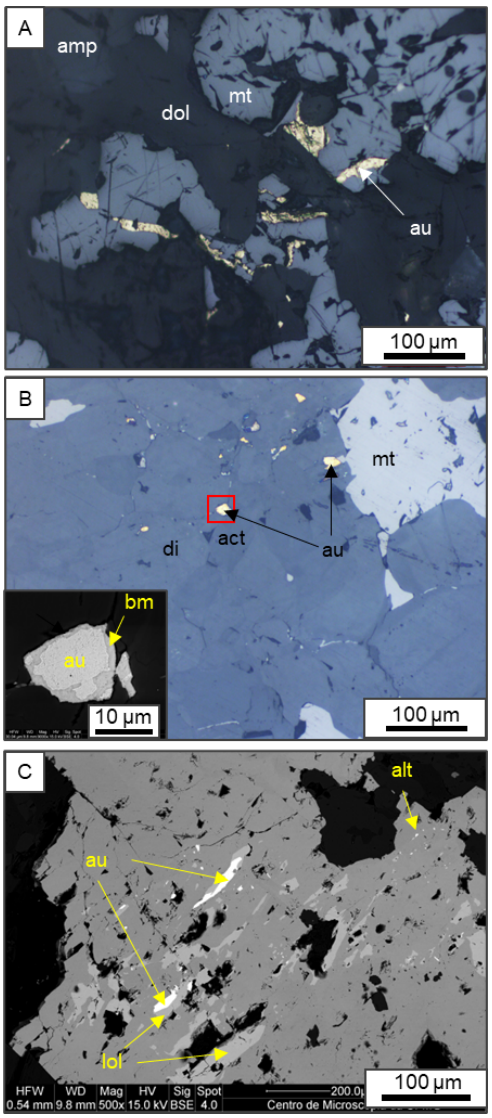

Figure 4. A) Visible gold (au) in apparent equilibrium with pyrrhotite (po) and arsenopyrite (asp), in an altered marble (dol – dolomite). B) Visible gold in amphibole (amp) that replaces subequant diopside (di) grains along grain boundaries. The inset in the lower left corner highlights one of the gold grains being surrounded by bismuthinite (bm). C) Equilibrium gold and loellingite (lol) lamellae hosted in a coarse-grained arsenopyrite. Very fine-grained altaite (alt) inclusions are also documented. A) and B) are photomicrographs taken under plane polarized reflected light, and C) is a backscattered electron image.

Equilibrium assemblage pyrrhotite-loellingite-arsenopyrite enables the use of the arsenopyrite geothermometer (Kretschmar and Scott 1976). Textural evidence suggests simultaneous crystallization of pyrrhotite and loellingite and subsequent retrograde solid-solid reaction to produce arsenopyrite. Thus, a temperature estimate using this geothermometer would track the cooling path as the system crosses the arsenopyrite – pyrrhotite + loellingite buffer curve in the $\log a_{S_2}$-T space (Figure 5, Kretschmar and Scott 1976, modified by Sharp et al. 1985). In fact, temperature estimates at 500 ± 17 °C (1σ, n = 6), are significantly lower than those obtained using silicate minerals, yet complying with the high-temperature character of this alteration event.

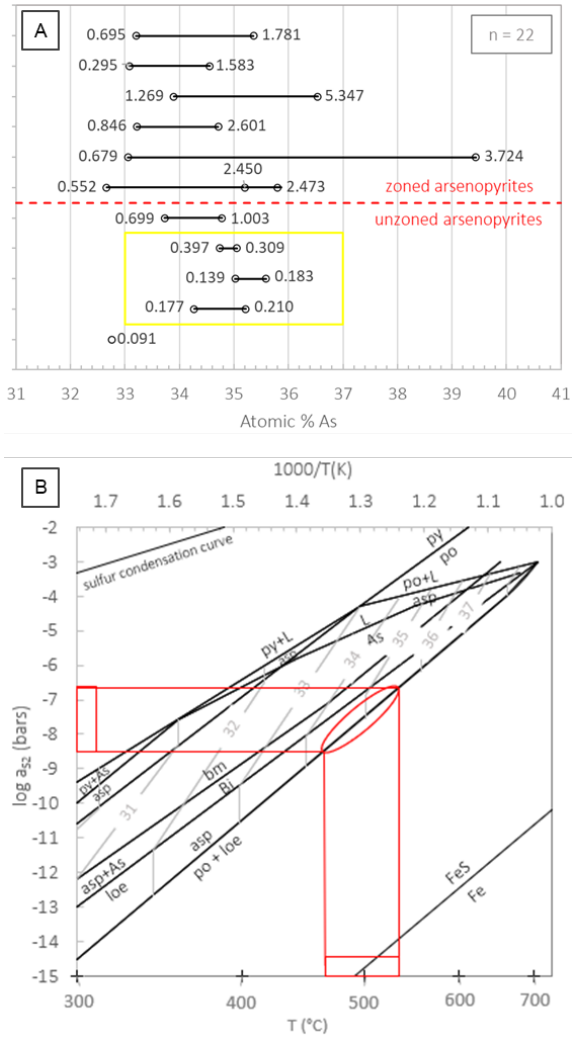

Figure 5. A) Atomic % As measured in core-margin pairs of arsenopyrite grains in zoned and unzoned crystals. Figures beside data points indicate the weight percent sum of trace elements (Co+Ni+Sb). The yellow box outlines the data points used for temperature estimates, i.e., grains having <1 atomic As % difference between core and margin and low trace elements. B) Arsenopyrite geothermometer (Sharp et al. 1985, after Kretschmar and Scott 1976) showing with red lines the crystallization conditions of arsenopyrite in logas_2 – temperature space.

5 Conclusions

The Tucano gold deposit is a shear-zone hosted hydrothermal system with distinct high temperature alteration assemblages in marble (tremolite-actinolite - hornblende - phlogopite - diopside - garnet - magnetite - pyrrhotite) and BIF (ferroactinolite - grunerite - hedenbergite - magnetite - pyrrhotite). Gold is found in equilibrium with sulfides (pyrrhotite, arsenopyrite), loellingite, silicates and magnetite.

Arsenopyrite geothermometry suggests minimum temperatures of 500 ± 17 °C (1σ) during the main stage of hydrothermal alteration. These temperatures are compatible with the amphibolite metamorphic facies conditions, as indicated by the garnet-biotite and Ti-in-biotite geothermometers. The equilibrium assemblage gold-loellingite, the location of gold in silicates and the high temperature alteration assemblages suggest that gold mineralization at the Tucano gold deposit is part of an orogenic, hypozonal gold system (Kolb et al. 2015). Tucano distinguishes itself from most described orogenic hypozonal gold deposits by the significant amount of hydrothermal magnetite and Na-bearing silicates in the proximal alteration zone.

Acknowledgements

This work has been supported through the South American Exploration Initiative. We thank AMIRA Global and industry sponsors, as well as Great Panther Mining for their support of the project, especially their exploration team that kindly assisted us during field activities and provided us with crucial data indispensable for the success of this project. We also thank Coordenação de Aperfeiçoamento de Pessoal de Nível Superior (CAPES) for the granted scholarship.

References

Barbosa JPO, Costa Neto MC, Rosa-Costa LT, Anjos GC, Chaves CL (2015) Geologia e recursos minerais da Folha Macapá NA.22-Y-D, estado do Amapá, escala 1:250.000: Belém, Brazil. Brazilian Geological Survey – CPRM, 118 p. (in Portuguese).

Groves DI, Goldfarb RJ, Gebre-Mariam M, Hagemann SG, Robert F (1998) Orogenic gold deposits: a proposed classification in the context of their crustal distribution and relationship to other gold deposit types. Ore Geol Rev 13(1-5):7-27.https://doi.org/10.1016/S0169-1368(97)00012-7

Henry DJ, Guidotti CV, Thomson JA (2005) The Ti-saturation surface for low- to medium-pressure metapelitic biotites: implications for geothermometry and Ti-substitution mechanisms. Am Min 90(2-3):316-328. https://doi.org/10.2138/am.2005.1498

Holdaway MJ (2000) Application of new experimental and garnet Margules data to the garnet-biotite geothermometer. Am Min 85(7):881-892. https://doi.org/10.2138/am-2000-0701

Kolb J, Dziggel A, Bagas L (2015) Hypozonal lode gold deposits: A genetic concept based on a review of the New Consort, Renco, Hutti, Hira Buddini, Navachab, Nevoria and the Granites deposits. Precambrian Res 262:20-44. https://doi.org/10.1016/j.precamres.2015.02.022

Kretschmar U, Scott SD (1976) Phase relations involving arsenopyrite in the system Fe-As-S and their application. Can Mineral 14:364-386.

Rosa-Costa LT (2006) Geocronologia 207Pb/206Pb, Sm-Nd, U-Th-Pb e 40Ar-39Ar do segmento sudeste do Escudo das Guianas: evolução crustal e termocronologia do evento transamazônico. PhD thesis, Federal University of Pará.

Scarpelli W, Horikava EH (2017) Gold, iron and manganese in central Amapá, Brazil. Braz J Geol 47(4):703-721. https://doi.org/10.1590/2317-4889201720170114

Sharp ZD, Essene EJ, Kelly WC (1985) A re-examination of the arsenopyrite geothermometer: pressure considerations and applications to natural assemblages. Can Mineral 23(4):517-534.

Tomkins AG (2010) Windows of metamorphic sulfur liberation in the crust: Implications for gold deposit genesis: Geochim Cosmochim Acta 74:3246-3259. https://doi.org/10.1016/j.gca.2010.03.003

Wu CM (2019) Original calibration of a garnet geobarometer in metapelite. Minerals 9(9):540. https://doi.org/10.3390/min9090540

World-class gold deposits and emerging exploration opportunities in the Loulo district, West Africa

Thomas Stapley[1], Paul Stenhouse[1], James Lambert-Smith[2], Andrew Allibone[1], David Lawrence[1], Dioumacor Senghor[1], Germain Crestin[1]
[1]*Barrick Gold Corporation, Toronto, ON, Canada*
[2]*School of Earth and Environmental Sciences, Cardiff University, Main Building, Cardiff CF10 3AT, United Kingdom*

Abstract. The Paleoproterozoic Loulo district in Western Mali contains +20Moz of gold, representing a key gold producing district on the African continent and host to the world-class Yalea, Gara and Gounkoto deposits. The Loulo district is comprised of two contrasting geological domains: the metasediment-dominated Kofi domain to the east, and the intrusion-dominated Falémé domain to the west which hosts the voluminous Falémé batholith and associated intrusions. At the district scale, the syn-deformation and syn-mineralisation, high-K, calc-alkaline Falémé intrusives are interpreted to be an important source of heat for the mineralising system. Stable isotope and fluid inclusion studies also support direct involvement of magmatic fluids in several of the deposits, particularly within and proximal to the Falémé domain. At the target-scale, mineralisation within the Kofi domain is commonly associated with local reactivation of N-striking, D1 structures, withing jogs/relays/bends, intersections, and minor folds commonly localising ore shoots. In contrast, exploration within the Falémé domain has begun to highlight possible oxidised intrusion-related styles of mineralisation, associated with lower syn-mineralisation strain hosted in magmatic-hydrothermal breccias and adjacent porphyries and metasedimentary rock.

1 Introduction

The Paleoproterozoic (Birimian) gold deposits of the Loulo district in Western Mali, including the world-class Gara, Yalea and Gounkoto deposits, contain a combined +20Moz endowment (Figure 1). The district is one of three major gold systems (wider Loulo, Sadiola, Sabodala-Massawa), within a window of the Paleoproterozoic Birimian (ca. 2300-2100 Ma), known as the Kedougou-Kenieba Inlier (KKI). The KKI is the second most highly endowed region in West Africa and a key global gold producer.

This article summarises and expands upon key studies from the Loulo district over the past decade (Allibone et al. 2020, Lambert-Smith et al. 2020, Lawrence et al. 2013b), incorporating recent findings from the underexplored Falémé domain.

2 Geological setting of the Loulo district

The Loulo district hosts two contrasting geological domains, the western, intrusive-dominated Falémé domain, and the eastern, metasediment-dominated Kofi domain (Figure 2). Previously, the district-scale boundary between these two domains was interpreted as a crustal-scale shear zone known as the Senegal-Mali Shear Zone (SMSZ), but the existence of the SMSZ at surface has been largely disproven. The nature of the domain boundary is still debated, with some outcrops suggesting a direct intrusive relationship with the Kofi domain.

The sedimentary succession in the Kofi domain comprises siliciclastic, marble and evaporitic rocks deposited around 2120-2105 Ma. In contrast, the Falémé domain is dominated by voluminous high-K, calc-alkaline granitoids (2100-2065 Ma), associated Fe-skarns, and subordinate magmatic-hydrothermal breccia systems intruding a siliciclastic- and carbonate-dominated sedimentary package that is similar to the Kofi domain metasediments (Figure 2).

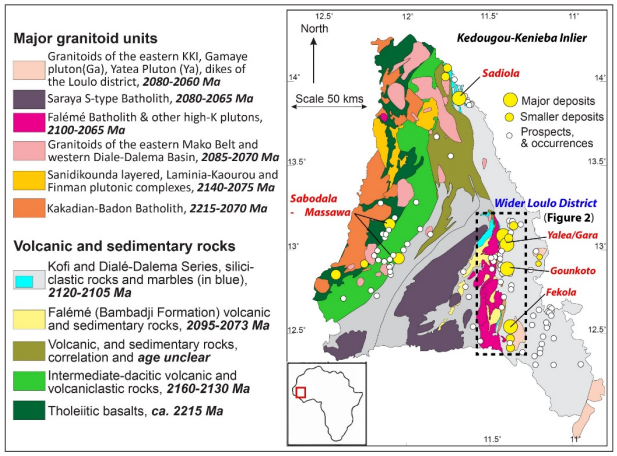

Figure 1. Geological map of the KKI, showing three key gold districts including Sabodala-Massawa, Sadiola and the wider Loulo district (modified after Allibone et al. 2020).

Two deformation phases have been recognised in the Loulo district between 2100 and 2070 Ma. D1 is associated with an early contractional period in which the Kofi sediments were folded and thrusted into their current sub-vertical geometries. D2 comprises one or more minor phases of deformation that involved localised folding and reactivation of N-striking D1 structures (Allibone et al. 2020). The kinematics of D2 are complex, with evidence for both normal and sinistral slip directions. Mineralisation in the district occurred between 2090 and 2070 Ma, which is broadly synchronous with emplacement of the high-K, calc-alkaline Falémé batholith and Fe±Au skarn formation.

3 Major gold deposits of the Loulo district

More than 30Moz of gold endowment in the wider Loulo district occurs along a narrow corridor, only 4-5km wide and +100km in strike (Figure 2), where most of the gold is hosted in four key deposits: Gara, Yalea, Gounkoto, and Fekola to the south.

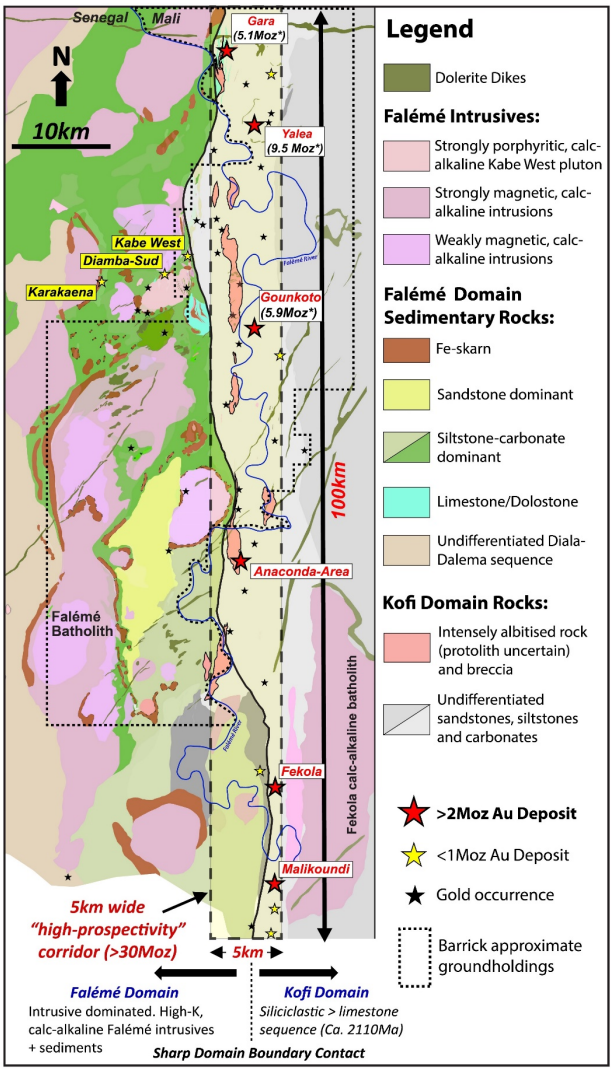

Figure 2. Simplified geological map of the wider Loulo district, showing locations of key deposits and prospects.

3.1 The Gara Deposit (5.1Moz @ 3.9g/t)

The Gara orebody comprises a stockwork of quartz-carbonate-pyrite-tourmaline veinlets and subordinate disseminated pyrite within an F2-folded layer of a quartz-rich sandstone, typically <30m thick (Figure 3A). An early phase of carbonate alteration is overprinted by strong tourmaline-quartz alteration. The tourmaline alteration increased competency, causing the host unit to fracture during deformation, increasing permeability, whilst adjacent rocks deformed in a dominantly ductile manner.

Mineralised veins at Gara are typically <5 cm thick but comprise between 10-50% of the volume of the sandstone host, with vein density greatest where early tourmaline-quartz alteration is strongest (Figure 3C). The dominant sulfide at Gara is pyrite, approximately 15% of which is a Ni-Co-rich variety. Accessory sulfide minerals include chalcopyrite, gersdorffite, pentlandite, pyrrhotite, and monazite, with only trace amounts of arsenopyrite having been observed (Lawrence et al. 2013b).

Mineralised vein orientations in the fold limbs are comparable to those in the fold hinges, implying veining occurred late- or post-F2. However, the overall shallow-SSW plunge of the orebody is sub-parallel to the $F2_A$ fold axes, while high-grade shoots within are more sub-parallel to the steeper $F2_B$ fold axes, suggesting some relationship between folding and vein formation (Figure 3B).

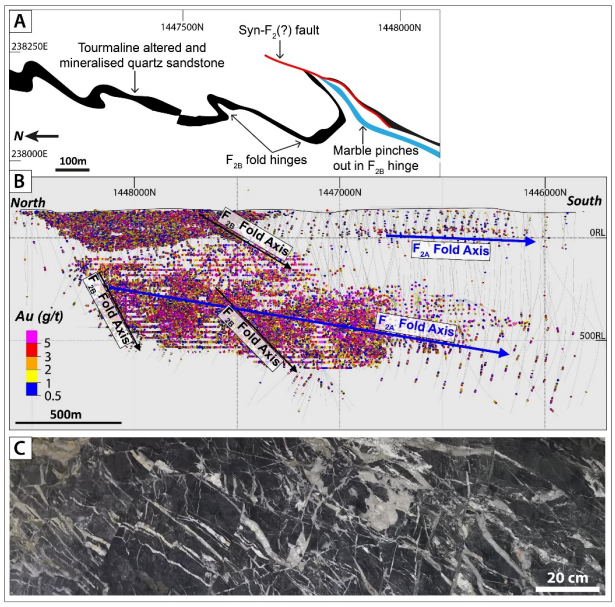

Figure 3. A Plan map showing the folded tourmalinised sandstone host. **B** Gara gram-tonne long section (looking east), showing the dominant $F2_A$ and sub-ordinate $F2_B$ fold controls on grade distribution. **C** Quartz-carbonate stockwork veining in tourmalinised sandstone at Gara.

3.2 The Yalea Deposit (9.5Moz @ 5.06g/t)

In contrast to Gara, Yalea is hosted along a 2.5km, N-striking, dominantly E-dipping shear zone comprised of variably altered, foliated and brecciated siliciclastic rocks and subordinate strongly sheared marble layers. Within the core of Yalea, these altered and deformed units range from 250m to <30m wide (Allibone et al. 2020).

The alteration and deformation at Yalea is attributed to two main N-striking, E-dipping structures, the Yalea Shear Zone and the Yalea Structure, which are broadly coincident through most of the deposit. The Yalea Shear Zone is discontinuous, mineralised and interpreted to have a syn-D2 timing, while the Yalea Structure is considered to be an early D1 structure that is continuous beyond the limits of the deposit and locally juxtaposes domains with different dips.

Ore shoots within the Yalea orebody are mostly shallowly S-plunging and related to both changes in the geometry of the Yalea Shear Zone, particularly increases in dip or rotations to a westerly dip direction, and structural intersections (Figure 4).

Mineralisation is intimately associated with zones of early, pervasive albite alteration which increased the competency of the host rocks and was subsequently overprinted by mineralised, carbonate-pyrite ± arsenopyrite ± sericite ± chlorite shear zones, fault breccias and vein/fracture

stockworks, with >10g/t zones commonly associated with massive pyrite-arsenopyrite.

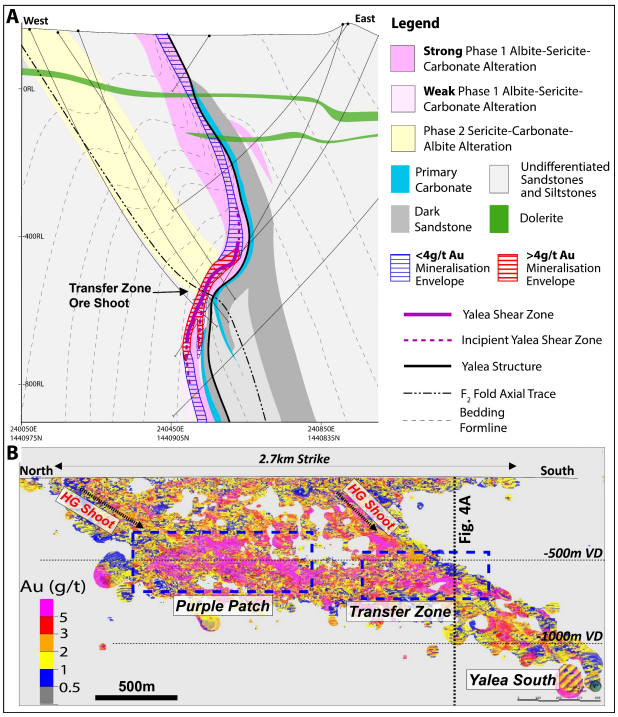

Figure 4. A Yalea Transfer Zone cross-section showing key structural control on high-grade (+4g/t) within a prominent rotation of the structure into a westerly dip. **B** Yalea gram-tonne long section looking east, sub-horizontal, high-grade Purple-Patch and Transfer Zone, and plunging Yalea South.

3.3 The Gounkoto Deposit (5.9Moz @ 4.09g/t)

The N-striking, E-dipping Gounkoto deposit occurs approximately 20km south of Yalea and Gara (Figure
5) and shares many similarities with Yalea, including its geometry, shear-hosted style of mineralisation, alteration assemblage (including albite, carbonate, and chlorite), and the reactivation of an early D1 structure which coincides with discontinuous sheared marbles and a change in dip of the dominant fabric (Figure 5). Intensely altered rocks in the vicinity of mineralised lodes grade outward, into haloes of partially to pervasively albitised rock up to 50m wide, comparable to that of Yalea.

High-grade mineralisation is characterised by auriferous pyrite-chlorite-carbonate ± magnetite ± hematite ± arsenopyrite shear zones, locally grading in and out of hydrothermal fault breccias and albitite.

Controls on high-grade mineralisation at Gounkoto include left-hand bends and relays along the main N-striking shear zone, and intersections with hangingwall and footwall structures (Figure 5). In contrast to Yalea and Gara, the geometry of high-grade (>8g/t Au) shoots is variable, ranging from steep- to shallow-plunging orientations.

4 An emerging gold district in the Falémé domain showing magmatic affinities

Recent exploration in the intrusive-dominated Falémé domain has highlighted substantial differences in the mineralisation style and structural setting compared with deposits in the Kofi domain. These differences are typified by the Kabe West deposit, where gold mineralisation is dominantly associated with disseminated pyrite ± tellurides ± chalcopyrite in the cement/matrix of clast-supported to matrix-supported hydrothermal breccia pipes and dykes (Figure 6A). These breccia systems comprise numerous cross-cutting breccia generations, with some phases containing possible juvenile mafic clasts (Figure 6B). Subordinate disseminated and vein-hosted mineralisation also occurs within adjacent primary carbonates and porphyry dykes and sills. Deposit-scale structures at Kabe West are incipient and syn-mineralisation strain is much lower than in most Kofi domain deposits.

Known deposits within the Falémé domain are all spatially associated with voluminous, hypabyssal intrusives with common porphyritic textures (Figure 6C) but variable compositions. Most of these Falémé intrusives fall within the magnetite-series, highlighting the possibility that these deposits might be oxidised intrusion-related systems, comparable to more typical porphyry-epithermal mineralisation. The combined total resources for the three main Falémé domain projects, Kabe West, Diamba-Sud and Karakaena now exceeds 1Moz, demonstrating that the domain has potential to become a significant mining district with further exploration (Figure 2).

5 Isotopic and fluid-inclusion analyses

The $\delta^{34}S$ signatures from vein and host rock material across the Kofi domain show a distinct metasedimentary source ($\delta 34S_{CDT}$: 5.8 – 15.5‰), contrasting that of prospects occurring closer to the Falémé batholith which show $\delta^{34}S$ signatures more indicative of sulfur having likely been sourced from a

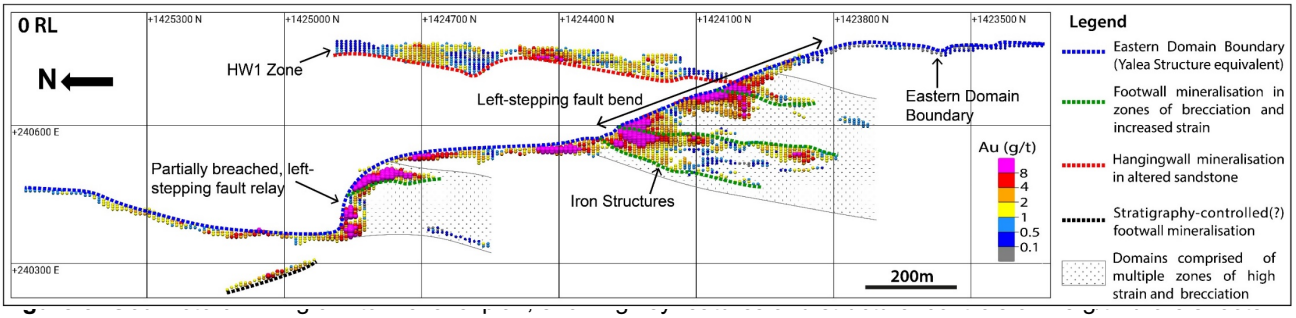

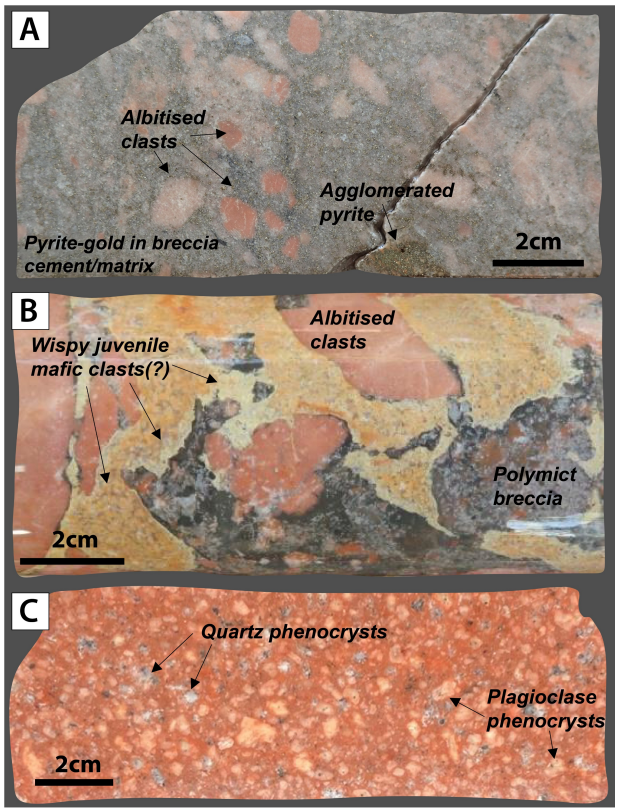

Figure 6. A Mineralised Kabe West breccia with disseminated semi-massive pyrite in cement/matrix. **B** Possible juvenile mafic clasts/fragments occurring within the mineralised polymict breccias. **C** Feldspar-quartz porphyry, typical of the hypabyssal intrusions commonly spatially associated with breccia formations and mineralisation occurrences.

magmatic fluid, particularly at Kabe West ($\delta^{34}S_{CDT}$: –4.6 to 3.9‰) (Lambert-Smith et al. 2020). Carbonate vein $\delta^{18}O$ and $\delta^{13}C$ compositions from Gara, Yalea and Gounkoto are consistent with water-rock reactions between a metamorphic fluid and the Kofi Series carbonates. However, carbonate vein compositions from Kabe West and other prospects closer to the Falémé domain have $\delta^{13}C_{PDB}$ values between -5.9 and -8.6‰ and $\delta^{18}O_{SMOW}$ values between 13.3 and 14.8‰, which is consistent with the direct involvement of cooling magmatic fluids (Lambert-Smith et al. 2020). Furthermore, fluid inclusion studies have indicated mixing with magmatic fluids elsewhere in the Loulo district, particularly at Gara where atypical H_2O-CO_2-NaCl-$FeCl_2$ inclusions occur (Lawrence et al. 2013b).

6 Discussion and Conclusions

The Loulo district can be subdivided into two domains based on differences in geology and mineralisation styles. The eastern Kofi domain is dominated by metasedimentary rocks and mineralisation is more typically orogenic, with gold focussed along reactivated D1 structures and pre-mineralisation alteration playing an important role by creating competency contrasts. In contrast, the western Falémé domain contains large amounts of broadly syn-mineralisation, high-K, calc-alkaline intrusive rocks (i.e., the Falémé batholith) and mineralisation is similar to oxidised intrusive-related systems with distinctly lower syn-mineralisation strain and mineralisation spatially associated with large hydrothermal ± magmatic breccia complexes, hypabyssal intrusives and primary carbonates.

While mapping indicates the SMSZ does not appear to exist at surface, it is considered probable that the intrusion of the Falémé batholith was accommodated along a trans-lithospheric structure. Heat from the emplacement of the Falémé batholith was probably an important driver of the synchronous, district-scale hydrothermal system in both the Falémé and Kofi domains. There is also isotopic and fluid inclusion evidence for the direct involvement of magmatic-derived fluids in mineralisation, particularly within and adjacent to the Falémé domain. Evidence for magmatic fluids generally becomes more equivocal to the east (Lambert-Smith et al. 2020).

This reinterpretation of the structural break implied by the previously interpreted SMSZ and the increasing evidence for magmatic influence in both the Falémé and Kofi domains has emphasised the link between the Falémé batholith and mineralisation in the Loulo district. It has also highlighted the exploration potential of the Falémé domain, which is underexplored compared to the Kofi domain.

In addition to ongoing exploration focussed on assessing the endowment of the Falémé domain, further work will also involve increasing confidence in the classification of the Falémé domain mineralisation and assessing any differences in the depth of mineralisation, as implied by the transition from orogenic-like mineralisation to the east, to oxidised intrusive-related mineralisation to the west.

Acknowledgements

Special thanks go to the authors responsible for the supporting studies discussed in this article, and to Barrick Gold Corporation for funding/access.

References

Allibone A, Lawrence DM, Scott J, Fanning M, Lambert-Smith J, Stenhouse P, Harbidge R, Vargas C, Turnbull R, Holliday J (2020). Paleoproterozoic gold deposits of the Loulo district, Western Mali. Society of Economic Geologists 23: 141-162. doi: 10.5382/SP.23.07

Lambert-Smith JS, Allibone A, Treloar PJ, Lawrence DM, Boyce AJ, Fanning M (2020). Stable C, O, and S isotope record of magmatic-hydrothermal interactions between the Falémé Fe skarn and the Loulo Au systems in western Mali. Economic Geology, 115: 1537-1558. doi: 10.5382/econgeo.4759

Lawrence DM, Treloar PJ, Rankin AH, Boyce A, Harbidge P, (2013b). A fluid inclusion and stable isotope study at the Loulo mining district, Mali, West Africa: Implications for multifluid sources in the generation of orogenic gold deposits. Economic Geology 108: 229–257. doi: 10.2113/econgeo.108.2.229

Insights into the formation of high-grade gold mineralisation at the 10 Moz. Jundee gold camp of Western Australia

Sumail[1], Nicolas Thébaud[1], Quentin Masurel[1], Chris Fisher[1]
[1]Centre for Exploration Targeting, School of Earth Science, The University of Western Australia, Perth, Australia

Abstract. Although orogenic gold deposits form one unified class, individual deposits vary significantly in terms of their mineral paragenesis, deformation styles and associated gold grades. Understanding the processes that control the variation in gold grade has significant implications for predicting how and more importantly where high-grade mineralisation is formed. In this study, we focus on the 10 M oz. Jundee gold camp, located in the Yandal greenstone belt in the Yilgarn Craton of Western Australia. The mining camp comprises the high-grade Jundee gold mine (9 Moz. at 5 g/t Au) and the low-grade Bogada deposit (1 Moz.) hosted in Archean mafic sequences. Detailed structural evolution of the gold camp reveals that gold mineralisation developed over at least three distinctive events. Early low-grade mineralisation hosted in shallow-crustal veins is overprinted by dominantly brittle structures comprising free gold mineralisation. Late thrusting in the gold camp is further associated with the gold remobilisation. At the Bogada deposit, limited evidence exists for punctuated gold episodes and gold mineralisation resulted from a single low-grade event. Based on the detailed structural and paragenetic framework established in this study, we conclude that the high-grade gold mineralisation at Jundee resulted from gold enrichment over three polyphased deformation events.

1 Introduction

Ore quality in orogenic gold deposits can be classified into two categories; free milling and refractory, based on the recovery efficiency of the metallurgical processes (Lunt and Weeks 2005; Petrella et al. 2021). Refractory-style gold mineralisation hosted in sulfide ore usually corresponds to lower gold grade and requires more sophisticated processes for extraction of gold. Contrarily, high-grade free-gold mineralisation is relatively easily recovered with significantly lower energy consumptions. Understanding the physical and chemical processes leading to enrichment of high-grade free-Au mineralisation is critical and important for a more efficient targeting of such ores.

High-grade gold mineralisation has been previously suggested to form as a result of subsequent enrichment of gold over several episodes of mineralisation. However, deciphering individual events in such systems can be extremely challenging and requires understanding the detailed paragenetic evolution of such deposits.

Our study focusses on the 10 Moz. Jundee gold camp comprising of the high-grade Jundee gold mine (9 Moz. at 5 g/t Au) and the low-grade Bogada deposit (1 Moz.) hosted in mafic-ultramafic sequences. The occurrence of high-grade and low-grade mineralisation in a single gold camp provides a unique opportunity to understand the process leading to the formation of high-grade gold mineralisation. By combining structural geology and mineralogy, this study examines in detail the structural and alteration paragenesis at the two deposits and places relative timing constraints on events leading to the formation of gold mineralisation.

2 Regional Geology

2.1 Yandal greenstone belt

The Neoarchean Jundee gold camp is located 600 km north of Kalgoorlie in the Yandal greenstone belt (Figure 1) of the Eastern Goldfields Superterrane (EGST) that hosts several other major deposits including Bronzewing and Darlot in the south. The Yandal greenstone belt represents a 300-km-long and 40-km-wide, poorly exposed N-NW-trending litho-tectonic complex (Figure 2) of metamorphosed and poly-deformed Archean volcanic and sedimentary rocks which are flanked by Late Archean granitoids on either side (Yeats et al. 2001; Baggott et al. 2005). In addition to the Jundee deposit, the Yandal greenstone belts host several other major deposits (> 1 M oz. Au; figure 2) including Bronzewing (Phillips et al. 1998), Mount McClure and Mt Joel in the centre of the belt, and Darlot in its southern end. Rocks in the Yandal belt have been metamorphosed to lower greenschist facies with amphibolite facies metamorphism restricted to granitoid margins (Vearncombe et al. 2000). The stratigraphic succession of the belt reciprocates that of EGST and comprises of mafic-ultramafic volcanism, differentiated mafic sills, felsic volcanics and clastic sedimentary rocks (Kohler and Phillips 2003).

The Yandal belt has been affected by polyphase deformation and thus not all but most of the primary contacts coincide with shear zones (Vearncombe 1998). To the west, the belt is bounded by the Moongarnoo and Moilers shear zones and to the east by Celia shear zone, which at the outcrop-scale, are characterised by protomylonites and foliated schists. The protomylonitic fabric exhibits a steeply dipping geometry, parallel to the greenstone bedding and is dominated by a flattening strain with locally developed asymmetric S-C fabrics (Vearncombe et al. 2000). The structural evolution of the Yandal belt was first described by Vearncombe (1998) through

his works on shear zones, which he later summarised into three progressive deformation events (Vearncombe et al., 2000), consistent with the regional D2 – D4 deformation event scheme proposed for the EGST by (Swager 1997).

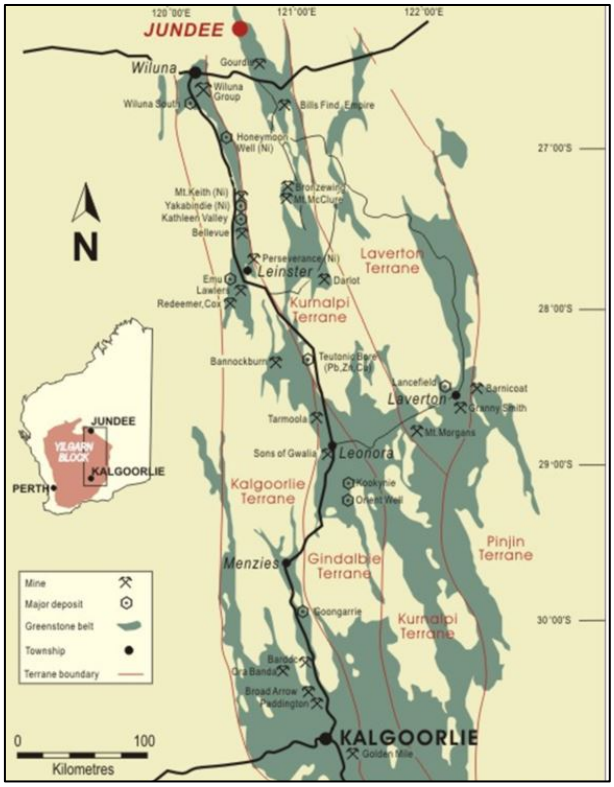

Figure1. Map showing location of Jundee gold deposit in the Yandal greenstone belt of the Eastern Goldfields Superterrane of Yilgarn Craton. Modified after Newmont (2008).

The Yandal greenstone belt is characterised by crosscutting brittle-ductile shear zones which trend from 000-150° and correlate with the D4 event (Kohler and Phillips 2003) in the D1 – D4 regional deformation scheme outlined for the EGST by (Swager 1989). The D3 event in the Yandal is represented by the Moilers, Moongarnoo and Celia shear zones resulting from an E-W progressive shortening deformation. An episode of NNW-trending upright folding has been recognised in the southern Yandal belt and results from an ENE-WSW shortening D2 deformation (Phillips et al. 1998; Vearncombe et al. 2000). Like elsewhere in EGST, evidence for D1 N-S shortening deformation is cryptic in the Yandal belt (Kohler and Phillips 2003).

2.2 Jundee goldfields

The 9 Moz. Jundee gold deposit is located in the northern end of the Yandal greenstone belt with host sequence striking NNW and dipping moderately (40-55°) towards the SW (Yeats et al. 2001). The mine sequence at Jundee (Figure 2) has an approximate thickness of ~2.5 km and is dominated

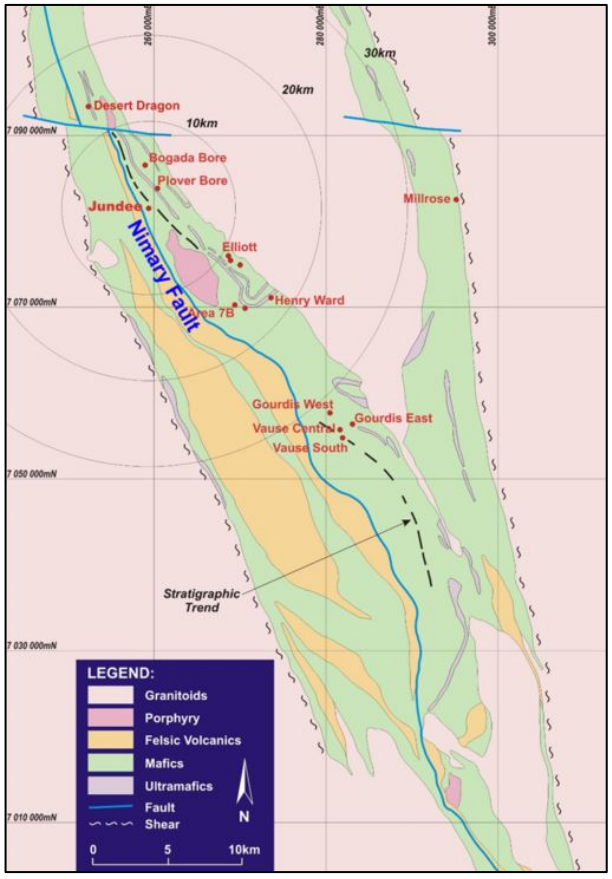

Figure 2: Detailed map displaying the geology of the Yandal greenstone belt. Modified after Newmont (2008).

by tholeiitic basaltic rocks, the Fisher and Lyons basalts which were originally separated by an horizon of 100 m thick sedimentary rocks (carbonaceous shales, cherts and siltstone). The present-day geometry is such that this sedimentary horizon has been separated into four individual units as it has been intruded by three strike-continuous differentiated gabbroic sills (Barton, Hughes and Lyons Dolerites). The differentiated sills represent individual separate intrusions based on geochemical analysis and absence of tectonic repetition (Hergt et al. 2000). A deformed succession of dacitic –to - rhyodacitic volcanoclastic rocks with minor shale, chert and basalt lies to the west of the mine sequence and is interpreted to be related to the Lake Violet Sequence (Phillips et al. 1998; Vearncombe et al. 2000). The mine sequence at Jundee is intruded by suites of dacitic porphyries, porphyritic granodiorites and lamprophyres which range from pre- to post-mineralisation in age. The dacitic porphyries are common, have variable trends, host economic gold mineralisation and can be up to 300 m thick (Yeats et al., 2001). These pre-mineralisation dacitic intrusions are dated at 2678 ± 5 Ma, thus providing a minimum age for the main mineralisation event (Yeats et al. 2001). The granodiorite porphyry dykes lack economic mineralisation (> 0.7 g/t Au) and are mostly barren and usually truncate the gold-bearing structures. These dykes can be up to 50 m wide and have a consistent NE to NNE-orientation (Kohler and Phillips 2003).

Gold mineralisation is hosted by a network of brittle-ductile cross-cutting shear zones trending 000-160° with variable dips. Vearncombe et al. (2000) argued that these faults represented a conjugate set where the NE-striking (040-060°) shear zones displayed dextral kinematics and the SE-striking (090-120°) shear zones were sinistral. Most veins consist of massive- to variably laminated, amorphous and finely crystalline quartz, with carbonate and minor chlorite, muscovite, pyrite and arsenopyrite. Visible gold is common, and grades can range up to several thousands of grams per tonne Au. Vein margins are usually sharp and planar, but locally exhibit evidence of wall rock replacement. Some veins show millimetre- to centimetre-wide, symmetrical, wall rock alteration zones. Some basalt-hosted shear zones, contain syn-deformational crustiform- and colloform-textured veins containing multiple, subparallel, quartz-carbonate bands 0.5 - 10 mm thick. The grade of the veins is rarely more than 2-3 g/t Au.

3 Structural Setting of the Jundee Gold Camp

3.1 V_{J1} veins

Thin (<5cm) fault-fill veins dominated by a chlorite calcite composition are ubiquitously present throughout the Jundee system and provide the evidence for first hydrothermal activity in the deposit. These veins are dominantly found along the lithological contacts between basalts, gabbros and dacitic porphyries. The V_{j1} veins display a consistent NW-trending orientation parallel to the stratigraphy along with an N-S trending conjugate pair. These early veins are barren in terms of gold and lack any significant associated alteration.

3.2 V_{J2A} Colloform veins

Relatively thick (up to 2 m wide) V_{J2A} veins show occurrences of colloform-crustiform textures along with cockade textured breccias. These open-space growth textures are commonly interpreted to form in shallow crustal environments. The V_{J2A} colloform veins represent the first introduction of gold in the Jundee system. These veins have a consistent NW-trending and SW-dipping structural orientation and are associated with normal kinematics. The colloform veins are also frequently associated with conjugate pairs and vertical tension veins which together suggest their formation in an extensional setting. These dominantly brittle, mineralised structures lack any significant displacement along them with limited evidence for associated kinematics such as slickenlines or stepfibres. However, where present, mineral lineation associated with the colloform veins plunges shallowly (15° - 20°) towards the SE. Gold mineralisation associated with the colloform veins is low-grade (<2 g/t), where gold is dominantly hosted in sulfides alteration associated with such veins.

3.3 V_{J2B} hydrothermal breccia and laminated veins

The V_{J2B} structures account for the high-grade gold event at Jundee and represent bulk of the gold mineralisation at the Jundee deposit. These highly endowed structures form a network of dominantly brittle fractures with multiple orientation o gold-bearing shear zones that parallel and cross-cut the stratigraphy. The V_{J2B} structures are characterised by tabular zones of dominantly brecciated and veined rocks that hosts the high-grade gold mineralisation. These structures consistently reactivates earlier preferentially oriented structures. The V_{J2B} structures dominantly occurs as hydrothermal breccia in basalts and as laminated veins in doleritic host rocks. Gold grades associated with these structures can be as high as 10 wt % of the rock volume. The mineralised structures are often narrow (up to 2 m wide) with strikes continuous over a few tens to several hundreds of metres. Although considerably variable in orientation, the mineralised V_{J2B} structures can be categorised into broad discrete trends based on associated kinematics. Shear zones striking NW to WNW appear to host most of the gold mineralisation in the deposit and are dominantly associated with normal kinematics with minor sinistral strike-slip component. These bedding parallel structures are occasionally associated with ENE-trending vertical tension veins further suggestion their formation in an extensional setting. Secondary trends includes the ENE-trending faults dipping moderately towards the SE. These faults often form a conjugate pair the WNW-trending mineralised faults which display evidence for normal displacements. Mineralisation related lineation associated with the ENE-trending faults plunges down-dip the structures with step-fibres suggesting a dominantly normal-dextral kinematics associated with the gold mineralisation. The dominant free-Au occurring mineralisation found in the Jundee deposit occurs mostly in the hydrothermal matrix. Matrix composition comprises of fine crystalline grey groundmass dominated with a quartz-calcite composition along with chlorite, muscovite and sulfide. The sulfide composition is dominated by pyrite along with arsenopyrite, tennantite and chalcopyrite. Pyrite occurs ubiquitously either in disseminated form or as millimetre-wide stingers. Euhedral to subhedral pyrite grains form larger irregular composites. SEM imaging of the pyrite grains reveals evidence for complex internal zoning with inclusion-rich spongy cores surrounded by arsenic-rich pyrite mantles. Gold preferentially occupies internal boundaries between zoned pyrite and there is significant evidence present for remobilisation of gold from internal pyrite zones to external parts of pyrite and outside pyrite grains.

3.4 V_{J3} gold rich veins

The high-grade V_{J2A} hydrothermal breccias are locally overprinted and crosscut by dark green chlorite-calcite V_{J3} veins. The V_{J3} veins are thin (<2 cm) and continuous over few 10's of metres. The V_{J3} veins hosts abundant visible gold mineralisation that can be >10 % of the vein material. Vein composition is dominated by a calcite-quartz with minor amounts of chlorite. However, interestingly the V_{J3} veins themselves host a low grade (<2 g/t) mineralisation when distant from the V_{J2B} hydrothermal breccias. These V_{J3} veins are dominantly associated with reverse kinematics resulting in thrusting of earlier structures. The occurrence of V_{J3} faults in the Jundee system is extremely limited and often observed when overprinting the earlier structures.

4 Summary

Through a detailed evaluation of the structural framework for the Jundee-Bogada gold camp, we have been able to establish that (i) the poorly preserved V_{J1} calcite-chlorite veins are the first evident hydrothermal event at the Jundee deposit; (ii) the widespread colloform-crustiform veins (V_{J2A}) represent the first introduction of gold in the Jundee deposit; (iii) the most prominent structural event 'V_{J2B}' and associated high-grade gold mineralisation accounts for the majority of gold mined at the Jundee deposit; (iv) locally occurring ultra-high grade V_{J3} veins represent the third and last evidence for gold mineralisation in the Jundee deposit. In the high-grade Jundee deposit, initial low-grade gold mineralisation hosted in the colloform structures (V_{J2A}) is overprinted by a high-grade gold mineralising event (V_{J2B}). Moreover, there is further evidence for a third event associated with the V_{J3} chlorite-calcite veins. The local enrichment of gold in these veins is restricted to localities where they intersect the earlier high-grade V_{J2B} structures. Therefore, we propose that some (if not all) of the gold may be locally remobilised from the high-grade V_{J2B} structures into the V_{J3} veins.

5 Conclusions

At the 10 M oz. Jundee gold camp of EGST, two distinctive orogenic gold deposits exist within 2 km of each other: the 9 M oz. Jundee gold deposit and the 1 M oz. Bogada gold deposit. The two deposits are characterised by significantly contrasting gold grades with high-grade (>10 g/t) gold mineralisation hosted at the Jundee deposit and low-grade mineralisation (< 2g/t) at the Bogada deposit. The structural paragenesis established at the two deposits provides evidence for a protracted and polyphased deformation associated with multiple episodes of gold mineralisation. The first episode of gold mineralisation hosted in colloform veins includes refractory-style gold associated with sulphide assemblage dominated by pyrite, sphalerite and tennantite. The second mineralisation event resulted in dominantly free-Au mineralisation associated with complexly pyrite, arsenopyrite, tennantite and chalcopyrite. Evidence for the last gold mineralisation episode is recorded by thrust faults associated with contractional deformation. This late gold mineralisation resulted in dominantly refractory ore except where remobilising from previous stages (V_{J3}). Our results demonstrate that a key characteristic of the high-grade Jundee gold deposit is the overprinting of successive mineralisation events compared to the single gold event at the low-grade Bogada deposit.

Acknowledgements

This study would like to acknowledge its parent project 'Yilgarn 2020' (MRIWA M530) for providing the financial and technical support required for this study. The authors would also like to acknowledge the in-kind and financial support provided by Northern Star Resources and Creasy Group, specifically Jamie Rogers, Peter Le Roux, Chris Scott and Kris Wright for their invaluable input.

References

Baggott MS, Vielreicher NM, Groves DI, McNaughton NJ, Gebre-Mariam M (2005) Zircons, Dikes, and Gold Mineralization at Jundee-Nimary: Post ca. 2.66 Ga Archean Lode Gold in the Yandal Belt, Western Australia. Economic Geology 100:1389-1405.

Hergt JM, Preston P, Bright RMJ, Phillips GN (2000) Differentiated mafic sills in the Yandal greenstone belt. AIG Bulletin 32:55-67.

Kohler EA, Phillips GN (2003) Jundee goldfield, Yandal gold province, Yilgarn Craton, Western Australia. National Library of Australia CSIRO Exploration & Mining, Box 312, Clayton South, Victoria.

Lunt D, Weeks T (2005) Process flowsheet selection. Developments in Mineral Processing 15:73-96.

Newmont (2008) Jundee Geology Overview. Newmont Pty Ltd, Australia.

Petrella L, Thébaud N, Evans K, LaFlamme C, Occhipinti S (2021) The role of competitive fluid-rock interaction processes in the formation of high-grade gold deposits. Geochimica et Cosmochimica Acta 313:38-54.

Phillips GN, Vearncombe JR, Eshuys E (1998) Yandal greenstone belt, Western Australia: 12 million ounces of gold in the 1990s. Mineralium Deposita 33:310-316.

Swager C (1989) Structure of Kalgoorlie Greenstones: Regional Deformation History and Implications for the Structural Setting of the Golden Mile Gold Deposits. Report25:59-84.

Swager C (1997) Tectono-stratigraphy of late Archaean greenstone terranes in the southern Eastern Goldfields, Western Australia. Precambrian Research 83:11-42.

Vearncombe JR (1998) Shear zones, fault networks, and Archean gold. Geology 26:855-858.

Vearncombe JR, Kohler E, Meyers J, Phillips GN, Rothery E, Ryan D (2000) Regional, structural and exploration geology in a terrain with minimal outcrop—the Yandal belt. Yandal greenstone belt: Perth, Australian Institute of Geoscientists, Bulletin 32:17-39.

Yeats CJ, Kohler EA, McNaughton NJ, Tkatchyk LJ (2001) Geological setting and SHRIMP U–Pb geochronological evidence for ca. 2680–2660 Ma lode-gold mineralization at Jundee–Nimary in the Yilgarn Craton, Western Australia. Mineralium Deposita 36:125-136.

Early crustal architecture revealed by multidisciplinary data integration: implications for gold exploration targeting

Nicolas Thébaud[1], Quentin Masurel[1,2], Alan Aitken[1], Hugh Smithies[3], Klaus Gessner[3], Chris Fisher[1], Yongjun Lu[3]
[1]Centre for Exploration Targeting, School of Earth Sciences, The University of Western Australia, 35 Stirling Hwy, Crawley 6009, Western Australia
[2] Minerals Targeting International Pty Ltd, West Perth, Wester Australia
[3]Geological Survey of Western Australia, Department of Mines, 100 Plain Street, East Perth 6004, Western Australia

Abstract. Metallogenic systems are intimately linked with zones of mechanical weakness that occur in the lower-middle crust and continental lithospheric mantle. Where preserved, these zones of lithospheric heterogeneity ("lithospheric discontinuities") reflect the finite cumulative lithospheric damage associated with paleo-tectonic events such as rifting and collision. Understanding this fundamental architecture is crucial for explorers to enhance their predictive capacity, as it exerts a primary control on the location of tier one ore deposits. To identify and map this architecture in the deep crust and continental lithospheric mantle, we conducted a multidisciplinary study of the Yilgarn Craton. Our analysis revealed regional scale lineaments, some of which oblique to the main structural grain established during the craton's assembly. We propose that these lineaments were active during intra-cratonic rifting and the emplacement of the Kalgoorlie-Kurnalpi supracrustal cover between c. 2720 and 2690 Ma. They were subsequently reactivated during the Kalgoorlie Orogen, c. 2680-2635 Ma, and played a critical role in controlling the location of tier one gold deposits in the region.

1 Introduction

Transcrustal to translithospheric discontinuities have been suggested to exert control over a diverse array of mineral systems. Such discontinuities are thought to provide the fundamental pathways connecting enriched continental lithospheric mantle domains to the upper crust (e.g. Hronsky et al. 2012). As noted by Holdsworth et al. (2001), hydrous fluids and magmas tend to migrate preferentially along long-lived, inherited structures in continental margins. This phenomenon has been observed in many mineral-rich areas worldwide, particularly at the intersection of fundamental basement structures with orogen-parallel crustal-scale structures. For example, orogenic gold deposits have been found to occur in such settings (Love et al. 2004), as have epithermal gold deposits (Bahiru et al. 2019) and porphyry Cu-Au deposits (Gow and Walshe 2005).

Identifying the crustal and lithospheric architecture within a continental mass is challenging due to its cryptic nature. In the field, such features are frequently overlooked or misinterpreted. As an alternative the early craton architecture may be indirectly mapped via a set of techniques including large-wavelength geophysical methods (e.g. gravity, magnetics), and radiogenic isotopes (e.g. Lu-Hf and U-Pb on zircon). Such an approach has been instrumental in revealing the architecture of the Yilgarn Craton of Western Australia and evaluating the role of this architecture in the generation of gold and nickel mineral systems (Fig 1., Mole et al. 2014).

2 Regional geology

The Yilgarn Craton, located in Western Australia, is divided into several terranes, including the Narryer Terrane, Youanmi Terrane, South West Terrane, and Eastern Goldfields Superterrane. The latter encompasses the Kalgoorlie, Kurnalpi, Burtville, and Yamarna terranes. The Narryer Terrane and northern Southern Cross Domain are ancient crustal blocks within the Yilgarn Craton and have a shared geological history extending back to c. 4000 Ma (Mole et al. 2019). A major felsic magmatic event affected the proto-craton between c. 3050 and 2900 Ma (e.g. Mole et al. 2019). An embryonic stage of subduction occurred between c. 2830 and 2740 Ma and resulted in the docking of the Narryer Terrane against the Youanmi Terrane at c. 2740 Ma. At c. 2720-2690 Ma, the Kalgoorlie-Kurnalpi Large Igneous Province (Hayman et al. 2015) occurred in a failed intra-cratonic rift related to a mantle upwelling zone focused along a zone of pre-existing lithospheric heterogeneity referred to as the Ida Fault (Masurel et al. 2022).

The tectonic inversion of the Kalgoorlie-Kurnalpi intracontinental rift occurred during the Kalgoorlie Orogen between c. 2680 and 2630 Ma. At that time the NNW-striking structural grain of the Eastern Goldfields Superterrane was acquired under ENE-WSW-directed bulk crustal shortening (Swager 1997).

3 Methodology

Our approach relies on the interpretation of multidisciplinary dataset combining aeromagnetic, gravity and seismic data together with radiogenic isotopic data (Sm-Nd) and the regional geological record. In this study, we: (i) identify the orientations of basement discontinuities in the lower-middle crust and continental lithospheric mantle of the Yilgarn Craton through the integrated geological interpretation of isotopic and deep-penetrating geophysical data; and (ii) assessing their geological robustness through comparison between independent dataset.

Our approach involves the interpretation of a multidisciplinary dataset that combines aeromagnetic, gravity, and seismic data, as well as radiogenic isotopic data (Sm-Nd), with the regional geological record. Here, we aim to (i) identify the orientations of basement discontinuities in the lower-middle crust and continental lithospheric mantle of the Yilgarn Craton by integrating isotopic and deep-penetrating geophysical data and (ii) evaluate their geological robustness by comparing them with independent datasets. Our approach enables us to validate the lineaments delineated in the range of datasets analyzed and to assess their relative timing of emplacement. We suggest that this combination is crucial for confidently verifying the presence of an inferred lithospheric architecture and refining its geological origin.

4 Results

The documented basement discontinuities can be grouped into three main categories. The first category consists of orogen-parallel trends that were likely acquired during the protracted assembly of the Yilgarn Craton. The second category mimics that of the craton's margins, and likely indicates post-cratonization modifications of the Yilgarn Craton. The third category comprises orogen-oblique trends, the origin of which remains cryptic.

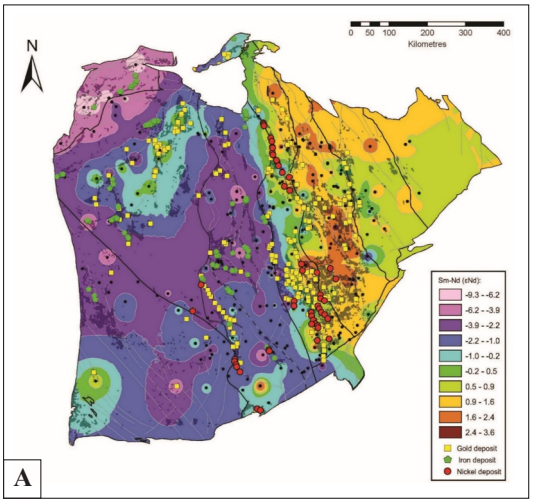

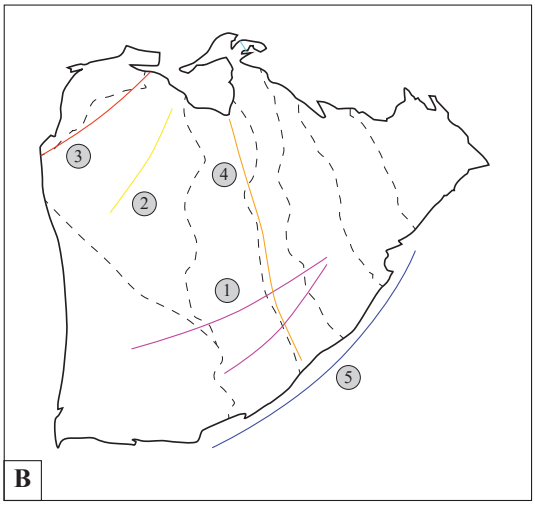

Figure 1. A) Sm-Nd isotopic contour map showing the spatial variation of εNd values (modified after Mole et al. 2013). B) Cartoon showing major structural architecture of the Yilgarn Craton: (1) Intracratonic rift zone across the Yilgarn proto-craton between c. 3050 and 2900 Ma resulting in the eruption of the Forrestania and Lake Johnston ultramafic units. (2) Intra-continental rift zone the Murchison Domain of the Youanmi Terrane between c. 2825 and 2740 Ma. (3) Collision front between the Narryer and Youanmi Terranes at c. 2740 Ma. (4) Kalgoorlie-Kurnalpi failed intracratonic rift axis (5) Albany-Fraser intracratonic rift at c. 1805 Ma. Dash line represents Terranes.

5 Discussion

5.1 Interpreting oblique-orogen structural architecture

Our analysis of potential field, topographic, isotopic, and seismic data indicates that both the orogen-parallel trends and trends parallel to the margins of the Yilgarn Craton exhibit similar expressions. Through comparison with existing geological knowledge of the Yilgarn Craton's evolution, we have validated each identified trend as representing a preserved expression of multiple tectonic events that affected the crust from the Neoarchean to the Proterozoic.

The geological validity of orogen-oblique trends identified in potential field, topographic, seismic, and isotopic data is harder to evaluate within the geological record of the Yilgarn Craton. Yet, the coincidence of the orogen-oblique lineaments in multiple datasets provides a higher degree of confidence with regards to their existence. The problem remains as to explain what these orogen-oblique trends may represent.

In the Yilgarn Craton, the development of the Kalgoorlie-Kurnalpi terranes developed within an extensional environment (e.g. Masurel et al. 2022). Stratigraphic, isotopic, and geochemical data, collectively, indicate that emplacement of the c. 2720-2690 Ma occurred in a failed intra-continental rift and was related to a mantle upwelling zone focused along the NNW-striking Ida Fault (e.g.

Hayman et al. 2015). Within such extensional context, one may suggest that oblique-orogen structures may represent ancient transfer faults that helped accommodating rifting of the proto-Yilgarn continental mass.

Such interpretation echoes with that made in more recent geological terrains of the Andes whereby orogen-oblique structures have been recognised across scales. For instance, in the Cu-Zn Antamina mine in Peru, the deposit architecture and structural setting is controlled by orogen-oblique structures that have been interpreted as transform segments accommodating early rifting of the continental margin (Love et al. 2004). Wiemer et al. (2022) did generalise this conclusion suggesting that cross structural lineaments along the NW-striking Peruvian crustal architecture were related to transfer structures that had accommodated the rifting of the continental margin associated with the Rodinia break up.

5.2 Implication for Gold mineralisation

In recent studies, a strong connection has been proposed between the formation of ore deposits and the inversion of early tectonic architecture. In the Cu-Zn Antamina mine, the oblique-orogen structure is interpreted to have controlled the intrusion and related mineralised skarn development during the rift inversion that took place during the Eocene and Miocene (Love et al. 2004). Following a similar interpretation, Wiemer et al. (2022) investigated the northern Peruvian Andean Cordillera and suggested that successive inversion of the Andean margin played a primary role in the clustering of gold deposits. There, the intersection between the so-called oblique-orogen Pataz lineament appear to mark the locus of a cluster of major Carboniferous and Cenozoic gold deposits in northern Peru. Such spatial coincidence is suggested to highlight the critical role of early rifting architecture in providing the plumbing system required to efficiently transfer ore-fertile magmas and fluids in the crust (Wiemer et al. 2022).

We propose that the spatial association between oblique-orogen structures in the Yilgarn Craton and gold deposit clusters in the Kalgoorlie and Kurnalpie Terrane supports the hypothesis that these structures play a crucial role in ore deposit localization. This conclusion is consistent with previous studies conducted at the camp scale, such as St Ives (Miller et al., 2010) and Yakabindie (Perring, 2016), as well as with interpretations presented in Doutre (2017). These studies suggest that oblique-orogen basement structures were either incipiently reactivated and upward-propagated through overlying c. 2720-2690 Ma greenstones; or remained inactive but controlled the segmentation and geometry of transfer zones along orogen-parallel upper to mid-crustal shear zones during the structural inversion that occurred between c. 2690 and 2650 Ma.

6 Conclusion

The identification and mapping of the fundamental early architecture of the deep crust is crucial for explorers to enhance their predictive capability. In the Yilgarn Craton, we identify strike-extensive lineaments, some of which appear oblique to the main structural grain established during tectonic assembly. We propose that this architecture developed between c. 2720 and 2690 Ma during lithospheric thinning, forming the critical early architecture that controlled the emplacement of tier-1 gold deposits in the region during c. 2690-2650 Ma basin inversion. Although the geological and structural expression of such architecture may be cryptic, the multidisciplinary workflow developed in this study provides a toolbox that can help validate its occurrence at the craton scale.

Acknowledgements

The authors acknowledge support from the Minerals Research Institute of Western Australian, Northern Star Resources Ltd, Gold Road Resources Ltd, BHP - Nickel West Pty Ltd, Evolution Mining Ltd, Gold Fields Australia Ltd, and Bogada Gold Ltd under the MRIWA collaborative research project M0530 Yilgarn 2020.

References

Bahiru, E.A., Rowland, J.V., Eccles, J., kellett, R.L., 2019. Regional crustal-scale structural control on epithermal deposits within the Hauraki Goldfield, Coromandel Volcanic Zone, New Zealand: insight from integrated geological and aeromagnetic structural patterns. New Zealand Journal of Geology and Geophysics 62

Holdsworth, R.E., Stewart, M., Imber, J., Strachan, R.A., 2001. The structure and rheological evolution of reactivated continental fault zones: a review and case study. Geological Society of London Special Publication 184:115–137.

Doutre R (2018) Multi-scale organisation and geological controls on large orogenic gold deposits. Doctoral Thesis, 10.26182/5bb2bacd25b5c

Hayman PC, Thébaud N, Pawley MJ, Barnes SJ, Cas RAF, Amelin Y, Sapkota J, Squire RJ, Campbell IH, Pegg I (2015) Evolution of a ~2.7 Ga large igneous province: a volcanological, geochemical and geochronological study of the Agnew Greenstone Belt, and new regional correlations for the Kalgoorlie Terrane (Yilgarn Craton, Western Australia). Precambr. Res. 270:334–368.

Hronsky JMA, Groves DI, Loucks RR, Begg GC (2012) A unified model for gold mineralisation in accretionary orogens and implications for regional-scale exploration targeting methods. Mineralium Deposita 47:339–358.

Love DA, Clark AH, and Glover JK (2004), The lithologic, stratigraphic, and structural setting of the giant Antamina copper-zinc skarn deposit, Ancash, Peru: Economic Geology, 99:887–916.

Miller J, Blewett R, Tunjic J, Connors K (2010) The role of early formed structures on the development of the world class StIves Goldfield, Yilgarn, WA. Precambrian Res.183,292–315.

Mole DR, Fiorentini ML, Cassidy KF, Kirkland CL, Thébaud N, McCuaig TC, Doublier MP, Duuring P, Romano SS, Maas R, Belousova EA, Barnes SJ and Miller J (2013) Crustal evolution, intra-cratonic architecture and the metallogeny

of an Archaean craton, Geological Society, London, Special Publications, 393
Mole DR, Kirkland CL, Fiorentini ML, Barnes SJ, Cassidy KF, Isaac C, Belousova EA, Hartnady M, Thébaud N (2019) Time-space evolution of an archean craton: a Hf-isotope window into continent formation. Earth-Science Rev. 196, 102831.
Perring CS, (2016) Yakabindie revisited – volcanological and structural controls on the komatiite-hosted Six Mile Well and Goliath North deposits and implications for the architecture of the 2.7 Ga rift event in the Agnew-Wiluna belt, Yilgarn Craton, Western Australia. Econ. Geol. 111:1159-1185.
Wiemer D, Hagemann, SG, Hronsky J, Kemp AIS, Thébaud, N, Ireland T, Villanes C 2022 Ancient structural inheritance explains gold deposit clustering in northern Perú. Geology 50/10:1197-1201

Mineralogy and geochemistry of the A2 and New A2 gold deposits in the Nwe Yon–Kwinthoneze gold district, central Myanmar

Aung Myo Thu[1,2], Adam Piestrzyński[1], Gabriela A. Kozub-Budzyń[1], Krzysztof Foltyn[1]
[1]Faculty of Geology, Geophysics and Environmental Protection, AGH University of Science and Technology in Krakow, Poland
[2]Department of Geology, Mandalay University, Myanmar

Abstract. The A2 and New A2 gold deposits are located in the New Yon-Kwinthoneze gold district in central Myanmar. The ore bodies are primarily hosted in marble and gneiss, and the contact between these two host rocks. The principal ore minerals are pyrite, chalcopyrite, sphalerite, pyrrhotite, marcasite, native gold, and telluride assemblages. Native gold occurs as fissure filling, inclusions in sulphide minerals, and Au-Ag-Te associations. Gangue minerals are mostly quartz, calcite, siderite, ankerite, W-bearing rutile, and minor chlorite. The wall-rock hydrothermal alterations include silicification and carbonatization. C-O isotopic compositions suggest that the ore-forming fluids were most likely derived from magma with limited contributions from the host rocks and later mixed with the meteoric water. The $\delta^{34}S$ values of sulphides from the A2 and New A2 deposits are consistent with a homogeneous magmatic source. The analyses of S, C, and O isotopic data suggested that the ore-forming fluids were mainly derived from the magmatic fluids and later mixed with meteoric water in the ore-forming process.

1 Introduction

In the last two decades, intrusion-related gold systems have been considered separately from orogenic gold systems (Thompson and Newberry 2000; Baker 2002; Hart and Goldfarb 2005). However, the distinction between these two gold systems remains a subject of debate because of many similarities (e.g., Sillitoe and Thompson 1998; Hart and Goldfarb 2005). Myanmar has more than 300 gold occurrences, including intrusion-related gold deposits (IRGDs), orogenic gold deposits (OGDs), and skarn type Au-(Cu) deposits (Swe et al. 2017).

The Mogok Metamorphic Belt (MMB) is one of the most important metallogenic belts in Myanmar (e.g., Zaw 2017), and gold is by far the most important mineral product after gemstones (Mitchell 2017). The Nwe Yon-Kwinthoneze gold district is located in the middle segment of the MMB and contains two significant economic orebodies (i.e., A2 and New A2 deposits). Artisanal mining started in at least the 1980s, and more recently, commercial-scale underground mining developed in this gold district (Mitchell 2017). However, the total gold reserves and the resources are not available. There are two viewpoints on the genesis of the Nwe Yon-Kwinthoneze gold district: (1) epithermal and skarn affinity (Myint et al. 2014) and (2) epizonal orogenic gold deposit (Myint et al. 2022).

In this paper, we present a detailed investigation of geological, mineralogical, and stable (C, O, S) isotopic studies conducted to determine the possible sources of the ore-forming fluid and the genesis of the A2 and New A2 deposits in the Nwe Yon – Kwinthoneze gold district.

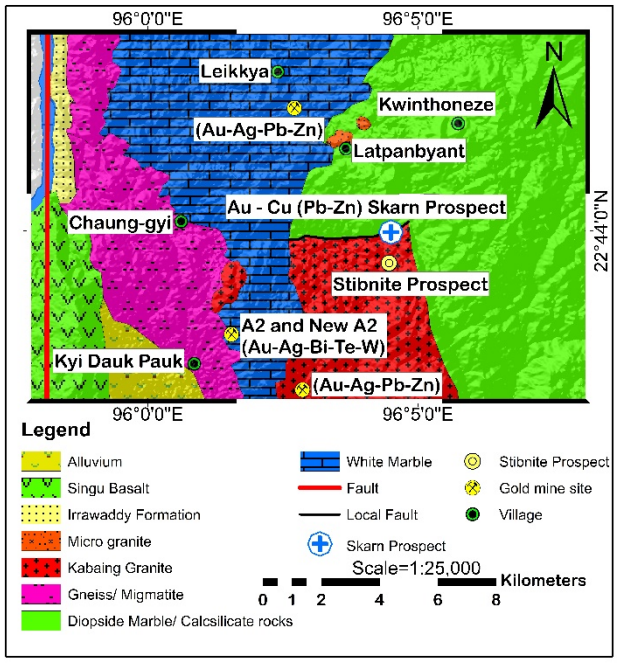

Figure 1. Geological map of the Nwe Yon-Kwinthoneze gold district (modified after Lamont et al. 2021).

2 Geological setting

Myanmar can be divided geologically into two parts: eastern and western provinces, which were separated by the 1200 km long north-south trending, dextral strike-slip Sagaing fault. The eastern province is a part of the Sibumasu Block and the western province is the West Burma Block. The MMB is located between Sibumasu Block and West Burma Block. It contains Jurassic to Early Cretaceous subduction-related magmatism and was exhumed by compressional deformation during the Tertiary metamorphic event (Searle et al. 2007).

The ore-hosting rocks in the Nwe Yon-Kwinthoneze gold district are dominated by the Mogok Metamorphic groups of migmatitic biotite gneiss, biotite-gneiss, garnet-biotite migmatite, white marble, diopside marble, phlogopite marble, and calc-silicates, which were intruded by Kabaing granite and minor micro-granite to the east of the Sagaing Fault (Figure 1). The Kabaing granite is the

largest intrusive body in this gold district. The age of the granite is constrained by zircon U-Pb ages of 16.8±0.5 Ma near the Mogok Valley to the north of the study area (Gardiner et al. 2016). Minor occurrences and thin (less than 15 cm wide) pegmatite dykes crosscut the Kabaing granite and biotite-rich hornfels near the Zee Phyu Kone skarn formation (Thu et al. 2022). The high-grade Mogok metamorphic groups are unconformably overlain by the Late Miocene-Pliocene Irrawaddy Formation and Singu Quaternary trachybasalt in the southern part of the study area (Figure 1). The metamorphism in this segment has been dated by using the monazite U-Pb method on migmatites from the Kyi-Tauk-Pauk gold mining area. It shows an early high-grade granulite event at 43–32 Ma and a later, upper amphibolite facies, sillimanite-grade event peaking at 23–20 Ma (Lamont et al. 2021).

The A2 and New A2 gold deposits are situated in the Nwe Yon – Kwinthoneze gold district. The host rock geology of these deposits is similar, primarily comprising marble and gneiss, and the contact between these two host rocks. The currently known A2 and New A2 Au-ore segments contain more than 16 auriferous quartz veins of NNE striking, parallel gold lodes, with a spacing of 40–50 m. Individual gold lodes strike between 10° and 35°, dipping 40° to 60° northeast, and parallel to the metamorphic foliations of the host rocks. Each lode is typically 50–150 m long and 0.5–1 m wide, locally wedged out along fracture zones, and shows typical pinch-and-swell features. The structure of the A2 and New A2 deposits are dominated by NE–SW trending compressional–shear faults. The primary contact between marble and gneiss, the A2 and New A2 shear zones, formed due to the rheological differences. The gold orebodies are characterized by sulphide-quartz-carbonate veins, disseminated, and massive sulphides. The principal ore minerals in the A2 and New A2 deposits are pyrite, chalcopyrite, sphalerite, pyrrhotite, marcasite, native gold, and telluride assemblages. Gangue minerals are mostly quartz, calcite, siderite, ankerite, W-bearing rutile, and minor chlorite.

The A2 and New A2 ore bodies have the same wall-rock hydrothermal alteration, mainly silicification and carbonatization. Silicification is the most widespread and significant alteration along the quartz veins in the host rocks (gneiss and marble). It is closely related to gold mineralization. Carbonatization is also common, with euhedral–subhedral carbonate minerals such as calcite and siderite occurring in veins and veinlets.

3 Analytical techniques

Detailed textural observation and preliminary mineral identification were performed using optical microscopy and EPMA (JEOL 8230) at the laboratory of Critical Elements AGH-KGHM at AGH-UST. Sulphur, Carbon, and Oxygen isotopes were analysed at the Laboratory of Petroleum Geochemistry at AGH University of Science and Technology, Krakow.

4 Results

4.1. Selected ore mineralogy

Pyrite, the most abundant sulphide phase, is the major host for gold and telluride minerals in the A2 and New A2 deposits. It forms at every stage of mineralization and usually occurs as euhedral to anhedral grains. The largest crystals, ranging from coarse to medium-grained (sizes ranging from 100 µm to 3 mm), have a porous, spongy texture and are commonly filled with sulphide minerals and native gold (Figure 2A).

Chalcopyrite and sphalerite are primarily subhedral to anhedral minerals that replace the gold-hosting pyrite and/or fracture fill within micro-fissures in pyrite (Figure 2A, B). Minor pyrrhotite inclusions are observed in chalcopyrite (Figure 2C).

Two types of gold occurrences were observed in the A2 and New A2 deposits. Native gold independently occurs as fissure filling, inclusions in sulphide minerals, and Au-Ag-Te associations (Figure 2A, B). The telluride minerals are petzite, hessite, tellurobismuthite, altaite, melonite, coloradoite, and mettagamite. Gold is widespread and exists as irregular grains, typically along the grain boundaries or as a filling of microfractures in quartz, pyrite, chalcopyrite, and telluride minerals.

Petzite is closely associated with gold and hessite (Figure 2B). Individual grains range in size from 5 to 100 µm. The EPMA analysis of some petzite grains shows a lower Au content (19.91-28.81 wt.%;) compared to ideal petzite (25.39 wt.%;), and its formula based on average composition is calculated as $Ag_{2.87-3.45}Au_{0.78-1.12}Te_{1.56-2.03}$.

Hessite frequently coexists with petzite, altaite, and native gold in the form of medium- to fine-grained, irregular grains and is also observed as cluster inclusions in pyrite. Hessite contains 60.03-60.40 wt.% Ag and 35.56-39.38 wt.% Te, with its calculated chemical formula as $Ag_{1.89-2.0}Te_{0.95-1.05}$.

Tellurobismuthite is less abundant than petzite and hessite, and it was observed as lath-shaped crystals that overprinted the hessite (Figure 2C). It has 50.55-50.36 wt.% Bi and 46.41-46.79 wt.% Te. Its chemical formula can be expressed as $Bi_{1.94-2.01}Te_{2.92-2.95}$.

Altaite is grey-white and less abundant than Au-Ag tellurides. It occurs commonly along the edge of or as inclusions in pyrite and chalcopyrite and is also closely associated with pyrrhotite and hessite (Figure 2D). Altaite contains 58.25 to 59.94 wt.% Pb, 36.56 to 37.26 wt.% Te (n = 5). The calculated general formula of altaite is $Pb_{0.91-1.19}Te_{0.75-0.95}$.

Melonite is the only Ni-telluride mineral detected in the A2 gold deposit. It is observed as inclusion and associated with hessite in chalcopyrite (Figure 2D). It contains 17.93 to 18.41 wt.% Ni, 81.40 to 82.37 wt.% Te, and a trace amount of Ag (0.19 wt.%), Bi (0.15 wt.%), and Sb (0.50 wt.%) on average (n = 3).

The general formula of melonite is $Ni_{0.93-0.97}Te_{1.95-1.99}$.

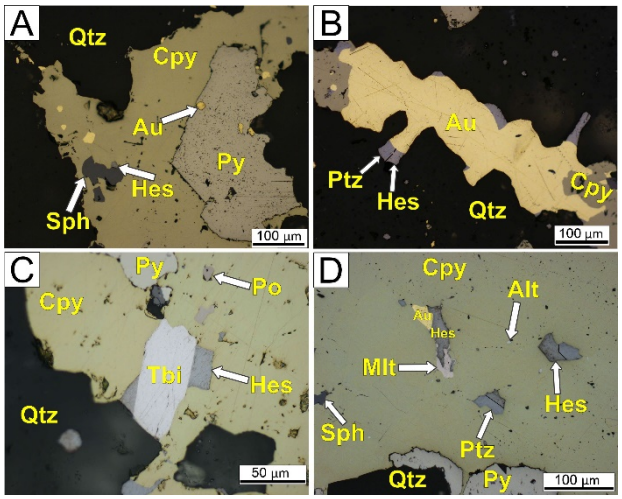

Figure 2. Representative gold-telluride mineralization of the A2 and New A2 gold deposits. Py-pyrite, Cpy-Chalcopyrite, Po- Pyrrhotite, Sph- Sphalerite, Au- Native gold, Hes- Hessite, Ptz- Petzite, Mlt- Melonite, Alt- Altaite, Tbi- Tellurobismuthite, Qtz- Quartz.

4.2 Carbon, oxygen, and sulphur isotopic compositions

The carbon and oxygen isotopic compositions of five calcite samples from the quartz-carbonate veins of the A2 and New A2 deposits, together with the Zee Phyu Kone Au-Cu-(Pb-Zn) skarn prospect (Thu et al. 2022), and local gold prospects around these deposits (unpublished data), are illustrated in Figure 3. The $\delta^{13}C_{PDB}$ values of calcite grains from the quartz-carbonate veins of the A2 and New A2 deposits range from -4.5 to 2.6‰, with $\delta^{18}O_{PDB}$ values of -17.2‰ to -12.3‰, and calculated $\delta^{18}O_{SMOW}$ values are in the range of 13.1‰ to 18.2‰.

The sulphur isotope compositions of six pyrite, six chalcopyrite, and three sphalerite samples from the A2 and New A2 deposits are illustrated in Figure 4. The auriferous $\delta^{34}S$ values of pyrite range from 2.1 to 3.4‰, chalcopyrite from 2.1 to 2.7‰, and those of sphalerite from 1.6 to 2.6‰, respectively.

5 Discussion

Hydrothermal calcite precipitation is generally controlled by fluid mixing, CO_2 degassing, and fluid-rock interactions (Zheng and Hoefs 1993). In the $\delta^{13}C_{PDB}$ vs. $\delta^{18}O_{SMOW}$ diagram, one wall rock sample from this gold district falls into the meta-carbonate field, and all of the hydrothermal calcite shows a depletion trend, which is evidence of the fluid-rock interaction (e.g., Bowman et al. 1985). All hydrothermal calcite samples from the Nwe Yon-Kwinthoneze area have ^{13}C values lower than seawater (0‰; Ohmoto and Goldhaber 1979), much higher than reduced carbon in sedimentary or metamorphic rocks (-25‰; Hoefs 2015), and close to magmatic fluids and/or mantle CO_2 (-7 to -2‰; Deines and Gold 1973). All of the samples fall into the field between within or close to the metasedimentary carbonate field to the meteoric water field in the late ore-forming stage (Figure 3), which is distinct from marine carbonate and organic matter, indicating that the carbon in the calcite perhaps was related to deep-seated magma or a mixed crustal source with limited contribution from the host rocks. The ore-forming fluids most probably experienced the involvement of meteoric water in the late stage. So, the primary source of carbon for the Nwe Yon-Kwinthoneze gold district was magmatic-hydrothermal.

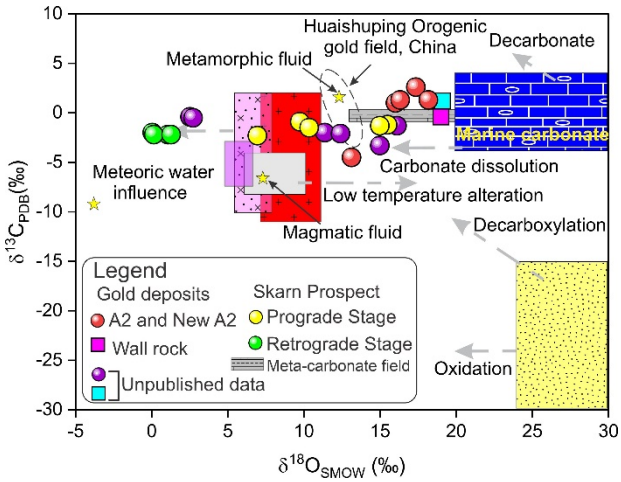

Figure 3. Carbon and oxygen isotopic compositions of calcite from the Nwe Yon-Kwinthoneze gold district comparison with the most known rock types (mineralising fluid and Huaishuping orogenic gold field are adapted from Wang et al. 2021).

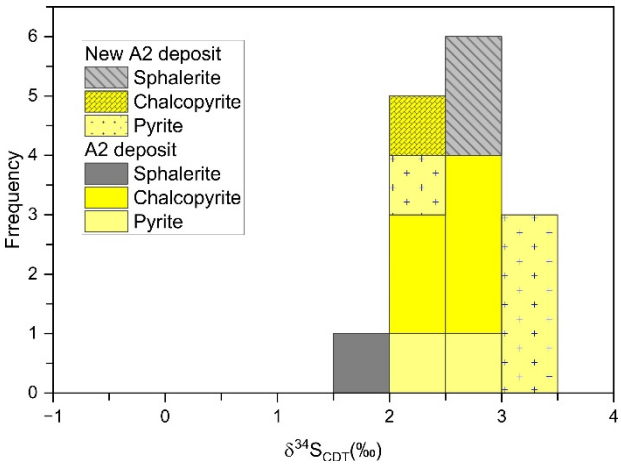

Figure 4. Sulphur isotope of the sulphides from the A2 and New A2 gold deposits.

The $\delta^{34}S$ values of sulphides from the A2 and New A2 deposits range from 1.6‰ to 3.4‰ (mean = 2.5; n= 15), which is consistent with many magmatic deposits with $\delta^{34}S$ values of -3‰ to +3‰ (Hoefs 2015). Furthermore, the uniformity of $\delta^{34}S$ values of sulphides indicates that the sulphur sources may be the same and are of the homogeneous magmatic sulphur source (Ohmoto and Goldhaber 1979).

Many telluride-rich gold deposits are associated with alkaline igneous rocks (e.g., Ciobanu et al. 2010) and tellurium is transported preferentially in the gaseous phase in magmatic fluids (Cooke &

McPhail 2001). Based on previous geochronological data of ore-hosting metamorphic rocks (23–20 Ma, Lamont et al. 2021) and the timing of magmatic intrusion (16.8±0.5 Ma, Gardiner et al. 2016), the gold-telluride mineralization of the A2 and New A2 deposits is thought to have resulted from the Kabaing granite intrusion. The analyses of S, C, and O isotopic data also showed that the ore-forming fluids mainly derived from the magmatic fluids and later mixed with meteoric water during the ore-forming process. Therefore, based on mineral assemblages, and C-O-S isotopic data, the A2 and New A2 deposits of the Nwe Yon-Kwinthoneze gold district can be classified as intrusion-related gold deposits. Moreover, metal zonation and a temporal and/or spatial relationship with I-type granite (Kabaing granite) with evidence of hydrothermal fluid generation (Zee Phyu Kone Au-Cu-(Pb-Zn) skarn alteration), which is typical of the intrusion-related gold deposits (Sillitoe and Thompson 1998; Lang et al. 2000), could be found (Figure 1).

6 Conclusions

(1) Orebodies of the A2 and New A2 deposits are primarily hosted in marble, gneiss, and contact between these two rocks. The principal ore minerals are pyrite, chalcopyrite, sphalerite, pyrrhotite, native gold, and telluride assemblages: petzite, hessite, tellurobismuthite, altaite, melonite, coloradoite, and mettagamite.
(2) C-O isotopic compositions suggest that the ore-forming fluids were most likely derived from magma with limited contributions from the host rocks and later mixed with the meteoric water into the ore-forming process. The sulphur isotopic compositions of the A2 and New A2 are homogeneous and indicative of a magmatic source of sulphur.
(3) Based on the mineral assemblages, and C-O-S isotopic data, the A2 and New A2 deposits of the Nwe Yon-Kwinthoneze gold district can be classified as intrusion-related gold deposits.

Acknowledgments

This study was financially supported by UNESCO-AGH and the Newmont Mining Corporation Fund of the Society of Economics Geologists.

References

Baker T (2002) Emplacement depth and carbon dioxide-rich fluid inclusions in intrusion-related gold deposits. Econ Geol 97:1111-1117.

Bowman JR, O'Neil JR, & Essene EJ (1985) Contact skarn formation at Elkhorn, Montana; II, Origin and evolution of COH skarn fluids. American Journal of Science, 285:621-660.

Ciobanu CL, Birch WD, Cook NJ, Pring A & Grundler PV (2010) Petrogenetic significance of Au–Bi–Te–S associations: the example of Maldon, Central Victorian gold province, Australia. Lithos, 116:1-17.

Cooke DR & McPhail DC (2001) Epithermal Au-Ag-Te mineralization, Acupan, Baguio district, Philippines: numerical simulations of mineral deposition. Econ Geol, 96:109-131.

Deines P & Gold DP (1973) The isotopic composition of carbonatite and kimberlite carbonates and their bearing on the isotopic composition of deep-seated carbon. Geochimica et Cosmochimica Acta, 37:1709-1733.

Gardiner NJ, Robb LJ, Morley CK, Searle MP, Cawood PA, Whitehouse MJ, Kirkland CL, Roberts NM., Myint TA (2016) The tectonic and metallogenic framework of Myanmar: a tethyan mineral system. Ore Geol Rev 79, 26–45.

Hart CJR & Goldfarb RJ (2005) Distinguishing intrusion-related from orogenic gold systems. In New Zealand Minerals Conference Proceedings (Vol. 2005, pp. 125-133).

Hoefs J (2015) Stable Isotope Geochemistry, (Vol. 2015, pp. 1–389). Switzerland.

Lamont TN, Searle MP, Hacker BR, Htun K, Htun KM, Morley CK, White RW (2021) Late Eocene-Oligocene granulite facies garnet-sillimanite migmatites from the Mogok Metamorphic belt, Myanmar, and implications for timing of slip along the Sagaing Fault. Lithos, 386, 106027.

Lang JR, Baker T, HART CJ & Mortensen JK (2000) An exploration model for intrusion-related gold systems. SEG Discovery, 40:1-15.

Mitchell AHG (2017) Geological Belts, Plate Boundaries and Mineral Deposits in Myanmar. Elsevier.

Myint TA, Than TN, Min A (2014) Precious and Base Metal Mineralization in Kwinthonze-Nweyon area, Singu, and Thabeikkyin Townships, Mandalay Region, Myanmar. Proc. Sundal. Resources. Indonesia.

Myint, AZ, Wagner T & Zaw K (2022) Telluride-bearing Au-Ag mineralization in the Singu-Tabeikkyin gold District, Mogok metamorphic Belt, Myanmar: New constraints on an intermediate-sulfidation epizonal orogenic ore system. Journal of Asian Earth Sciences, 227, 105120.

Ohmoto H, Rye RO (1979) Isotopes of sulphur and carbon. In: Barnes HL (ed) Geochemistry of hydrothermal ore deposits. Wiley, New York, pp 509–567.

Searle MP, Noble SR, Cottle JM, Mitchell AHG, Hlaing T, Horstwood MSA (2007) Tectonic evolution of the Mogok metamorphic belt, Burma (Myanmar) constrained by U-Th-Pb dating of metamorphic and magmatic rocks. Tectonics 26, TC3014.

Sillitoe RH, & Thompson JF (1998) Intrusion–Related Vein Gold Deposits: Types, Tectono-Magmatic Settings and Difficulties of Distinction from Orogenic Gold Deposits. Resource Geology, 48:237-250.

Swe YM, Aye CC & Zaw K (2017) Chapter 25 Gold Deposits of Myanmar. Geological Society, London, Memoirs, 48: 557-572.

Thompson JF & Newberry RJ (2000) Gold deposits related to reduced granitic intrusions. Econ Geol, v. 13, p. 377–400.

Thu AM, Piestrzyński A, Foltyn K, Kozub-Budzyń G (2022) Formation of the Zee Phyu Kone Au-Cu (Pb-Zn) skarn mineralization in the Mogok Metamorphic Belt, Central Myanmar: Insights from mineral chemistry and C-O-S isotopes. In: Christie AB (ed.) Proceedings of the 16th SGA Biennial Meeting, 28-31 March 2022, 1:384-387.

Wang C, Deng J, Bagas L, He X, Zhang J (2021). Origin and classification of the Late Triassic Huaishuping gold deposit in the eastern part of the Qinling-Dabie Orogen, China: implications for gold metallogeny. Miner Depos, 56, 725-742.

Zaw K (2017) Overview of mineralization styles and tectonic metallogenic setting in Myanmar. In Barber AJ, Zaw K and Crow MJ (eds.) Myanmar: Geology, resources, and tectonics, Geological Society Memoirs 48, London.

Zheng YF & Hoefs J (1993) Carbon and oxygen isotopic covariations in hydrothermal calcites: Theoretical modelling on mixing processes and application to Pb-Zn deposits in the Harz Mountains, Germany. Miner Depos, 28, 79-89.

Spatial distribution and structural control on gold mineralisation in the Barberton Greenstone Belt (South Africa, Eswatini)

Laurine Travers[1,2], Jérémie Lehmann[2], Alain Chauvet[1]
[1] *Géosciences Montpellier, University of Montpellier, CNRS, France*
[2] *Department of Geology, University of Johannesburg, South Africa*

Abstract. The Barberton Greenstone Belt (BGB) contains over 350 gold occurrences and an estimated production of 342 tons, mainly from Fairview, New Consort, Sheba and Agnes mines. Many studies target these active mines to understand gold mineralisation. This study focuses on the distribution and structural control of hydrothermal veins, including in old mining areas and low-grade gold occurrences. The gold-bearing event is studied using spatial statistical analysis combined with structural field geology and mineralogical analysis. The hydrothermal/gold occurrences are distributed in several clusters. Two main tectonic events are involved in the formation of hydrothermal veins. A main deformation event related to large-scale folding and thrusting controls emplacement of gold-bearing veins during a single or pulsed NW-SE shortening in the northern BGB, and during an E-W shortening in the southern BGB. A late deformation event, produced by NE-SW shortening in the southern BGB is also related to late hydrothermal quartz veins. Quartz-carbonate veins are found in the northern mineralised system, whereas quartz-tourmaline-feldspars-carbonate +/- sulfides veins are present mainly in the southern BGB. The mineralised event in the BGB is structurally controlled by the main NW-SE to E-W shortening whereas additional quartz systems, not mineralised, seem to be controlled by an enigmatic NE-SW shortening.

1 Introduction

The Barberton Greenstone Belt in South Africa and Eswatini is a typical Archean belt with over 350 gold occurrences and has an estimated production of 342 tons of gold (Anhaeusser 2019), mainly extracted from the Fairview, Sheba, New Consort and Agnes mines. These mines are located in the northern BGB, mainly in a complex fold and thrust zone. Nevertheless, hundreds of lower grade, poorly studied, gold occurrences occur elsewhere within the belt. These occurrences may represent significant information for the formation mode of the gold-bearing event and its spatial distribution at the belt scale.

Figure 1. Location of the Barberton Greenstone Belt and geological map (modified from the metallogenic map Council for Geoscience 2000) with gold occurrences and extracted Kernel Density map (blue is high density, white is low density).

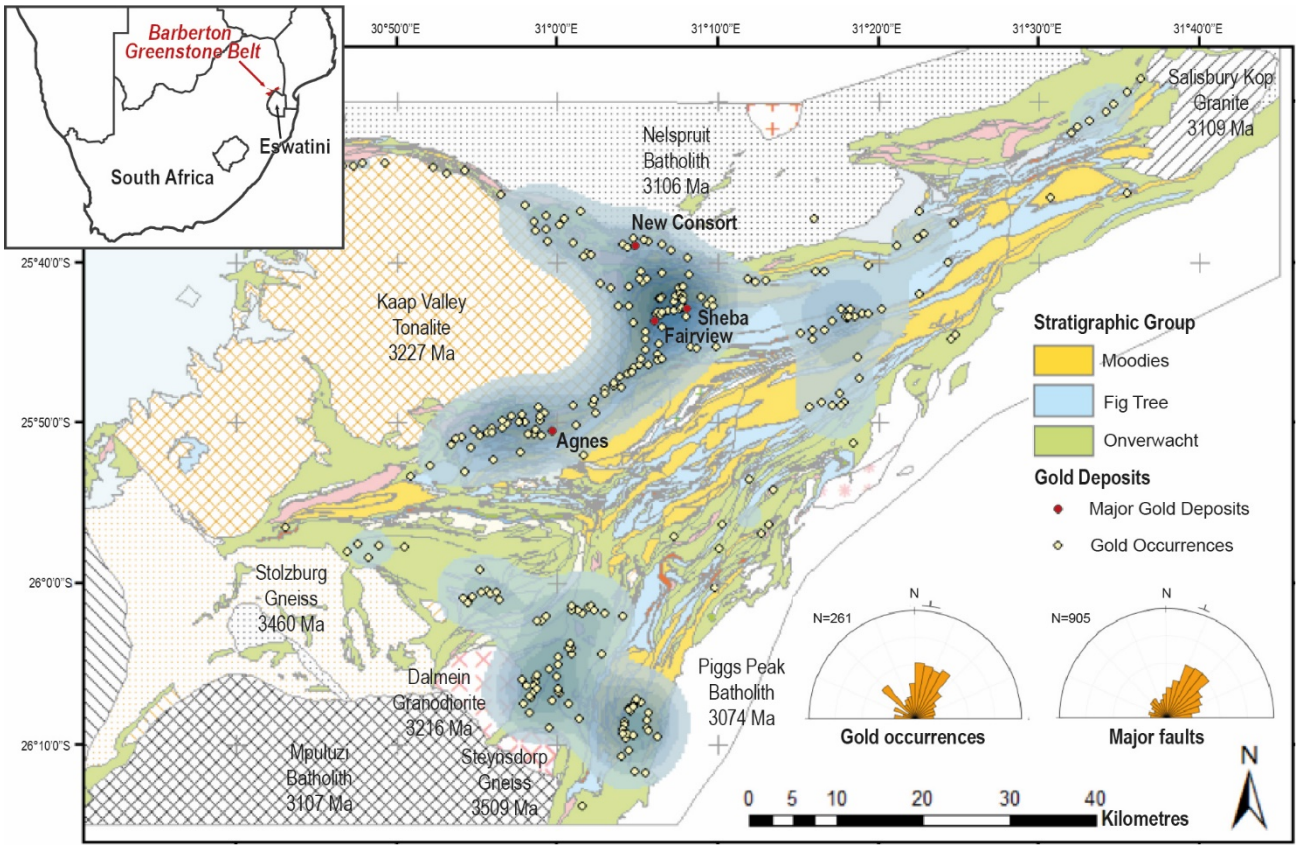

This study aims to establish the structural framework of the multiple gold occurrences within the Barberton Greenstone Belt. The objective is to understand the gold forming event and its potential link with regional deformation and magmatism. A detailed structural, microstructural and mineralogical analysis leads to propose a model for the tectonic-hydrothermal evolution of the study area. This model suggests that gold-bearing quartz veins formed during the shortening of the entire belt and perhaps involves the role of some neighbouring granites. The structural characterisation of the Archean gold event in the Barberton Greenstone Belt allows for a better understanding of the formation of Archean gold deposits and of Archean geodynamics.

2 Geological setting

The Barberton Greenstone Belt (BGB), in South Africa and Eswatini, is located in the eastern part of the Kaapvaal Craton. It is composed of volcano-sedimentary units surrounded by variably gneissic TTG rocks (Tonalite-Trondhjemite-Granodiorite), in turn intruded by granite batholiths. The stratigraphic succession of the BGB shows three main units named, from bottom to top: Onverwacht, Fig Tree and Moodies groups (Lowe and Byerly 2007, Figure 1). The Onverwacht Group (3.55 to 3.29 Ga) is mainly a mafic to ultramafic meta-volcano-sedimentary series. The Fig Tree Group (3.26 to 3.22 Ga) is formed by calc-alkaline lavas and detrital rocks. Lastly, the Moodies Group (3.22 to 3.21 Ga) represents the upper detrital series. The architecture of the BGB seems to be the result of several contraction events mainly oriented NW-SE (De Ronde and de Wit 1994).

Over the 350 gold occurrences in the BGB (Barberton 1:100,000 metallogenic map, Council for Geoscience, 2000), the most studied and best-known ones are the active Fairview, Sheba and New Consort mines, which are all located in the northern BGB (Figure 1). The numerous other gold occurrences are mainly former mines and mining exploration areas which few have been the subject of in-depth studies, which will be the focus of this study.

Overall, there are two opposing theories on the interpretation of the Barberton gold mineralisation, it may have formed during: i) a late phase of regional extension (Otto et al. 2007; Dziggel et al. 2010), which postdates the tectonic and thermal stabilisation of the belt (Dirks et al. 2013), or ii) a late NW-SE shortening episode (Gloyn-Jones and Kisters 2019; Jones and Kisters 2022; Cerdas et al. 2022).

Several ages for the mineralisation have been published. At New Consort, the mineralisation has been dated at ca. 3027 ± 7 Ma (Dziggel et al. 2010), which is consistent with the age between 3009 ± 16 Ma and 3017 ± 18 Ma obtained at Golden Quarry (Dirks et al. 2013), but younger than the 3084 ± 18 Ma obtained at Fairview (de Ronde et al. 1991). Thus, the ages of the gold mineralisation appear to be spread over a long period of time (i.e., 100 Myr), suggesting that several mineralising episodes of different nature may co-exist, and/or that the dating of the mineralisation is not well constrained.

3 Distribution of the gold occurrences

The predictive spatial analysis was carried out by digitisation of the Barberton 1:100,000 metallogenic map (Council for Geoscience, 2000) and all the gold occurrences and their characteristics (i.e., orientation, size, morphology, mining status, name) were imported and processed in a GIS platform (ArcGIS Pro).

Several methods of analysis were performed to investigate the distribution of gold occurrences according to their host stratigraphy, regional structures, density and gold grade. The weight of evidence analysis has shown that stratigraphy was not the major factor controlling the spatial occurrence of gold. The Kernel density map of the occurrences shows that the occurrences are distributed within four main clusters: Barberton, Steynsdorp, Malolotja, and Barbrook areas (Figure 1). The Inverse Distance Weighting interpolation map shows that the deposits have a higher tonnage along the northern flank of the belt. Overall, the angular difference between the trend of occurrences as extracted from the 1:100,000 scale map and the strike of the nearest fault is rather small (55% of the gold occurrences have an angular difference smaller than 20°), suggesting that the BGB gold occurrences may be structurally controlled. This hypothesis has been tested through detailed field structural geological analysis as summarised below.

4 Structural control of the hydrothermal and gold mineralisation events

4.1 Regional deformation

In the field, we observe three schistosities which were defined according to their mutual overprinting relationships Se (early), Sm (main) and Sl (late). The schistosity Se is defined by aligned small micas and talc sheets, and is steep and E-W to NW-SE striking. It is often observed folded by Fm folds with N-S striking axial planes in the southern BGB and NE-SW-striking ones in the northern BGB. The schistosity Sm is axial planar to Fm folds. Sm is very prominent throughout the entire belt. Petrographic observations reveal that Sm is marked by the alignment of small micas sheets. In a few areas, especially in the south, Sm is commonly folded into Fl folds with steep NW-SE axial planes. The last schistosity Sl is axial planar to Fl fold and is mostly observed in the southern BGB. Sl is defined in microscopy by the alignment of micas (Figure 2a, b and c).

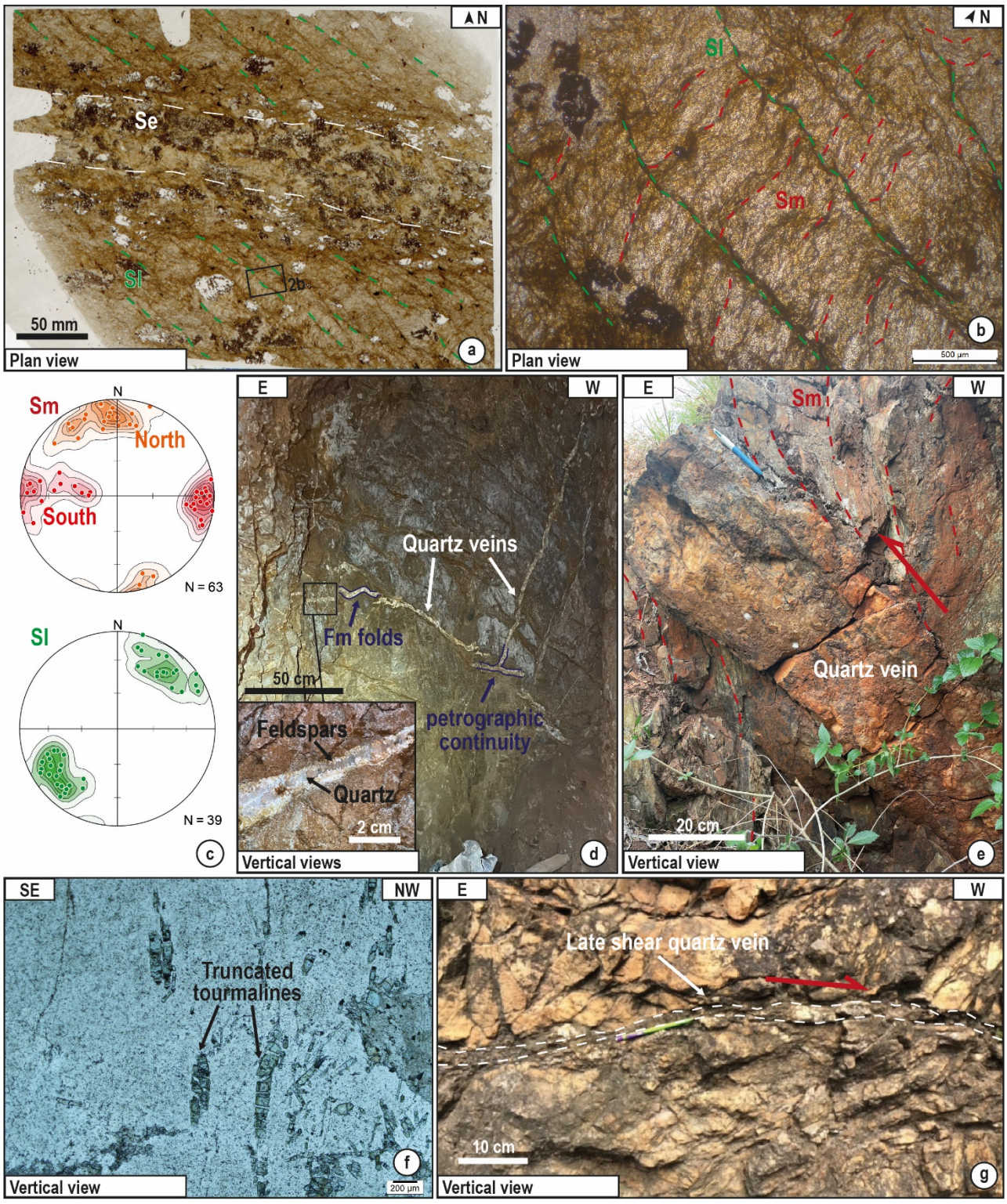

Figure 2. a Thin section scan of a sample showing the overprinting relations between Se and Sl. **b** Close up of photo a, with Sm deformed by Sl. **c** Equal-area lower hemisphere projections of Sm and Sl as pole to planes throughout the belt. **d** Field photo of synchronous shallow-dipping folded and steep quartz veins. Inset is a close up view on the quartz-feldspar vein. **e** Photo of a quartz vein located in a shear zone with a reverse motion as seen by the drag folds of the schistosity Sm. The quartz vein is internally brecciated. **f** Photomicrograph of vertical truncated tourmalines in a horizontal quartz-tourmaline vein. **g** Field photo of a late shear horizontal quartz vein.

4.2 Hydrothermal vein system

The mineralised system is mainly expressed by shallow-dipping and steep to vertical (Figure 2d and e) mm- to m-thick quartz veins cutting Se, and in places Sm. These two vein sets are in petrographic continuity; hence they are interpreted to form synchronously. Horizontal veins exhibit, in several places, vertical comb quartz or quartz fibres, which can be interpreted as formed by mode I opening as tension gashes resulting from horizontal shortening. In the southern BGB, the quartz veins contain

vertical tourmaline grains, which are truncated by horizontal fractures filled with vein quartz (Figure 2f), also suggesting syn-tectonic mineralisation during horizontal shortening and vertical stretching. These horizontal veins are commonly folded into open to tight buckles, with axial plane parallel to schistosity Sm. Some sub-vertical veins show reverse kinematics particularly in the Steynsdorp and Barberton areas (Figure 2e). This reverse kinematics is consistent with a Dm shortening in thrust or back-thrust (i.e., verging towards the interior of the belt) positions.

The sum of these observations demonstrates that the mineralisation event is syn- to late-Dm. This interpretation is supported by pene-contemporaneous, variably Dm-folded, sub-horizontal tension gashes and sub-vertical veins exhibiting reverse motion. The gold-bearing quartz veins are structurally controlled by the main shortening of the entire belt, which is E-W in the south and NW-SE to N-S in the north.

In several places, crosscutting quartz veins are shear sub-horizontal veins (Figure 2g) or en-echelon quartz veins. This late hydrothermal event seems to have formed by a NE-SW shortening, compatible with Dl. These veins do not appear to be mineralised.

5 Mineralogy

The mineralised veins are divided into two types on the basis of contrasting mineralogy. The southern vein system is composed of quartz with a variable amount of tourmaline, feldspar (albite, K-feldspar and plagioclase, Figure 2d and f) and carbonate with alteration halo composed of white mica, albite and tourmaline. Few sulfides are present – mostly pyrite and minor arsenopyrite. The northern vein system is composed of quartz and carbonate veins with a higher amount of sulfides (mostly pyrites). The alteration halo on the edges of the veins is formed by chlorite, micas, and sulfides.

The presence of tourmaline and feldspars in the southern vein system questions the origin of the mineralised fluid, i.e., magmatic-hydrothermal vs orogenic. However, as the potential impact of magmatism on the mineralised event in the southern part of the BGB is not established, this hypothesis remains presently uncertain

6 Conclusion

The Barberton Greenstone Belt contains numerous gold occurrences that are heterogeneously distributed throughout the belt. Some areas show higher concentration of gold occurrences, particularly around major structures such as folds and thrust zones. The hydrothermal system is characterised by complex quartz vein networks controlled by two shortening directions. The origin of the NE-SW shortening that formed the late veins is enigmatic. Although the mineralisation seems to be the result of the same structural control, mineralogical differences in the hydrothermal system between the south and the north have been identified and remain to be further explored.

Acknowledgements

This work benefited greatly from the scientific and financial support of IRP BuCOMO team (https://bucomo.fr/). Chistoph Heubeck, Andrea Els from Barberton Adventure, Astrid Christianson and Teddy Dlamini are acknowledged for their assistance in the field.

References

Anhaeusser CR (2019) The geology and tectonic evolution of the northwest part of the Barberton Greenstone Belt, South Africa: A review. South African Journal of Geology 122:421–454. https://doi.org/10.25131/sajg.122.0033

Cerda LP, Jones C, Kisters A (2022) The effects of fault-zone architecture, wall-rock competence and fluid pressure variations on hydrothermal veining and gold mineralization along the Sheba Fault, Barberton Greenstone Belt, South Africa. Journal of African Earth Sciences 192:104554. https://doi.org/10.1016/j.jafrearsci.2022.104554

de Ronde CEJ, de Wit MJ (1994) Tectonic history of the Barberton greenstone belt, South Africa: 490 million years of Archean crustal evolution. Tectonics 13:983–1005. https://doi.org/10.1029/94TC00353

de Ronde CEJ, Kamo S, Davis DW, et al (1991) Field, geochemical and U-Pb isotopic constraints from hypabyssal felsic intrusions within the Barberton greenstone belt, South Africa: Implications for tectonics and the timing of gold mineralization. Precambrian Research 49:261–280. https://doi.org/10.1016/0301-9268(91)90037-B

Dirks PHGM, Charlesworth EG, Munyai MR, Wormald R (2013) Stress analysis, post-orogenic extension and 3.01Ga gold mineralisation in the Barberton Greenstone Belt, South Africa. Precambrian Research 226:157–184. https://doi.org/10.1016/j.precamres.2012.12.007

Dziggel A, Poujol M, Otto A, et al (2010) New U–Pb and 40Ar/39Ar ages from the northern margin of the Barberton greenstone belt, South Africa: Implications for the formation of Mesoarchaean gold deposits. Precambrian Research 179:206–220. https://doi.org/10.1016/j.precamres.2010.03.006

Gloyn-Jones J, Kisters A (2019) Ore-shoot formation in the Main Reef Complex of the Fairview Mine—multiphase gold mineralization during regional folding, Barberton Greenstone Belt, South Africa. Miner Deposita 54:1157–1178. https://doi.org/10.1007/s00126-019-00865-9

Jones C, Kisters A (2022) Regional and local controls of hydrothermal fluid flow and gold mineralization in the Sheba and Fairview mines, Barberton Greenstone Belt, South Africa. Ore Geology Reviews 144:104805. https://doi.org/10.1016/j.oregeorev.2022.104805

Lowe DR, Byerly GR (2007) Chapter 5.3 An Overview of the Geology of the Barberton Greenstone Belt and Vicinity: Implications for Early Crustal Development. In: Developments in Precambrian Geology. Elsevier, pp 481–526

Otto A, Dziggel A, Kisters AFM, Meyer FM (2007) The New Consort Gold Mine, Barberton greenstone belt, South Africa: orogenic gold mineralization in a condensed metamorphic profile. Miner Deposita 42:715–735. https://doi.org/10.1007/s00126-007-0135-5

Tracing gold origin: A neural network approach to trace element geochemistry

Angel Verbel[1,2], Maria Emilia Schutesky[1], Daniel Gregory[2]
[1]*Universidade de Brasilia*
[2]*University of Toronto*

Abstract. Gold grains have long been used as a vectoring tool for ore deposits, and in recent years, the combination of their geochemistry with conventional machine learning techniques has yielded encouraging results for determining their original ore deposit. Using a personalized neural network, we were able to make better predictions on the origin of individual gold grains while reducing the number of steps required in the classification process. These advances can be used as an exploration tool to constrain the possible origin of gold deposits along with the geological criteria of the target area.

1 Introduction

Despite the fact that techniques for integrating artificial intelligence (AI) with data science have existed since the late 1950s (Rosenblatt 1958), their use in geosciences and geochemistry has mostly occurred in the last 20 years (Farnham et al. 2002; Taylor et al. 2010; Ghannadpour et al. 2013; Cone et al. 2020; Liu et al. 2021; Liu and Beaudoin 2021). Given that geosciences applications of AI are still a relatively unexplored area, it opens up opportunities for innovation and the use of AI to comprehend intricate natural processes.

Gold geochemistry is often employed primarily as an exploratory technique to discover ore deposits. In addition to its morphology, which is connected to transportation in the basin, its chemistry is defined by physicochemical processes of formation as well as the geological framework of the deposit (McClenaghan 2005; Chapman et al. 2009; McClenaghan and Cabri 2011; Moles and Chapman 2019). Furthermore, since the 1960s, the introduction of the electron probe micro analyzer (EPMA) has made it possible to determine the chemical composition of natural gold from the diverse range of deposits that it is formed from with high degrees of precision (Rinaldi and Llovet 2015). Antweiler and Campbell (1977) revealed a connection between the temperature at which certain deposits originate and the amounts of Ag, Bi, Pb, and Cu in gold. Later, Morrison et al. (1991) determined the variations in gold fineness from different deposits. Then, Huston et al. (1992) evaluated the variations of trace elements and fineness of VMS deposits in Australia, finding that the content of trace elements in electrum depends on the complexity in the ore fluid. Later, Pochon et al. (2021) established that, given the presence of Ag, Cu, and Hg, it is feasible to distinguish legal from illegal gold that is extracted using Hg in French Guiana. Finally, Liu et al. (2021) and Liu and Beaudoin (2021) identified the chemical signature of gold in each style of deposit, with a rate of successful prediction ranging from 50 up to 97%, depending on the deposit type. They did this by using trace element geochemistry of natural gold grains from a wide variety of deposits around the world in combination with a machine learning algorithm.

2 Materials and methods

A total of 674 analyses of gold by EPMA were used to develop the model, these analyses were performed by Liu et al. (2021) and Liu and Beaudoin (2021), as well as 460 LA-ICP-MS for trace element analysis. These data correspond to 5 deposit types in a wide range of geological settings hosted by rocks varying in composition from mafic to sedimentary and ages varying from Archean to Neogene.

2.1 Data Processing

Pre-processing of the geochemical data was preformed prior to cluster analysis (Templ et al. 2008). The three datasets were pre-processed by: (1) geochemical feature selection; (2) substitution of censored (below the limit of detections) data; (3) screening missing values; (4) data transformation, to a more symmetric distribution, preserving the modes and removing skewness; and (5) standardization. A parameter was excluded from the database if it could be related through a different parameter (e.g., Fe reported as pct and ppm in this case the analysis with the higher resolution was selected) or >60% of the parameter are censored analysis with the higher resolution will be selected) or >60% of the parameter are ruled out. To process the data the package zCompositions was used in R 4.2.2 (Palarea-Albaladejo and Martín-Fernández 2015). Then the data was replaced and standardized to avoid biasing the model due to an overweight of high concentration elements like Ag. Z-scores were generated for the data set as a standardization procedure, using the following equation where z is the z-score, x is the concentration, μ is the population mean and σ something missing here is the standard deviation of the population (Guilloux et al. 2011):

$$z = \frac{x - \mu}{\sigma}$$

2.2 Neural network

The architecture of the neural network consists of a single hidden activation layer of 35 neurons, each of which was activated depending on the Rectified-Linear-Unit (ReLU) activation function to avoid gradient dispersion. The supervised algorithm architecture was completed with the numpy package in Python 3.9.13.

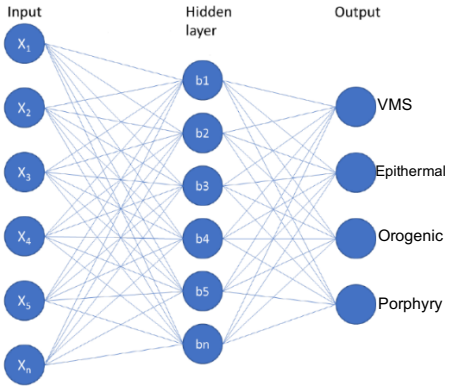

Figure 1. Sketch diagram of the architecture of the neural network.

3. Results

The first neural network used Au, Ag, Co, Cu, Fe, S, and Hg values in ppm (Figure 2A) as an input layer (normalized raw data); this data was processed with the artificial neural network, generating a total of 495 weights and biases. These results are the heart of the prediction model, since the model is generated under random initial conditions, the data presented provides reproducibility of the results when new data is presented.

Maintaining the same architecture for both models, the results were slightly improved when the LA-ICP-MS data was evaluated in all the deposits that have data with more resolution. For this analysis, the elements used were Ag, Bi, Cd, Cu, Hg, Pb, Pd, S, Sb, and Tl as shown in Figure 2B. In this case Fe was left out given the preliminary results that show that it brought noisy results, decreasing the accuracy for all the ore deposits.

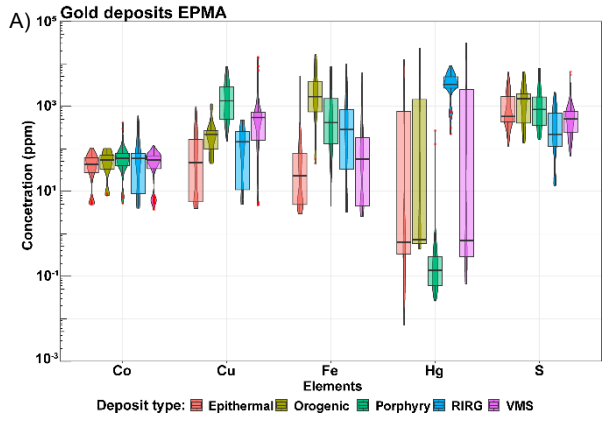

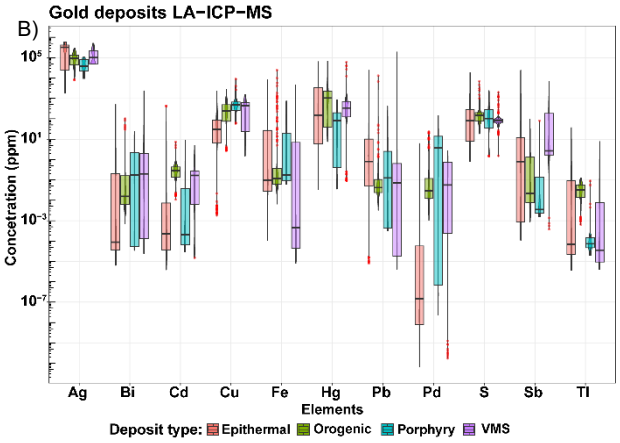

Figure 2. Multi-element box (25th & 75th percentile) and whisker (5th & 95th percentile) for selected elements. A) EPMA and B) LA-ICP-MS.

Testing the model with blind data (70 gold analyses randomly selected) for EPMA as well as the LA-ICP-MS model, results in an accuracy of well-classified deposits using the EPMA model of 81% for orogenic deposits, 75% for RIRG deposits, 55% for porphyry deposits, 68% for VMS deposits, and 60% for epithermal deposits (Figure 3A). In contrast, the accuracy of well classified deposits using the LA-ICP-MS model is 85% for orogenic deposits, 62% for porphyry deposits, 72% for VMS deposits, and 64% for epithermal deposits (Figure 3B).

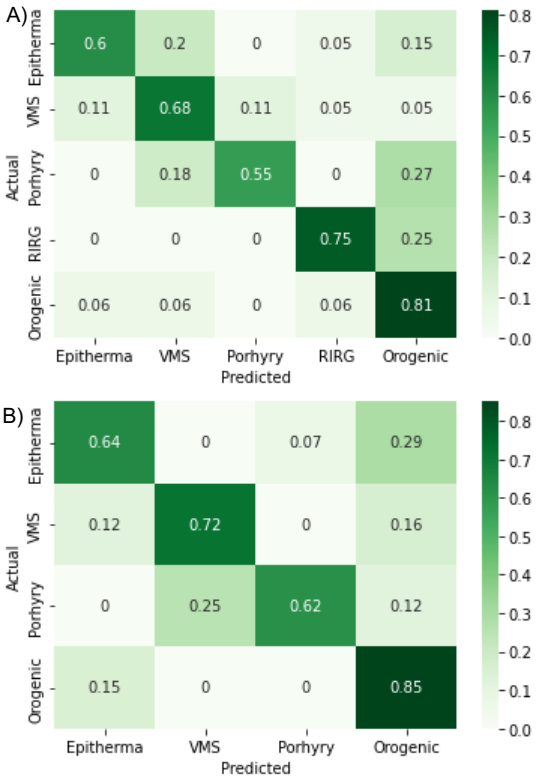

Figure 3. Confusion matrix of the results of a neural network algorithm for classification applied on blind data with A) EPMA and B) LA-ICP-MS.

4. Discussion

Many attempts have been made to find the relationship between the trace element composition of gold and deposit types (Townley et al. 2003; Chapman et al. 2009; Moles and Chapman 2019; Liu et al. 2021). Generally, the resulting classification tends to be shown as a discrimination diagram (usually ternary diagrams) with fields of large overlaps that do not make a clear classification of the data. In addition, there are ore deposit types that share similar fluid compositions and, therefore, similar trace element content in gold, like orogenic and RIRG deposits (Hart and Goldfarb 2005). For these reasons, the use of a nonlinear machine learning algorithm was selected as an approach to unveil the intricate geochemical signature of gold.

The work of Liu and Beaudoin (2021) and Liu et al. (2021) provided a first inside on the use of machine learning algorithms to understand the chemical signatures of gold as well as the necessary database for a baseline for further applications. In addition to the use of a different machine learning algorithm, our approach used the raw data as a starting point, which simplified the processing of the data, along with a larger blind dataset (i.e., over 3 times larger) than the one used by Liu and Beaudoin (2021), which led to a smaller accuracy compared with the one presented by them but ensured that the result obtained is not affected by a sample bias.

Despite the differences in variability between EPMA and LA-ICP-MS, the results of both neural networks can be taken as similar except for porphyry deposits, which have shown a notable increase in precision. It is believed that this improvement is caused by the addition of new elements, (e.g., Bi, Pb, Pd, Sb) that contribute to the differentiation of these sorts of deposits without affecting them much.

These results could be improved by pre-processing the data with a matrix factorization technique to minimize data dimensionality, but at the expense of increased processing time.

5. Conclusions

The use of artificial neural networks to evaluate chemical signatures of natural gold appears to be a powerful technique to unveil this complicated nonlinear problem even with overlaps presented in the trace element concentrations of some deposits.

Chemical zoning in gold could lead to a misclassification of single grains but using the right sample size can ensure the best classification possible for a population of gold grains. The use of this model in gold grains of unknown origin (placer deposits) could be used as an exploration technique to utilize the correct geologic model to find the original source of gold.

Acknowledgements

This study was financed in part by the Coordenação de Aperfeiçoamento de Pessoal de Nível Superior - Brasil (CAPES) - Finance Code 001 and the Conselho Nacional de Desenvolvimento Científico e Tecnológico (CNPq) by the grant (140810/2021-8).

References

Antweiler JC, Campbell WL (1977) Application of Gold Compositional Analyses to Mineral Exploration in the United States. In: Developments in Economic Geology. Elsevier, pp 17–29

Chapman RJ, Leake RC, Bond DPG, et al (2009) Chemical and Mineralogical Signatures of Gold Formed in Oxidizing Chloride Hydrothermal Systems and their Significance within Populations of Placer Gold Grains Collected during Reconnaissance. Economic Geology 104:563–585. https://doi.org/10.2113/gsecongeo.104.4.563

Cone KA, Palin RM, Singha K (2020): Unsupervised machine learning with petrological database ApolloBasaltDB reveals complexity in lunar basalt major element oxide and mineral distribution patterns. Icarus 346:113787. https://doi.org/10.1016/j.icarus.2020.113787

Farnham IM, Singh AK, Stetzenbach KJ, Johannesson KH (2002): Treatment of nondetects in multivariate analysis of groundwater geochemistry data. Chemometrics and Intelligent Laboratory Systems 60:265–281. https://doi.org/10.1016/S0169-7439(01)00201-5

Ghannadpour S, Hezarkhani A, Farahbakhsh E (2013): An Investigation of Pb Geochemical Behavior Respect to Those of Fe and Zn Based on kMeans Clustering Method. 291-302 1:

Guilloux J-P, Seney M, Edgar N, Sibille E (2011): Integrated behavioral z-scoring increases the sensitivity and reliability of behavioral phenotyping in mice: Relevance to emotionality and sex. Journal of Neuroscience Methods 197:21–31. https://doi.org/10.1016/j.jneumeth.2011.01.019

Hart CJR, Goldfarb RJ (2005) Distinguishing intrusion-related from orogenic gold systems. pp 125–133

Huston DL, Bottrill RS, Creelman RA, et al (1992) Geologic and geochemical controls on the mineralogy and grain size of gold-bearing phases, eastern Australian volcanic-hosted massive sulfide deposits. Economic Geology 87:542–563. https://doi.org/10.2113/gsecongeo.87.3.542

Liu H, Beaudoin G (2021) Geochemical signatures in native gold derived from Au-bearing ore deposits. Ore Geology Reviews 132:104066. https://doi.org/10.1016/j.oregeorev.2021.104066

Liu H, Beaudoin G, Makvandi S, et al (2021) Multivariate statistical analysis of trace element compositions of native gold from orogenic gold deposits: Implication for mineral exploration. Ore Geology Reviews 131:104061. https://doi.org/10.1016/j.oregeorev.2021.104061

McClenaghan MB (2005) Indicator mineral methods in mineral exploration. GEEA 5:233–245. https://doi.org/10.1144/1467-7873/03-066

McClenaghan MB, Cabri LJ (2011) Review of gold and platinum group element (PGE) indicator minerals methods for surficial sediment sampling. GEEA 11:251–263. https://doi.org/10.1144/1467-7873/10-IM-026

Moles NR, Chapman RJ (2019) Integration of Detrital Gold Microchemistry, Heavy Mineral Distribution, and Sediment Geochemistry to Clarify Regional Metallogeny in Glaciated Terrains: Application in the Caledonides of Southeast Ireland. Economic Geology 114:207–232. https://doi.org/10.5382/econgeo.2019.4628

Morrison GW, Rose WJ, Jaireth S (1991) Geological and geochemical controls on the silver content (fineness) of gold in gold-silver deposits. Ore Geology Reviews 6:333–

364. https://doi.org/10.1016/0169-1368(91)90009-V
Palarea-Albaladejo J, Martín-Fernández JA (2015) zCompositions — R package for multivariate imputation of left-censored data under a compositional approach. Chemometrics and Intelligent Laboratory Systems 143:85–96. https://doi.org/10.1016/j.chemolab.2015.02.019
Pochon A, Desaulty A-M, Bailly L, Lach P (2021) Challenging the traceability of natural gold by combining geochemical methods: French Guiana example. Applied Geochemistry 129:104952. https://doi.org/10.1016/j.apgeochem.2021.104952
Rinaldi R, Llovet X (2015) Electron Probe Microanalysis: A Review of the Past, Present, and Future. Microsc Microanal 21:1053–1069. https://doi.org/10.1017/S1431927615000409
Rosenblatt F (1958) The perceptron: A probabilistic model for information storage and organization in the brain. Psychological Review 65:386–408. https://doi.org/10.1037/h0042519
Taylor GJ, Martel LMV, Karunatillake S, et al (2010) Mapping Mars geochemically. Geology 38:183–186. https://doi.org/10.1130/G30470.1
Templ M, Filzmoser P, Reimann C (2008) Cluster analysis applied to regional geochemical data: Problems and possibilities. Applied Geochemistry 23:2198–2213. https://doi.org/10.1016/j.apgeochem.2008.03.004
Townley BK, Hérail G, Maksaev V, et al (2003) Gold grain morphology and composition as an exploration tool: application to gold exploration in covered areas. GEEA 3:29–38. https://doi.org/10.1144/1467-787302-042

Early structural architecture controlling komatiite-hosted nickel sulphide and orogenic gold mineralisation at Beta-Hunt Au-Ni mine, Kambalda, WA

Lauri T. Virnes[1], Nicolas Thébaud[1], Laura Petrella[1], Helen B. Mcfarlane[2], Laure Martin[3], Denis Fourgerouse[4]
[1]*Centre for Exploration Targeting (CET), University of Western Australia*
[2]*Commonwealth Scientific and Industrial Research Organisation (CSIRO)*
[3]*Centre for Microscopy, Characterisation & Analysis (CMCA), University of western Australia*
[4]*The Institute for Geoscience Research (TIGeR), Curtin University*

Abstract. At the Beta-Hunt mine, orogenic gold and komatiite-hosted massive nickel sulphide mineralisation are locally coincident, indicating that crustal architecture could play a role in the localisation of the two mineral systems. A structural framework was derived based on field observations to evaluate how early crustal architecture may have influenced both mineral systems. We propose that SW-dipping D_0 growth faults controlled the deposition of komatiite-hosted massive nickel sulphide mineralisation and that these structures were reactivated during SW-NE-directed basin inversion (D_1). During the inversion, strain was partitioned into SW-dipping reverse shear planes along lithological contacts and steeply SW-dipping foliation corridors associated with early growth faults. Deformation was assisted by fluid migration causing strong hydrothermal alteration and deposition of gold. During subsequent local D_2 extension, the steep foliation corridors became dilated. D_2 phase coincided with a major fluid flux, which led to the formation of moderately and steeply NE-dipping hydraulic extension veins and thick sub-vertical breccia bodies following the steep D_1 structural corridors. D_2 hydrothermal veins represent the main phase of gold deposition. We suggest that at Beta-Hunt, early growth faults related to the formation of nickel sulfide mineralisation were also critical for the localisation of high-grade gold mineralisation.

1 Introduction

Understanding deposit scale structural architecture is essential in mid-crustal orogenic gold deposits where fluid flow is highly channelised (Cox 2020). Structural components formed at different times during a deposit's progressive or discrete deformation history control the localisation of fluid channels, enabling the accumulation of economic mineral reserves. At the same time, the presence of fluids changes the mechanical behaviour of rocks during deformation and can influence strain partitioning patterns (Fossen and Cavalcante 2017). Consequently, fluid-assisted deformation is expected to form self-organising systems where fluid flow and localisation of deformation are coupled (Cox 2020). The earliest components of a deposit scale structural architecture can therefore serve as nucleation points for processes that develop into self-enhancing fluid channels, concentrate deformation, and eventually lead to metal accumulation over vast geological time frames spanning multiple mineralising events (Sibson 2020).

This work focuses on the combined komatiite-hosted nickel sulphide and orogenic gold mineralisation of the Beta-Hunt mine in Kambalda, Western Australia, where fluid-enhanced deformation led to the juxtaposition of a structurally controlled orogenic gold mineralisation and a pre-existing komatiite-hosted massive nickel sulphide mineralisation (Neall and Phillips 1987; Stone et al. 2005).

2 Geological background

2.1 Regional geology

The Norseman-Wiluna greenstone belt is in the central southern part of the Archean Yilgarn Craton, Western Australia, located in the southern part of the Kalgoorlie terrane (Cassidy et al. 2006). The greenstone belt is characterised by a greenstone-greywacke succession containing basalts, komatiites, felsic volcanic and volcanoclastic rocks and clastic sediments (Blewett et al. 2010). The southern Kalgoorlie terrane's stratigraphic sequence chronicles a tectonic history that includes an early failed rifting event of the Yilgarn proto-craton and later basin inversion, with reactivation of crustal-scale fault-shear zones, formation of new regional deformation zones, granitic doming, and rapid uplift. (Miller et al. 2010). A simplified stratigraphic column typical for the research area is shown in Figure 1B.

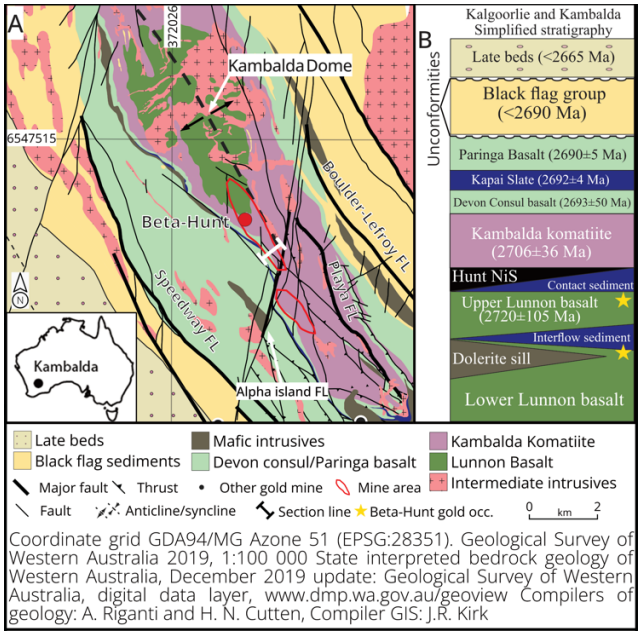

Figure 1. Local geology of the Beta-Hunt mine area. A) Geological map of the mine area, modified after GSWA regional map. B) Local stratigraphy modified after Blewett et al. (2010).

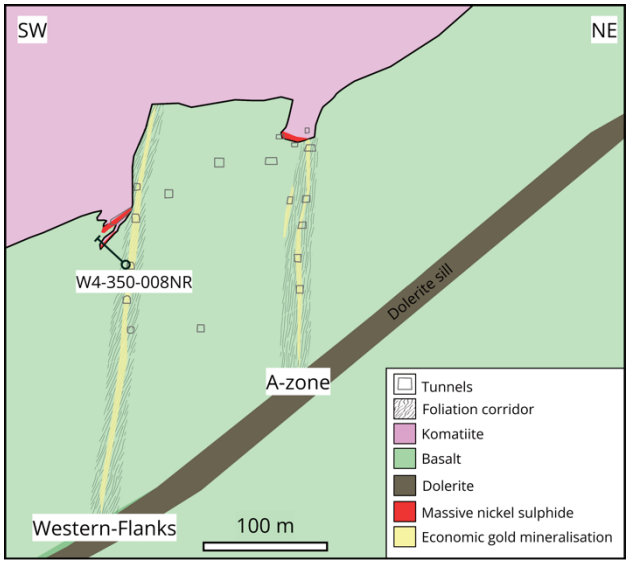

Figure 2. General cross-section of the mine looking NW. Section line in Figure 1A.

2.2. Local geology

The Beta-Hunt mine is in Western Australia, 55 km SE from the city of Kalgoorlie-Boulder. Karora Resources own the mine and currently produces both gold and nickel ore. The mine is located in the NW part of the Saint-Ives and Kambalda district on the SW limb of the Kambalda anticline, close to the anticline hinge zone (Figure 1A). Consequently, only the lowermost stratigraphic units of the gold district are exposed (Figure 1B). The stratigraphic basement is formed by a thick unit of tholeiitic basalt called the Lunnon Basalt, which is split loosely into two sub-units (Said et al. 2010). A thin discontinuous interflow sediment and a strata sub-parallel dolerite sill mark a transitional interface between the Upper and Lower Lunnon basalts (Figure 1B). The 1 km thick Kambalda Komatiite forms the stratigraphic hanging wall of the deposit (Gresham and Loftus-Hills 1981; Miller et al. 2010). However, only the komatiite's lower contact, associated cherty sedimentary sequence ("the contact sediment") and the nickel sulphide mineralisation lenses are exposed within the mine area.

Nickel sulphide mineralisation occurs as basal, massive sulfides in troughs at the footwall contact as well as disseminated to net-textured, semi-massive sulfides either on top of the massive nickel sulphide bodies or as isolated lenses completely enclosed by komatiite (Gresham and Loftus-Hills 1981).

The gold mineralisation located within the footwall of the Kambalda komatiite is primarily found along steeply SW-dipping, NW-striking structural corridors (the "A-zone" and the "Western Flanks"), where the corridors are primarily marked by zones of strong foliation (Figure 2). Auriferous hydraulic extension veins and breccias form the main portion of the minable gold within and immediately adjacent to the zones of foliation. The gold deposition has been estimated to have occurred at approximately 3-6 km crustal depth at the temperature of 280 – 350 °C and confining pressure of 80 – 180 MPa (Neall and Phillips 1987).

3. Methodology

Structural data and observations were collected during detailed underground mapping of the Western Flanks mineralised corridor and the Kambalda komatiite's lower contact. Underground observations were augmented with data from oriented diamond drill cores from the A-zone and Western Flanks gold mineralisation and from the nickel mineralised zone where gold mineralisation is in direct contact with the massive nickel sulphides (drill core W4-350-008NR, Figure 2). Structural orientations presented below are median orientations calculated from the accumulated structural dataset.

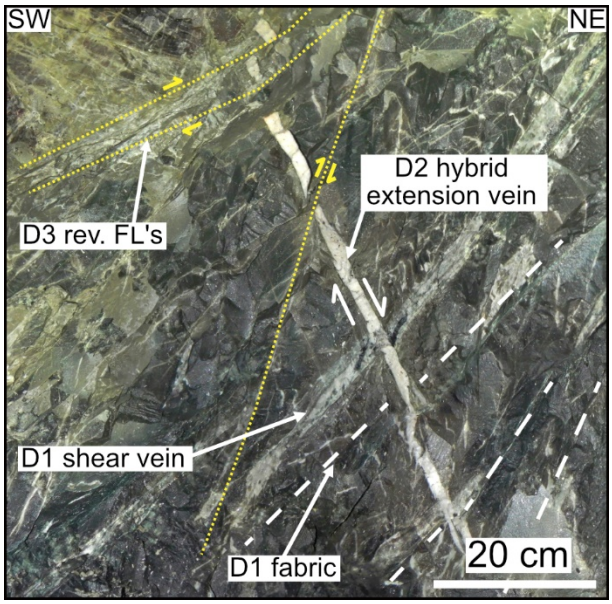

Figure 3. Crosscutting relationships between SW-dipping D1 fabric and fabric parallel shear vein, NE-dipping D2 hybrid extension vein, and strongly bleached D3 reverse faults linked to sub-vertical D3 strike-slip faults. At this underground outcrop, the D1 fabric-related pyrite alteration carries 0.5 - 7 g/t Au, and D2 veins carry gold grades between 7 - 19 g/t Au.

4. Results: Structural elements

A structural framework for the deposit scale structural architecture of the Beta-Hunt mine was derived from structural observations, analysis and relative timing relationships. Structures related to the four phases are described below:

D_0-structures comprise the stratigraphic interfaces formed before and during the regional and district-wide early extension. At Beta-Hunt mine, these boundaries, on average, dip shallowly to moderately to SW (~30/220). Especially

important contacts are the major Kambalda Komatiite-Lunnon Basalt contact and associated massive nickel sulphide troughs, forming the gold mineralisation's hanging wall boundary (Figure 1A and Figure 2). Another important D_0 interface, which is not as well constrained as the komatiite contact, is the transition zone between Upper and Lower Lunnon Basalt marked by the interflow sediment and the dolerite sill. These are usually oriented similarly to the komatiite-basalt contact. Finally, steeply SW-dipping, apparent normal faults that offset the komatiite-basalt contact from meters up to a hundred meters are likewise considered as D_0 structures.

D_1 structures comprise the dominant ductile foliations within the deposit area. Shallow to moderately SW-dipping (~45/230) foliations are most prominently developed along or in the proximity of the primary lithological boundaries, especially along the komatiite-basalt contact and along the dolerite sill (Figure 2). The shallow, anastomosing foliations are associated with asymmetric meso- and microscale deformation fabrics that indicate apparent NE-verging transport. Steeply SW-dipping (~72/226) foliations, highlighted by pervasive biotite-pyrite alteration, define the major corridors of economic mineralisation between the komatiite-basalt contact and the transition between Upper and Lower Lunnon Basalts. Both foliation trends can be associated with foliation parallel, discontinuous quartz-carbonate banding. In addition, a relatively minor set of shallow dipping (~20/252) D_1 tension veins crosscut the steep foliations within the mineralised corridors. A sampling of the production headings shows that D_1 veins carry low to moderate gold grades (0.3 – 2 g/t Au). Further, the D_1 foliations contain very fine-grained free gold where biotite-pyrite alteration is strong (unpublished report, Karora Resources).

D_2 structures contain most of the gold associated with the deposit (Figure 3). D_2 veins are confined to the steeply dipping and pervasively altered D_1 foliation corridors. Veins are usually medium to coarse-grained and composed of quartz-albite-carbonates±sulphide±gold. Two sets of coeval veins are recognised: 1) the most common auriferous veins are millimetre- to decimetre-scale, moderately to steeply NE-dipping (~55/034) hydraulic extension veins, which crosscut the D_1 fabrics at a nearly perpendicular angle (Figure 3). The extension veins occur in en-echelon vein sets soft-linked with 2) less numerous but locally dominant, up to 6 meters wide, and very steeply SW-dipping to sub-vertical D_2 hydraulic breccia veins. NE-dipping vein sets sometimes branch off or join with the breccia veins. Meanwhile, the breccia veins locally propagate into the wall rocks exploiting the D_1 foliation, resulting in much shorter, irregular SW-dipping veins branching from the wider breccia veins.

The most dominant D_3 structure is the Alpha Island Fault, which shows an apparent right-lateral movement and displaces the whole deposit by about 500 meters (Figure 1A). Smaller structures include numerous minor strike-slip faults (~70/290 and ~60/330), minor reverse faults (~55/214), and rare sub-vertical tension veins (~70/325) that overprint all previous structural features. The various D_3 structures are inferred to be coeval due to similarities in crosscutting relationships and diagnostic pale green sericitisation alteration signatures (Figure 3). The D_3 structures are only grade-bearing, where they directly crosscut pre-existing gold-bearing D_1-D_2 veins and foliations.

5. Discussion

5.1. Komatiite-hosted nickel sulphide mineralisation

Previous research has recognised the extensive early growth fault network within the Saint-Ives and Kambalda district, highlighting its control on gold mineralisation (e.g., Miller et al. 2010). Here we suggest that this early to syn-magmatic architecture could have been an important control for localising massive nickel sulphide ore bodies. Low-viscosity komatiitic lavas are preferentially channelled along topographic lows, which would develop along fault scarps (Barnes 2006). Such interpretation is further supported when looking at the northern parts of the Kalgoorlie terrane, where a preferential accumulation of nickel mineralisation has been shown to occur where komatiitic lavas cross fault lines (Perring 2015). Recent modelling has further demonstrated that the accumulation of nickel sulfide droplets on the hanging wall of a normal fault is flow-dynamically feasible (Yao and Mungall 2022). The channelisation of komatiitic lavas along deep and narrow channels increases physical contact with substrate rocks leading to thermomechanical erosion, crustal assimilation and sulfur saturation (Staude et al. 2017). At the Beta-Hunt mine, undeformed komatiite and massive nickel sulfide - mineralisation occur in troughs on the hanging wall side of the D_0 normal faults, which clearly offset the komatiite footwall basalt contact (Figure 2).

5.2. D_1 Reverse reactivation of early normal faults

The dominant D_1 foliations formed during SW-NE trending sub-horizontal compression. The strain was partitioned along D_0 lithological contacts (Sz) and along moderately to steeply dipping structural corridors (S), which bound lava flow channels hosting nickel sulfide mineralisation at the komatiite-basalt contact. We suggest that stratigraphic interfaces were favourably oriented for flexural slip as the development of the Kambalda anticline tilted the rock strata and led to NE-verging transport along the shallow Sz-shear foliations during broadly NE-SW directed shortening (Stone et al. 2005). S-planes, on the other hand, may have essentially recorded coaxial-dominated deformation and formed sub-vertical compressional foliations. Foliations are associated with strong biotite-pyrite-

ankerite alteration, indicating that hydrothermal fluid circulation assisted the ductile deformation.

Fluid-induced reactivation is especially effective during compressional tectonics (Sibson 2020). Reactivation and strain partitioning along pre-existing structure architectural components are favoured as fluid flow becomes highly channelised below ~2 km of crustal depth (Cox 2020). Channelisation occurs as the presence of fluids changes the behaviour of rocks during deformation, enhancing ductile and brittle mechanisms (Fossen 2017). As a region progresses from one deformation phase to another, the coupling of fluid flow and deformation causes pre-existing deformation zones and their damage zones to become preferentially "selected" for reactivation due to their enhanced permeability and mechanical weakness. At the Beta-Hunt mine, this process led to the formation of discrete foliation corridors while the surrounding basaltic host rocks remained relatively undeformed (Figure 2).

5.3. Reactivation of D_1 fabrics

Analysis of the D_2 extension and breccia veins indicates that both are syntectonic fractures that developed into the mesoscopic hydraulic veins observed today during local vertical shortening. Fracturing coincided with a major fluid flux into the system, evident from the decimeter to several meter thicknesses of the veins. During D_2, the steeply dipping D_1 S-planes became favourable oriented for dilation. Minor deflections of D_1 foliations adjacent to D_2 breccia veins indicate that these veins are dilated normal faults. D_2 veining does not extend significantly into the Kambalda Komatiite or the nickel sulphide mineralised bodies. This is likely because the mechanically weak serpentinised komatiite in the hanging wall was too mechanically weak to brittlely deformed during D_2. This may have prevented the fluids from migrating upwards through the ~1 km thick komatiite. Instead, fluid capping led to sustained and relatively stable elevated pressure along the D_1 deformation corridors, driving propagation and dilation of the hydraulic veins, lateral fluid advection and gold deposition.

6. Conclusion

At the Beta-Hunt mine, structural analysis suggests that early rifting-related growth faults may have contributed to the deposition of massive nickel sulphide ore bodies. These faults were reactivated during D_1 compression and developed into gold-mineralised corridors where gold was further enriched in hydraulic veins during local extensional D_2 deformation. Natural fluid flow networks tend to form along pre-existing zones of weakness in the middle and lower crust, and the ability of fluids to enhance deformation has caused the repeated reactivation of the structural components of the deposit, resulting in the co-occurrence of gold and nickel sulfide mineralisations.

Acknowledgements

The study is funded by Australian Research Councils linkage project LP 200200897. Authors would like to give special thanks to Karora Resources and their technical team for their support.

References

Barnes SJ (2006) Komatiite-Hosted Nickel Sulfide Deposits: Geology, Geochemistry, and Genesis Nickel Deposits of the Yilgarn Craton: Geology, Geochemistry, and Geophysics Applied to Exploration. Society of Economic Geologists, pp 0.

Blewett RS, Czarnota K, Henson PA (2010) Structural-event framework for the eastern Yilgarn Craton, Western Australia, and its implications for orogenic gold. Precambrian Research 183:203-229. doi: 10.1016/j.precamres.2010.04.004.

Cassidy K, Champion DC, Krapez B, Barley ME, Tyler IM (2006) A revised geological framework for the Yilgarn Craton: Western Australia. Western Australia Geological Survey, Record 2006/8:8 p.

Cox SF (2020) Chapter 2: The Dynamics of Permeability Enhancement and Fluid Flow in Overpressured, Fracture-Controlled Hydrothermal Systems In: Rowland JV, Rhys DA (eds) Applied structural geology of ore-forming hydrothermal systems. Society of Economic Geologists, pp 25- 82.

Fossen H, Cavalcante GCG (2017) Shear zones – A review. Earth-Sci Rev 171:434–455. doi: 10.1016/j.earscirev.2017.05.002.

Gresham JJ, Loftus-Hills GD (1981) The geology of the Kambalda nickel field, Western Australia. Economic Geology 76:1373-1416. doi: 10.2113/gsecongeo.76.6.1373.

Miller J, Blewett R, Tunjic J, Connors K (2010) The role of early formed structures on the development of the world class St Ives Goldfield, Yilgarn, WA. Precambrian Res 183:292–315. doi: 10.1016/j.precamres.2010.08.002.

Neall FB, Phillips GN (1987) Fluid-wall rock interaction in an Archean hydrothermal gold deposit; a thermodynamic model for the Hunt Mine, Kambalda. Economic Geology 82:1679-1694. doi: 10.2113/gsecongeo.82.7.1679.

Perring CS (2015) Volcanological and Structural Controls on Mineralization at the Mount Keith and Cliffs Komatiite-Associated Nickel Sulfide Deposits, Agnew-Wiluna Belt, Western Australia—Implications for Ore Genesis and Targeting. Econ Geol 110:1669–1695. doi: 10.2113/econgeo.110.7.1669.

Said N, Kerrich R, Groves D (2010) Geochemical systematics of basalts of the Lower Basalt Unit, 2.7Ga Kambalda Sequence, Yilgarn craton, Australia: Plume impingement at a rifted craton margin. Lithos 115:82-100. doi: 10.1016/j.lithos.2009.11.008.

Sibson RH (2020) Preparation zones for large crustal earthquakes consequent on fault-valve action. Earth, Planets and Space 72. doi: 10.1186/s40623-020-01153-x.

Stone WE, Beresford SW, Archibald NJ (2005) Structural Setting and Shape Analysis of Nickel Sulfide Shoots at the Kambalda Dome, Western Australia: Implications for Deformation and Remobilisation. Econ Geol 100:1441–1455. doi: 10.2113/gsecongeo.100.7.1441.

Yao Z, Mungall JE (2022) Transport and deposition of immiscible sulfide liquid during lateral magma flow. Earth-Sci Rev 227:103964. doi: 10.1016/j.earscirev.2022.103964

Mineral-specific deportment of gold and other elements in mine tailings from the Witwatersrand goldfields

Bjorn von der Heyden[1], Steve Chingwaru[1], Margreth Tadie[2]
[1] Department of Earth Sciences, Stellenbosch University, Private Bag X1, Matieland, 7602, South Africa
[2] Department of Process Engineering, Stellenbosch University, Private Bag X1, Matieland, 7602, South Africa

Abstract. The Witwatersrand Basin is the world's largest gold province hosting over 53 000 tons of native Au predominantly in quartz pebble conglomerates. The Witwatersrand gold tailings dumps are subjected to secondary mining operations which involve traditional extraction techniques (cyanide leaching) that lead to 30-50 % recovery of gold missed by the historical beneficiation. This leaves a projected 1325-1855 tons of refractory gold together with an estimated 30 million tons of sulfide material which reports to the discard stream after secondary mining. The mineralogical deportment of this remaining or refractory gold is not well constrained. Results from the analyses indicate that about 0.71 – 10.21 g/ton of gold is distributed in the heavy mineral concentrates which are predominantly made up of sulfides (35-76%) and oxides (9-20%). Detailed in situ analyses suggest the gold in the concentrate fraction is hosted predominantly in pyrite and arsenian pyrite, Au grades range from 0.1 – 2729 g/ton. Given that the Witwatersrand Goldfield is historically a native gold deposit, identification of 'invisible' gold in detrital pyrites represents a potentially under-exploited resource which explains in part the refractory nature of the 50-70 % Au remaining after secondary mining.

1 Introduction

The Witwatersrand Basin represents the world's largest gold mineralization, having produced around 53 000 tons of gold since its discovery in 1884 (Frimmel 2019). Despite having an extensive history of mining the origin of gold mineralisation is still highly debated, with provenance described by metallogenic models. These include the placer model, the modified placer model, and the epigenetic model (Frimmel et al. 1993; Robb and Meyer 1995; Tucker et al. 2016). Recent studies suggest microbial fixation by cyanobacteria on coastal environments, these Au-rich organic mats are reworked mechanically to form the Au-bearing conglomerate placer deposits of the Central Rand Group (Frimmel 2019). The placer- and modified placer models state that the origin of gold within the Witwatersrand Basin was initially concentrated within dense native gold placers then later redistributed and re-precipitated because of several hydrothermal events (Frimmel and Minter 2002). Therefore, gold is suggested to enter the quartz pebble conglomerates (QPC) along with other detrital minerals such as pyrite, uraninite and other oxide phases all these being liberated and eroded from an Archean granite-greenstone hinterland.

Several of these remnants of Archean granite-greenstone exist with notable concentrations of gold mineralization (Pearton and Viljoen 2017). A good example of these vestiges is the Barberton greenstone belt, which hosts countable gold deposits, in which the majority is defined as 'invisible' or 'refractory gold that is incorporated into the sulfide structures of pyrite, arsenopyrite and arsenian pyrite via solid-solution substitution or nanoparticulate inclusions (Anhaeusser 2019; Hofmann et al. 2019). Similarly, invisible gold mineralization (described as very fine ~10 µm) is hosted in the Banded-iron formation Kalgold deposit of the Kraaipan Greenstone, associated with fine-grained sulfides (Harmony Gold 2018; Pearton and Viljoen 2017). This chemical nature of the greenstone belt gold deposits proposes that a considerable percentage of the detrital sulfides within the Witwatersrand QPC should be mineralized in Au. This has been proven to be true by limited data from Witwatersrand detrital pyrite (up to 8 ppm Au and as high as 1400 ppm; (da Costa et al. 2020)).

The traditional Witwatersrand processing methods of standard milling (up to 80% of material less than top-size 75 µm), cyanidation, and carbon-in-pulp have been designed to liberate gold from the ore. These historical liberation methods have efficiencies of ca. 95% (Vaughan 2004), implying 5% of the total gold (i.e., ca. 2650 t Au) is still available for extraction in the historical tailing dumps. Tailing reprocessing units that also make use of cyanidation run at 30-50% efficiency, again implying 50-70% (representing 1325-1855 t Au) is not extracted from the ore. One of the possible explanations is that a significant proportion of the Witwatersrand gold deposits contain 'invisible' or refractory gold, which is inaccessible via cyanidation.

Therefore, the purpose of the study is to conduct mineral-specific gold deportment characterisation to determine the variability and nature of gold in the Witwatersrand tailings.

2 Methods

Duplicates of 150 kg of sample material were acquired from four tailings dams storage facilities associated with mining in the Evander, Carletonville, Central Rand and Klerksdorp Goldfields of the Witwatersrand Basin (Fig.1). After homogenisation and representative splitting of these bulk samples, ~1 kg subsamples were further subjected to a series of pre-concentration procedures. The applied techniques were desliming, superpanning and a two-stage heavy liquid separation using tetrabromoethane at 2.95 g/cm^3 density and lithium metatungstate at 2.71 g/cm^3 density. The resultant

density-defined mineral fractions were a slimes fraction (particle size < 25 µm), a light mineral fraction (< 2.95 g/cm^3) and a heavy mineral fraction (> 2.95 g/cm^3). Approximately 0.3 g of representative aliquots from each of the density-defined mineral fractions was placed as a monolayer in an epoxy mount, and subsequently diamond polished to a 1 µm finish.

The pre-concentrated samples were subjected to a variety of analytical techniques. Aqua regia digestion and inductively coupled plasma mass spectrometry (ICP-MS) analyses were conducted to determine the bulk trace element concentrations (As, Au, Co, Cu, Hg, Ni, Pb, Sb, Se, Zn & U). This was done on approximately 0.55 g duplicates from each bulk sample, each density fraction and on three blank samples at the Central Analytical Facilities (CAF), Stellenbosch University. Textural descriptions of each epoxy mount were afforded by optical petrography, scanning electron microscopy (Stellenbosch University) and QEMSCAN (University of Cape Town). The QEMSCAN approach was incorporated into the study to determine bulk mineral percentages of the heavy mineral fraction, which in turn was used to validate the assay data derived from acid digestion and for mass balance calculations. Additionally, a false image colour map was generated to assist with the identification of 'visible gold' and potential gold carriers, as well as a visual aid to identify potential grains for subsequent LA ICP-MS analysis.

LA ICP-MS was carried out on 800 grains of oxides (hematite, goethite/limonite, rutile) and sulfides (pyrite, arsenopyrite, galena, sphalerite, chalcopyrite, pentlandite and pyrrhotite) from the heavy minerals fraction mounts using a grid method at CAF, Stellenbosch University with a Resolution 193 nm Excimer laser from Applied spectra, coupled with an Agilent 7700 Q ICP-MS. This was done to obtain concentrations of trace elements (Co, Ni, Cu, Zn, As, Se, Ag, Sb, Te, Au, Hg, Pb and Bi) hosted within each of the mineral phases. Resultant data were processed using LADR from Norris Scientific.

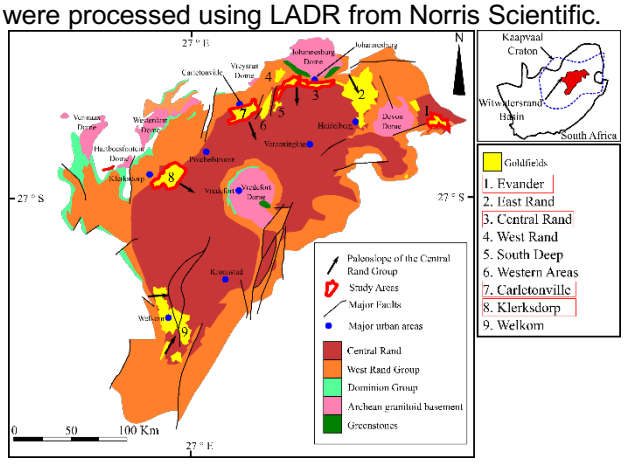

Figure 1. A surface geological map of the Witwatersrand basin, displaying the goldfields referred to in the text (from Chingwaru et al. 2023).

3 Results and Discussion

3.1 Gold deportment according to operational definitions and according to mineralogy

The first step towards identifying the main gold 'carriers' in the Witwatersrand tailings materials was to identify the operationally-defined units which hosted the highest proportions of gold (Fig. 2a). Across all four goldfields evaluated, the heavy mineral fraction consistently hosts the largest relative proportion of gold with aqua regia measured grades of between 0.71 and 10.12 ppm (Fig. 2a). This accounts for 0.89 to 13.23 % for the mass of gold in the samples. The light mineral fraction (d < 2,95 g.cm^{-3}; size 15-75 µm) and slimes fraction (< 10 µm) have measured gold concentrations that are an order of magnitude lower, measuring across the four goldfields between 0,05-0,22 ppm and 0,17-0.76 ppm respectively. This preferential partitioning of gold into the heavy mineral fraction may be explained by the presence of nano-particulate native gold grains, or by a chemical association between gold and heavy gangue minerals such as sulfides and oxides (Goodall 2008; Coetzee et al. 2011; Goodall and Butcher 2012).

To elucidate the main mineralogical carriers of gold within the heavy mineral fraction, we utilised the QEMSCAN imagery to identify, locate and quantify the different sulfide minerals present in this fraction. Coupled with optical and SEM microscopy, our results highlight that the mineralogical composition of the heavy mineral fraction comprises 13-44% silicates; 35-76% sulfides; 9-20% oxides; 0.01-0.34% carbonates and phosphates, and no native or 'free' gold observed. Pyrite was the dominant sulfide mineral and textural observations from microscopy (Fig. 2b-d) enabled textural sub-classes of pyrite to be identified (e.g., da Costa et al. 2020). Using the QEMSCAN imagery as a guide, LA ICP-MS was used to quantify the deportment of gold per mineral phase within the heavy mineral fraction. From the pie charts depicted in Figure 2b, it is clear that pyrite and arsenian pyrite host the majority of gold within this fraction. For example, these two minerals account for approximately 65% of gold in the Klerksdorp heavy mineral fraction, 78% of gold in the Carletonville heavy mineral fraction and 85% of gold in the Evander heavy mineral fraction (Fig. 2a). Gold deportment into goethite/limonite, hematite and other sulfide minerals is quantitatively less important (i.e., typically accounting for ~1 – 6% of total gold in the heavy mineral fraction), with the largest concentrations observed in goethite/limonite (0.78 ppm), hematite (0.64 ppm), and pyrrhotite (0.34 ppm) respectively. Based on the textural classification of pyrite grains, we discerned that rounded pyrite grains comprise the highest concentration of gold, recording an average spot concentration value of 21.36 ppm gold and a maximum of 2700 ppm gold. We conform to previous authors' designation of this rounded pyrite class as being detrital in origin, with rounding having occurred during fluvial processing and sedimentation of the Witwatersrand conglomerates (e.g., Agangi et al.

2015; da Costa et al. 2020).

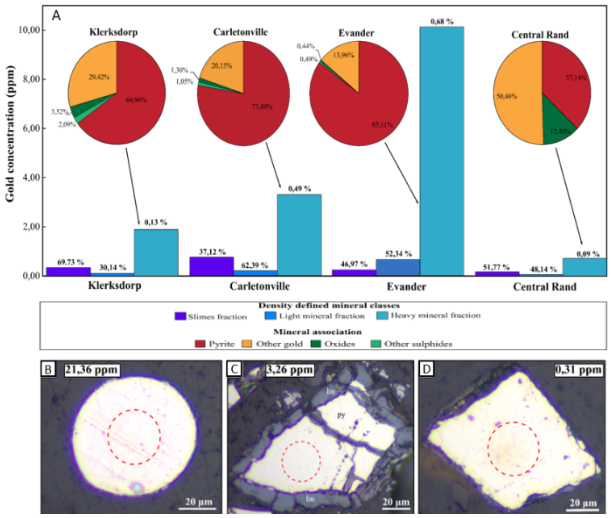

Figure 2a. Gold distributions summarised per operational definition and per individual mineral phase. **b-d.** Example spot loci in various pyrite morphological types (**b:** rounded/detrital pyrite, **c:** oxide rim pyrite, and **d:** euhedral pyrite classes respectively). Figures adapted from Chingwaru et al. 2023.

3.2 Pyrite chemistry: implications for provenance, economic extraction and the environment

The binary plot of As vs Au is a useful tool for considering the gold endowment of individual pyrite grains in the context of the maximum solubility of gold within the mineral structure (Reich et al. 2005). The upper limit of this stability is given by the gold saturation line (Fig. 3a), above which Au is expected to be present as nanoparticulate inclusions within the confines of the pyrite mineral. Figure 3 plots the chemistry of the pyrite grains investigated in this study, which we believe to represent a cross-section of a variety of pyrite types present in the Witwatersrand sediments (e.g., authigenic pyrite, hydrothermal pyrite formed during modification, detrital pyrite that is not derived from Au deposits, and pyrite derived from possible hinterland Au deposits). Applying the concept of the Clarke value (Fig. 3b), we suggest that the random sampling ensured by our pre-concentration approach and subsequent LA ICP-MS analysis approach should ensure that the bulk of our measurements falls within the low-Au 'normal crustal abundance' main peak of the Clarke distribution. Applying this to our empirical distribution shown on the binary plot (Fig. 3a), we suggest that the low-Au 'normal crustal abundance' field could fall below the line $C_{Au} = 0.0022.C_{As} + 0.2$. The data points for tailings pyrite grains that fall above this line may be representative of pyrite that derives from an Au-enriched source, for example, from possible hinterland orogenic Au deposits. For comparison, we show empirical LA ICP-MS data published for pyrite sampled from orogenic gold deposits in the Barberton greenstone belt, the chemical signatures of which we deem to be representative of a possible granite-greenstone hinterland gold source.

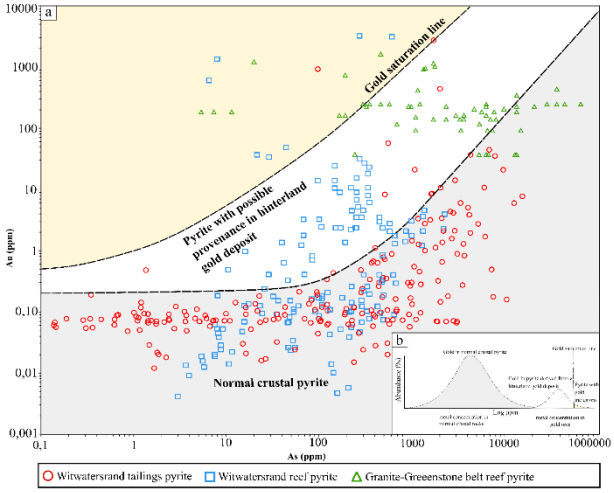

Figure 3a. An arsenic/gold scatter plot with concentration points from the Witwatersrand tailings pyrite (this study), Witwatersrand reef pyrite (Large & Maslennikov, 2020; Large et al., 2013; Morishita et al., 2019) and Granite-Greenstone belt auriferous pyrite (Agangi et al., 2014). The gold saturation line by Reich et al. (2005) represents the gold/arsenic limit in which gold occurs as free gold particles in pyrite. Inset diagram (**b**) uses the concept of a bi-modal distribution for metal grades, where Clarke values represent the broad main peak (reflecting normal crustal rocks), whereas the second peak represents the metal distribution specifically in ore deposits and occurrences. Figure from Chingwaru et al. 2023.

The finding that auriferous sulfides are located within the surficial materials of the mine tailings dumps scattered across the Witwatersrand mining precinct has meaningful implications for the secondary mining of this Au resource. Historical mining and processing as well as more recent reprocessing have focussed predominantly on the native gold endowment of the Witwatersrand auriferous conglomerates, thus overlooking the economic opportunity of auriferous pyrite. This 'invisible' gold is known to be inaccessible through direct cyanidation (Coetzee et al. 2011), and may thus be a significant contributor to the 50-70% recovery inefficiencies associated with secondary beneficiation of the Witwatersrand tailings. From an economic standpoint, extraction of auriferous pyrite from these tailings is deemed more favourable due to fine grain sizes and surficial location, respectively negating comminution and the high overheads associated with underground mining.

Environmental benefits would emanate from targeted re-mining of the sulfide fraction of the Witwatersrand tailings dumps. Mass balance calculations from our deportment study highlight that in addition to hosting high gold concentrations, the sulfide fraction hosts on the order of 95% of Zn, Cu, As and Pb; 55-97% of Ni; 64-99% of Co; 77-99% of Se and 84-99% of Sb. Removal of the sulfide component additionally would remove a major contributor to the acid mine drainage pollution

problem in some parts of the Witwatersrand area (e.g. Tutu et al. 2008). The value proposition of such an approach would be further enhanced by the recovery of high-demand heavy metals such as Co, Cu and Ni as by-products, which respectively have average calculated concentrations of 9755 ± 2330 ppm Co, 8771 ± 1817 ppm Cu and 9822 ± 1810 ppm Ni within the sulfide mineral fraction.

4 Conclusion

The study suggests that the fraction of gold inaccessible to conventional processing technologies in the Witwatersrand tailings ore material is attributed to a percentage of invisible gold, predominately within the arsenian pyrite and pyrite. Preserved rounded detrital pyrite classes within the tailings dump material exhibit the highest concentration of gold, with a maximum gold concentration similar to auriferous pyrite from existing granite-greenstone belt gold deposits. The residual sulfides in the tailings dump potentially represent a large under-exploited economic resource of up to 420 tons of gold, in which pre-treatment beneficiation can directly improve gold recovery by ~22 % during secondary reprocessing. This will further alleviate the growing ramifications of AMD and effluents with deleterious elements in the Witwatersrand mining region, while potentially recovering additional high-demand by-product metals.

Acknowledgements

This research was funded by the DST-NRF Centre of Excellence for Integrated Mineral and Energy Resource Analysis (CIMERA) and the Society of Economic Geologists (SEG) Tim Nutt Fund. Thank you to the analytical staff at CAF, Stellenbosch University and QEMSCAN unit, University of Cape Town. We further extend our thanks to the mining houses Harmony Gold limited, DRD Gold Limited and Pan African Resources for sample donations.

References

Agangi, A., Hofmann, A., Rollion-Bard, C., Marin-Carbonne, J., Cavalazzi, B., Large, R. & Meffre, S. 2015. Gold accumulation in the Archaean Witwatersrand Basin, South Africa-Evidence from concentrically laminated pyrite. Earth-Science Reviews. 140:27–53.

Anhaeusser, C. 2019. The geology and tectonic evolution of the northwest part of the Barberton Greenstone Belt, South Africa: A review. South African Journal of Geology. 122.

Chingwaru, S.J., Von der Heyden, B. and Tadie, M., 2023. An underexploited invisible gold resource in the Archean sulphides of the Witwatersrand tailings dumps. Scientific Reports, 13(1), p.3086.

Coetzee, L.L., Theron, S.J., Martin, G.J., Merwe, J.D. Van Der & Stanek, T.A. 2011. Modern gold deportments and its application to industry. Minerals Engineering. 24(6):565–575.

da Costa, G., Hofmann, A. & Agangi, A. 2020. A revised classification scheme of pyrite in the Witwatersrand Basin and application to placer gold deposits. Earth-Science Reviews. 201.

Frimmel, H.E., Le Roex, A.P., Knight, J. & Minter, W.E.L. 1993. A case study of the postdepositional alteration of the Witwatersrand Basal reef gold placer. Economic Geology.

Frimmel, H.E. & Minter, W.E.L. 2002. Recent Developments Concerning the Geological History and Genesis of the Witwatersrand Gold Deposits, South Africa. In Society of Economic Geologists Integrated Methods for Discovery: Global Exploration in the Twenty-First Century.

Frimmel, H.E. 2019. The Witwatersrand Basin and Its Gold Deposits. In A. Kröner & A. Hofmann (eds.). Cham: Springer International Publishing The Archaean Geology of the Kaapvaal Craton, Southern Africa. 255–275.

Goodall, W.R. 2008. Characterisation of mineralogy and gold deportment for complex tailings deposits using QEMSCAN®. Minerals Engineering. 21(6):518–523.

Goodall, W.R. & Butcher, A.R. 2012. The use of QEMSCAN in practical gold deportment studies. In Vol. 121 Transactions of the Institutions of Mining and Metallurgy, Section C: Mineral Processing and Extractive Metallurgy. 199–204.

Harmony Gold. 2018. Kalgold Greenstone exploration - Harmony Gold Mining. [Online], Available: https://www.harmony.co.za/invest/presentations/2018/send/131-2018/3486-kalgold-greenstone-exploration [2020, November 09]

Hofmann, A., Anhaeusser, C., Dixon, J., Kröner, A., Saha, L., Wilson, A. & Xie, H. 2019. Archaean Granitoid–Greenstone Geology of the Southeastern Part of the Kaapvaal Craton. In Springer The Archaean Geology of the Kaapvaal Craton, Southern Africa. 33–54.

Large, R.R. & Maslennikov, V. V. 2020. Invisible gold paragenesis and geochemistry in pyrite from orogenic and sediment-hosted gold deposits. Minerals. 10(4).

Large, R.R., Meffre, S., Burnett, R., Guy, B., Bull, S., Gilbert, S., Goemann, K. & Danyushevsky, L. 2013. Evidence for an intrabasinal source and multiple concentration processes in the formation of the carbon leader reef, Witwatersrand Supergroup, South Africa. Economic Geology. 108(6):1215–1241.

Morishita, Y., Hammond, N.Q., Momii, K., Konagaya, R., Sano, Y., Takahata, N. & Ueno, H. 2019. Invisible gold in pyrite from epithermal, banded-iron-formation-hosted, and sedimentary gold deposits: Evidence of hydrothermal influence. Minerals. 9(7):447.

Pearton, T. & Viljoen, M. 2017. Gold on the Kaapvaal Craton, outside the Witwatersrand Basin, South Africa. South African Journal of Geology. 120:101–132.

Reich, M., Kesler, S.E., Utsunomiya, S., Palenik, C.S., Chryssoulis, S.L. & Ewing, R.C. 2005. Solubility of gold in arsenian pyrite. Geochimica et Cosmochimica Acta. 69(11):2781–2796.

Robb, L.J. & Meyer, F.M. 1995. The Witwatersrand Basin, South Africa: Geological framework and mineralization processes. Ore Geology Reviews.

Tucker, R.F., Viljoen, R.P. & Viljoen, M.J. 2016. A Review of the Witwatersrand Basin - The World's Greatest Goldfield. Episodes. 39(2):105–133.

Tutu, H., McCarthy, T.S. & Cukrowska, E. 2008. The chemical characteristics of acid mine drainage with particular reference to sources, distribution and remediation: The Witwatersrand Basin, South Africa as a case study. Applied Geochemistry. 23(12):3666–3684.

Vaughan, J.P. 2004. The process mineralogy of gold: The classification of ore types. Jom. 56(7):46–48.

An integrated approach towards unravelling the gold mineralisation processes around Ardtalnaig, Scotland.

Shane Webb[1], Taija Torvela[2], Robert Chapman[3], David Selby[4], Robert Gooday[5]
[1-4]School of Earth and Environment, University of Leeds, U.K.
[2]Durham University, Department of Earth Sciences, Durham University, UK
[3]National Museums Scotland, UK

Abstract. In the Caledonides of Britain and Ireland, there are several gold deposits of commercial interest hosted within the Grampian Terrane, which is comprised of Neoproterozoic metasedimentary rocks. One Scottish region that has been the focus of exploration in recent years is the southern margin of Loch Tay, where polymetallic quartz±carbonate veins sporadically outcrop throughout a 100km^2 swathe of the Dalradian Supergroup. Genetic aspects of the mineralisation here remain poorly constrained, particularly with regards to the source of the ore-forming fluids. We have used an integrated approach involving petrography, geochronology, sulphur isotope geochemistry and gold microchemistry to rectify this. Rhenium-Osmium (Re-Os) dating of molybdenite from the Tomnadashan Mine, in addition to our paragenetic study, confirms that the initial stage of mineralisation around Loch Tay occurred at ca. 423Ma. The sulphur isotope and gold microchemical data demonstrate that this area, along with the high-grade gold prospect named Lead Trial, likely comprises a magmatic-hydrothermal mineral system in the region. The extent and relation of the Tomnadashan-Lead Trial system to the metasediment-hosted veins throughout the region, which recorded $\delta^{34}S$ values of 5-10‰, remains unknown. It may be possible for other researchers to replicate our integrated approach towards metallogenic studies on other gold deposits.

1 Introduction

Around the southern margins of Loch Tay, which is situated in the Perthshire region of Scotland (Figure 1a), there are several gold and base metal deposits. The Tomnadashan and Coire Buidhe mines (Figure 1b) were worked by artisanal methods in the 19th century (Pattrick 1980), whilst the other occurrences of mineralisation were explored by junior exploration companies during the 1980s and 1990s (Corkhill et al. 2010). Neoproterozoic SEDEX mineralisation has been mined for barytes at Foss (Figure 1b) since the 1970s. Green Glen Minerals, a junior exploration company, are currently investigating the auriferous potential of the Lead Trial, which is one of several occurrences of gold mineralisation within the Ardtalnaig Estate (Figure 1c). Despite the extensive history of mineral exploration and extraction around Loch Tay, the genetic aspects of the mineral system are poorly understood. The veins consistently strike NW-SE (120-140°) (Corkhill et al. 2010). This may indicate a contemporaneous mineralisation event throughout the wider region (Figure 1b), with localised paragenetic and mineralogical variations representing subsequent mineralisation events that have affected some localities but not others.

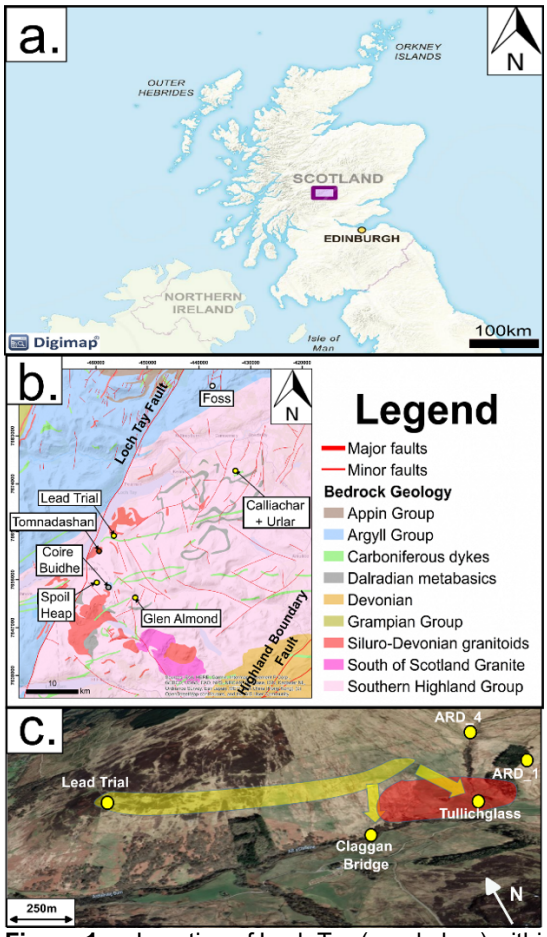

Figure 1. a. Location of Loch Tay (purple box) within the northern British Isles. **b.** Geological map of the Study Area, with localities colour coded according to the commercial or historic commodity of interest (yellow = gold, grey = silver, brown = copper, white = barytes). Localities other than Ardtalnaig and Tomnadashan are known as the 'metasediment-hosted veins.' **c.** Sampling localities (yellow) within the Ardtalnaig Estate. The arrows show a detrital contribution of gold from the peak of the hill, whilst the red colouration demonstrates the likely source of gold panned at Claggan Bridge.

The fractures infilled by the veins formed in response to sinistral motion along the Loch Tay Fault during the Scandian phase of the Caledonian Orogeny between 435 and 390Ma (Chew and Strachan 2013). The source of the ore-forming fluids around Loch Tay is unknown. At Calliachar and Urlar (Figure 1b), the fluid inclusion data revealed CO_2 contents and salinities typical of 'orogenic' gold deposits (Ixer et al. 1997). However, Tomnadashan has been described as a Cu-Mo porphyry (Pattrick 1984), and the elevated Bi concentrations observed across Figure 1b may be

the result of magmatic mineralisation processes (Corkhill et al. 2010). It can therefore be argued that an intrusion was the source of the ore-forming fluids throughout the region. The issue is complicated further by the ongoing debate regarding the genesis of gold deposits in orogenic belts, with several models involving metamorphic and magmatic fluids being recognised (Mortensen et al. 2022). We have used several analytical techniques to elucidate this problem around Loch Tay. The Re-Os geochronological analyses on molybdenite from Tomnadashan, in addition to a paragenetic study, provide a constraint on the age of the regional mineralising system. We also utilised $\delta^{34}S$ studies on sulphides to assess potential sources of ore-forming fluids, with gold compositional data being used to scrutinise variations within the mineral system around Ardtalnaig (Figure 1c).

2 Methodology

A molybdenite sample (TOM_MOLY_SM) was collected from a mineralised quartz stringer at Tomnadashan for Re-Os dating by isotope-dilution negative ion mass spectrometry (ID-NTIMS). This was conducted at Durham University. Whilst paragenetic studies on Tomnadashan do exist (Table 1), these are not supported with petrographic images. To contextualise the Re-Os age for the molybdenite and confirm the paragenesis, we conducted SEM studies on polished blocks of the mineralisation. This work was partially carried out using equipment at a facility operated by National Museums Scotland.

Compositional data was derived from gold particles that were panned from Ardtalnaig (Figure 1c) and Tomnadashan. Particles from each locality were dried and separated into groups of similar sizes. The samples were mounted on polished blocks. An SEM and Electron Microprobe were used to determine the inclusions present and the alloy composition. For the $\delta^{34}S$ studies, sulphides were analysed using an Elementar PYRO cube coupled to an IsoPrime continuous flow mass spectrometer. The samples were weighed into 8 x 5 mm tin cups and combusted at 1150°C.

3 The age and paragenetic context of molybdenite at Tomnadashan

TOM_MOLY_SM yielded a Re-Os age of 423±2Ma. At Tomnadashan, a NW-SE trending quartz vein (similar to the other Loch Tay veins) crosscuts the porphyry exposed on the surface (Figure 1b). This vein contains most of the Tomnadashan mineralisation (Naden 2010), which is also disseminated in the granitoid wallrock. The mineralisation postdates emplacement of the porphyry and therefore does not belong to the 'Cu-Mo porphyry' style of mineral deposits. Fluid inclusion data (Naden 2010) still supports a magmatic origin for the ore-forming fluids at Tomnadashan.

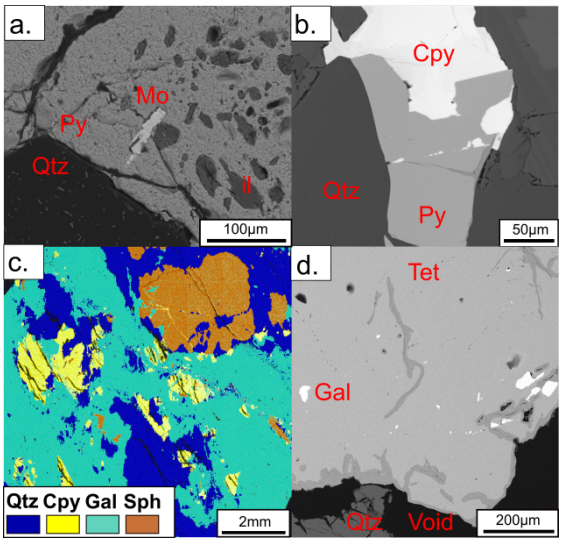

Figure 3. SEM images of the mineralisation at Tomnadashan. **a.** Molybdenite inclusion within a large pyrite crystal. **b.** Chalcopyrite overgrowing and crosscutting pyrite. **c.** Phase map demonstrating the co-occurrence of galena, sphalerite and chalcopyrite. **d.** Galena inclusions within tetrahedrite. Figure 3a represents mineralisation disseminated in the granitoid, whilst Figures 3b-d are from the vein. Figures 3a and 3c © National Museums Scotland.

The paragenetic study on Tomnadashan found that molybdenite coprecipitates with pyrite, which is crosscut and overprinted by an event involving chalcopyrite, galena and tetrahedrite precipitation (Figure 3).

Stage	Description
1	Pyrite + molybdenite + bismuthinite + tennantite + aikinite + gold.
2	Chalcopyrite + galena + native bismuth + tetrahedrite.

Table 1. A combination of the paragenetic interpretations that have previously been produced for Tomnadashan (Pattrick 1984; Smith et al. 2003).

Our paragenetic interpretation corresponds with previous work (Table 1). However, the paragenesis we describe here is not comprehensive and there are uncertainties; we need to confirm that the pyrite that is crosscut by the later base metal mineralisation belongs to the same generation as the material coprecipitating with the molybdenite (Figure 3a). There may in fact be several generations of pyrite and chalcopyrite at Tomnadashan. Furthermore, we did not observe all the phases (e.g. gold, tennantite) that were originally described (Table 1). Regardless, our study demonstrates an association between molybdenite and pyrite, with no evidence for multiple generations of molybdenite observed so far. The resulting Re-Os age of ca. 423Ma likely pertains to the initial stage of mineralisation at Tomnadashan. Further Re-Os dating will be

undertaken on the pyrite-hosted molybdenite that is disseminated throughout the granitoid (Figure 3a). This will help us to confirm that all occurrences of molybdenite belong to the same paragenetic stage.

4 Sources of ore-forming fluids

The following $\delta^{34}S$ results represent a regional study aimed at establishing the range of $\delta^{34}S$ variation throughout the region.

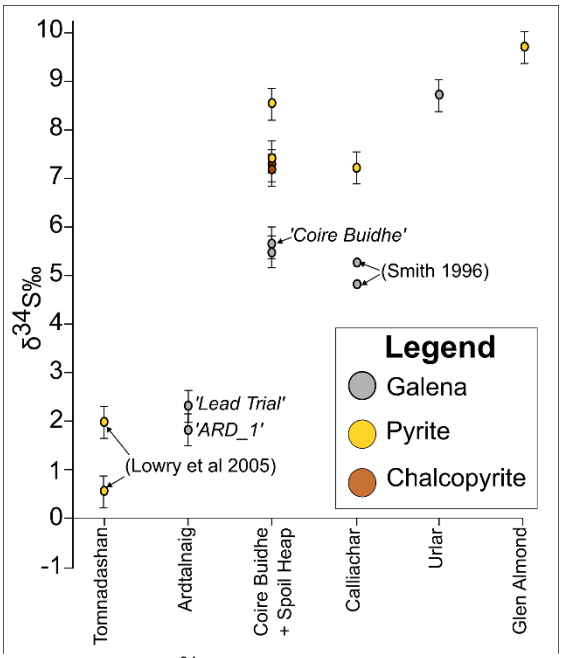

Figure 4. The $\delta^{34}S$ values of sulphides at several localities throughout the Loch Tay region. Results from previous studies have been added for context.

Around Ardtalnaig, $\delta^{34}S$ signatures are low relative to the metasediment-hosted veins. Although $\delta^{34}S$ values between different sulphides cannot be directly compared (due to differing isotopic fractionation rates during crystallisation), values <+5‰ typify magmatic sulfur (Ohmoto and Rye 1979). The Tomnadashan pyrite values therefore represent a magmatic source of sulfur too. The metasediment-hosted veins show $\delta^{34}S$ values that are significantly heavier than Tomnadashan and Lead Trial (Figure 4). These results are typical of 'orogenic' gold deposits and may indicate a crustal source of sulfur.

5. The microchemical signature of gold around Tomnadashan and Ardtalnaig

The similar microchemical characteristics between Lead Trial and Ardtalnaig (Figure 5) represents a detrital contribution of gold from Lead Trial into the Ardtalnaig Burn (Figure 1c).

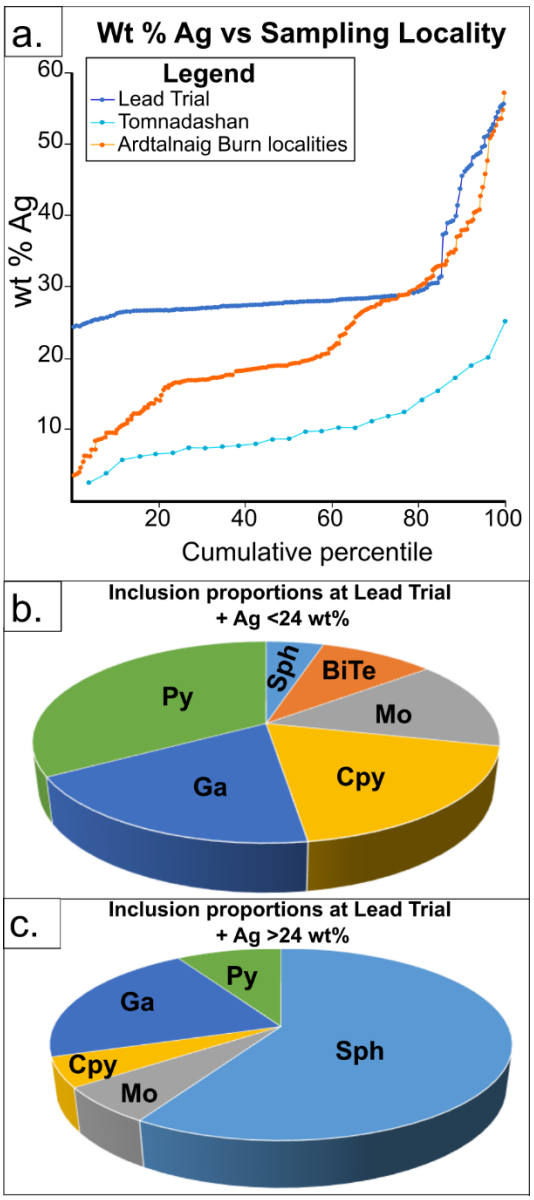

Figure. 5a. Wt% Ag in the alloy comprising the gold particles by locality. **b + c.** Pie charts showing inclusion types by proportion.

Gold particles characterised by the higher Ag contents have an inclusion assemblage that is dominated by sphalerite (Figure. 5c; Savastano et al. 2023). Particles from Claggan Bridge and Tullichglass, which are distinguishable by their lower Ag contents (Figure 5a), contain a greater proportion of pyrite inclusions. This phase is rare in the Ag >24 wt% gold particles (Figure 5c), and may indicate the presence of a vertically graded mineralising system at Ardtalnaig, with Lead Trial representing the peak. Further down the hill (Figure 1c), localities such as Tullichglass may demarcate deeper portions of the system, a transition marked by a pyrite + galena assemblage. Gold particles panned from Tomnadashan had much lower Ag contents when compared to the Ardtalnaig localities (Figure 5a). This may represent the deepest known portion of this Ardtalnaig-Tomnadashan system.

6. Conclusions

The contemporaneous formation of the veins around Loch Tay means that the age of one deposit (Tomnadashan) is likely to be widely applicable. The paragenetic context of molybdenite here – in the initial stage of mineralisation – indicates that the ca. 423 Ma age of molybdenite likely reflects the upper age of the Loch Tay mineralising system, with the lower age remaining uncertain. Our age of 423±2Ma overlaps with the 425Ma age often quoted for the slab-break off event at the end of the Caledonian Orogeny (Oliver et al. 2008). The $\delta^{34}S$ values from Ardtalnaig and Tomnadashan also support a link between magmatism and mineralisation around Loch Tay. However, the gold microchemical data has revealed that different populations exist within this area, potentially indicating a vertically graded mineral system. Lead Trial represents the peak, with the ore assemblage becoming more pyritic and enriched in Bi and Te with depth. This culminates in the assemblage of porphyry-type minerals preserved at Tomnadashan. Galena from ARD_1 and Lead Trial shows overlapping $\delta^{34}S$ values (Figure 4) - this further supports the notion that mineralisation processes around Ardtalnaig are genetically related and gold compositional variations simply reflect different portions of the same hydrothermal event.

There remains uncertainty regarding the relationship between the metasediment-hosted veins and the Tomnadashan-Ardtalnaig magmatic-hydrothermal system. Isotopically heavy $\delta^{34}S$ values, such as the ones recorded from the metasediment-hosted veins, are typical of 'orogenic' fluids. However, given the contemporaneous nature of mineralisation across the Loch Tay region, these veins are probably not associated with a mineralisation style preceding the formation of the Tomnadashan molybdenite. A more probable scenario involves a magmatic-hydrothermal system originating beneath the Tomnadashan pluton. As ore-forming fluids migrated away from this pluton, they may have mixed with isotopically lighter fluids stored in the metasediments, explaining the elevated $\delta^{34}S$ values observed in the metasediment-hosted veins (Figure 4). However, further research is needed to confirm this hypothesis.

Acknowledgements

Shane Webb is a PhD student supported by the NERC Panorama Doctoral Training Partnership under grant NE/2445151.

References

Corkhill C, Ixer R, Mason J, Irving D, Pattrick R (2010) Polymetallic auriferous vein mineralization near Loch Tay, Perthshire, Scotland. Scott J Geol, 46:23-30

Chew D, Strachan R (2013) The Laurentian Caledonides of Scotland and Ireland. Geol Soc Lond Spec Publ, 390:45-91

Ixer R, Pattrick R, Stanley C (1997). Geology, mineralogy and genesis of gold mineralization at Calliachar-Urlar Burn, Scotland. Trans Inst Min Metall Sect B Appl Earth Sci, 106:99-108.

Lowry D, Boyce A, Fallick A, Stephens E, Grassineau N (2005). Terrane and basement discrimination in northern Britain using sulphur isotopes and mineralogy of ore deposits. Geol Soc Lond Spec Publ, 248:133-151.

Mortensen J, Craw D, MacKenzie, D (2022). Concepts and revised models for Phanerozoic orogenic gold deposits. Geol Soc Lon Spec Publ, 516.

Naden J, Gunn A, Shephard T (2010). Fluids and mineralisation in the Scottish Dalradian. Br Geol Surv Intern Rep, OR/09/054.

Ohmoto H, Rye R (1979) Isotopes of sulfur and carbon. In: Barnes H (ed) Geochemistry of Hydrothermal Ore Deposits, 2nd edn. John Wiley and Sons, New York, pp 509-567

Oliver G, Wilde S, Wan Y (2008). Geochronology and geodynamics of Scottish granitoids from the late Neoproterozoic break-up of Rodinia to Palaeozoic collision. J Geol Soc, 165:661-674

Pattrick R (1984). Sulphide mineralogy of the Tomnadashan copper deposit and the Corrie Buie lead veins, south Loch Tayside, Scotland. Mineral Mag, 48:85-91

Savastano L, Chapman R, Torvela T (2023). Metallogeny of gold (from in-situ to placer) in the Loch Tay area of Central Scotland. 17th SGA Bienn Meet.

Smith G, Gunn A, Shepherd T, Coats J, Wiggans G (2003). Gold in the Dalradian terrane: a review of previous work. Br Geol Surv Intern Rep, p. 191.

Smith D (1996) Fractures and mineralisation in the Scottish Dalradian. PhD Thesis, University of Manchester.

Superimposed orogeny as key to gold hotspot formation at the north Peruvian Gondwana margin

Daniel Wiemer[1], Steffen G. Hagemann[1], Anthony I.S. Kemp[1], Jon Hronsky[1,2], Laure Martin[1], Trevor Ireland[3], Nicholas Thébaud[1], Carlos Villanes[4]
[1]Centre for Exploration Targeting, University of Western Australia, Crawley, WA, Australia
[2]Western Mining Services Pty Ltd, Perth, WA, Australia
[3]University of Queensland, St. Lucia, QLD, Australia
[4]Compañia Minera Poderosa S.A., Lima, Peru

Abstract. The geodynamic processes responsible for the formation of economic gold deposits remain controversial. It is postulated that the generation of gold-rich parental magma plays a crucial role. Two contrasting models prevail: i) selective uptake of gold as an incompatible element during low-degree partial melting of a crustal or upper mantle source, and ii) reactivation of a previously enriched source reservoir. We present bulk-geochemical and zircon U-Pb, Hf and O isotopic data from intrusive rocks that host the north Peruvian Carboniferous Pataz-Parcoy gold vein system to identify potential gold parental magmas and characterize their source. We find that hydrous, metal-enriched mafic rocks were emplaced episodically into the mid crust from ~370 Ma onwards. Zircon Hf isotopic data indicate that these magmas derived from an upper mantle domain that was likely pre-enriched during preceding Ordovician subduction. Sub-mantle $\delta^{18}O$ zircon values imply the presence of remnant subducted oceanic crust, part of which is preserved as an ophiolite, within the upper mantle source. Furthermore, evidence of hydrothermally modified zircon attests to ore-fluid expulsion upon parental magma recharge concomitant with repeated amphibole break-down. The gold vein system formed after final magma emplacement and solidification at ~332 Ma, marking a tectonic switch towards back-arc magmatic activity.

1 Introduction and background

The geometry of gold veins hosted within Carboniferous plutonic rocks in the Pataz-Parcoy gold districts of northern Peru is controlled by the inheritance of structures belonging to the Famatinian basement orogen that strikes at oblique angle to the Carboniferous and subsequent Andean orogenic belts (Fig. 1; Wiemer et al., 2021). Major gold deposits are situated in the hanging-wall of the inferred cryptic Famatinian suture between the Gondwana margin and the Paracas micro-terrane (Wiemer et al., 2022). The Famatinian Paracas collision seeded the development of a regional-scale dilational jog as a response to Carboniferous dextral-strike slip along the Rio Marañon Fault (Fig. 1; Wiemer et al., 2021; 2022). The Pataz-Parcoy gold vein system displays characteristics of orogenic gold deposits, although its extent is largely restricted to host rocks ascribed to the Western Plutonic Belt that intruded the Famatinian basement (Fig. 1). The Eastern Plutonic Belt does not host auriferous veins akin to the mesothermal Pataz-Parcoy system and intrusive relationships imply a later relative timing of magmatism. Thus, the timing and geochemical-isotopic signatures of the relatively older Western Plutonic Belt may inform about critical magmatic processes and parental magma and source characteristics responsible for gold deposit formation.

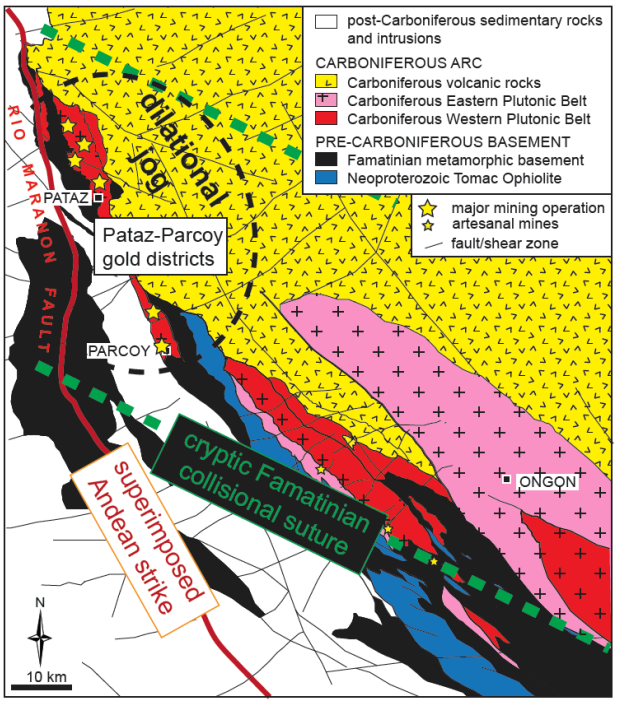

Figure 1. Simplified geologic map of the study area, Pataz region, northern Peru (modified after Wiemer et al., 2022).

2 Methodology

In combination with petrographic investigations (University of Western Australia, UWA), bulk-rock XRF major oxide and ICP-MS trace element geochemical data were acquired (Bureau Veritas, Canada) from a total of 48 unaltered/fresh samples, including plutonic, sub-volcanic and volcanic rocks from both the Eastern and the Western Plutonic Belt (Fig. 1). Zircon from a total of 14 plutonic rocks from the Eastern and the Western suite and from one metasedimentary rock of the adjacent basement were characterized by CL-SEM imaging (UWA) and selected spots were analyzed by SHRIMP for U-Pb age determination (Australian National University). On the same spots (and/or same zircon domains), LA-ICP-MS trace element and Lu-Hf isotopic data and SIMS O-isotopic data were acquired (UWA).

3 Results

3.1 Bulk-rock geochemistry

The bulk-rock geochemical data show that the most primitive (~46-58 wt.% SiO_2) Pataz rocks, which intruded repeatedly (based on field relationships), are relatively enriched in Au and Cu compared to more evolved igneous components (Fig. 2a and b). The primitive and evolved rocks are separated by a conspicuous silica gap (58-64 wt.% SiO_2) that corresponds to a change in the fractionation behaviour, conforming with petrographic observations. The primitive rocks are controlled by initial amphibole accumulation and show no to only weak Eu anomalies, indicating hydrous conditions and suppression of plagioclase crystallization, whereas increasing negative Eu anomalies and decreasing Dy/Yb ratios in the evolved rocks are in accordance with plagioclase and amphibole fractionation (Fig. 2c and d).

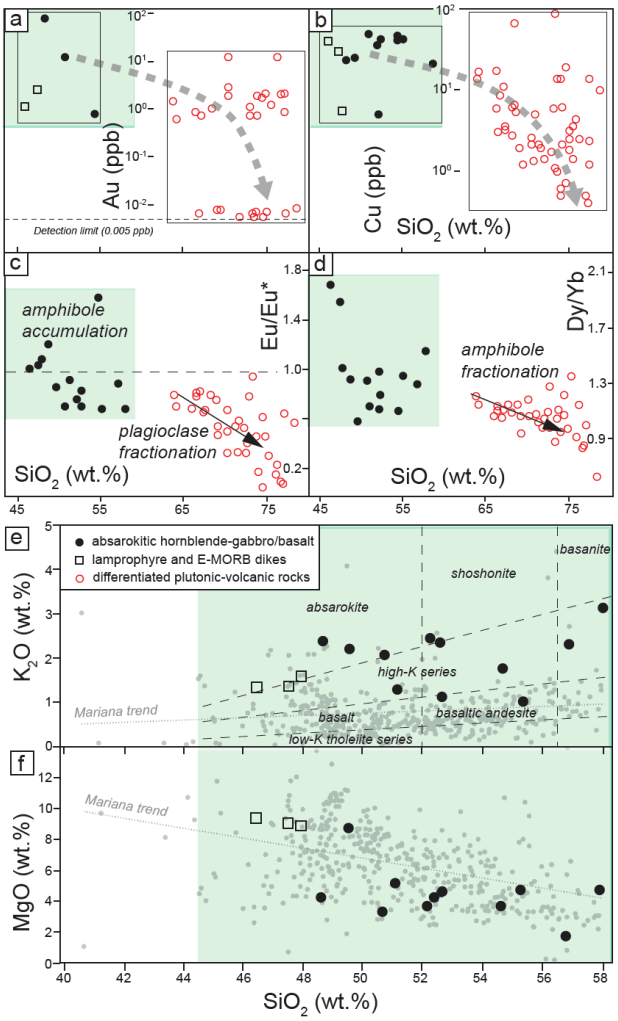

Figure 2. Bulk-rock Harker plots using SiO_2 as an index of differentiation. **a** Cu. **b** Au. **c** Eu/Eu*. **d** Dy/Yb. **e** K_2O. **f** MgO. Mariana arc reference suite downloaded from the GEOROC database (https://georoc.eu/).

The most primitive rocks show elevated K_2O contents at corresponding MgO contents that are in the range of typical arc magmas (Mariana arc reference suite (GEOROC database, https://georoc.eu/) and thus can be classified as absarokites/appinites (Fig. 2e and f). The Pataz absarokitic rocks are also relatively enriched in other incompatible elements, such as Ba, and display a strong affinity to gold parental rocks in the graph of Figure 3 (Loucks and Ballard, 2002). Figure 3 reaffirms the role of hornblende accumulation and suppressed plagioclase crystallization due to hydrous conditions, expressed in the Sr/Y ratio as the denominator in the ordinate of the graph.

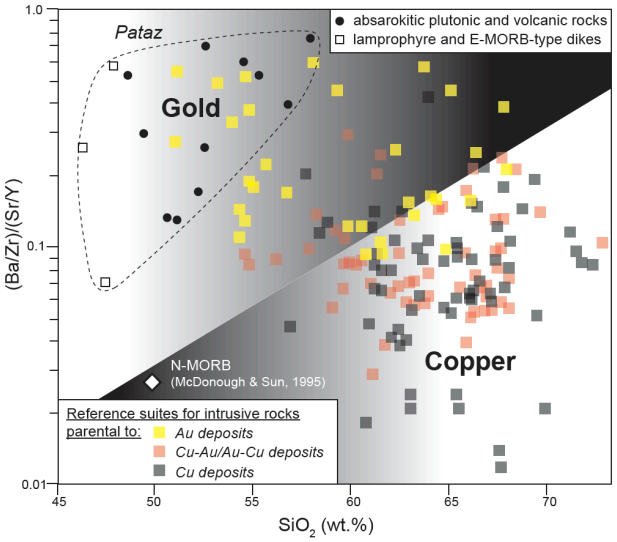

Figure 3. Bulk-rock chemical plot distinguishing Au, Au-Cu, and Cu parental intrusive rocks (reference suites after Loucks and Ballard, 2002).

3.2 Zircon trace elements, U-Pb geochronology, and Hf-O isotopes

Zircon CL imaging reveals relatively complex internal structures attesting to the presence of multiple truncating domains in all samples. In combination with trace element chemical data magmatic, recrystallized, and hydrothermally modified domains are identified, noting that hydrothermal domains do not occur within zircon from the primitive absarokitic gabbros (Fig. 4a). All analyzed zircons largely fall within the field of the Cu-Au fertile reference suite (Fig. 4b; Lu et al., 2016) and rare earth element (REE) pattern mimic the absence or presence of Eu anomalies of respective bulk-rock samples (Fig. 4c). Magmatic domains yield Ti-temperatures (calculated after Watson and Harrison, 2005) between ca. 650-810°C, indicating that zircon crystallized both from near-solidus melt and from high(er) temperature melt ascribed to repeated recharge episodes. Indeed, due to the re-occurrence of distinct U-Pb age domains throughout all samples, geochronological data are evaluated based on the overall spot age frequency distribution (Fig. 5a). The frequency distribution shows multiple age peaks associated with antecrystic zircon domains. The age peaks are interpreted to reflect episodic recharge

and thermal rejuvenation over a >30-Myr duration for the Western Plutonic suite, whereby troughs in the age distribution match the observation of truncating zircon domains. Outermost oscillatory-zoned magmatic domains (autocrystic) suggest that final magma emplacement of the Western suite occurred between ca. 340-332 Ma (Fig. 5a), followed by a brief episode of apparent magmatic quiescence that correlates with a reported Re-Os molybdenite age for initial gold vein formation (Szappanosné-Vágó et al., 2010) and confirms the required brittle nature (i.e., magma solidification) for fault-fill vein development envisaged by Wiemer et al. (2021).

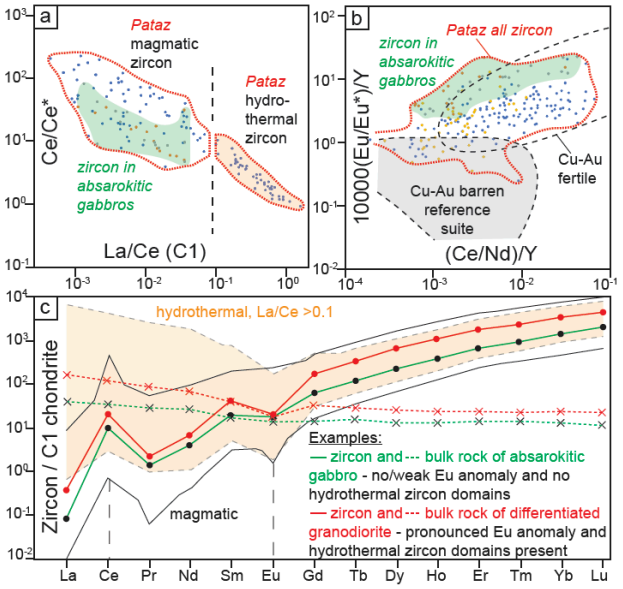

Figure 4. **a** Chemical discrimination of magmatic and hydrothermally modified zircon. **b** Zircon Cu-Au fertility index plot (reference suites after Lu et al., 2016). **c** REE pattern (chondrite values after McDonough and Sun, 1995).

Zircon Hf isotopic compositions of early antecryst domains from the absarokitic gabbros correspond to εHf(t) values of ca. -3 at the onset of magmatic crystallization at ca. 370-360 Ma (Fig. 5b). The εHf(t) of younger antecrystic and autocrystic domains follow near-linear trends for respective samples that can be approximated by their average $^{176}Lu/^{177}Hf$ ratio (~0.0017). The onset of "new" crystallization series in younger sample populations appears to be shifted towards slightly more unradiogenic compositions, i.e., towards εHf(t) of ca. +2 at ca. 340 Ma. On the other hand, either single domains or entire sample populations from the most evolved rock types are characterized by εHf(t) values of ca. -5 to -10 (Fig. 5b). The latter εHf(t) values fall in the range of, and/or approach, those of the adjacent basement metasedimentary rock. The youngest detrital zircon population from the metasedimentary rock yield $^{206}Pb/^{238}U$ spot ages between 494-462 Ma and εHf(t) values between -5.8 and -16.1 (recalculated at 340 Ma using their average zircon $^{176}Lu/^{177}Hf$ ratio of ~0.0008).

Zircon $\delta^{18}O$ values from the Western Plutonic suite largely range between ca. 5.2 and 6.8, generally overlapping the upper limits of the mantle array (Fig. 5c). Zircon from the most evolved rocks (high negative εHf) display elevated $\delta^{18}O$ values of ca. 6.5 to 8, similar to those detected in the basement metasedimentary rocks ($\delta^{18}O$ = 5.6 to 8.3). Samples with younger onset of zircon crystallization indicate the increasing influence of a sub-mantle $\delta^{18}O$ component (Fig. 5c).

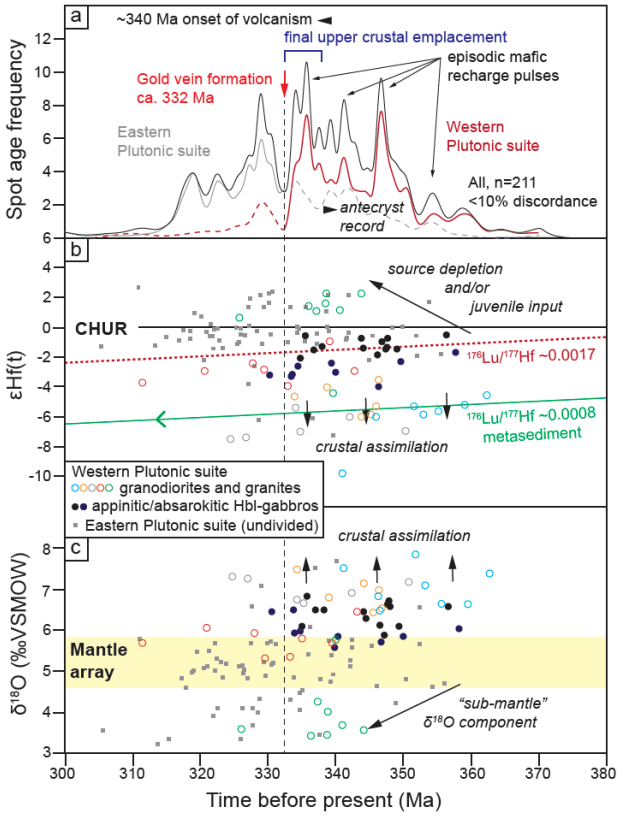

Figure 5. **a** Zircon $^{206}Pb/^{238}U$ spot age frequency Kernel distribution. **b** εHf versus time. **c** $\delta^{18}O$ versus time.

To further test if particularly the isotopic signatures from the absarokitic gabbros are pristine, i.e., characterizing their mantle source, uncontaminated by post-extraction intracrustal assimilation, we introduce the inherited zircon index (IZI; this study). The IZI describes the percentage of inherited (in this case pre-Carboniferous) zircon within a sample population. It is noted that our initial analytical spot selection was conducted irrespective of the internal position of distinct zircon domains, in other words representing a random statistical probe. As shown in Figure 6a and b, the IZI correlates well with the presented Hf and O isotopic data. The samples that contain a high proportion of inherited grains are those that display high negative εHf and high $\delta^{18}O$ values matching the zircon from the basement metasedimentary rock. In contrast, inherited zircons are entirely absent from the absarokitic gabbro samples. Given the overall well-preserved record of zircon domains in combination with Ti-zircon temperatures of up to 810°C we discard the possibility of significant zircon

dissolution. Hence, the overall primitive character of the absarokitic gabbros precludes magma genesis through partial melting of lower crustal rocks, and the absence of inherited zircons supports the fact that no intracrustal assimilation affected the magmas. This suggest that the presented isotopic signatures are pristine and reflect the composition of the mantle source.

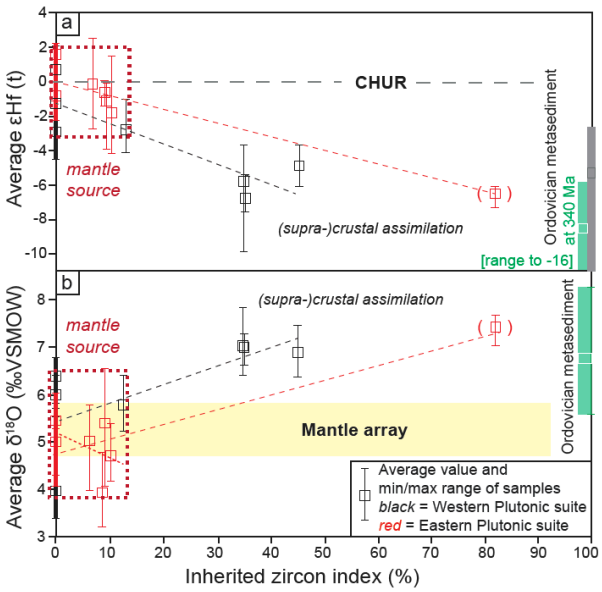

Figure 6. **a** εHf and **b** $\delta^{18}O$ versus the inherited zircon index (IZI; this study).

4 Discussion and conclusions

Our data show that most primitive absarokitic gabbros represent the parental magmas for gold in the Pataz region of northern Peru. These magmas intruded episodically since the very onset of Carboniferous subduction-related magmatic activity at ca. 370-360 Ma. Elevated incompatible major and trace element concentrations (K_2O, Ba) in combination with enrichment in Au and Cu relative to high MgO and low SiO_2 contents suggest that the magmas were generated from a metasomatized, pre-enriched ore fertile upper mantle. This is confirmed by trace element concentrations in zircon. Furthermore, Hf-O zircon isotopic data indicate that only some of the most evolved granitic components in the Pataz magmatic system interacted with adjacent (supra-)crustal components, whereas pristine εHf(t) values (ca. -3) of zircon from the primitive absarokitic gold parental rocks confirm the pre-enriched nature of the mantle source at ca. 370-360 Ma. Mantle pre-enrichment can be ascribed to the preceding Famatinian subduction-collision that has been documented in the area (Wiemer et al., 2022). Indeed, the early onset and repeated intrusion, as well as the overall observed volume of the absarokitic gabbros and equivalent volcanic rocks in the study area, and the inferred genetic link to the more evolved igneous rocks, favour a geodynamic scenario that does not require low-degree partial source melting to selectively uptake gold as an incompatible element. Instead, the preceding Famatinian subduction sufficiently pre-enriched and fertilized the upper mantle. We argue that at the onset of Carboniferous arc formation, heat from subduction related magma production caused the re-melting of fertile portions/regions within the established fossil Famatinian lithospheric mantle, giving rise to the repeated generation of gold-rich absarokitic magma. The episodic nature of recharge remains unclear but may be discussed in the context of energy (heat) transitions upon major bulk melt extraction in the source. Concomitant source depletion (increasing εHf towards +2) was accompanied by increasing consumption of remnant previously subducted oceanic crust (towards sub-mantle $\delta^{18}O$ values, e.g., Cartwright and Valley, 1991). The episodic inferred mid-crustal absarokitic magma replenishment resulted in repeated thermal rejuvenation associated with amphibole break-down that spawned magmatic-hydrothermal transitions, ore-fluid expulsion, hydrothermal zircon modification, and batch extraction of evolved magmas. Magma and fluid discharge from the accumulated mid-crustal reservoir into upper crustal levels occurred between 340-332 Ma.

Acknowledgements

This research was fully funded by the Compañia Minera Poderosa S.A. (Lima, Perú). The authors thank D. Sologuren Arias and F. Cueva (Compañia Minera Poderosa S.A.) for their continued support.

References

Cartwright, I., and Valley, J.W. (1991): Low-18O Scourie dike magmas from the Lewisian complex, northwestern Scotland. Geology, v. 19, p. 578-581.

Loucks, R.R., and Ballard, J.R. (2002): Predictive guides to copper and gold mineralization at circum-pacific convergent plate margins. Report 2A: Distinguishing characteristics, petrogenesis and tectonic habitat of copper ore-forming arc magmas, p. 1-105.

Lu, Y.-J., Loucks, R.R., Fiorentini, M., McCuaig, C., Evans, N.J., Yang, Z.-M., Hou, Z.-Q., Kirkland, C.L., Parra-Avila, L.A., and Kobussen, A. (2016): Zircon compositions as pathfinder for porphyry Cu ± Mo ± Au mineral deposits. Society of Economic Geologists. Special Publications Series v. 19, p. 329-347.

McDonough, W.F., and Sun, S.-S. (1995): The composition of the Earth. Chemical Geology, v. 120, p. 223-253.

Szappanosné-Vágó, E., Moritz, R., and Barra, F. (2010): Fluid inclusion investigation and Re-Os dating of the Pataz-Parcoy intrusion-hosted gold deposits, Eastern Cordillera, Peru. EG51, Crustal fluids and gold, p. 260.

Watson, E.B., and Harrison, T.M. (2005): Zircon thermometer reveals minimum melting conditions on earliest Earth. Science, v. 308, p. 841-844.

Wiemer D., Hagemann, S.G., Thébaud, N., and Villanes, C. (2021): Role of basement structural inheritance and strike-slip fault dynamics in the formation of the Pataz gold vein system, Eastern Andean Cordillera, northern Peru. Economic Geology, v. 116, p. 1503-1535.

Wiemer, D., Hagemann, S.G., Hronsky, J., Kemp, A.I.S., Thébaud, N., Ireland, T., and Villanes, C. (2022): Ancient structural inheritance explains gold deposit clustering in northern Peru. Geology, v. 50, p. 1197-1201.

